

Design of New Spin-crossover Materials for Surface Deposition

Izar Capel Berdiell

Submitted in accordance with the requirements for the degree of
Doctor of Philosophy

University of Leeds
School of Chemistry

June 2019

The candidate confirms that the work submitted is his/her own, except where work which has formed part of jointly-authored publications has been included. The contribution of the candidate and other authors to this work has been explicitly indicated below. The candidate confirms that appropriate credit has been given within the thesis where reference has been made to the work of others.

Four papers containing work from my PhD have been published at the time of writing, which contain results from Chapters 2, 3 and 6 of the thesis. I contributed to the preparation of these manuscripts, but the final versions were completed by my supervisor Professor Halcrow, who is also the corresponding author on the papers. I am also corresponding author on the paper in ACS Omega due to my huge contribution for its manufacturing. The description of these results in Chapters 2, 3 and 6 is not directly reproduced from the papers, and has been written in my own words. The references are:

“Iron(II) Complexes of 2,4-Dipyrazolyl-1,3,5-triazine Derivatives—The Influence of Ligand Geometry on Metal Ion Spin State”, I. Capel Berdiell, R. Kulmaczewski, and M. A. Halcrow*, *Inorganic Chemistry*, **2017**, 56 (15), 8817-8828.

“An Incomplete Spin Transition Associated with a $Z'=1 \rightarrow Z'=24$ Crystallographic Symmetry Breaking”, I. Capel Berdiell, R. Kulmaczewski, O. Cespedes and M. A. Halcrow*, *Chemistry – A European Journal*, **2018**, 24, 5055-5059.

“Silver(I) Complexes of Bis- and Tris-(pyrazolyl)azine Derivatives – Dimers, Coordination Polymers and a Pentametallic Assembly”, I. Capel Berdiell, S. L. Warriner, and M. A. Halcrow*, *Dalton Transactions*, **2018**, 47, 5269-5278.

“Heterometallic Coordination Polymer Gels Supported by 2,4,6-Tris(pyrazol-1-yl)-1,3,5-triazine” I. Capel Berdiell*, A. N. Kulak, S. L. Warriner, and M. A. Halcrow*, *ACS Omega*, **2018**, 3, 18466-18474.

This copy has been supplied on the understanding that it is copyright material and no quotation from the thesis may be published without proper acknowledgement.

The right of Izar Capel Berdiell to be identified as Author of this work has been asserted by him in accordance with the Copyright, Designs and Patents Act 1988.

Acknowledgements

Thanks to Malcolm Andrew Halcrow for offering me the position in his research group, a PhD position which I really enjoyed in the scientific aspect. In Halcrow's group I learnt several characterization techniques but also how to write a manuscript or a mobility grant application on my own. I would like to acknowledge him for his advice and help in many ways.

Thanks to Rafal Kulmaczewski for offering me your home. I spent a marvellous time with you and your family. I am also grateful for your numberless suggestions towards my project, some of which were very good and some others were horrible but all of them helped me developing the work that I performed at the beginning of my PhD. Finally, I want to acknowledge him for teaching me how to process SQUID data, powder XRD and almost everything I know of crystallography. Dejian Zhou, every advice I gathered from you was very useful. Thanks to Alexander Kulak for taking SEM images for me and thanks to Stuart Warriner for helping me with direct injection mass spectroscopy.

Thanks to all the inorganic team. Danny Davies and Sarah Farmiloe for being the nicest Padawans I could ask for. Ahmed Gamal for the banter and showing me the proper English. Thanks to Sam Greatorex, Jonny Fowler and Matthew Allison for all the parties and fun we had during the beginning of my PhD. In that respect I should also acknowledge Ryan Gonciarz, Lewis Turner and Aaron Wilkinson for making me laugh all night long. Thanks to Iurii Galadzhun for being always nice and honest. Also I want to acknowledge him for providing snacks and coca cola at a reasonable price. The best sportsmen mates of the chemistry department go for; Jordan Holmes, James Green, Raf, James Duncan, Robert Dawber, Sam Griggs and Ryan McBerney we had very good games together. Thanks to the mates from the other groups, Pablo Carames for those conversations in Spanish at late hours. Laurenleigh Taylor for all our chats, jokes and laughs. You were a great support. Laura Gandhi for including me in the climbing group and other adventures/trips we had along with Irene Arrata, Kris Paraschiv etc. Sam Oldknow for inviting us several times to that nice apartment for drinks, and playing games. Cecilia Madzivire for being always funny with me. Ed Britton you were the best DIAMOND partner. Chris Pask you are so nice, thank you for helping everyone.

Gracias a mi familia. Mis padres, que siempre me habeis apoyado y a mi hermana Andrea. Gracias Gisela por ayudarme siempre. Tambien a mis amigos que habeis venido a visitarme durante mi estancia en Leeds: Bernad, Dani, Migue, Sergio, Gascon, Gisela, Tania, Alba, Xavi, Clara, Ares y Elsa. Por ultimo, si algun dia vuelvo a leer la tesis... quiero recordar a todos los amigos que me llevo de aqui: Borja, Shauny, Azahara, Lidia, Pablo Martinez, Ellie, Jordan, Julz, Joana, Juanjo, Ibai, Sofia, Monica, Angela, Silvia, Carlos, Isa, Ana, Jaime, Josh, Lauri, Sherin, Natalee, Alvaro, Claire, Alah, Roman, Dimi, Bea, Javi, Pablo, Patri, Estefania, Eric, Andrea, Toni, Carmen, Ana, Cesar, Jose el resto de churritos y Albert Sanz.

Abstract

This thesis comprises the synthesis and characterization of a variety of compounds and systems whose magnetic behaviour has been tested orienting into the spin crossover phenomenon (SCO). The first chapter is an introduction of generic knowledge related to spin crossover, including the techniques used to determine SCO and the stimuli which are relevant and contribute to it.

The modification of the 2,6-bis(pyrazol-1-yl)pyridine (1-bpp) scaffold was proposed as an easier alternative way to produce iron(II) SCO complexes. A new family of iron(II) mononuclear complexes of 2,4-di(pyrazol-1-yl)-1,3,5-triazine based ligands, with different substituents in the 6-position of the triazinyl ring or at the pyrazolyl group are studied (Chapter 2), DFT calculations highlight the nature of these HS compounds is due to a geometric factor. New heterometallic coordination polymer gels (CPGs) with different first row transition metal complexes of 2,4,6-tris(pyrazol-1-yl)-1,3,5-triazine (TPT) combined with silver(I) salts are characterized in the following study. Production of SCO CPGs is attempted by modification of the TPT ligand. Related coordination polymers of silver(I) salts and a linear iron(III) trimer bridged by fluorine are also described at chapter 3. Various polymeric and polymetallic compounds assembled from 1,3,5-triazine and 1,3-pyrimidine based ligands acting as bis-bidentate ligands (Chapter 4). Modification of the ligands affects the coordination type and the magnetic properties of such assemblies.

Moreover, a second modification of 1-bpp family of ligands is studied together in chapter 5 with the magnetic behaviour of their iron(II) mononuclear complexes. Geometric isomers of 2,6-di(1,2,3-triazol-yl)pyridine based behave differently. DFT calculations of the free ligands determined that the most energetic lone pair could determine whether it is tridentate or linear coordinating ligand.

Potential linkers between the 2,6-di(pyrazol-1-yl)-pyridine scaffold and a tether group are assessed. Iron(II) complexes of the simpler analogue compounds show varying magnetic behaviours, including the highest symmetry breaking associated to SCO ever reported (Chapter 6). Successful deposition of novel iron(II) complexes of 2,6-di(pyrazol-1-yl)-pyridine based tethered ligands on gold or metal-oxides was developed at the ICMol (Valencia). However the integrity of SCO at the surface was not proved by the current techniques (Chapter 7). The account of all experimental details for the compounds and analytical techniques which are the subject of discussion in this work are described in the last chapter, 8.

Table of Contents

Acknowledgements.....	II
Abstract.....	III
Table of Contents.....	IV
List of Figures.....	VIII
List of Tables	XVII
List of Abbreviations	XIX
Chapter 1 – Introduction.....	1
1.1 Theoretical foundations.....	1
1.1.1 Crystal field theory (CFT).....	1
1.1.2 Ligand field theory (LFT) and electronic configuration	2
1.1.3 Diamagnetism and paramagnetism	4
1.2 Magnetic bistability.....	6
1.2.1 Spin-crossover (SCO)	7
1.2.2 Transition types.....	9
1.2.3 LIESST.....	10
1.2.4 Pressure influence	11
1.2.5 Magnetic field	12
1.2.6 Uv-vis absorption spectra.....	12
1.3 Ligand design	13
1.3.1 Spin-crossover: iron complexes	13
1.3.2 Cooperativity.....	13
1.3.3 Jahn-Teller distortions.....	14
1.4 Computational methods.....	17
1.4.1 DFT calculations	18
1.5 Bibliography	20
Chapter 2 – Bis (Pyrazolyl) Triazine Derivatives and their Iron(II) Complexes	25
2.1 Introduction	25
2.1.1 Bis pyrazolyl pyridine (bpp) iron(II) complexes.....	25
2.1.2 Bis pyrazolyl triazine (bpt) iron(II) complexes.....	25
2.2 Results and discussion.....	26

2.2.1	Synthesis and characterization of the ligands.....	26
2.2.2	Synthesis of iron(II) complexes	28
2.2.3	Single crystal and powder X-Ray diffraction.....	29
2.2.4	Crystallographic analysis of bpt iron(II) complexes	34
2.2.5	Magnetic susceptibility analysis.....	38
2.2.6	Uv-vis spectra.....	40
2.2.7	DFT calculations	40
2.3	Conclusions	45
2.4	Bibliography	45
Chapter 3 – New Heterometallic Coordination Polymer Gels Combining Silver(I) Salts with [2,4,6-Tris(Pyrazolyl)-1,3,5-Triazine] First Row Metal(II) Complexes..... 48		
3.1	Introduction	48
3.1.1	Silver (I) and first row metals in CPGs	48
3.1.2	2,4,6-Tri(pyrazolyl)-1,3,5-triazine (TPT), ligand (2).....	48
3.2	Results and discussion.....	49
3.2.1	Crystallographic analysis of the monomer $[M(TPT)_2](X)_2$	49
3.2.2	Synthesis of the coordination polymer gels (CPGs)	51
3.2.3	Characterization of CPGs.....	53
3.2.4	Can we make spin-crossover coordination polymer gels?	59
3.2.5	Silver coordination polymers	59
3.2.6	Different polymer crosslink	65
3.2.7	Structural model	66
3.2.8	Novel iron(II) and iron(III) complexes	67
3.2.9	DFT calculations	74
3.3	Conclusions	77
3.4	Bibliography	78
Chapter 4 – Polymetallic and Polymeric Structures Derived from Iron(II) Complexes of 1,3,5-Triazine and 1,3-Pyrimidine Based Ligands 83		
4.1	Introduction	83
4.2	Results and discussion.....	84
4.2.1	Self-assemblies of 2,4-di(4,5,6,7-tetrahydro-2-indazol-2-yl)-6-chloro-1,3,5-triazine and iron(II)/(III) centres	84
4.2.2	Structures derived from 2,4-di(pyrazol-1-yl)-1,3,5-triazine.....	90
4.2.3	Cubic cluster derived from 4,6-di(pyrazol-1-yl)-pyrimid-2-one.....	93

4.2.4	Novel 4,6-di-pyrazolyl-1,3-pyrimidine-based iron(II) complexes and coordination polymers.....	102
4.2.5	Novel ligands derived from 4,6-di(pyrazol-1-yl)-pyrimid-2-one with methylated pyrazole derivatives.....	108
4.3	Conclusions	111
4.4	Bibliography	112
Chapter 5 – Isomeric Bis (Triazolyl) Pyridine Ligands and their Iron Complexes....		115
5.1	Introduction	115
5.1.1	Examples of bis-(azolyl) pyridine ligands in the literature	115
5.1.2	Bis 1,2,3-triazolyl pyridine ligands (bTp)	116
5.2	Results and discussion.....	116
5.2.1	Synthesis of 2,6-di(1,2,3-triazol-1-yl)pyridine isomers (30), (31) and (33). 116	
5.2.2	Metal complexes of 2,6-di(1,2,3-triazol-1-yl)pyridine M[30]X	117
5.2.3	Iron(II) complex of 2,6-bis(1,2,3-triazol-2-yl)-pyridine (31).....	121
5.2.4	DFT calculations	122
5.2.5	Synthesis of 2-(1-methyl-1,2,3-triazol-4-yl)-6-(1-methyl-1,2,3-triazol-3-yl)-pyridine (34) and 2,6-di(1-methyl-1,2,3-triazol-3-yl)-pyridine (35) ligands	133
5.2.6	Iron(II) complexes of 2-(1-methyl-1,2,3-triazol-4-yl)-6-(2-methyl-1,2,3-triazol-1-yl)-pyridine (34)	133
5.2.7	Iron(II) complexes of 2,6-(2-methyl-1,2,3-triazol-1-yl)-pyridine (35) ...	135
5.2.8	Cobalt(II) complexes of 2,6-(1,2,3-triazol-4-yl)-pyridine (32)	140
5.3	Conclusions	142
5.4	Bibliography	142
Chapter 6 – Pursuit of Bpp Derivatives Containing Tether Group for Covering Surfaces and Nanoparticles		145
6.1	Introduction	145
6.2	Results and discussion.....	146
6.2.1	Target molecule n.1; 2,6-di(pyrazol-1-yl)-4-(R)-thiolipoate-pyridine (36) 146	
6.2.2	Target molecule n.2, (41); obtainment of 2,6-Di(pyrazol-1-yl)-4-(3,4-dimethoxythiophenol)-pyridine (42)	151
6.2.3	Target molecule n.3; 2,6-Di(pyrazol-1-yl)-4-(R)-(5-(1,2-dithiolan-3-yl)pentanecarbamoyl)-pyridine (43) and 2,6-di(pyrazol-1-yl)-4-acetamide-pyridine (44).....	154
6.3	Conclusions	165

6.4	Bibliography	165
Chapter 7 – Coating Surfaces with SAMs of Spin-Crossover Materials.		169
7.1	Introduction	169
7.2	Results and discussion	171
7.2.1	Synthesis and characterization of the 1,2dithiolane tethered ligands and their iron(II) complexes.....	171
7.2.2	Synthesis and characterization of carboxylic acid tethered ligands and their iron(II) complexes	176
7.2.3	Coating surfaces with the complexes	180
7.2.4	Characterization of the coated surfaces.....	183
7.2.5	Coating gold nanoparticles.....	189
7.3	Conclusions	193
7.4	Bibliography	193
Chapter 8 – Experimental		199
8.1	Methods and instrumentation	199
8.1.1	NMR Spectroscopy	199
8.1.2	Mass Spectrometry	199
8.1.3	X-ray Crystallography.....	199
8.1.4	Magnetic susceptibility	200
8.1.5	Elemental Analysis.....	200
8.1.6	Scanning Electron Microscopy (SEM)	200
8.1.7	UV-vis/NIR	200
8.1.8	Evans Method.....	200
8.1.9	Melting point.....	200
8.1.10	Dynamic light scattering (DLS)	201
8.1.11	Transmission electron microscopy (TEM).....	201
8.1.12	X-ray photoelectron spectroscopy (XPS).....	201
8.1.13	Atomic force microscopy (AFM).....	201
8.1.14	X-ray absorption spectroscopy (XAS)	201
8.2	Experimental details of ligands and metal complexes related to Chapter 2	202
8.3	Experimental details of ligands and metal complexes related to Chapter 3	212
8.4	Experimental details of ligands and metal complexes related to Chapter 4	222
8.5	Experimental details of ligands and metal complexes related to Chapter 5	235
8.6	Experimental details of ligands and metal complexes related to Chapter 6	241

8.7	Experimental details of ligands and metal complexes related to Chapter 7	247
8.8	Crystallographic tables	263
8.9	Bibliography	264

List of Figures

Figure 1.1	1
Figure 1.2	2
Figure 1.3	3
Figure 1.4	6
Figure 1.5	7
Figure 1.6	8
Figure 1.7	9
Figure 1.8	9
Figure 1.9	10
Figure 1.10	11
Figure 1.11	11
Figure 1.12	12
Figure 1.13	13
Figure 1.14	14
Figure 1.15	14
Figure 1.16	15
Figure 1.17	15
Figure 1.18	16
Figure 1.19	16
Figure 2.1	25
Figure 2.2	26
Figure 2.3	26
Figure 2.4	27

Figure 2.5	27
Figure 2.6	28
Figure 2.7	29
Figure 2.8	29
Figure 2.9	30
Figure 2.10	30
Figure 2.11	31
Figure 2.12	31
Figure 2.13	32
Figure 2.14	32
Figure 2.15	32
Figure 2.16	33
Figure 2.17	33
Figure 2.18	33
Figure 2.19	34
Figure 2.20	37
Figure 2.21	37
Figure 2.22	38
Figure 2.23	39
Figure 2.24	40
Figure 2.25	41
Figure 2.26	42
Figure 2.27	43
Figure 2.28	44
Figure 2.29	44
Figure 3.1	49
Figure 3.2	49
Figure 3.3	50

Figure 3.4	50
Figure 3.5	51
Figure 3.6	52
Figure 3.7	52
Figure 3.8	53
Figure 3.9	53
Figure 3.10	54
Figure 3.11	54
Figure 3.12	55
Figure 3.13	56
Figure 3.14	57
Figure 3.15	57
Figure 3.16	58
Figure 3.17	58
Figure 3.18	59
Figure 3.19	59
Figure 3.20	60
Figure 3.21	60
Figure 3.22	61
Figure 3.23	61
Figure 3.24	62
Figure 3.25	62
Figure 3.26	62
Figure 3.27	63
Figure 3.28	63
Figure 3.29	63
Figure 3.30	64
Figure 3.31	64

Figure 3.32	65
Figure 3.33	65
Figure 3.34	66
Figure 3.35	67
Figure 3.36	67
Figure 3.37	68
Figure 3.38	69
Figure 3.39	70
Figure 3.40	71
Figure 3.41	72
Figure 3.42	72
Figure 3.43	73
Figure 3.44	73
Figure 3.45	74
Figure 3.46	74
Figure 3.47	76
Figure 4.1	83
Figure 4.2	84
Figure 4.3	84
Figure 4.4	85
Figure 4.5	86
Figure 4.6	86
Figure 4.7	87
Figure 4.8	87
Figure 4.9	88
Figure 4.10	88
Figure 4.11	89
Figure 4.12	89

Figure 4.13	89
Figure 4.14	90
Figure 4.15	90
Figure 4.16	91
Figure 4.17	91
Figure 4.18	92
Figure 4.19	92
Figure 4.20	92
Figure 4.21	93
Figure 4.22	93
Figure 4.23	94
Figure 4.24	94
Figure 4.25	94
Figure 4.26	95
Figure 4.27	96
Figure 4.28	97
Figure 4.29	97
Figure 4.30	98
Figure 4.31	98
Figure 4.32	98
Figure 4.33	99
Figure 4.34	99
Figure 4.35	100
Figure 4.36	100
Figure 4.37	101
Figure 4.38	101
Figure 4.39	102
Figure 4.40	102

Figure 4.41	103
Figure 4.42	104
Figure 4.43	105
Figure 4.44	106
Figure 4.45	107
Figure 4.46	107
Figure 4.47	108
Figure 4.48	109
Figure 4.49	110
Figure 4.50	110
Figure 4.51	110
Figure 5.1	115
Figure 5.2	115
Figure 5.3	116
Figure 5.4	116
Figure 5.5	116
Figure 5.6	117
Figure 5.7	118
Figure 5.8	118
Figure 5.9	119
Figure 5.10	119
Figure 5.11	120
Figure 5.12	120
Figure 5.13	121
Figure 5.14	121
Figure 5.15	122
Figure 5.16	123
Figure 5.17	124

Figure 5.18	124
Figure 5.19	125
Figure 5.20	126
Figure 5.21	126
Figure 5.22	128
Figure 5.23	129
Figure 5.24	129
Figure 5.25	130
Figure 5.26	131
Figure 5.27	131
Figure 5.28	132
Figure 5.29	132
Figure 5.30	133
Figure 5.31	133
Figure 5.32	133
Figure 5.33	134
Figure 5.34	135
Figure 5.35	135
Figure 5.36	136
Figure 5.37	136
Figure 5.38	137
Figure 5.39	139
Figure 5.40	139
Figure 5.41	140
Figure 5.42	141
Figure 5.43	141
Figure 6.1	145
Figure 6.2	145

Figure 6.3	146
Figure 6.4	146
Figure 6.5	147
Figure 6.6	147
Figure 6.7	147
Figure 6.8	148
Figure 6.9	149
Figure 6.10	149
Figure 6.11	150
Figure 6.12	151
Figure 6.13	151
Figure 6.14	151
Figure 6.15	152
Figure 6.16	153
Figure 6.17	153
Figure 6.18	153
Figure 6.19	154
Figure 6.20	154
Figure 6.21	155
Figure 6.22	155
Figure 6.23	156
Figure 6.24	158
Figure 6.25	159
Figure 6.26	159
Figure 6.27	160
Figure 6.28	161
Figure 6.29	163
Figure 6.30	163

Figure 6.31	164
Figure 6.32	164
Figure 7.1	169
Figure 7.2	170
Figure 7.3	171
Figure 7.4	171
Figure 7.5	171
Figure 7.6	172
Figure 7.7	172
Figure 7.8	173
Figure 7.9	173
Figure 7.10	173
Figure 7.11	174
Figure 7.12	174
Figure 7.13	175
Figure 7.14	175
Figure 7.15	176
Figure 7.16	176
Figure 7.17	177
Figure 7.18	177
Figure 7.19	178
Figure 7.20	179
Figure 7.21	179
Figure 7.22	179
Figure 7.23	180
Figure 7.24	181
Figure 7.25	183
Figure 7.26	183

Figure 7.27	184
Figure 7.28	184
Figure 7.29	184
Figure 7.30	186
Figure 7.31	186
Figure 7.32	187
Figure 7.33	187
Figure 7.34	188
Figure 7.35	189
Figure 7.16	190
Figure 7.16	191
Figure 7.16	191
Figure 7.16	192
Figure 7.16	192

List of Tables

Table 1-1	4
Table 1-2	19
Table 2-1	36
Table 2-2	39
Table 2-3	43
Table 2-4	43
Table 2-5	44
Table 3-1	57
Table 3-2	57
Table 3-3	69
Table 3-4	70

Table 3-5	72
Table 3-6	75
Table 3-7	75
Table 3-8	76
Table 4-1	91
Table 4-2	95
Table 4-3	97
Table 4-4	100
Table 4-5	105
Table 4-6	106
Table 4-7	108
Table 4-8	109
Table 5-1	122
Table 5-2	123
Table 5-3	123
Table 5-4	125
Table 5-5	125
Table 5-6	127
Table 5-7	127
Table 5-8	128
Table 5-9	129
Table 5-10	130
Table 5-11	131
Table 5-12	134
Table 5-13	138
Table 5-14	140
Table 5-15	141
Table 6-1	148

Table 6-2	150
Table 6-3	152
Table 6-4	157
Table 6-5	160
Table 6-6	161
Table 6-7	162
Table 6-8	164
Table 7-1	177
Table 7-2	178
Table 7-3	182
Table 7-4	185
Table 7-5	190
Table 7-6	192

List of Abbreviations

1-bpp	2,6-Di(pyrazol-1-yl)-pyridine
1-btp	2,6-Di(1,2,4-triazol-1-yl)-pyridine
1-bTp	2,6-Di(1,2,3-triazol-1-yl)-pyridine
2-bTp	2,6-Di(1,2,3-triazol-2-yl)-pyridine
Δ_o	Crystal field splitting
AFM	Atomic force microscopy
AuNPs	Gold nanoparticles
bptOEt	2,4-Di(pyrazol-1-yl)-6-ethoxy-1,3,5-triazine
bptNMe ₂	2,4-Di(pyrazol-1-yl)-6-(dimethylamino)-1,3,5-triazine
btpSIP	2,4-Di(pyrazol-1-yl)-6-(isopropylsulfanyl)-1,3,5-triazine
CFT	Crystal Field Theory
CHCl ₃	Chloroform

CPGs	Coordination polymer gels
DCC	N,N'-Dicyclohexylcarbodiimide
DCE	Dichloroethane
DCM	Dichloromethane
DCU	Dicyclohexylurea
DFT	Density Functional Theory
DLS	Dynamic light scattering
DMAP	4-Dimethylaminopyridine
DMSO	Dimethylsulfoxide
DSC	Differential Scanning Calorimetry
EDX	Energy Dispersive X-ray
<i>et al</i>	<i>“et alia”</i> “and others”
EtCN	Propionitrile
EtOAc	Ethyl acetate
EtOH	Ethanol
ESMS	Electrospray Mass spectrometry
EWG	Electron-withdrawing groups
HF	Hartree-Fock
HOMO	Highest Occupied Molecular Orbital
HS	High spin
\hat{H}	Hamiltonian
ICMol	Instituto de ciencia molecular, Valencia (Spain)
ISC	Intersystem crossing
J-T	Jahn-Teller
KS	Kohn-Sham
L	Ligand
LFT	Ligand Field Theory
LIESST	Light-Induced Excited Spin-State Trapping

LS	Low spin
LUMO	Lowest Unoccupied Molecular Orbital
M-L	Metal-Ligand
Me ₂ CO	Acetone
MeCN	Acetonitrile
MeNO ₂	Nitromethane
MeOH	Methanol
NMR	Nuclear Magnetic Resonance
py	Pyridine
pz	Pyrazole
RMS	Root mean square roughness
SAMs	Self-assembled monolayers
SCO	Spin-crossover
SEM	Scanning Electron Microscopy
TEM	Transmission Electron Microscopy
SQUID	Superconducting Quantum Interference Devices
T _{1/2}	Temperature which HS molar fraction occupancy = LS
TPT	2,4,6-Tri(pyrazol-1-yl)-1,3,5-triazine
THF	Tetrahydrofuran
TMS	Tetramethylsilane
UHV	Ultra high vacuum
UV-vis-NIR	Ultraviolet-visible-near infra-red
VT	Variable temperature
XAS	X-ray absorption spectroscopy
XPS	X-ray photoelectron spectroscopy
[L]B	Tetrafluoroborate complex of L
[L]C	Perchlorate complex of L

Chapter 1 – Introduction

1.1 Theoretical foundations

IUPAC defines spin-crossover as a type of molecular magnetism that is the result of electronic instability caused by external constraints which induce structural changes at molecular and lattice levels¹. In order to understand this phenomenon, which is mostly characteristic of first-row transition metal complexes, a crystal field theory introduction is needed.

1.1.1 Crystal field theory (CFT)

CFT is a purely electrostatic model which describes the bonding and electronic configuration for d-metal complexes. *d* orbitals from a free metal ion are degenerate. However, they are split in energy when subjected to a finite ligand field. For octahedral geometry, the orbital lobes of $d_{x^2-y^2}$ and d_{z^2} orbitals (termed the e_g set) are oriented towards the surrounding ligands so, they are raised in energy by the electrostatic repulsion of electrons. Simultaneously, the t_{2g} orbital set (d_{xy} , d_{xz} and d_{yz}) are stabilized from the barycentre (Figure 1.1).

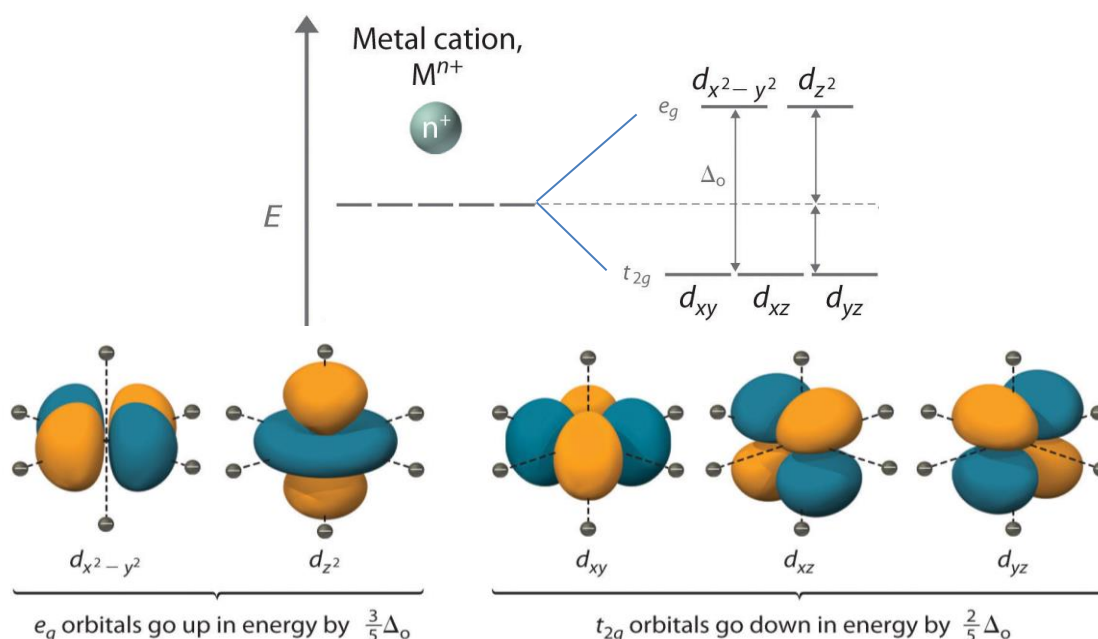


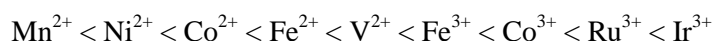
Figure 1.1: *d* orbitals are split into two set energy levels due to octahedral arrangement².

The energy gap between the orbital sublevels t_{2g} and e_g is known as the octahedral splitting energy (Δ_o). $10 Dq$ symbolizes the semi-empirical value of Δ_o and it can be

Chapter 1

determined by UV-vis spectroscopy. Its magnitude is related to the following three factors of the metal atom.

Among atoms of the same row of the periodic table the field varies irregularly but usually increases from left to right. Almost all elements from second and third row have a significantly stronger Δ_o . For the same element, a higher oxidation state implies higher octahedral splitting energy. Some examples describe the observed tendency³;



Here, ions are arranged in function of the strength of the crystal field they produce in any specific ligand environment.

1.1.2 Ligand field theory (LFT) and electronic configuration

The LFT model builds on CFT, is more complex and takes into account the overlap of M-L orbitals. It gives better explanations for a wide range of properties of complexes such as their electronic structure. Therefore, Δ_o also depends on the ligand field bound to the metal ion.

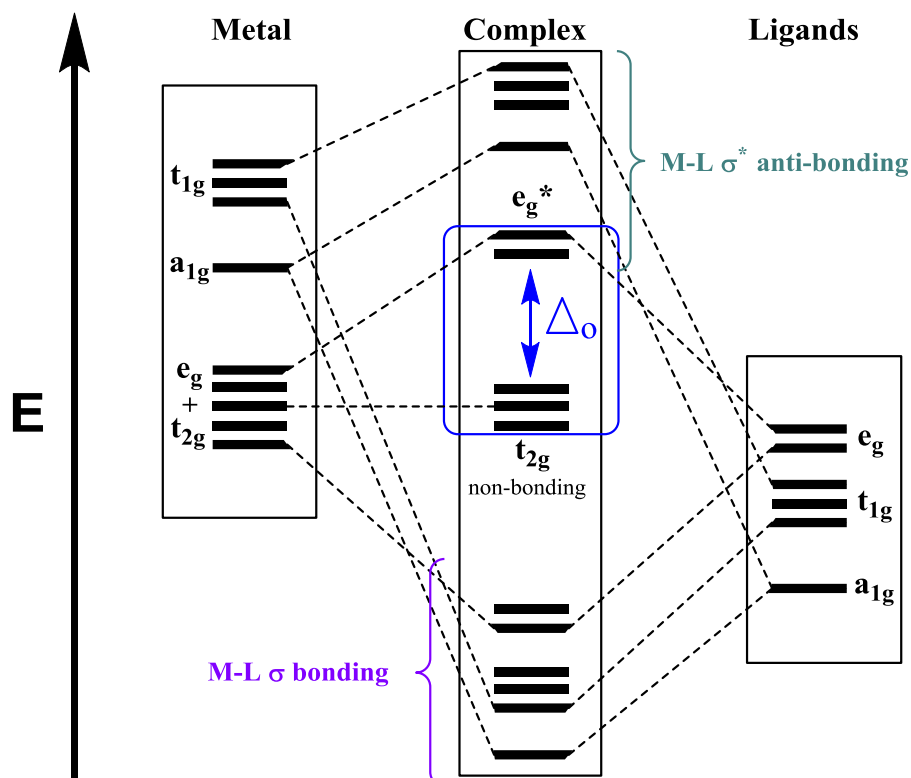
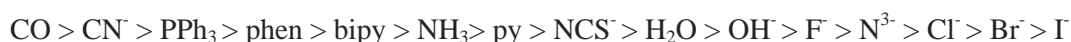


Figure 1.2: Molecular orbital energy levels for octahedral complexes. Inside the blue box are the frontier orbitals.

In principle, good σ -donor ligands which give strong M-L overlap would result in strongly antibonding e_g^* orbitals, in other words, a high Δ_o (Figure 1.2). However, π orbitals of

Chapter 1

the ligand also interfere with the ligand field splitting. When they overlap with d orbitals of the metal, the t_{2g} combination is no longer purely non-bonding. A π -donor ligand has filled π orbitals, thus the t_{2g} combination reaches higher energy, decreasing Δ_o . Conversely, for ligands with empty π orbitals, e.g. PPh_3 or CO , the bonding t_{2g} combination lies lower in energy, making the energy gap between it and e_g stronger⁴. The spectrochemical series is an empirically-derived list of ligands ordered by the size of the splitting Δ_o that they produce;



Accordingly, carbon monoxide and cyanide (π -acceptor type) are considered strong-field ligands while halides are weak-field ligands and give rise to a low energy gap.

Two electrons of a given atom cannot have identical quantum numbers as indicated by Pauli's exclusion principle. Thus, electrons in the same orbital have opposite spin and will repel one another. This repulsion is called spin pairing energy (Π). The electronic configuration for a metal complex follows Hund's rules. For the same orbital energetic sublevel the electrons are arranged such the number of parallel and unpaired electrons is maximum. For d^{4-7} octahedral complexes it is possible to have two electronic configurations depending on if the energetic difference between t_{2g} and e_g (Δ_o) is higher or lower than Π .

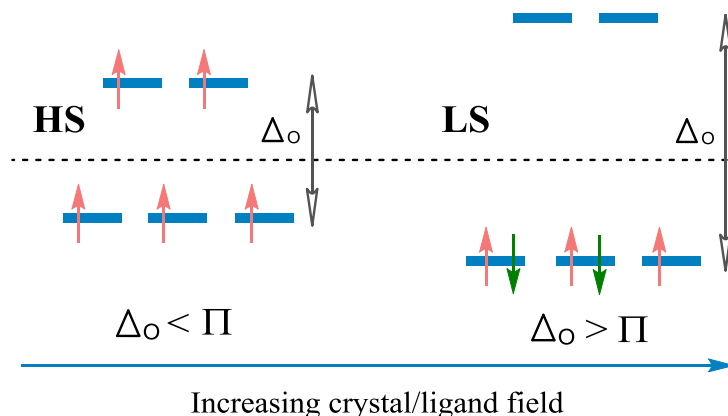


Figure 1.3: High spin and low spin configurations for d^5 octahedral metal complex.

The two possible electronic distributions for Fe(III) which has the general configuration $[\text{Ar}] 3d^5$, are defined in Figure 1.3; high spin (HS) and low spin (LS) respectively. A weak-field ligand allows the complex to arrange its fourth and fifth electron onto anti-bonding e_g orbitals instead of pairing them in the non-bonding t_{2g} , hence $r(\text{M-L})$ becomes weaker and longer.

The nephelauxetic effect (degree of M-L bond covalency) is related to the overlap of ligand orbitals with metal d orbitals. The orbitals size increase with the consequent decreasing of electronic repulsion⁵. This effect is minimized for HS complexes were the orbital overlap is lower.

Chapter 1

1.1.3 Diamagnetism and paramagnetism

The magnetism of materials arises from the movement of electrons because the magnetic moment is inversely proportional to particle mass (the magnetic moment of an electron is about 1000 times higher than that of a proton). When two electrons occupy the same orbital they have opposite spin quantum numbers. Almost all compounds of elements in the main group of the periodic table have completely filled orbitals with paired electrons. Despite these molecules having no net spin momentum, the application of a magnetic field causes their electrons to induce a small magnetic field which opposes the applied field. This behaviour, termed diamagnetism, is characteristic of substances which do not have any unpaired electrons.

On the other hand, the situation is very different when a compound has unpaired electrons. Paramagnetism is the phenomenon linked to the existence of any unpaired electrons. These electrons give net spin angular momentum (\vec{S}) and may originate an orbital angular momentum (\vec{L}) if they can move around the nucleus (the unpaired electron has \vec{L} , when the orbital it occupies can be transformed into another which is equivalent and degenerate by rotation, for example d_{xy} and d_{xz}), giving rise to a magnetic moment. This magnetic moment is positioned parallel to the externally applied magnetic field and enhances it. The magnitude of paramagnetism is the effective magnetic moment (μ_{eff}). It depends on the orbital and spin angular momenta from the unpaired electrons, (Eq. 1).

$$\mu_{eff} = \sqrt{\vec{L}(\vec{L} + 1) + 4\vec{S}(\vec{S} + 1)}\mu_B \quad (\text{Equation 1})$$

The magnetism of a transition metal complex is mainly produced by the d orbitals and their electrons. However, when d orbitals are perturbed by the ligands, the rotations which move electrons between the degenerate orbitals are not possible for low symmetry complexes. In other words, for first-row transition metals the orbital angular momentum is typically quenched $\vec{L} \approx 0$. Therefore, spin-only formula (Eq. 2) is a good approximation to calculate the magnetic moment:

$$\mu_{eff} = \sqrt{n(n + 2)}\mu_B \quad (\text{Equation 2})$$

where n is the number of unpaired electrons. From this equation μ_{eff} can be predicted in good agreement with experimental values^{3b}. (See table 1-1)

Unpaired electrons (n)	Effective magnetic moment calculated (μ_{eff})	Example of observed magnetic moment (μ_B)
1	1.73	$V^{4+} \rightarrow 1.7 - 1.8$
2	2.83	$Ni^{2+} \rightarrow 2.8 - 3.5$
3	3.87	$Cr^{3+} \rightarrow 3.7 - 3.9$
4	4.90	$Fe^{2+} \rightarrow 5.1 - 5.7$
5	5.92	$Fe^{3+} \rightarrow 5.7 - 6.0$

Table 1-1: Application of spin-only formula.

Chapter 1

In magnetochemistry, the magnetic susceptibility (χ) is a dimensionless proportionality constant that indicates the degree of magnetization of a material in response to an externally applied magnetic field. The molar magnetic susceptibility can be determined experimentally and relates to μ_{eff} as described in equation 3;

$$\mu_{\text{eff}} = \sqrt{\frac{3 \cdot k \cdot T \cdot \chi}{N \cdot \mu_B^2}} \approx 2.8278 \sqrt{\chi_m T} \quad (\text{Equation 3})$$

where χ_m is the molar magnetic susceptibility ($\text{cm}^3 \cdot \text{mol}^{-1}$) determined at temperature T in the Kelvin scale. There are a few methods to determine χ_m ; the classic Gouy method, paramagnetic NMR Evans method or SQUID magnetometry.

Currently, the most common way of detecting the molar magnetic susceptibility of a solid is the modern superconducting quantum interference device (SQUID) which is more sensitive (magnetic fields of 10^{-6} emu can be detected) than a Gouy balance and can collect data over a wide range of T quickly. Its principle is based on two superconductors separated by thin weak insulating layers (Josephson junctions) which measure variations in magnetic flux³.

The information extracted from this experiment is the magnetization ($M_g = \text{emu} \cdot \text{G}$) of the sample for each exact temperature within the range. In order to obtain the $\chi_m T$ vs T curve, processing the data using equation 4 is required;

$$\chi_m(T) = \left(\frac{M_{g_{\text{corr}}(T)}}{H \cdot n} - \chi_{\text{dia}} \right) \cdot T \quad (\text{Equation 4})$$

where $M_{g_{\text{corr}}}$ are the values obtained once the blank is subtracted, H is the magnetic field (Oe), n is the number of moles and χ_{dia} is the diamagnetic correction from the Pascal's constants approximation (Eq. 5);

$$\chi_{\text{dia}} \approx -\frac{M}{2} \cdot 10^{-6} \text{ emu mol}^{-1} \quad (\text{Equation 5})$$

which is "directly proportional" to the molar mass M of the compound analysed⁶.

Another particularly practical method for determining χ_m from a liquid solution samples is Evans Method where the SQUID magnetometer is not required. ¹H NMR can be collected over a range of temperatures however, the melting and boiling points of the solvent limit the technique.

A special insert containing a blank solution is required inside the NMR tube for the measurements. The reference peaks are split between the blank signal and the shifted peak influenced by the paramagnetism of the sample. The $\chi_m T$ vs T curve is obtained by measuring the shifting (Δf) and applying the equation 6;

$$\chi_m(T) = \left(\frac{3 \cdot \Delta f(T)}{4\pi \cdot f \cdot c(T)} + \chi_{\text{o}(T)} \right) \cdot M \cdot T \quad (\text{Equation 6})$$

Chapter 1

It is important to consider the density variation ($d(T)$) of the solvent which is often linearly dependent with temperature. Because of this variation there are few terms of equation 6 which are T dependent. The mass susceptibility of the solvent (χ_o) term is described by equation 7;

$$\chi_o = \frac{\chi}{d(T)} \quad (\text{Equation 7})$$

where χ is the magnetic susceptibility for the solvent (usually described in the literature), Δf is the observed frequency splitting measured directly from the spectrum (Hz), f is the spectrophotometer frequency (Hz), c is the concentration of the paramagnetic sample ($\text{g}\cdot\text{cm}^{-3}$) and M is its molecular weight.

The molar mass susceptibility (χ_m) can be calculated by using this method with an agreement of 5-10%⁷.

1.2 Magnetic bistability

Some materials are able to switch between their electronic states and have been proposed as potential building blocks to obtain molecular switching devices⁸ (Figure 1.4), where the ultimate goal could be to manipulate information at the molecular level, using them as sensors or as display devices. One well known example of this is valence tautomerism⁹. However, our research was focused on spin-crossover (SCO) compounds.

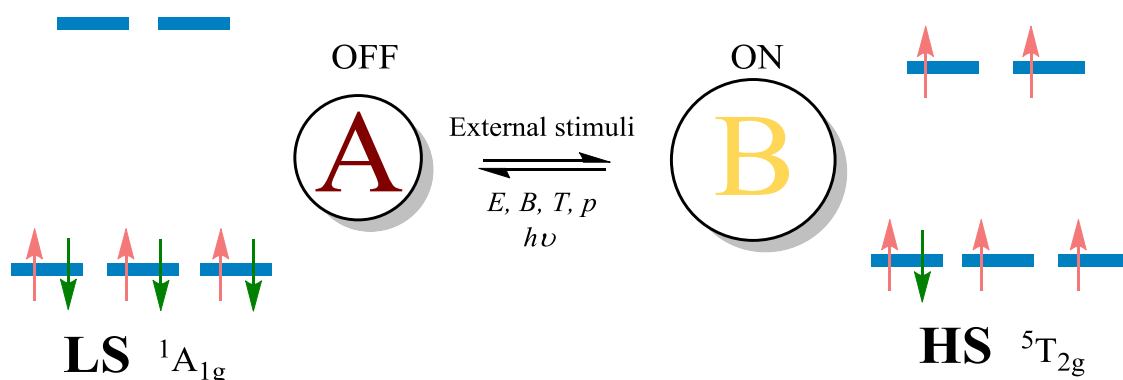


Figure 1.4: Model of a molecular switching device based on d^6 transition metal complex SCO phenomenon.

For d^6 octahedral complexes, the $^1A_{1g}$ (t_{2g}^6) term describes the LS state. $^1A_{1g}$ means the material is a singlet (no unpaired electrons). On the other hand, the HS state is represented by the lowest energy level quintuplet $^5T_{2g}$ ($t_{2g}^4 e_g^2$) term, and it is related to four unpaired electrons¹⁰.

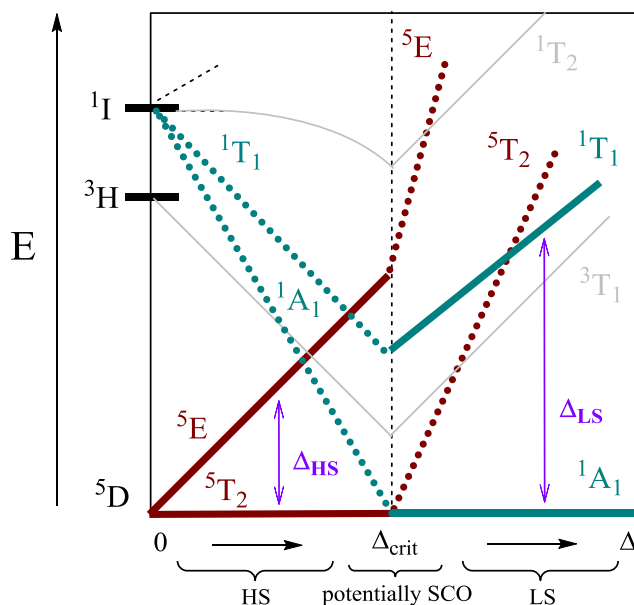


Figure 1.5: Simplified Tanabe-Sugano diagram for a d^6 system. Few transitions hidden for clarity.

Considering a d^6 complex CFT assigns the d-d transition maximum absorption band to the ${}^5T_{2g}(t_{2g}^4 e_g^2) \rightarrow {}^5E_g(t_{2g}^3 e_g^3)$ or to the ${}^1A_{1g}(t_{2g}^6) \rightarrow {}^1T_{1g}(t_{2g}^5 e_g^1)$ transition depending on if it is HS or LS respectively (Figure 1.5). Although these transitions are spin allowed, they show weak intensity because they are Laporte forbidden^{1*}. When a vibration alters the geometry from the perfect octahedron (e.g. Jahn-Teller distortion) the centre of symmetry is eliminated and those transitions became partially allowed.

If the ligand field splitting has intermediate values, close to Δ_{crit} , a spin transition may be possible. The idea of having two values for the ligand field parameter is graphically represented in Figure 1.6 as potential energy wells following a harmonic oscillator model which is described by the next expression (Eq. 8):

$$E = \frac{1}{2} \cdot k \cdot x^2 \quad (\text{Equation 8})$$

where k is the force constant and x is $\Delta r(M-L)^{10b}$. When the difference between $E_{HS}^o - E_{LS}^o$ is sufficiently small an equilibrium between two “electronic isomers” is established which can be displaced by a minor external stimulus.

1.2.1 Spin-crossover (SCO)

The SCO phenomenon is a reversible and repeatable transition between the electronic states which is usually triggered by varying temperature, pressure¹¹ or photoirradiation. The

^{1*} An orbital which possesses a centre of symmetry is termed gerade (g), while if it does not possess it is called ungerade (u). Allowed transitions by the Laporte selection rule must involve a change in parity, $g \rightarrow u$ and $u \rightarrow g$.

Chapter 1

discovery of the LIESST (light-induced excited spin state trapping) effect suggested that those compounds could be used as optical switches¹². The SCO event is accompanied by physical changes such as the material's colour, M-L bond lengths, magnetic moment, optical spectra and electrical resistance.

For systems in solution the SCO behaviour can be interpreted as a thermal equilibrium involving a Boltzmann distribution over the vibronic levels of both spin states. In terms of thermodynamics, the Gibbs free energy equation (Eq. 9) determines whether a process is energetically favoured or not.

$$\Delta G = \Delta H - T \cdot \Delta S \quad (\text{Equation 9})$$

Simplifying, a reversible transition SCO should be understood as a thermodynamic equilibrium ($\Delta G = 0$) between its two electronic states where the equilibrium can be shifted by applying external stimuli; e.g. by raising the temperature. The enthalpy of the LS state is thermodynamically more stable since its M-L bonds are stronger, its magnitude changes by about +2.4 to +5 kcal/mol over the LS→HS transition. However, the entropic term which favours the HS configuration is more decisive in this process (Eq. 10).

$$\Delta S = \Delta S_{el} + \Delta S_{vib} + \Delta S_{lattice} \quad (\text{Equation 10})$$

High spin electrons are arranged in a larger number of orbitals increasing the electronic entropy (ΔS_{el}). In addition, HS vibrational sublevels are wider with a smaller energy gap between them and electrons can move between them more easily (ΔS_{vib} , schematic representation in Figure 1.6). Finally, the increase of $r(\text{M-L})$ leads to a big lattice disorder ($\Delta S_{lattice}$). The $T \cdot \Delta S$ term usually reaches from 12 to 19 kcal/mol¹³.

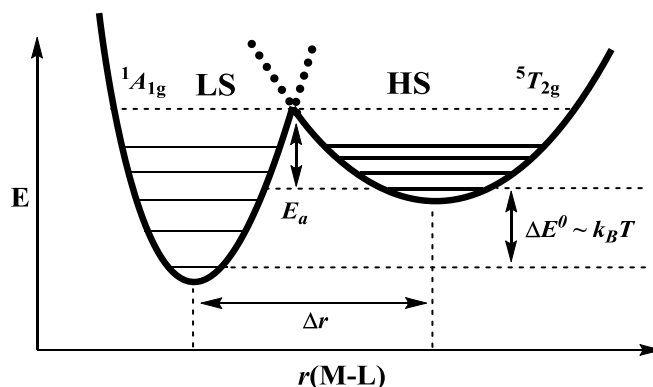


Figure 1.6: Potential energy wells of the electronic states of d^6 transition metal complexes.

In summary, SCO is entropically driven. When $E_{LS}^0 - E_{HS}^0$ is comparable to $k_B T$ ($k_B =$ Boltzmann constant) the transition is thermodynamically feasible and it may happen at that T . However the activation energy is also strongly related to $r(\text{M-L})$. In the case of $\Delta E^0 \approx k_B T$ compounds, if the potential energy wells are distant along the coordinate system the overlap between them may decay increasing the energy barrier (E_a). As a result, this will lead to a kinetically unfavourable SCO.

1.2.2 Transition types

Liquid solutions, crystalline and amorphous solids, can all present SCO. Although the origin of this phenomenon has a molecular level basis, it is strongly influenced by the surroundings in the crystal lattice. This effect is termed cooperativity¹⁴. Not all spin transitions are equivalent, and several types of magnetic curves can be observed (Figure 1.7), exhibiting different shapes or varying the temperature at which the transition occurs. $T_{1/2}$ is the temperature when the molar fractions of the HS and LS states are equal and 0.5, this temperature is considered the point when the SCO transition happens.

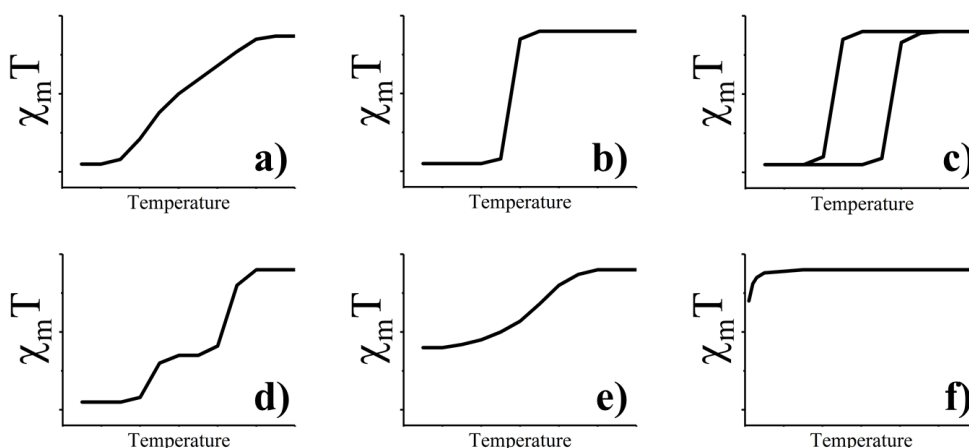


Figure 1.7: Classification of transitions. A) The most common is the gradual which undergoes over a wide temperature range. B) Abrupt transition. C) Hysteresis loop. D) The transition may happen in two or more steps, also it can be incomplete or even not happen E) and F). Examples apply for a material able of switching its paramagnetism on and off such as iron(II) d^6 .

An abrupt transition (Figure 1.7, b) implies that metallic centres changing their spin state promote the transition in their neighbours cooperatively. Typically, when high cooperativity accompanies the transition, enhancement of hysteresis may result¹⁵.

The term hysteresis is referred to any property depending on external stimuli which remains intact when that stimulus disappears. In this context, thermal hysteresis is a lag in the magnetic response on changing the temperature. A good example is illustrated at Figure 1.8 where the $\chi_m T$ vs T curve follows different paths on the cooling and heating mode;

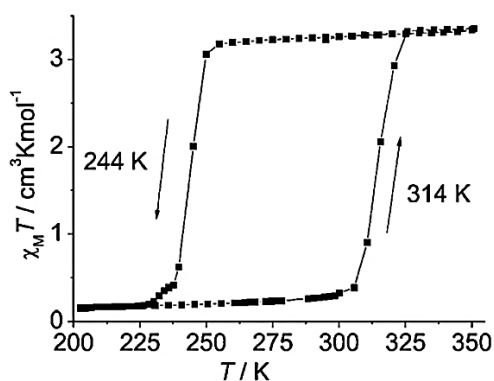


Figure 1.8: Example of wide hysteresis with 70K loop¹⁵.

It is said that this material shows magnetic bistability between 244K and 314K which implies the two electronic states are stable over this certain temperature range. All these features can be used to produce molecular devices as was mentioned above. In order to use such systems in real applications $T_{1/2}$ values should be around room temperature. For this, having control over the critical temperature at which the transition takes place or the enhancement of hysteresis effects is a requirement.

1.2.3 LIESST

As explained above, external stimuli can shift to a greater or lesser degree the SCO thermodynamic equilibrium. In other words, they affect the temperature at which the spin transition occurs. Light-Induced Excited Spin State Trapping (LIESST) is an alternative pathway to trigger the transition from LS to HS without applying thermal energy. Figure 1.9 describes the LIESST mechanism and reverse LIESST presented by Gütllich and Hauser in 1990¹⁶. Currently a large number of Fe(II) complexes have been reported to display this phenomenon¹⁷, along with a smaller number of Fe(III) examples¹⁸.

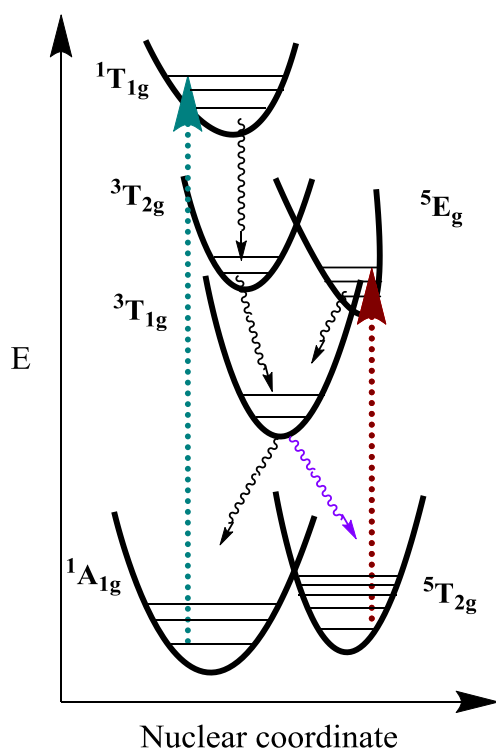


Figure 1.9: Schematic LIESST mechanism.

The HS state is kinetically metastable at low temperature where E_a cannot be reached. However the system can relax back into the LS by increasing the temperature ($T_{(LIESST)}$). The $T_{(LIESST)}$ experiment involves a “strict protocol”; irradiating the sample at 10 K and warming at 0.3 Kmin^{-1} rate while measuring $\chi_m T$ until it decays to LS. Example shown in Figure 1.10;

A sample is irradiated at very low temperatures (when LS is the ground state) with the characteristic d-d absorption band, promoting the $^1A_{1g} \rightarrow ^1T_{1g}$ transition which will decay by intersystem crossing (ISC) into $^1T_{1g} \rightarrow ^3T_{2g} \rightarrow ^3T_{1g}$ due to spin-orbit coupling. From that electronic state, a $^3T_{1g} \rightarrow ^5E_g$ ISC transition can happen (violet relaxation, Figure 1.9) concluding the transition to HS.

At this stage, in order to induce reverse LIESST specific irradiation again is needed which would allow the $^5T_{2g} \rightarrow ^5E_g$ transition, and finally a $^5E_g \rightarrow ^3T_{1g} \rightarrow ^1A_{1g}$ ISC could convert back the system to LS state.

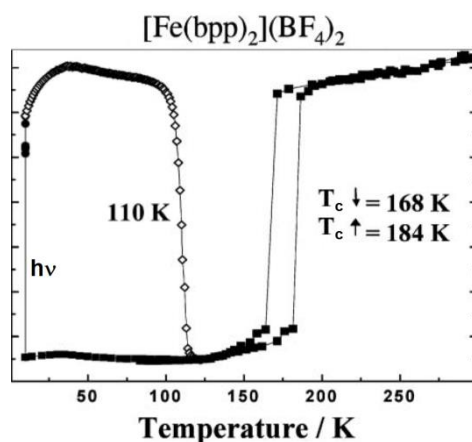


Figure 1.10: Example of T(LIESST) experiment for an iron(II) complex. This graph has been adapted from¹⁷.

It is important to be consistent with the method because the process is entropically driven. It has been reported the scan rate of T variation affects the shape and $T_{(\text{LIESST})}$ ¹⁹.

1.2.4 Pressure influence

Pressure is an external stimulus able to shift the SCO equilibrium. This effect arises because $r(\text{M-L})$ decreases under pressure increasing the ligand field. High spin geometry is expanded compared to that for LS due to its anti-bonding electronic occupancy. Therefore, in a situation where the difference between unit cell volumes of HS and LS is significant, applying pressure would stabilize the LS state and raise $T_{1/2}$. An example is in Figure 1.11;

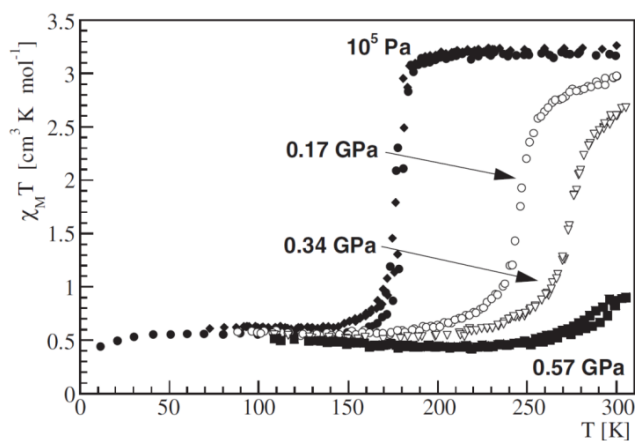


Figure 1.11 Plot of pressure influence in the $\chi_{\text{m}}T$ vs T curves. This picture has been taken from Gütlich et al²⁰.

Gutlich, Létard *et al.* conducted several studies regarding pressure influence in SCO or VT transitions, Figure 1.11²¹. Since typical values of $T_{1/2}$ are low temperatures, the approach of increasing it close to room temperature is very important for potential application as a sensor or memory storage devices. However in practice, typical pressures needed to shift low $T_{1/2}$ close to room temperature are too high to be applied in a realistic way for such applications.

1.2.5 Magnetic field

Varying the applied magnetic field another stimulus which interacts with $T_{1/2}$. Among two spin states available the one which has more unpaired electrons is stabilised (HS) when increasing the magnetic field. However, the effect observed for cases reported in the literature is small in magnitude. For instance; an increment in the magnetic field from 1 to 5.5 Tesla was applied and only $\Delta T_{1/2} = -0.10 \pm 0.04$ K was found²².

1.2.6 Uv-vis-NIR absorption spectra

The crystal field splitting (Δ_o) can be experimentally measured by Uv-vis-NIR. Hence, this technique is an interesting tool for predicting the magnetic behaviour of metal complexes. Nevertheless, the application is limited because d-d bands are Laporte forbidden.

The semi-empirical $10 Dq$ term represents Δ_o mathematically and its value differs depending on the spin state; $Dq^{HS} < Dq^{LS}$ because M-L bond lengths change along the transition, Figure 1.12. Despite the larger nephelauxetic effect for LS complexes, spin pairing energy (Π , black straight line in Figure 1.12) is considered equivalent for both HS or LS Fe(II) complexes with a magnitude around $14000-17000 \text{ cm}^{-1}$ ²³.

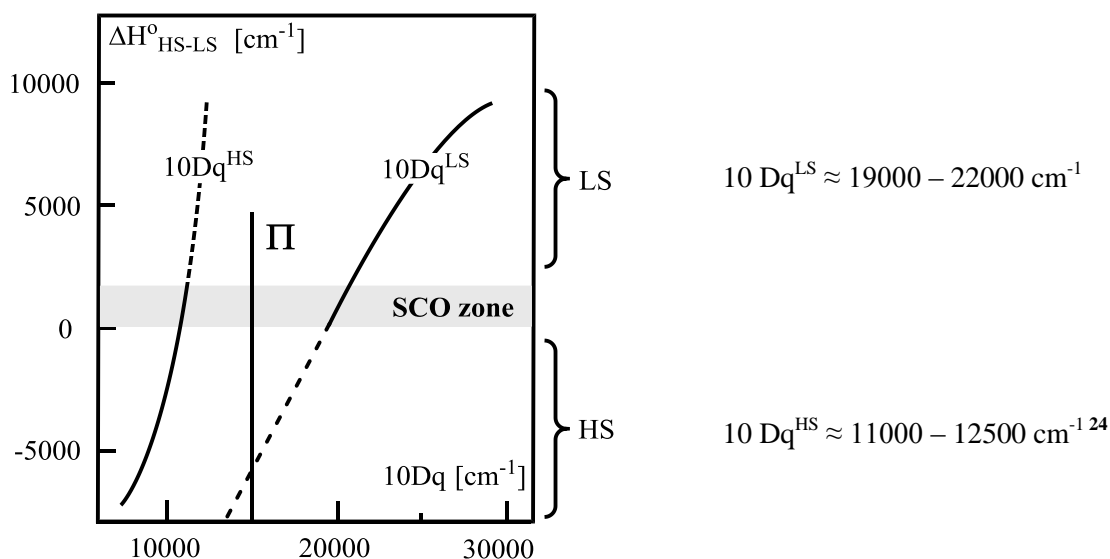


Figure 1.12: Energetic difference between the two electronic states versus the ligand field strength. Pairing energy (Π). Typical Dq SCO values are related such as $Dq^{LS}/Dq^{HS} \approx 1.75$; and $0 < \Delta H^\circ < +2000 \text{ cm}^{-1}$.

The transition is impossible when $10 Dq^{HS} < 10000 \text{ cm}^{-1}$ because ΔH° is negative. In this case, HS is the ground state and LS state cannot be populated. Furthermore, when $10 Dq^{LS} > 23000 \text{ cm}^{-1}$ ΔH° is too high to thermally populate the HS state without destroying the complex¹⁰.

1.3 Ligand design

Ligand design is one of the most important issues in the SCO research since even the smallest variation of a ligand can strongly affect the magnetic properties of its metal complex.

1.3.1 Spin-crossover: iron complexes

Since Cambi and Szegő reported the first SCO compounds in 1931²⁵, much progress has been made on this topic. Several metal ions from different coordination geometries undergo spin-crossover; manganese(III)²⁶, iron(III) and (II), cobalt(II)²⁷ mononuclear complexes, dinuclear²⁸ or even polynuclear²⁹ clusters are some examples found in the literature. Nevertheless, the field is dominated by six coordinate iron(II) complexes of N-donor ligands³⁰.

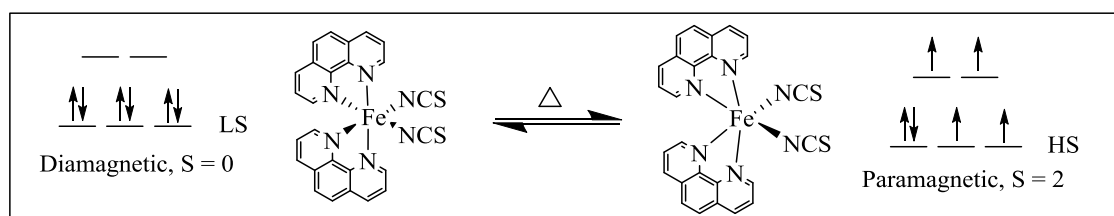


Figure 1.13 First iron(II) SCO reported. This transition involves two electrons and a spin variation of $\Delta S = 2$.

The first SCO Fe(II)-6 N-donor combination was reported in 1964 by Baker and Bobonich³¹ (Figure 1.13), however it was not until 1966 when König and Madeja³² proposed the SCO phenomenon as a thermal transition between the spin states. The electronic occupancy of the antibonding e_g orbitals for the HS state is translated into an elongation of the metal-ligand (M-L) bond length average³³.

That combination is one of the most studied spin-crossover systems since the structural difference between their spin states is greater than for other metal-ligand combinations³⁰. This fact helps to propagate the transition through the material more efficiently, leading to an abrupt switching transition. In addition, the high spin state is usually pale in colour, while the low spin state is strongly coloured making it easily recognizable. Finally, spin-crossover in iron(II) (d^6) switches the paramagnetism of material on and off. Iron(II) complexes of 2,6-di(pyrazolyl)pyridine ligands (bpp) (Figure 1.14) and its derivatives are a well-known example of this combination.

1.3.2 Cooperativity:

The arrangement of the complexes along the crystal lattice is determinant for the SCO phenomenon. The use of different counter-anions has also a notable effect on the magnetic behaviour in two main ways. Very often counter-anions have H-bonding acceptor atoms. When

interacting with the ligand through a position close enough to the coordinating nitrogen donor, they can withdraw some electron density weakening the M-L bond, hence stabilising the HS state³⁴. On the other hand, the size of the counter-anion also usually makes a difference³⁵. The solvent molecules within the crystal lattice can also have a similar H-bonding or size impact as counter-anions³⁶. Figure 1.14 displays examples of such effects.

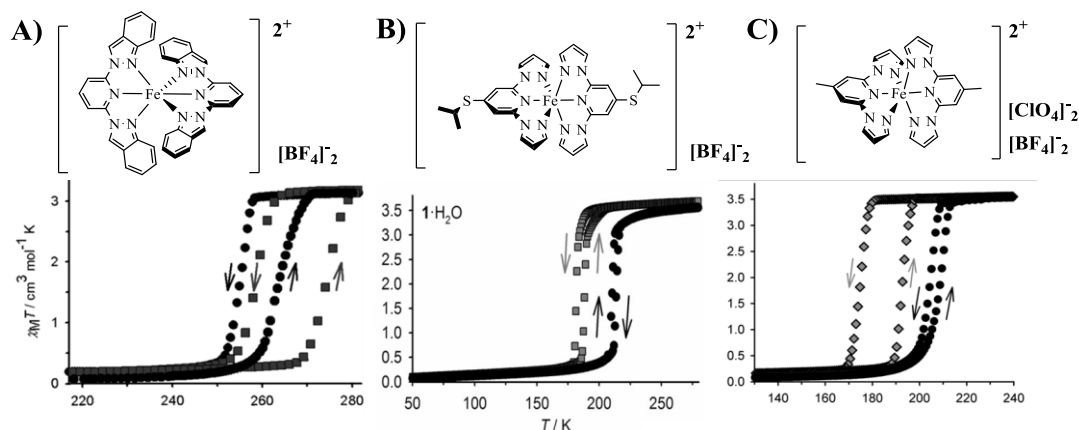


Figure 1.14: A) Wider and closer to room temperature hysteresis loop due to the enhanced mechanical coupling between the complexes over the lattice³⁷. B) $[\text{FeL}_2](\text{BF}_4)_2$ ($L = 2,6\text{-di}(\text{pyrazol-1-yl})\text{-4}(\text{isopropylsulfanyl})\text{pyridine}$; recrystallized from different solvents shows varying SCO behaviours even though they are isostructural³⁸. C) SCO active complex despite its large Jahn-Teller distortion. Its magnetism is affected by the counter-anion used³⁹.

Cooperative effects cannot be understood at molecular level. Small variations in the system will have a strong effect if they influence the steric arrangement in the crystal lattice or its rigidity. Structures with greater structural differences between HS and LS states will show strong cooperativity leading to abrupt transitions⁴⁰.

1.3.3 Distortions parameters, Jahn-Teller:

The morphology of a complex plays a determining role towards the spin transition. Hendrickson *et al* introduced the parameters which describe the deviation of octahedral metal complexes from the ideal octahedral geometry (ideal O_h : $\Sigma = \Theta = 0$)⁴¹ (Figure 1.15);



Figure 1.15: Where α_i are the 12 cis N-Fe-N angles and θ_j are 24 unique N-Fe-N angles measured from the triangular projections along the pseudo-threefold axis. Both Σ and Θ are usually much larger for HS state than the LS.

Chapter 1

The Σ rhombic distortion parameter gives information about the overall O_h distortion, and the Θ trigonal parameter is more indicative of the type of distortion observed. Later, Guionneau *et al.* used these parameters to describe the spin state of iron(II) complexes and to determine the extent of distortion produced during the spin transition by comparing HS and LS structures⁴². The HS configuration is more flexible and susceptible to distortion than LS due to its extra anti-bonding e_g^* electrons (Figure 1.16).

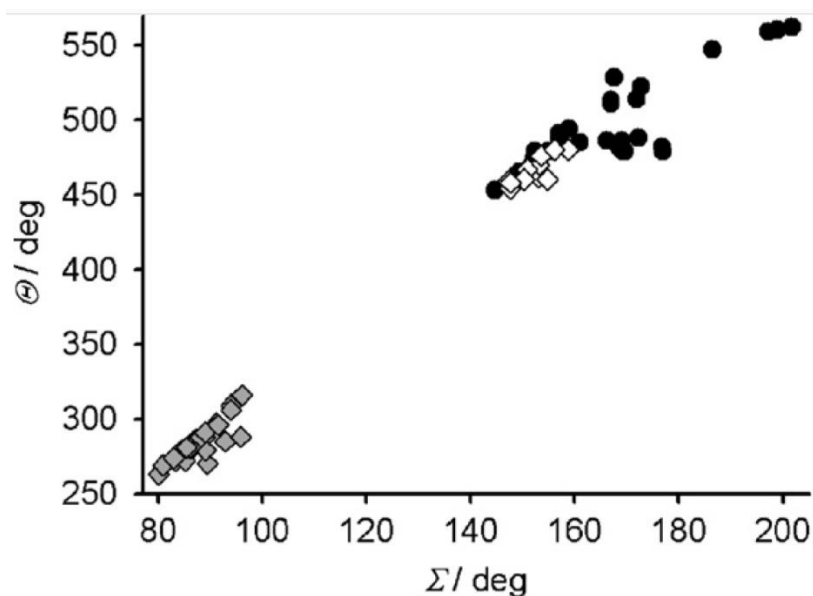


Figure 1.16: Complexes remaining LS at room temperature are represented by “ \diamond ”, complexes trapped in HS state at low temperatures corresponds to “ \bullet ” and finally, the complexes which trigger a spin-crossover transition are “ \diamond ”⁴³.

The Jahn-Teller (J-T) theorem states that every non-linear geometry with a degenerate ground state is unstable so a distortion will break the symmetry, decreasing the energy of the system. Notice that the ideal symmetry for complexes with planar tridentate chelating ligands such as bpp is not O_h anymore, it is D_{2d} instead⁴⁴ (Figure 1.17).

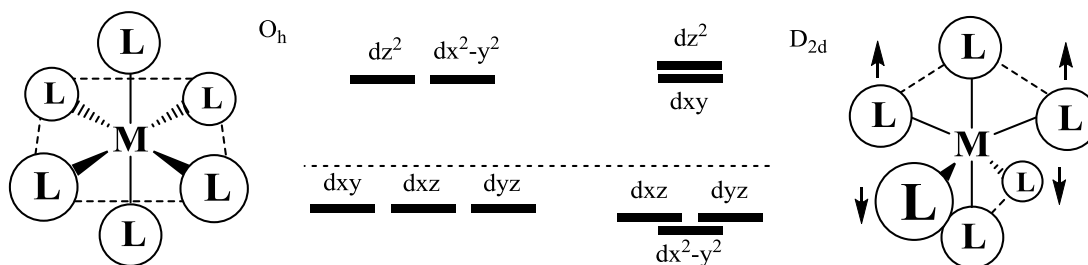


Figure 1.17: Energy levels of d orbitals for O_h and D_{2d} geometries.

The HS geometry for this type of complexes is characteristically distorted from D_{2d} symmetry to C_2 under a Jahn-Teller effect described by the following two angles (Figure 1.18).

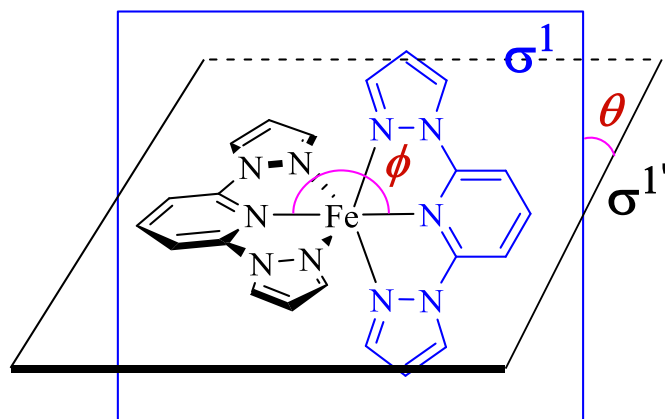


Figure 1.18: Definition of θ and ϕ , Jahn-Teller distortion angles.

where $\phi < 180^\circ$ is the *trans*-N[pyridine]-Fe-N[pyridine] angle which measures the bending of the molecule along the main C_2 fold axis and $\theta < 90^\circ$ is the twist angle between the two planes generated from the ligands ($\sigma^1 \nrightarrow \sigma^{1'}$).

The SCO phenomenon is often inhibited for systems whose geometries of both electronic states strongly differ from each other, so the structural change over the lattice required during the transition would be too energetic to be accessible. It is said that these complexes are trapped in their HS state. The geometric distortion parameters of several $[\text{Fe}(\text{bpp})_2]^{2+}$ salts are plotted against their capacity of undergo SCO (Figure 1.19)⁴³.

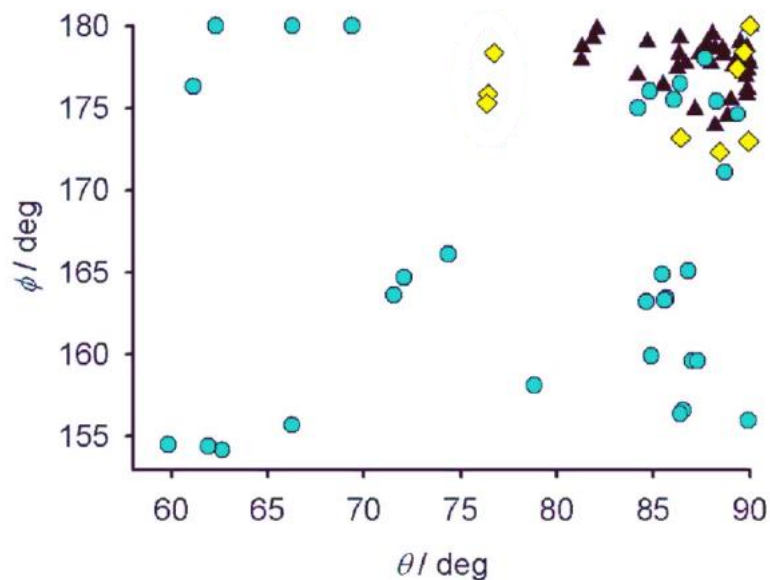


Figure 1.19: Complexes remaining LS at room temperature are represented by “▲”, complexes trapped in HS state at low temperatures corresponds to “●” and finally, the complexes which trigger a spin-crossover transition are “◆”⁴⁵.

1.4 Computational methods

The use of computational methods for exploring the properties of individual molecules and materials has increased over the last two decades. The calculations currently can be performed in small computers where the ultimate goal is the solution of the time-independent, non-relativistic Schrödinger equation (S.E., Eq. 11):

$$\hat{H} \cdot \Psi = E \cdot \Psi \quad (\text{Equation 11})$$

where wavefunction (Ψ) describes the quantum state of a system, E is the energy and Hamiltonian operator (\hat{H}) operates the wavefunction to determine permitted energy levels of a molecule. The Schrödinger equation only can be solved exactly for molecules with $N \leq 1$ (N = no. electrons). For more complex systems approximations must be made. Currently, there are two main approaches to solve the S.E.; semi-empirical methods and *ab initio* methods which use the first principles of quantum theory to calculate structures.

The Hamiltonian represents E so it must contain terms for kinetic energy and the potential energy of electrons (e^-) and nuclei (n^+). It is represented by five-terms: $E_k n^+$, $E_k e^-$, $E_p n^+ - E_p n^+$, $E_p e^- - E_p e^-$, $E_p n^+ - E_p e^-$. After the Born-Oppenheimer approximation is taken into account^{2*} \hat{H} becomes a three-term \hat{H}_{elec} . Ideally, for molecules with $N > 1$, the S.E. would be solved one e^- at a time for all the electrons in the system and summed together which will give an overall solution with N atomic orbitals. However, electron motion is correlated meaning that every electron is related to every other and by adding electrons to the system the increase of variables is exponential. This is known as the “many-body” problem. Hartree assumed that each e^- moves in a uniform field generated by all the other electrons of the system instead of considering every movement of e^- individually. In other words, he proposed how to solve the S.E. one e^- at a time by ignoring electronic correlation. Fock included the electron exchange model due to Pauli’s exclusion principle. Thereby they created Hartree-Fock (HF) theory, an iterative method which converges until self-consistency is attained and calculates the “best” solution for the Schrödinger equation. It is the most basic level of *ab initio* calculation and is only an exact calculation for $N \leq 1$ systems.

When having multi-electronic systems HF approximates the wave function with a single Slater determinant in the one-electron wave function basis. “*Every normalizable antisymmetric wave function can be expressed as the sum of a series of Slater determinants built up from a complete basis set of one-electron functions*”⁴⁶.

For building the Hamiltonian the no. of electrons (N), atomic numbers (Z_A) and atomic positions (R_A) are required: $(N, Z_A, R_A) \rightarrow \hat{H} \rightarrow \Psi \rightarrow E$, $E = E[N, Z_A, R_A]$. Thus, the energy is

^{2*} Owing to the mass of the electrons compared to the mass of protons and neutrons is negligible, we consider that the nucleus is static while electrons are orbiting around it.

a function of those parameters. The energy of the ground state can be calculated with the variational method for the minimum Ψ allowed. The variational principle states that the energy computed from a guessed Ψ is an upper bound to the true ground-state energy E_0 .

HF can be taken as starting point for higher levels of theory by adding extra approximation of the missing correlation energy. The Møller-Plesset series or couple cluster models are examples. Although an *ab initio* approach based on $4N$ variables; $N(e^-) \Psi = f(3N \text{ spatial} + N \text{ spin variables})$ is reliable, its equations are too complex and it is too computationally expensive for complicated structures. On the other hand, semi-empirical methods which require either experimental data and/or so many approximations are applicable to different molecules with an almost limitless number of atoms since they are not very complex calculations.

1.4.1 DFT calculations

This is an alternative variational procedure of solving the Schrödinger equation, which since the 1980s has been growing in popularity. The mean unsigned error of DFT on a broad chemistry energetic database has been improved by a factor of 3.7^{47} . It can be considered either as an *ab initio* or semi-empirical method since some of its common functionals use empirical parameters. In DFT, the electronic energy functional is minimized with the electronic density ρ .

$\rho(r)$ represents the likelihood for any electron N of being in a volume dr , which can be experimentally determined e.g. by X-ray diffraction. Knowing the following properties:

$$\rho(\mathbf{r}) \geq 0 \quad \text{Equation 12}$$

$$\rho_{(\mathbf{r} \rightarrow \infty)} = 0 \quad \text{Equation 13}$$

$$\int \rho(\mathbf{r}) d\mathbf{r} = N \quad \text{Equation 14}$$

$$\lim_{\mathbf{r} \rightarrow R_A} \left[\frac{d}{dr} + 2Z_A \right] \vec{\rho}(\mathbf{r}) = 0 \quad \text{Equation 15}$$

electron density is a non-negative function (Eq. 12) which vanishes at infinity (Eq. 13), the nuclear positions are maxima for the function (R_A), it integrates the total number of electrons for the system (Eq. 14), and also give information about nuclear charge (Z_A , Eq 15). One could say that ρ contains enough information to define the previously described Hamiltonian. $(\rho) \rightarrow \hat{H} \rightarrow \Psi^2 \rightarrow E, \mathbf{E}_0 = \mathbf{E}[\rho_0]$

The main problem with the DFT method is that even being an exact theory it is only applicable as an approximation except for the simplest models. The total energy of a system can be written again as the sum of e^-n^+ interactions (E_{Ne}), kinetic energy (T) and e^-e^- interactions (E_{ee}). See eq. 16.

$$\mathbf{E}[\rho] = \mathbf{E}_{Ne}[\rho] + \mathbf{T}[\rho] + \mathbf{E}_{ee}[\rho] \quad \text{(Equation 16)}$$

Chapter 1

where the blue terms are unknown^{3*}. Kohn and Sham suggested the calculation of the exact kinetic energy of a non-interacting reference system with the same density as the real, interacting one. That $E_{xc}[\rho]$ contains everything that is unknown (Eq. 17).

$$E[\rho] = E_{Ne}[\rho] + J[\rho] + T_s[\rho] + E_{xc}[\rho] \quad (\text{Equation 17})$$

where $E_{Ne}[\rho]$ is the e^-n^+ interaction, $J[\rho]$ is the classical Coulomb interaction between electronic clouds, $T_s[\rho]$ is kinetic term which is not equal to the real kinetic energy of the system and $E_{xc}[\rho]$ is the exchange-correlation functional. The explicit form of the $E_{xc}[\rho]$ functional is the major challenge in DFT.

When the Schrödinger equation is expressed in terms of ρ it becomes a set of equations termed Kohn-Sham equations which are solved iteratively until a self-consistent calculation is achieved. Total energy is expressed in terms of electron density distribution $\rho = \Psi^2$ rather than the wave function Ψ itself. This is a great advantage since electronic density is a much simpler term than a wavefunction. When having a system with N electrons, ρ only depends on three spatial variables whereas *ab initio* methods depend on $4N$ variables. In other words, DFT calculations can be very accurate with the advantage of being less computationally demanding when compared with *ab initio* methods. The use of DFT is remarkable for d-metals in giving better agreement with experimental values than obtained with other methods.

The spin-polarized Kohn–Sham (KS) formalism involves a Slater determinant formed from a set of N fictitious single-particle spin-orbitals corresponding to a non-interacting system of electrons with the same spin densities. Therefore, KS orbitals satisfy a set of coupled analogous equations to the HF but contain the exchange-correlation potential instead HF exchange potential⁴⁹. (Table 1-2).

	e ⁻ /e ⁻ correlation	e ⁻ /e ⁻ exchange
HF theory	ignores	exact
DFT	approximate	approximate
Hybrid DFT	approximate	exact

Table 1-2: Comparison between the two systems of approximation.

There are several levels of calculation among the computational methods, for example BLYP (Generalized Gradient Approximation). In fact, DFT is often combined with HF theory to create hybrid DFT. B3LYP (Global Hybrid Generalized Gradient Approximation) is a very popular example because is faster than post-HF methods and quite accurate. There is a term known as Jacob’s ladder which compares the different methods according to their quality:

^{3*} See the Tomas-Fermi model, which expresses all energetic terms as an electron density functional with poor approximation of the kinetic energy⁴⁸. Eschrig, H., *The Fundamentals of Density Functional Theory*. Vieweg+Teubner Verlag, Wiesbaden: 1996.

Chapter 1

“Earth”

Hartree-Fock → LDA → GGA → meta-GGA → hybrids → generalized RPA →

Chemical accuracy.

“Heaven”

Despite this, there is no systematic way of improving the results of a calculation. The most effective modus operandi is to choose the method that gives the best results by comparison with experimental values or with some higher level calculations, independent of its position in Jacob’s ladder.

Appropriate levels of theory and basis sets need to be chosen for a calculation. In other words, we need to model the atomic radial distribution of the electrons. The basis sets are optimised for atoms so atomic orbitals are calculated instead of molecular orbitals. Thus, adding polarization functions represented by (*) is a good approximation. Diffuse functions (+) which make larger versions of the atomic orbitals, can be important for atoms carrying extra charge. Common basis sets are the Split-valence, for example 6-31-G* and 6-311G*. The classification of basis sets follows as the higher the number and the more numbers the better.

All DFT calculations presented here were performed by the SPARTAN’16 or SPARTAN’ 18 Software⁵⁰. Equilibrium geometries were estimated by using B86PW91 method (GGA) with def2-SVP basis set (Karlsruhe). This functional/basis set combination has performed well in other computational studies of spin state properties in compounds related to those in this thesis⁵¹.

1.5 Bibliography

1. McNaught, A. D.; Wilkinson, A., *IUPAC. Compendium of Chemical Terminology, 2nd ed. (the "Gold Book")*. WileyBlackwell; 2nd Revised edition edition.
2. Chemistry-LibreText [Crystal_Field_Theory. chem.libretexts.org/Bookshelves/Inorganic_Chemistry/Supplemental_Modules_\(Inorganic_Chemistry\)/Crystal_Field_Theory/Crystal_Field_Theory](https://chem.libretexts.org/Bookshelves/Inorganic_Chemistry/Supplemental_Modules_(Inorganic_Chemistry)/Crystal_Field_Theory/Crystal_Field_Theory).
3. Housecroft, C.; Sharpe, A. G., *Inorganic Chemistry*. Pearson Education Limited: 2012.
4. Atkins, P.; De Paula, J., *Physical Chemistry + Exploring Physical Chemistry Access Card + Physical Chemistry Ebook Access Card, 12 Month Access*. Macmillan Higher Education: 2011.
5. Tchougréeff, A. L.; Dronskowski, R., Nephelauxetic effect revisited. *International Journal of Quantum Chemistry* **2009**, *109* (11), 2606-2621.
6. Bain, G. A.; Berry, J. F., Diamagnetic Corrections and Pascal's Constants. *Journal of Chemical Education* **2008**, *85* (4), 532.

Chapter 1

7. Yatsunyk, L. A.; Walker, F. A., Structural, NMR, and EPR Studies of $S = 1/2$ and $S = 3/2$ Fe(III) Bis(4-Cyanopyridine) Complexes of Dodecasubstituted Porphyrins. *Inorganic Chemistry* **2004**, *43* (2), 757-777.
8. Hayami, S.; Holmes, S. M.; Halcrow, M. A., Spin-state switches in molecular materials chemistry. *Journal of Materials Chemistry C* **2015**, *3* (30), 7775-7778.
9. Evangelio, E.; Ruiz-Molina, D., Valence tautomerism: new challenges for electroactive ligands. *European Journal of Inorganic Chemistry* **2005**, *2005* (15), 2957-2971.
10. Launay, J. P.; Verdager, M., *Electrons in Molecules: From Basic Principles to Molecular Electronics*. OUP Oxford: 2013.
11. Maryunina, K. Y.; Zhang, X.; Nishihara, S.; Inoue, K.; Morozov, V. A.; Romanenko, G. V.; Ovcharenko, V. I., A heterospin pressure sensor. *Journal of Materials Chemistry C* **2015**, *3* (30), 7788-7791.
12. Decurtins, S.; Gütllich, P.; Köhler, C. P.; Spiering, H.; Hauser, A., Light-induced excited spin state trapping in a transition-metal complex: The hexa-1-propyltetrazole-iron (II) tetrafluoroborate spin-crossover system. *Chemical Physics Letters* **1984**, *105* (1), 1-4.
13. König, E., Nature and dynamics of the spin-state interconversion in metal complexes. In *Complex Chemistry*, Springer Berlin Heidelberg: Berlin, Heidelberg, 1991; pp 51-152.
14. Elhaik, J.; Kilner, C. A.; Halcrow, M. A., Insight into structure: function relationships in a molecular spin-crossover crystal, from a related weakly cooperative compound. *European Journal of Inorganic Chemistry* **2014**, *2014* (26), 4250-4253.
15. Brooker, S., Spin crossover with thermal hysteresis: practicalities and lessons learnt. *Chemical Society Reviews* **2015**, *44* (10), 2880-2892.
16. Gütllich, P.; Hauser, A., Thermal and light-induced spin crossover in iron(II) complexes. *Coordination Chemistry Reviews* **1990**, *97*, 1-22.
17. Letard, J.-F., Photomagnetism of iron(ii) spin crossover complexes-the T(LIESST) approach. *Journal of Materials Chemistry* **2006**, *16* (26), 2550-2559.
18. Hayami, S.; Hiki, K.; Kawahara, T.; Maeda, Y.; Urakami, D.; Inoue, K.; Ohama, M.; Kawata, S.; Sato, O., Photo-Induced Spin Transition of Iron(III) Compounds with π - π Intermolecular Interactions. *Chemistry – A European Journal* **2009**, *15* (14), 3497-3508.
19. (a) Kulmaczewski, R.; Olguín, J.; Kitchen, J. A.; Feltham, H. L. C.; Jameson, G. N. L.; Tallon, J. L.; Brooker, S., Remarkable Scan Rate Dependence for a Highly Constrained Dinuclear Iron(II) Spin Crossover Complex with a Wide Thermal Hysteresis Loop. *Journal of the American Chemical Society* **2014**, *136* (3), 878-881; (b) Yamasaki, M.; Ishida, T., Heating-rate dependence of spin-crossover hysteresis observed in an iron(ii) complex having tris(2-pyridyl)methanol. *Journal of Materials Chemistry C* **2015**, *3* (30), 7784-7787.
20. Gütllich, P.; Ksenofontov, V.; Gaspar, A. B., Pressure effect studies on spin crossover systems. *Coord Chem Rev* **2005**, *249*.
21. Gütllich, P.; Goodwin, H. A., *Spin Crossover in Transition Metal Compounds III*. Springer: 2004.

Chapter 1

22. Negre, N.; Goiran, M.; Bousseksou, A.; Haasnoot, J.; Boukheddaden, K.; Askenazy, S.; Varret, F., High magnetic field induced spin transition, H.M.F.I.S.T. effect, in [Fe_{0.52}Ni_{0.48}(btr)₂(NCS)₂]H₂O. *Synthetic Metals* **2000**, *115* (1–3), 289-292.
23. Hauser, A., Ligand Field Theoretical Considerations. In *Spin Crossover in Transition Metal Compounds I*, Gütllich, P.; Goodwin, H. A., Eds. Springer Berlin Heidelberg: Berlin, Heidelberg, 2004; pp 49-58.
24. Robinson, M. A.; Curry, J. D.; Busch, D. H., Complexes Derived from Strong Field Ligands. XVII. Electronic Spectra of Octahedral Nickel(II) Complexes with Ligands of the α -Diimine and Closely Related Classes. *Inorganic Chemistry* **1963**, *2* (6), 1178-1181.
25. Cambi, L.; Szegö, L., Über die magnetische susceptibilität der komplexen verbindungen. *Berichte der deutschen chemischen Gesellschaft (A and B Series)* **1931**, *64* (10), 2591-2598.
26. Martinho, P. N.; Gildea, B.; Harris, M. M.; Lemma, T.; Naik, A. D.; Müller-Bunz, H.; Keyes, T. E.; Garcia, Y.; Morgan, G. G., Cooperative spin transition in a mononuclear manganese(III) complex. *Angewandte Chemie International Edition* **2012**, *51* (50), 12597-12601.
27. Hayami, S.; Komatsu, Y.; Shimizu, T.; Kamihata, H.; Lee, Y. H., Spin-crossover in cobalt(II) compounds containing terpyridine and its derivatives. *Coordination Chemistry Reviews* **2011**, *255* (17–18), 1981-1990.
28. Trzop, E.; Buron-Le Cointe, M.; Cailleau, H.; Toupet, L.; Molnar, G.; Bousseksou, A.; Gaspar, A. B.; Real, J. A.; Collet, E., Structural investigation of the photoinduced spin conversion in the dinuclear compound [[Fe(bt)(NCS)₂]₂(bpym)]: toward controlled multi-stepped molecular switches. *Journal of Applied Crystallography* **2007**, *40* (1), 158-164.
29. (a) Schneider, C. J.; Moubaraki, B.; Cashion, J. D.; Turner, D. R.; Leita, B. A.; Batten, S. R.; Murray, K. S., Spin crossover in di-, tri- and tetranuclear, mixed-ligand tris(pyrazolyl)methane iron(ii) complexes. *Dalton Transactions* **2011**, *40* (26), 6939-6951; (b) Newton, G. N.; Nihei, M.; Oshio, H., Cyanide-bridged molecular squares – The building units of prussian blue. *European Journal of Inorganic Chemistry* **2011**, *2011* (20), 3031-3042.
30. Halcrow, M. A., The foundation of modern spin-crossover. *Chemical Communications* **2013**, *49* (93), 10890-10892.
31. Baker, W. A.; Bobonich, H. M., Magnetic Properties of Some High-Spin Complexes of Iron(II). *Inorganic Chemistry* **1964**, *3* (8), 1184-1188.
32. König, E.; Madeja, K., Unusual magnetic behaviour of some iron(II)-bis-(1,10-phenanthroline) complexes. *Chemical Communications (London)* **1966**, (3), 61-62.
33. Oliver, J. D.; Mullica, D. F.; Hutchinson, B. B.; Milligan, W. O., Iron-nitrogen bond lengths in low-spin and high-spin iron(II) complexes with poly(pyrazolyl)borate ligands. *Inorganic Chemistry* **1980**, *19* (1), 165-169.
34. Lemerrier, G.; Bréfuel, N.; Shova, S.; Wolny, J. A.; Dahan, F.; Verelst, M.; Paulsen, H.; Trautwein, A. X.; Tuchagues, J.-P., A Range of Spin-Crossover Temperature $T_{1/2} > 300$ K

Chapter 1

Results from Out-of-Sphere Anion Exchange in a Series of Ferrous Materials Based on the 4-(4-Imidazolylmethyl)-2-(2-imidazolylmethyl)imidazole (trim) Ligand, $[\text{Fe}(\text{trim})_2]\text{X}_2$ (X=F, Cl, Br, I): Comparison of Experimental Results with Those Derived from Density Functional Theory Calculations. *Chemistry – A European Journal* **2006**, *12* (28), 7421-7432.

35. Renovitch, G. A.; Baker, W. A., Spin equilibrium in tris(2-aminomethylpyridine)iron (II) halides. *Journal of the American Chemical Society* **1967**, *89* (24), 6377-6378.

36. Sorai, M.; Ensling, J.; Hasselbach, K. M.; Gütllich, P., Mössbauer effect study on low-spin $^1\text{A}_1 \rightleftharpoons$ high spin $^5\text{T}_2$ transition in $[\text{Fe}(\text{2-pic})_3]\text{Cl}_2$. *Chemical Physics* **1977**, *20* (2), 197-208.

37. Santoro, A.; Kershaw Cook, L. J.; Kulmaczewski, R.; Barrett, S. A.; Cespedes, O.; Halcrow, M. A., Iron(II) complexes of tridentate indazolylpyridine ligands: enhanced spin-crossover hysteresis and ligand-based fluorescence. *Inorganic Chemistry* **2015**, *54* (2), 682-693.

38. Cook, L. J. K.; Kulmaczewski, R.; Cespedes, O.; Halcrow, M. A., Different spin-state behaviors in isostructural solvates of a molecular iron(II) complex. *Chemistry – A European Journal* **2016**, *22* (5), 1789-1799.

39. Kershaw Cook, L. J.; Thorp-Greenwood, F. L.; Comyn, T. P.; Cespedes, O.; Chastanet, G.; Halcrow, M. A., Unexpected spin-crossover and a low-pressure phase change in an iron(II)/dipyrazolylpyridine complex exhibiting a high-spin Jahn–Teller distortion. *Inorganic Chemistry* **2015**, *54* (13), 6319-6330.

40. Halcrow, M. A., Recent advances in the synthesis and applications of 2,6-dipyrazolylpyridine derivatives and their complexes. *New Journal of Chemistry* **2014**, *38* (5), 1868-1882.

41. McCusker, J. K.; Rheingold, A. L.; Hendrickson, D. N., Variable-Temperature Studies of Laser-Initiated $5\text{T}_2 \rightarrow 1\text{A}_1$ Intersystem Crossing in Spin-Crossover Complexes: Empirical Correlations between Activation Parameters and Ligand Structure in a Series of Polypyridyl Ferrous Complexes. *Inorganic Chemistry* **1996**, *35* (7), 2100-2112.

42. (a) Marchivie, M.; Guionneau, P.; Letard, J.-F.; Chasseau, D., Photo-induced spin-transition: the role of the iron(II) environment distortion. *Acta Crystallographica Section B* **2005**, *61* (1), 25-28; (b) Guionneau, P.; Marchivie, M.; Bravic, G.; Létard, J.-F.; Chasseau, D., Co(ii) molecular complexes as a reference for the spin crossover in Fe(ii) analogues. *Journal of Materials Chemistry* **2002**, *12* (8), 2546-2551.

43. Halcrow, M. A., Iron(II) complexes of 2,6-di(pyrazol-1-yl)pyridines—A versatile system for spin-crossover research. *Coordination Chemistry Reviews* **2009**, *253* (21–22), 2493-2514.

44. Holland, J. M.; McAllister, J. A.; Kilner, C. A.; Thornton-Pett, M.; Bridgeman, A. J.; Halcrow, M. A., Stereochemical effects on the spin-state transition shown by salts of $[\text{FeL}_2]^{2+}$ [L = 2,6-di(pyrazol-1-yl)pyridine]. *Journal of the Chemical Society, Dalton Transactions* **2002**, (4), 548-554.

Chapter 1

45. Halcrow, M. A., Structure: function relationships in molecular spin-crossover complexes. *Chemical Society Reviews* **2011**, 40 (7), 4119-4142.
46. Löwdin, P.-O., Quantum theory of many-particle systems. I. Physical interpretations by means of density matrices, natural spin-orbitals, and convergence problems in the method of configurational interaction. *Physical Review* **1955**, 97 (6), 1474.
47. Peverati, R.; Truhlar, D. G., Quest for a universal density functional: the accuracy of density functionals across a broad spectrum of databases in chemistry and physics. *Philosophical Transactions of the Royal Society A: Mathematical, Physical and Engineering Sciences* **2014**, 372 (2011).
48. Eschrig, H., *The Fundamentals of Density Functional Theory*. Vieweg+Teubner Verlag, Wiesbaden: 1996.
49. Kohn, W.; Sham, L. J., Self-Consistent Equations Including Exchange and Correlation Effects. *Physical Review* **1965**, 140 (4A), A1133-A1138.
50. Inc, W. *SPARTAN' 18*, Irvine CA, 2018.
51. Houghton, B. J.; Deeth, R. J., Spin-State Energetics of FeII Complexes – The Continuing Voyage Through the Density Functional Minefield. *European Journal of Inorganic Chemistry* **2014**, 2014 (27), 4573-4580.

Chapter 2 – Bis (Pyrazolyl) Triazine Derivatives and their Iron(II) Complexes

2.1 Introduction

The synthesis of the bpt family of ligands is described along with the characterization of their iron(II) complexes obtained.

2.1.1 Bis (pyrazolyl) pyridine (bpp) iron(II) complexes

Iron(II) complexes with 2,6-di(pyrazol-1-yl)pyridine ligands (1-bpp) (Figure 2.1a) and several derivatives are well known within the spin crossover community and have been studied in Halcrow group for the last 15 years¹. There are various synthetic routes available for bpp ligands with different substituents. Many of these iron(II) complexes present SCO in solution however, and only around half of them trigger the spin transition in the solid state². It is clear that functionalising the pyridine or the pyrazole rings has a strong effect on SCO behaviour³. Derivatizing the bpp backbone by adding second functionalities is a powerful method to produce multifunctional SCO compounds⁴. However, synthesizing this kind of ligand generally involves tedious multistep procedures with low yields. Thus, finding an alternative family of ligands which is more easily modifiable than bpp ligands was our goal.

2.1.2 Bis (pyrazolyl) triazine (bpt) iron(II) complexes

Iron(II) complexes of other similar tridentate ligands with different azabenzenes have recently been reported as SCO active. Examples include, iron(II) salts of 2,6-di(pyrazol-1-yl)pyrazine (Figure 2.1b)⁵ and 2,6-di(pyrazol-1-yl)pyrimidine (Figure 2.1c)⁶.

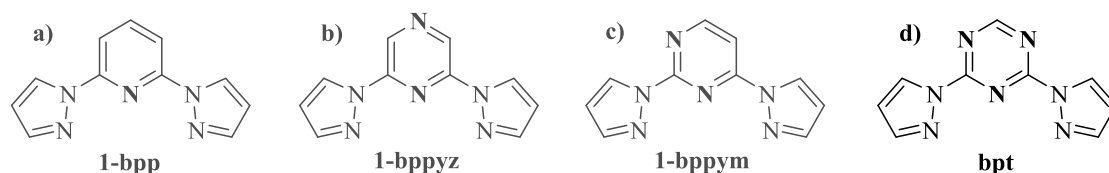


Figure 2.1: New family of ligands proposed “d” and related scaffolds whose iron(II) complexes undergo SCO.

2,4-Di(pyrazol-1-yl)1,3,5-triazine ligands (Figure 2.1d), designed by increasing the nitrogen content of the 6-membered ring in the centre of the molecule, were proposed as a potential new SCO family of ligands which can be easily tunable.

2.2 Results and discussion

2.2.1 Synthesis and characterization of the ligands

The new family of bpt ligands synthesized in this work was based on the 2,4-di(pyrazol-1-yl)-1,3,5-triazine scaffold (Figure 2.2) varying the substituents in either the 6-position of the triazine ring (R_1) or the 3,4,5-pyrazole sites (R_2). The bpt ligand (where $R_1 = H$ and $R_2 = H$) was also synthesized, however it will be discussed later in chapter 4.

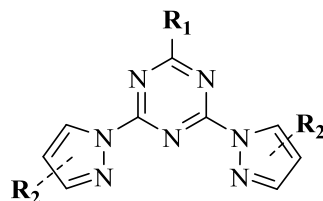


Figure 2.2: Bis (pyrazolyl) triazine scaffold (bpt).

Cyanuric chloride is the precursor of the new ligands. Aerobic conditions, room temperature and non-dry solvents were used for the reactions discussed here (Figure 2.3).

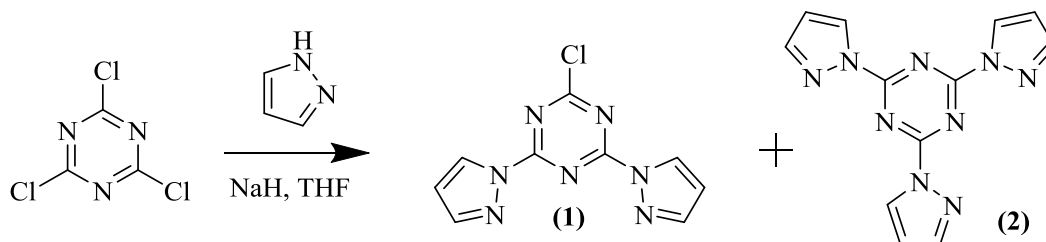


Figure 2.3: Synthetic scheme of the starting material (1) and (2).

Pyrazolate attacks the strongly electrophilic cyanuric chloride carbon atoms triggering a nucleophilic aromatic substitution of the chloride group. 2,4-Di(pyrazol-1-yl)-6-chloro-1,3,5-triazine (**1**) (Figure 2.3) was selected as a starting material for the other ligands, analogously to de Hoog *et al*⁷. However, mixtures of (**1**) and (**2**) were always obtained from this reaction. The yields of (**1**) were low and hard to control due to the highly reactive nature of 1,3,5-triazine ring.

Triethylamine is a weaker base, so it was used as an alternative to NaH in order to shift the previous reaction towards ligand (**1**). A combination of (**1**), (**2**) and (**3**) (Figure 2.4) was obtained instead. These results contrast with the ones reported by Rothmann *et al* in an analogous reaction with carbazole as the nucleophile, where *n*-BuLi was used as base at high temperature (70°C) to yield the di substituted ligand⁸.

The reactivity of the 1,3,5-triazine ring allowed the use of ligand (**2**) as a starting material for the synthesis of the new bpt R_1 family of ligands through nucleophilic aromatic substitution (Figure 2.4).

Chapter 2

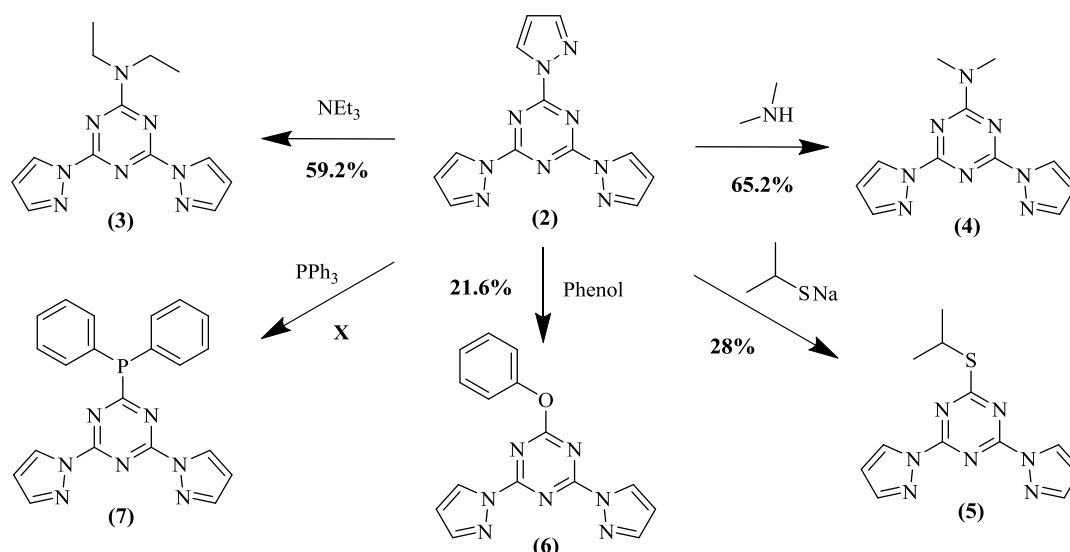


Figure 2.4: Synthetic scheme of bptR₁ ligands. Both (1) or (2) ligands can be used as starting material. Yields are given as %.

Compounds (2) and (3) were described in the literature before^{9,10}. Three novel organic compounds; 2,4-di(pyrazol-1-yl)-6-chloro-1,3,5-triazine, (1), 2,4-di(pyrazol-1-yl)-6-(dimethylamino)-1,3,5-triazine, (4) and 2,4-di(pyrazol-1-yl)-6-(isopropylsulfanyl)-1,3,5-triazine, (5) have been fully characterized by ¹H NMR, ¹³C NMR, microanalysis, ESMS, melting point, and X-ray single crystal diffraction. Although ligand 2,4-di(pyrazol-1-yl)-6-phenoxy-1,3,5-triazine, (6) was novel too, we decided to stop investing time on it before the full characterization was completed. It was similar to ligand (12) (Figure 2.6) which was not synthesized but whose iron(II) complex was obtained. The synthesis approach for ligand (7) was analogous to the synthesis of ligand (3) with PPh₃ instead of NEt₃. (7) was not isolated in its neutral form and due to solubility problems it was not purified. When this crude ligand was reacted with iron perchlorate, it assembled into a supramolecular complex [7*] through hydrogen bonds with a pyrazolium cation (Figure 2.6). No more research was performed in that direction.

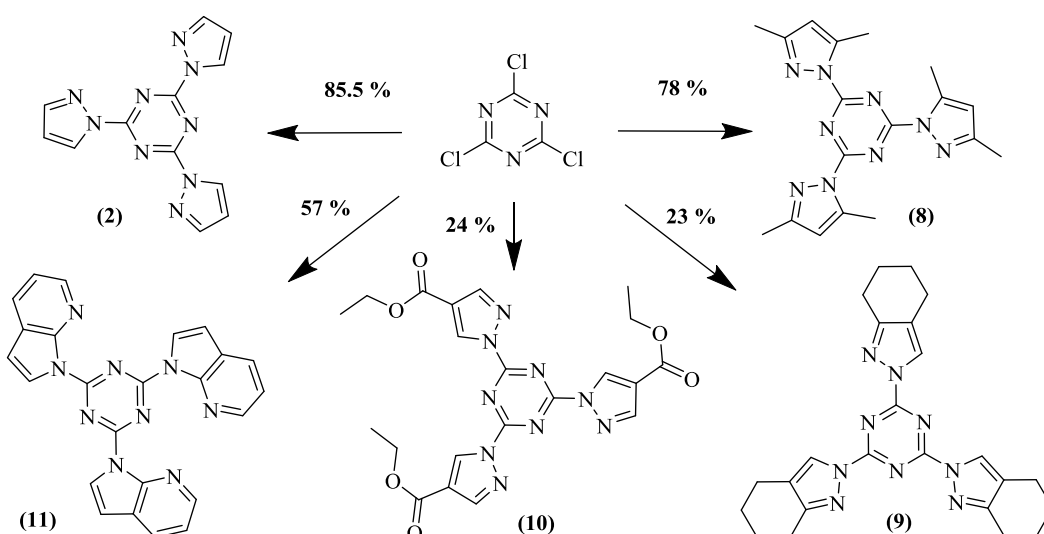


Figure 2.5: Synthetic scheme of bptR₂ ligands. Yields given as %.

Additionally, a few other bptR_2 type ligands were synthesized by using different nucleophiles in the same reaction with cyanuric chloride, Figure 2.5. Compounds (2), (8) and (11) had been published previously^{9b, 10a, 11}. Ligand (10) was discarded because no iron(II) complex was isolated from it. Therefore, only the novel ligand 2,4,6-tris(4,5,6,7-tetrahydro-2-indazol-2-yl)-1,3,5-triazine (9) was fully characterized.

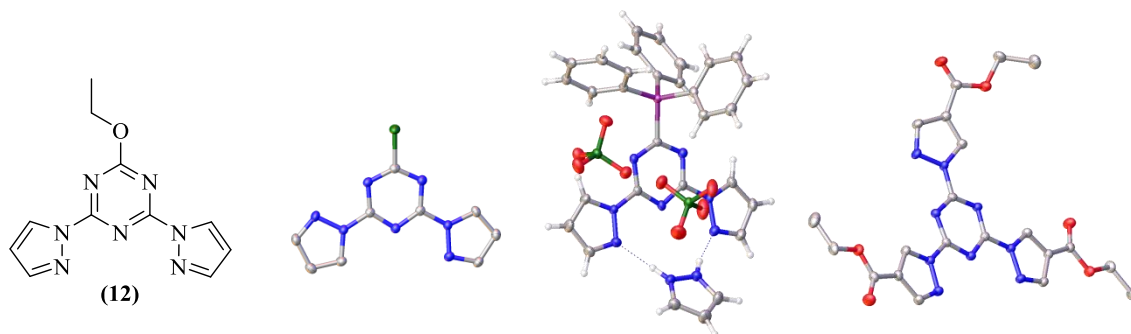


Figure 2.6: Structure of ligand (12) which was not synthesized in this work. Few examples of the crystal structures obtained ordered from left to right; (1) $P2_1/c$, $[7^*] P\bar{1}$ and (10) $P2_1/n$. Solvent molecules and hydrogen atoms of structures (1) and (10) have been removed for clarity.

In conclusion, the 1,3,5-triazine skeleton is very reactive. All these reactions work reasonably well in mild conditions but the yields are unreliable. Thus, it is believed that cyanuric chloride would react with any nucleophile present in THF solution.

Ligands (4), (5) and (12) have different substituents in the 6-position of the triazine (-NR₂, -SR and -OR), and were abbreviated with words; **bptOEt**, **bptNMe₂** and **bptSIP** respectively.

2.2.2 Synthesis of iron(II) complexes

The labelling criteria of the metal complexes are the following; the homoleptic complex of a given ligand (X) such as bis(X)iron(II) tetrafluoroborate is labelled as [X]B, or as [X]C if perchlorate is the counter-anion used. For compounds with more than one structure or polymorph, a third parameter identifying each one is added; α , β , γ , and so on. All complexes were made from iron(II) salts unless otherwise stated. Other important considerations will be explained during the discussion when needed.

Complex formation was monitored for the appearance of a characteristic yellow colour immediately when ligands were mixed in solution with iron(II) salts. The first complexation procedure (Figure 2.7) was described by Baker et al.¹² It consists in mixing ligands and metal salts in hot ethanol and slowly cooling the mixture. Ligand (1) yielded single crystals of complex [12]B by this route, where ethanol has performed an aromatic nucleophilic substitution with its chlorine moiety. Similar reactions were reported before¹³, therefore protic solvents were discarded for this study.

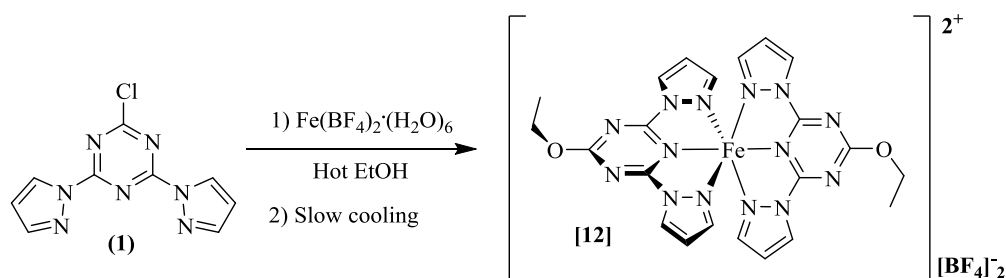


Figure 2.7: Method 1 of complexation and crystallization of $[\text{Fe}(\text{bptOEt})_2](\text{BF}_4)_2$, [12]B.

The strategy used subsequently was described by Cook *et al*¹⁴ and is similar to the previous one (Figure 2.8). However, in this case the complex was isolated by addition of antisolvent. Single crystals were obtained by diffusing ether into a concentrated complex solution. Variations in the solvent system used are detailed in Chapter 8.

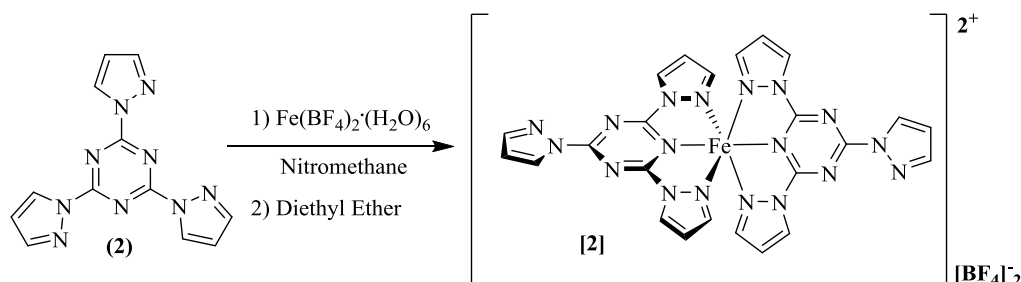


Figure 2.8: Example of the crystallization method used for the rest of complexes.

Iron(II) salts containing ligands (1), (10) and (11) were not obtained. The chloride moiety of ligand (1) becomes susceptible to hydrolysis as soon as a transition metal coordinates the ligand. Some polymetallic structures could be present in the mixture precluding the purification of the complex; a similar scenario will be discussed in Chapter 3. The bpt family of complexes showed unexpected weak pyrazolyl-iron bonds (Experimentally determined, Table 2-1). Besides, electron withdrawing groups (EWG) in the 4-position of the pyrazole ring weaken the M-L bond for this type of complex³. Therefore, the iron(II) complex of ligand (10) with ethyl carboxylate in the 4-position was not stable. Finally, in an attempt to favour the LS state, ligand (11) was proposed. The two azaindazolyl N-donor are very close to each other whereas the triazinyl nitrogen is too far away compared to the rest of bpp-like ligands. Such a geometry could prevent the complexation itself.

2.2.3 Single crystal and powder X-Ray diffraction

Crystal structures of the following iron(II) salts were collected; [12]B, [2]_aB, [2]_βB, [2]_αC, [3]_αB, [3]_βB, [3]C, [4]B, [5]B, [6]B, [8]_αB, [8]_βB and [9]B. An iron(III) complex of ligand (3) was also prepared; Fe^(III)[3]C. Powder patterns were obtained from the bulk

precipitate from adding ether to the complex solution and compared with the pattern simulated from the crystal structures using the Mercury software¹⁵.

2.2.3.1 Complex [12]B

Complex $[\text{Fe}(\mathbf{12})_2](\text{BF}_4)_2$ **[12]B** crystallized in $I4_1/a$ space group, and the asymmetric unit cell contains half of the complex (Figure 2.9).

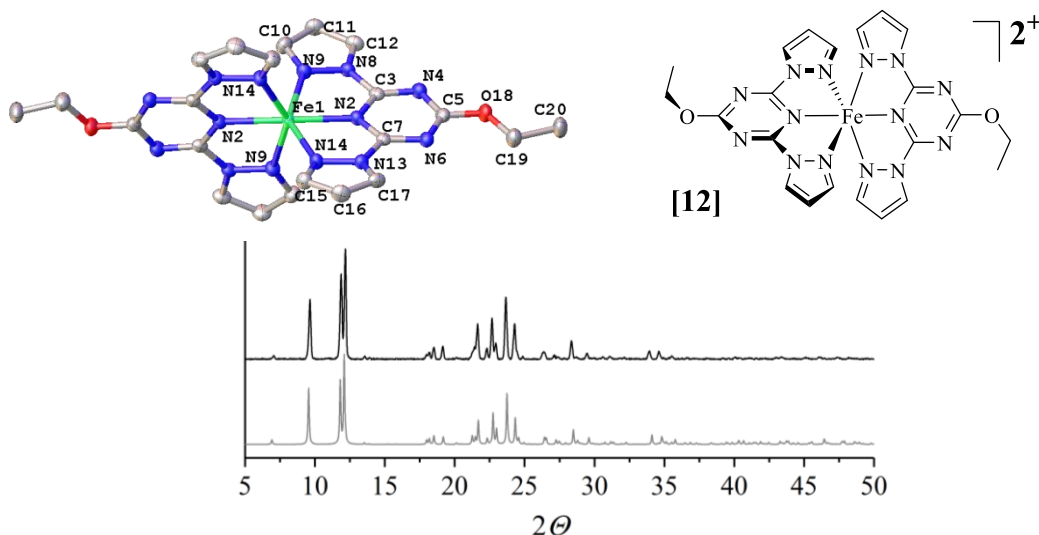


Figure 2.9: Crystal structure and powder diffraction pattern of **[12]B** complex. Counter-anions and hydrogen atoms of structures have been removed for clarity. The colour assignment in the plot is black for the experimental and grey for the simulated XRD.

2.2.3.2 Complexes $[\mathbf{2}]_\alpha\mathbf{B}$, $[\mathbf{2}]_\beta\mathbf{B}$ and $[\mathbf{2}]C$

Complex $[\text{Fe}(\mathbf{2})_2](\text{BF}_4)_2$ **[2]B** crystallized as two polymorphs. Polymorph α ($[\mathbf{2}]_\alpha\mathbf{B}$) is arranged in the cubic crystal system, in the $Ia\bar{3}d$ space group, and was mainly obtained during this work as octahedral-spherical yellow crystals. Polymorph β ($[\mathbf{2}]_\beta\mathbf{B}$) was observed only once as yellow needles. In that case the space group is tetragonal, $I4_1/acd$. The contents of the asymmetric unit cells are different. The main polymorph α contains 1/6 of the molecule while the second, polymorph β consists of 1/4. Both polymorphs exhibit symmetry-imposed disorder (Figure 2.10).

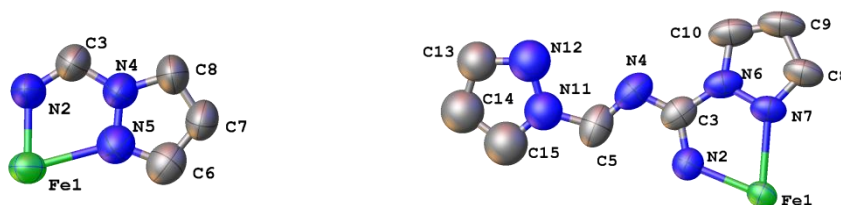


Figure 2.10: Asymmetric unit cell of $[\mathbf{2}]_\alpha\mathbf{B}$ on the left and $[\mathbf{2}]_\beta\mathbf{B}$ on the right. Counter-anions and hydrogen atoms of structures have been removed for clarity.

The main difference between the two models is that the iron occupancy is a random distribution along the cubic array of ligands in $[\mathbf{2}]_\alpha\mathbf{B}$ whereas it is fixed for $[\mathbf{2}]_\beta\mathbf{B}$. Perchlorate

salt **[2]C** was also prepared and it was isostructural with **[2]_αB**. See powder diffraction patterns (Figure 2.11).

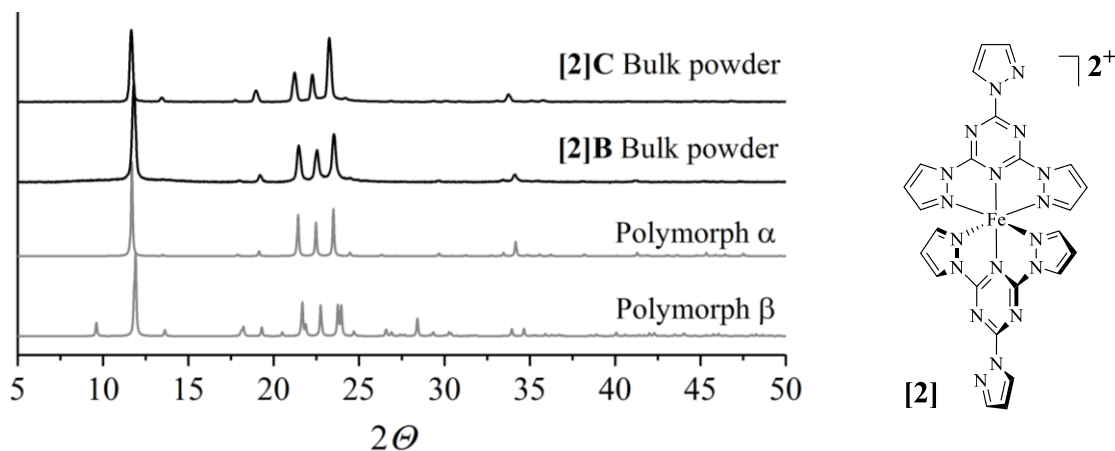


Figure 2.11: Powder diffraction pattern of **[2]B** and **[2]C** compared with the simulated polymorphs. The colour assignment in the plot is black for the experimental and grey for the simulated XRD.

2.2.3.3 Complexes **[3]_αB**, **[3]_βB** and **[3]C**

Two pseudopolymorphs were collected from $[\text{Fe}(\mathbf{3})_2](\text{BF}_4)_2$ and modelled in the triclinic $P\bar{1}$ space group. **[3]_αB** contains two unique complexes and a half molecule of DCM in the asymmetric unit cell while **[3]_βB** contains three complexes and approximately half a molecule of DCM disordered over several positions (Figure 2.12).

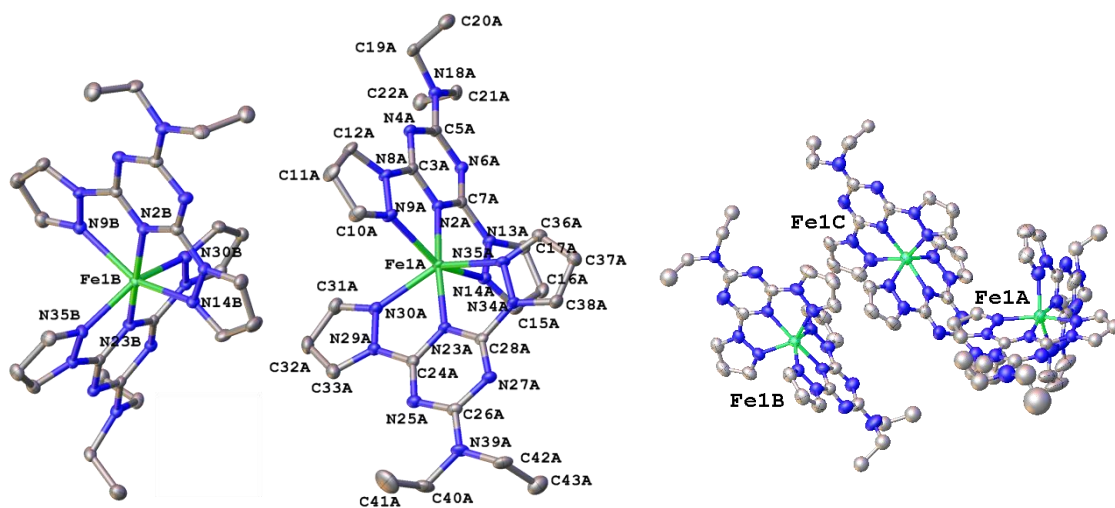


Figure 2.12: Crystal structure of **[3]_αB** and **[3]_βB** respectively. Counter-anions, solvent molecules and hydrogen atoms of structures have been removed for clarity.

The powder pattern of the bulk sample did not fit any of the polymorphs. However when a few mg of pure single crystal of **[3]_βB** were ground the result was positive (Figure 2.13).

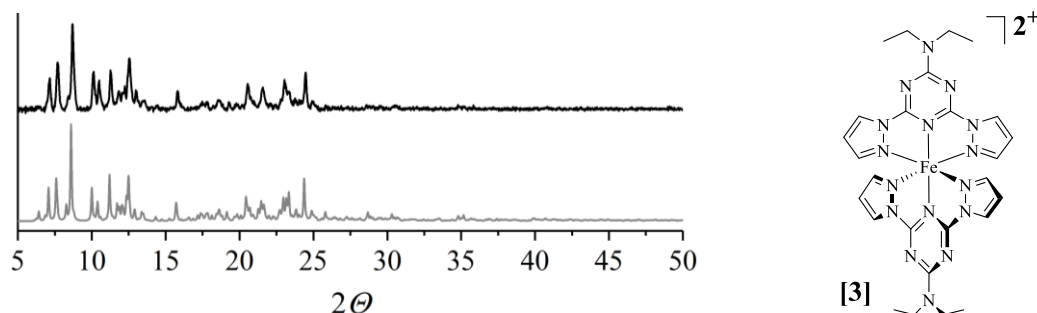


Figure 2.13: Powder pattern diffraction of polymorph β . The colour assignment in the plot is black for the experimental and grey for the simulated XRD.

Complex [3]C was crystallized in a different symmetry to any of the two [3]B structures, $P2_1/c$. It contains three molecules of nitromethane and one complex in the asymmetric unit cell.

2.2.3.4 Complex [4]B

$[\text{Fe}(\mathbf{4})_2](\text{BF}_4)_2$, [4]B crystallized in the tetragonal $I4_1/a$ space group, the asymmetric unit contains half of the complex and a disordered molecule of acetonitrile (Figure 2.14).

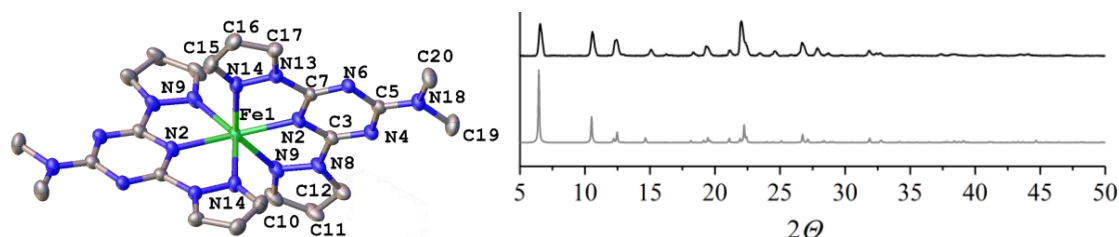


Figure 2.14: Crystal structure of [4]B and powder diffraction pattern. Counter-anions and hydrogen atoms of structures have been removed for clarity. The colour assignment in the plot is black for the experimental and grey for the simulated XRD.

2.2.3.5 Complex [5]B

$[\text{Fe}(\mathbf{5})_2](\text{BF}_4)_2$, [5]B complex crystallized in the monoclinic $P2_1/c$ space group, the asymmetric unit contains the complex (Figure 2.15).

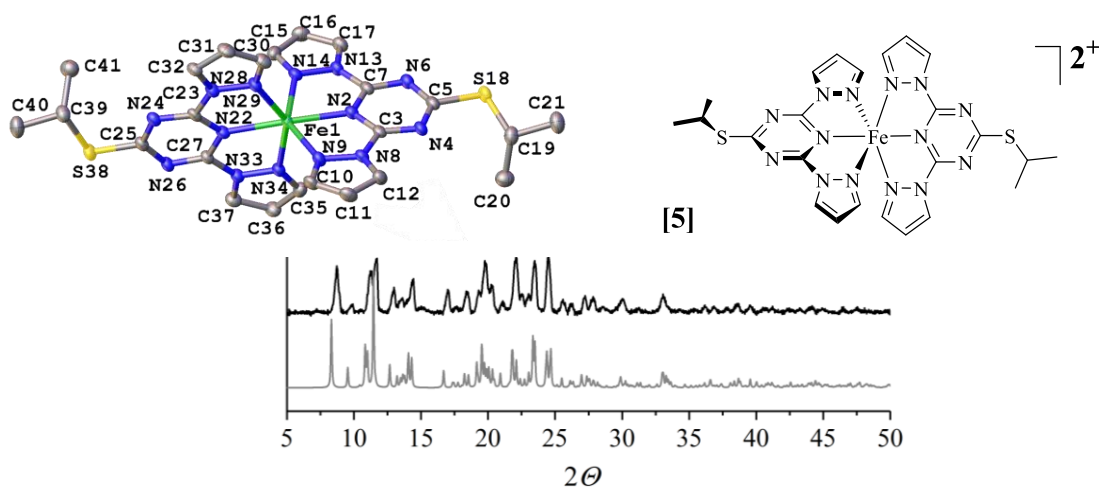


Figure 2.15: Crystal structure of [bptSIP]B, [5]B and powder diffraction pattern. Counter-anions and hydrogen atoms of structures have been removed for clarity. The colour assignment in the plot is black for the experimental and grey for the simulated XRD.

2.2.3.6 Complex [6]B

$[\text{Fe}(\mathbf{6})_2](\text{BF}_4)_2$, **[6]B** complex crystallized in the tetragonal $I4_1/a$ space group. The asymmetric unit contains half of the complex (Figure 2.16).

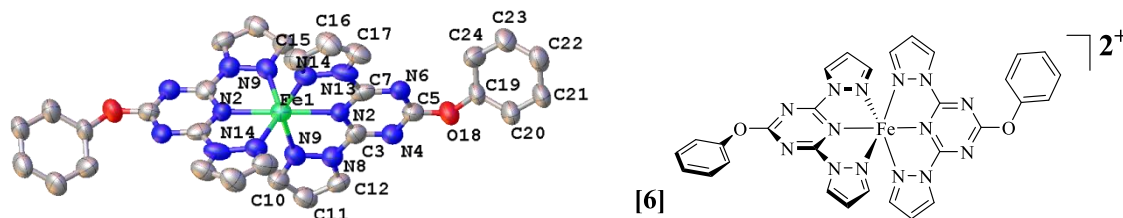


Figure 2.16: Crystal structure of **[6]B**. Hydrogen, Counter-anions and hydrogen atoms of structures have been removed for clarity.

2.2.3.7 Complexes $[\mathbf{8}]_{\alpha}\mathbf{B}$ and $[\mathbf{8}]_{\beta}\mathbf{B}$

$[\text{Fe}(\mathbf{8})_2](\text{BF}_4)_2$, **[8]B** crystallized as two different pseudopolymorphs; $[\mathbf{8}]_{\alpha}\mathbf{B}$ crystallized in the monoclinic $C2/c$ space group and contains half complex and one molecule of DCM in the asymmetric unit cell. $[\mathbf{8}]_{\beta}\mathbf{B}$ was triclinic $P\bar{1}$ containing three unique complexes, two DCM molecules and one molecule of diethyl ether in the refinement model. However, some electron density may remain unidentified due to the quality of the data (Figure 2.17).

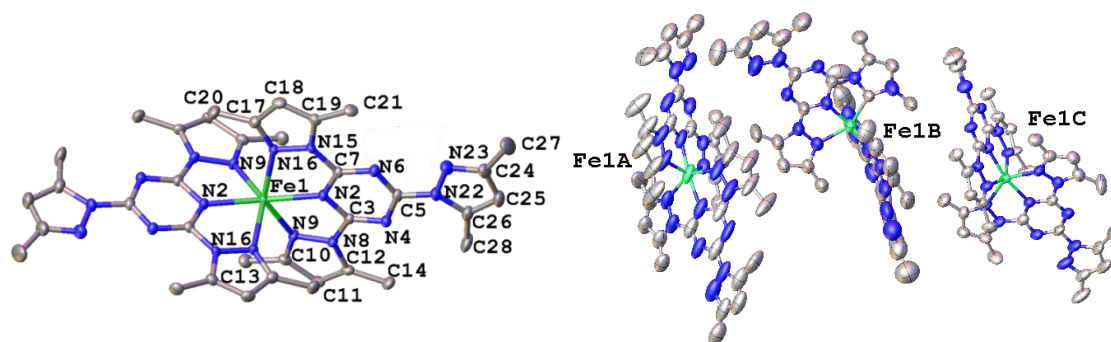


Figure 2.17: $[\mathbf{8}]_{\alpha}\mathbf{B}$ and $[\mathbf{8}]_{\beta}\mathbf{B}$ polymorphs respectively. Counter-anions, solvent molecules and hydrogen atoms of structures have been removed for clarity.

This compound became an amorphous powder even when a sample of pure single crystals was ground (Figure 2.18).

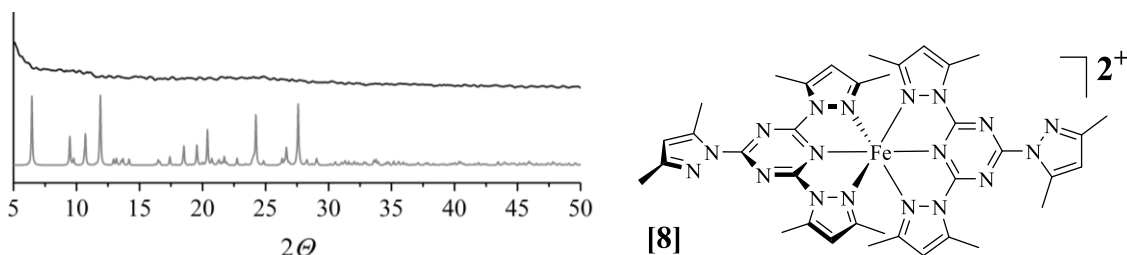


Figure 2.18: Powder pattern diffraction of **[8]B**. The colour assignment in the plot is black for the experimental and grey for the simulated XRD.

2.2.3.8 Complex [9]B

Finally, $[\text{Fe}(\mathbf{9})_2](\text{BF}_4)_2$, **[9]B** was crystallized in the triclinic $P\bar{1}$ space group. The asymmetric unit contains the complex and 1.55 disordered molecules of MeCN with 0.45 molecule of DCM (Figure 2.19).

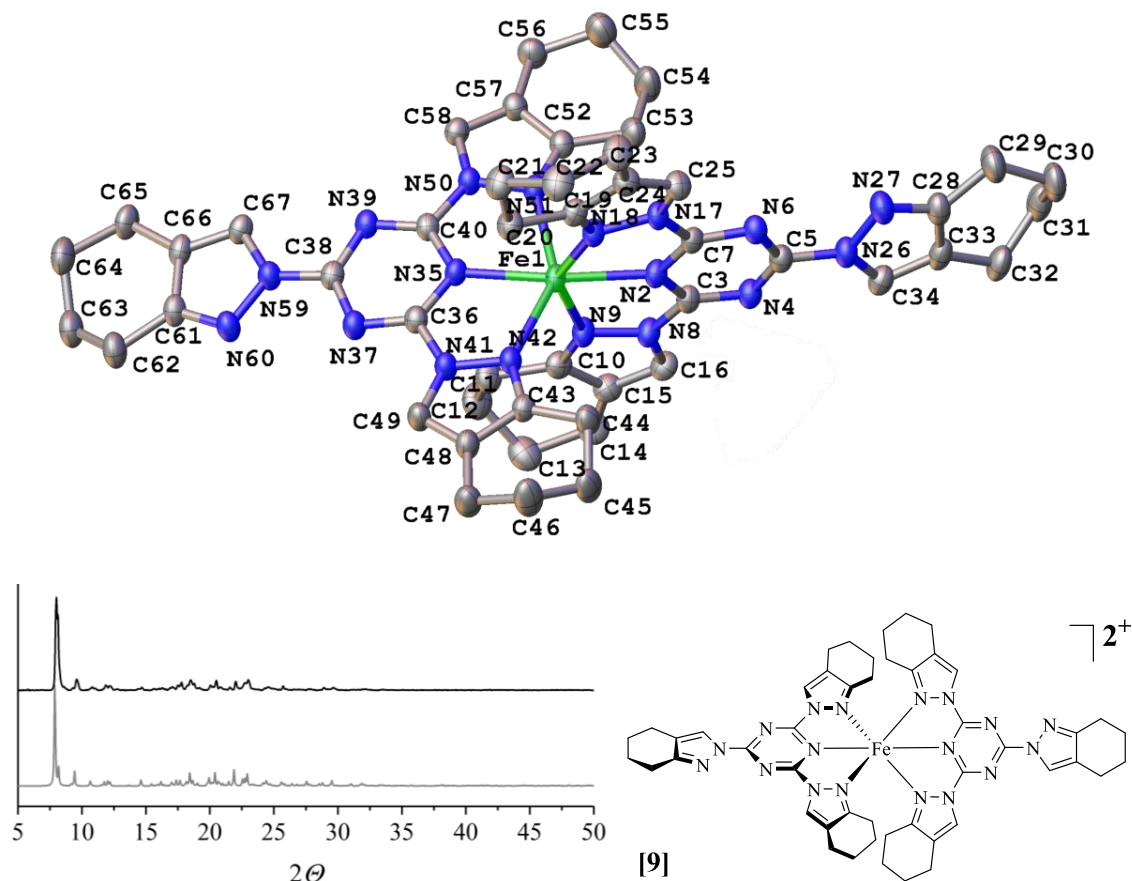


Figure 2.19: Crystal structure of **[9]B** and powder diffraction pattern. Counter-anions, solvent molecules and hydrogen atoms of structures have been removed for clarity. The colour assignment in the plot is black for the experimental and grey for the simulated XRD.

2.2.4 Crystallographic analysis of bpt iron(II) complexes

Single crystal X-ray diffraction is one of the most useful techniques to analyse the electronic state of iron(II) complexes and it is widely used in SCO characterization.¹⁶ Typical low spin iron(II) complexes present Fe-N bond lengths between 1.9 and 2.0 Å while the HS form shows longer bond lengths (2.1-2.4 Å) and larger unit cells.¹⁷ All crystal structures in this work have been collected at 120 K unless it is specified otherwise. The crystallographic parameters for the iron(II) complexes describing their spin state can be found in the following Table 2-1 (Check section 1.3.3 in Chapter 1, for definition of the distortion parameters).

Chapter 2

	[12]B bptOEt	[2]_αB	[2]_βB
Fe–N[triazinyl]	2.0972 (18)	1.9078(7)	2.097(5)
Fe–N[pyrazolyl]	2.2048(19), 2.2146(19)	2.301(12)	2.224(3)
V _{Oh}	12.108(8)	12.15(5)	12.358(11)
Σ	171.5(4)	175(3)	177.8(6)
Θ	542.4(7)	474(6)	538.8(12)
φ	168.75(10)	180(0)	180(0)
θ	74.03(3)	69.9(3)	71.88(4)

	[2]_αC,	[3]_αB, molecule A	[3]_αB, molecule B
Fe–N[triazinyl]	1.9465(5)	2.0789(16), 2.0907(16)	2.0823(16), 2.0907(16)
Fe–N[pyrazolyl]	2.455(12)	2.2140(17) - 2.2474(17)	2.2040(17) - 2.2607(17)
V _{Oh}	14.26(5)	12.374(6)	12.445(6)
Σ	167(2)	175.1(2)	162.5(2)
Θ	449(4)	533.7(6)	531.6(6)
φ	180(0)	173.53 (6)	171.79(7)
θ	70.09(4)	73.535(17)	79.999(17)

	[3]_βB, molecule A	[3]_βB, molecule B	[3]_βB, molecule C
Fe–N[triazinyl]	2.075(4), 2.152(10)	2.077(4), 2.083(4)	2.099(4), 2.100(4)
Fe–N[pyrazolyl]	2.212(4) - 2.282(12)	2.222(4) - 2.271(4)	2.215(4) - 2.257(4)
V _{Oh}	12.54(3)	12.457(14)	12.297(14)
Σ	166.1(11)	163.7(5)	167.8(6)
Θ	550(3)	531.8(12)	561.4(13)
φ	168.8(3)	168.61(14)	163.69(15)
θ	84.52(2)	81.83(4)	87.80(4)

Chapter 2

	[3]C	[4]B bptNMe ₂	[5]B bptSIP
Fe–N[triazinyl]	2.076(2), 2.1006(18)	2.108(3)	2.087(4), 2.102(4)
Fe–N[pyrazolyl]	2.2353(19) - 2.2591(19)	2.219(3), 2.269(3)	2.206(4) - 2.244(4)
V _{Oh}	12.581(7)	12.102(11)	12.284(16)
Σ	168.1(3)	174.2(6)	166.8(6)
Θ	538.1(6)	568.8(11)	532.2(14)
φ	173.63(7)	154.19(15)	167.50(16)
θ	81.953(17)	82.35(4)	75.82(4)

	[6]B	[8] _α B	[8] _β B, molecule A
Fe–N[triazinyl]	2.110(8)	2.100(2)	2.094(7), 2.097(6)
Fe–N[pyrazolyl]	2.203(9), 2.244(9)	2.193(2), 2.258(2)	2.169(7) - 2.254(7)
V _{Oh}	12.26(4)	11.989(10)	12.07(3)
Σ	169.3(16)	174.7(4)	170.6(9)
Θ	558(4)	587.7(10)	563(2)
φ	165.2(5)	159.62(13)	165.1(3)
θ	79.51(2)	89.06(3)	84.67(8)

	[8] _β B, molecule B	[8] _β B, molecule C	[9]B
Fe–N[triazinyl]	2.0805(16), 2.102(9)	2.127(10), 2.178(12)	2.093(2), 2.099(2)
Fe–N[pyrazolyl]	2.1500(19) - 2.2051(15)	2.157(9) - 2.212(11)	2.188(2) - 2.249(3)
V _{Oh}	11.638(18)	12.20(4)	12.494(9)
Σ	175.4(5)	175.7(15)	166.6(3)
Θ	577.0(17)	561(4)	547.3(8)
φ	167.4(3)	173.4(4)	166.10(10)
θ	83.69(5)	84.6(13)	84.02(3)

Table 2-1: Crystallographic parameters determined directly from the crystal structure by using Olex2¹⁸.

Chapter 2

The first parameter examined in order to determine the spin state of iron(II) complexes is the M-L bond lengths (Figure 2.20).

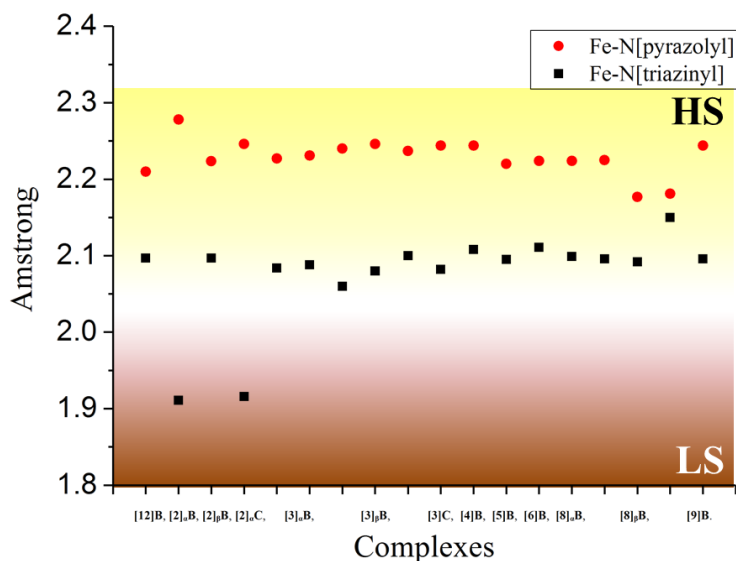


Figure 2.20: Plot of Fe-N bond lengths for all complexes. The values are averaged and extracted from table 2-1.

Two conclusions were drawn from Figure 2.20; all complexes are HS at 120 K, all Fe-N[pyrazolyl] bond lengths are approximately 0.1Å longer than Fe-N[triazinyl]. Although [2]aB and [2]cC Fe-N[triazinyl] bond lengths are around 1.9Å, the Fe-N[pyrazolyl] distances are too high to be LS complexes. Hence, this might be an artifact of the symmetry-imposed disorder in those crystals.

The next parameters examined from the table are the Jahn-Teller distortion parameters (Figure 2.21).

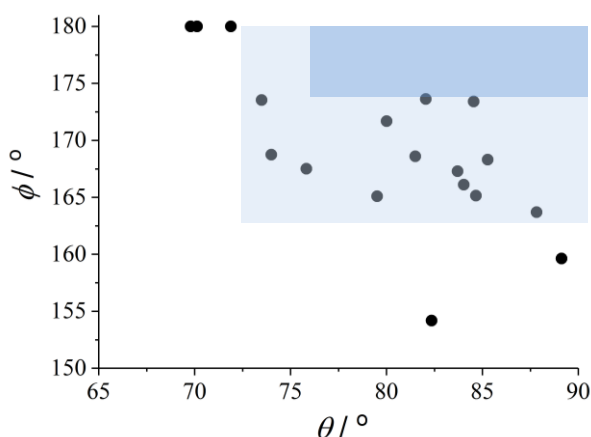


Figure 2.21: Distortion from idealized D_{2d} symmetry, in the Jahn-Teller distortion parameters of the complexes discussed here. HS complexes in the shaded regions of the graph commonly (dark blue) or rarely (pale blue) exhibit SCO. Complexes outside the shaded part never undergo SCO in the solid state.

[Fe(bptR)] X_2 complexes exhibit significant distortions at least in parameter from an ideal D_{2d} symmetric coordination geometry. There is a kind of relationship between the distortions

observed. For example, [8]_aB and [3]_βB, molecule C are not twisted at all ($\theta \approx 90^\circ$), however they are very bent. In contrast, the complexes [2]X are the opposite, they exhibit $\phi = 180^\circ$ which is characteristic of LS complexes but their θ parameter is very distorted. The other complexes show reasonably large distortions of both parameters. As a curiosity the complex [4]B is very deviated from D_{2d} symmetry, it shows a quite strong twist parameter ($\theta : 82.3^\circ < 90^\circ$). In addition it is extremely bent ($\phi : 154^\circ \ll 180^\circ$).

In order to confirm the spin state of the complexes more data can be highlighted from Table 2-1. Typical LS complexes of this type present a value of V_{Oh} around $9.5 \pm 0.4 \text{ \AA}^3$ whereas for HS configuration the volume is around $12.2 \pm 0.8 \text{ \AA}^3$ ¹⁹. The value of Θ parameter is also in agreement with iron(II) HS complexes values around 500 ± 100 . In conclusion, all iron(II) 2,4-di(pyrazol-1-yl)-1,3,5-triazine based complexes are HS at low temperature (120 K).

2.2.5 Magnetic susceptibility analysis

Magnetic susceptibility (χT) versus temperature (T) data were determined in the solid state by SQUID. The measurement was performed in cooling mode from 300 to 3 K, Figure 2.22;

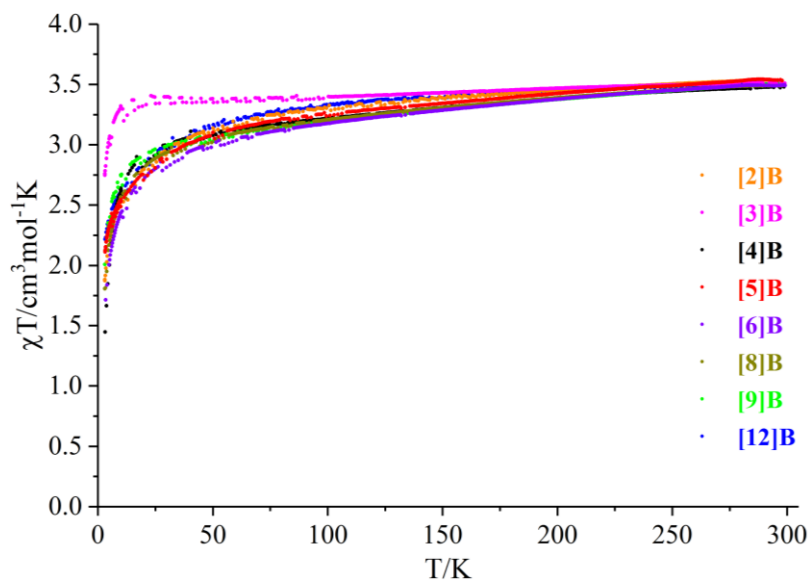


Figure 2.22: Solid state variable temperature magnetic susceptibility measurement.

All the complexes remain HS over the range of temperatures. This result is in agreement with the conclusions drawn from the crystallographic analysis (Section 2.2.4). The zero field splitting effect explains the fact that susceptibility value is constant at 3.5 until 55 K when it decreases.²⁰

2.2.5.1 Evans Method

χT vs T data were also determined in liquid solution of acetonitrile by paramagnetic NMR Evans Method. Data points were taken every 10 K from 340 K to 240 K. (Figure 2.23)

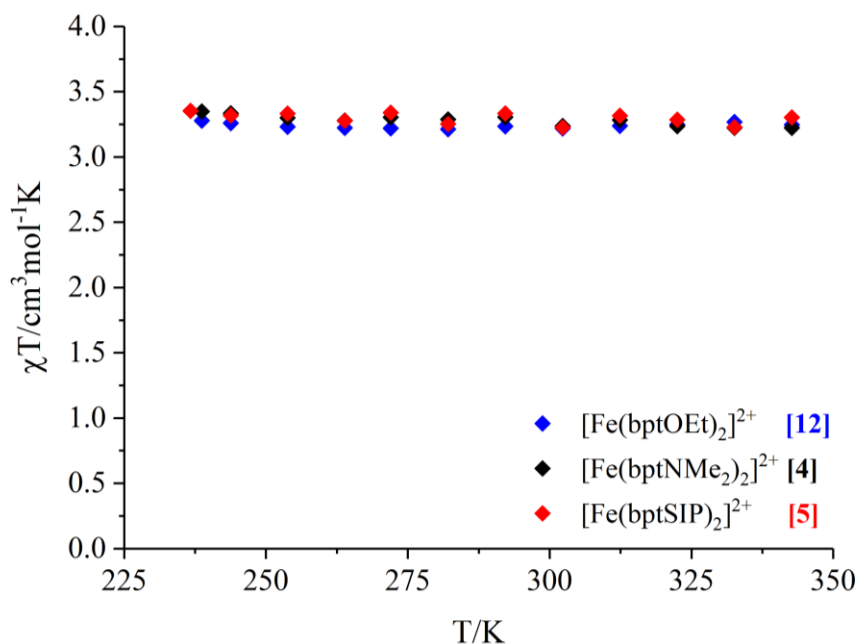


Figure 2.23: Liquid state variable temperature magnetic susceptibility measurement in acetonitrile.

Evans method reflect the HS nature of the complexes, not only because the strong geometric distortions observed, but for the weak ligand field imposed by bpt donor ligands.

2.2.5.2 Complex $\text{Fe}^{\text{III}}[\mathbf{3}]\text{C}$

Increasing the oxidation state of an octahedral complex ion, while maintaining all other features equal, raises Δ_o about 40-80%²¹. Therefore, with the aim of favouring the LS state, ligand (**3**) was reacted with iron(III) perchlorate yielding a black powder which crystallized in the *Pccn* space group.

Despite the efforts, the crystallographic parameters (Table 2-2) indicated that $\text{Fe}^{\text{III}}[\mathbf{3}]\text{C}$ was high spin at 120 K. SQUID magnetic measurement also confirmed that χT remains ≈ 4.5 $\text{cm}^3 \text{mol}^{-1} \text{K}$ over the cooling cycle.

	$\text{Fe}^{\text{III}}[\mathbf{3}]\text{C}$
Fe–N[triazinyl]	2.072(3), 2.077(3)
Fe–N[pyrazolyl]	2.176(3) - 2.214(3)
V_{Oh}	11.836(12)
Σ	161.9(5)
θ	527.1(11)
ϕ	166.13(13)
θ	80.66(4)

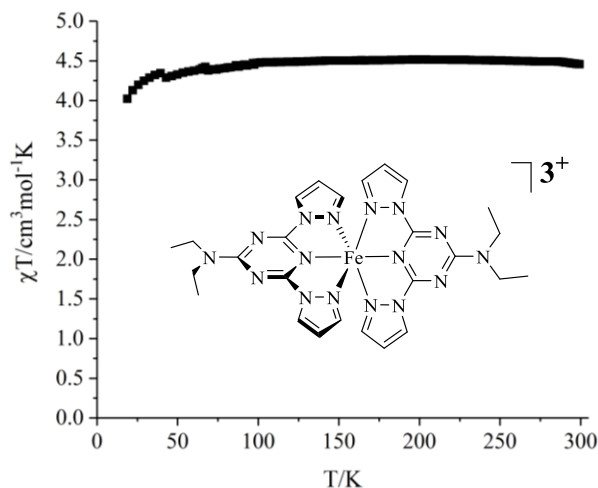


Table 2-2: Geometric parameters and SQUID curve on cooling mode for $\text{Fe}^{\text{III}}[\mathbf{3}]\text{C}$ complex.

2.2.6 Uv-Vis-NIR spectra

Uv-Vis-NIR spectra of some $[\text{Fe}(\text{bptR})_2]^{2+}$ complexes in acetonitrile (**[4]B** and **[5]B**) or nitromethane (**[8]B** and **[9]B**) solutions were collected in order to evaluate the value of Δ_o experimentally, see Figure 2.24;

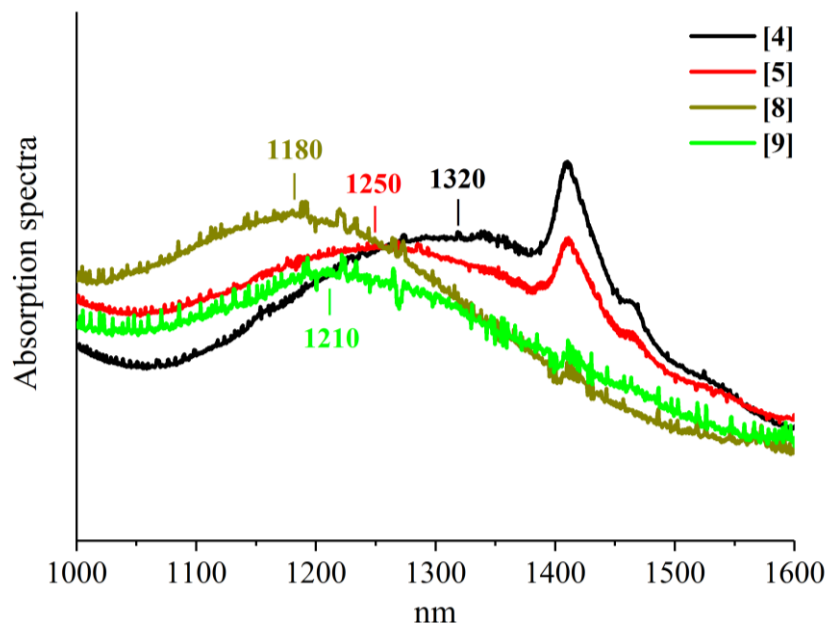


Figure 2.24: d-d bands of **[4]**, **[5]**, **[8]** and **[9]** determined by Uv-Vis-NIR in nm, the spectrum only shows NIR region for clarity.

The transitions were weak in intensity because they are Laporte forbidden. Wavelengths $[\lambda, (\text{m})]$ are inversely proportional to the energy of an electromagnetic wave. Thus, the energetic band gap Δ_o can be calculated in eV, kcal/mol or in cm^{-1} by using equation 1;

$$\Delta E = \frac{h \cdot c}{\lambda} \quad (\text{Equation 1})$$

where h is Planck's constant ($4.1357 \cdot 10^{-15}$ eV·s) and c is the speed of light ($2.998 \cdot 10^8$ m/s). The experimental values given in cm^{-1} are roughly; **[4]** = 7576 cm^{-1} , **[5]** = 8000 cm^{-1} , **[8]** = 8475 cm^{-1} and **[9]** = 8265 cm^{-1} . The complexes of ligands containing electron-donor substituents in the pyrazolyl show slightly larger Δ_o as expected³. However these values are too low for these compounds to possibly accommodate a LS state (Chapter 1, Figure 1.12).

2.2.7 DFT calculations

The magnetic properties of the iron(II) bpt complexes detailed here were unexpected. Gas phase DFT calculations gave some understanding of this behaviour. The calculations performed used the B86PW91 functional which is the most similar to BP86 among those available in SPARTAN'16²², and def2-SVP basis set. BP86 was widely used in a study of transition metals and performed well in other calculations of comparative spin state energies for iron compounds²³.

Chapter 2

An equilibrium geometry DFT calculation generates a series of energy levels with high precision, but variable accuracy, termed Kohn-Sham (KS) orbitals. SPARTAN'16 displays a 3D graphical representation of the electron density for any of those orbitals. The energy of KS orbitals has no chemical/physical significance, except for the HOMO energy level. DFT states that this energy is equal to the first ionization potential, however the experimental value will differ from it in practise²⁴.

In principle, it is easy to assign the KS energy levels to the chemically expected M-L d orbitals by looking at the shape of their electron density. Although the gap between KS HOMO and KS LUMO does not necessarily correspond to the energy band gap between t_{2g} and e_g , usually M-L d orbitals are near in energy to the frontier KS orbitals (Figure 2.25). Similar behaviour is expected for any diamagnetic transition metal with octahedral geometry. Note that the e_g set is composed by d_z^2 and d_{xy} because this kind of complexes have a reduction in symmetry from O_h to D_{2d} . That leads the ligands to rearrange facing d_{xy} orbital lobes and $d_{x^2-y^2}$ nodes rearranging the energetic levels.

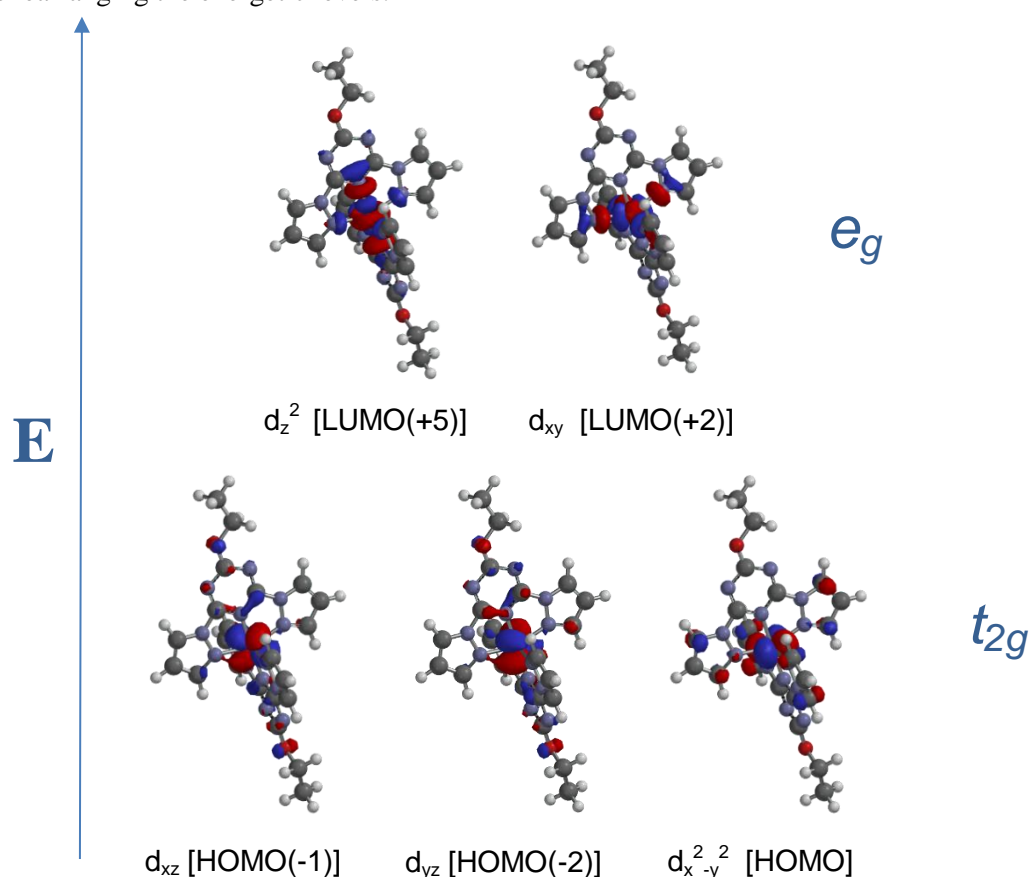


Figure 2.25: 3D graphic representation of KS orbitals calculated in SPARTAN'16 assigned to the d orbitals of $[\text{Fe}(\text{bptOEt})_2]^{2+}$ in its LS state. The value of energy is given in electron-volts, for example; HOMO(-1) = -10.68708 eV is associated to d_{xz} orbital.

Equilibrium geometry calculations were performed on pairs of complexes from the bpp and bpt series. The parent molecules $[\text{Fe}(\text{bpp})_2]^{2+}$ ²⁵ and $[\text{Fe}(\text{bpt})_2]^{2+}$ (which was not synthesized), as well as the compounds bearing thioisopropyl (SIP) substituents;

$[\text{Fe}(\text{bppSIP})_2]^{2+}$ ¹⁶ and $[\text{Fe}(\text{bptSIP})_2]^{2+}$ [5] were investigated. Two other bpt complexes bearing different substituents were also calculated; $[\text{Fe}(\text{bptOEt})_2]^{2+}$ [12] and $[\text{Fe}(\text{bptNMe}_2)_2]^{2+}$ [4], Figure 2.26.

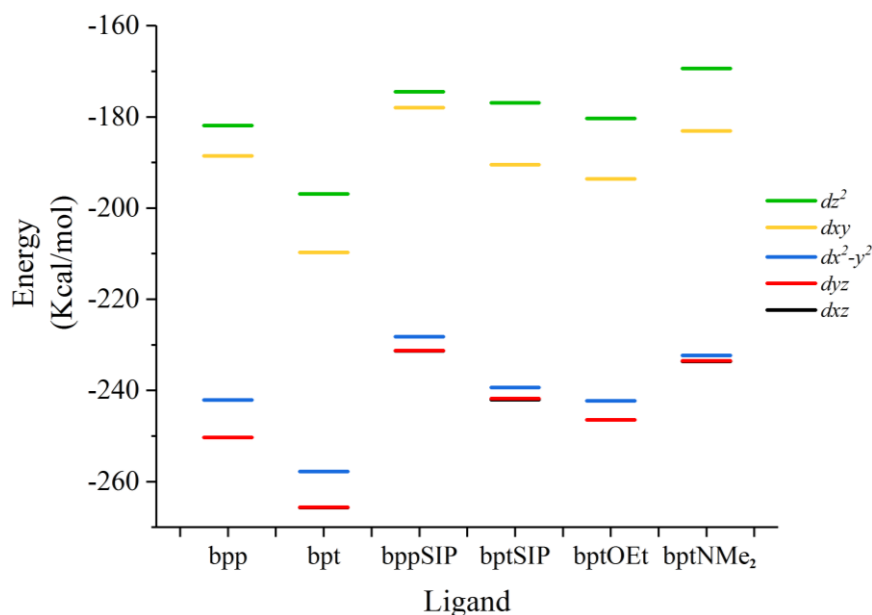


Figure 2.26: Plot of the energy levels for iron(II) complexes calculated in the LS state.

The band gap Δ_o calculated by direct average of the e_g and t_{2g} set components is around 60 kcal/mol for all complexes, table 2-4. DFT calculations of $[\text{Fe}(\text{bpyz})_2]^{2+}$ and $[\text{Fe}(\text{bpym})_2]^{2+}$ complexes were also performed in order to trace a tendency related to the N content in the main aromatic ring¹⁹. The result of Δ_o was as follow;

$$[\text{Fe}(\text{bpyz})_2]^{2+} (62.6) \approx [\text{Fe}(\text{bpp})_2]^{2+} (62.3) > [\text{Fe}(\text{bpym})_2]^{2+} (61.1) > [\text{Fe}(\text{bpt})_2]^{2+} (59.6)$$

Experimental values of Δ_o for $[\text{Fe}(\text{bptNMe}_2)_2]^{2+}$ and $[\text{Fe}(\text{bptSIP})_2]^{2+}$ calculated from UV-Vis-NIR experiment by using equation 1 were 21.7 and 22.8 kcal/mol respectively. However, these values are not comparable with the ones calculated in table 2-4 because the complexes are experimentally HS while they were considered LS in this calculation, $\Delta_{o(\text{LS})} \neq \Delta_{o(\text{HS})}$.

In terms of DFT calculation, the story changes when one or more unpaired electrons are found in the transition metal. HS iron(II) complexes hold four unpaired electrons. The unrestricted DFT calculation method is strongly recommended when working with paramagnetic systems. Different spin electrons $^{+1/2}$ and $^{-1/2}$ are considered individually so that two KS equations are calculated. In other words, energy levels are expressed by two distinct energy sets, called α and β .

Unrestricted Kohn-Sham equations were used to calculate the HS state of the same complexes. However it was not possible to assign the d orbitals among the two α and β energy sets (See Figure 2.27) as for the LS calculation which uses restricted identical Kohn-Sham equations. Therefore, it was not possible to determine the value of Δ_o calculated for the HS species.

Chapter 2

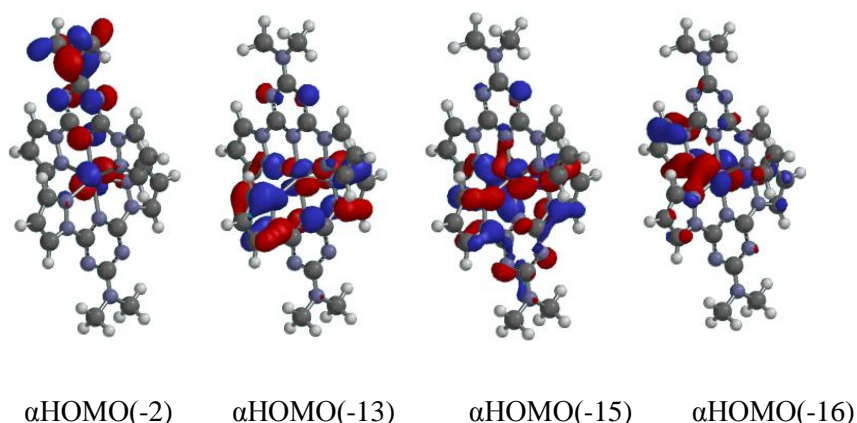


Figure 2.27: Few examples of KS α HOMO orbitals where the electron density is observed in both the ligand and M-L bond.

Despite that, the HS calculation was still useful. The total energy in the ground state was compared for both LS and HS calculations and in the following Table 2-3.

Complex	E(HS), Hartrees	E(LS), Hartrees	ΔE (HS-LS), Kcal/mol	ΔE_{rel} (HS-LS), Kcal/mol
[Fe(bpp) ₂] ²⁺	-2659.474284	-2659.501049	16.8	0
[Fe(bpt) ₂] ²⁺	-2723.588283	-2723.605836	11.0	-5.8
[Fe(bppSIP) ₂] ²⁺	-3691.507709	-3691.531735	15.1	-1.7
[Fe(bptSIP) ₂] ²⁺	-3755.65119	-3755.665395	8.9	-7.9
[Fe(bptOEt) ₂] ²⁺	-3031.196078	-3031.209848	8.6	-8.2
[Fe(bptNMe ₂) ₂] ²⁺	-2991.519173	-2991.533036	8.7	-8.1

Table 2-3: Energetic comparison between the ground state of LS and HS calculations.

Notably lower values of $\Delta E_{\text{HS-LS}}^{\circ}$ were calculated for the bpt compared with the bpp derived complexes, which translates to a relative HS stabilization. The larger contributor to Δ_0 [Fe(bpp)₂]²⁺ > Δ_0 [Fe(bpt)₂]²⁺ is the reduced energy for the d_{xy} orbital related to the energy of d_z^2 orbital observed for all the bpt derivatives, see energy levels of Figure 2.26, Table 2-4 for the $\Delta d_z^2 - d_{xy}$ parameter. Although the calculated Δ_0 (LS) showed an inconsistent trend (smaller for Fe(bppSIP)₂ than bpt complexes, Table 2-4), this is because the real Δ_0 is described by a combination of the LS and HS calculations and the value of Δ_0 (HS) calc. was not determined.

Complex	[Fe(bpp) ₂] ²⁺	[Fe(bpt) ₂] ²⁺	[Fe(bppSIP) ₂] ²⁺	[Fe(bptSIP) ₂] ²⁺	[Fe(bptOEt) ₂] ²⁺	[Fe(bptNMe ₂) ₂] ²⁺
Δ_0 (LS) calc.	62.4	59.7	54.0	57.4	58.1	56.9
$\Delta d_z^2 - d_{xy}$	6.7	12.8	3.4	13.5	13.3	13.7

Table 2-4: Energy increments are given in Kcal/mol. $\Delta d_z^2 - d_{xy}$ of bpt is at least twice larger than that for the bpp analogous complex.

Strong orbital overlap translates into wider splitting between bonding and anti-bonding M-L combinations. Hence, the energy decay of the orbital d_{xy} which is geometrically associated with the Fe-N[pyrazolyl] bonds according to the axis system, implies a weaker Fe-N[pyrazolyl] bond for bpt than bpp derived complexes.

As the N atom content increases in the azabenzene, the computed values of Fe-N[azinyl] bond lengths decreases and Fe-N[pyrazolyl] raises, accompanied by a narrowing by 1.3° of the bite angle (α)¹⁹ defined in Figure 2.28:

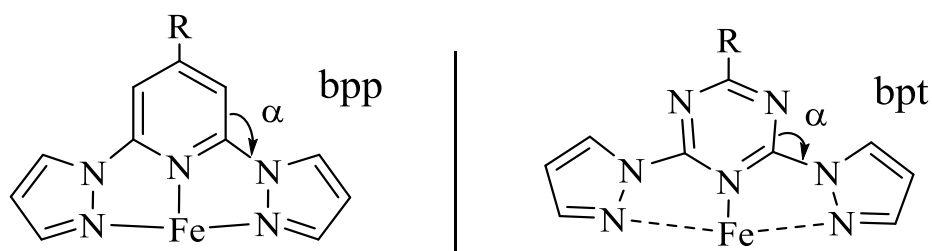


Figure 2.28: Schematic representation of the ligand conformation variation.

Two geometric factors of the ligand conformation itself are responsible for the narrowing of α , and thus the widening of the chelating ligand. First, a 1,3,5-triazine ring is more compact than a pyridine ring because C-N bonds are 0.05 \AA shorter than C-C bonds in pyridine²⁵. In addition, the C[azinyl]-N[pyrazolyl] (C2-N7 and C6-N12) bond length becomes shorter as the content of N atom increases (Figure 2.29, and Table 2-5);

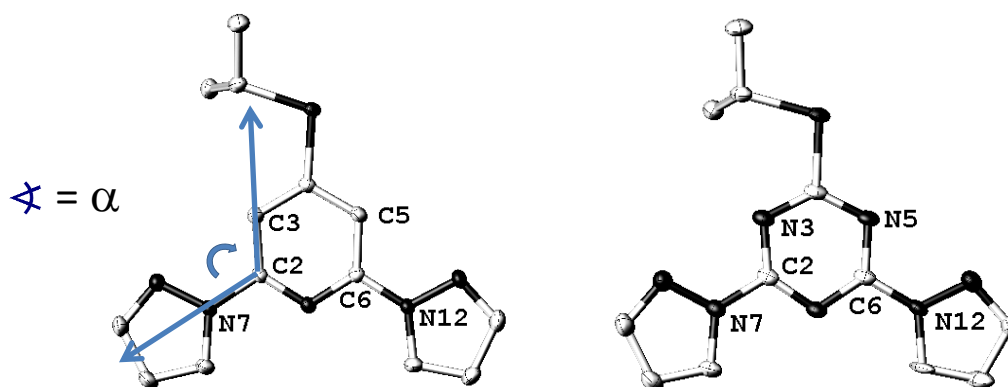


Figure 2.29: Example of two equivalent bpp and bpt ligands. The crystal structure of bppSIP was collected by Dr Rafal Kulmaczewski.

Ligand	C2-C/N3	C6-C/N5	C2-N7	C6-N12	α_1	α_2
Bpp-SIP	1.389(3)	1.391(3)	1.422(3)	1.402(3)	119.2(2)	120.17(19)
Bpt-SIP	1.330(4)	1.336(4)	1.399(4)	1.393(4)	117.0(3)	116.6(3)

Table 2-5: Experimental evidence of the geometric factors discussed above.

2.3 Conclusions

A number of 2,4-di(pyrazol-1-yl)-6-R-1,3,5-triazine (bptR)-containing complexes of the type $[\text{Fe}(\text{bptR})_2](\text{X})_2$ (where R is isopropylsulfanyl, ethoxide, dimethyl or diethyl amine and X = BF_4 or ClO_4) were synthesized as a new family of easily modifiable potential SCO iron(II) complexes. They were analysed by different methods including X-ray crystallography, Uv-Vis-NIR spectroscopy and SQUID magnetometry. Contrary to what was expected, it was demonstrated that none of those complexes exhibit SCO either in solid or liquid state, and showed strong distortion from the ideal D_{2d} molecular geometry. Density Functional Theory (DFT) calculations were performed for some of the complexes and their analogous 2,6-di(pyrazol-1-yl)-pyridine (bpp)-containing complexes. DFT highlighted the weakening of Fe-N-[pyrazolyl] bond in the bptR complexes, associated with the narrowing of the chelate bite angle due to geometric factors of the triazine based ligands. In summary, the geometry of (bpt)-containing ligands favours the HS state of their iron(II) complexes because the M-L orbital overlap is weaker than for (bpp)-containing ligands.

2.4 Bibliography

1. Halcrow, M. A., Recent advances in the synthesis and applications of 2,6-dipyrazolylpyridine derivatives and their complexes. *New Journal of Chemistry* **2014**, 38 (5), 1868-1882.
2. Haryono, M.; Heinemann, F. W.; Petukhov, K.; Gieb, K.; Müller, P.; Grohmann, A., Parallel Crystallization of a “Static” and a Spin-Crossover Polymorph of an Iron(II) Complex from the Same Solution. *European Journal of Inorganic Chemistry* **2009**, 2009 (14), 2136-2143.
3. Kershaw Cook, L. J.; Kulmaczewski, R.; Mohammed, R.; Dudley, S.; Barrett, S. A.; Little, M. A.; Deeth, R. J.; Halcrow, M. A., A Unified Treatment of the Relationship Between Ligand Substituents and Spin State in a Family of Iron(II) Complexes. *Angewandte Chemie International Edition* **2016**, 55 (13), 4327-4331.
4. (a) Devid, E. J.; Martinho, P. N.; Kamalakar, M. V.; Šalitroš, I.; Prendergast, Ú.; Dayen, J.-F.; Meded, V.; Lemma, T.; González-Prieto, R.; Evers, F.; Keyes, T. E.; Ruben, M.; Doudin, B.; van der Molen, S. J., Spin transition in arrays of gold nanoparticles and spin crossover molecules. *ACS Nano* **2015**, 9 (4), 4496-4507; (b) Pukenas, L.; Benn, F.; Lovell, E.; Santoro, A.; Kershaw Cook, L. J.; Halcrow, M. A.; Evans, S. D., Bead-like structures and self-assembled monolayers from 2,6-dipyrazolylpyridines and their iron(II) complexes. *Journal of Materials Chemistry C* **2015**, 3 (30), 7890-7896.
5. (a) Elhaik, J.; Money, V. A.; Barrett, S. A.; Kilner, C. A.; Evans, I. R.; Halcrow, M. A., The spin-states and spin-crossover behaviour of iron(ii) complexes of 2,6-dipyrazol-1-

Chapter 2

ylpyrazine derivatives. *Dalton Transactions* **2003**, (10), 2053-2060; (b) Mohammed, R.; Chastanet, G.; Tuna, F.; Malkin, T. L.; Barrett, S. A.; Kilner, C. A.; Létard, J.-F.; Halcrow, M. A., Synthesis of 2,6-Di(pyrazol-1-yl)pyrazine Derivatives and the Spin-State Behavior of Their Iron(II) Complexes. *European Journal of Inorganic Chemistry* **2013**, 2013 (5-6), 819-831.

6. Bushuev, M. B.; Pishchur, D. P.; Logvinenko, V. A.; Gatilov, Y. V.; Korolkov, I. V.; Shundrina, I. K.; Nikolaenkova, E. B.; Krivopalov, V. P., A mononuclear iron(ii) complex: cooperativity, kinetics and activation energy of the solvent-dependent spin transition. *Dalton Transactions* **2016**, 45 (1), 107-120.

7. de Hoog, P.; Gamez, P.; Driessen, W. L.; Reedijk, J., New polydentate and polynucleating N-donor ligands from amines and 2,4,6-trichloro-1,3,5-triazine. *Tetrahedron Letters* **2002**, 43 (38), 6783-6786.

8. Rothmann, M. M.; Haneder, S.; Da Como, E.; Lennartz, C.; Schildknecht, C.; Strohmriegl, P., Donor-substituted 1,3,5-triazines as host materials for blue phosphorescent organic light-emitting diodes. *Chemistry of Materials* **2010**, 22 (7), 2403-2410.

9. (a) Guerrero, A.; Jalon, F. A.; Manzano, B. R.; Claramunt, R. M.; Cabildo, P.; Infantes, L.; Cano, F. H.; Elguero, J., The Structure of Tris(3',5'-dimethylpyrazol-1-yl)-s-triazine and Its Use as a Ligand in Coordination Chemistry. *Chemistry of Heterocyclic Compounds* **2003**, 39 (10), 1396-1403; (b) Zhou, H.-P.; Gan, X.-P.; Li, X.-L.; Liu, Z.-D.; Geng, W.-Q.; Zhou, F.-X.; Ke, W.-Z.; Wang, P.; Kong, L.; Hao, F.-Y.; Wu, J.-Y.; Tian, Y.-P., Anion-Induced Assembly of Five-Coordinated Mercury(II) Complexes and Density Functional Theory Calculations to Study Bond Dissociation Energies of Long Hg–N Bonds. *Crystal Growth & Design* **2010**, 10 (4), 1767-1776.

10. (a) Quinonero, D.; Deya, P. M.; Carranza, M. P.; Rodriguez, A. M.; Jalon, F. A.; Manzano, B. R., Experimental and computational study of the interplay between C-H/[small pi] and anion-[small pi] interactions. *Dalton Transactions* **2010**, 39 (3), 794-806; (b) Wang, J.-X.; Zhu, Z.-R.; Bai, F.-Y.; Wang, X.-Y.; Zhang, X.-X.; Xing, Y.-H., Molecular design and the optimum synthetic route of the compounds with multi-pyrazole and its derivatives and the potential application in antibacterial agents. *Polyhedron* **2015**, 99, 59-70.

11. Huang, W.-H.; Jia, W.-L.; Wang, S., 7-Azaindolyl- and indolyl-functionalized starburst molecules with a 1,3,5-triazine or a benzene core — Syntheses and luminescence. *Canadian Journal of Chemistry* **2006**, 84 (4), 477-485.

12. Baker, A.; Craig, D.; Dong, G.; Rae, A., Metal complexes of 1,3-bis(Pyridin-2-yl)pyrazole: spectral, magnetic and structural studies. *Australian Journal of Chemistry* **1995**, 48 (6), 1071-1079.

13. Xiao, L.; Pöthig, A.; Hintermann, L., 2-Amino-1,3,5-triazine chemistry: hydrogen-bond networks, Takemoto thiourea catalyst analogs, and olfactory mapping of a sweet-smelling triazine. *Monatshefte für Chemie - Chemical Monthly* **2015**, 146 (9), 1529-1539.

Chapter 2

14. Kershaw Cook, L. J.; Shepherd, H. J.; Comyn, T. P.; Baldé, C.; Cespedes, O.; Chastanet, G.; Halcrow, M. A., Decoupled spin crossover and structural phase transition in a molecular iron(II) complex. *Chemistry – A European Journal* **2015**, *21* (12), 4805-4816.
15. Macrae, C. F.; Edgington, P. R.; McCabe, P.; Pidcock, E.; Shields, G. P.; Taylor, R.; Towler, M.; van de Streek, J., Mercury: visualization and analysis of crystal structures. *Journal of Applied Crystallography* **2006**, *39* (3), 453-457.
16. Cook, L. J. K.; Kulmaczewski, R.; Cespedes, O.; Halcrow, M. A., Different spin-state behaviors in isostructural solvates of a molecular iron(II) complex. *Chemistry – A European Journal* **2016**, *22* (5), 1789-1799.
17. Kershaw Cook, L. J.; Mohammed, R.; Sherborne, G.; Roberts, T. D.; Alvarez, S.; Halcrow, M. A., Spin state behavior of iron(II)/dipyrazolylpyridine complexes. New insights from crystallographic and solution measurements. *Coordination Chemistry Reviews* **2015**, 289–290, 2-12.
18. Dolomanov, O. V.; Bourhis, L. J.; Gildea, R. J.; Howard, J. A. K.; Puschmann, H., OLEX2: a complete structure solution, refinement and analysis program. *Journal of Applied Crystallography* **2009**, *42* (2), 339-341.
19. Capel Berdiell, I.; Kulmaczewski, R.; Halcrow, M. A., Iron(II) Complexes of 2,4-Dipyrazolyl-1,3,5-triazine Derivatives—The Influence of Ligand Geometry on Metal Ion Spin State. *Inorganic Chemistry* **2017**, *56* (15), 8817-8828.
20. Boča, R., Zero-field splitting in metal complexes. *Coordination Chemistry Reviews* **2004**, *248* (9–10), 757-815.
21. González-Gutiérrez, M.; Domínguez-Alcázar, J.; Quintero-Rivera, E.; Ramírez-Jiménez, S.; Martínez-Bulit, P.; Barba-Behrens, N., Estrategias de diseño para materiales con entrecruzamiento de espín (SCO). *Educación química* **2014**, *25*, 425-431.
22. Inc, W. *SPARTAN' 18*, Irvine CA, 2018.
23. (a) Kershaw Cook, L. J.; Kulmaczewski, R.; Mohammed, R.; Dudley, S.; Barrett, S. A.; Little, M. A.; Deeth, R. J.; Halcrow, M. A., A unified treatment of the relationship between ligand substituents and spin state in a family of iron(II) complexes. *Angewandte Chemie* **2016**, *128* (13), 4399-4403; (b) Houghton, B. J.; Deeth, R. J., Spin-State Energetics of FeII Complexes – The Continuing Voyage Through the Density Functional Minefield. *European Journal of Inorganic Chemistry* **2014**, *2014* (27), 4573-4580.
24. Stowasser, R.; Hoffmann, R., What Do the Kohn–Sham Orbitals and Eigenvalues Mean? *Journal of the American Chemical Society* **1999**, *121* (14), 3414-3420.
25. Gordon, A. J., ; J. Ford, R. A., *The Chemist's Companion: A Handbook of Practical Data, Techniques, and References*. New York, USA, 1972; p 108.

Chapter 3 – New Heterometallic Coordination Polymer Gels Combining Silver(I) Salts with [2,4,6-Tris(Pyrazolyl)-1,3,5-Triazine] First Row Metal(II) Complexes.

3.1 Introduction

Unravelling soft matter systems is a rich field of scientific investigation. Over the last decades, supramolecular gels have gained attention due to their diverse promising applications including catalysis, sensors, surface science, tissue engineering and pollutant removal¹. Supramolecular gels are usually formed by low molecular weight gelator molecules assembled in a 3D network, which traps a bulk amount of solvent via non-covalent interactions². The reversible and dynamic nature of the supramolecular interactions provides a mechanism for sensing, or physical transformations in response external stimuli³.

Coordination polymer gels (CPGs) or metallogels have also been widely reported recently, where metal ions play a crucial role in the assembly of the 3D network⁴. Inclusion of transition metals in the gel assembly brings tunability to the coordination strength, as well as new redox, optic, electronic and magnetic properties which are intrinsic to the metal ion. These new properties afford additional possibilities for applications in catalysis, luminescence and adhesives as well as new types of sensing functionality^{3,5}.

3.1.1 Silver(I) and first row metals in CPGs

CPGs of first row transition ions are often supported by pyridyl gelators⁶, but can also be prepared from more diverse organic scaffolds based on other donor groups⁷. In some cases, the organic components were found to be selective gelators for particular metal ions or salts⁸. Moreover, a typical class of CPGs are silver(I)-containing metallogels of pyridyl-containing gelators⁹, which can template the formation of silver nanoparticles under mild heating or reduction¹⁰. Nevertheless, combining two different metals where both are critically involved in the self-assembly of the 3D polymer has not been widely studied although rare examples of heterometallic CPGs have been reported¹¹.

3.1.2 2,4,6-Tri(pyrazolyl)-1,3,5-triazine (TPT), ligand (2)

Homometallic CPGs supported by a different di or trisubstituted 1,3,5-triazine scaffold have been described in a previous study^{6b, 12}. 2,4,6-Tri(pyrazolyl)-1,3,5-triazine¹³ (TPT, (2), Figure 3.1) and its derivatives are well known coordinating ligands for transition metals¹⁴.

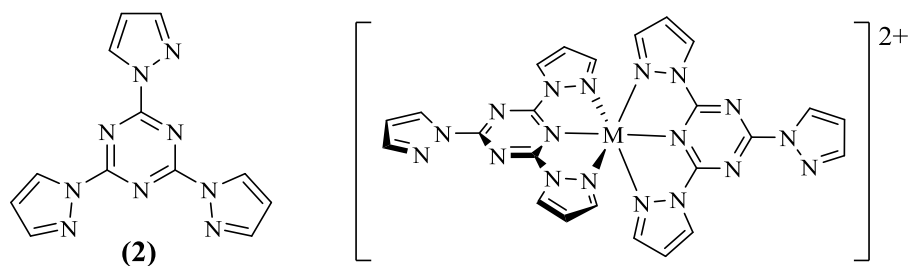


Figure 3.1: Scheme of TPT, ligand (2). Divalent metal complexes where M = Fe, Co and Ni.

Metallogels lie between highly ordered aggregates (crystals) and amorphous solids. Crystal engineering studies contribute to our understanding of their networks, but their final structures are still far from elucidation. Hence, understanding of the nature of non-covalent interactions and metal-ligand coordination in metal-organic gels is needed^{4a}. Designing and developing novel rational gelators is a challenging task which will significantly impact the comprehension of such supramolecular interactions and the coordination polymer gels themselves. Therefore, our aim was to make 1D coordination polymers by combining silver(I) salts which are well known within the coordination polymer gel chemistry, with solutions of mononuclear $[M(TPT)_2]^{2+}$ complexes which have free pyrazolyl moieties and strong non-covalent interactions in the lattice of the crystal¹⁵.

3.2 Results and discussion

3.2.1 Crystallographic analysis of the monomer $[M(TPT)_2](X)_2$

The spin state of $[Fe(TPT)_2]^{2+}$ (Figure 3.1, M = Fe), was investigated in Chapter 2. An exotic cubic crystal structure with strong anion- π interactions was observed for **[2]B** and **[2]C** complexes^{14a} (Figure 3.2). We proposed $[Fe(TPT)_2]^{2+}$ centers might be linked into larger assemblies by coordination to exogenous silver ions through the dangling pyrazole donor group.

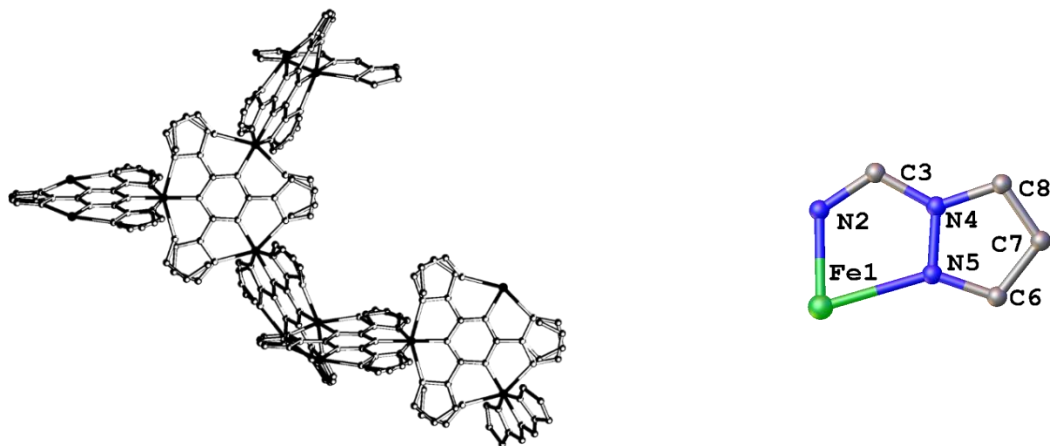


Figure 3.2: Grown structure of [2]B showing the disorder of the pyrazolyl and the iron(II). Hydrogen atoms and counter-anions were removed for clarity. Asymmetric unit cell (right) containing 1/6 of the complex.

Chapter 3

The 1,3,5-triazine ring has been widely reported as π -acid functional group which can form strong anion- π interactions¹⁶. Similar interactions were found where the counter-anion was placed perfectly in between the centroids of the two triazine rings (Figure 3.3).

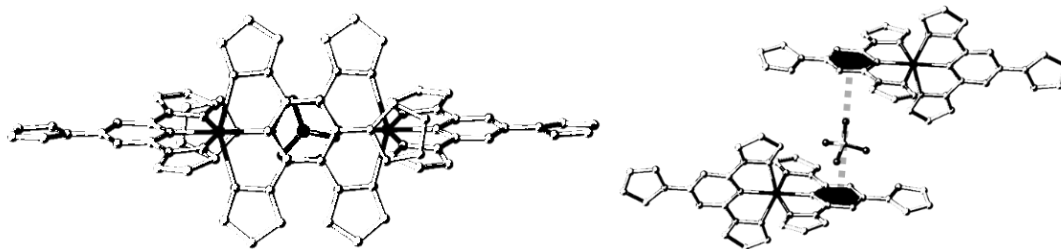


Figure 3.3: Anion- π interactions [3F atoms plane - triazine centroid 1 = 2.647(5) Å and F atom - triazine centroid 2 = 3.586(7) Å] for $\text{Fe}(\text{TPT})_2(\text{BF}_4)_2$. Hydrogen atoms were removed for clarity.

The best way to understand the structure of [2]X is assuming a cubic array of ligands linked in pairs through a random distribution of iron atoms. Different transition metal salts were also reacted with ligand (2) following the procedure described previously; $\text{Mn}(\text{ClO}_4)_2$, $\text{Fe}(\text{BF}_4)_2$, $\text{Fe}(\text{ClO}_4)_2$, $\text{Co}(\text{BF}_4)_2$, $\text{Ni}(\text{ClO}_4)_2$, $\text{Ni}(\text{BF}_4)_2$ and $\text{Cu}(\text{BF}_4)_2$. All of them crystallized in the same cubic space group ($Ia\bar{3}d$) apart from $\text{Cu}[2]\text{B}$ which yielded a mixture of crystals where the majority component is the following hydrolysed compound (Figure 3.4).

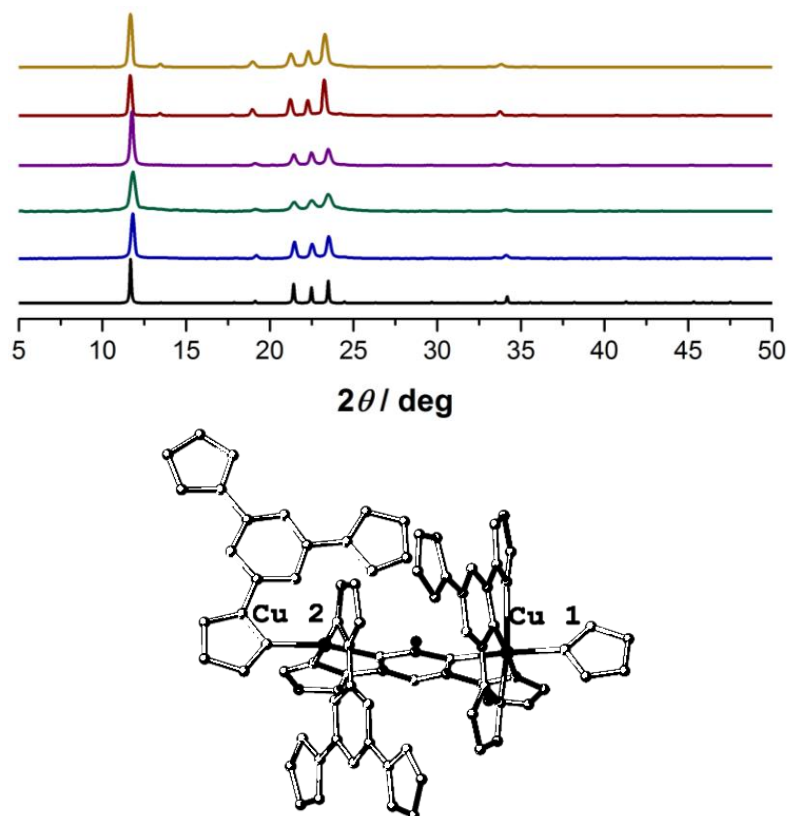


Figure 3.4: Powder pattern diffraction of; ■ simulated from crystal structure of [2]B, ■ experimental from [2]B, ■ experimental from $\text{Co}[2]\text{B}$, ■ experimental from $\text{Ni}[2]\text{B}$, ■ experimental from [2]C, ■ experimental from $\text{Ni}[2]\text{C}$ (top). Main structure obtained from the copper mixture with (2). It contains 3 TPT ligands, 2 copper(II) and one hydrolysed TPT plus the free pyrazole detached from the ligand, hydrogen atoms and counter-anions were removed for clarity (bottom).

Although $[\text{Cu}(\text{TPT})_2](\text{BF}_4)_2$ was reported by Quiñero *et al*^{14d} in a similar synthesis performed here, copper and other strong metals are well-known as hydrolysing agents of 1,3,5-triazine in a variety of conditions¹⁷. Because of that, copper was discarded for this study.

3.2.2 Synthesis of the coordination polymer gels (CPGs)

In order to obtain 1D heterometallic polymers, nitromethane solutions of a silver(I) salt and mononuclear complex $\text{M}[\text{TPT}]\text{X}$ ($\text{M} = \text{Mn}, \text{Fe}, \text{Co}$ or Ni and $\text{X} = \text{BF}_4^-$ or ClO_4^-) were mixed at 1:1 ratio. New CPGs assembled almost immediately (Figure 3.5).

The mononuclear complexes were also soluble in several solvents such as methanol, acetone, acetonitrile, dimethyl formamide and dimethyl sulfoxide. However, nitromethane was the only solvent trapped in the 3D network of a gelator system.

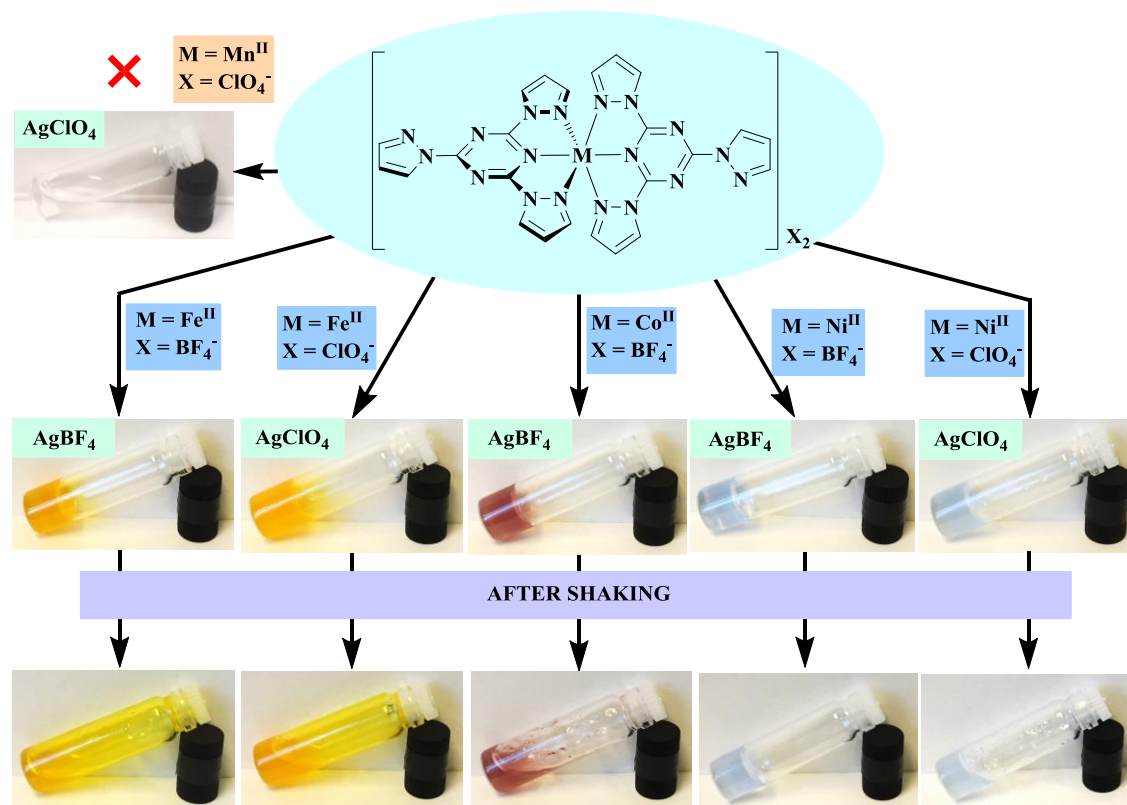


Figure 3.5: Heterometallic CPGs studied in this work.

Both tetrafluoroborate and perchlorate silver salts produced similar gels whereas by using silver hexafluoroantimonate the gel weakened. A similar effect was observed when more than one equivalent of silver was used, and no gelation occurred with 3 equivalents of silver(I) salt (Figure 3.6).

Chapter 3

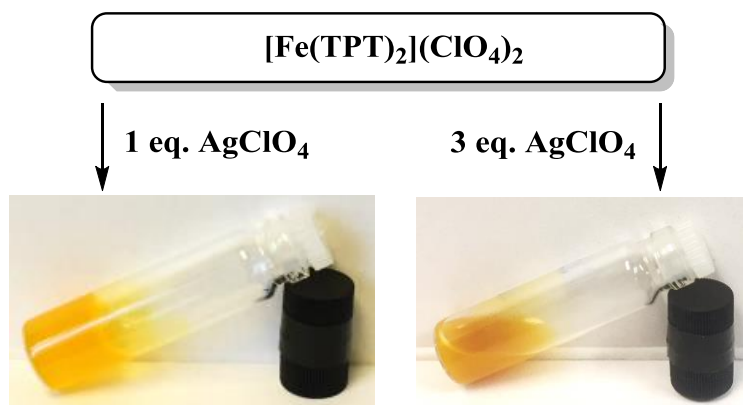


Figure 3.6: Effect of different $[\text{Fe}(\text{TPT})_2](\text{ClO}_4)_2:\text{AgClO}_4$ stoichiometry on the gel formation.

All concentrated complex solutions became viscous when silver salt was added apart from $\text{Mn}[2]\text{C}$ which remained as a liquid (Figure 3.5). A remarkable fact is that iron and cobalt gels showed irreversible thixotropy while nickel gel remained viscous after shaking. All these facts can be explained with the Irving-Williams Series¹⁸. Irving-Williams series refers to the relative stabilities of complexes formation and applies to high-spin complexes of the divalent ions of first-row transition metals (Figure 3.7).

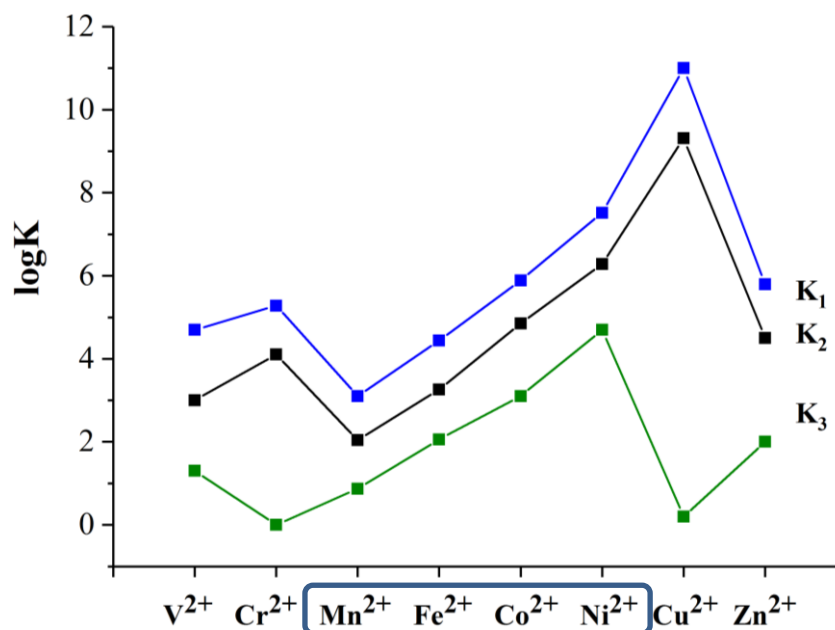


Figure 3.7: Representation of $\log K_n$ values calculated for the complexation of ethylenediamine ligand. Plot adapted from¹⁹.

When the number of coordinated ligands increases, the step-wise formation constant decreases, as expected based on entropy and steric hindrance considerations. $\log K_3$ for Cu^{2+} is out of line because Cu^{2+} does not easily form six-coordinate complexes due to the extreme Jahn-Teller distortion found in these complexes. By following the plot of the Figure 3.7 can be concluded that Mn^{2+} was the weakest coordinating metal of our study. This fact was in agreement with the paramagnetic NMR of the four complexes in deuterated nitromethane (Figure 3.8).

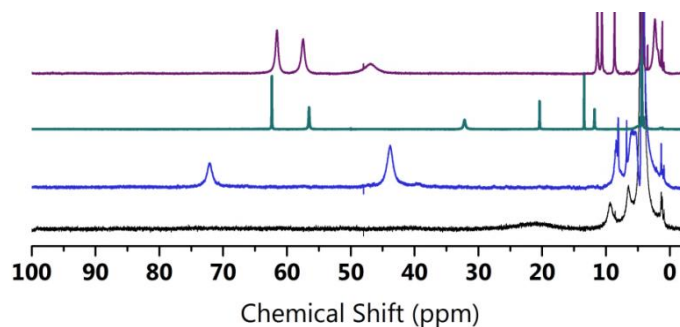


Figure 3.8: Paramagnetic ^1H NMR of; ■ $[\text{Mn}(\text{TPT})_2](\text{ClO}_4)_2$, ■ $[\text{Fe}(\text{TPT})_2](\text{BF}_4)_2$, ■ $[\text{Co}(\text{TPT})_2](\text{BF}_4)_2$, ■ $[\text{Ni}(\text{TPT})_2](\text{BF}_4)_2$.

Iron, cobalt and nickel complexes of TPT show well-defined peaks whereas manganese complex show very broad peaks which reflects its rapid electron-nuclear relaxation typical of $S = 5/2$ metal ion. The spectrum of **Mn[2]** could also be indicative of ligand lability in solution. Therefore, the CPG cannot be assembled given the weakness of the **Mn[2]C** complex.

3.2.3 Characterization of CPGs

3.2.3.1 Scanning Electron Microscopy (SEM)

Several images were taken of three iron-silver, cobalt-silver and nickel-silver CPGs. SEM samples were prepared by three different procedures; slow evaporation of the gel, freeze-drying of the gel and evaporation of diluted gel. The images were taken either with a Circular Backscatter Detector (CBS) or an Everhart-Thornley Detector (ETD) for iridium coated samples. A few nanometre-sized silver nanoparticles were observed homogeneously dispersed through all three samples when the gels were dried overnight (Figure 3.9). Similar results were reported before²⁰.

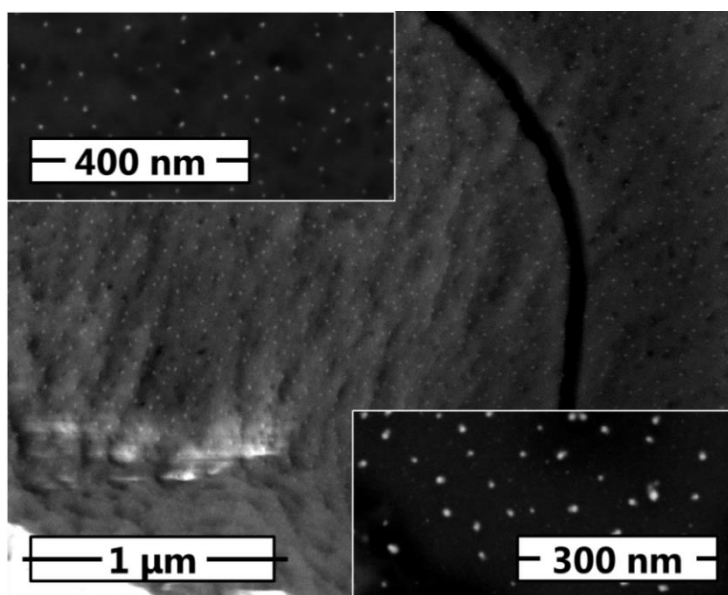


Figure 3.9: SEM images of slow evaporated iron-silver CPG (big picture and top-left for zoom). Bottom-right corresponds to a zoom of nickel-silver CPG.

Chapter 3

Fibrous amorphous material was observed using freeze-drying method, Figure 3.10;

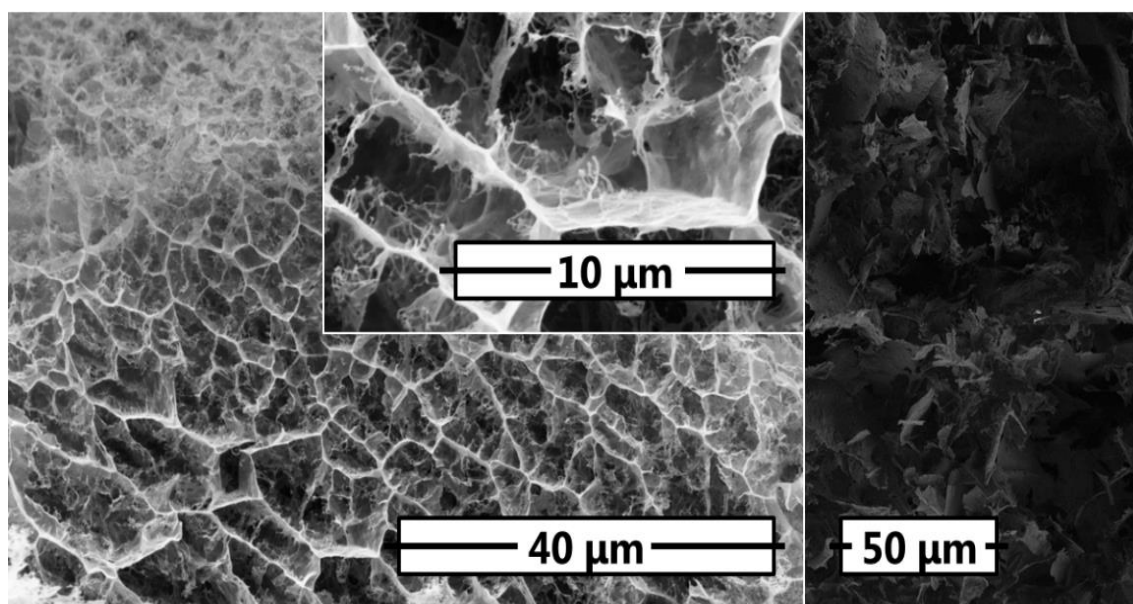


Figure 3.10: SEM images of freeze-drying nickel-silver CPG (big picture and top-centre for zoom). The right corresponds to the iron-silver CPG.

On the other hand, the slow evaporation of diluted solutions yielded fibres more crystalline, see Figure 3.11;

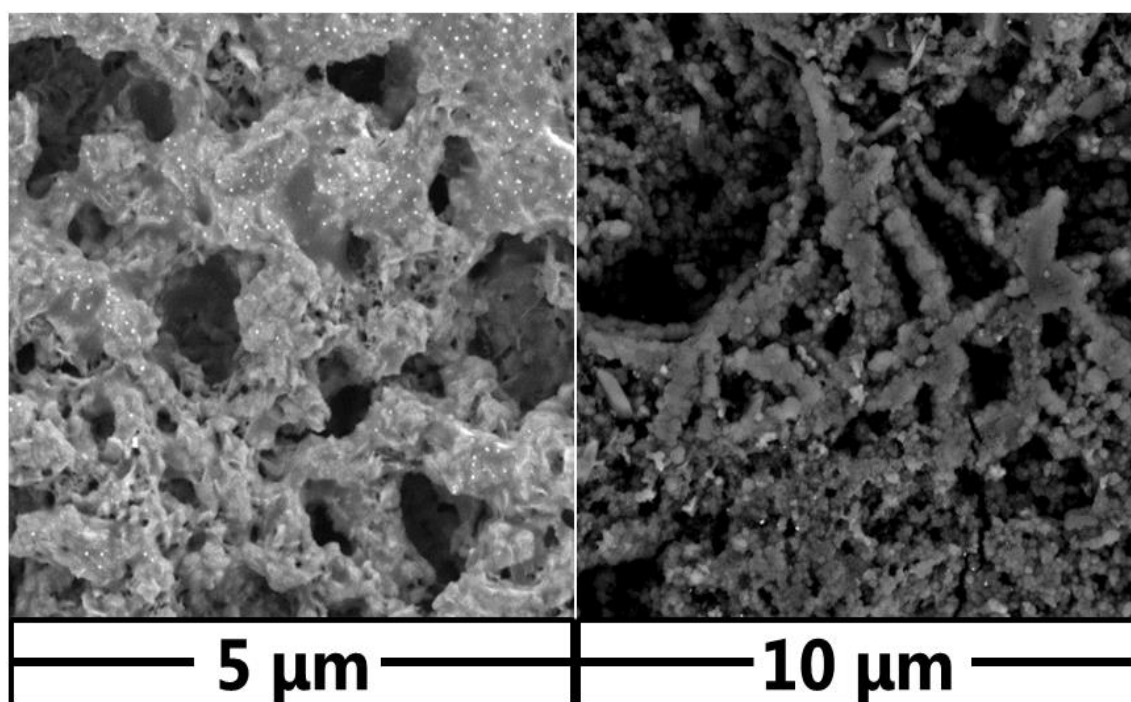


Figure 3.11: SEM images of slow evaporating solutions of cobalt-silver left and iron-silver right.

3.2.3.2 Energy dispersive X-ray (EDX)

EDX mapping proved the homogeneous distribution of the two metals (Figure 3.12).

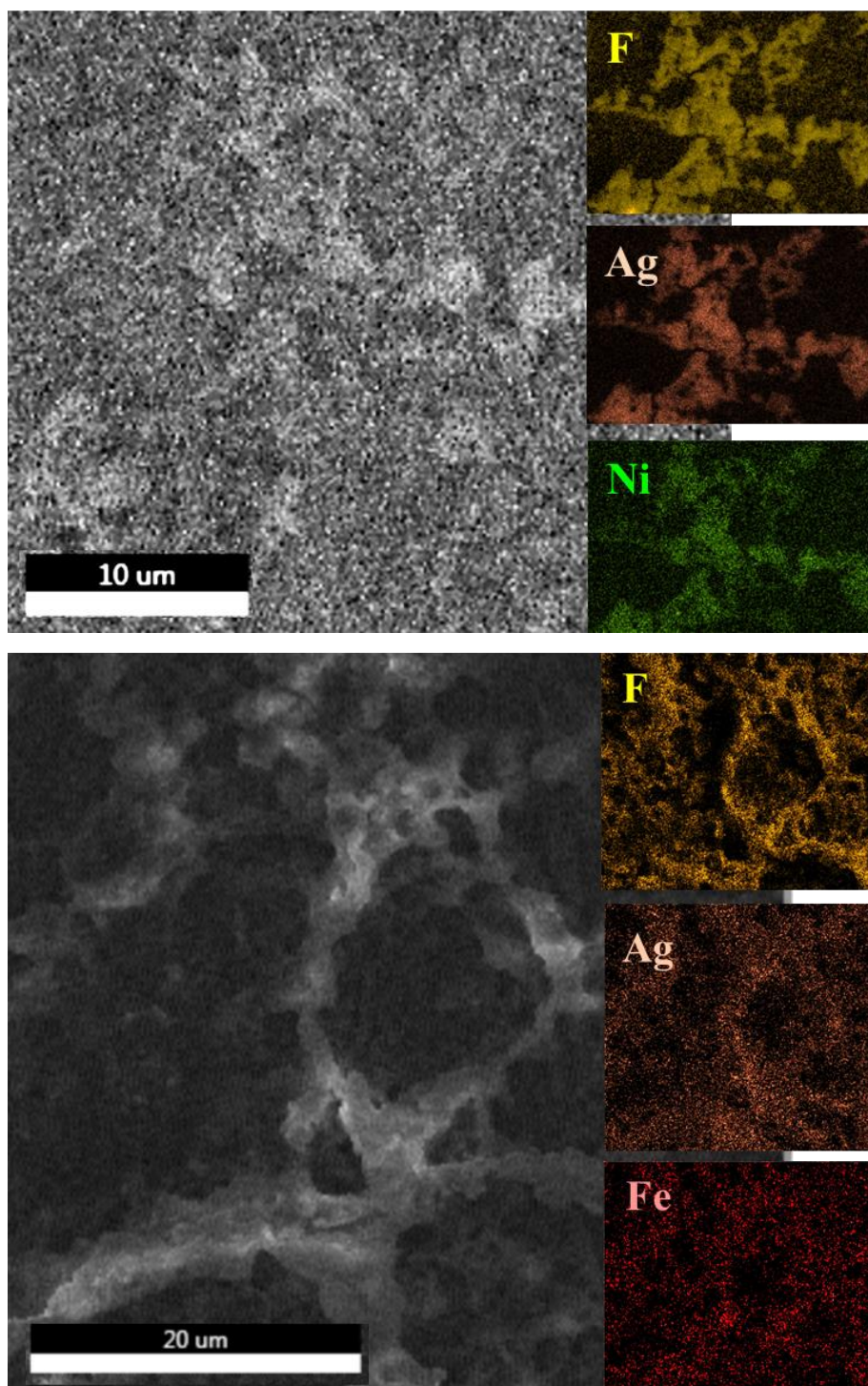


Figure 3.12: Examples of EDX mapping for the nickel-silver (top) and iron-silver (bottom) CPGs.

Qualitative elemental analysis was investigated by EDX spectroscopy where silver (2.9), fluorine (0.7), nickel (7.5), cobalt (6.9) and iron (6.4) atoms were the most representative peaks observed (Figure 4.16). A strong silicon (1.7) signal was always observed due to the silicon wafer used to mount the sample in the microscope.

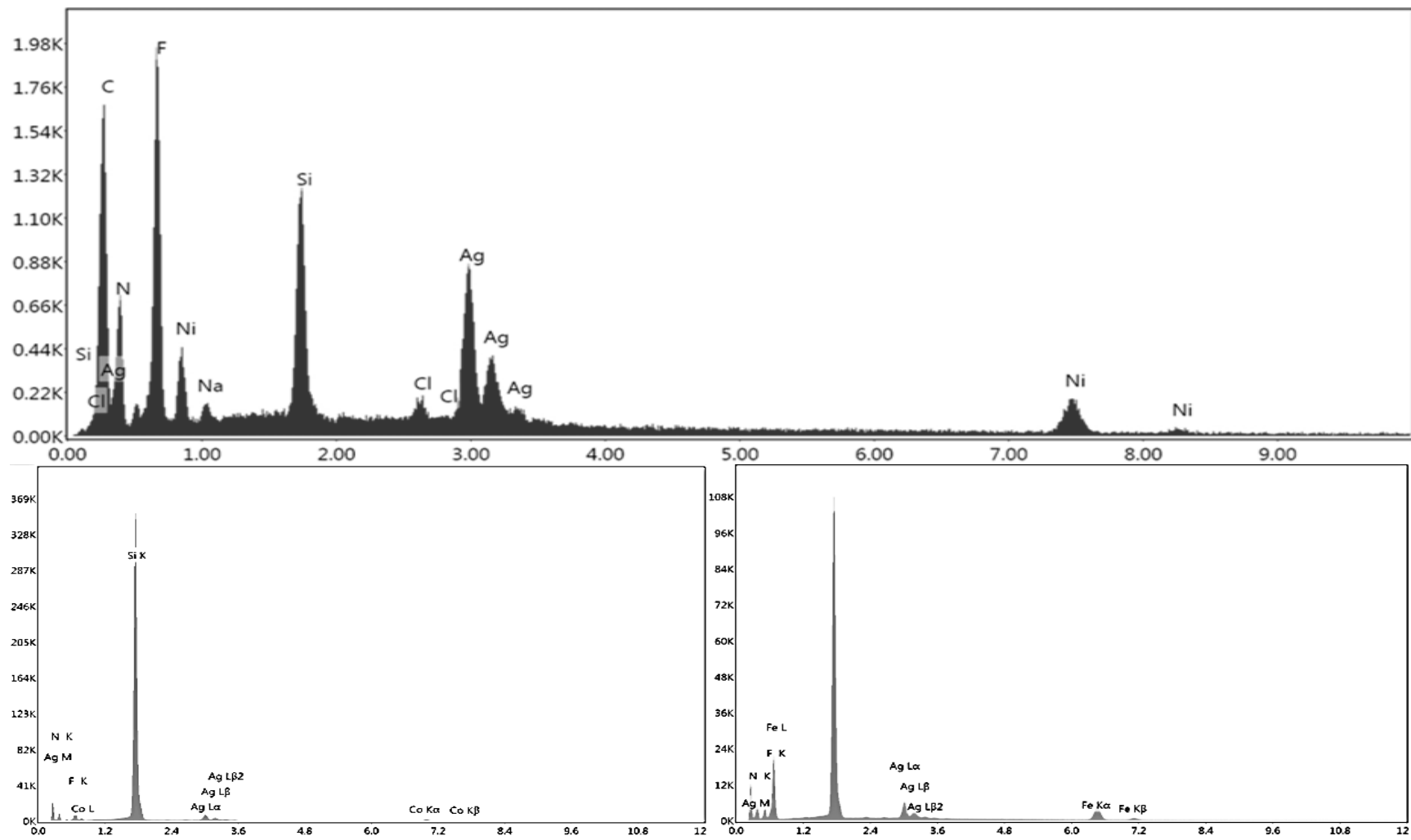


Figure 3.13: Energy Dispersive X-ray Analysis. Nickel (top), cobalt (lower-left) and iron (lower-right).

Chapter 3

3.2.3.3 High resolution ES-MS

Direct injection mass spectrometry was used to characterize solutions of the diluted CPGs. The most representative peaks of two examples were assigned in the tables below. The hydrolysed ligand btpO^- was only observed for the BF_4^- gels²¹ (Figure 3.14 and Figure 3.15).

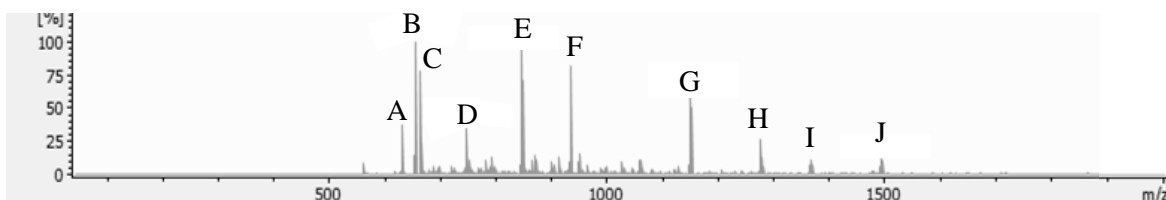


Figure 3.14: Mass spectrum of Fe[2]B-AgBF₄ CPG.

A	633.1464 ⁺	Fe(TPT) ₂ F ⁺	F	936.1291 ⁺	Fe ₂ (TPT) ₂ (btpO)F ₂ ⁺
B	657.0391 ⁺	Fe ₂ (TPT)(btpO)F ₂ ⁺	G	1152.0255 ⁺	Fe ₂ (TPT) ₃ AgF ₃ H ⁺
C	665.1108 ⁺	Ag(TPT) ₂ ⁺	H	1279.9297 ⁺	Fe ₂ (TPT) ₃ Ag ₂ F ₆ H ⁺
D	749.0126 ⁺	Fe(TPT) ₂ NaF ₃ (H ₂ O) ₃ H ⁺	I	1369.9219 ⁺	Fe ₃ (TPT) ₃ Ag ₂ F ₆ (OH)H ₂ O ⁺
E	849.0288 ⁺	Fe ₂ (TPT) ₂ AgF ₂ (OH) ₂ ⁺	J	1495.8227 ⁺	Fe ₃ (TPT) ₃ Ag ₃ F ₇ (OH)H ₂ O ⁺

Table 3-1: Assignment of peaks for iron CPG.

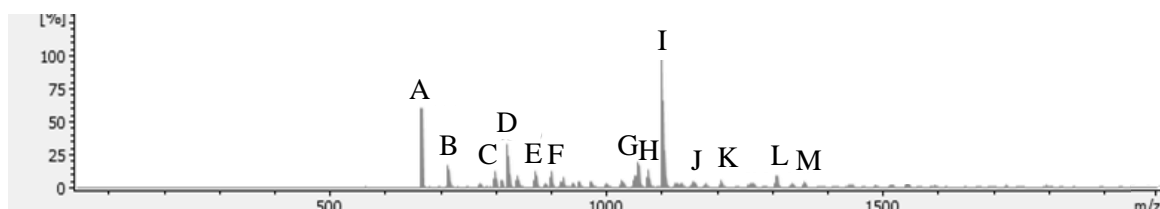


Figure 3.15: Mass spectrum of Ni[2]C-AgClO₄ CPG.

A	665.1108 ⁺	Ag(TPT) ₂ ⁺	H	1076.1092 ⁺	Ni ₂ (TPT-H ⁺) ₃ Ag(OH) ⁺
B	715.2322 ⁺	Ni(TPT) ₂ (ClO ₄) ⁺	I	1102.2377 ⁺	Ni(TPT) ₃ Ag(ClO ₄)-H ⁺
C	800.1696 ⁺	Ag ₂ (TPT) ₂ (CN) ⁺	J	1160.0795 ⁺	Ni ₂ (TPT-H ⁺) ₃ Ag(ClO ₄) ⁺
D	823.0896 ⁺	Ni(TPT) ₂ Ag(ClO ₄)-H ⁺	K	1208.1080 ⁺	Ni(TPT-H ⁺) ₃ Ag ₂ (ClO ₄)+H ⁺
E	873.1275 ⁺	Ni ₂ (TPT) ₂ (ClO ₄) ₂ -H ⁺	L	1310.1290 ⁺	Ni(TPT) ₃ Ag ₂ (ClO ₄) ₂ -H ⁺
F	901.1173 ⁺	Ni(TPT) ₂ Ag ₂ (OH) ₄ +H ⁺	M	1360.1321 ⁺	Ni ₂ (TPT) ₃ Ag(ClO ₄) ₃ -H ⁺
G	1058.0958 ⁺	Ni ₂ (TPT-H ⁺) ₃ Ag-H ⁺			

Table 3-2: Assignment of peaks for nickel CPG.

3.2.3.4 Nuclear Magnetic Resonance ^1H

Paramagnetic NMR spectra of the CPGs were compared with their respective mononuclear complex solutions in nitromethane, Figure 3.16;

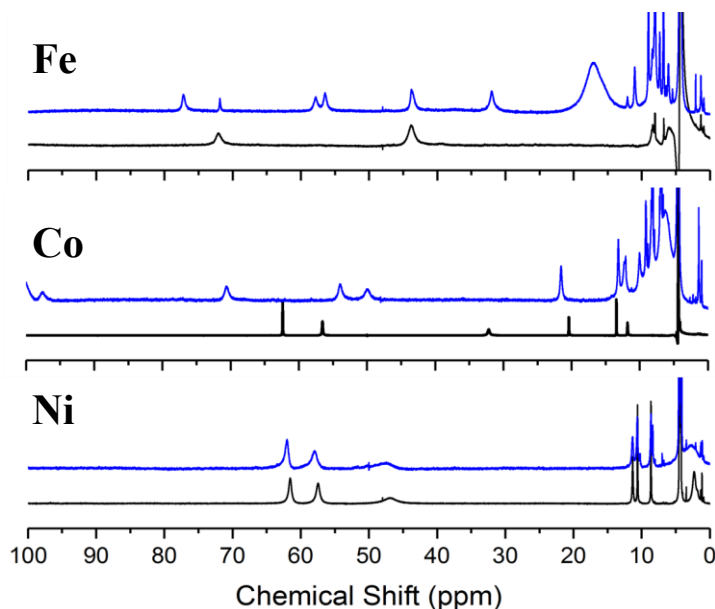


Figure 3.16: Comparison of mononuclear complex (■) with the respective CPG (■). The order of the spectra is as follow; top corresponds to iron, middle is cobalt and nickel derived compounds are in the bottom.

There was a notable difference in terms of the paramagnetic environments when comparing the “weak” gel spectra (iron and cobalt which show irreversible thixotropy) with the corresponding complex solution presenting only the three shifted peaks corresponding to the pyrazolyl rings (black spectra). Addition of silver ions lowers the NMR symmetry of the tpt ligand from C_2 to C_1 , which indicates formation of a heterometallic $M/\text{Ag}/\text{tpt}$ species. Assignment of the peaks is not possible because the structure of the gels was not determined. However the strong nickel CPG presented exactly the same spectrum for both; mononuclear complex solution and the heterometallic coordination polymer gel, suggesting that silver ions did not displace TPT ligand from $[\text{Ni}(\text{TPT})_2]^{2+}$ in MeNO_2 solution.



Figure 3.17: Picture of the Ni[2]B-AgBF₄ CPG after 20 months.

The nickel-based gels retain their viscosity when stored for a period of years at room temperature, in closed vials.

3.2.4 Can we make spin-crossover coordination polymer gels?

The magnetic behaviour of $[\text{Fe}(\text{TPT})_2]^{2+}$ was discussed in Chapter 2 and no SCO phenomenon was observed^{14a}. Three other complexes whose ligands were based on a pyridine and pyrimidine skeleton²², were approached for potential SCO CPGs (Figure 3.18).

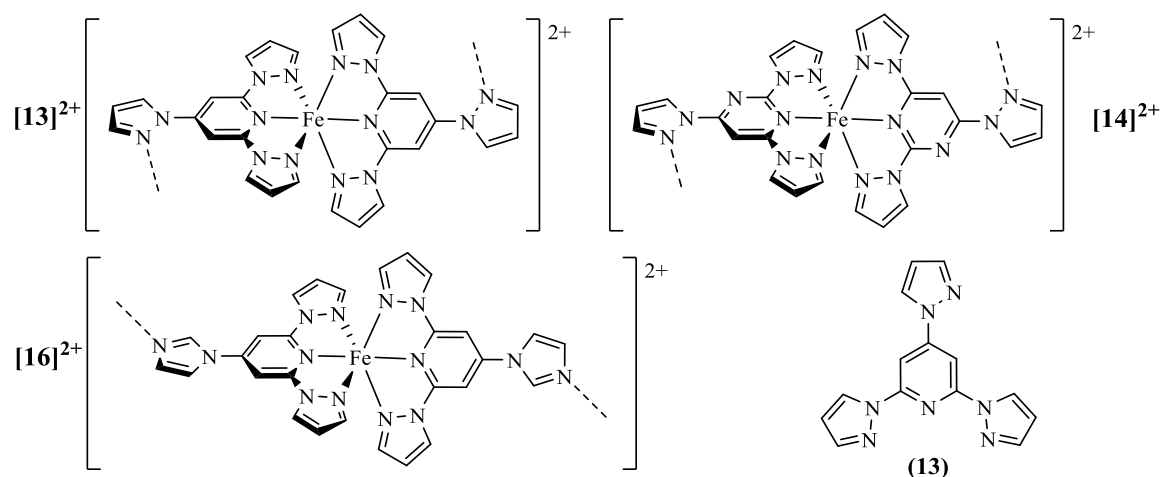


Figure 3.18: Iron(II) complexes designed as SCO gelator; [13], [14] and [16]. Structure of ligand (13) first synthesized by Lawrence Kershaw Cook.

The experiments described here provided deep understanding of the CPGs structure. Bis(2,4,6-tris-(pyrazolyl)-pyridine)iron(II) tetrafluoroborate; $[\text{Fe}(\mathbf{13})_2](\text{BF}_4)_2$ was previously synthesised by Dr Lawrence Kershaw Cook and presents SCO²³. However $[\mathbf{14}]^{2+}$ and $[\mathbf{16}]^{2+}$ were novel compounds synthesized and characterized in this work. Similar ligands to **(16)** produced CPGs with silver cations²⁴ and imidazolyl is well-known as linear coordinating ligand²⁵. Unfortunately, none of these three complexes assembled into a CPG upon the silver(I) salt addition.

3.2.5 Silver coordination polymers

In order to understand the connectivity of silver ions in the CPGs, silver(I) salts were reacted with the above mentioned ligands; **(2)**, **(13)**, **(14)** and **(16)** (Figure 3.19). The same general procedure was followed for all; solutions of ligand and silver salt in either MeNO_2 or MeCN were mixed and they were crystallized through a diethyl ether atmospheric diffusion.

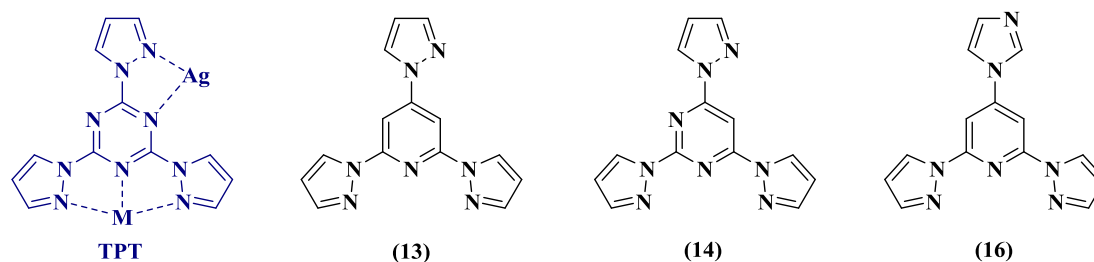


Figure 3.19: Ligands discussed as possible gelator. Only $[\text{M}(\text{TPT})_2]^{2+}\text{-Ag}^+$ assembled into an heterometallic CPG, highlighted in dark blue.

Chapter 3

The TPT ligand with AgBF_4 crystallized as 1D polymer with linear connectivity and strong intermolecular interactions (space group, $P2_1$), (Figure 3.20 and Figure 3.21).

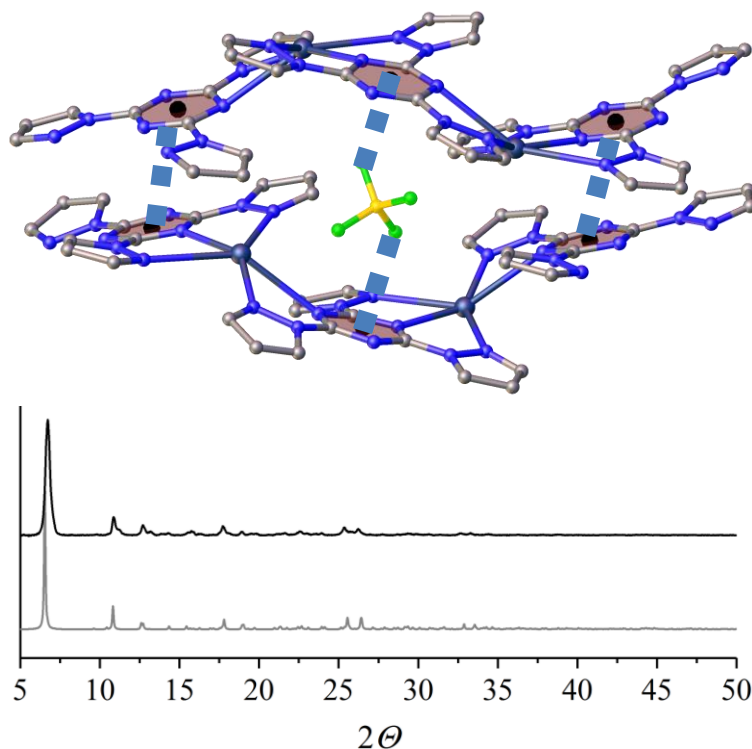


Figure 3.20: 1D $\text{Ag}[\text{TPT}]\text{B}^{\infty}$ polymeric structure showing π - π interactions involving triazine rings and π -anion interactions. Hydrogen atoms were removed for clarity. The colour assignment in the plot is black for the experimental and grey for the simulated XRD.

Supramolecular interactions involving triazine rings are π - π interactions between the two triazine rings [3.576(6) Å], strong π -anion interactions with the top chain [F atom-plane 2.789(5) Å and F atom-centroid 2.832(6) Å] and with the bottom chain [F atom-plane 2.805(5) Å and F atom-centroid 2.866(5) Å].

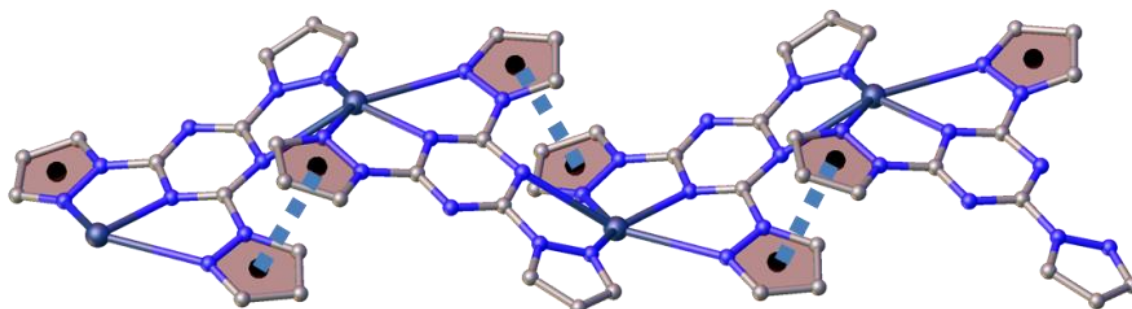


Figure 3.21: Different view of $\text{Ag}[\text{TPT}]\text{B}^{\infty}$ with supramolecular interactions involving pyrazolyl rings highlighted (3.424(5) Å). Hydrogen atoms and counter-anions were removed for clarity.

Strictly speaking the coordination number of silver for this polymer is 4, with bond lengths from 2.372(7) to 2.416(5) Å. However, weak interaction between a free pyrazolyl-Ag 2.877(4) Å is a potential fifth N-Ag bond. Different polymorphs of $\text{Ag}(\text{TPT})\text{X}$ ($\text{X} = \text{BF}_4^-$ and ClO_4^-) were obtained with helical connectivity when trifluoroethanol or acetone were used as solvents, in the space group $Pca2_1$ (Figure 3.22).

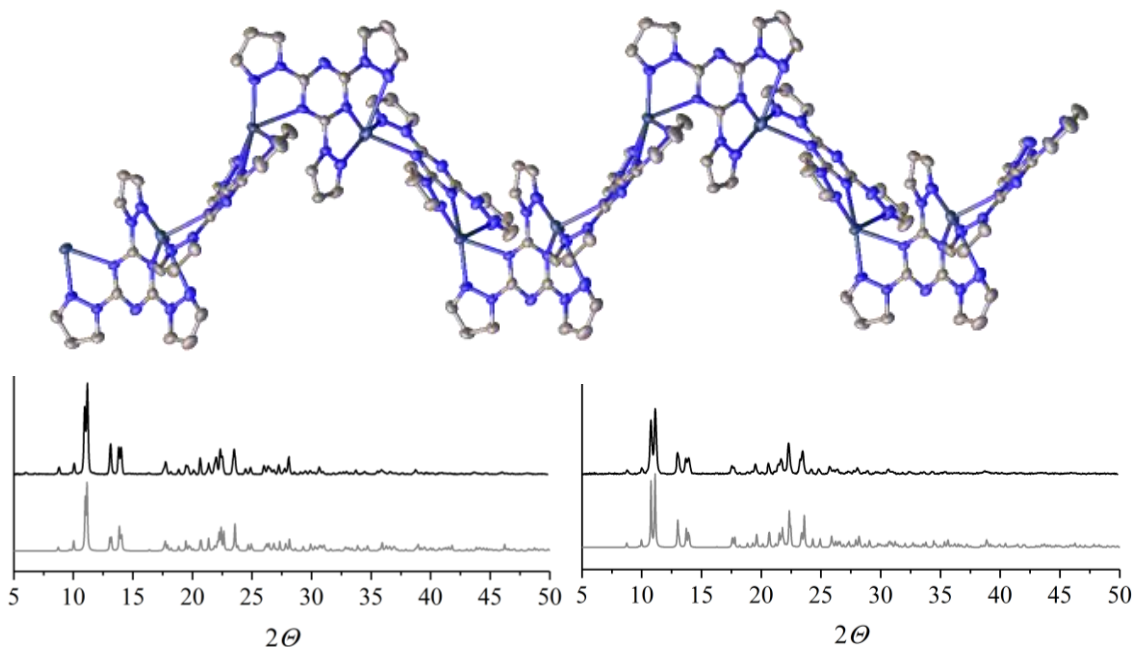


Figure 3.22: Helicoid 1D polymer $\text{Ag}[\text{TPT}]\text{X}^\infty\beta$, $\text{X} = \text{BF}_4^-$ and ClO_4^- , space group $P2_1/c$. Powder pattern of both salts, left tetrafluoroborate and right perchlorate. Hydrogen atoms and counter-anions were removed for clarity. The colour assignment in the plot is black for the experimental and grey for the simulated XRD.

Ligand (**13**)²³ combined with silver tetrafluoroborate in acetonitrile gave rise to a dimer where each silver atom has coordinated one molecule of solvent (Figure 3.23).

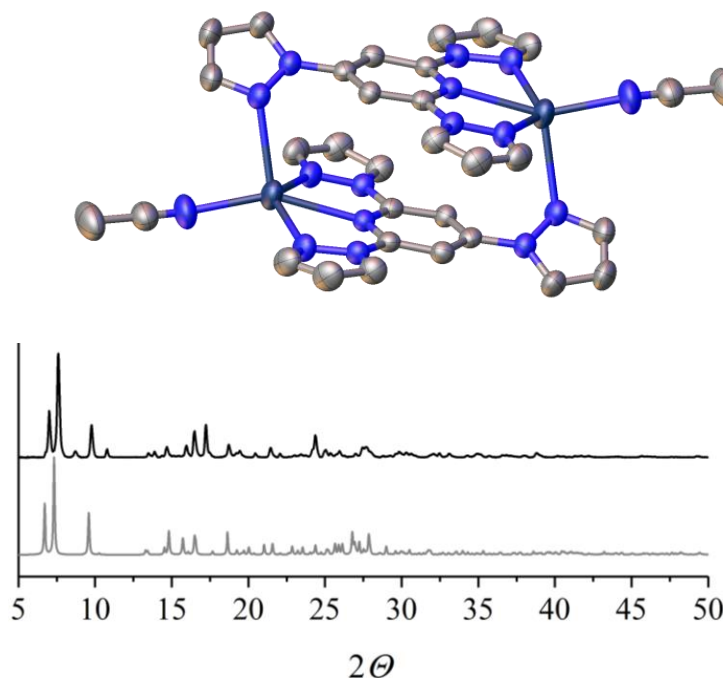


Figure 3.23: Structure of $\text{Ag}[\mathbf{13}]\text{B-MeCN}$ dimer and powder diffraction pattern, space group $P2_1/c$. Hydrogen atoms and counter-anions were removed for clarity. The colour assignment in the plot is black for the experimental and grey for the simulated XRD.

In contrast, when the same compound was prepared from nitromethane, an interesting crystalline compound with Ag-Ag metallophilic interactions was obtained, see Figure 3.24;

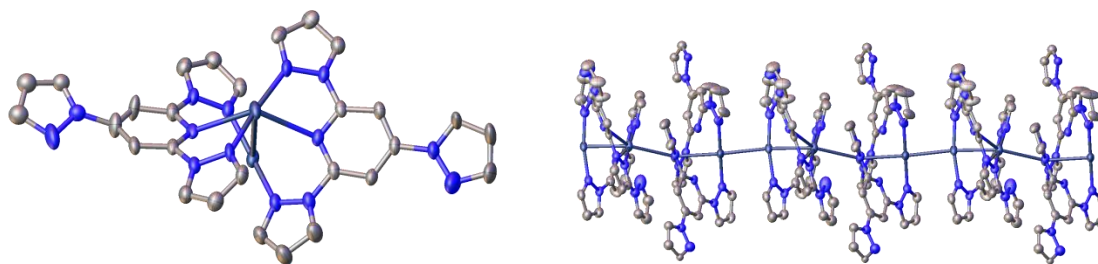


Figure 3.24: Linear polymer $\text{Ag}[13]\text{B}^\alpha$, space group $P2_1/c$. Hydrogen atoms and counter-anions were removed for clarity.

An infinite chain of silver atoms is arranged due to strong metallophilic interactions (2.9 Å). This kind of interaction is common for silver and other d^{10} metals²⁶. This solvatomorph contained four ligands, four silver, four BF_4^- and 0.3 nitromethane molecules in the asymmetric unit cell. When diethyl ether escaped from the opened crystallization vial the crystals redissolved and crystallized upon drying in a different polymorph, changing the morphology from large and thick plates into small regular cubes (Figure 3.25).



Figure 3.25: Photography taken from the optical microscope of the crystals before (left) and after (right) the self-recrystallization.

Countless attempts to measure the experimental powder pattern for the first polymorph α failed because the second form β was stable upon grinding (Figure 3.27).

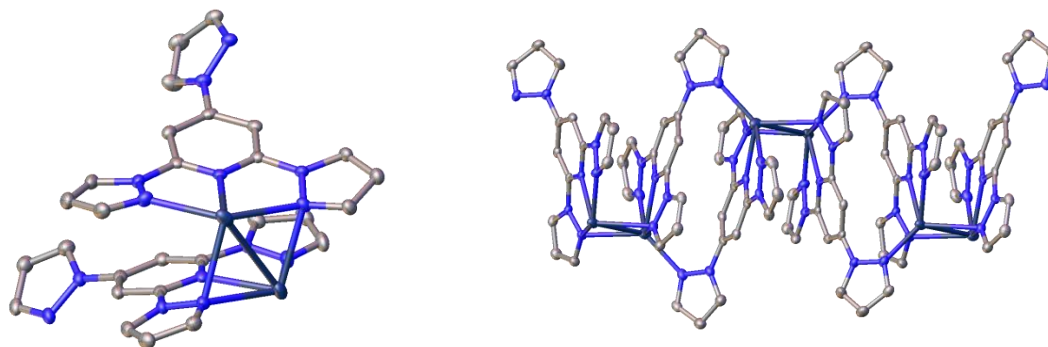


Figure 3.26: Crystal structure of linear polymer $\text{Ag}[13]\text{B}^\beta$, space group $P\bar{1}$. Hydrogen atoms and counter-anions were removed for clarity.

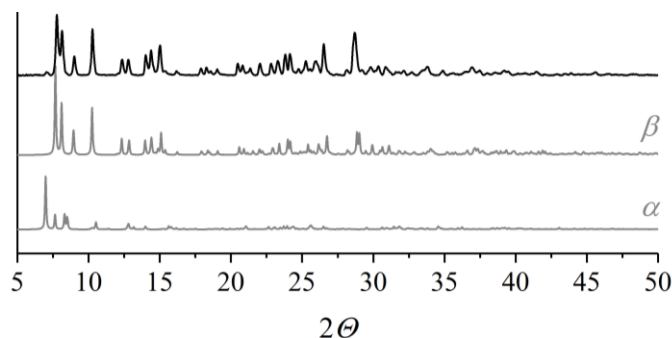


Figure 3.27: Powder pattern of $\text{Ag}(13)\text{BF}_4$. The colour assignment in the plot is black for the experimental and grey for the simulated XRD.

In that case the nitromethane content increased, $\text{Ag}[13]\text{B}^\alpha\beta$ contained two ligands, two silver, two BF_4^- and one nitromethane molecule in the asymmetric unit cell.

Although 2,4,6-tris-(pyrazolyl)-pyrimidine (**14**) was reported previously by Sarkar *et. al* the literature procedure was found to be inaccurate²⁷. Ligand (**14**) was prepared from 2,4,6-trichloro-pyrimidine²⁸ in a similar reaction as ligand (**2**), Figure 3.28;

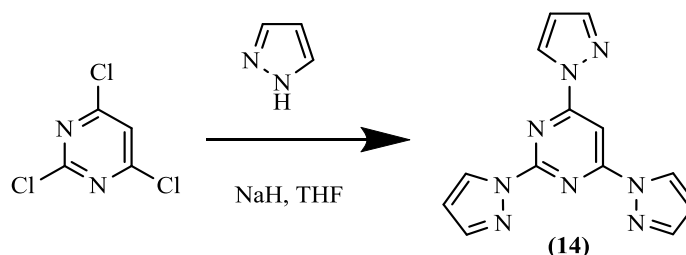


Figure 3.28: Synthetic scheme used for ligand (**14**).

Ligand (**14**) did not form a linear silver coordination polymer. Instead, a polymetallic structure was obtained (Figure 3.29), where 4 ligands shared 5 silver(I) atoms. A similar structure was reported before from a related ligand²⁹;

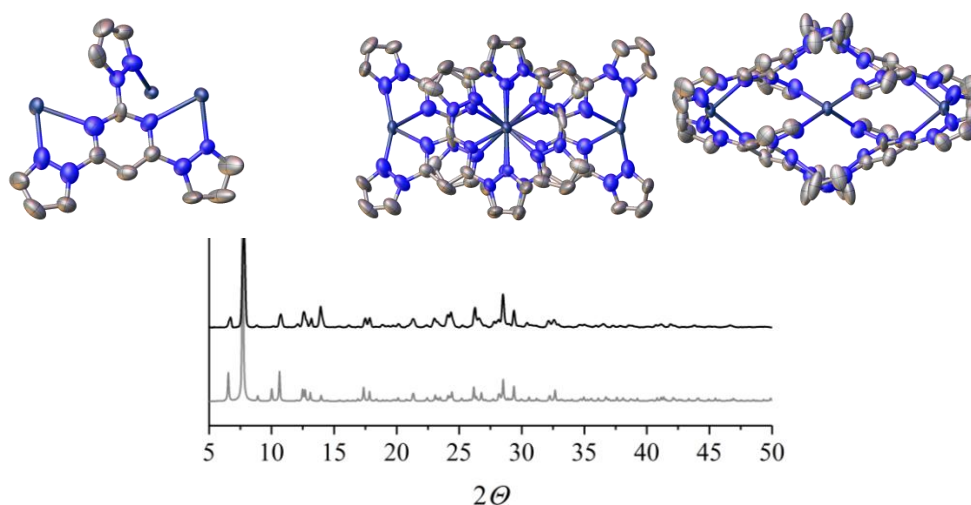


Figure 3.29: Crystal structure in space group $C2/c$ and powder diffraction pattern of $\text{Ag}[14]\text{B}$ cluster. Hydrogen atoms and counter-anions were removed for clarity. Asymmetric unit cell shown and different views of the cluster. The colour assignment in the plot is black for the experimental and grey for the simulated XRD.

Chapter 3

The cluster was crystallized from nitromethane. In contrast, when **(14)** and silver ions reacted in MeCN an analogous structure to the $\text{Ag}[\mathbf{13}]\text{B-MeCN}$ (Figure 3.23) dimer was obtained (Figure 3.30).

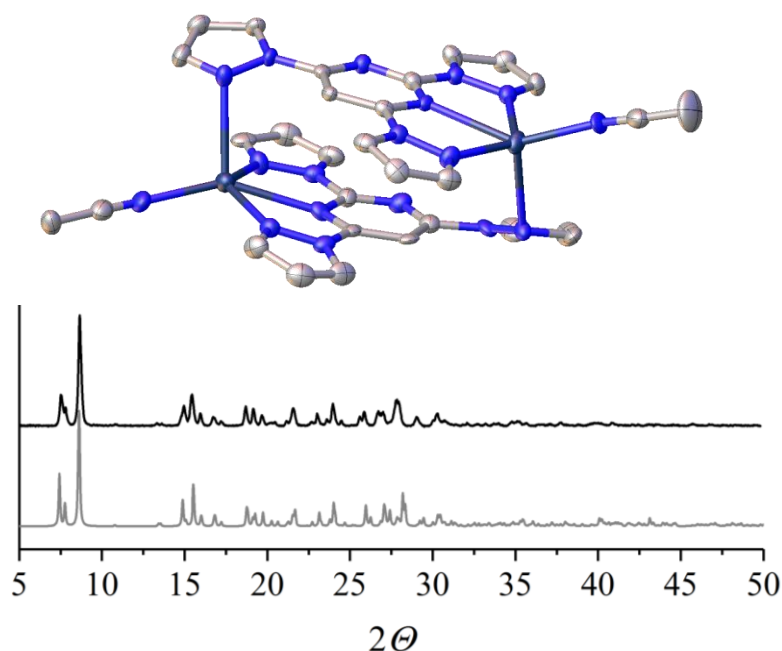


Figure 3.30: Crystal structure in space group $P2_1$ and experimental powder pattern of $\text{Ag}[\mathbf{14}]\text{B-MeCN}$. Hydrogen atoms and counter-anions were removed for clarity. The colour assignment in the plot is black for the experimental and grey for the simulated XRD.

Bis(2,6-bis(pyrazolyl)-4-(imidazolyl)-pyridine (**16**) was synthesized from 2,4,6-trifluoropyridine in a two step reaction with a 43% overall yield (Figure 3.31) and fully characterized.

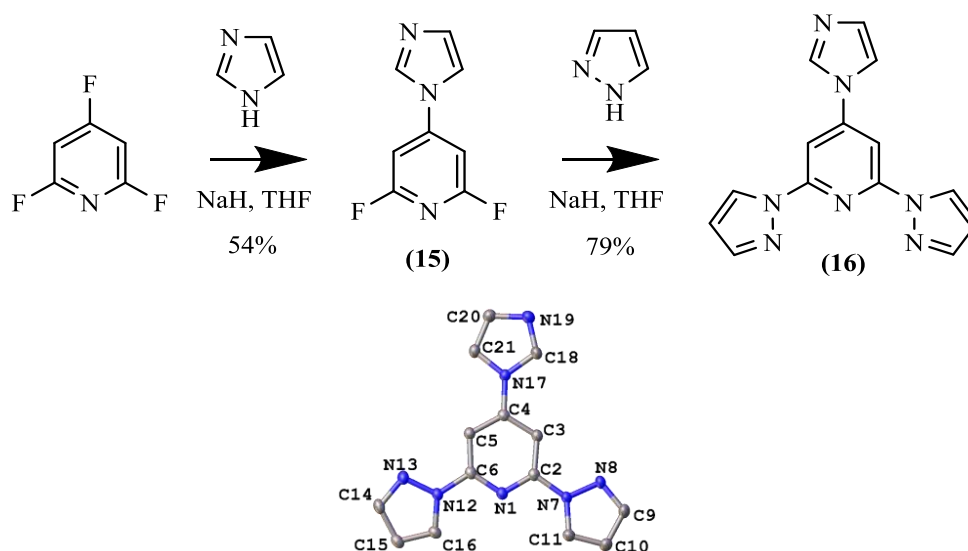


Figure 3.31: Synthetic scheme and crystal structure of ligand **(16)**. $Pna2_1$ space group with two unique molecules in the asymmetric unit cell. Hydrogen atoms were removed for clarity.

Finally ligand **(16)** was reacted in an analogous procedure but a very insoluble polymer precipitated immediately.

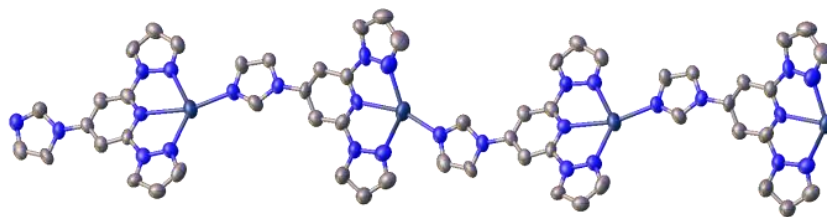


Figure 3.32: Crystal structure of the linear polymer Ag[16]B, space group $P\bar{1}$. Hydrogen atoms and counter-anions were removed for clarity.

Several solvents such as; methanol, ethanol, nitromethane or acetone were used however, only acetonitrile redissolve that polymer. Crystals were observed in a closed old vial containing MeCN solution which was very slowly evaporated (ca. six months). It was believed that acetonitrile solubilized the polymer by breaking it through the coordination of silver ions, similarly as for Ag[13]B-MeCN or Ag[14]B-MeCN (Figure 3.23 and Figure 3.30), however no crystal structure was observed to confirm that.

3.2.6 Different polymer crosslink

Manganese(II) trifluoroacetylacetonate was added to a concentrated solution in nitromethane of complex [2]B to form a new CPG assembly, but with no success. Hence, TPT ligand was reacted with Mn(tFacac)₂ in order to investigate the connectivity and the following structure was fully characterized (Figure 3.33).

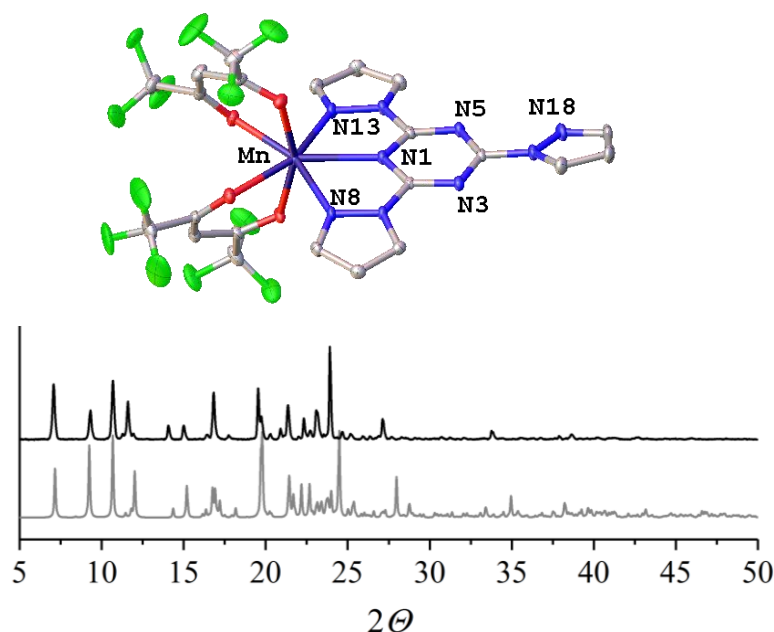


Figure 3.33: Structure obtained from the mixture of Mn(tFacac)₂ with ligand (2). Hydrogen atoms were removed for clarity. Similar geometry to the structure reported before by Zhou et al³⁰.

A three-dimensional polymer was expected³¹. However, Mn(tFacac)₂ complex coordinated to 3N donors yielding that seven coordination geometry through N1, N8 and N13. Polymer formation was prevented because only N3 and N18 were available.

3.2.7 Structural model

From the crystal structures discussed above and all the data collected for the CPG series, a plausible structure of the coordination polymer is the following (Figure 3.34a).

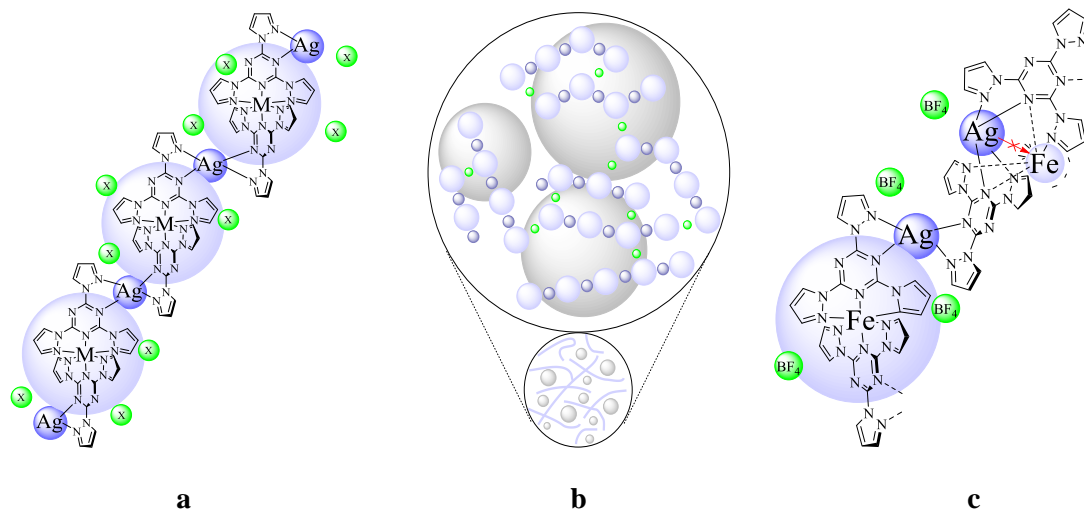


Figure 3.34: Model of; a) TPT heteronuclear coordination polymer, b) the assembly of the CPGs and c) representation of a potential intermediate for the “weak” gels.

The coordination polymer was possibly built through the free N-triazinyl and N-pyrazolyl not involved in the mononuclear complex formation; which bind a silver atom analogously to the $[\text{Ag}(\text{TPT})]\text{X}^\infty$ polymers. The three-dimensional network would be assembled due to the strong anion- π interactions between tetrahedral counter-anions and triazine rings (green dots represent the counter-anion acting as 3D bridges, Figure 3.34b).

Silver cations compete for TPT ligand against iron and cobalt atoms, but compete less against nickel which coordinates stronger the ligand (See Figure 3.7). This effect can be also monitored in solution by paramagnetic NMR of the CPGs (Figure 3.16). The irreversible thixotropy can be explained when considering the existence of an intermediate whose the coordination sphere has been altered (Figure 3.34c). The physical stress applied is enough to homogenize the sample promoting more replacement of M^{2+} by silver, and finally gathering the liquid solution (Figure 3.34c).

The reluctance of **[13]X**, **[14]X** and **[16]X** to undergo silver-induced gelation might be understood from the structures of the homoleptic silver complexes for those ligands. In the crystal structures of $[\text{Ag}(\text{TPT})]\text{X}$ ($\text{X}^- = \text{BF}_4^-$ or ClO_4^-), TPT ligand chelates to both silver ions that are coordinated to them, through their pyrazolyl and triazinyl N donors. Several other 1,3,5-triazine derivatives can also bridge between silver ions in a similar fashion in the solid state³². In contrast, **Ag[13]X** and **Ag[16]X** can only assemble into larger aggregates by monodentate binding through its pendant pyrazolyl substituent. Although chelation of a second silver ion by **Ag[14]X** through the pyrimidinyl N1 atom and N6-pyrazolyl substituents was feasible, it was not observed in practice. That may reflect a preferred transoid orientation of

those N-donors, which avoids an intramolecular steric clash between the pyrimidinyl C4 and pyrazolyl C5 C–H groups (steric hindrance highlighted in red in Figure 3.35).

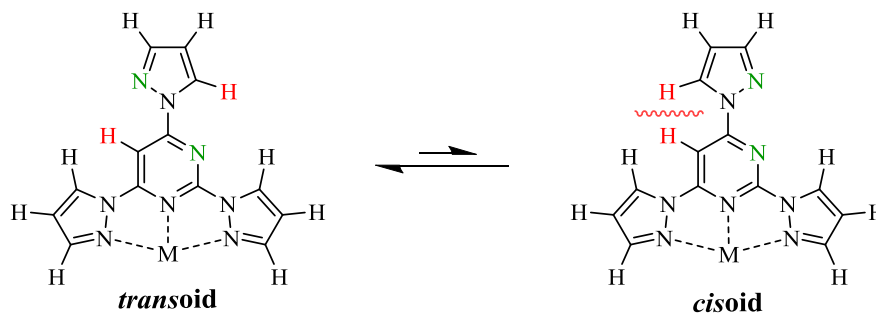


Figure 3.35: Cisoid and transoid conformations of the pendant pyrazolyl substituent in metal-bound tpym.

The transoid conformation is indeed observed crystallographically in [14]C (Figure 3.36; the pendant pyrazolyl conformation in the BF_4^- salt of this complex is uncertain because of symmetry imposed crystallographic disorder). Hence, out of the ligands considered in this work, only TPT has a proven ability to chelate two silver ions simultaneously, which will afford more stable mixed-metal assemblies in solutions of $[\text{M}(\text{TPT})_2]\text{X}_2$ and AgX . That might explain the unique gelation properties of the $[\text{M}(\text{TPT})_2]\text{X}_2/\text{AgX}$ system.

3.2.8 Novel iron(II) and iron(III) complexes

[14]B and [14]C were synthesised with the usual procedure, Figure 3.36;

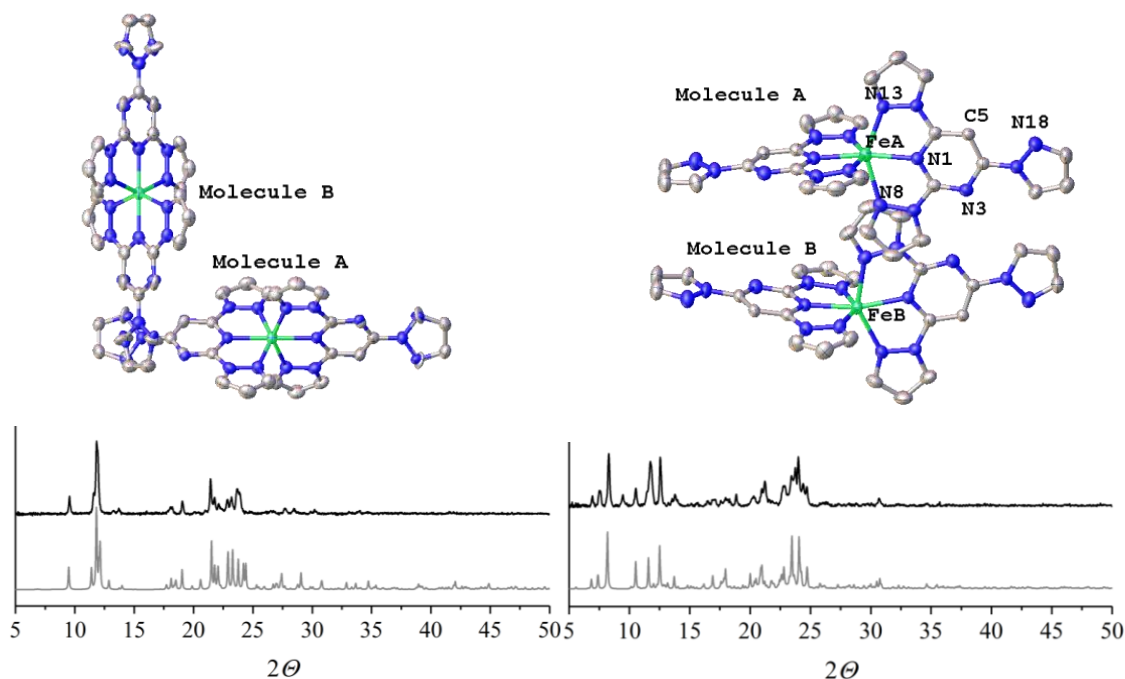


Figure 3.36: Crystal structures of [14]B (left) and [14]C (right). Hydrogen atoms and counter-anions were removed for clarity. Powder diffraction patterns of both are also shown, the colour assignment in the plot is black for the experimental and grey for the simulated XRD.

Chapter 3

Both compounds contained two unique complexes in the asymmetric unit cell. The first structure **[14]B** exhibited symmetry-imposed disorder (space group $Fddd$) while the perchlorate salt crystallized in $P2_1/n$.

In contrast, the perchlorate and tetrafluoroborate iron(II) salts of **(16)** were isostructural and solvent free. The two salts showed poor solubility and crystallized in the monoclinic $C/2c$ space group (Figure 3.37);

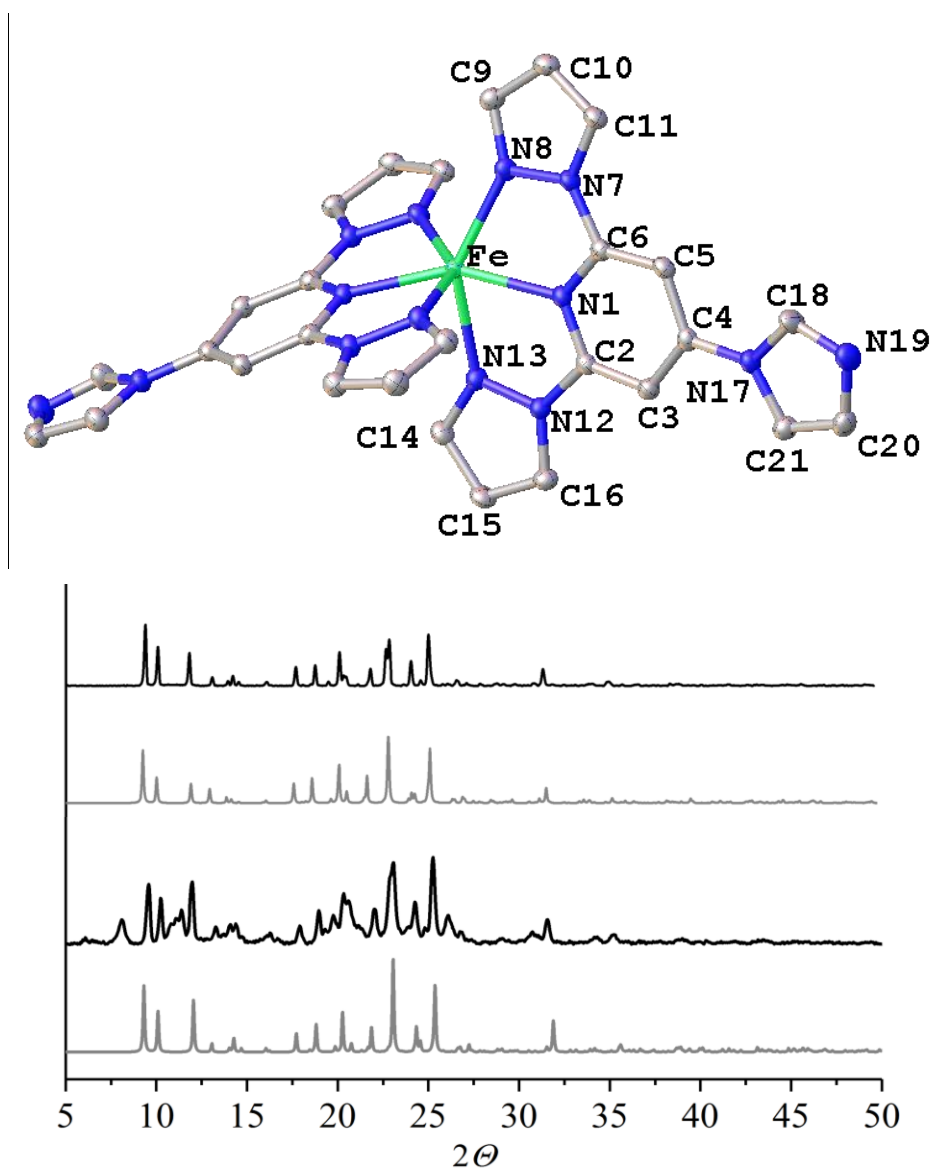


Figure 3.37: Crystal structures of **[16]X** which were isostructural. Hydrogen atoms and counter-anions were removed for clarity. Powder diffraction pattern of **[16]C** (top) and **[16]B** (bottom). The colour assignment in the plot is black for the experimental and grey for the simulated XRD.

The **[16]C** powder pattern was very clean however **[16]B** was collected several times and was always noisy. Bulk powder samples of **[16]B** were amorphous. Surprisingly the four novel iron(II) complexes prepared were HS at 120K (Table 3-3).

Chapter 3

	[14]B, Molecule A	[14]B, Molecule B	[14]C, Molecule A
Fe–N[py]	2.11765(11)	2.11029(8)	2.119873(19), 2.12174(2)
Fe–N[pz]	2.20227(6)	2.21423(7)	2.20850(2) - 2.22537(3)
V_{Oh}	12.3526(4)	12.3398(3)	12.42997(10)
Σ	164.176(10)	178.839(15)	160.258(2)
\varnothing	540.020(16)	524.050(13)	531.827(4)
ϕ	180.0(0)	180.0(0)	166.0676(3)
θ	76.400(3)	69.888(4)	88.3648(11)
	[14]C, Molecule B	[16]B	[16]C
Fe–N[py]	2.11586(2), 2.11769(2)	2.12965(12)	2.1323(2)
Fe–N[pz]	2.0378(3) - 2.22372(3)	2.17544(9), 2.19683(8)	2.1762(2), 2.19582(16)
V_{Oh}	12.46945(10)	11.3330(4)	11.3307(8)
Σ	158.882(2)	181.567(11)	182.567(11)
\varnothing	525.074(4)	557.217(19)	562.86(4)
ϕ	169.82489(19)	151.257(2)	151.459(4)
θ	88.7701(11)	68.275(4)	68.406(7)

Table 3-3: Crystallographic parameters for complexes [14]X and [16]X at 120K determined directly from the crystal structure by using Olex2³³.

Their magnetic behaviour of the crystals is in agreement with SQUID measurements. χT vs T was also determined in acetonitrile solution by Evans method (Figure 3.38).

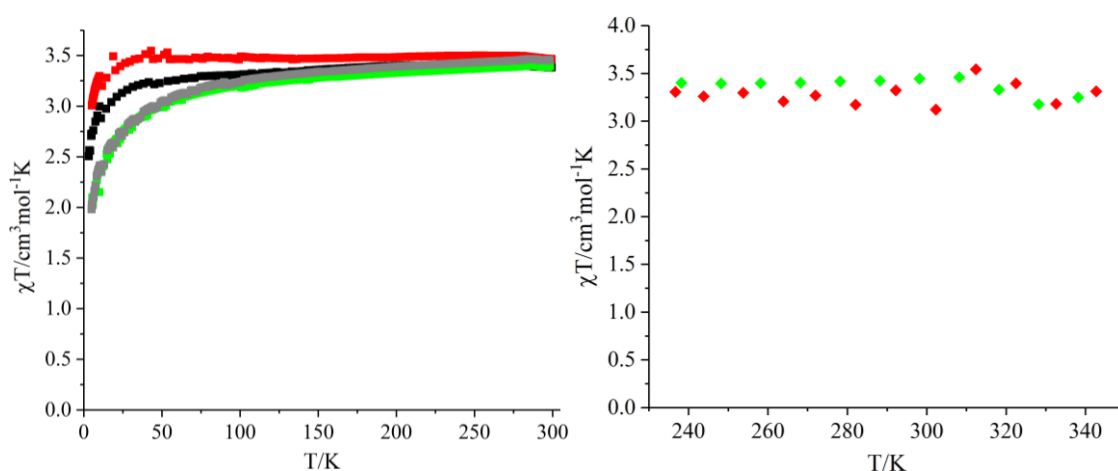


Figure 3.38: SQUID curves (left) and Evans method (right) of complexes [14]X and [16]X. The colour assignment in the SQUID plot is red for [16]C, black for [16]B, grey for [14]B and green for [14]C. Data points taken every 10 K.

Chapter 3

The magnetic behaviour of complexes **[16]X** contrasts with the one observed previously where **[13]B** was SCO acting in the solid state²³. Both ligands were based on 1-bpp scaffold with N-azolyl in the 4-position of the pyridine. Although such electronic difference between **[13]X** and **[16]X** was not expected at the molecular level, the **[16]X** complexes present extremely distorted structures. Detailed analysis of these structures highlighted the strong interactions of the counter-anions with rings and specially with the hydrogen atoms of C18,21-H, C3,5-H and C11,16-H, Figure 3.39;

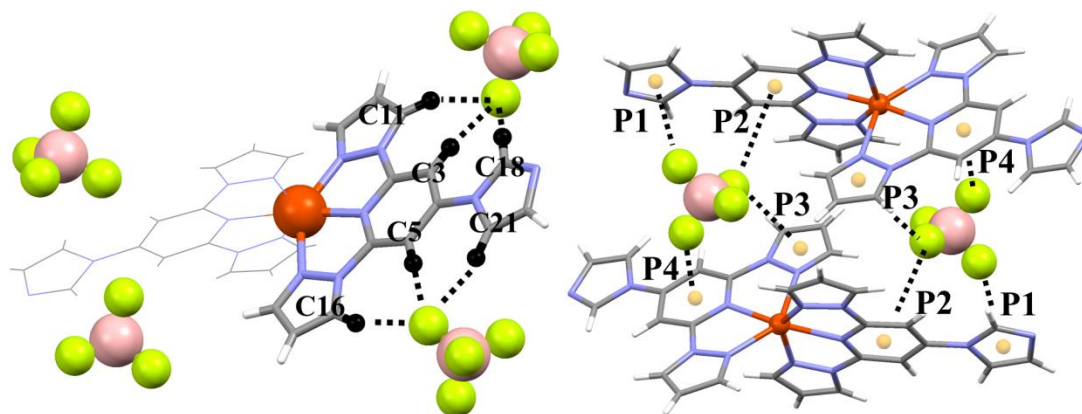


Figure 3.39: View of anion controlled short contact van der Waals interactions in **[16]X**.

The structures accommodate the counter-anions with short contacts in the four sides of the tetrahedral anion, see Table 3-4;

[16]B		[16]C	
BF ₃ -F [⋯] H-C3	2.245(3)	ClO ₃ -O [⋯] H-C3	2.285(2)
BF ₃ -F [⋯] H-C11	2.343(4)	ClO ₃ -O [⋯] H-C11	2.401(3)
BF ₃ -F [⋯] H-C18	2.602(4)	ClO ₃ -O [⋯] H-C18	2.591(2)
BF ₃ -F [⋯] H-C5	2.280(3)	ClO ₃ -O [⋯] H-C5	2.341(5)
BF ₃ -F [⋯] H-C16	2.483(4)	ClO ₃ -O [⋯] H-C16	2.513(3)
BF ₃ -F [⋯] H-C21	2.442(4)	ClO ₃ -O [⋯] H-C21	2.491(3)
BF ₃ -F [⋯] π _[imidazole] P1	3.360(4)	ClO ₃ -O [⋯] π _[imidazole] P1	3.330(2)
BF ₃ -F [⋯] π _[pyridine] P2	3.665(5)	ClO ₃ -O [⋯] π _[pyridine] P2	3.627(4)
BF ₃ -F [⋯] π _[pyrazole] P3	3.383(4)	ClO ₃ -O [⋯] π _[pyrazole] P3	3.344(2)
BF ₃ -F [⋯] π _[pyridine] P4	2.991(4)	ClO ₃ -O [⋯] π _[pyridine] P4	3.019(2)

Table 3-4: Values of the short contact between **[16]²⁺** molecules and the counter-anions observed in the crystal structures by using Olex2³³.

These strong interactions with the counter-anions were responsible for the poor solubility of the compounds. While **[16]C** was relatively easy to crystallize, the complex **[16]B** was

Chapter 3

extremely difficult, in fact it was only obtained once as single crystals. While trying several conditions and solvents, by using methanol as solvent, [16]B crystals were observed mixed with an unexpected three iron(III) cluster (Figure 3.40).

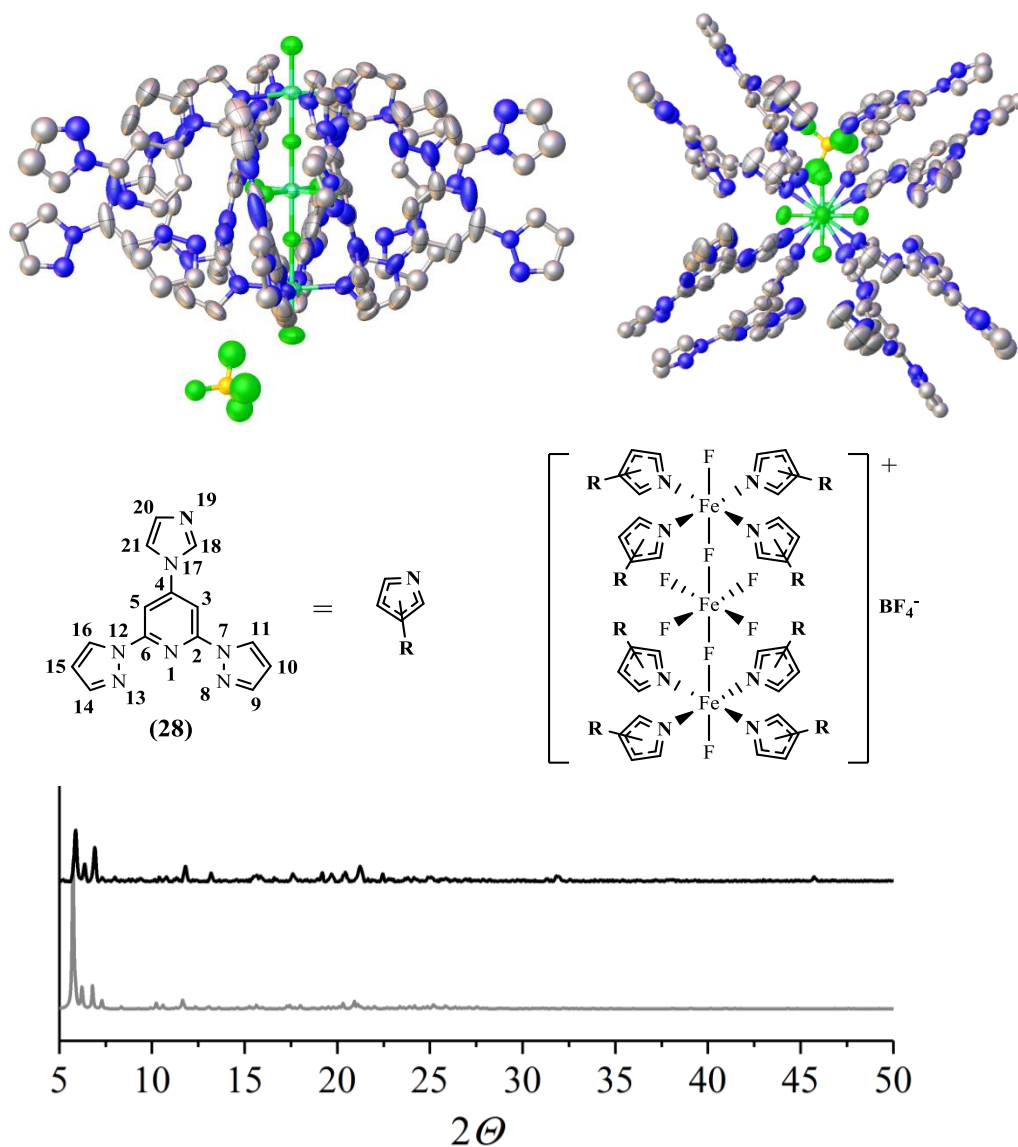


Figure 3.40: Two different views of the crystal structure $\text{Fe}^{\text{III}}_3[\text{16}]\text{F}_8$ (top). Hydrogen atoms were removed for clarity. Schematic representation drawn with labels for clarity (middle). Powder diffraction pattern of $\text{Fe}^{\text{III}}_3[\text{16}]\text{F}_8$ (bottom). The colour assignment in the plot is black for the experimental and grey for the simulated XRD.

The $\text{Fe}(\text{BF}_4)_2$ salt decomposed somehow into a $\text{Fe}^{\text{III}}\text{F}_x$ species³⁴. It was believed that the anion FeF_6^{2-} template the cluster formation³⁵ (Figure 3.41). This cluster was composed of three iron(III) bridged by fluorine atoms. The inner iron was coordinated to six fluorine atoms, two of them were bridging the outer iron atoms in a straight line. The other four fluorine atoms were on the perpendicular plane to this line, each of which presented two strong hydrogen bonding with the hydrogen of C18 (Ligand (16) labels in Figure 3.40, values of the interactions in Table 3-5). On the other hand, each of the outer iron atoms completed the coordination sphere with four N9 donor ligands and an external fluorine.

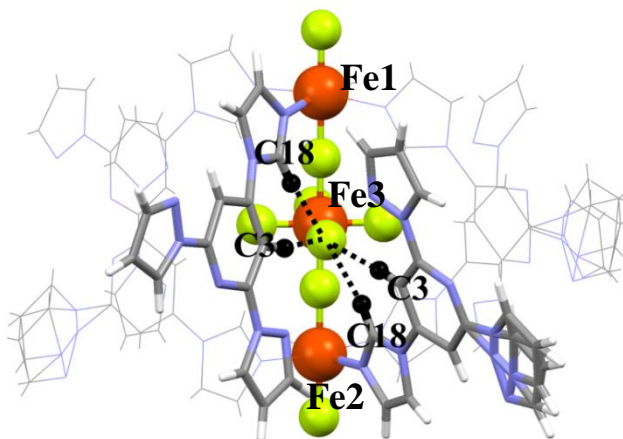


Figure 3.41: View of short the contacts C18-H \cdots F-Fe3F₅ and C3-H \cdots F-Fe3F₅ highlighted as black dashed line. Some ligands were removed and some were de-emphasised for clarity.

$\text{Fe}^{\text{III}}_3[16]\text{F}_8$	
Fe3F ₅ -F \cdots H-C3	2.371(4) - 2.461(3)
Fe3F ₅ -F \cdots H-C18	2.121(3) - 2.176(3)

Table 3-5: Range of values of the short contact between the eight (16) ligands and the anion templating $[\text{Fe}^{\text{III}}\text{F}_6]^{3-}$ observed in the crystal structure by using Olex2³³.

Two different polymorphs were observed depending on the crystallization method. Slow evaporation of methanol yielded large cubes which were twinned and not suitable for a good data collection by X-ray single crystal diffraction. The structure solved in the tetragonal $P4_322$ space group but the model had high residuals and unassigned electron density. Powder patterns of cubes $\text{Fe}^{\text{III}}_3[16]\text{F}$ always contained some $[16]\text{B}$ in the mixture and vice-versa (Figure 3.41). This fact was also in agreement with the microanalysis. Micro-analytically pure $[16]\text{B}$ was obtained from a nitromethane solution, although unfortunately that sample was amorphous.

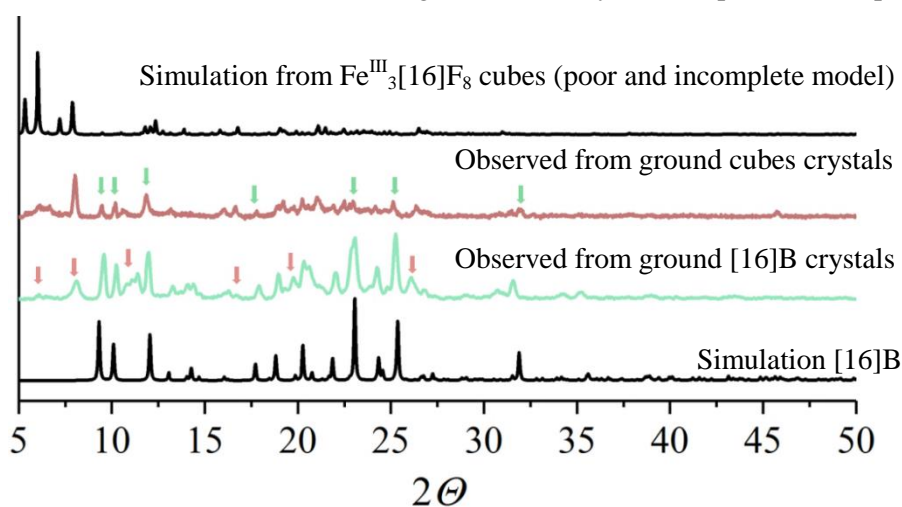


Figure 3.42: Experimental powder diffraction pattern of $\text{Fe}^{\text{III}}_3[16]\text{F}_8$ cubes polymorph (pale red line). The colour assignment in the plot was black for the simulations, compared with the experimental observed from ground “single crystals of $[16]\text{B}$ ”. Several arrows highlight the wrong peaks from each model which were found to be characteristic of each other compound.

Chapter 3

Thick needles were obtained from atmospheric diffusion of diethyl ether into a methanolic solution of one equivalent of sodium hexafluoroferrate, two equivalents of iron(II) tetrafluoroborate and eight equivalents of ligand (**16**). In that case the crystals were suitable for XRD analysis (Figure 3.40). Although the $\text{Fe}^{\text{III}}_3[\mathbf{16}]\text{F}_8$ cluster was not very soluble, it was possible to collect an ESMS spectrum in MeCN. The peaks corresponded to the cluster $[\mathbf{16}]^+ = [\text{Fe}^{\text{III}}\text{F}_6\text{CFe}^{\text{III}}_2(\mathbf{16})_8\text{F}_2]^+$ and to the double charged cluster when a fluorine was lost $[[\mathbf{16}]^+-\text{F}]^{2+}$ (Figure 3.43).

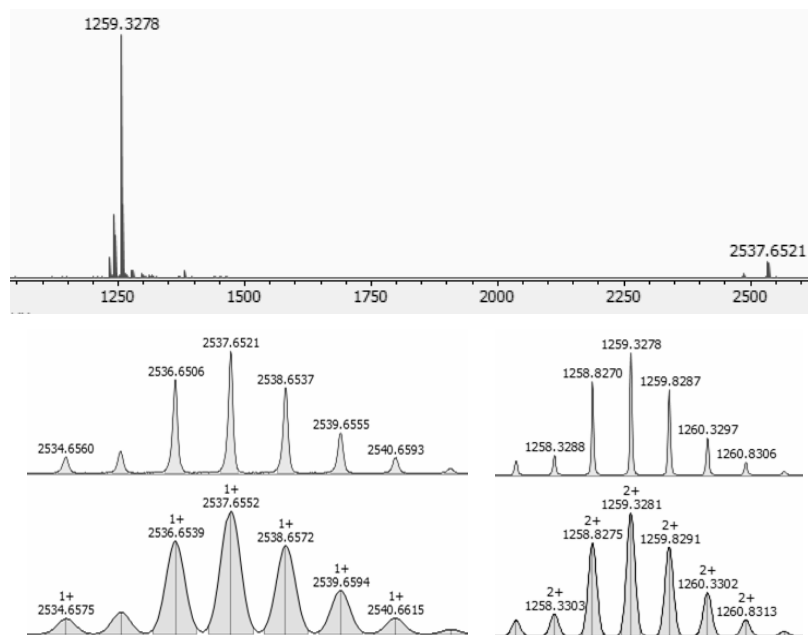


Figure 3.43: Mass spectrum of the cluster $\text{Fe}^{\text{III}}_3[\mathbf{16}]\text{F}_8$ (top). Zoom on the two major peaks, comparison of the isotopic patterns (bottom); orange for the experimental and black for the simulated.

The magnetic susceptibility of the material was measured on SQUID (Figure 3.45) where a horizontal line around $12 \text{ cm}^3 \text{ mol}^{-1} \text{ K}$ was expected for the three iron (III) HS. However the $\chi_{\text{M}}T$ values observed were lower. This reflects antiferromagnetic coupling between two next-to-nearest neighbour cations through a non-magnetic anion. In this case, we had a linear trimeric iron (III) cluster bridged by fluorine atoms, Figure 3.44;

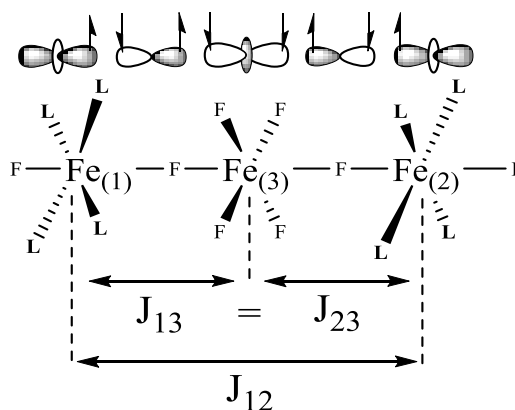


Figure 3.44: Scheme of the superexchange in the cluster $\text{Fe}^{\text{III}}_3[\mathbf{16}]\text{F}_8$.

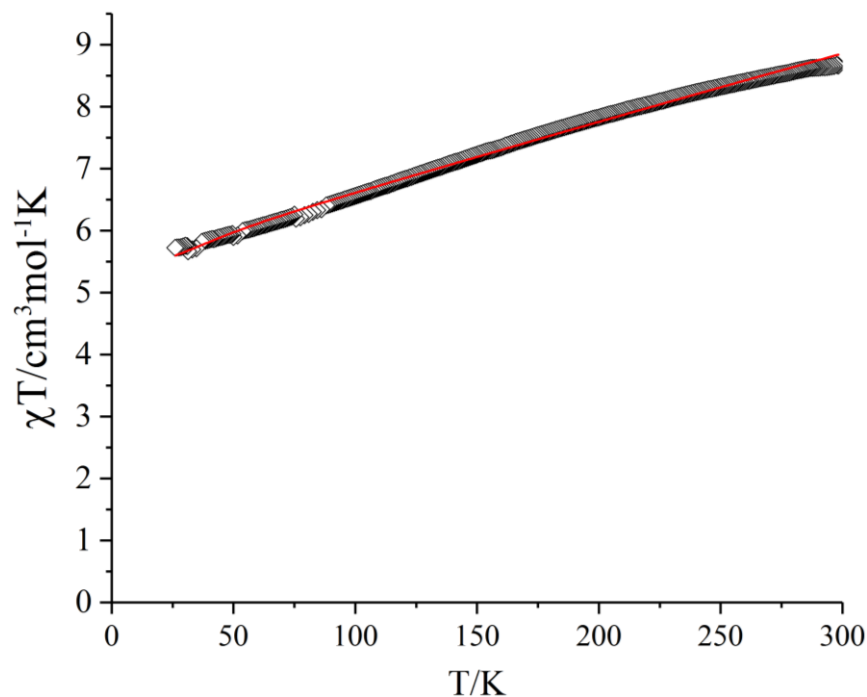


Figure 3.45: SQUID curve of $\text{Fe}^{\text{III}}_3[16]\text{F}_8$ overlaid with the fitting curve (red line).

The magnetic data are fitted using the PHI software³⁶. The g value calculated was 2.25, and the couplings were a strong antiferromagnetic coupling $J_{13} = J_{23} = -39.40$ between Fe3 and Fe2 or Fe1 which was equivalent, and a small ferromagnetic coupling $J_{12} = +1.30$.

3.2.9 DFT calculations

DFT calculations were performed using SPARTAN¹⁸ on the (16) free ligand in order to understand the cluster formation. It can exist in four conformations according to the rotation of the single bonds between pyrazolyl or imidazolyl and the pyridine rings, Figure 3.46;

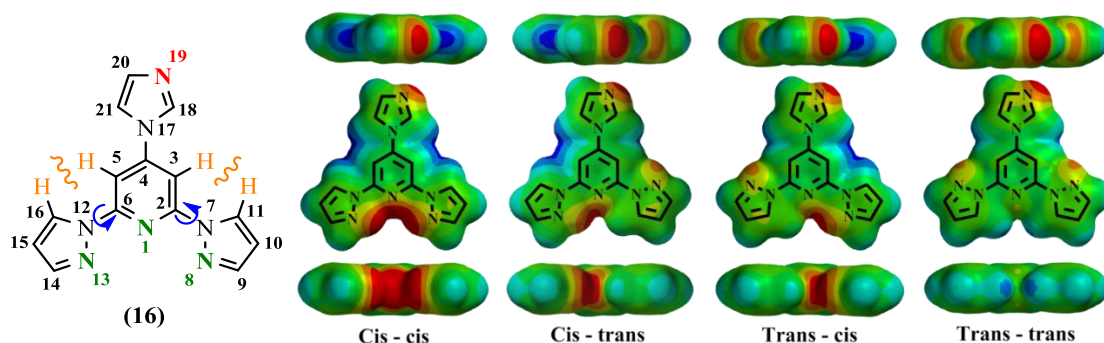


Figure 3.46: Scheme of conformer trans trans (C-c). Cis or trans define the relative position of N8 or N13 with respect to N1. Electrostatic potential map of the four major conformers.

Due to steric hindrance of hydrogen atoms in the pyridine (C3 or C5) with the ones in the pyrazole (C11 and C16 respectively), the Cis-cis conformation is the less favoured and the most stable is T-t, in agreement with the crystal structure of (16) (Figure 3.31). However all conformations were in equilibrium so all of them were considered.

Chapter 3

On its own Figure 3.46 does not give much information. However it showed qualitatively that N19 contained strong electron density in all conformations while the bpp region only in the C-c conformer which was also the less stable conformation (Table 3-6).

Conformer	C-c	C-t	T-c	T-t
Energy (Hartree)	-922.980103	-922.995284	-922.995448	-923.005694
Relative energy	0.025591	0.010410	0.010246	0

Table 3-6: Energy calculated of the equilibrium geometry for every conformer. The relative energy is normalized with the most stable T-t conformation.

In an attempt to obtain a more quantitative analysis of the electron density, values of atomic charges for the N-donor atoms of (**16**) were calculated and displayed in Table 3-7;

Cis - cis	N19	N1	N13	N8
Mulliken	-0.138	-0.009	-0.060	-0.059
Natural charge	-0.490	-0.454	-0.260	-0.259
Cis - trans	N19	N1	N13	N8
Mulliken	-0.138	-0.072	-0.074	-0.104
Natural charge	-0.491	-0.496	-0.273	-0.320
Trans - cis	N19	N1	N13	N8
Mulliken	-0.140	-0.072	-0.075	-0.105
Natural charge	-0.491	-0.496	-0.274	-0.320
Trans - trans	N19	N1	N13	N8
Mulliken	-0.139	-0.136	-0.101	-0.101
Natural charge	-0.492	-0.535	-0.317	-0.316

Table 3-7: Atomic charges of the N-donor from the equilibrium geometry calculations of all conformers of ligand (16**).**

The formulism of Mulliken charge and NPA charge are essentially identical, the key difference is that the Mulliken charge is calculated under original basis functions, while NPA charge is derived based on natural atomic orbitals. Although the Mulliken charge was significantly higher for N19 than for the other nitrogen atoms, natural charges observed did not present a clear trend towards drawing a conclusion. However the situation changed when looking at the molecular orbital energies (Table 3-8 and Figure 3.47).

Chapter 3

	Cis - cis	Cis - trans	Trans - cis	Trans - trans
HOMO	-5.89	-5.94	-5.86	-5.81
HOMO(-1)	-6.11	-5.99	-6.02	-5.98
HOMO(-2)	-6.14	-6.19	-6.30	-6.27
HOMO(-3)	-6.27	-6.29	-6.37	-6.39
HOMO(-4)	-6.32	-6.34	-6.38	-6.45
HOMO(-5)	-6.49	-6.42	-6.51	-6.55
HOMO(-6)	-6.49	-6.52	-6.54	-6.72
HOMO(-7)	-6.60	-6.62	-6.77	-7.00
HOMO(-8)	-6.82	-6.87	-6.96	-7.03
HOMO(-9)	-7.06	-7.08	-7.18	-7.20

Table 3-8: Molecular orbital energies, the N-atom lone pair orbitals were highlighted in bold.

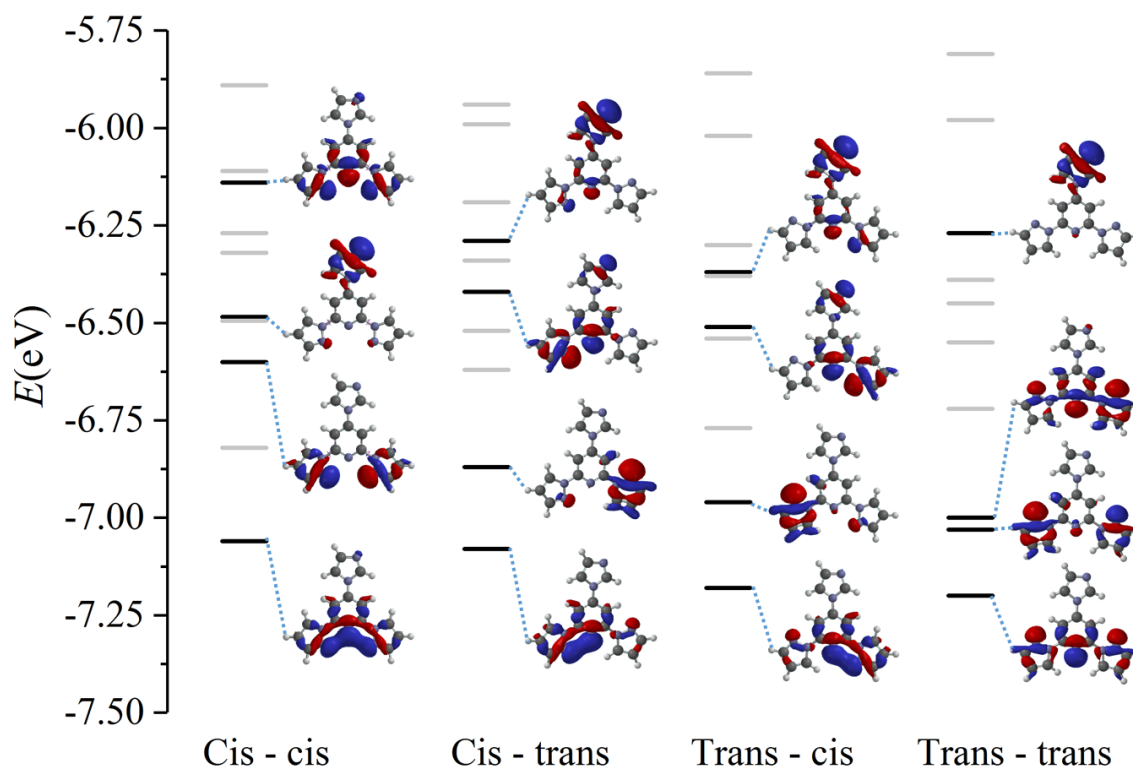


Figure 3.47: Molecular orbital HOMO – HOMO(-9) energy levels calculated for every conformation. π -orbitals were de-emphasised for clarity.

The most energetic lone pair for the three most stable conformations contains the electronic density around N19 which could imply its highly reactivity towards the metal ion compared to the bpp coordination site.

3.3 Conclusions

A new approach to coordination-based gelation without ancillary ligands was presented. Among the ligands discussed during this work, only 2,4,6-tris(pyrazolyl)-1,3,5-triazine (TPT, ligand **(2)**) acted as a gelator. The new family of CPGs reported is sensitive to physical stimuli or stress. On the other hand, they are quite thermo-stable maintaining the viscosity up to the boiling point of the solvent. The gels have been characterized by Electrospray Mass Spectrometry, ^1H Nuclear Magnetic Resonance, Energy Dispersive X-ray and Scanning Electron Microscopy, where silver precipitation as small silver nanoparticles was observed. X-ray single crystal structures of the M(II) complexes (monomer) and the $[\text{Ag(TPT)}]X_\infty$ 1D polymer present strong non-covalent interactions. They suggest a plausible arrangement of a 1D $\text{Ag-TPT-M-TPT}^\infty$ heterometallic polymer which self-assembly in a 3D network through non-covalent interactions. High resolution mass spectroscopy is in agreement with that structure. Both iron(II) and cobalt(II) derived-gel present irreversible thixotropy while nickel(II) gels maintain their viscosity after shaking. Here it has been proved the Irving-William series as plot describing the stability of complexes can be applied as well to predict the strength of the metallogels depending on the metal used.

The different ligands; **(2)**, **(13)**, **(14)** and **(16)** were reacted with silver(I) salts in order to study their coordination sphere. Several assemblies were observed; dimers, polymers and polymetallic structures which were isolated and fully characterized by ESMS, single crystal XRD and powder XRD.

Two novel iron(II) complexes were designed to undergo SCO, but surprisingly none of the **[14]X** or **[16]X** salts undergo the spin transition. While optimising the crystallization of **[16]B** a linear cluster containing three iron(III) atoms bridged by fluorine atoms was observed, $\text{Fe}^{\text{III}}_3[\text{16}]\text{F}_8$. It was fully characterized by ESMS, SQUID magnetometry, single crystal XRD and powder XRD. The template effect of the cluster was attributed to the strong affinity of (C11, C3 and C18)-H towards the counter-anions. The coupling of the iron(III) centres was calculated to be antiferromagnetic between the iron in the center (Fe_3) and the outer iron atoms, however the external iron(III) were weakly ferromagnetically coupled. DFT calculations highlighted the electron density around N19 in the most energetic lone pair.

3.4 Bibliography

1. Dong, S.; Zheng, B.; Wang, F.; Huang, F., Supramolecular Polymers Constructed from Macrocyclic-Based Host–Guest Molecular Recognition Motifs. *Accounts of Chemical Research* **2014**, *47* (7), 1982-1994.
2. Babu, S. S.; Praveen, V. K.; Ajayaghosh, A., Functional π -Gelators and Their Applications. *Chemical Reviews* **2014**, *114* (4), 1973-2129.
3. Jones, C. D.; Steed, J. W., Gels with sense: supramolecular materials that respond to heat, light and sound. *Chemical Society Reviews* **2016**, *45* (23), 6546-6596.
4. (a) Zhang, J.; Su, C.-Y., Metal-organic gels: From discrete metallogelators to coordination polymers. *Coordination Chemistry Reviews* **2013**, *257* (7), 1373-1408; (b) Piepenbrock, M.-O. M.; Lloyd, G. O.; Clarke, N.; Steed, J. W., Metal- and Anion-Binding Supramolecular Gels. *Chemical Reviews* **2010**, *110* (4), 1960-2004.
5. (a) Sutar, P.; Maji, T. K., Coordination polymer gels: soft metal–organic supramolecular materials and versatile applications. *Chemical Communications* **2016**, *52* (52), 8055-8074; (b) Ye, L.; Wan, L.; Huang, F., A class of polytriazole metallogels via CuAAC polymerization: preparation and properties. *New Journal of Chemistry* **2017**, *41* (11), 4424-4430.
6. (a) Jung, J. H.; Lee, J. H.; Silverman, J. R.; John, G., Coordination polymer gels with important environmental and biological applications. *Chemical Society Reviews* **2013**, *42* (3), 924-936; (b) Wu, J.-J.; Cao, M.-L.; Zhang, J.-Y.; Ye, B.-H., A nanocomposite gel based on 1D coordination polymers and nanoclusters reversibly gelate water upon heating. *RSC Advances* **2012**, *2* (33), 12718-12723; (c) Byrne, P.; Lloyd, G. O.; Applegarth, L.; Anderson, K. M.; Clarke, N.; Steed, J. W., Metal-induced gelation in dipyrindyl ureas. *New Journal of Chemistry* **2010**, *34* (10), 2261-2274.
7. (a) Sarkar, S.; Dutta, S.; Chakrabarti, S.; Bairi, P.; Pal, T., Redox-Switchable Copper(I) Metallogel: A Metal–Organic Material for Selective and Naked-Eye Sensing of Picric Acid. *ACS Applied Materials & Interfaces* **2014**, *6* (9), 6308-6316; (b) Sun, J.; Liu, Y.; Jin, L.; Chen, T.; Yin, B., Coordination-induced gelation of an l-glutamic acid Schiff base derivative: the anion effect and cyanide-specific selectivity. *Chemical Communications* **2016**, *52* (4), 768-771.
8. (a) Tanaka, K.; Yoshimura, T., A novel coordination polymer gel based on succinic acid–copper(ii) nitrate–DABCO: metal ion and counterion specific organogelation. *New Journal of Chemistry* **2012**, *36* (7), 1439-1441; (b) Zhong, J.-L.; Jia, X.-J.; Liu, H.-J.; Luo, X.-Z.; Hong, S.-G.; Zhang, N.; Huang, J.-B., Self-assembled metallogels formed from N,N',N''-tris(4-pyridyl)trimesic amide in aqueous solution induced by Fe(iii)/Fe(ii) ions. *Soft Matter* **2016**, *12* (1), 191-199.
9. (a) Xue, M.; Lü, Y.; Sun, Q.; Liu, K.; Liu, Z.; Sun, P., Ag(I)-Coordinated Supramolecular Metallogels Based on Schiff Base Ligands: Structural Characterization and Reversible Thixotropic Property. *Crystal Growth & Design* **2015**, *15* (11), 5360-5367; (b) Paul,

M.; Sarkar, K.; Dastidar, P., Metallogels Derived from Silver Coordination Polymers of C3-Symmetric Tris(pyridylamide) Tripodal Ligands: Synthesis of Ag Nanoparticles and Catalysis. *Chemistry – A European Journal* **2015**, *21* (1), 255-268; (c) Liu, Z.-X.; Feng, Y.; Zhao, Z.-Y.; Yan, Z.-C.; He, Y.-M.; Luo, X.-J.; Liu, C.-Y.; Fan, Q.-H., A New Class of Dendritic Metallogels with Multiple Stimuli-Responsiveness and as Templates for the In Situ Synthesis of Silver Nanoparticles. *Chemistry – A European Journal* **2014**, *20* (2), 533-541.

10. (a) Piepenbrock, M.-O. M.; Clarke, N.; Steed, J. W., Rheology and silver nanoparticle templating in a bis(urea) silver metallogel. *Soft Matter* **2011**, *7* (6), 2412-2418; (b) Lee, J. H.; Kang, S.; Lee, J. Y.; Jung, J. H., A tetrazole-based metallogel induced with Ag⁺ ion and its silver nanoparticle in catalysis. *Soft Matter* **2012**, *8* (24), 6557-6563; (c) Tatikonda, R.; Bertula, K.; Nonappa; Hietala, S.; Rissanen, K.; Haukka, M., Bipyridine based metallogels: an unprecedented difference in photochemical and chemical reduction in the in situ nanoparticle formation. *Dalton Transactions* **2017**, *46* (9), 2793-2802; (d) Qin, L.; Wang, P.; Guo, Y.; Chen, C.; Liu, M., Self-Assembled Soft Nanomaterials Via Silver(I)-Coordination: Nanotube, Nanofiber, and Remarkably Enhanced Antibacterial Effect. *Advanced Science* **2015**, *2* (11), 1500134.

11. (a) Qu, L.; Fan, J.; Ren, Y.; Xiong, K.; Yan, M.; Tuo, X.; Terech, P.; Royal, G., Homo- and heterodinuclear coordination polymers based on a tritopic cyclam bis-terpyridine unit: Structure and rheological properties. *Materials Chemistry and Physics* **2015**, *153*, 54-62; (b) Zhang, J.; Chen, S.; Xiang, S.; Huang, J.; Chen, L.; Su, C.-Y., Heterometallic Coordination Polymer Gels Based on a Rigid, Bifunctional Ligand. *Chemistry – A European Journal* **2011**, *17* (8), 2369-2372; (c) Weng, W.; Beck, J. B.; Jamieson, A. M.; Rowan, S. J., Understanding the Mechanism of Gelation and Stimuli-Responsive Nature of a Class of Metallo-Supramolecular Gels. *Journal of the American Chemical Society* **2006**, *128* (35), 11663-11672.

12. Xing, B.; Choi, M.-F.; Xu, B., Design of Coordination Polymer Gels as Stable Catalytic Systems. *Chemistry – A European Journal* **2002**, *8* (21), 5028-5032.

13. Claramunt, R.; Milata, V.; Cabildo, P.; Santa María, D.; Cornago, P.; Infantes, L.; H. Cano, F.; Elguero, J., *2,4,6-Tris(azol-1-yl)-1,3,5-triazines: A New Class of Multidentate Ligands*. 2001; Vol. 55.

14. (a) Capel Berdiell, I.; Kulmaczewski, R.; Halcrow, M. A., Iron(II) Complexes of 2,4-Dipyrazolyl-1,3,5-triazine Derivatives—The Influence of Ligand Geometry on Metal Ion Spin State. *Inorganic Chemistry* **2017**, *56* (15), 8817-8828; (b) Guerrero, A.; Jalon, F. A.; Manzano, B. R.; Claramunt, R. M.; Cabildo, P.; Infantes, L.; Cano, F. H.; Elguero, J., The Structure of Tris(3',5'-dimethylpyrazol-1-yl)-s-triazine and Its Use as a Ligand in Coordination Chemistry. *Chemistry of Heterocyclic Compounds* **2003**, *39* (10), 1396-1403; (c) Zhou, H.-P.; Gan, X.-P.; Li, X.-L.; Liu, Z.-D.; Geng, W.-Q.; Zhou, F.-X.; Ke, W.-Z.; Wang, P.; Kong, L.; Hao, F.-Y.; Wu, J.-Y.; Tian, Y.-P., Anion-Induced Assembly of Five-Coordinated Mercury(II) Complexes and Density Functional Theory Calculations to Study Bond Dissociation Energies of Long Hg–N Bonds. *Crystal Growth & Design* **2010**, *10* (4), 1767-1776; (d) Quinonero, D.; Deya, P.

Chapter 3

- M.; Carranza, M. P.; Rodriguez, A. M.; Jalon, F. A.; Manzano, B. R., Experimental and computational study of the interplay between C-H/[small pi] and anion-[small pi] interactions. *Dalton Transactions* **2010**, 39 (3), 794-806; (e) Capel Berdiell, I.; Warriner, S. L.; Halcrow, M. A., Silver(i) complexes of bis- and tris-(pyrazolyl)azine derivatives – dimers, coordination polymers and a pentametallic assembly. *Dalton Transactions* **2018**, 47 (15), 5269-5278.
15. Chifotides, H. T.; Dunbar, K. R., Anion- π Interactions in Supramolecular Architectures. *Accounts of Chemical Research* **2013**, 46 (4), 894-906.
16. Hung, C.-Y.; Singh, A. S.; Chen, C.-W.; Wen, Y.-S.; Sun, S.-S., Colorimetric and luminescent sensing of F⁻ anion through strong anion-[small pi] interaction inside the [small pi]-acidic cavity of a pyridyl-triazine bridged trinuclear Re(i)-tricarbonyl diimine complex. *Chemical Communications* **2009**, (12), 1511-1513.
17. (a) Wang, J.-X.; Wang, C.; Wang, X.; Wang, X.-Y.; Xing, Y.-H.; Sun, Q., Experimental and theoretical investigations of copper (I/II) complexes with triazine-pyrazole derivatives as ligands and their in situ C-N bond cleavage. *Spectrochimica Acta Part A: Molecular and Biomolecular Spectroscopy* **2015**, 142, 55-61; (b) Manzur, J.; Acuña, C.; Vega, A.; García, A. M., Copper(II) assisted hydrolysis of 2,4,6-tris(pyrazol-1-yl)-1,3,5-triazine. Crystal and molecular structure of catena- [CuL(H₂O)Cl]_n (L=2,4-dione-1,3,5-(1H)-triazin-1-amido). *Inorganica Chimica Acta* **2011**, 374 (1), 637-642; (c) Gómez-de la Torre, F.; de la Hoz, A.; Jalón, F. A.; Manzano, B. R.; Otero, A.; Rodríguez, A. M.; Rodríguez-Pérez, M. C.; Echevarría, A.; Elguero, J., Synthesis and Characterization of Palladium(II) Complexes with New Polydentate Nitrogen Ligands. Dynamic Behavior Involving Pd-N Bond Rupture. X-ray Molecular Structure of [[Pd(η^3 -C₄H₇)₂(Me-BPzTO)](4-MeC₆H₄SO₃)] [Me-BPzTO = 4,6-Bis(4-methylpyrazol-1-yl)-1,3,5-triazin-2-olate]. *Inorganic Chemistry* **1998**, 37 (26), 6606-6614; (d) Castro, I.; Faus, J.; Julve, M.; Amigo, J. M.; Sletten, J.; Debaerdemaeker, T., Copper(II)-assisted hydrolysis of 2,4,6-tris(2-pyridyl)-1,3,5-triazine. Part 3. Crystal structures of diaqua[bis(2-pyridylcarbonyl)amido]copper(II) nitrate dihydrate and aquabis(pyridine-2-carboxamide)copper(II) nitrate monohydrate. *Journal of the Chemical Society, Dalton Transactions* **1990**, (3), 891-897.
18. Irving, H.; Williams, R. J. P., 637. The stability of transition-metal complexes. *Journal of the Chemical Society (Resumed)* **1953**, (0), 3192-3210.
19. Toma, H. E., Magnetic nanohydrometallurgy: a nanotechnological approach to elemental sustainability. *Green Chemistry* **2015**, 17 (4), 2027-2041.
20. Sharma, M.; Sarma, P. J.; Goswami, M. J.; Bania, K. K., Metallogel templated synthesis and stabilization of silver-particles and its application in catalytic reduction of nitro-arene. *Journal of Colloid and Interface Science* **2017**, 490, 529-541.
21. Berdiell, I. C.; Kulak, A. N.; Warriner, S. L.; Halcrow, M. A., Heterometallic Coordination Polymer Gels Supported by 2,4,6-Tris(pyrazol-1-yl)-1,3,5-triazine. *ACS Omega* **2018**, 3 (12), 18466-18474.

Chapter 3

22. Bushuev, M. B.; Pishchur, D. P.; Logvinenko, V. A.; Gatilov, Y. V.; Korolkov, I. V.; Shundrina, I. K.; Nikolaenkova, E. B.; Krivopalov, V. P., A mononuclear iron(ii) complex: cooperativity, kinetics and activation energy of the solvent-dependent spin transition. *Dalton Transactions* **2016**, 45 (1), 107-120.
23. Kershaw Cook, L. J.; Mohammed, R.; Sherborne, G.; Roberts, T. D.; Alvarez, S.; Halcrow, M. A., Spin state behavior of iron(II)/dipyrazolylpyridine complexes. New insights from crystallographic and solution measurements. *Coordination Chemistry Reviews* **2015**, 289–290, 2-12.
24. Zhang, S.; Yang, S.; Lan, J.; Yang, S.; You, J., Helical nonracemic tubular coordination polymer gelators from simple achiral molecules. *Chemical Communications* **2008**, (46), 6170-6172.
25. (a) Zhu, H.-F.; Fan, J.; Okamura, T.-a.; Sun, W.-Y.; Ueyama, N., Syntheses and Structures of Zinc(II), Silver(I), Copper(II), and Cobalt(II) Complexes with Imidazole-Containing Ligand: 1-(1-Imidazolyl)-4-(imidazol-1-ylmethyl)benzene. *Crystal Growth & Design* **2005**, 5 (1), 289-294; (b) Fan, J.; Sun, W.-Y.; Okamura, T.-a.; Tang, W.-X.; Ueyama, N., Novel Metal–Organic Frameworks with Specific Topology from New Tripodal Ligands: 1,3,5-Tris(1-imidazolyl)benzene and 1,3-Bis(1-imidazolyl)-5-(imidazol-1-ylmethyl)benzene. *Inorganic Chemistry* **2003**, 42 (10), 3168-3175.
26. (a) Crespo, O.; Gimeno, M. C.; Laguna, A.; Larraz, C., Luminescent Silver(I) and Copper(I) Systems Containing Pyridyl Phosphine Bridges. In *Zeitschrift für Naturforschung B*, 2009; Vol. 64, p 1525; (b) Pinter, B.; Broeckart, L.; Turek, J.; Růžička, A.; De Proft, F., Dimers of N-Heterocyclic Carbene Copper, Silver, and Gold Halides: Probing Metallophilic Interactions through Electron Density Based Concepts. *Chemistry – A European Journal* **2014**, 20 (3), 734-744.
27. Tabassum, S.; Zaki, M.; Afzal, M.; Arjmand, F., Synthesis and characterization of Cu(II)-based anticancer chemotherapeutic agent targeting topoisomerase I α : In vitro DNA binding, pBR322 cleavage, molecular docking studies and cytotoxicity against human cancer cell lines. *European Journal of Medicinal Chemistry* **2014**, 74, 509-523.
28. Gelling, A.; Noble, D. R.; Orrell, K. G.; Osborne, A. G.; Sik, V., Synthesis and solution fluxionality of rhenium(I) carbonyl complexes of 2,4,6-tris(pyrazolyl)pyrimidines (L), [ReX(CO)3L](X = Cl, Br or I). Isolation and identification of the dinuclear complex [{ReBr(CO)3}2L]. *Journal of the Chemical Society, Dalton Transactions* **1996**, (14), 3065-3070.
29. Najafpour, M. M.; Hołyńska, M.; Amini, M.; Kazemi, S. H.; Lis, T.; Bagherzadeh, M., Two new silver(I) complexes with 2,4,6-tris(2-pyridyl)-1,3,5-triazine (tptz): Preparation, characterization, crystal structure and alcohol oxidation activity in the presence of oxone. *Polyhedron* **2010**, 29 (14), 2837-2843.
30. Zhou, S. Y.; Li, T.; Li, X.; Sun, Y. Q.; Wang, Q. L.; Liao, D. Z.; Tian, L., Syntheses, structures, and magnetic characterizations of five Mn(II) and Co(II) complexes based on 2,6-

Chapter 3

Pyridyl-substituted nitronyl and imino nitroxide radical. *Inorganica Chimica Acta* **2016**, *444*, 131-140.

31. Wang, H.-Y.; Wu, Y.; Leong, C. F.; D'Alessandro, D. M.; Zuo, J.-L., Crystal Structures, Magnetic Properties, and Electrochemical Properties of Coordination Polymers Based on the Tetra(4-pyridyl)-tetrathiafulvalene Ligand. *Inorganic Chemistry* **2015**, *54* (22), 10766-10775.

32. (a) Manzano, B. R.; Jalón, F. A.; Soriano, M. L.; Carrión, M. C.; Carranza, M. P.; Mereiter, K.; Rodríguez, A. M.; de la Hoz, A.; Sánchez-Migallón, A., Anion-Dependent Self-Assembly of Silver(I) and Diaminotriazines to Coordination Polymers: Non-Covalent Bonds and Role Interchange between Silver and Hydrogen Bonds. *Inorganic Chemistry* **2008**, *47* (19), 8957-8971; (b) Carranza, M. P.; Manzano, B. R.; Jalón, F. A.; Rodríguez, A. M.; Santos, L.; Moreno, M., First Examples of a Modulated Bridging μ_2 -1:2 κ N-Triazine in Double Helical Silver Compounds. Experimental and Theoretical Evidence. *Inorganic Chemistry* **2010**, *49* (8), 3828-3835; (c) Zhou, X.-P.; Zhang, X.; Lin, S.-H.; Li, D., Anion- π -Interaction-Directed Self-Assembly of Ag(I) Coordination Networks. *Crystal Growth & Design* **2007**, *7* (3), 485-487.

33. Dolomanov, O. V.; Bourhis, L. J.; Gildea, R. J.; Howard, J. A. K.; Puschmann, H., OLEX2: a complete structure solution, refinement and analysis program. *Journal of Applied Crystallography* **2009**, *42* (2), 339-341.

34. Abherve, A.; Clemente-Juan, J. M.; Clemente-Leon, M.; Coronado, E.; Boonmak, J.; Youngme, S., Tuning the nuclearity of iron(iii) polynuclear clusters by using tetradentate Schiff-base ligands. *New Journal of Chemistry* **2014**, *38* (5), 2105-2113.

35. Mooibroek, T. J.; Gamez, P., Halogen... phenyl supramolecular interactions in the solid state: hydrogen versus halogen bonding and directionality. *CrystEngComm* **2013**, *15* (9), 1802-1805.

36. Chilton, N. F.; Anderson, R. P.; Turner, L. D.; Soncini, A.; Murray, K. S., PHI: A powerful new program for the analysis of anisotropic monomeric and exchange-coupled polynuclear d- and f-block complexes. *Journal of Computational Chemistry* **2013**, *34* (13), 1164-1175.

37. Inc, W. *SPARTAN' 18*, Irvine CA, 2018.

Chapter 4 – Polymetallic and Polymeric Structures Derived from Iron(II) Complexes of 1,3,5-Triazine and 1,3-Pyrimidine Based Ligands

4.1 Introduction

Ligands are classified as unidentate, bidentate or polydentate depending on how many donor atoms are found in their structure. Metal ions have affinity for ligands attaching the central ion through coordinate bonds from two or more different donor atoms simultaneously forming a ring structure, this phenomenon is known as the chelate effect. A chelate ligand forms complexes more stable than the analogous complex made from monodentate ligands¹.

Self-assembly processes between organic ligands and metal ions may lead to the formation of supramolecular architectures exhibiting unusual properties. The template effect is an important element within self-assembly reactions. Some molecules can interact through non-covalent bonds with two or more reactive species in order to pre-organize the reactive sites close together, facilitating a reaction which otherwise is thermodynamically or kinetically unlikely. It can be considered a special case of supramolecular catalysis. The template may be as simple as a single metal ion or it may be extremely complex².

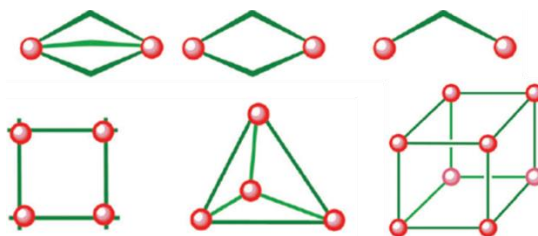


Figure 4.1: Examples of topologies observed for discrete polynuclear SCO complexes. Image adapted from, where the green lines represent di- to polydentated N-donor ligands³.

Tris(diimine) and bis(terimine) iron(II) complexes constitute two of the major classes of spin-crossover systems. The complexes studied in Chapter 2 were homoleptic bis(terimine) octahedral complexes⁴. In this chapter we present a set of unexpected structures observed during the work in chapters 2 and 3 and further research carried out, where the iron centres were coordinated by ligands acting in the bis-bidentate fashion. Several types of coordination assemblies have been reported from bis-bidentate ligands. Some examples are; 1D chains (ML)⁵, dinuclear (M₂L₃)⁶, [2 x 2] grid⁷, tetrahedral (M₄L₆) (which often contain an included counter-anion templating the assembly⁸) and more complex structures like (M₈L₁₂)⁹ or (M₁₂L₁₈) which were in equilibrium with other assemblies¹⁰. Iron(II) has also produced polymetallic assemblies with bis-bidentate NN-donor ligands¹¹, some of which also present spin-crossover¹² (Figure 4.1).

4.2 Results and discussion

4.2.1 Self-assemblies of 2,4-di(4,5,6,7-tetrahydro-2-indazol-2-yl)-6-chloro-1,3,5-triazine and iron(II)/(III) centres

During the synthesis of 2,4,6-tri(4,5,6,7-tetrahydro-2-indazol-2-yl)-1,3,5-triazine (**9**) in Chapter 2, the disubstituted derivate (**17**) was also isolated from the product mixture through a flash column chromatography (Figure 4.2).

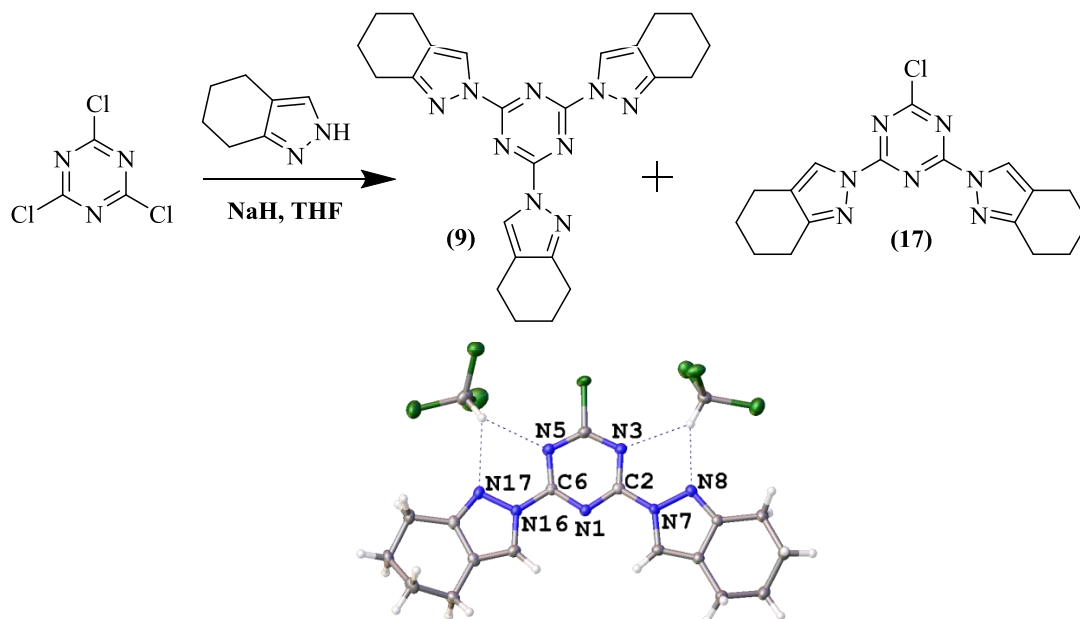


Figure 4.2: Synthetic scheme and crystal structure of (**17**) in $P\bar{1}$ space group, showing hydrogen bonds between two molecules of chloroform and both N[triazinyl] and N[pyrazolyl] ($H\cdots N = 2.377(10)$ - $2.549(11)$ Å).

The $[Fe(L)_2](BF_4)_2$ -type homoleptic complex (Figure 4.3, A) was expected from combining iron(II) tetrafluoroborate with (**17**), which is a NNN donor of the terimine type. However in addition to the terimine coordinating site (N8, N1 and N17), it contains two “non-coordinating” triazinyl lone pairs, N5 and N3. Figure 4.3;

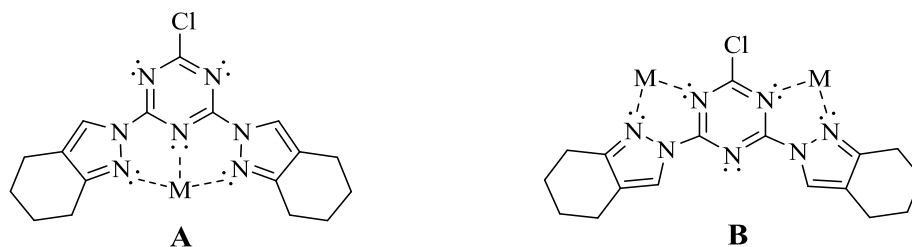


Figure 4.3: A) Expected coordination. B) Observed coordination of ligand (**17**).

These extra lone pairs allow the possibility of coordination mode B (Figure 4.3). In principle, coordination mode A should be thermodynamically favoured by the chelate effect. However, the geometry of the 1,3,5-triazine ring-based ligand reduces that effect by its narrow bite angle, favouring the bis-bidentate conformation (Chapter 2).

Various motifs self-assembled from the combination of (17) with iron(II) tetrafluoroborate were observed by varying the template molecules; M_4L_4 , [18] α , M_8L_{12} , [18] β and $M_{10}L_{12}$ [18] γ . All of them contain the deprotonated hydrolysed ligand (18), (Figure 4.10) because the chloro substituent is activated when a metal is bound to the ligand.

4.2.1.1 [2 x 2] grid assembly (M_4L_4), [18] α

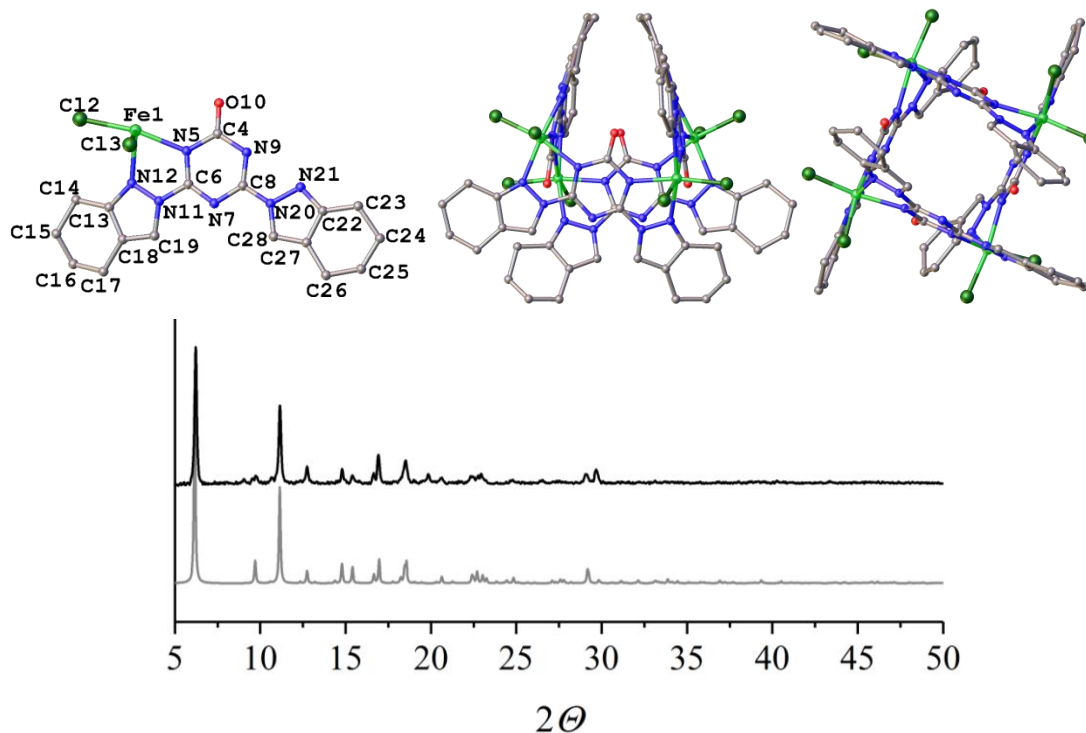


Figure 4.4: Asymmetric unit cell, and two views of the crystal structure of grid [18] α , $I4_1/a$ space group. Hydrogen atoms were removed for clarity. The colour assignment in the plot is black for the experimental and grey for the simulated XRD.

The neutral compound $[\text{Fe}^{\text{III}}_4(\mathbf{18})_4(\text{Cl})_8] = [\mathbf{18}]\alpha$ contains four negatively charged ligands (18) and four metal ions. Iron(II) was oxidized to the +3 oxidation state and the hydrolysed chloride acts as a coordinating ligand. That compound appeared as red needle-shaped crystals only twice inside aged crystallization vials. Unfortunately no more characterization was obtained due to the solubility of the material.

4.2.1.2 Cubic shaped assembly (M_8L_{12}), [18] β

The second assembly, [18] β was a cubic shaped complex $[\text{Fe}^{\text{III}}(\text{H}_2\text{O})_6\text{CFe}^{\text{II}}_8(\mathbf{18})_{12}](\text{BF}_4)_4(\text{FeCl}_4)_3$ where twelve (18) ligands form the edges of the cube and iron(II) atoms are the eight vertices (Figure 4.5). A related structure was reported using cobalt(II) by Cao *et al.*¹³. This structure was reproducible in acetonitrile. The structure was collected several times and with different unit cells and mixtures of BF_4^- and FeCl_4^- counter-anions. Crystals of [18] β became slightly amorphous upon grinding but the main phase could be recognised (Figure 4.5).

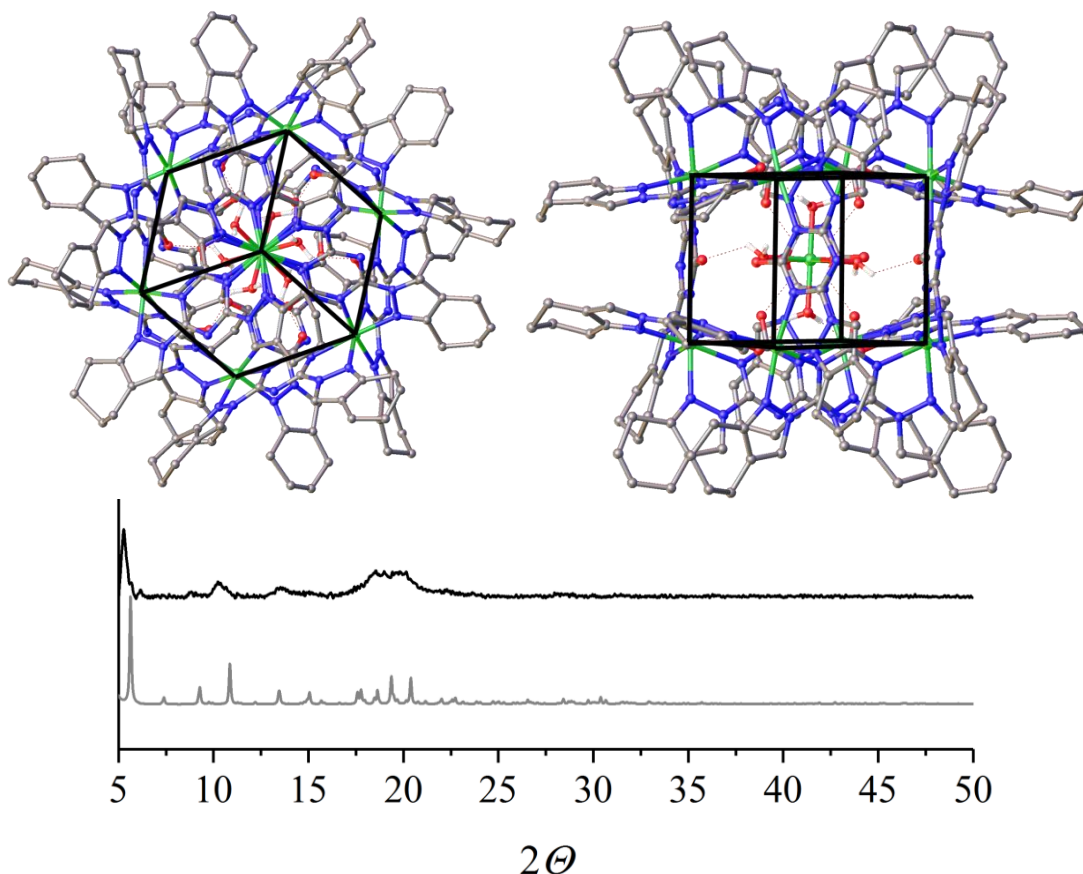


Figure 4.5: Different views of the cubic structure $[18]\beta$, $R\bar{3}$ space group. Cube represented with black lines on top of the structure. Hydrogen atoms and counter-anions were removed for clarity. The colour assignment in the plot is black for the experimental and grey for the simulated XRD.

Fe-N bond lengths are between 2.150(2) – 2.222(3) Å and V_{Oh} 13.045(14) – 13.096(14) Å³ taken from the crystal structure. These values suggested the HS state of the iron in the vertices of the cube at 120 K. The $[\text{Fe}(\text{H}_2\text{O})_6]^{3+}$ cation in the centre of the structure interacts through hydrogen bonding with the negatively charged ligands (**18**), acting as a template of the cube. The compound was analysed in solution by ES⁺-MS, Figure 4.6.

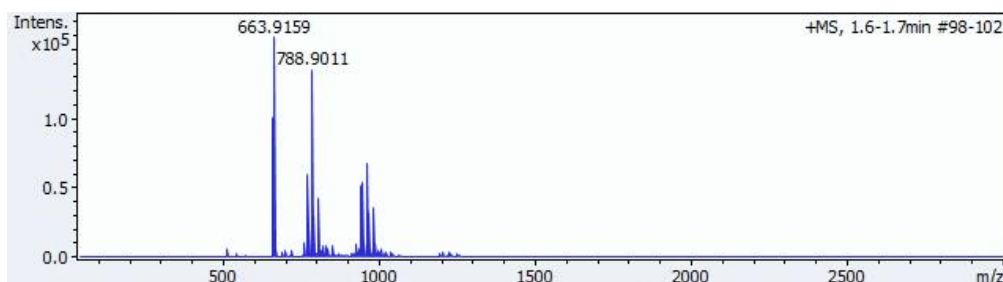


Figure 4.6: Mass spectrum of $[18]\beta$.

The assignment of the peaks was simple; the first peak from the right (663.9 m/z) corresponds to the $[18]\beta$ cation = $[\text{Fe}^{\text{III}}(\text{H}_2\text{O})_6\text{CFe}^{\text{II}}_8(\mathbf{18})_{12}]^{7+}$, followed by (774.4 m/z) $[[18]\beta\text{-H}^+]^{6+}$, (788.9 m/z) $[[18]\beta + \text{BF}_4]^{6+}$, (964.1 m/z) $[[18]\beta + (\text{BF}_4)_2]^{5+}$ and so forth. The counter anion FeCl_4^- was also identified by ES⁺-MS; for example (986.3 m/z) $[[18]\beta + \text{FeCl}_4 + \text{BF}_4]^{5+}$. More detailed analysis is in the experimental section (Chapter 8).

4.2.1.3 Super-tetrahedral assembly ($M_{10}L_{12}$), [18] γ

Finally, a tetrahedron shaped complex $[BF_4 \subset Fe_{10}(\mathbf{18})_{12}(H_2O)_{12}](FeCl_4)_2(BF_4)_2$ formed where four iron(II) coordinated by three ligands act as vertices of the pyramid, and six iron(II) atoms are placed in the edges of the pyramid coordinating two ligands ($\mathbf{18}$) and two water molecules, (Figure 4.7).

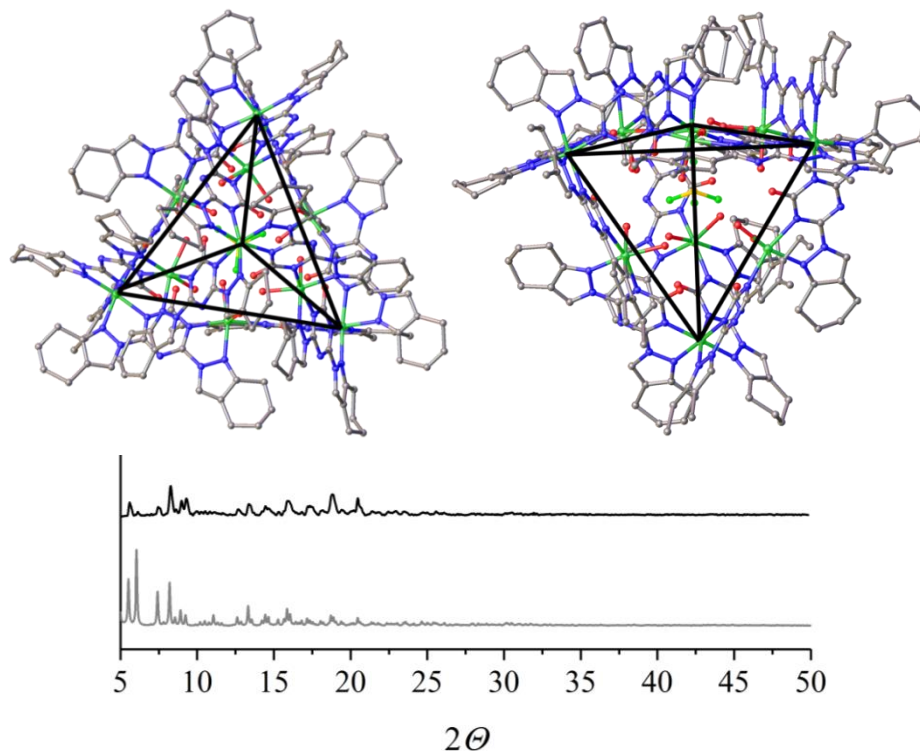


Figure 4.7: Different views of the structure [18] γ , $P2_13$ space group. Tetrahedron represented with black lines on top of the structure. Hydrogen atoms and counter-anions were removed for clarity. The colour assignment in the plot is black for the experimental and grey for the simulated XRD.

A BF_4^- counter-anion was found in the centre of the structure whose fluorine atoms pointed perfectly towards each face of the super tetrahedron. It is believed that BF_4^- acts as a template through hydrogen bonding with the water molecules bound to the iron(II) in the edges of the pyramid. This compound was observed only once, inside a one year old dried crystallization vial. The compound was also analysed in solution by ES^+ -MS, (Figure 4.8).

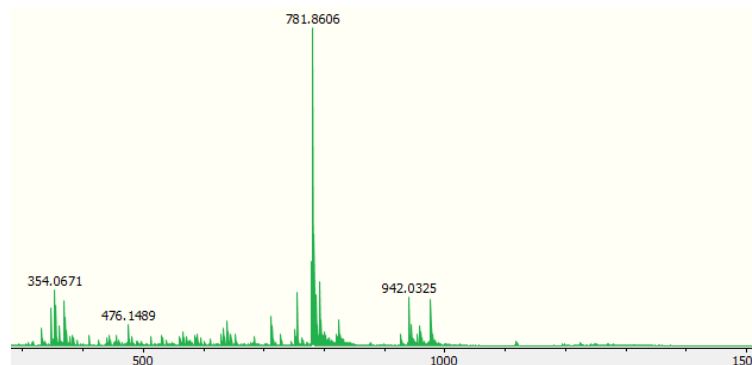


Figure 4.8: Zoom mass spectrum of [18] γ . Main peak assigned to $[BF_4 \subset Fe_{10}(\mathbf{18})_{12}(H_2O)_{12}](FeCl_4)_2(BF_4)_2$.

Chapter 4

Summarizing, three different assemblies from a simple mixture of ligand (17) with iron(II) tetrafluoroborate salt were identified up to now containing ligand (18) (Figure 4.9).

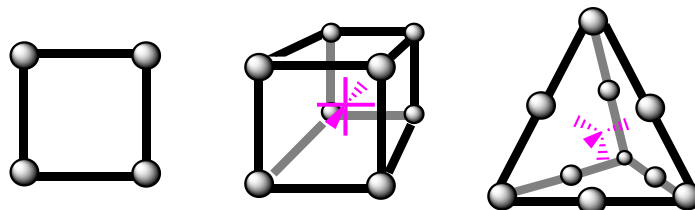


Figure 4.9: Schematic representation of the three motifs identified, [18] α , [18] β and [18] γ respectively. The template molecules are represented in magenta.

Unfortunately, none of these assemblies was isolated in analytical purity, probably due to contamination with mixtures of these or other M_xL_y combinations or other yet unknown. The template effect was found to be a determining factor of each assembly. Iron atoms acted as connectors, ligand (18) as linker and hydrogen bonding towards the faces of each polymetallic assembly templated the formation. All three compounds showed in one way or another chloride ions coordinated to iron centres. Unfortunately, the counter anions in [18] β and [18] γ were extremely disordered, hence the refined models were incomplete and presented high residuals. The counter-anion $FeCl_4^-$ was detected by ES^+ -MS (Figure 4.6 and Figure 4.8).

There is little understanding of the chemical reactions happening behind the structures here discussed, but a mechanism of how ligand (17) may evolve into (18) was detailed below, Figure 4.10.

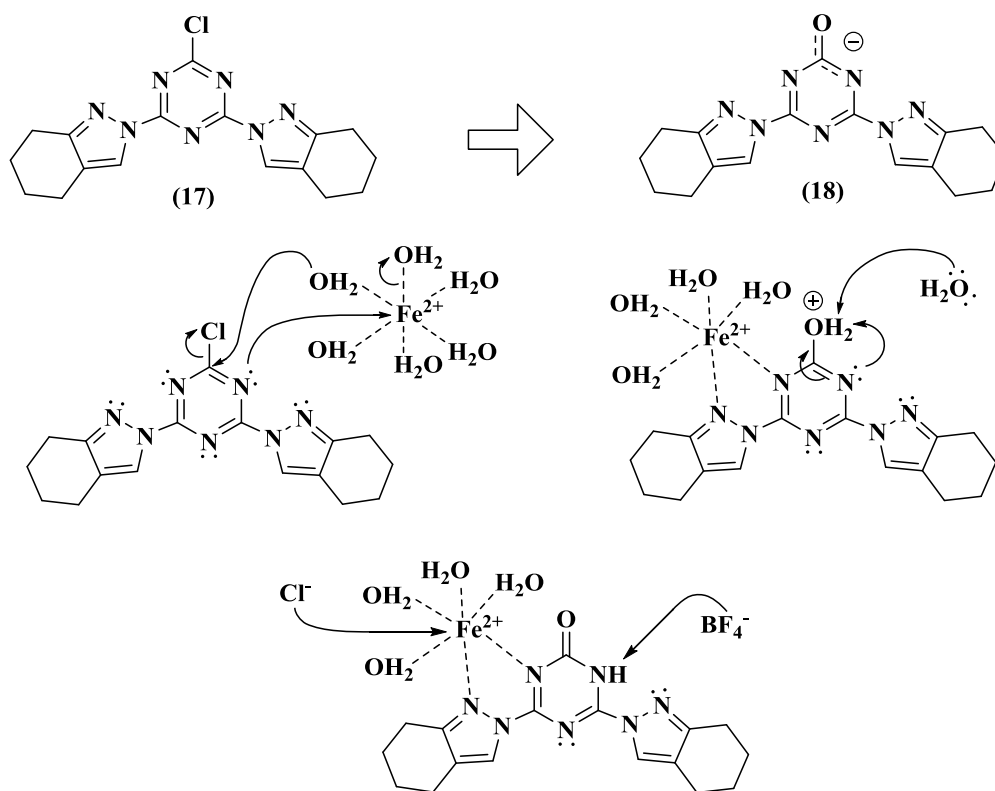


Figure 4.10: Proposed mechanism of hydrolysis and deprotonation of ligand (17).

Chapter 4

Ligand (17) forms coordinate bonds with the metal ion when the activated chloro group is hydrolyzed. An acid-base equilibrium with the media gives the more stable tautomer. Finally the chloride ion coordinates iron(II) while the tetrafluoroborate counter-anion, which is sensitive to hydrolysis under several conditions¹⁴, deprotonates the ligand as a non-innocent counter-anion. Occasionally pale yellow crystals were observed in the vials. That crystal structure could be in agreement with the mechanism proposed (Figure 4.11), where the chloro substituent was replaced by a methoxy group.

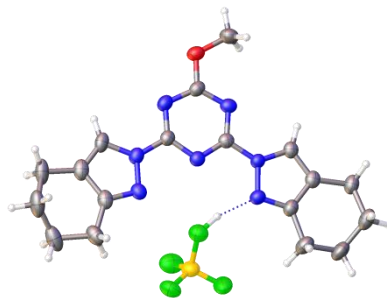


Figure 4.11: Crystal structure of [18]OMe-HBF₄, *P2₁/c* space group (monoclinic).

HBF₄ was observed in that crystal structure while the chlorine atom did not appear. The lability of the chloride bound to a 1,3,5-triazine ring was also observed for ligand (19) (Figure 4.12).

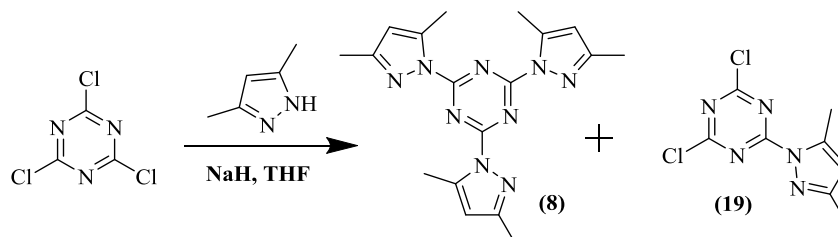


Figure 4.12: Synthetic scheme of ligand (19)

In this case, iron tetrafluoroborate was reacted with ligand (19) in 1:3 M:L ratio in methanol and the following structures were observed (Figure 4.13).

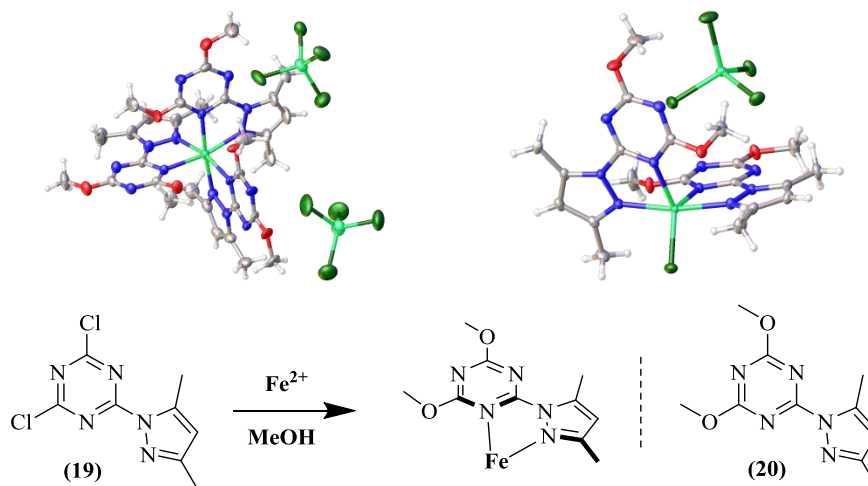


Figure 4.13: Crystal structures of [20]α and [20]β, *P1* and *P2₁/c* space groups.

Ligand (**20**) was reported previously under similar circumstances¹⁵. The two chlorine atoms of (**19**) were substituted by methoxy groups when the ligand was activated by the Lewis acid, and the FeCl_4^- counter-anion was observed again as for [**18**] β and [**18**] γ (Figure 4.5 and Figure 4.7).

4.2.2 Structures derived from 2,4-di(pyrazol-1-yl)-1,3,5-triazine

Ligand 2,4-di(pyrazol-1-yl)-1,3,5-triazine (**21**) was synthesized as follows, Figure 4.14.

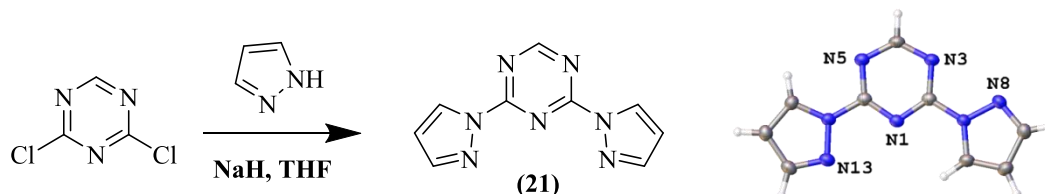


Figure 4.14: Synthetic scheme and crystal structure of (**21**), bpt ligand.

The ligand (**21**) was extremely difficult to crystallize, but crystals in the $P2_1/n$ space group formed by slow evaporation of a chloroform solution. This compound was prepared aiming to complete the study of the magnetic behaviour of the homoleptic complexes $[\text{Fe}(\text{bptR})_2]^{2+}$ in Chapter 2. However (**21**) appears to be geometrically predefined as bis-bidentate (Figure 4.15).

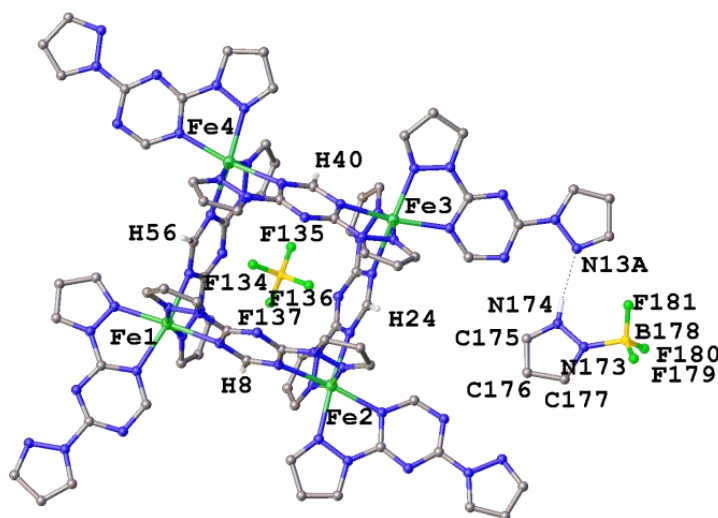


Figure 4.15: Crystal structure of [**21**]**B**, $P\bar{1}$ space group. Hydrogen atoms and some counter-anions were removed for clarity.

This structure was similar to [**18**] α (Figure 4.4) with the difference that there was no “labile” chlorine in the ligand so an extra ligand coordinates each iron from the outside the grid. Moreover, a tetrafluoroborate molecule was found in the centre of the grid showing strong anion $\cdots\pi$ interactions with F_3 -plane to triazine-centroid distances of 2.7652(16) – 2.7995(15) Å, which could template the M_4L_8 assembly formation. Crystals of [**21**]**B** were only observed once inside an NMR tube, which might reflect the potential existence of different species in solution, for instance a 1D polymer or even the homoleptic $[\text{Fe}(\text{bptR})_2]^{2+}$ complex (Figure 4.16).

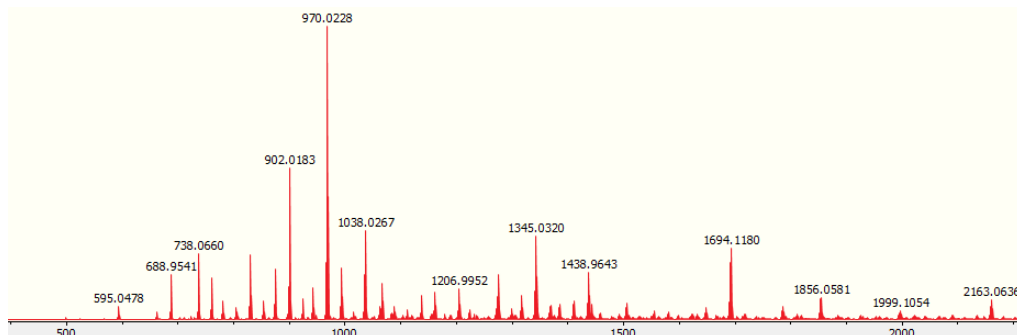


Figure 4.16: Fragment of the direct injection ESMS spectrum of [21]B.

Where the most intense peak (970.0^+ m/z) is assigned to $[\text{Fe}^{\text{II}}_3(\mathbf{21})_3(\text{BF}_4)\text{F}_4]^+$, a more detailed analysis is described in the experimental section in chapter 8 (page 228) where different M_xL_y ratios are identified using different conditions in the instrument. The compound [21]B did not undergo SCO as shown in Table 4-1;

	[21]B
Fe ₁ -N	2.089(4) - 2.263(4)
Fe ₁ V _{Oh}	12.844(13)
Fe ₂ -N	2.107(4) - 2.296(3)
Fe ₂ V _{Oh}	13.254(14)
Fe ₃ -N	2.109(4) - 2.325(4)
Fe ₃ V _{Oh}	13.235(14)
Fe ₄ -N	2.116(4) - 2.276(4)
Fe ₄ V _{Oh}	13.195(14)

Table 4-1: Crystallographic parameters of the grid [21]B at 120K where all iron(II) centres are clearly HS. SQUID curve which is in agreement with the crystal structure.

On a different note, the presence of pyrazolyl-BF₃ in the crystal structure (Figure 4.15, labelled as N173, N174, C175, C176 and C177) suggested that more complex reactions than a simple M-L coordination took place in solution. Although the pyrazolyl-BF₃ could not be rationalised in [21]B a similar compound has been reported before¹⁶. In some reactions of this type, crystals containing hydrolysed ligands were also found, (Figure 4.17).

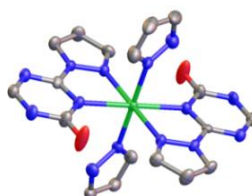


Figure 4.17: Example of a hydrolysed species found in the crystallization vials. Hydrogen atoms, counter-anions were removed and only one co-crystallized complex is shown for clarity.

Chapter 4

Therefore, ligand (**21**) was sensitive to hydrolysis in contact with iron salts. Hypothetically the free pyrazole could react with BF_4^- anion giving rise the pyrazolyl- BF_3 and HF. The systematic hydrolysis of the ligand (**21**) could also explain the difficulties found when trying to crystallize its iron(II) complexes. The following calcium complex was once observed in a reaction mixture of (**21**) with iron(II) perchlorate (Figure 4.18), but no $[\text{Fe}_x(\mathbf{21})_y](\text{ClO}_4)_z$ species was observed.

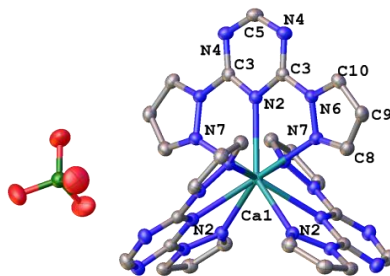


Figure 4.18: Crystal structure of $[\text{Ca}(\mathbf{21})_3]\text{ClO}_4$ which crystallized in $P\bar{3}c1$ space group. Hydrogen atoms were removed for clarity

Ignoring the fact that the source of the Ca^{2+} remains unknown, the existence of such a compound could mean that the ligand (**21**) is easily hydrolysed by hard transition metals like Fe^{2+} , Co^{2+} and Ni^{2+} while maintaining its integrity against softer metal ions. Therefore it was reacted with silver(I) tetrafluoroborate¹⁷ (Figure 4.19).

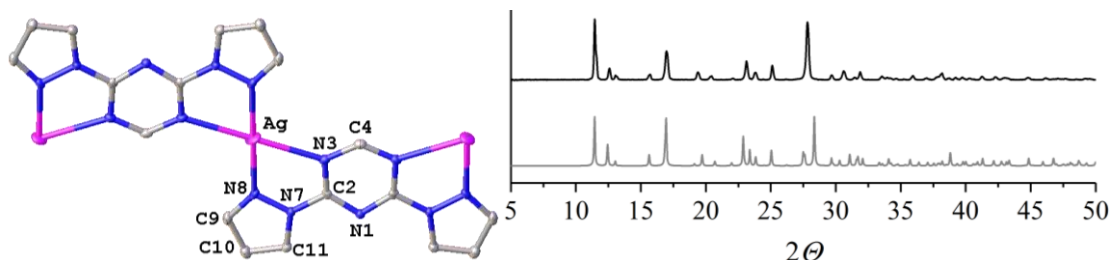


Figure 4.19: Crystal structure of $[\text{Ag}(\mathbf{21})]\text{BF}_4$ 1D chain. Hydrogen atoms and counter-anions were removed for clarity. The colour assignment in the plot is black for the experimental and grey for the simulated XRD.

Similar ligands to (**21**) with different substituents on the pyrazole groups were synthesized by Sarah Farmiloe during her MChem project under the candidate's supervision (Figure 4.20).

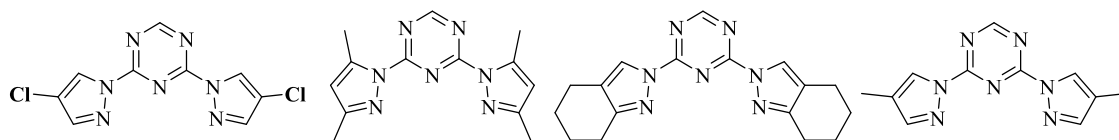


Figure 4.20: Modifications of ligand (**21**) synthesized by Sarah Farmiloe.

Such ligands were reacted with several salts of different transition metals for instance; Fe^{2+} , Fe^{3+} , Co^{2+} , Ni^{2+} , Mn^{2+} , Ag^+ and so forth. Interestingly, only silver(I) and manganese(II) yielded crystalline materials. When using silver salts, various M_4L_4 or 1D-chain assemblies were observed, depending on the ligand and counter-anion used. This study was in agreement

Chapter 4

with our hypothesis stated above where the integrity of the ligand is guaranteed when coordinated to softer transition metals.

4.2.3 Cubic cluster derived from 4,6-di(pyrazol-1-yl)-pyrimid-2-one

The impurity (**22**) was obtained during the synthesis of (**14**)¹⁸ in the previous chapter (Figure 4.21).

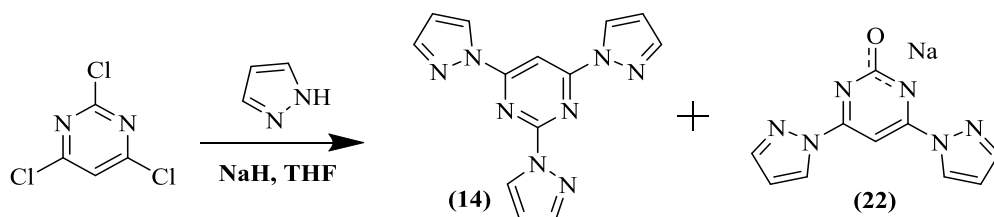


Figure 4.21: Synthetic scheme of (**14**), which usually produced the sodium salt of (**22**) as an impurity.

Due to the solubility of (**22**) (Figure 4.23), the mixture of ligands (**14**) and (**22**) was reacted with iron(II) tetrafluoroborate prior to purification as test reaction with the aim of obtaining $[\text{Fe}(\mathbf{14})_2](\text{BF}_4)_2$ single crystals. Instead, the same M_8L_{12} cubic assembly as $[\mathbf{18}]\beta$ (Figure 4.5) was unexpectedly observed, $[\text{Fe}^{\text{III}}(\text{H}_2\text{O})_6\text{CFe}^{\text{II}}_8(\mathbf{22})_{12}](\text{BF}_4)_7$ (Figure 4.22).

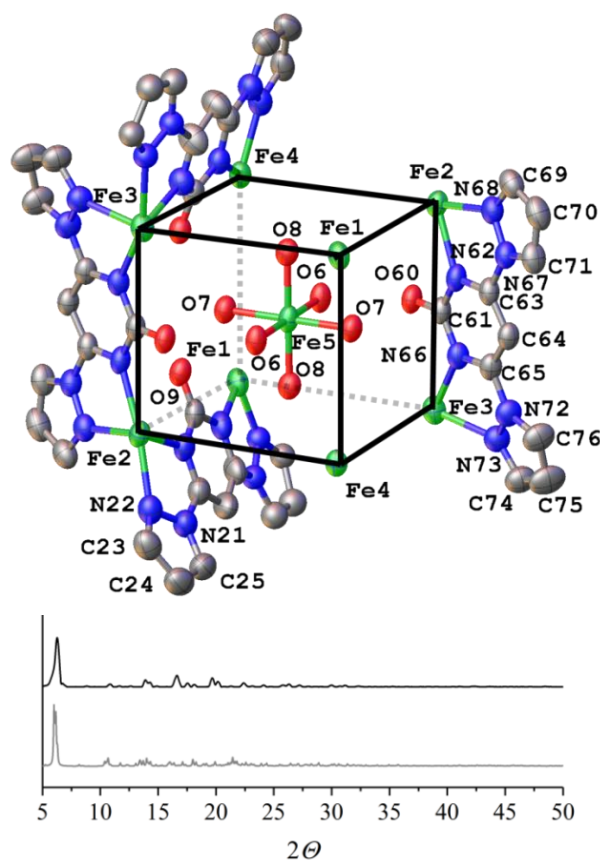


Figure 4.22: View of the cubic structure, $[\mathbf{22}]\alpha\text{B}$ at 100 K. Hydrogen atoms and counter-anions were removed and only four bridging ligands shown for clarity. $C2/c$ space group. The colour assignment in the plot is black for the experimental and grey for the simulated XRD.

The following strategy was proposed for obtaining ligand **(24)** pure in a reasonably yield (34.6%, Figure 4.23).

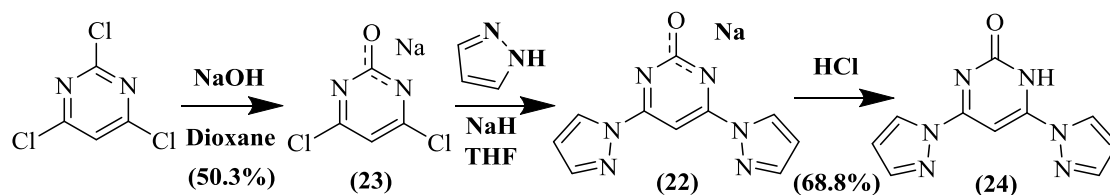


Figure 4.23: Synthetic scheme of **(24)**.

Ligand **(23)** was synthesized following a previously reported procedure¹⁹ and a crystal structure was collected (Figure 4.24).

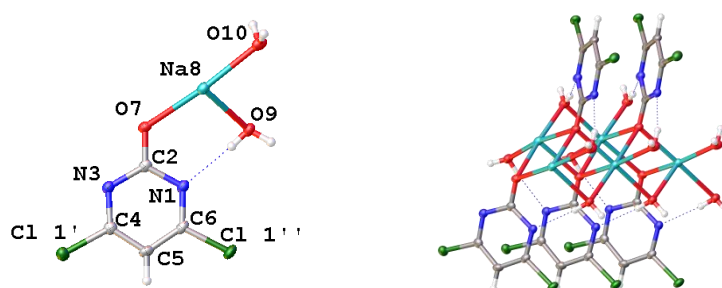


Figure 4.24: Crystal structure of **(23)**, $C2/c$ space group.

Pyrazole and sodium hydride were added giving **(22)** as its sodium salt. Then, 1 equivalent HCl was added to neutralize the ligand giving rise the neutral form **(24)**.

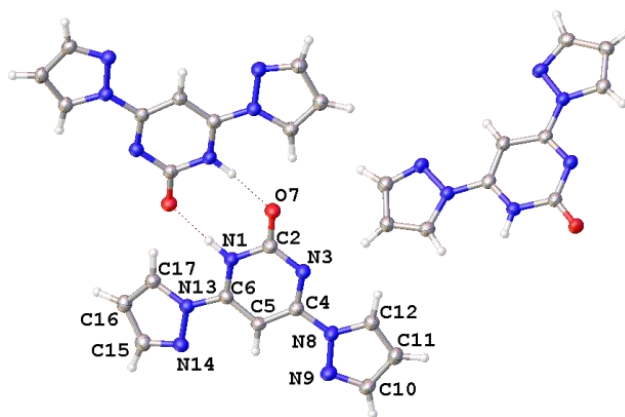


Figure 4.25: Crystal structure of **(24)**, $C2/c$ space group.

The reaction of pure **(24)** with iron(II) tetrafluoroborate yielded the same **[22]αB** structure (Figure 4.22). Bond valence sum (BVS)²⁰ were calculated for the atoms of the cube and demonstrated that iron atoms of the vertices were iron(II) while the central cation was iron(III). Iron(II) atoms of the cube were related by a centre of symmetry as pairs in the opposite vertices, in other words there were four crystallographically unique iron atoms (Figure 4.22). The singularity of **[22]αB** structure is that Fe 1 and its symmetry equivalent were LS at 100 K. A VT X-ray experiment was performed to confirm the SCO phenomenon (Table 4-2).

Chapter 4

100 K	Fe 1	Fe 2	Fe 3	F 4
Fe–N[averaged]	2.01	2.16	2.21	2.19
V_{Oh}	10.365(3)	12.331 (4)	12.626(4)	12.824(4)
200 K	Fe 1	Fe 2	Fe 3	F 4
Fe–N[averaged]	2.12	2.18	2.22	2.19
V_{Oh}	11.990(7)	12.618(8)	12.630(8)	12.814(8)

Table 4-2: VT experiment crystallographic parameters for [22]αB.

According to crystallographic parameters of Table 4-2, two out of eight iron(II) in the vertices of the cube exhibit gradual spin crossover in the solid state. This fact was proved by SQUID magnetometry (Figure 4.26), Mössbauer Spectroscopy (Figure 4.27), and by the LIESST effect observed when the sample was irradiated with green light (Figure 4.28).

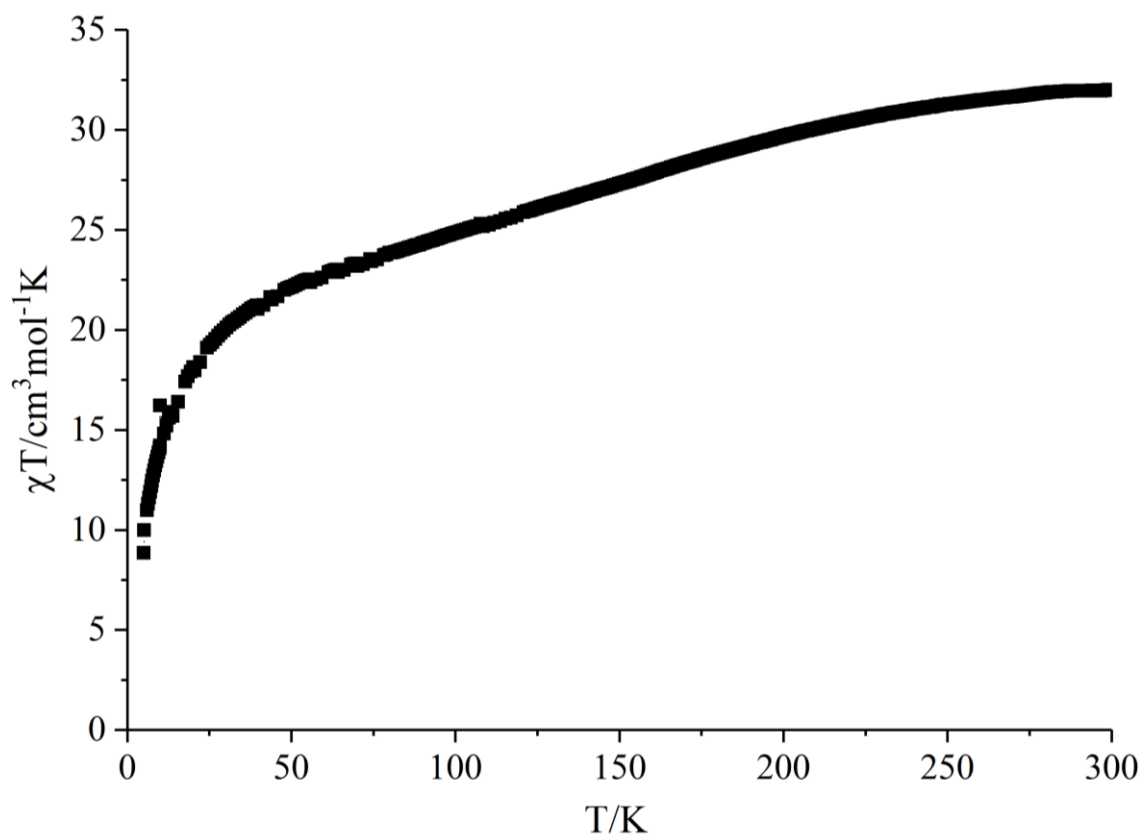


Figure 4.26: SQUID curve of [22]αB.

It was very challenging to prove the SCO only with the SQUID measurement, because the magnetic curve was influenced by three different processes; gradual SCO, superexchange interactions between iron(II) centers and the zero-field splitting. Thus, extra experiments confirmed the transition, (Figure 4.27, Table 4-3 and Figure 4.28).

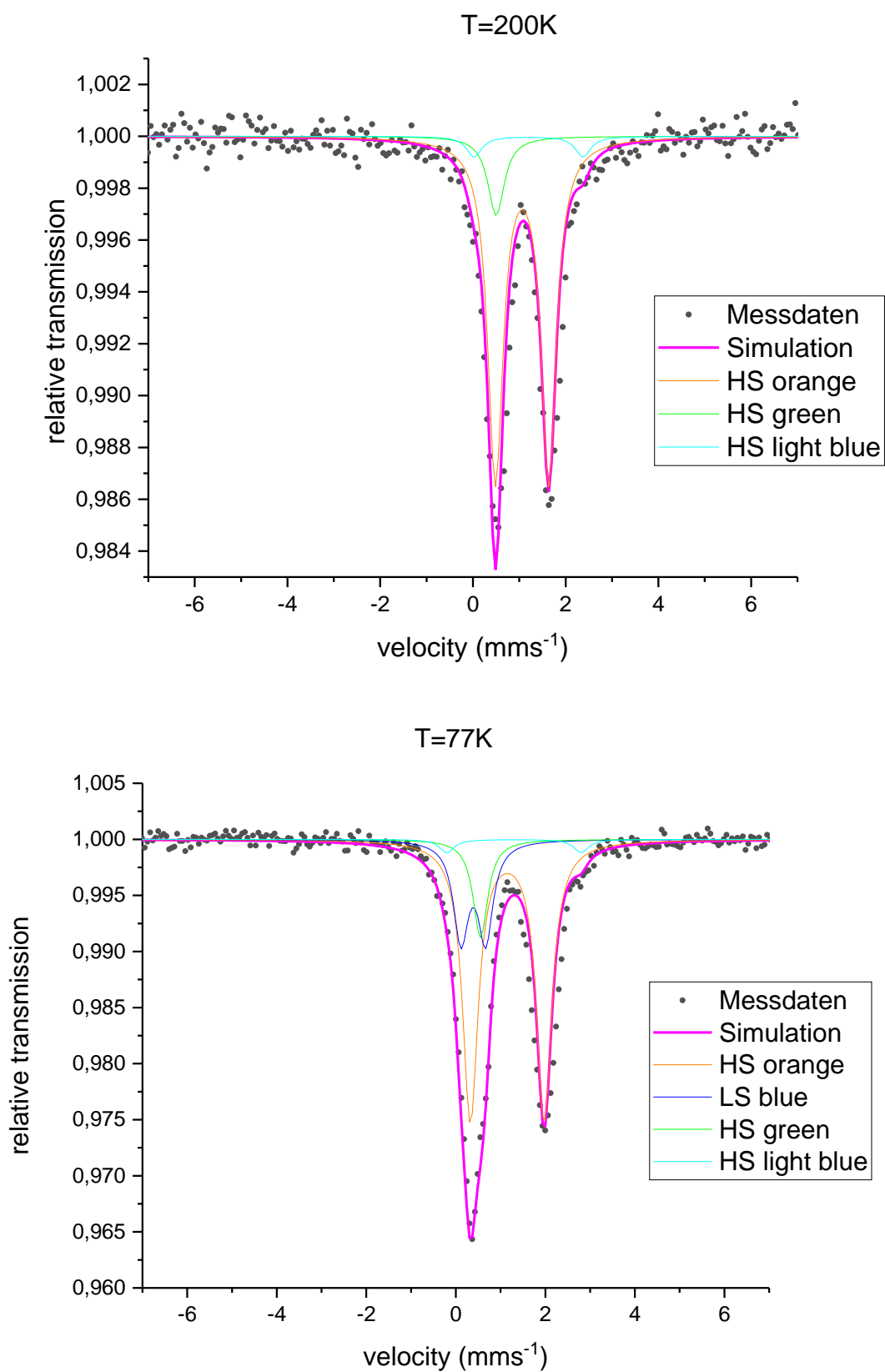


Figure 4.27: Mössbauer spectrum at 200K where all iron(II) are HS (top). Mössbauer spectrum at 77K where 2 iron(II) switched into LS (bottom). Experiment performed in collaboration with Prof. Dr. V. Schünemann of Department of Physics, University of Kaiserslautern (Germany).

	77 K	100 K	150 K	175 K	200 K	298 K
Area HS [%]	64,7 ± 1,0	71,4 ± 1,0	79,8 ± 1,0	83,8 ± 1,0	84,3 ± 1,0	82,8 ± 1,0
Area LS [%]	21,6 ± 1,0	15,6 ± 1,0	6,8 ± 1,0	0	0	0

Table 4-3: Mössbauer VT parameters for [22]αB.

The results fit with the presence of a LS fraction only below 175K which increases gradually on cooling.

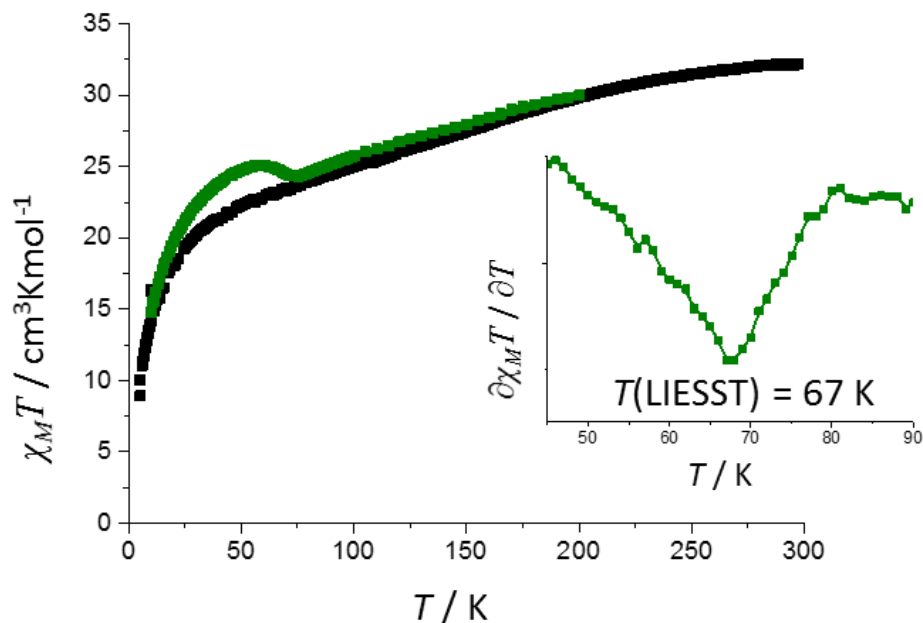


Figure 4.28: Solid state magnetic susceptibility data of [22]αB upon cooling (black line), and rewarming following irradiation at 650 nm at 10 K (green line). The first derivative of the data from the irradiated sample is also shown, whose minimum corresponds to $T(\text{LIESST}) = 67 \text{ K}$.

The sample was irradiated at 10K and some excitation was observed which proves that some iron(II) fraction was LS at 10K. The metastable HS state relaxed back to LS at $67 \text{ K} = T(\text{LIESST})$. This experiment was performed in collaboration with Dr. G. Chastanet in CNRS, Univ. Bordeaux, ICMCB (France).

This compound retained its integrity in solution (Figure 4.29 and Figure 4.30).

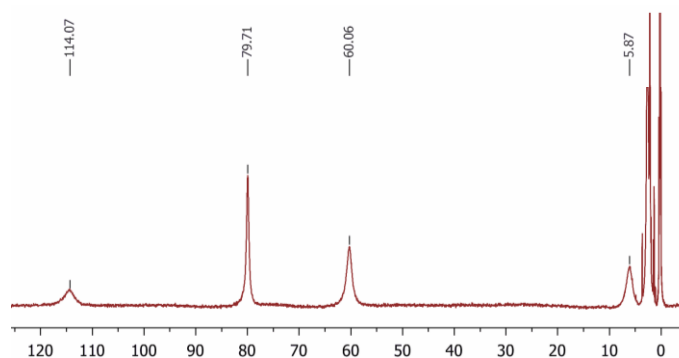


Figure 4.29: ^1H NMR(400 MHz, CD_3CN) spectrum of the cube, [22]αB.

Chapter 4

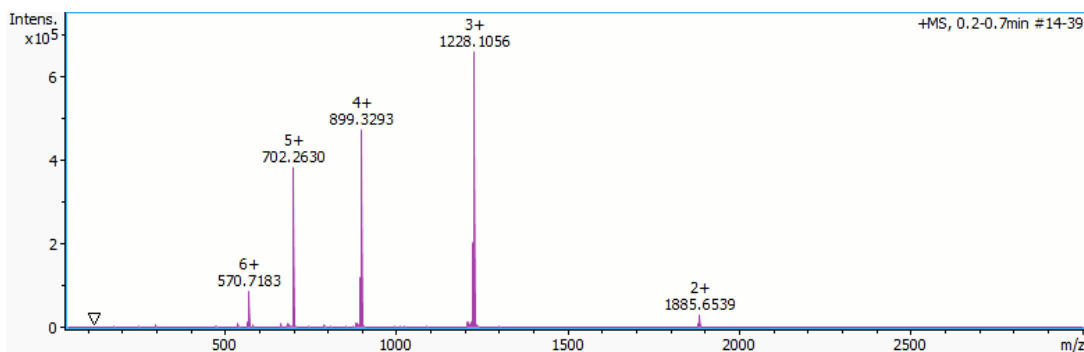


Figure 4.30: Mass spectrum of the cube, [22]αB.

The mass spectrum of [22]αB is very clean, showing the progression peaks from $[[22] + \text{BF}_4]^{6+}$ to $[[22] + 5\text{BF}_4]^{2+}$ by adding one counter-anion at a time ($[22]$ cation = $[\text{Fe}^{\text{III}}(\text{H}_2\text{O})_6\text{CFe}^{\text{II}}_8(22)_{12}]^{7+}$).

Therefore, χT vs T was also determined in liquid solution of acetonitrile by paramagnetic NMR Evans Method. Data points were taken every 10 K from 340 K to 240 K (Figure 4.31). Unfortunately, the temperature of any transition was lower than the freezing point of MeCN.

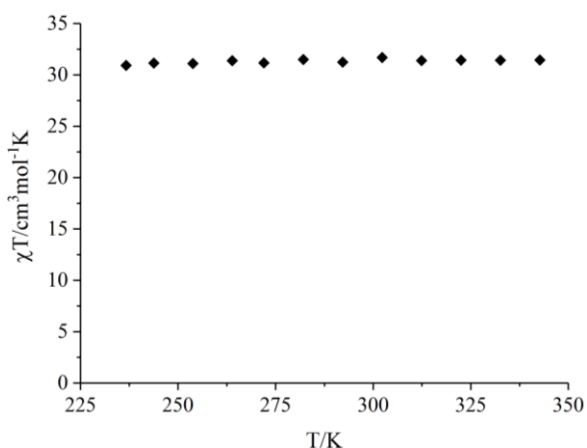


Figure 4.31: Liquid state variable temperature magnetic susceptibility measurement of [22]αB.

Homogeneous bulk sample crystals of [22]αB as red blocks were regularly obtained. But small yellow crystals were occasionally observed in the walls of the crystallization vials which corresponded to the following structure (Figure 4.32), which could be the paramagnetic impurity detected by Mössbauer spectroscopy (light blue line, Figure 4.27).

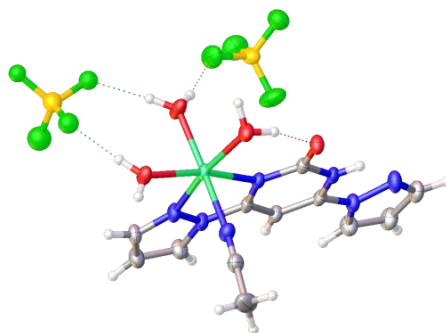


Figure 4.32: Crystal structure of [24]B, $P\bar{1}$ space group.

Unfortunately, not enough crystals of **[24]B** were obtained to fully characterize the compound. Ligand **(24)** was also reacted with iron(II) perchlorate and triflate, but none of those salts template the same M_8L_{12} assembly. The mixture of **(24)** with triflate salt crystallized as small twinned crystals which generated genuinely poor data and the structure could barely be solved. In contrast, the perchlorate salt produced twinned but larger crystals which were suitable for X-ray single crystal analysis (Figure 4.33).

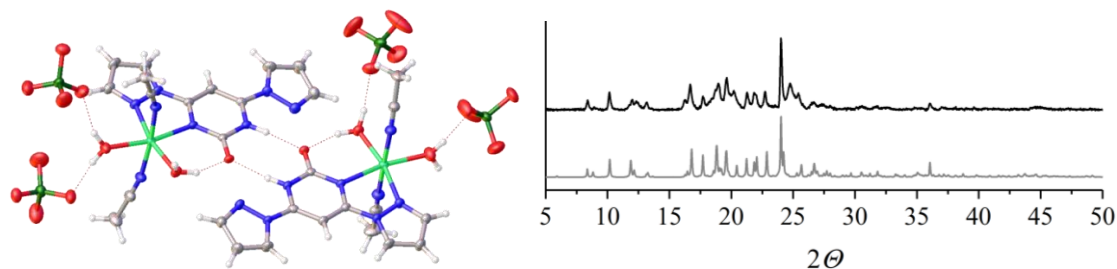


Figure 4.33: Crystal structure of **[24]C**, $C2/c$ space group. The colour assignment in the plot is black for the experimental and grey for the simulated XRD.

Notably, the ligands found in both **[24]C** and **[24]triflate** structures were in their neutral form. Only the BF_4^- counter-anion was basic enough to promote the full deprotonation of **(24)**, and therefore to allow the cubane formation. Hence, the pure sodium salt of **(24)** (ligand **(22)**, Figure 4.23) was reacted with iron(II) tetrafluoroborate in acetonitrile hoping to increase the yield of **[22]αB**. However the structure obtained by diffusion of diisopropyl ether was a different cubic assembly $M_{10}L_{10}$ (Figure 4.34), $[Fe^{III}-F-Fe^{III} \subset Fe^{II}_8(22)_{10}(F)_2(OH, MeCN \text{ or } H_2O)_4](BF_4)_8 \text{ or } 9$ **[22]βB**. Disordered counter-anions were found in the lattice, hence it is unclear from the model whether there are eight or nine tetrafluoroborate molecular formula. Elemental microanalysis results did not fit either of these options.

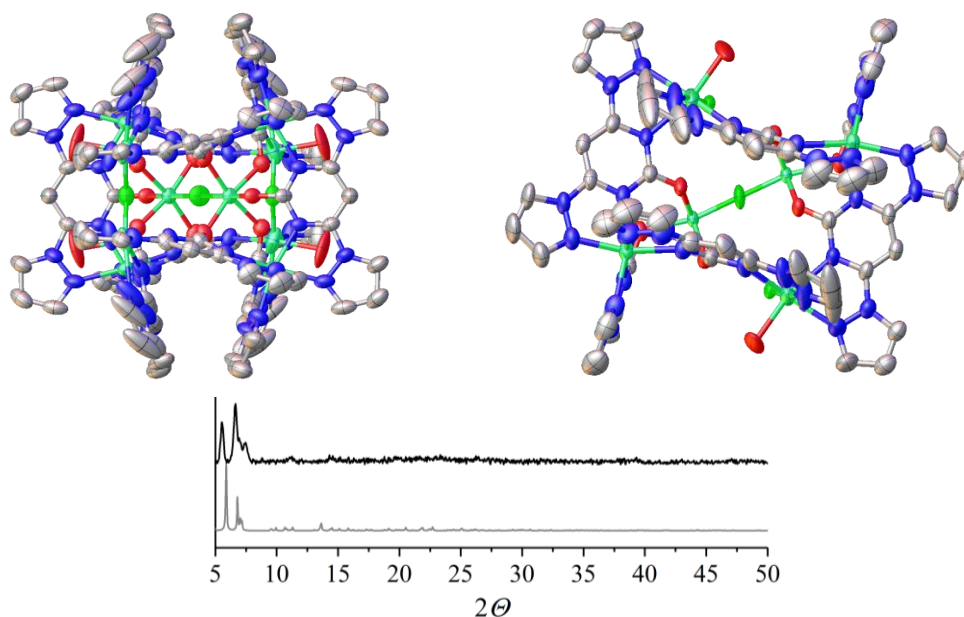


Figure 4.34: Different views of the crystal structure of **[22]βB**, $C2/c$ space group. Hydrogen atoms and counter-anions were omitted for clarity. The colour assignment in the plot is black for the experimental and grey for the simulated XRD.

Chapter 4

This extraordinary assembly is templated by two iron(III) atoms which are directly coordinated by O-donors from (22). [22]βB is constituted by two central iron-(III) atoms bridged by a fluoride ion and coordinated by two sets of five (22) ligands through their oxygen donors. In addition, every outer ligand is coordinating two iron(II) in a bis-bidentate fashion (Figure 4.35). The positions of the iron(II) atoms were the vertices of a cube. In summary, every ligand coordinates to three metal ions simultaneously. Metal ions in the vertices are related by symmetry in groups of four, therefore only two iron(II) atoms and one central iron(III) were unique crystallographically.

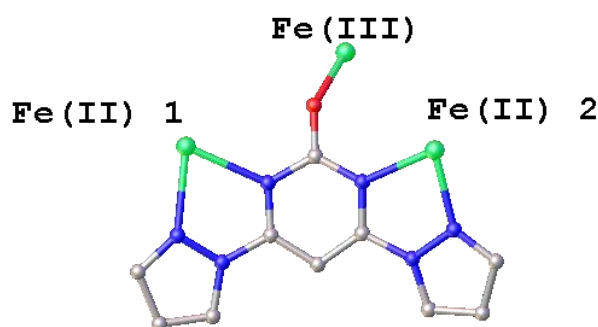


Figure 4.35: Coordination fashion of every (22) in the crystal structure of [22]βB.

120 K	Fe(II) 1	Fe(II) 2	Fe(III)
Fe–L[averaged]	2.126(3)	2.235(3)	1.98(3)
V_{Oh}	12.230(4)	12.779(4)	10.313(3)

Table 4-4: VT experiment crystallographic parameters for [22]βB.

According to crystallographic parameters of Table 4-4, all iron(II) in the vertices were HS at 120 K. However the colour of the crystal clearly changed upon cooling (Figure 4.36).

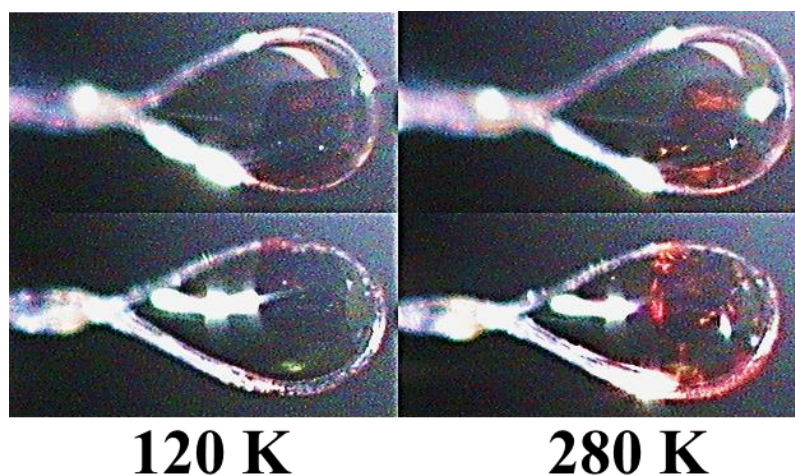


Figure 4.36: Images taken by the camera connected to the cryostream of the Agilent SuperNova diffractometer at different temperatures.

Darkening of crystals upon cooling is indicative of spin-crossover²¹. Since iron(II) in the vertices were HS while iron (III) atoms in the centre of the assembly were LS at 120 K (Table 4-4), the SCO was attributed to the two iron(III) atoms. VT cells were collected every 10 K in cooling cycle. The volume of the unit cell gradually decreased by 3.6% (Figure 4.37).

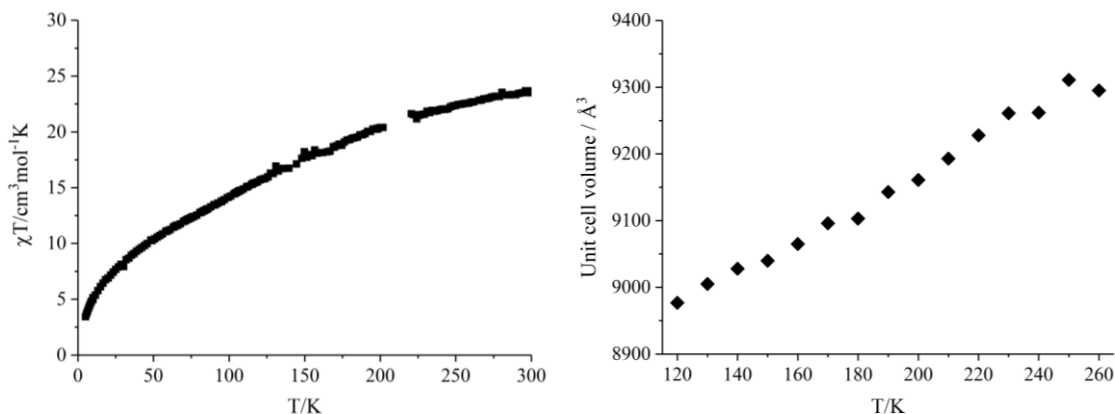


Figure 4.37: SQUID curve of [22]βB. VT X-ray diffraction experiment showing the gradual decrease on the unit cell volume.

Expected χT values for [22]βB at room temperature are around 36 and 30 cm³ mol⁻¹ K at low temperature. However, the measurement is suspect because the sample was not pure and the SQUID temperature controller had a fault (Figure 4.37). Unfortunately the compound was not obtained a second time.

ESMS spectroscopy was used to analyse the stability of the new M₁₀L₁₀ assembly. Although in this case the spectrum of [22]βB was not as clean as [22]αB (Figure 4.30), it was also stable and present in solution (Figure 4.38).

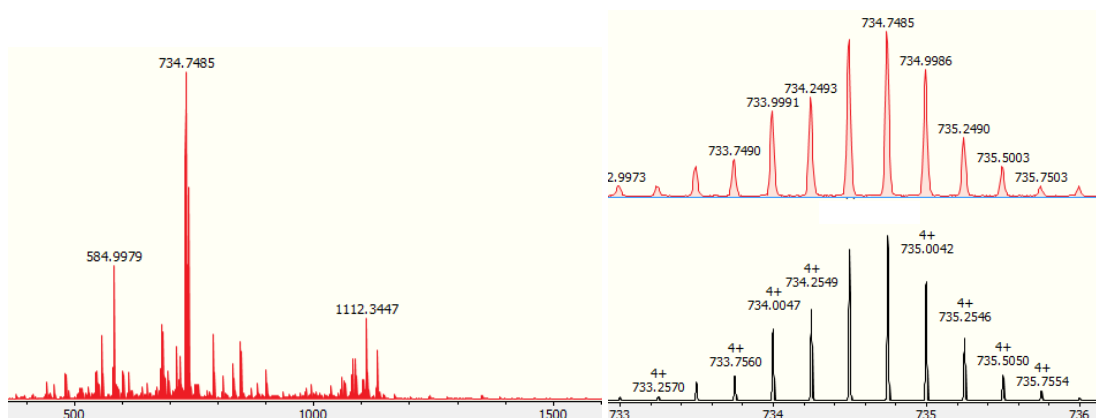


Figure 4.38: Mass spectrum of the second cubic assembly, [22]βB (left). Comparison of the isotopic patterns (right); red for the experimental and black for the simulated.

The most intense peak corresponds to the [22]βB cation = [Fe^{III}F-Fe^{III}CFe^{II}(22)₁₀O₂F₃]⁴⁺.

4.2.4 Novel 4,6-di-pyrazolyl-1,3-pyrimidine-based iron(II) complexes and coordination polymers

Ligands 2-methyl-4,6-di(pyrazol-1-yl)-1,3-pyrimidine (**25**), 2-amino-4,6-di(pyrazol-1-yl)-1,3-pyrimidine (**26**) and 4,6-di(pyrazol-1-yl)-1,3-pyrimidine (**27**) were easily synthesized following the procedure reported by Ortiz *et al.*²² and Ikeda *et al.*²³ and were crystallized (Figure 4.39).

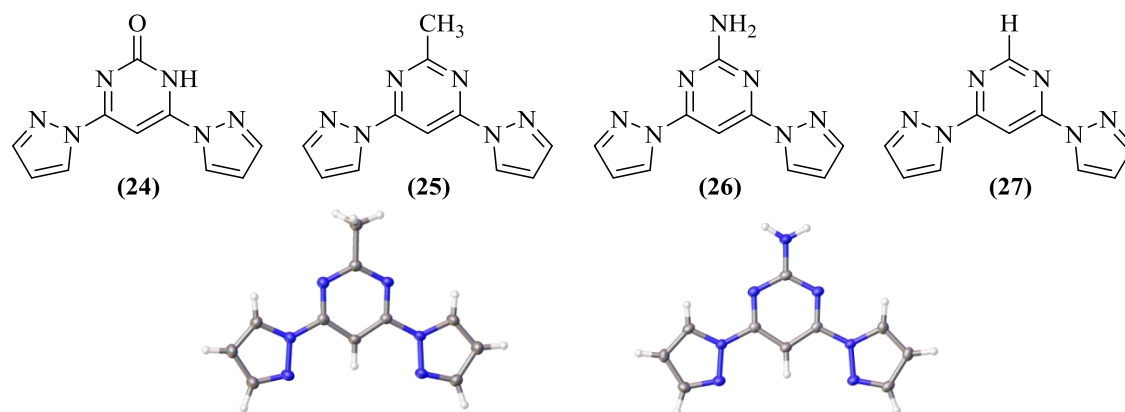


Figure 4.39: Ligands based on the pyrimidine ring. Crystal structures of (**25**) and (**26**), in the $P2_1/c$ and $P2_12_12_1$ space groups respectively.

Those ligands were first synthesized aiming to repeat the same cubic structure $[22]aB$ with different magnetic properties by varying the substituent in the 2-position of the pyrimidine. However, the template effect between the iron(III) hexaaqua and the oxygen of the ligand (**24**) is crucial towards the cubic assembly formation. Different 1D-coordination polymer topologies are presented (Figure 4.40).

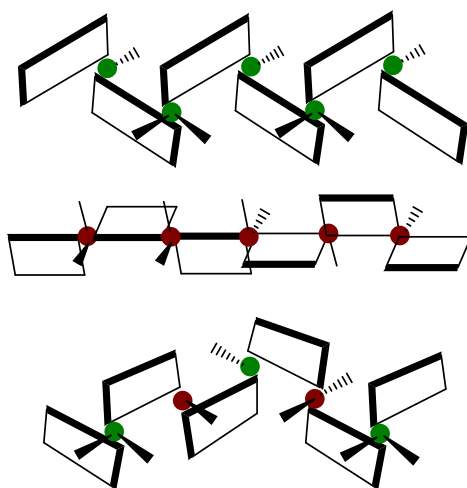


Figure 4.40: Varying topologies of 1D coordination polymers observed. Iron(II) atoms forming an angle of 90° with the two ligands are pictured in green, those forming the 180° angle are pictured in red.

1D-coordination polymers $[25]B^\infty$, $[26]C^\infty$ and $[27]C^\infty$ were obtained, where the solvent molecules and counter-anions played an important role in the assembly through hydrogen bonding (Figure 4.41).

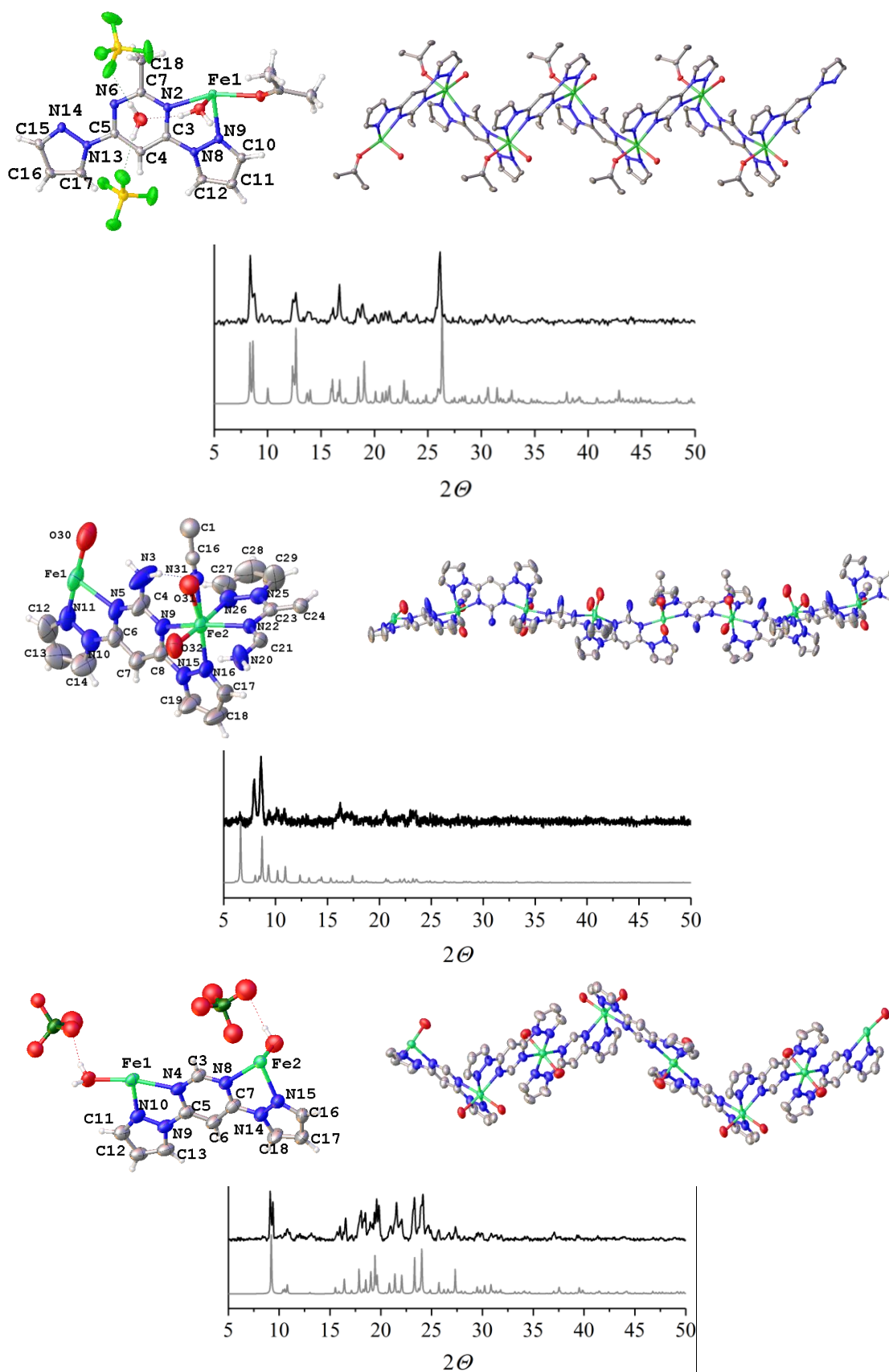


Figure 4.41: Polymeric structures [25]B $^{\infty}$, [26]C $^{\infty}$ and [27]C $^{\infty}$ crystallized in monoclinic $P2_1/n$, tetragonal $P4_2/nm$ and monoclinic $C2/c$ space groups respectively. The colour assignment in the plot is black for the experimental and grey for the simulated XRD. Counter-anion in [26]C $^{\infty}$ model were extremely disordered and were omitted for clarity.

Bulk powders of $[26]C^\infty$ were amorphous, so single crystals were used for the powder XRD experiment which produced a spectrum where the correct peaks can be observed but with different relative intensities compared to the simulation (Figure 4.41). These results contrasted with the previous reports where copper(I) based grids $[2 \times 2]$ were obtained from the same ligands^{22, 24}. Two solvent molecules coordinate the iron(II) centres in the three polymeric structures. $[25]B^\infty$ was crystallized from acetone by diffusion of diethyl ether. It contains one molecule of acetone and one molecule of water acting as coordinating ligand in a *cis* geometry. Planes of the two (25) ligands bound to each iron atom make a 90° angle. $[26]C^\infty$ was crystallized in acetonitrile by diffusion of diisopropyl ether. This structure contains two unique crystallographically iron(II) atoms, the first coordinates two bidentate ligands and two water molecules. The second iron coordinates two ligands and, one fully occupied water molecule, while the last coordination site is shared between a mixture of water and acetonitrile. In this case the least squares planes of (26) are parallel and the solvent coordination sites are in *cis*. $[27]C^\infty$ crystallized from slow evaporation of a nitromethane solution. This structure presents two different alternating environments of iron(II) with parallel and perpendicular oriented ligands, where the solvent molecules coordinate in *trans* and *cis* configurations respectively.

4.2.4.1 Thiocyanate and selenocyanate salts

Complexes of type; $[Fe(N\text{-donor})_4(NCS)_2]$ are well established SCO compounds in both *cis* or *trans* configurations²⁵. Therefore, it was believed that by replacing the solvent coordination sites in the above structures by NCS, a novel SCO coordination polymer could be developed. $Fe(NCS)_2$ was generated *in situ* and added to methanolic solutions of the four ligands (Figure 4.39). (25) and (26) produced isostructural 1D polymers (Figure 4.43) while (27) crystallized as a mononuclear complex which was collected as methanol solvate and solvent free forms. Unfortunately, the $[24]NCS$ reaction yielded an amorphous black powder which was not identified.

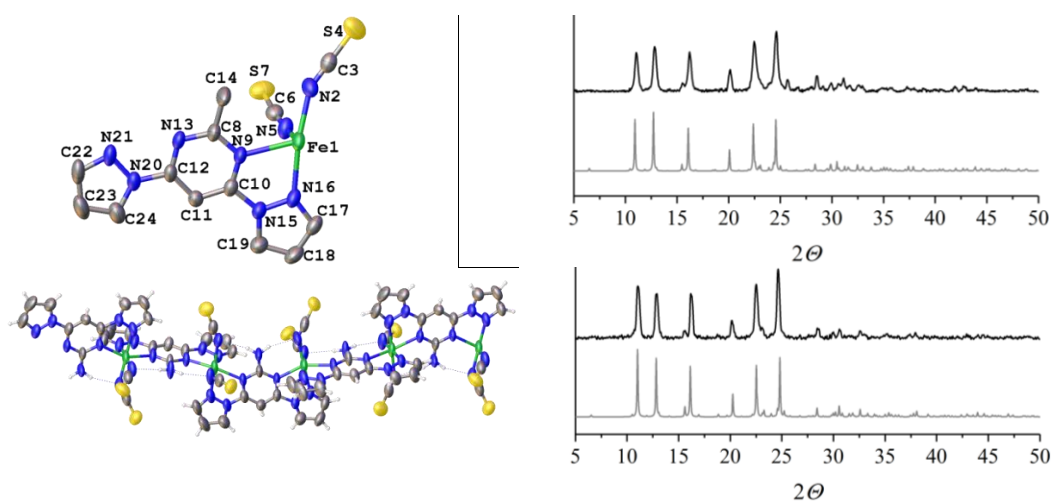


Figure 4.42: Both $[25]NCS^\infty$ and $[26]NCS^\infty$ polymers crystallized in the tetragonal $I4_1/a$ space group. The colour assignment in the plot is black for the experimental and grey for the simulated XRD. $[25]NCS^\infty$ (top) and $[26]NCS^\infty$ (bottom).

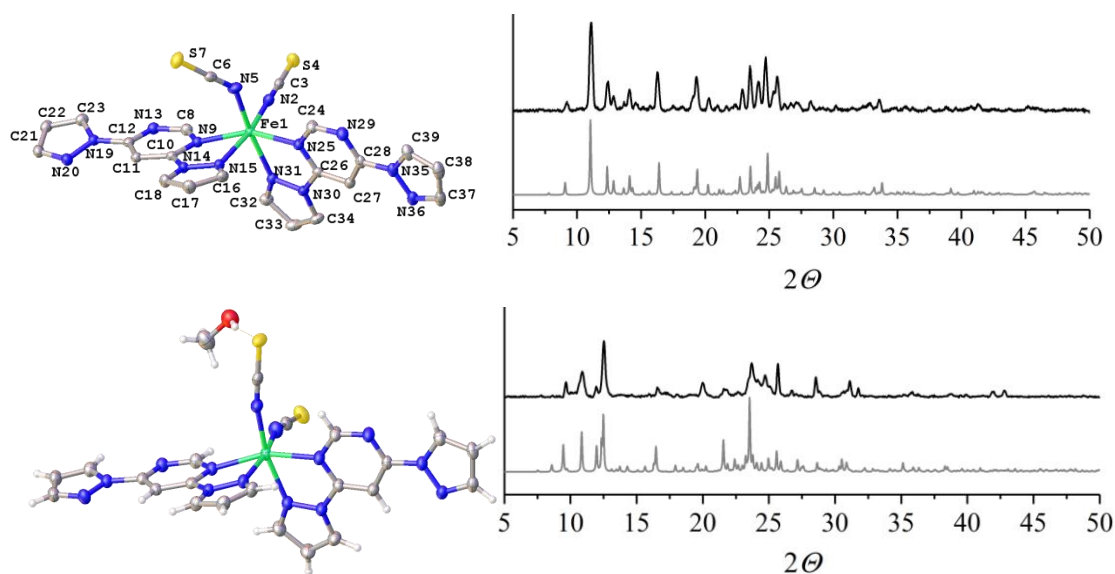


Figure 4.43: Complexes [27]NCS and [27]NCS(MeOH) were triclinic $P\bar{1}$ and monoclinic $P2_1/n$ respectively. The colour assignment in the plot is black for the experimental and grey for the simulated XRD.

Unexpectedly, all the complexes are HS at low temperatures. The [25]NCS[∞] and [27]NCS data sets were collected at 120 K while [26]NCS[∞] was collected in Diamond at 100 K (Table 4-5).

	[25]NCS [∞]	[26]NCS [∞]
Fe-N_[pzi]	2.184(4), 2.194(3)	2.178(5), 2.181(5)
Fe-N_[pym]	2.231(3), 2.245(3)	2.202(4), 2.206(4)
Fe-N_[NCS]	2.051(4), 2.139(4)	2.036(6), 2.113(7)
V_{Oh}	12.692(12)	12.722(18)
	[27]NCS	[27]NCS (MeOH)
Fe-N_[pzi]	2.171(2), 2.192(2)	2.184(2), 2.185(2)
Fe-N_[pym]	2.197(2), 2.210(2)	2.202(2), 2.214(2)
Fe-N_[NCS]	2.067(2), 2.107(2)	2.053(2), 2.104(2)
V_{Oh}	12.916(6)	12.933(7)

Table 4-5: Crystallographic parameters of thiocyanate polymers and complexes.

Selenocyanate acts as stronger σ -donor ligand than thiocyanate, thus increasing the ligand field splitting. Hence, complexes like [Fe(N-donor)₄(NCSe)₂] where NCS⁻ is replaced by NCSe⁻ present a stabilization of their low spin state²⁶. With that in mind, the following compounds [25]NCSe, [26]NCSe and [27]NCSe were prepared (Figure 4.44).

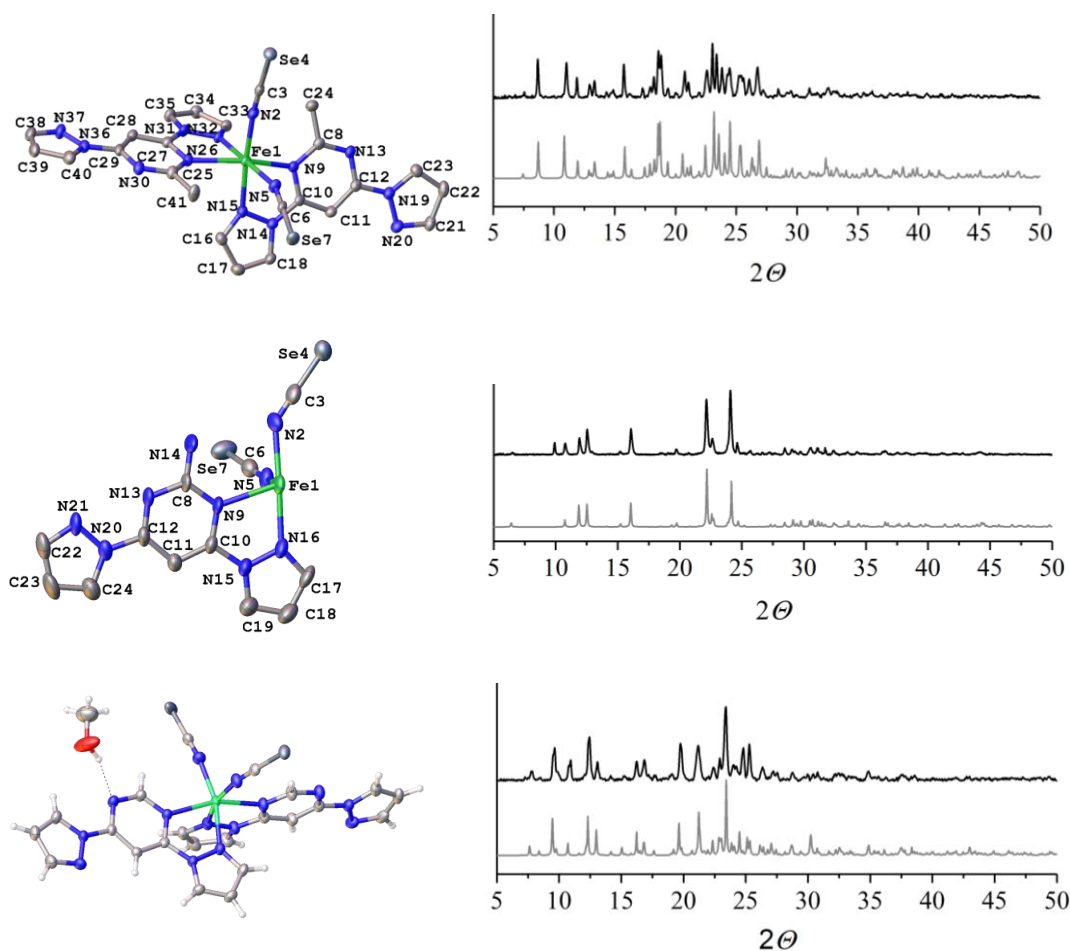


Figure 4.44: Crystal structures of complexes $[25]\text{NCSe}$ and $[27]\text{NCSe}$ which crystallized in $P\bar{1}$ space group, and $[26]\text{NCSe}^\ominus$ polymer, which was isostructural to the NCS polymers described above, in the $I4_1/a$ space group. The colour assignment in the plot is black for the experimental and grey for the simulated XRD, $[25]\text{NCSe}$ (top), $[26]\text{NCSe}^\ominus$ (middle) and $[27]\text{NCSe}$ (bottom).

All these structures were also HS at 120 K (Table 4-6).

	$[25]\text{NCSe}$	$[26]\text{NCSe}^\ominus$	$[27]\text{NCSe}$ (MeOH)
$\text{Fe-N}_{[\text{pz}]}$	2.151(3), 2.158(3)	2.160(5), 2.162(5)	2.168(4), 2.1774(4)
$\text{Fe-N}_{[\text{pym}]}$	2.272(3), 2.305(3)	2.195(4), 2.201(4)	2.205(3), 2.231(3)
$\text{Fe-N}_{[\text{NCS}]}$	2.085(3), 2.114(3)	2.073(5), 2.131(5)	2.059(4), 2.107(4)
V_{Oh}	13.103(11)	12.769 (17)	12.958(13)

Table 4-6: Crystallographic parameters of selenocyanate polymers and complexes.

Singularly, although all these reactions were set up initially with a 1:1 $[\text{Fe}(\text{NCX})_2]$ -ligand stoichiometry, only three of them crystallized as 1D polymers. Magnetic susceptibility measurements versus temperature were recorded and confirmed what was concluded from X-ray crystallography (Figure 4.45).

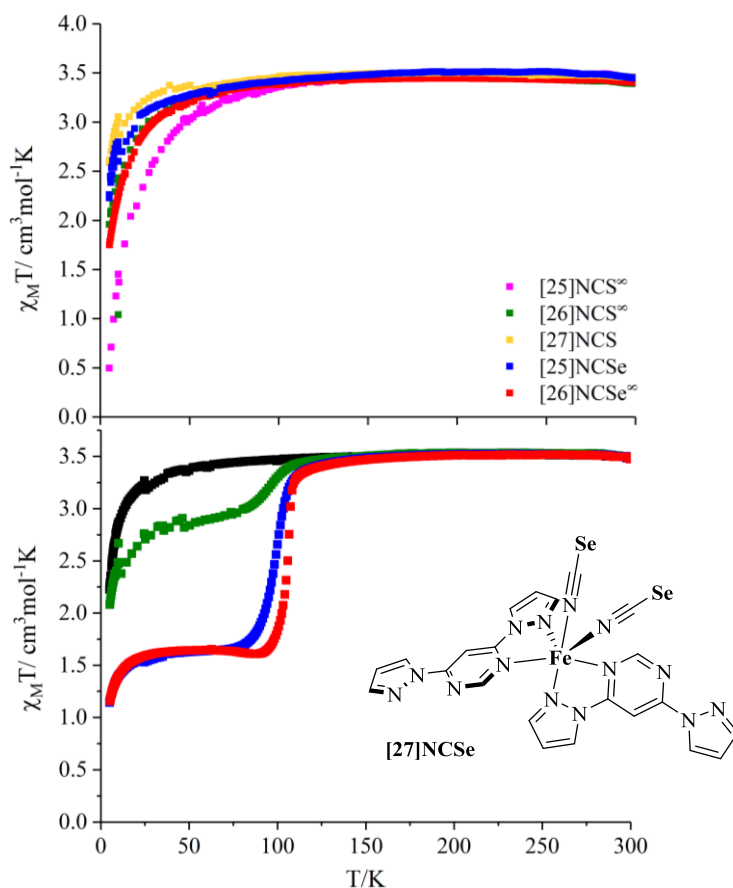


Figure 4.45: SQUID curves of the bis-pyrazolyl-pyrimidine coordination complexes and polymers discussed above. At the top are plotted the five HS complexes whereas at the bottom is [27]NCSe methanol solvate (black line), which starts losing solvent after a few hours (green line) and after 24 h in the vacuum oven (blue and red cooling and warming cycles).

As was concluded from the crystallographic parameters (Table 3-4 and Table 3-5) all complexes were HS at 120K. Therefore none of these compounds were subject of SCO above this temperature. However the complex [27]NCSe undergoes an incomplete hysteretic spin transition at 97 K \downarrow – 106 K \uparrow upon drying (Figure 4.45). Unfortunately no crystals of the solvent free phase were obtained despite trying other solvents, where isostructural solvatomorphs to [27]NCS (MeOH) containing ethanol or acetone in the lattice were obtained.

As further research the following ligands (Figure 4.46) were proposed to give potential SCO coordination polymers with Fe(NCS) $_2$ salt. The geometry of the pyrimidine-pyridine certainly entails a stronger crystal ligand field, which would favour the LS if iron(II) complexes compared to pyrimidine-pyrazole synthesized above. A similar comparison holds between bpp and terpy ligands. The synthesis of the new ligands was reported²⁷ and some interesting materials were synthesized previously²⁸. However this was not investigated due to lack of time.

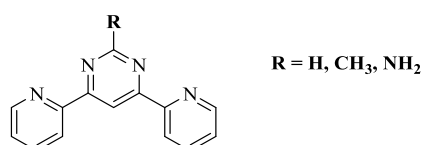


Figure 4.46: Ligands based on the pyrimidine ring, potential SCO coordination polymers.

4.2.5 Novel ligands derived from 4,6-di(pyrazol-1-yl)-pyrimid-2-one with methylated pyrazole derivatives.

As a second modification of (24), the new ligands 4,6-di(4-methyl-pyrazol-1-yl)-pyrimid-2-one (28) and 4,6-di(3,5-dimethyl-pyrazol-1-yl)-pyrimid-2-one (29), were synthesized following the same synthetic procedure as (24) (Figure 4.23). The same cubic pyrimidine-based structure [22]αB with a higher $T_{1/2}$ was sought by adding methyl groups (EDGs) to the pyrazole²⁹.

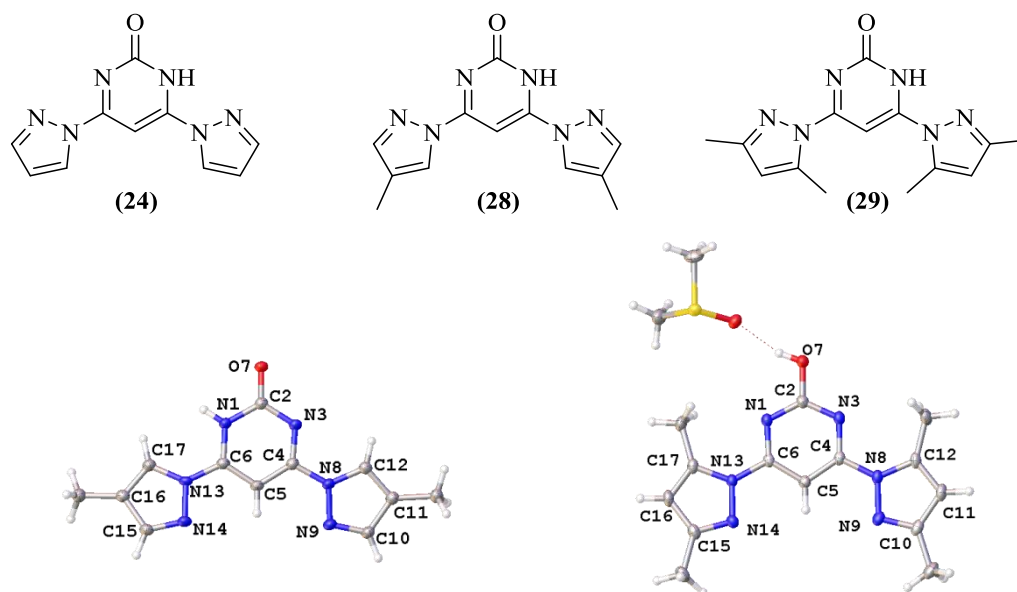


Figure 4.47: Drawings of ligand (24) and novel ligands (28) and (29) with their crystal structures.

Hydrogen bond between a DMSO molecule and the hydroxyl group (O7-H, Figure 4.47) of ligand (29) showed evidence of the more stable tautomer; 2-hydroxy-4,6-di(3,5-dimethyl-pyrazol-1-yl)-pyrimidine. This differs from (24) and (28), whose pyrimidine tautomer is observed in the solid state (Table 4-7).

	(24)	(28)	(29)
O7-C2	1.240(2)-1.249(3)	1.240(2)	1.3334(17), 1.3364(17)
N1-C2	1.390(3)-1.395(3)	1.391(2)	1.3339(18), 1.3333(18)
N3-C2	1.355(3)-1.358(3)	1.360(2)	1.3365(18), 1.3353(18)

Table 4-7: Bond lengths surrounding C2 of the three ligands.

This difference is probably due to the steric hindrance between the C17-CH₃ substituent in (29) with the N1-H group in the pyrimidine tautomer of that compound. Unfortunately no crystalline material was obtained from ligand (29) when reacted with iron(II) tetrafluoroborate salt. In contrast the analogous structure to [22]αB was observed from ligand (28) (Figure 4.48).

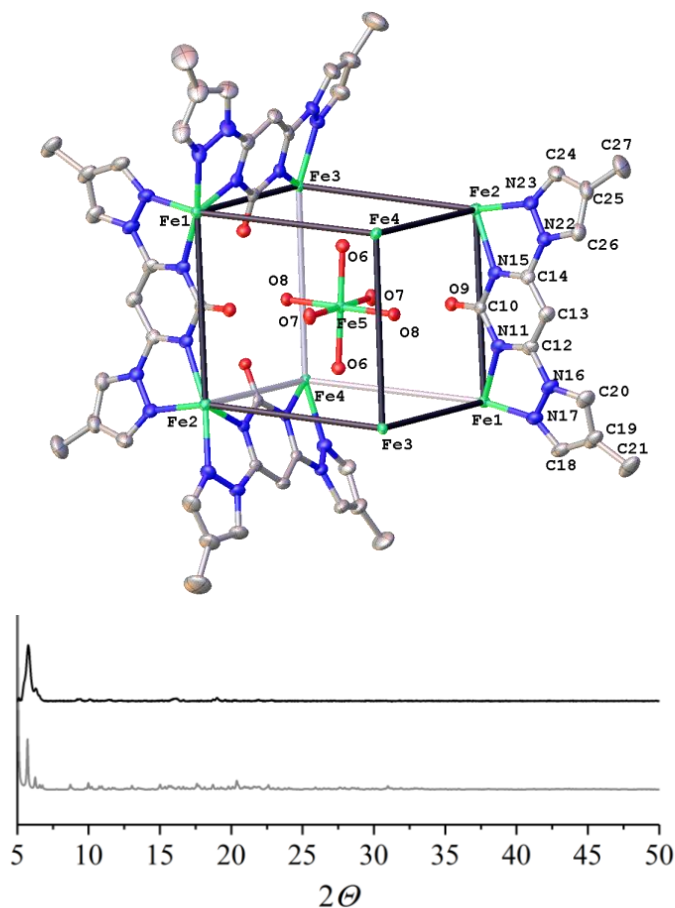


Figure 4.48: View of the cubic structure, [28]B at 100 K. Hydrogen atoms and counter-anions were omitted and only four bridging ligands shown for clarity. $P2_1/n$ space group. The colour assignment in the plot is black for the experimental and grey for the simulated XRD.

The [22]αB and [28]B are not isostructural but they have some things in common; the two cubic structures were composed of four opposed pairs of iron (II) related by inversion symmetry, and in both structures only two opposite iron(II) switched from their HS to LS states (Table 4-8).

125 K	Fe 1	Fe 2	Fe 3	F 4
Fe–N[averaged]	2.072(10)	2.171(3)	2.193(3)	2.158(3)
V_{Oh}	11.38(3)	12.674(10)	12.916(10)	12.504(10)
250 K	Fe 1	Fe 2	Fe 3	F 4
Fe–N[averaged]	2.189(5)	2.178(5)	2.181(5)	2.182(5)
V_{Oh}	12.881(17)	12.889(17)	12.833(17)	12.868(17)

Table 4-8: VT experiment crystallographic parameters for [28]B.

Unfortunately the cryo-system of the diffractometer could not reach 100 K due to problems with the drying unit during the last year of the PhD. Gradual spin-crossover was observed from 250 K to 125 K. However in this case the SQUID curve had well-defined spin-crossover (Figure 4.49).

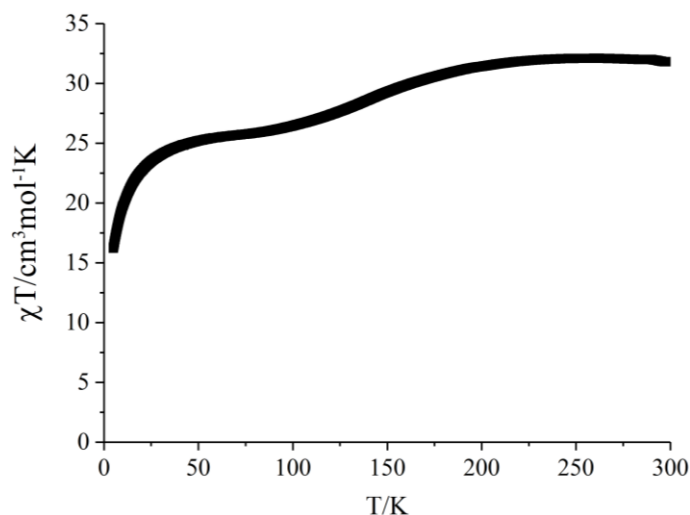


Figure 4.49: SQUID curve of [28]B.

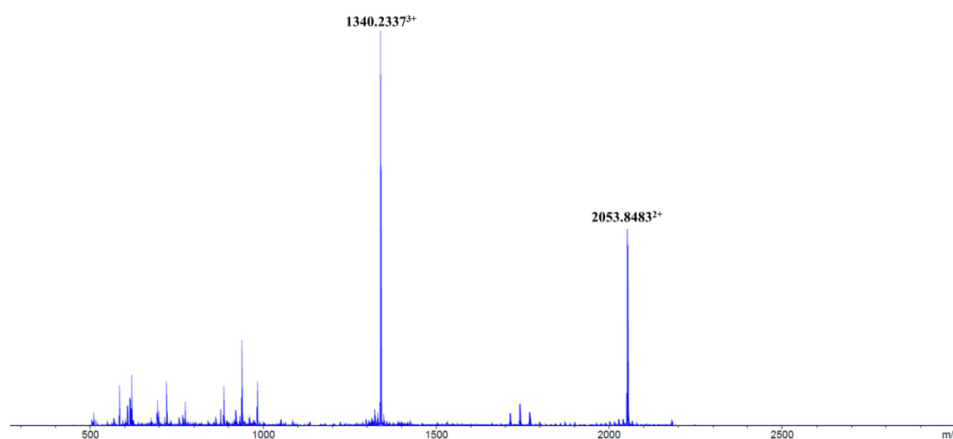


Figure 4.50: Mass spectrum of the cubic assembly [28]B.

The two main peaks were assigned to $[[28](\text{BF}_4)_5]^{2+}$ and $[[28](\text{BF}_4)_4]^{3+}$ respectively ($[28]$ cation = $[\text{Fe}^{\text{III}}(\text{H}_2\text{O})_6\text{CFe}^{\text{II}}_8(28)_{12}]^{7+}$).

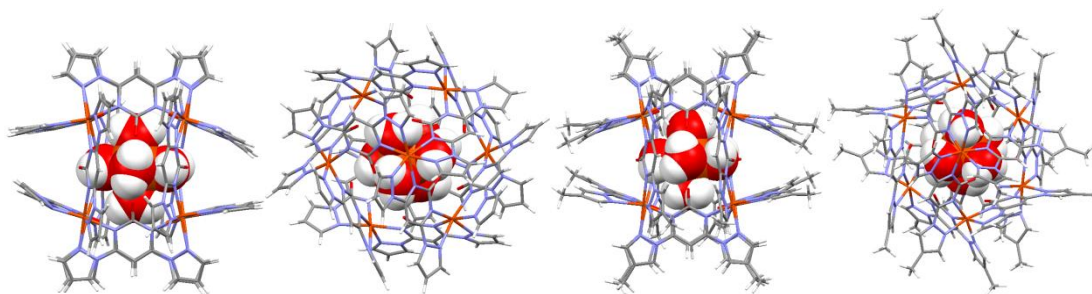


Figure 4.51: Space fill view of the template molecules in [22]αB and [28]B.

The iron(III) hexaaqua template inside the assembly occupies the internal volume of the cluster, which may afford steric hindrance to the complex interfering with the full spin transition of the eight iron(II). Another difference between them is the disordered found in the crystal lattice, while ligands in the cubic structure [22]αB are disordered over different positions, ligands in [28]B fully occupy their positions in the lattice. This could explain the difference observed in the SQUID curves (Figure 4.26 and Figure 4.49).

4.3 Conclusions

2,4-Di(4,5,6,7-tetrahydro-2-indazol-2-yl)-6-chloro-1,3,5-triazine (**17**) reacted with iron(II) tetrafluoroborate as a bis-bidentate ligand yielding a set of M_4L_4 , M_8L_{12} and $M_{6+4}L_{12}$ assemblies containing ligand (**18**). It was not possible to fully characterize those because of reproducibility problems where mixtures of these and other unknown assemblies were probably obtained. On the other hand, 2,4-di(1H-pyrazol-1-yl)-1,3,5-triazine (**21**) also adopted a bis-bidentate conformation producing an unexpected grid M_4L_8 which was characterized by ES⁺MS, X-ray, SQUID and elemental analysis. The nature of ligand (**21**), which hydrolyses easily in contact with iron salts, prevented the synthesis of [**21**]C and other related compounds with different 3d transition metal ions. The bis-bidentate geometric conformations in these compounds can be justified by the conclusions of Chapter 2. Ligands (**17**) and (**21**) have in common the absence of a bulky group in the 6-position of the triazine, which could disfavour the bis-bidentate conformation, when compared to the other 1,3,5-triazine-based ligands (**1**) - (**9**), which produced the homoleptic complexes in Chapter 2.

The cubic-shaped structure M_8L_{12} , where 12 deprotonated ligands act as edges of the cube while iron(II) atoms are the vertices, was reproduced using 4,6-di(pyrazol-1-yl)-1,3-pyrimid-2-one (**24**). Two iron(II) atoms of the cubane vertices undergo a gradual spin transition between 200 and 100 K. This compound has been characterized by single crystal X-ray diffraction, powder pattern diffraction, diffuse reflectance, Mössbauer Spectroscopy, ES⁺MS mass spectrometry, ¹H NMR, SQUID magnetometry, LIESST and Evans method. The sodium salt (**22**) assembled in a different cubic assembly ($M_{10}L_{10}$) which presents gradual SCO in the central iron(III) atoms. They were bridged by a fluorine atom and are coordinated by five O-donor atoms from ligand (**22**).

One-dimensional coordination polymers were obtained from the mixtures of iron(II) salts with 2-methyl-4,6-di(pyrazol-1-yl)-1,3-pyrimidine (**25**), 2-amino-4,6-di(pyrazol-1-yl)-1,3-pyrimidine (**26**), and 4,6-di(pyrazol-1-yl)-1,3-pyrimidine (**27**). In order to promote SCO, thiocyanate and selenocyanate were coordinated into the free coordination sites in these assemblies. These were also HS over the temperature ranges although the compound [**27**]NCSe when dried, undergoes an incomplete hysteretic spin transition.

The methylated derivatives 4,6-di(4-methyl-pyrazol-1-yl)-pyrimid-2-one (**28**) and 4,6-di(3,5-dimethyl-pyrazol-1-yl)-pyrimid-2-one (**29**) were synthesized and fully characterized. They assembled into the analogous cubic M_8L_{12} structure. [**28**]B was characterized by ES⁺MS, single crystal and powder XRD, and SQUID. The [**29**]B was not isolated in more than few crystals which were not suitable for single crystal analysis.

4.4 Bibliography

1. Carter, M. J.; Beattie, J. K., Kinetic chelate effect. Chelation of ethylenediamine on platinum(II). *Inorganic Chemistry* **1970**, *9* (5), 1233-1238.
2. Paul, R. L.; Bell, Z. R.; Jeffery, J. C.; McCleverty, J. A.; Ward, M. D., Anion-templated self-assembly of tetrahedral cage complexes of cobalt(II) with bridging ligands containing two bidentate pyrazolyl-pyridine binding sites. *Proceedings of the National Academy of Sciences* **2002**, *99* (8), 4883-4888.
3. Hogue, R. W.; Singh, S.; Brooker, S., Spin crossover in discrete polynuclear iron(ii) complexes. *Chemical Society Reviews* **2018**, *47* (19), 7303-7338.
4. Capel Berdiell, I.; Kulmaczewski, R.; Halcrow, M. A., Iron(II) Complexes of 2,4-Dipyrazolyl-1,3,5-triazine Derivatives—The Influence of Ligand Geometry on Metal Ion Spin State. *Inorganic Chemistry* **2017**, *56* (15), 8817-8828.
5. Chi, Y.-N.; Huang, K.-L.; Cui, F.-Y.; Xu, Y.-Q.; Hu, C.-W., Structural Diversity of Silver(I) 4,6-Dipyridyl-2-Aminopyrimidine Complexes: Effect of Counteranions and Ligand Isomerism. *Inorganic Chemistry* **2006**, *45* (26), 10605-10612.
6. Tuna, F.; Lees, M. R.; Clarkson, G. J.; Hannon, M. J., Readily Prepared Metallo-Supramolecular Triple Helicates Designed to Exhibit Spin-Crossover Behaviour. *Chemistry – A European Journal* **2004**, *10* (22), 5737-5750.
7. Barboiu, M.; Dumitru, F.; Petit, E.; Legrand, Y. M.; Lee, A. V. D., Mesomeric metallosupramolecular grid architectures. *Supramolecular Chemistry* **2015**, *27* (5-6), 393-400.
8. (a) Hall, B. R.; Adams, H.; Ward, M. D., A family of tetrahedral coordination cages with different symmetries by assembly of bis-bidentate bridging ligands with first-row transition metal dications. *Supramolecular Chemistry* **2012**, *24* (7), 499-507; (b) Lindoy, L. F., Tetrahedral metallocages assembled from oligopyridine ligands and transition metal ions. *Journal of Inclusion Phenomena and Macrocyclic Chemistry* **2018**.
9. Train, J. S.; Wragg, A. B.; Auty, A. J.; Metherell, A. J.; Chekulaev, D.; Taylor, C. G. P.; Argent, S. P.; Weinstein, J. A.; Ward, M. D., Photophysics of Cage/Guest Assemblies: Photoinduced Electron Transfer between a Coordination Cage Containing Osmium(II) Luminophores, and Electron-Deficient Bound Guests in the Central Cavity. *Inorganic Chemistry* **2019**, *58* (4), 2386-2396.
10. Cullen, W.; Hunter, C. A.; Ward, M. D., An Interconverting Family of Coordination Cages and a meso-Helicate; Effects of Temperature, Concentration, and Solvent on the Product Distribution of a Self-Assembly Process. *Inorganic Chemistry* **2015**, *54* (6), 2626-2637.
11. Meng, W.; Ronson, T. K.; Nitschke, J. R., Symmetry breaking in self-assembled M_4L_6 cage complexes. *Proceedings of the National Academy of Sciences* **2013**, *110* (26), 10531-10535.

Chapter 4

12. Steinert, M.; Schneider, B.; Dechert, S.; Demeshko, S.; Meyer, F., Spin-State Versatility in a Series of Fe₄[2 × 2] Grid Complexes: Effects of Counteranions, Lattice Solvent, and Intramolecular Cooperativity. *Inorganic Chemistry* **2016**, *55* (5), 2363-2373.
13. Cao, M.-L.; Hao, H.-G.; Zhang, W.-X.; Ye, B.-H., Assembly of a Cubic Nanocage Co₈L₁₂ and a Hydrogen-Bonded 3D NbO Net Based on the [(HCO₃)₂]²⁻ Synthone and Water. *Inorganic Chemistry* **2008**, *47* (18), 8126-8133.
14. Freire, M. G.; Neves, C. M. S. S.; Marrucho, I. M.; Coutinho, J. A. P.; Fernandes, A. M., Hydrolysis of Tetrafluoroborate and Hexafluorophosphate Counter Ions in Imidazolium-Based Ionic Liquids. *The Journal of Physical Chemistry A* **2010**, *114* (11), 3744-3749.
15. Wang, J.-X.; Wang, C.; Wang, X.; Wang, X.-Y.; Xing, Y.-H.; Sun, Q., Experimental and theoretical investigations of copper (I/II) complexes with triazine-pyrazole derivatives as ligands and their in situ C–N bond cleavage. *Spectrochimica Acta Part A: Molecular and Biomolecular Spectroscopy* **2015**, *142*, 55-61.
16. (a) Schröter, M.; Lork, E.; Mews, R., Über das Donor-Verhalten von Bis(pyrazolyl)-Schwefel-Derivaten. *Zeitschrift für anorganische und allgemeine Chemie* **2005**, *631* (9), 1609-1614; (b) Nielsen, D. J.; Cavell, K. J.; Skelton, B. W.; White, A. H., Tetrafluoroborate anion B–F bond activation—unusual formation of a nucleophilic heterocyclic carbene:BF₃ adduct. *Inorganica Chimica Acta* **2003**, *352*, 143-150.
17. Capel Berdiell, I.; Warriner, S. L.; Halcrow, M. A., Silver(i) complexes of bis- and tris-(pyrazolyl)azine derivatives – dimers, coordination polymers and a pentametallic assembly. *Dalton Transactions* **2018**, *47* (15), 5269-5278.
18. Berdiell, I. C.; Kulak, A. N.; Warriner, S. L.; Halcrow, M. A., Heterometallic Coordination Polymer Gels Supported by 2,4,6-Tris(pyrazol-1-yl)-1,3,5-triazine. *ACS Omega* **2018**, *3* (12), 18466-18474.
19. Hübsch, W.; Pfeleiderer, W., Pteridines. Part XLI. Synthesis and properties of 6,7,8-trimethyl-4-thiolumazine. *Helvetica Chimica Acta* **1989**, *72* (4), 738-743.
20. Liu, W.; Thorp, H. H., Bond valence sum analysis of metal-ligand bond lengths in metalloenzymes and model complexes. 2. Refined distances and other enzymes. *Inorganic Chemistry* **1993**, *32* (19), 4102-4105.
21. Halcrow, M. A., The foundation of modern spin-crossover. *Chemical Communications* **2013**, *49* (93), 10890-10892.
22. Ortiz, M. I.; Soriano, M. L.; Carranza, M. P.; Jalón, F. A.; Steed, J. W.; Mereiter, K.; Rodríguez, A. M.; Quiñero, D.; Deyà, P. M.; Manzano, B. R., New [2 × 2] Copper(I) Grids as Anion Receptors. Effect of Ligand Functionalization on the Ability to Host Counteranions by Hydrogen Bonds. *Inorganic Chemistry* **2010**, *49* (19), 8828-8847.
23. Ikeda, M.; Maruyama, K.; Nobuhara, Y.; Yamada, T.; Okabe, S., Cytoprotective Effects of 4, 6-Bis(1H-pyrazol-1-yl)pyrimidine and Related Compounds on HCl/Ethanol-Induced Gastric Lesions in Rats. *CHEMICAL & PHARMACEUTICAL BULLETIN* **1997**, *45* (3), 549-551.

Chapter 4

24. Manzano, B. R.; Jalón, F. A.; Soriano, M. L.; Carrión, M. C.; Carranza, M. P.; Mereiter, K.; Rodríguez, A. M.; de la Hoz, A.; Sánchez-Migallón, A., Anion-Dependent Self-Assembly of Silver(I) and Diaminotriazines to Coordination Polymers: Non-Covalent Bonds and Role Interchange between Silver and Hydrogen Bonds. *Inorganic Chemistry* **2008**, *47* (19), 8957-8971.
25. (a) Moliner, N.; Gaspar, A. B.; Muñoz, M. C.; Niel, V.; Cano, J.; Real, J. A., Light- and Thermal-Induced Spin Crossover in $[\text{Fe}(\text{abpt})_2[\text{N}(\text{CN})_2]_2]$. Synthesis, Structure, Magnetic Properties, and High-Spin \leftrightarrow Low-Spin Relaxation Studies. *Inorganic Chemistry* **2001**, *40* (16), 3986-3991; (b) Trzop, E.; Buron-Le Cointe, M.; Cailleau, H.; Toupet, L.; Molnar, G.; Bousseksou, A.; Gaspar, A. B.; Real, J. A.; Collet, E., Structural investigation of the photoinduced spin conversion in the dinuclear compound $[[\text{Fe}(\text{bt})(\text{NCS})_2]_2(\text{bpym})]$: toward controlled multi-stepped molecular switches. *Journal of Applied Crystallography* **2007**, *40* (1), 158-164; (c) Kulmaczewski, R.; Halcrow, M. A., Structures and spin states of crystalline $[\text{Fe}(\text{NCS})_2\text{L}_2]$ and $[\text{FeL}_3]^{2+}$ complexes (L = an annelated 1,10-phenanthroline derivative). *CrystEngComm* **2016**, *18* (14), 2570-2578; (d) Galet, A.; Gaspar, A. B.; Muñoz, M. C.; Levchenko, G.; Real, J. A., Pressure Effect and Crystal Structure Reinvestigations on the Spin Crossover System: $[\text{Fe}(\text{bt})_2(\text{NCS})_2]$ (bt = 2,2'-Bithiazoline) Polymorphs A and B. *Inorganic Chemistry* **2006**, *45* (24), 9670-9679.
26. Figg, D. C.; Herber, R. H., Spin crossover and light-induced excited-spin-state trapping in bis(thiocyanato)bis(2,2'-bi-2-thiazoline)iron(II) and bis(selenocyanato)bis(2,2'-bi-2-thiazoline)iron(II). *Inorganic Chemistry* **1990**, *29* (11), 2170-2173.
27. Shigeru, T.; Tomohiro, S.; Katsuya, S.; Katsuya, M.; Masato, K.; Hiroshi, N., Syntheses of New Pyrimidine Based Compounds and Their Peculiar Emission Behaviors. *Chemistry Letters* **2002**, *31* (6), 628-629.
28. (a) Ishida, T.; Kawakami, T.; Mitsubori, S.-i.; Nogami, T.; Yamaguchi, K.; Iwamura, H., Antiferromagnetic coupling of transition metal spins across pyrimidine and pyrazine bridges in dinuclear manganese(ii), cobalt(ii), nickel(ii) and copper(ii) 1,1,1,5,5,5-hexafluoropentane-2,4-dionate complexes. *Journal of the Chemical Society, Dalton Transactions* **2002**, (16), 3177-3186; (b) Hearn, N. G. R.; Korčok, J. L.; Paquette, M. M.; Preuss, K. E., Dinuclear Cobalt Bis(dioxolene) Complex Exhibiting Two Sequential Thermally Induced Valence Tautomeric Transitions. *Inorganic Chemistry* **2006**, *45* (22), 8817-8819.
29. Kershaw Cook, L. J.; Kulmaczewski, R.; Mohammed, R.; Dudley, S.; Barrett, S. A.; Little, M. A.; Deeth, R. J.; Halcrow, M. A., A unified treatment of the relationship between ligand substituents and spin state in a family of iron(II) complexes. *Angewandte Chemie* **2016**, *128* (13), 4399-4403.

Chapter 5 – Isomeric Bis (Triazolyl) Pyridine Ligands and their Iron Complexes

5.1 Introduction

As discussed in Chapter 2, the 1-bpp scaffold was modified by increasing the nitrogen content in the six-membered ring. This strategy yielded the novel $[\text{Fe}(\text{bpt})_2]^{2+}$ family of complexes with unexpected magnetic properties. The magnetic behaviour was not suited to our purposes, hence we proposed an alternative modification where the number and position of the nitrogen atoms were modified in the five-membered rings of the backbone.

5.1.1 Examples of bis-(azolyl) pyridine ligands in the literature

Diverse tridentate ligand analogues to 1-bpp family containing different azoles than pyrazol-1-yl have been reported in the past. For example, iron(II) salts of 2,6-di(pyrazol-3-yl)pyridine (3-bpp, Figure 5.1a) and its alkylated versions were widely studied¹. Other ligands such as 2,6-di(imidazol-2-yl)pyridine (2-bip, Figure 5.1b)^{2,3} or 2,6-di(1,2,4-triazol-5-yl)pyridine (5-btp, Figure 5.1c) formed iron(II) complexes that were also SCO active⁴.

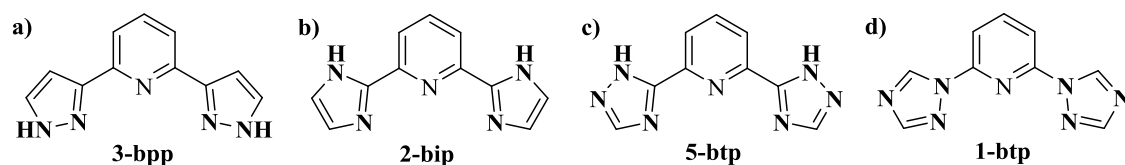


Figure 5.1: Some bis azolyl pyridine ligands found in the literature.

Contrary to a, b or c; 2,6-di(1,2,4-triazol-1-yl)pyridine (1-btp, Figure 5.1d) did not form the typical mononuclear complex ($[\text{ML}_2]^{x+}$) of this type of tridentate ligands. Several transition metals were coordinated linearly with 1-btp through $\text{N}_4[\text{triazolyl}]^{5,6,7}$, (Figure 5.2) instead of the expected geometry through the $\text{N}[\text{pyridine}]$ and the two $\text{N}_2[\text{triazolyl}]$.

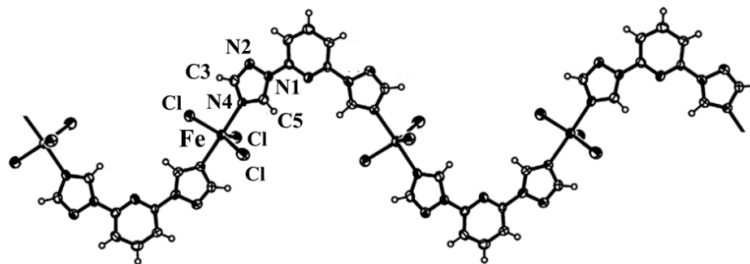


Figure 5.2: Coordination polymer of 1-btp with FeCl_3 . Picture adapted from Youm et al⁸.

Some ligands containing other heteroatoms than nitrogen in the azole moiety of the 2,6-pyridine positions such as pybox and its derivatives also produced SCO iron(II) salts^{9,10}.

5.1.2 Bis 1,2,3-triazolyl pyridine ligands (bTp)

The two tridentate isomers of 2,6-di(1,2,4-triazolyl)-pyridine ligands (btp) were reported previously (Figure 5.1 c and d). On the other hand, the 2,6-di(1,2,3-triazol-1-yl)-pyridine isomers (30) and (31) were novel (Figure 5.3). In order to distinguish between them; 1,2,4-triazolyl-pyridine based ligands are abbreviated as “btp” while 1,2,3-triazolyl-pyridine are “bTp”.



Figure 5.3: Scheme of novel ligands proposed as potential family of iron(II) SCO complexes.

In contrast with (30) and (31), the coordination chemistry of several alkylated derivatives of the isomer (32) (Figure 5.4) was widely studied¹¹. There are some examples of iron(II) complexes derived from this scaffold in the literature whose magnetic properties were detailed¹². However the homoleptic iron(II) complex of ligand (32) itself are unknown.

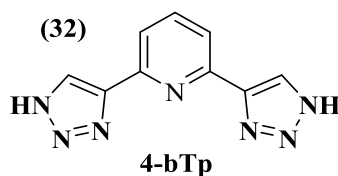


Figure 5.4: Scheme of the ligand (32) commercially available, 2,6-di(1,2,3-triazol-4-yl)pyridine.

D. Davies synthesized $[\text{Fe}(4\text{-bTp})_2](\text{BF}_4)_2$; [32]B and $[\text{Fe}(4\text{-bTp})_2](\text{ClO}_4)_2$; [32]C during his MChem project under the candidate’s supervision. The complexes were both LS in the solid and liquid states up to 350 K. Nevertheless, methylation of ligand (32) in the N1 or N2 positions has not yet been reported.

5.2 Results and discussion

5.2.1 Synthesis of 2,6-di(1,2,3-triazol-1-yl)pyridine isomers (30), (31) and (33).

The novel ligand 1-bTp (30) was first synthesized by J. Woodworth as an undergraduate summer project and it was reproduced here by a similar procedure where the 2-bTp (31) and 1T-2Tp (33) ligands were also isolated (Figure 5.5).

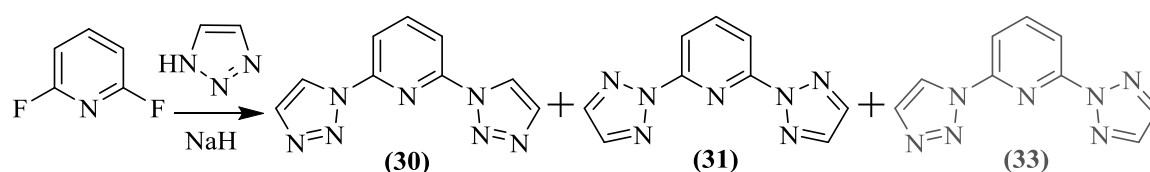


Figure 5.5: Synthetic procedure for 1-bTp and 2-bTp ligands (30) and (31). Ligand (33) is de-emphasised because it was not obtained pure in a reproducible way.

The reaction is a nucleophilic aromatic substitution similar to the previous reactions. Ligand (**33**) was very difficult to isolate in a pure form because it had almost the same retardation factor as (**31**) in every elution attempted with different solvent combinations as the mobile phase.

5.2.2 Metal complexes of 2,6-di(1,2,3-triazol-1-yl)pyridine M[**30**]X

Various metal-ligand combinations were prepared from the novel ligand (**30**). When it reacted with iron(II) tetrafluoroborate in hot nitromethane the colour of the solution turned red immediately and gradually converted into a yellowish suspension. Yellow single crystals were obtained only once when the solution slowly cooled in an NMR tube (Figure 5.6).

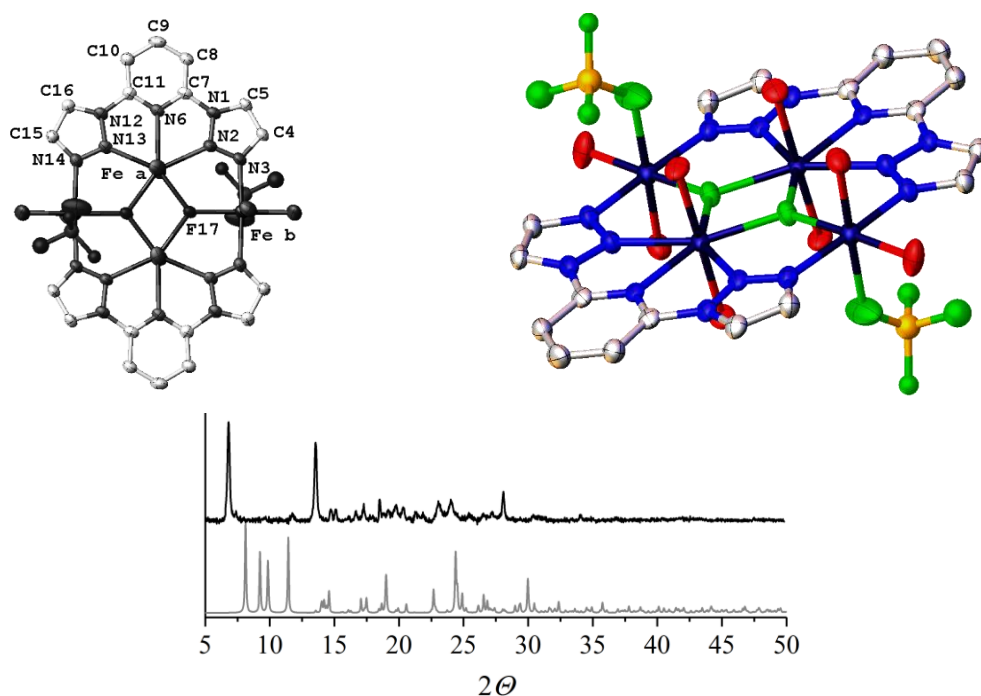


Figure 5.6: Crystal structure of [30]B and powder pattern. Non-binding and disordered counter-anions, solvent molecules and hydrogen atoms of the structure were removed for clarity. The colour assignment in the plot is black for the experimental and grey for the simulated XRD.

Structure [**30**]B with the formula $C_{18}H_{32}N_{14}O_9Fe_4B_6F_{26}$, crystallized in the monoclinic $P2_1/n$ space group. It was a four iron-two fluorine cluster assembled through two trigonal planar F bridging. The cluster was coordinated by two coplanar ligand (**30**) in an unexpected pentadentate fashion. The NNN bpp-like terimine coordination site (N2, N6, N13) bound Fe a, while N3 and N14 coordinated linearly two Fe b atoms. Fe a presented an hepta-coordination geometry with NNN bpp-like donor, two water molecules and two F⁻ bridges. In contrast, the Fe b octahedron was completed by two N3 linear, two water molecules, F⁻ and BF₄⁻ acting as ligand. Four extra BF₄⁻ molecules compensate the charge balance of the molecule. A cluster with similar geometry but with oxo bridges was reported¹³ and the trigonal geometry of fluorine was observed in a pentanuclear iron(II) and (III) complex¹⁴.

Chapter 5

It was believed that the crystal structure [30]B corresponds to an unstable intermediate species according to the discrepancy with the powder XRD pattern in Figure 5.6. Experimental powder patterns of bulk samples from different solvents were consistent with that result. This theory could also explain why the experimental microanalysis were inconsistent with that composition.

The SQUID measurement of the powder sample is noisy because there was a fault with the temperature controller of the instrument but it was enough to see some gradual decrease in χT which could reflect antiferromagnetic coupling between iron(III) centres. The experiment was not recollected because the compound was not identified or characterized (Figure 5.7).

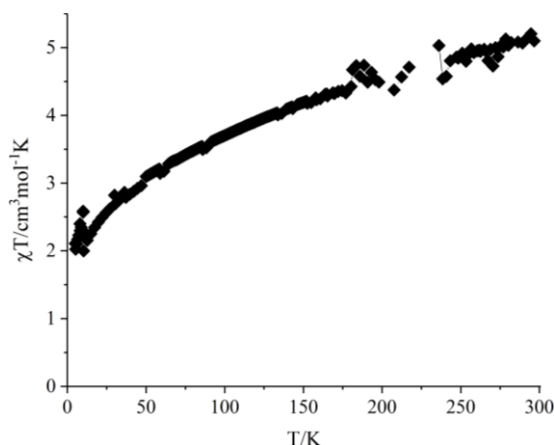


Figure 5.7: SQUID curve of the unknown [30]B powder.

On the other hand, when (30) reacted with iron(II) perchlorate in acetonitrile the solution colour barely changed and transparent crystals were grown by ether diffusion (Figure 5.8).

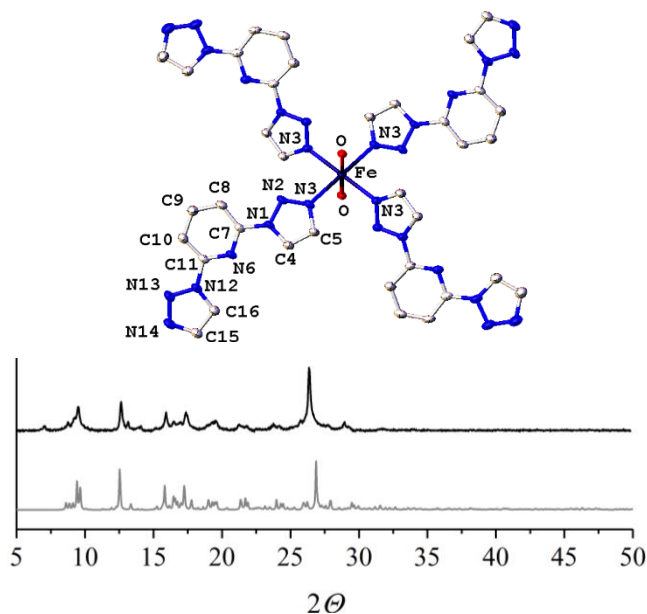


Figure 5.8: Crystal structure of [30]C in the triclinic $P\bar{1}$ space group, and powder pattern. Counter-anions, solvent molecules and hydrogen atoms of the structure were removed for clarity. The colour assignment in the plot is black for the experimental and grey for the simulated XRD.

Although the reaction was first performed with a 1:2 metal-ligand ratio, a mononuclear complex composed by four (**30**) ligands coordinating linearly to the central ion through N3[triazoly] was obtained. The octahedral geometry was completed by two water molecules. The behaviour of ligand (**30**) was similar to the one observed for the 1-btp ligand (Figure 5.1d and Figure 5.2). The complex [**30**]C was expected to be HS because water molecules induce a weaker ligand field than N-donor imines. That was confirmed by SQUID data (Figure 5.9).

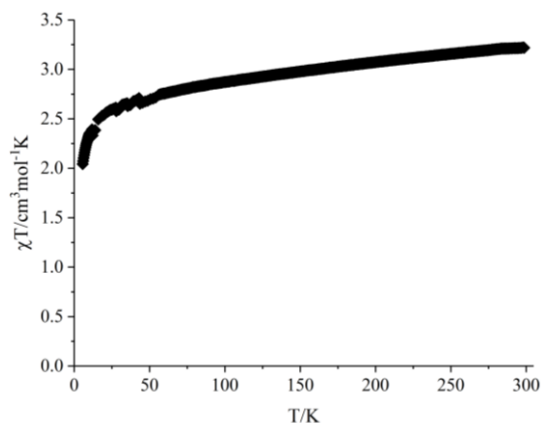


Figure 5.9: SQUID curve of [**30**]C.

It was suggested that replacing the coordination sites occupied by water in [**30**]C (Figure 5.8), with thiocyanate could produce a novel SCO iron(II) complex¹⁵. The addition of two equivalents of thiocyanate to a complex [**30**]C solution resulted in a mixture of dark amorphous powder, thin transparent needles and few small yellow crystals (Figure 5.10).

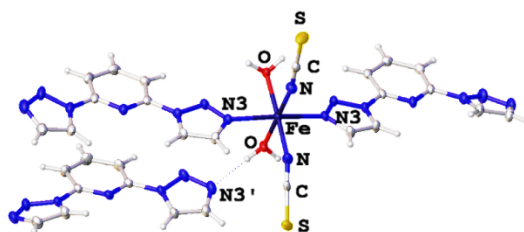


Figure 5.10: Crystal structure of [**30**]NCS, monoclinic *Pc* space group.

The complex [**30**]NCS showed two (**30**) linearly coordinating ligands through N3[triazoly], two thiocyanate molecules and two water molecules. This complex co-crystallized with a free ligand in the lattice. In view of the results, different approach where the Fe(NCS)₂ salt was prepared in-situ and added to a solution of ligand (**30**) was attempted. Surprisingly the same results were observed either with 1:1 or 1:4 metal-ligand ratios. The compound [**30**]NCS was not isolated in pure form from these mixtures.

Ligand (**30**) (1-bTp), which was proposed as a novel tridentate ligand analogous to bpp, coordinated iron(II) through N3 and N14 in both the [**30**]B and [**30**]C structures. The interesting penta-coordination of [**30**]B though N2, N3, N6, N13 and N14 (Figure 5.6) provoked curiosity and (**30**) was also reacted with other metals whose geometries are not usually octahedral; AgClO₄ and Cu(BF₄)₂.

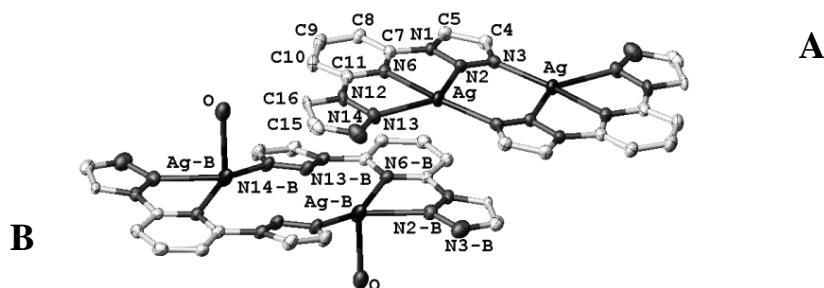


Figure 5.11: Crystal structure of $[30]AgC$ in the triclinic $P\bar{1}$ space group. Counter-anions and hydrogen atoms of the structure were removed for clarity.

The crystallizations from silver perchlorate yielded almost homogenous samples of thin needles which were not suitable for single crystal analysis, however some large transparent crystals were occasionally found which correspond to $[30]AgC$ in Figure 5.11. This complex also presented the two coplanar ligands and N3-14 participated in the coordination of silver(I). Two type of clusters were co-crystallized in the lattice of $[30]AgC$. The cluster A was a plane of two (30) molecules acting as “tetradentate” ligand and two silver(I) whereas the cluster B was similar but included one extra coordinating water to each silver(I).

In contrast, the copper structure $[30]Cu$ grew into a two-dimensional coordination polymer (Figure 5.12).

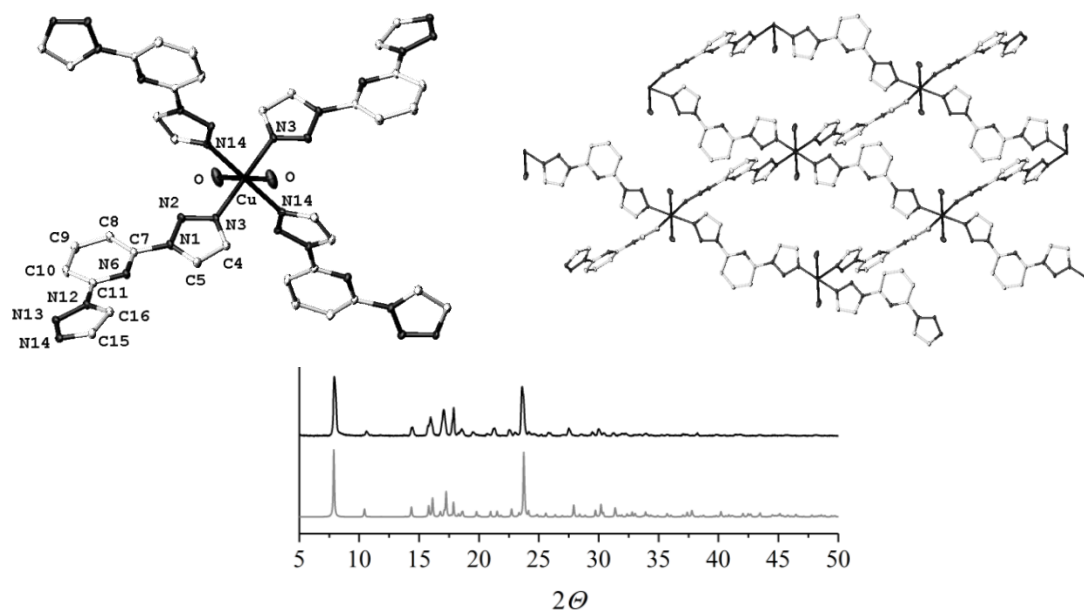


Figure 5.12: Crystal structure of $[30]Cu$ in the monoclinic $C2/c$ space group and powder pattern. Counter-anions, solvent molecules and hydrogen atoms of the structure were removed for clarity. The colour assignment in the plot is black for the experimental and grey for the simulated XRD.

This structure is similar to $[30]C$ however in this case the initial stoichiometry 1:2 was maintained in the coordination polymer ($[30]Cu$, Figure 5.12).

In summary, none of the complexes studied from ligand (30) displayed the tridentate coordination expected through the nitrogen 2, 6 and 13. All of them contain water molecules in the coordination sphere of the metal.

5.2.3 Iron(II) complex of 2,6-bis(1,2,3-triazol-2-yl)-pyridine (31)

The 2-bTp ligand coordinated iron (II) perchlorate as expected (Figure 5.13).

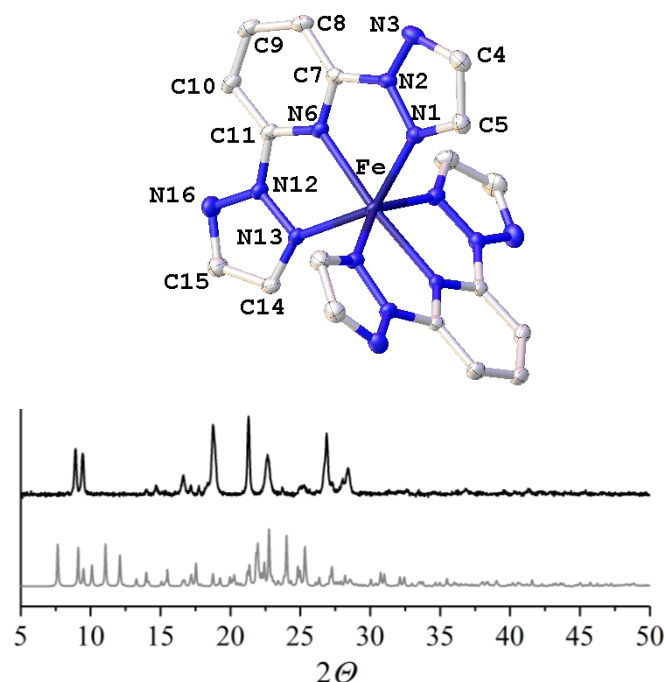


Figure 5.13: Crystal structure of [31]C in the triclinic $P\bar{1}$ space group and powder pattern. Counter-anions, solvent molecules and hydrogen atoms of the structure were removed for clarity. The colour assignment in the plot is black for the experimental and grey for the simulated XRD.

The experimental powder XRD (Figure 5.13) and the CHN analysis did not fit the crystal structure of [31]C. This could be explained by the two nitromethane molecules found in asymmetric unit of the crystal lattice. The solvent could be replaced by water over time or upon thermal cycling. The crystallographic parameters at 120 K were typical of an iron(II) HS complex, with Fe-N bond lengths from 2.1-2.2 Å and V_{Oh} of 12 Å³ (Table 5-1).

It was confirmed by SQUID that [31]C was high spin and does not undergo SCO in solid state, or in solution by Evans method NMR (Figure 5.14).

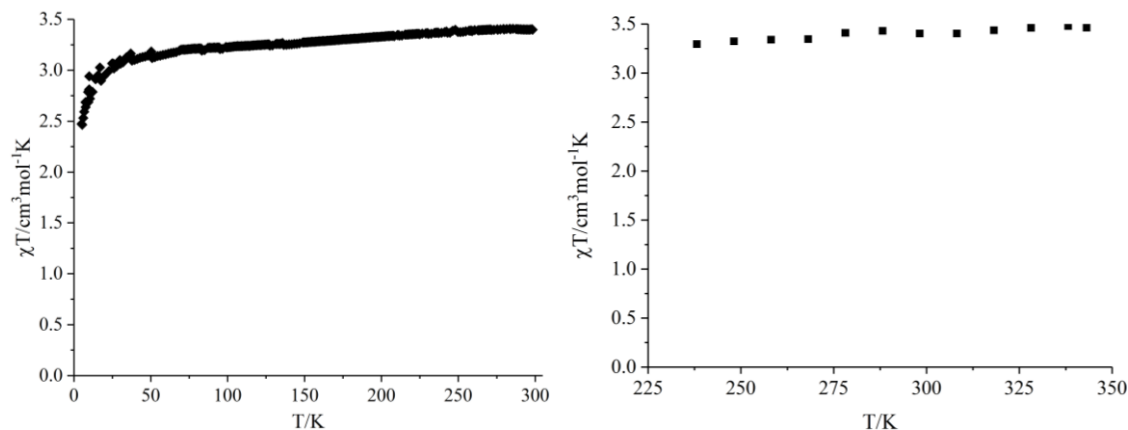


Figure 5.14: SQUID curve (left) and Evans method in solution (right), data points were taken every 10 K in acetonitrile solution of [31]C.

	[31]C
Fe–N[pyridinyl]	2.133(2), 2.135(2)
Fe–N[triazolyl]	2.194(2), 2.204(2)
V_{Oh}	12.470(8)
Σ	154.1(3)
Θ	508.6(7)
ϕ	170.33(8)
θ	88.31(2)

Table 5-1: Crystallographic parameters determined directly from the crystal structure by using Olex2¹⁶.

5.2.4 DFT calculations

DFT is a powerful tool widely used to explain or predict several experimental behaviour. A recent study on free ligands¹⁷ encouraged our DFT calculations of several similar ligands trying to find a trend which explains why the linear coordination was favoured for ligand **1-bTp** (**30**) instead of terdentate-like (Figure 5.15). The labels for N[pyridyl], N[chelating] and N[linear] are also shown in Figure 5.15.

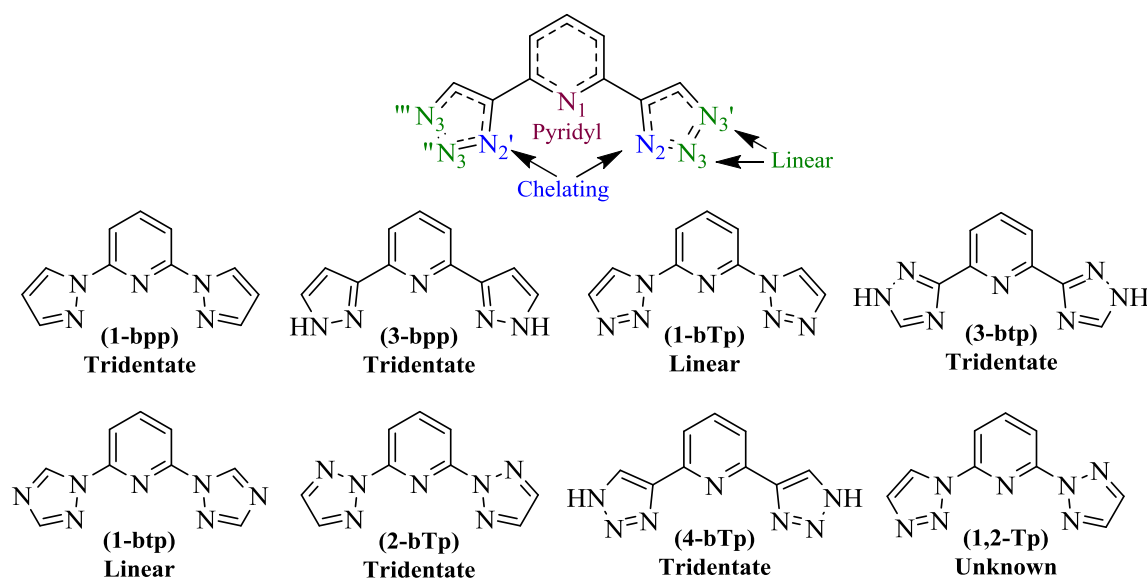


Figure 5.15: Scheme of all the ligands discussed here. defining N1 [pyridyl], N2 [chelating] and the two possible N3 [linear] coordinating imines.

Every isomer for the above ligands was calculated in SPARTAN'18 using the B86PW91 functional and def2-SVP basis set (Figure 5.15).

Chapter 5

Calculations on ligand **1-bTp**, (**30**) were performed in order to understand why it behaves similarly to **1-btp** (Figure 5.1) coordinating through N₃ rather than acting as terdentate through N₁, N₂, N₂' as was initially expected (Figure 5.16).

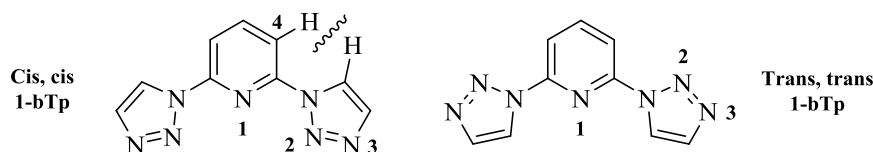


Figure 5.16: Scheme of ligand (**30**) including labels of the imines of interest. The steric hindrance between the hydrogen atoms for this kind of ligands with position C₄ of the pyridine was highlighted.

Ligand (**30**) can exist in three conformers due to the free rotation of triazolyl-pyridine single bonds. The calculations were performed in all of them. The lowest energy form was in agreement with the crystal structure (Table 5-2).



Cis, cis	Cis, trans	Trans, trans
-730.070057 hartree	-730.084399 hartree	-730.092855 hartree

Table 5-2: Crystal structure of ligand (**30**), collected by J. Woodworth. Total energies calculated for every isomer. Trans, trans (TT) conformer was highlighted in bold as it was the energetically more stable.

The DFT calculations were performed because it was believed that the electron density would be concentrated in N₃ rather than N₁ or N₂. Calculated values of Natural (NPA) and Mulliken charges of the N₁, N₂ and N₃ obtained directly from the equilibrium geometry using SPARTAN 18' were displayed in (Table 5-3).

1-bTp	N ₃ (linear)			N ₂ (chelating)			N ₁ (pyridinyl)			
Cis, cis	-0.247	-0.122		-0.026	-0.004		-0.439	-0.005		
Cis, trans	-0.249	-0.248	-0.123	-0.125	-0.042	-0.081	-0.022	-0.049	-0.481	-0.064
Trans, trans	-0.247	-0.122		-0.077	-0.046		-0.519	-0.122		
CHARGES	Natural	Mulliken		Natural	Mulliken		Natural	Mulliken		

Table 5-3: Values of natural and Mulliken charges for the three imine N atoms of ligand (**30**). The highest charge of the three N-donor was highlighted in bold for every conformer.

Chapter 5

The formulism of Mulliken charge and NPA charge are essentially identical, the key difference is that the Mulliken charge is calculated under original basis functions, while NPA charge is derived based on natural atomic orbitals. Although N_1 had the highest natural charge, N_2 had notably lower values compared to N_3 (Linear). The situation was different for mulliken charges, where the most negative charges were found for N_3 .

Images of the Highest Occupied Molecular Orbital (HOMO) and its subsequent series of near frontier orbitals were computed using SPARTAN 18 in order to identify the lone pairs of the ligand (Figure 5.17).

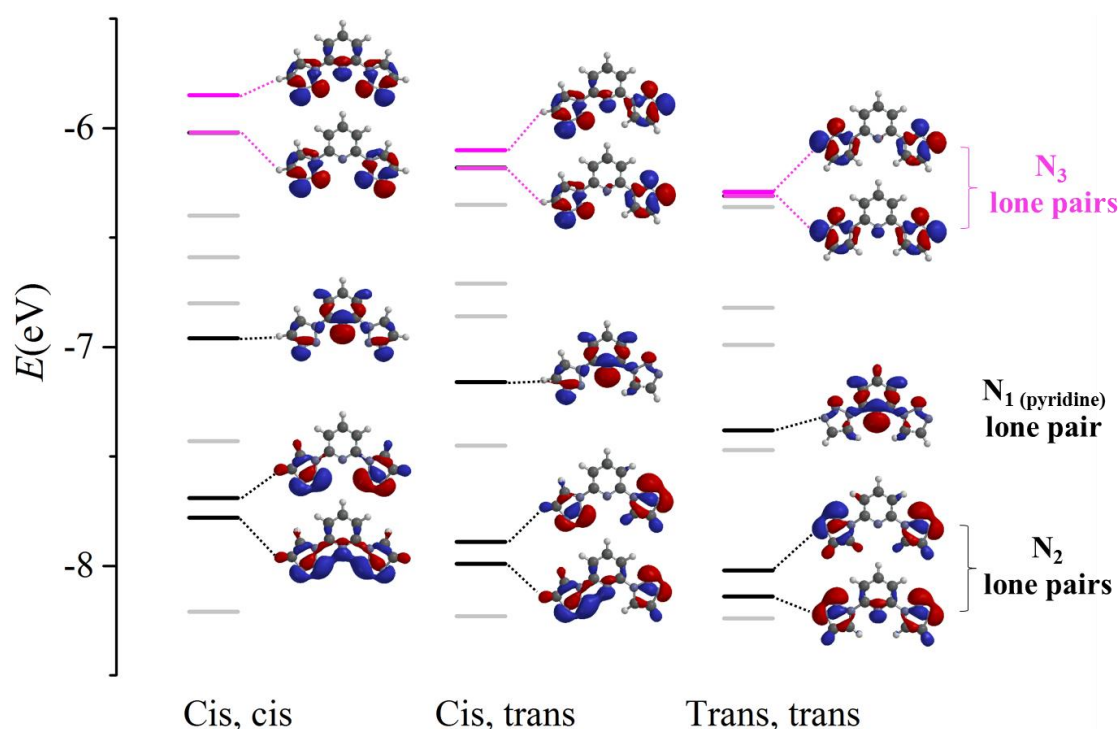


Figure 5.17: Images of energy levels calculated for the three conformers. The N atom lone pair orbitals are highlighted in black, and π -orbitals are de-emphasised for clarity. The most energetic lone pair was highlighted in pink.

The most energetic lone pair should be the more reactive and the most energetic one contained bigger orbital lobes around N_3 (Figure 5.17). The tridentate coordination site also contained some electronic occupancy in the HOMO of the cis isomers which could explain the penta-coordinated **[30]B** structure, however it is clear from the figure that lobes around N_3 are larger.

Calculations of the **1-btp** ligand which behaved analogously to **1-bTp (30)**^{5,6,7}, were also performed to compare to the trends found and to draw a conclusion (Figure 5.18).

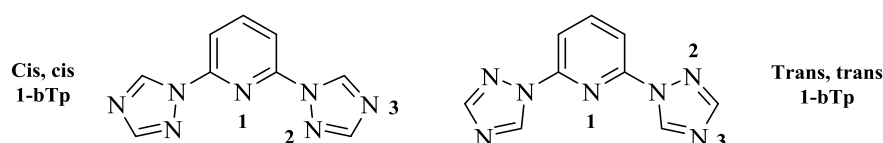


Figure 5.18: Scheme of ligand **1-btp** including labels of the imines of interest.

Chapter 5

Again the calculations were performed for the three conformers, and the most stable was Trans, trans (Table 5-4).

Cis, cis	Cis, trans	Trans, trans
-730.123719 hartree	-730.136225 hartree	-730.144705 hartree

Table 5-4: Total energies calculated for every isomer. Trans, trans (TT) conformer was highlighted in bold as it was the energetically more stable.

The values of Natural and Mulliken charges calculated for N₁, N₂ and N₃ are displayed in Table 5-5;

1-btp	N ₃ (linear)			N ₂ (chelating)			N ₁ (pyridinyl)			
Cis, cis	-0.513	-0.164		-0.278	-0.054		-0.446	-0.006		
Cis, trans	-0.513	-0.517	-0.163	-0.166	-0.291	-0.329	-0.068	-0.098	-0.484	-0.067
Trans, trans	-0.516	-0.166		-0.326	-0.095		-0.520	-0.126		
CHARGES	Natural	Mulliken		Natural	Mulliken		Natural	Mulliken		

Table 5-5: Values of natural and Mulliken charges for the three imine N atoms of 1-btp. The higher charges were highlighted in bold.

The same trend as for **1-bTp** was observed in the calculation of **1-bpt**. However, in this case similar or even higher values of natural charge were observed for N₃ than in N₁. Images of the KS energy levels were also in agreement with the trend observed above (Figure 5.19).

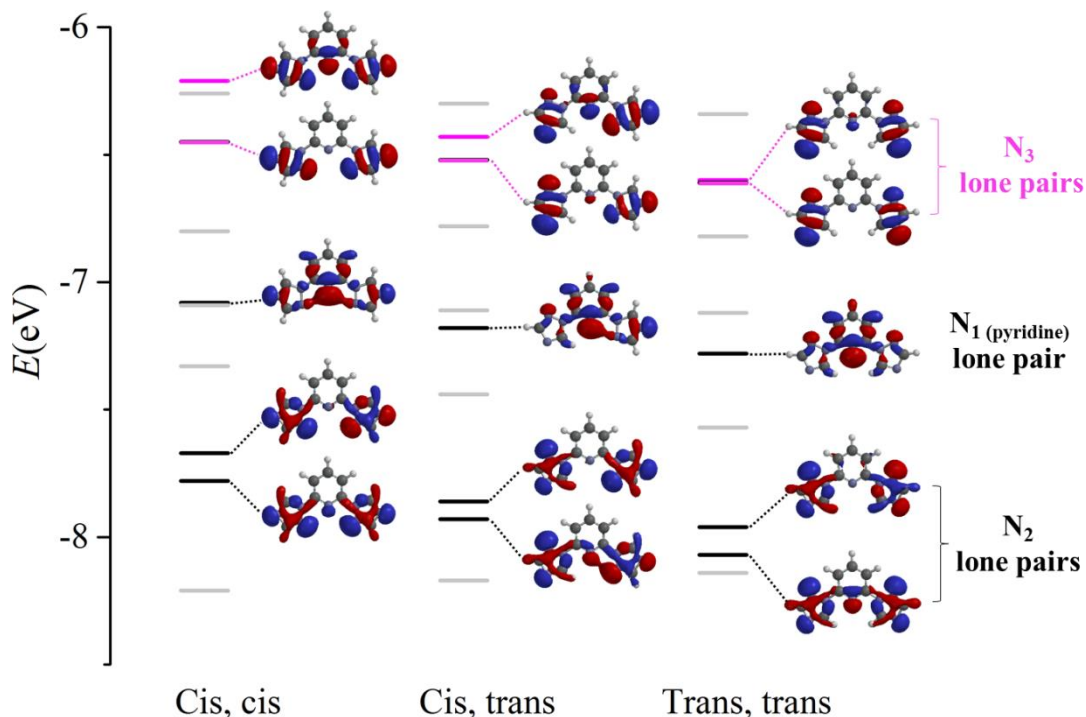


Figure 5.19: Images of energy levels calculated for the three conformers of 1-btp. The N atom lone pair orbitals are highlighted in black, and π -orbitals are de-emphasised for clarity. The most energetic lone pair was highlighted in pink.

Chapter 5

Since values of total energy (Table 5-2 and Table 5-4), charges (Table 5-3 and Table 5-5) and orbital shape (Figure 5.17 and Figure 5.19) of the CT isomer were intermediate between the CC and TT conformers they did not add to our knowledge of this system. Hence it was decided not to include them in the discussion of the following ligands despite having the calculations for all of them.

Completing the DFT study, several other ligands which bind in tridentate fashion were calculated in order to confirm the conclusions drawn, (Figure 5.20 and Figure 5.22).

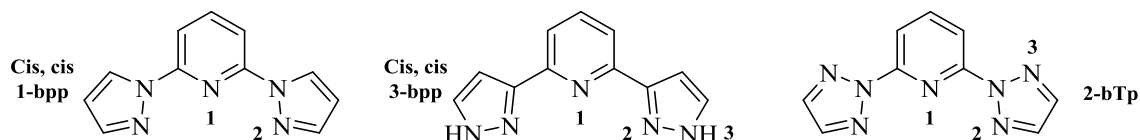


Figure 5.20: Scheme of tridentate ligands; 1-bpp, 3-bpp and 2-bTp calculated.

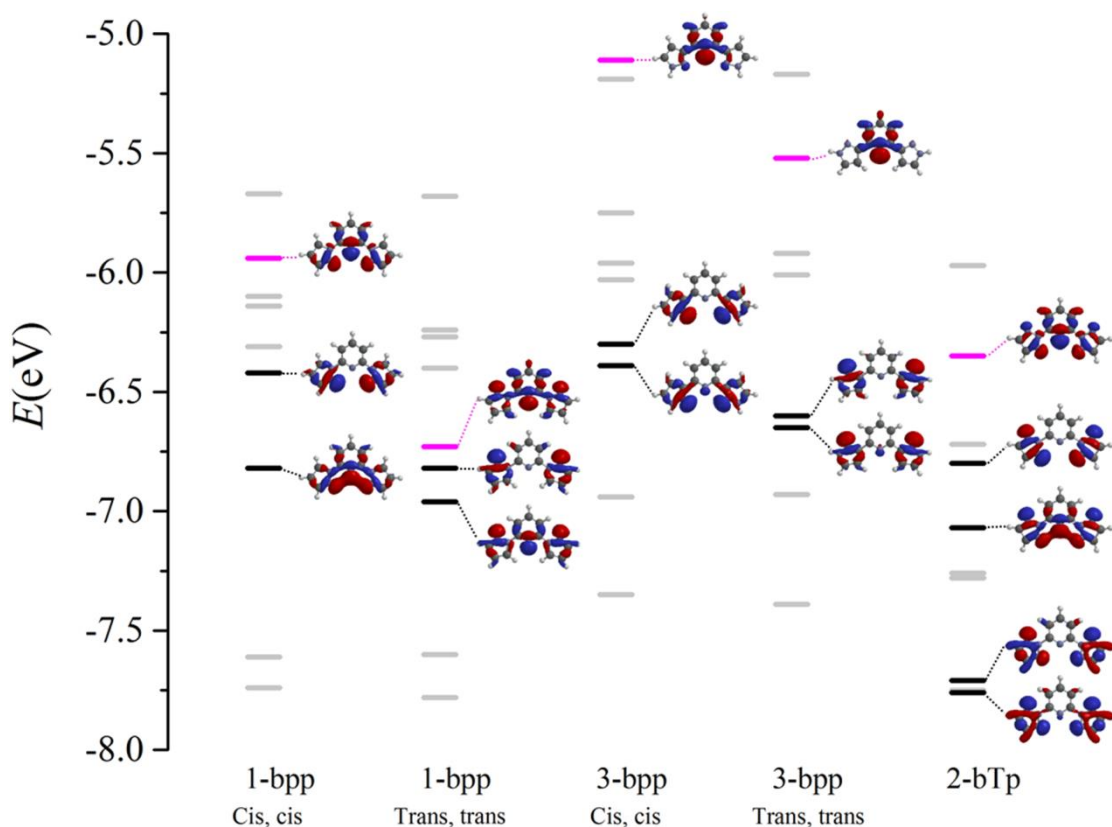


Figure 5.21: Images of energy levels calculated for the three tridentate ligands. The N atom lone pair orbitals are highlighted in black, and π -orbitals are de-emphasised for clarity. The most energetic lone pair was highlighted in pink.

In those examples the highest energy lone pair corresponded to the bonding orbital lobes of the tridentate coordinating site (imines N_1 , N_2 , N_2') for conformer cis, cis or N-donor lobe of pyridine N_1 when trans, trans conformation.

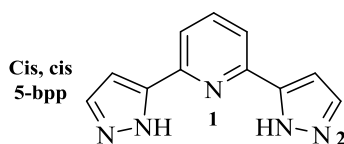
Chapter 5

The values of the charges for cis, cis conformations are given in Table 5-6;

	N ₁ (pyridinyl)		N ₂ (chelating)		N ₃ (linear)	
1-bpp	-0.450	<i>-0.008</i>	-0.261	<i>-0.062</i>	-	-
3-bpp	-0.513	<i>-0.051</i>	-0.253	<i>-0.100</i>	-	-
2-bTp	-0.453	<i>-0.022</i>	-0.240	<i>-0.039</i>	-0.291	<i>-0.076</i>
CHARGES	Natural	Mulliken	Natural	Mulliken	Natural	Mulliken

Table 5-6: Values of natural and Mulliken charges for the three tridentate ligands. The higher charges were highlighted in bold.

Note that for **3-bpp**, in addition to the 3 conformers of simple bond rotation, there is another structural isomer regarding the position of the labile H-N₃. In fact, the most stable isomer corresponds to **5-bpp** (Table 5-7).



	3-bpp	3,5-bpp	5-bpp
Cis, cis (CC)	-698.058074	-698.071334	-698.077156
Cis, trans (CT)	-698.066881	-698.063848	-698.072691
Trans, cis (TC)	=	-698.076517	=
Trans, trans (TT)	-698.073624	-698.070698	-698.066763

Table 5-7: Scheme of 5-bpp and crystal structure reported previously¹⁸. Total energies calculated for every isomer. Trans, trans (TT) conformer was highlighted in bold as it was the energetically more stable of 3-bpp.

The calculated orbitals and charges of **5-bpp** did not follow the trend discussed above because it did not contain the imine in the chelating position (N₂). Since the interconversion from **5-bpp** to **3-bpp** must take place when coordinating a transition metal, in order to understand the results, it was assumed that the difference of the total energy between the isomers was negligible compared to the complexation stability. Therefore those isomers were not considered.

It was difficult to imagine that any of the 5 previous ligands (**1-bpp**, **3-bpp** or **2-bTp**) could act as linear coordinating ligand. Firstly, **1-bpp** does not have any other N-donor imine competing with the N₁, N₂ and N₂' terimine. **3-bpp** has a hydrogen atom in the five-membered aromatic ring which makes the extra nitrogen (N₃) a secondary amine. Finally, N₃ of **2-bTp** has the steric hindrance of C₄-H avoiding a possible metal coordination.

Chapter 5

The same could not be said of the following two ligands; **3-btp** and **4-bTp**; both act as tridentate while having the possibility of acting as linear (N_3 , Figure 5.22). Why did they not act as a linear coordinating ligand?

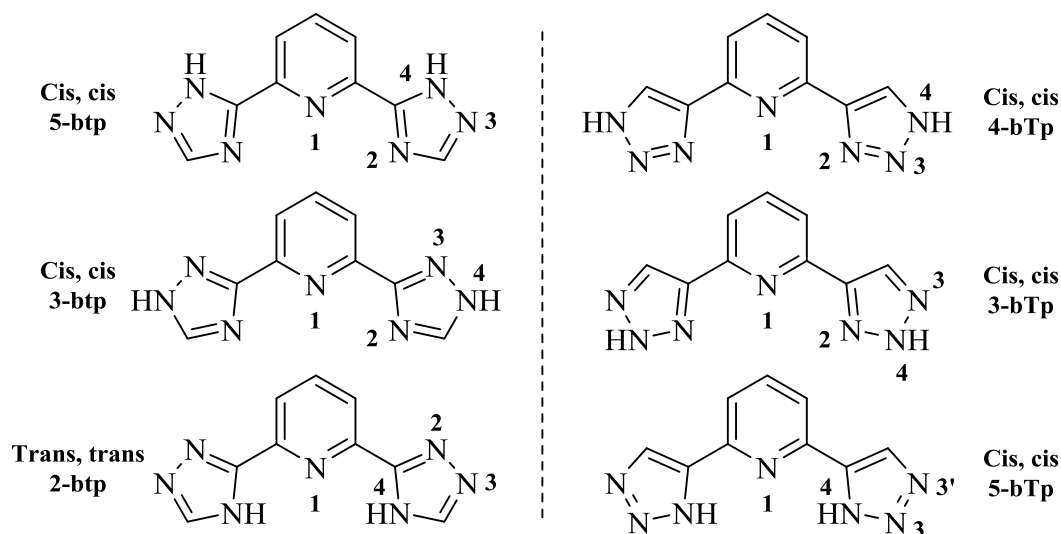


Figure 5.22: Scheme of ligands **3-btp** and **4-bTp** including the structural isomers.

Both ligands **3-btp** and **4-bTp**, (**31**) could exist in 21 different isomers and conformers depending of the position of the N-H and the rotation of the triazolyl-pyridine bond. All of them were calculated (Table 5-8) but again the isomers containing hydrogen in the chelating position as for example **5-bTp** (Figure 5.22) were discarded, since they were outliers of the experiment as for **3-bpp**. The main isomers of every ligand were compared (Table 5-8 where the total energy of every isomer was displayed).

	4-bTp	3-bTp	5-bTp	3,4	4,5	3,5
CC	-730.086950	-730.105667	-730.105465	-730.096575	-730.100865	-730.108871
CT	-730.099920	-730.113278	-730.101404	-730.104249	-730.093112	-730.101849
TC	=	=	=	-730.107952	-730.107517	-730.113469
TT	-730.107312	-730.119271	-730.095793	-730.113555	-730.102772	-730.108079

	5-btp	3-btp	2-btp	23	25	35
CC	-730.137886	-730.144628	-730.112895	-730.142021	-730.125531	-730.142092
CT	-730.154553	-730.146283	-730.133255	-730.143811	-730.142941	-730.158073
TC	=	=	=	-730.158073	-730.144690	-730.143795
TT	-730.163975	-730.147806	-730.142096	-730.159063	-730.153176	-730.159063

Table 5-8: Total energies calculated for every structural isomer and its conformers. Apart from ligands containing hydrogen at the chelating nitrogen atom, the main isomers are highlighted in bold.

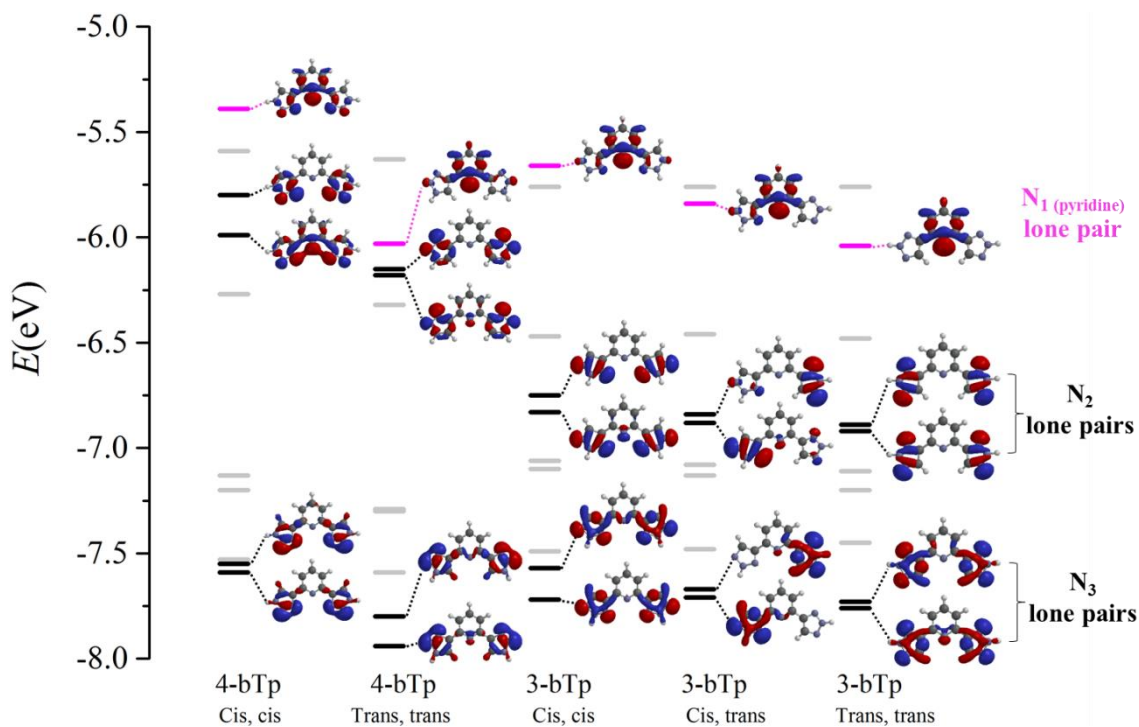


Figure 5.23: Images of energy levels calculated for the main conformers of 3- and 4-bTp. The N atom lone pair orbitals are highlighted in black, and π -orbitals are de-emphasised for clarity. The most energetic lone pair was highlighted in pink.

As demonstrated above for every table or figure, combination of structural isomers produced results in between the two (Figure 5.24).

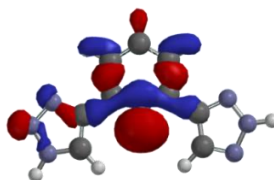


Figure 5.24: Example of asymmetric isomer 4,3-bTp TT whose HOMO orbital present similar lobes as shown for the 4-bTp and 3-bTp respectively.

Therefore only values of charges for the two main isomers in both conformations are reported (Table 5-9).

	N_1 (pyridinyl)		N_2 (chelating)		N_3 (linear)	
3-bTp (TT)	-0.477	<i>-0.103</i>	-0.277	<i>-0.111</i>	-0.277	<i>-0.088</i>
3-bTp (CC)	-0.432	<i>-0.054</i>	-0.235	<i>-0.077</i>	-0.279	<i>-0.086</i>
4-bTp (TT)	-0.490	<i>-0.113</i>	-0.266	<i>-0.145</i>	-0.066	<i>-0.043</i>
4-bTp (CC)	-0.422	<i>-0.040</i>	-0.222	<i>-0.111</i>	-0.064	<i>-0.042</i>
CHARGES	Natural	<i>Mulliken</i>	Natural	<i>Mulliken</i>	Natural	<i>Mulliken</i>

Table 5-9: Values of natural and Mulliken charges for the three imines of 3- and 4-bTp in both conformations. The higher energies were highlighted in bold.

Chapter 5

In general, higher charge values were observed in the terimine N_1 , N_2 and N_2' than for N_3 . As previously found for 1-bTp and 1-btp, N_1 has the highest natural charge. However, now N_2 [chelating] occupies the second position on average. The second difference between these compounds and 1-bTp/1btp is that the strongest Mulliken charges were for N_2 .

Images of the Highest Occupied Molecular Orbital (HOMO) and its subsequent series were also calculated for 2-, 3- and 5-btp and isomers (Figure 5.25).

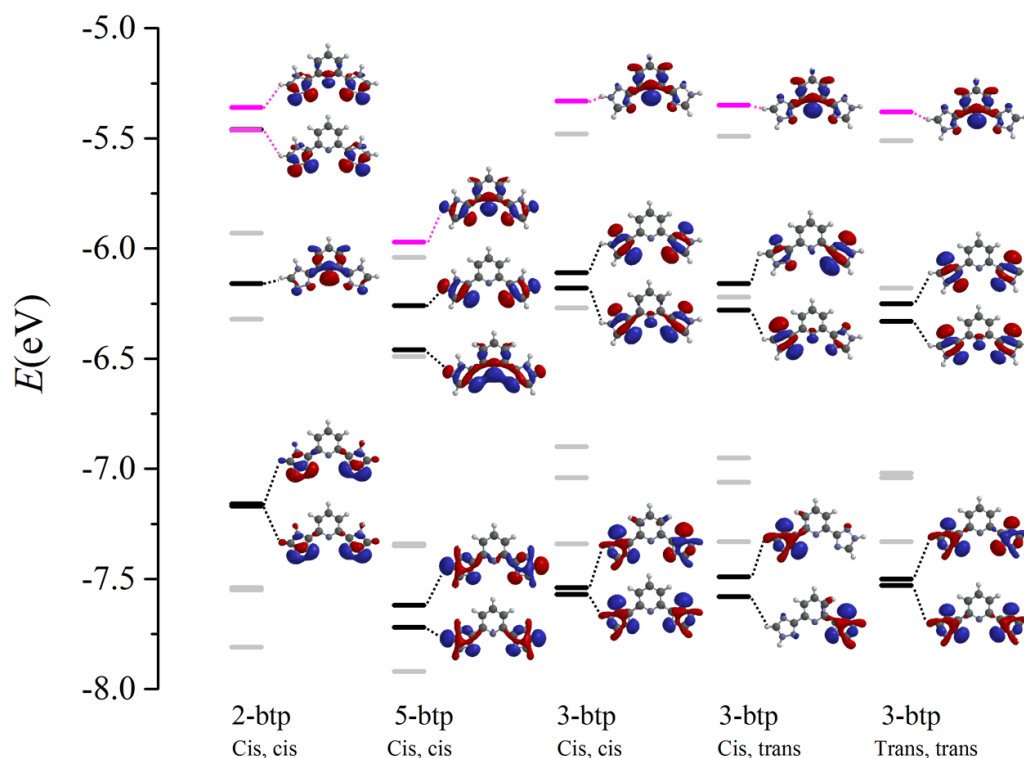


Figure 5.25: Images of energy levels calculated for the main conformers of 2, 3 and 5-btp ligand. The N atom lone pair orbitals are highlighted in black, and π -orbitals are de-emphasised for clarity. The most energetic lone pair was highlighted in pink.

In this case, 2- and 5-btp TT conformations were discarded because of the hydrogen at the chelating N position. As for the 4-bTp results, the highest energy lone pair was mainly the pyridine N_1 atom. However, for 2-btp CC the most energetic lone pair was N_2 followed by N_1 .

	N_1 (pyridinyl)		N_2 (chelating)		N_3 (linear)	
3-btp (CC)	-0.424	<i>-0.048</i>	-0.486	<i>-0.112</i>	-0.313	<i>-0.117</i>
3-btp (TT)	-0.432	<i>-0.062</i>	-0.530	<i>-0.154</i>	-0.269	<i>-0.077</i>
2-btp (CC)	-0.401	<i>-0.033</i>	-0.252	<i>-0.086</i>	-0.299	<i>-0.121</i>
5-btp (CC)	-0.403	<i>-0.035</i>	-0.481	<i>-0.120</i>	-0.304	<i>-0.105</i>
CHARGES	Natural	<i>Mulliken</i>	Natural	<i>Mulliken</i>	Natural	<i>Mulliken</i>

Table 5-10: Values of natural and Mulliken charges for the three imines of 2-, 3- and 5-btp. The higher energies were highlighted in bold.

Chapter 5

To gain more insight into these data, a new parameter which compares the charges of the linear imine (N_3) with the chelating N_2 donors was defined; ΔN_2-N_3 (Figure 5.26). This corresponds to the difference between the charges on N_2 and N_3 . The behaviour of the ligand could be rapidly recognized based on the positive or negative values of ΔN_2-N_3 .

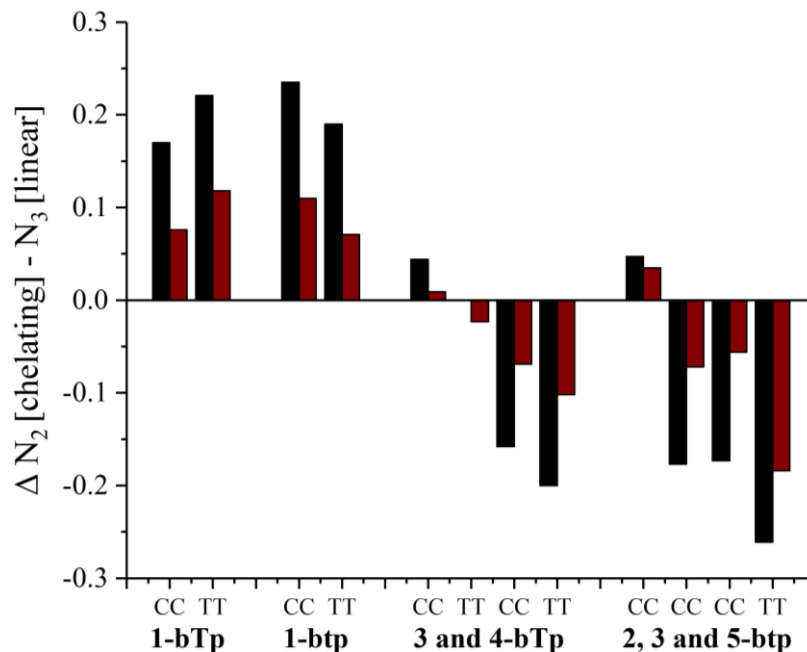


Figure 5.26: Parameter ΔN_2-N_3 plotted versus the main conformations of the four ligands discussed above which contained 5N-donor imines. The bars in black represents ΔN_2-N_3 Natural charges and the bars in dark red the Mulliken charges.

Knowing the trend discussed above, calculations of ligand (33) were also performed for both conformers (Figure 5.27).

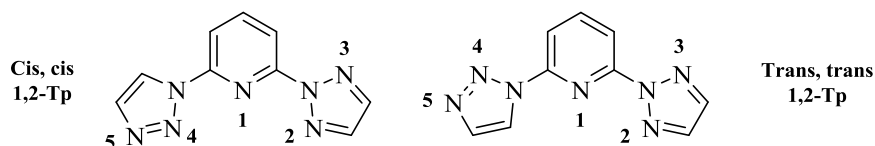


Figure 5.27: Scheme of ligand 1,2-Tp (33) including labels of the imines of interest.

The values of Natural and Mulliken charges of the N_1 , N_2 , N_4 and N_5 calculated are displayed in Table 5-11;

1,2-Tp (32)	N_5 (linear)		N_4 (chelating A)		N_2 (chelating B)	
Cis	-0.252	-0.125	-0.031	<i>-0.010</i>	-0.236	<i>-0.034</i>
Trans	-0.251	-0.127	-0.081	<i>-0.050</i>	-0.251	<i>-0.051</i>
CHARGES	Natural	Mulliken	Natural	Mulliken	Natural	Mulliken

Table 5-11: Values of natural and Mulliken charges for 1,2-Tp. The higher energies were highlighted in bold.

Chapter 5

When comparing natural charges of the nitrogen atoms we can see that the pyridine N₁ (not listed in Table 5-11) had values of -0.446 and -0.488 natural charges and -0.013 and -0.072 Mulliken charges for Cis and Trans conformations respectively. This has more natural charge than N₅, which in turn has higher natural charges than N₄ and N₂. In contrast, as for **1-bTp** and **1-btp** the most negative Mulliken charges were found in N₅.

The most energetic lone pair corresponds to the HOMO, and presents the largest lobes around N₅ (linear) (Figure 5.28).

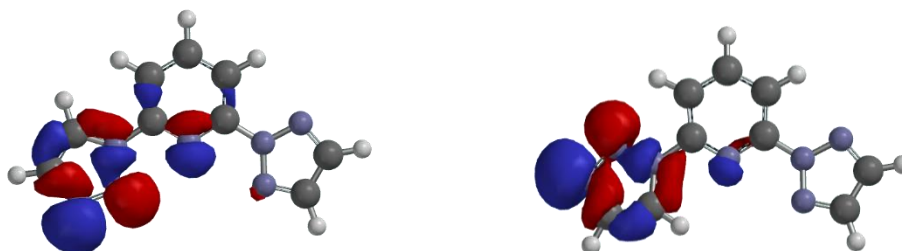


Figure 5.28: HOMO KS orbitals computed for both conformers of (33).

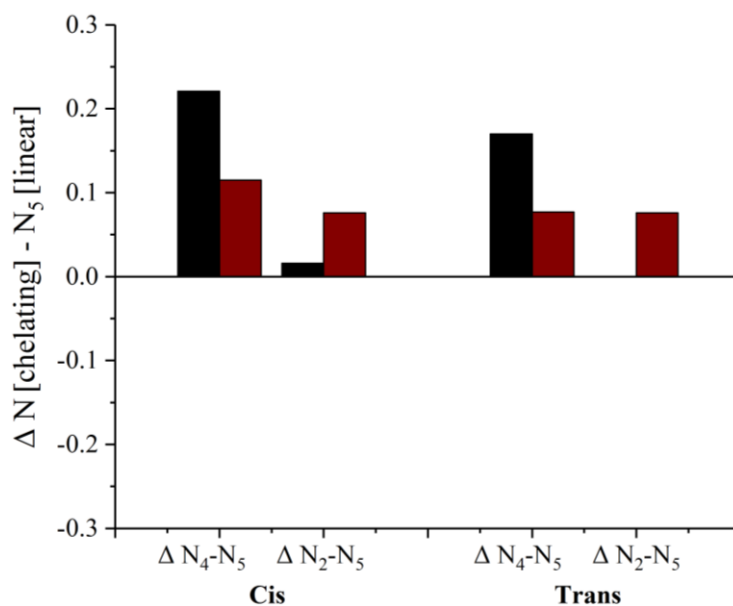


Figure 5.29: Parameters ΔN_{4-N_5} and ΔN_{2-N_5} plotted versus the two conformations of ligand (33). The bars in black represents natural charges and the bars in dark red the Mulliken charges.

Hereby, we can conclude that ligand (33) should behave similarly to **1-bTp** and **1-btp** rather than being tridentate like **1-bpp**. Although no crystal structure was obtained to prove it, when ligand (33) was mixed with iron(II) salts no strong yellow/red coloration occurred, similarly as when (30) reacted with iron(II) perchlorate. That result is evidence supporting the described theory.

The $\Delta N_{[\text{chelating}]} - N_{[\text{linear}]}$ parameter defines the nature of each coordinating ligand. Positive values were obtained for linear ligands and negative values for tridentate-like ligands. This discovery could be applied to other families of polyimine ligands, i.e. Figure 5.30:

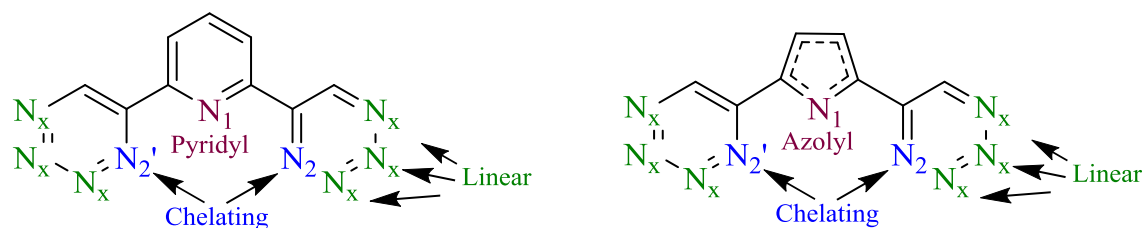


Figure 5.30: Two examples of scaffolds which would potentially follow the trend here discussed. N_1 [pyridyl/azolyl], N_2 [chelating] and the possible N [linear] coordinating imines were labeled.

5.2.5 Synthesis of 2-(1-methyl-1,2,3-triazol-4-yl)-6-(1-methyl-1,2,3-triazol-3-yl)-pyridine (34) and 2,6-di(1-methyl-1,2,3-triazol-3-yl)-pyridine (35) ligands

The complexes $[\text{Fe}(4\text{-bTp})_2]2\text{BF}_4$ and $[\text{Fe}(4\text{-bTp})_2]2\text{ClO}_4$ were low spin. This was attributed to the strong hydrogen bonding between H-N1 and counter-anions or solvent molecules. Hence, methylation of ligand (32) was proposed (Figure 5.31).

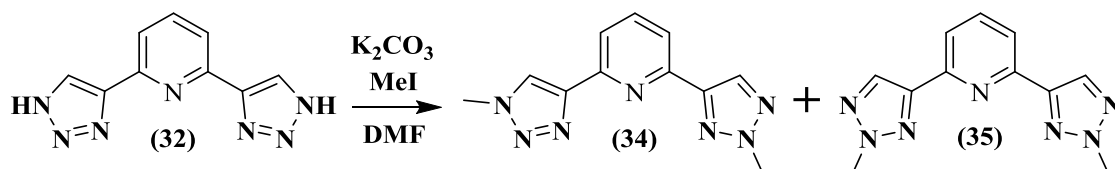


Figure 5.31: Synthetic procedure for ligands (34) and (35).

Methyl iodide and potassium carbonate were used in other similar nucleophilic substitution (S_N2) reactions¹⁹.

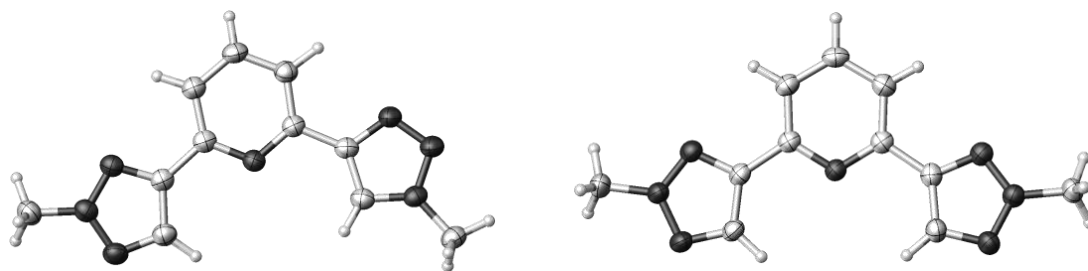


Figure 5.32: Crystal structures of ligands (34) and (34) in $P2_1/n$ and $P2_1/c$ respectively.

Both ligands (34) and (35) in Figure 5.31 were isolated through column chromatography moderate yields, of 27% and 33% respectively.

5.2.6 Iron(II) complexes of 2-(1-methyl-1,2,3-triazol-4-yl)-6-(2-methyl-1,2,3-triazol-1-yl)-pyridine (34)

As for previous complexation procedures, solutions of ligand (34) and iron(II) salts were mixed. Three solvatomorphs were collected from $[\text{Fe}(\mathbf{34})_2](\text{BF}_4)_2$; $[\mathbf{34}]_{\alpha}\mathbf{B}$ is the solvent free form, crystallized in the monoclinic $P2_1/c$ space group. $[\mathbf{34}]_{\beta}\mathbf{B}$ had 2.3 molecules of

acetonitrile and crystallized in the triclinic $P\bar{1}$ space group. Finally **[34]γB** was comprised by one molecule of water and one of acetonitrile ($C2/c$ space group). On the other hand, crystals of the perchlorate salt (**[34]C**) were of poor quality and considerably disordered.

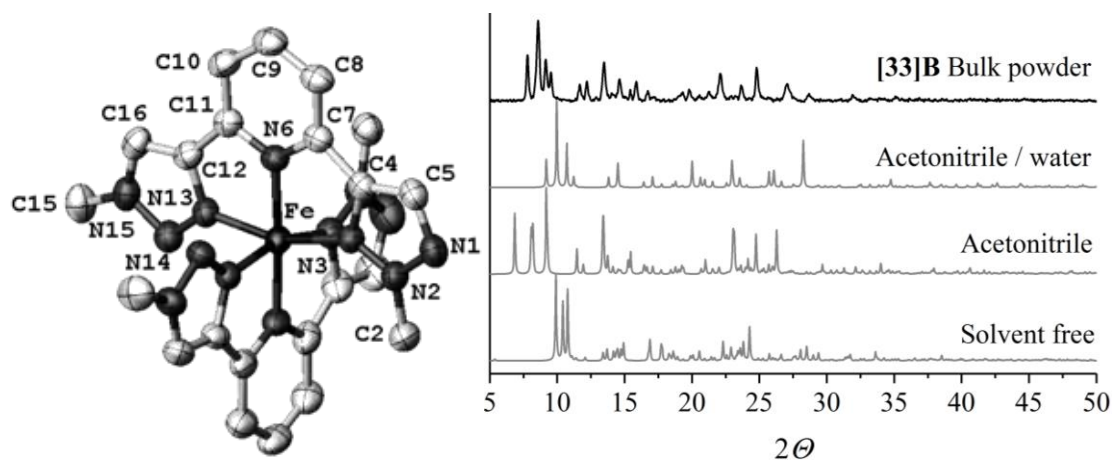


Figure 5.33: Crystal structure of **[34]αB and powder pattern. Counter-anions, solvent molecules and hydrogen atoms of the structure were removed for clarity. The colour assignment in the plot is black for the experimental and grey for the simulated XRD.**

Powder patterns of **[34]B** complexes were collected several times, including ground single crystals, but the results did not fit the simulation for any of the structures collected (Figure 5.33). All crystal structures were collected at 120 K unless specified otherwise (Table 5-12).

	[34]αB solvent free	[34]βB (MeCN) _{2.3}	[34]γB (H ₂ O)(MeCN)	[34]C (MeCN) _{2.5}
Fe–N _[py]	1.916(4), 1.925(4)	1.924(2), 1.928(2)	1.9325(18)	1.938(5), 1.943(5)
Fe–N _[tz]	1.943(4)	- 1.928(2) - 1.995(2)	1.9546(18), 1.9964(19)	1.933(4) - 1.990(5)
V _{Oh}	2.013(4)	9.593(7)	9.699(6)	9.626(14)
Σ	9.624(12)	87.2(3)	89.8(3)	90.9(6)
ϑ	86.4(6)	287.0(8)	296.4(7)	299.6(16)
ϕ	283.8(14)	176.62(9)	174.87(10)	174.70(19)
θ	176.24(16)	88.08(2)	87.36(2)	89.86(4)
	88.34(4)			

Table 5-12: Crystallographic parameters determined directly from the crystal structure using Olex2¹⁶.

The octahedral volume of **[34]X** complexes was close to 9.5 Å³, thus, all the crystal structures were low spin at 120 K. The spin state of the iron(II) in the solid state was confirmed by SQUID measurements (Figure 5.34).

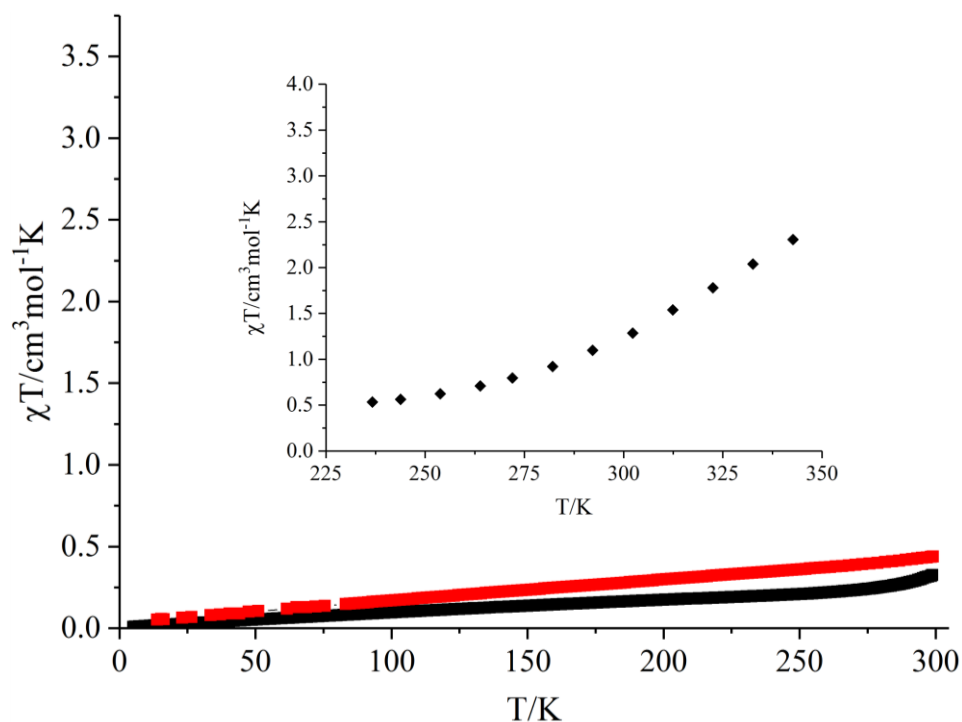


Figure 5.34: Magnetic susceptibility measurement of [43]X in solid and in liquid MeCN solution. SQUID curves of [34]B (black) and [34]C (red) are shown.

Both [34]B and [34]C were LS all over the temperature range in the solid state. However, this complex presented SCO in solution above room temperature.

5.2.7 Iron(II) complexes of 2,6-(2-methyl-1,2,3-triazol-1-yl)-pyridine (35)

In contrast with ligand (35), only the iron/perchlorate of ligand (35) salt was obtained as single crystals. Again three pseudopolymorphs were collected. The first one [35]αC contains half complex in the asymmetric unit cell and it is water solvated (Figure 5.35).

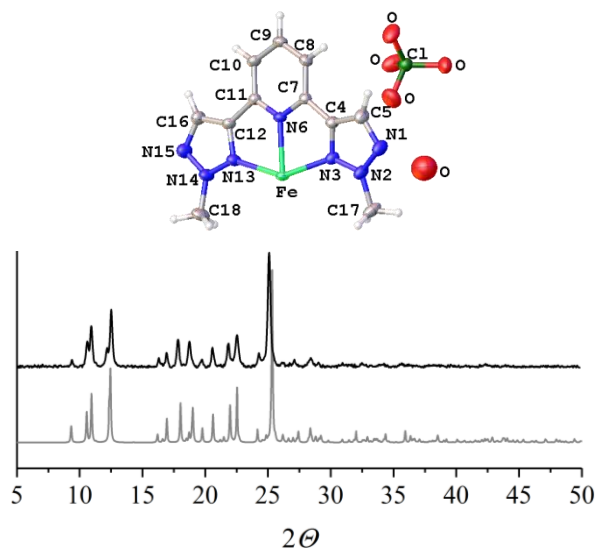


Figure 5.35: Crystal structure of [35]αB in the $C2/c$ space group and powder pattern. The colour assignment in the plot is black for the experimental and grey for the simulated XRD.

Chapter 5

The other two pseudopolymorphs were the nitromethane solvatomorphs; **[35]βC** crystallized in the triclinic $P\bar{1}$ space group as thin pale yellow needles. It contains three unique complexes in the HS state at 120 K and 2.8 molecules of nitromethane (Figure 5.36).

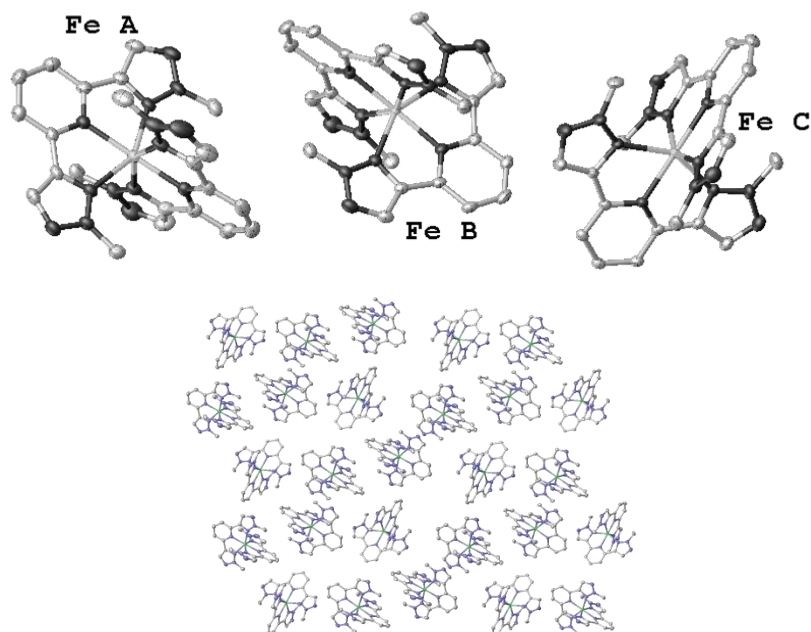


Figure 5.36: Crystal structure of **[35]βC** containing three HS complexes in the asymmetric unit cell. Counter-anions, solvent molecules and hydrogen atoms of the structure were removed for clarity. View of the crystal packing along the a axis where different orientations of **[35]βC** are observed.

In the same crystallization vials as **[35]βC**, **[35]γC** crystallized as big pear coloured blocks. **[35]γC** solvatomorph had also three unique complexes at 120 K in the asymmetric unit cell (Figure 5.38) where the amount of nitromethane was $[\text{Fe}(\mathbf{35})_2](\text{ClO}_4)_2 \cdot 3\text{MeNO}_2$. However the main difference between **[35]βC** and **[35]γC** was the crystal packing (Figure 5.37).

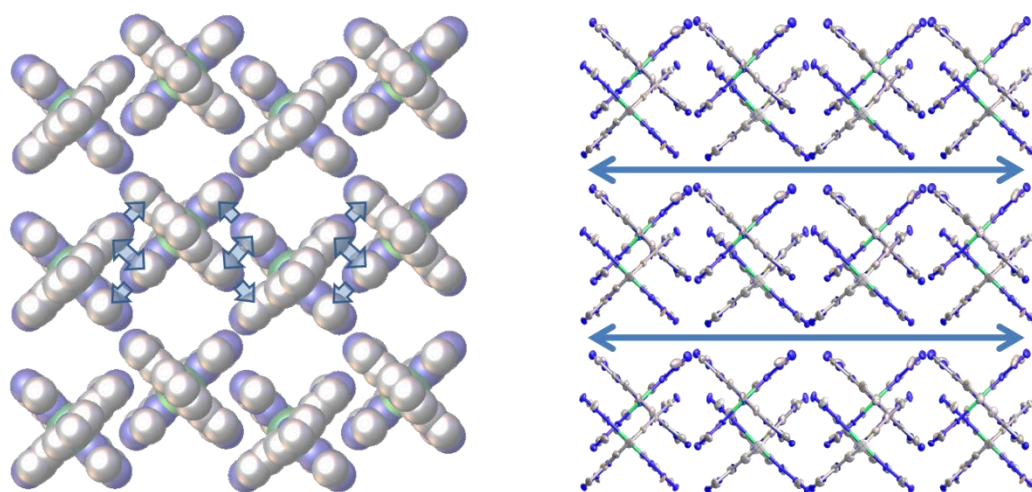


Figure 5.37: Space-filling representation of the packing of **[35]γC**. The octahedral complexes are viewed along their S_4 axes. Counter-anions, solvent molecules and hydrogen atoms of the structure were removed for clarity. The arrows in the left represent the intermolecular interactions typical of the terpyridine embrace, while the arrows in the right highlight the voids occupied by nitromethane and some perchlorate molecules.

Chapter 5

In this case the complexes pack in the same orientation and have intermolecular interactions between them (Figure 5.37). This type of packing receives the name of terpy embrace which involves two complexes attracted by one offset-face-to-face and two edge-to-face interactions by the outer pyridyl rings of the ligand²⁰ which in this case is triazolyl. Terpyridine embrace is typical of bis tridentate complexes. In crystals it is common to find networks of these embraces, combined in numerous ways, and extended in one-, two- or three-dimensions²¹. In this case the interactions were extended in one dimension. Nitromethane molecules were found between the one dimensional networks (Figure 5.37) where the parallel stacking motif of the adjacent layers was observed.

The cooperativity of a thermal spin-transition (whether it occurs gradually, abruptly, with or without hysteresis) is a function of the geometry and strength of intermolecular contacts between spin centres in the material. Terpyridine embrace packing motif reliably gives rise to a particular degree of cooperativity in iron(II) spin-crossover compounds²².

[35] γ C undergoes an incomplete spin transition associated with a $Z'=1 \rightarrow Z'=3$ crystallographic symmetry breaking, Table 5-13. The high temperature phase (180 K) was modelled in the monoclinic $P2/c$ space group, while the low temperature phase (120 K) is in $P2$.

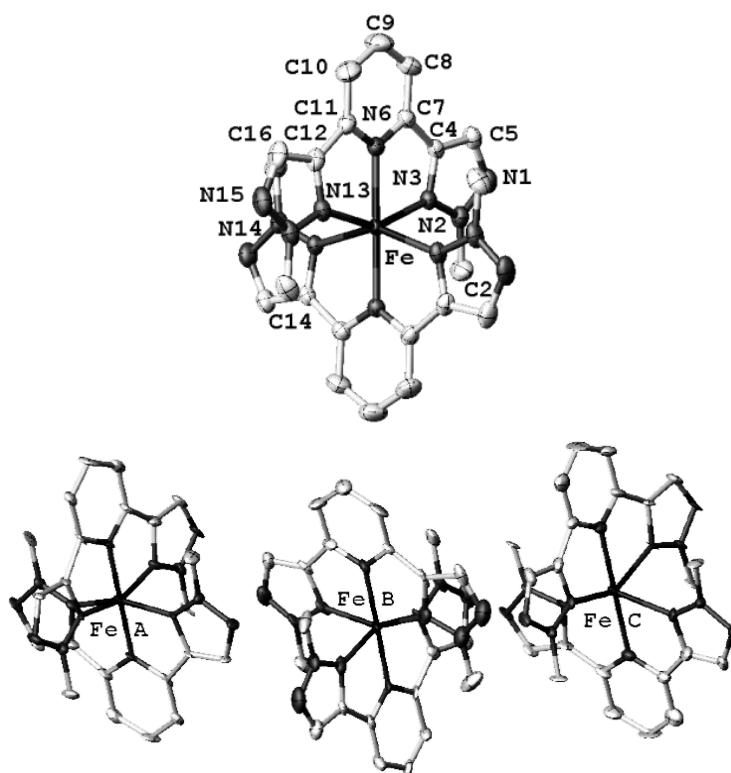


Figure 5.38: Crystal structure of [35] γ C at 180 K ($P2/c$) in the top and at 120 K in the right ($P2$).

The spin states of the three unique iron(II) atoms in [35] γ C at 120 K were; Fe A low spin with an $V_{Oh} \approx 10$, Fe B was in an intermediate spin state ($V_{Oh} \approx 11$), and finally Fe C was HS ($V_{Oh} \approx 13$). The crystals were warm up to 180 K and the asymmetric unit cell only contained one HS complex.

Chapter 5

All crystal structures mentioned in the Table 5-13 were collected at 120 K unless otherwise specified.

	[35] α C	[35] β C Molecule A	[35] β C Molecule B
Fe–N[pyridinyl]	2.136(2)	2.120(3), 2.125(3)	2.106(2), 2.110(2)
Fe–N[triazolyl]	2.203(2), 2.224(2)	2.191(3) - 2.212(2)	2.172(2), 2.218(2)
V_{Oh}	12.845(10)	12.669(9)	12.445(9)
Σ	145.0(4)	146.7(4)	143.1(3)
Θ	475.6(9)	463.3(8)	448.5(8)
ϕ	179.57(12)	178.83(10)	173.60(9)
θ	81.68(3)	82.15(2)	80.62(2)
	[35] β C Molecule C	[35] γ C Molecule A	[35] γ C Molecule B
Fe–N[pyridinyl]	2.125(2), 2.139(2)	1.918(7)	2.004(7)
Fe–N[triazolyl]	2.194(2), 2.229(2)	1.979(8), 1.999(9)	2.077(9), 2.096(9)
V_{Oh}	12.774(9)	9.82(3)	10.98(3)
Σ	144.1(3)	86.2(12)	118.6(11)
Θ	472.7(8)	283(3)	389(3)
ϕ	177.84 (9)	179.8(6)	179.0(4)
θ	83.82(2)	88.34(10)	87.90(9)
	[35] γ C Molecule C	[35] γ C, 180 K	
Fe–N[pyridinyl]	2.166(7)	2.117(3)	
Fe–N[triazolyl]	2.223(8), 2.259(9)	2.199(2), 2.214(2)	
V_{Oh}	13.43(4)	12.783(11)	
Σ	142.4(13)	138.3(5)	
Θ	467(3)	453.8(10)	
ϕ	179.7(6)	179.97(13)	
θ	87.51(11)	86.56(4)	

Table 5-13: Crystallographic parameters determined directly from the crystal structure by using Olex2¹⁶.

The magnetism of [35]C was confirmed by SQUID magnetometry measurements (Figure 5.39) showing an abrupt hysteretic transition for the [35] γ C solvatomorph.

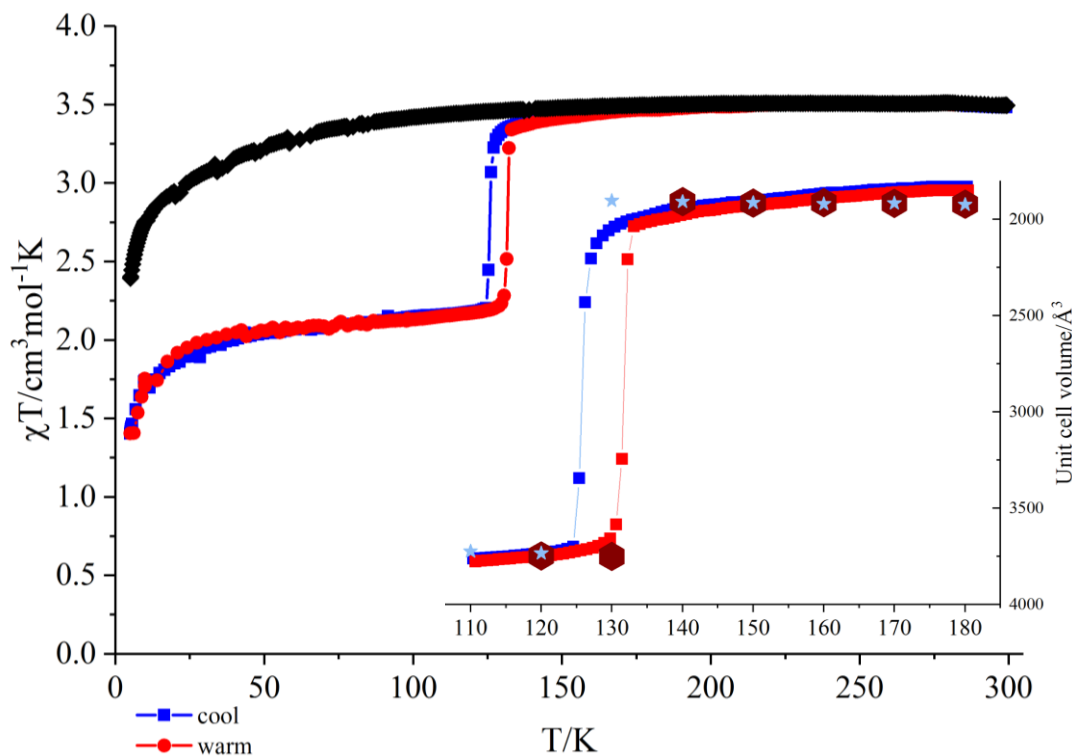


Figure 5.39: SQUID curves of; $[35]_a\text{C}$ black and $[35]_g\text{C}$ cooling and warming cycles blue and red respectively. Zoom in the hysteresis loop overlaid with VT crystallographic unit cells. Pale blue stars corresponded to cooling data points while big red hexagons were warming data points.

Although the nitromethane content was held constant in the single crystal sample inside a SQUID holder (Figure 5.39), solvent exchange occurred more rapidly when the sample was ground for powder XRD analysis. Powder diffraction patterns demonstrated that water solvatomorph is the most stable structure (Figure 5.40).

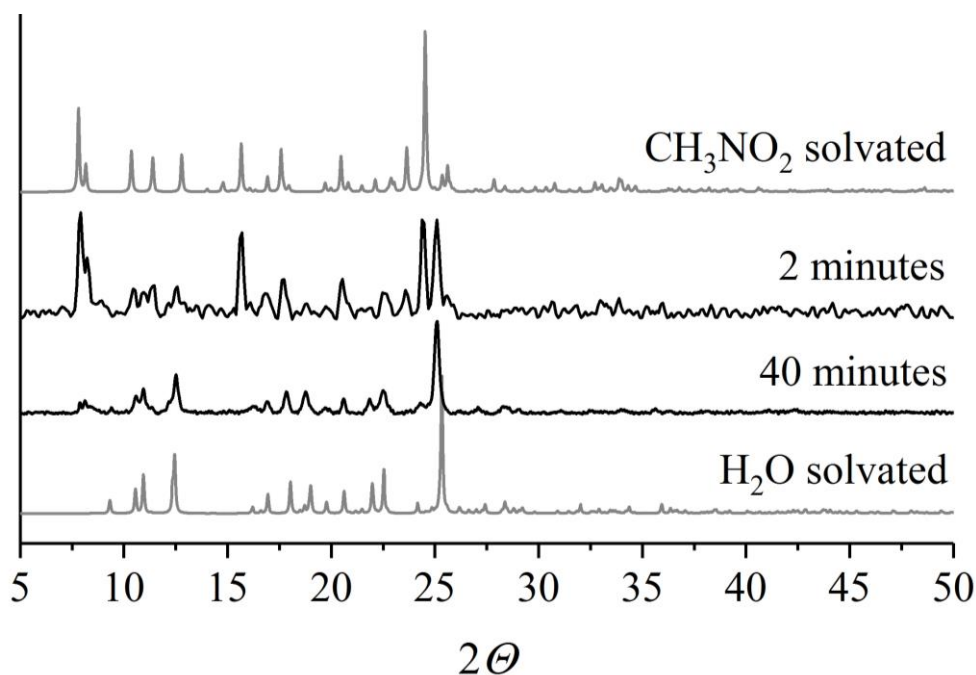


Figure 5.40: Powder diffraction patterns of ground single crystals of $[35]_g\text{C}$ at variable time. The colour assignment in the plot is black for the experimental and grey for the simulated XRD.

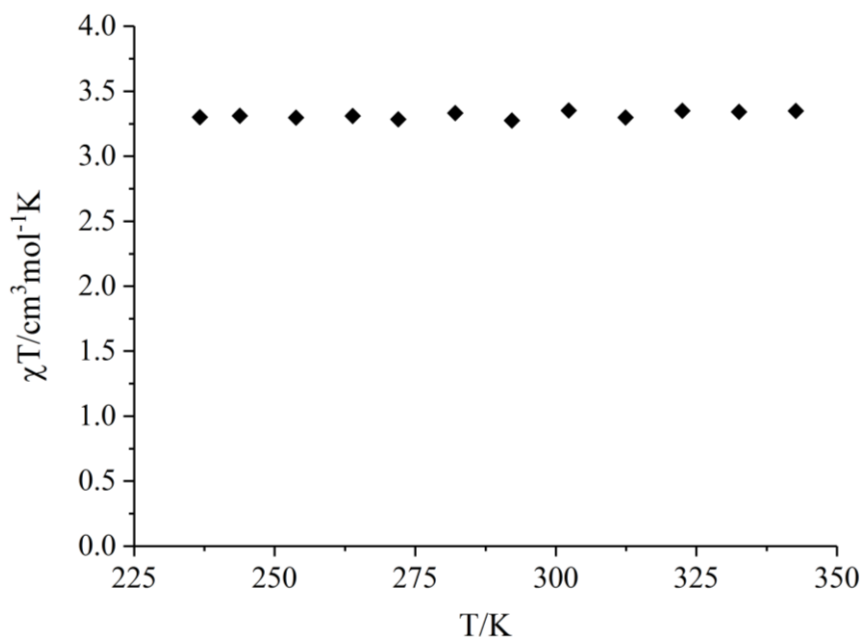


Figure 5.41: Magnetic susceptibility measurement in liquid solution of [35]C in acetonitrile.

Complex [35]C was HS in solution (Figure 5.41). In comparison with [35]X complexes which were fully LS, we have demonstrated that the addition of methyl groups in the ligand shift their iron(II) complexes to the HS state which is also dependent on the methyl position (Table 5-14).

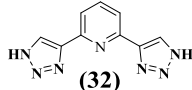
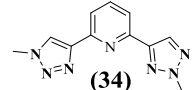
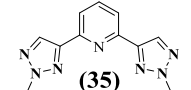
LIGAND	 (32)	 (34)	 (35)
Solution	LS	SCO	HS
Solid state	LS	LS	SCO / HS

Table 5-14: Summarised comparison of the magnetic behaviour of complexes [32], [34] and [35]X.

Certainly ligand (35) shifts its iron(II) complex towards HS in more degree than (34). It seems that the methyl groups in the 3-position exert steric hindrance on the coordination sphere making the Fe-N bond weaker. Similar effects were observed by the methylation of 1-bppz²³ and 1-bppz²⁴ in analogous positions.

5.2.8 Cobalt(II) complexes of 2,6-(1,2,3-triazol-4-yl)-pyridine (32)

Similarly as [Fe(terpy)₂]²⁺ complexes, iron(II) complexes of ligand (32) were low spin in solution and solid state. In contrast, [Co(terpy)₂]²⁺ and its derivative complexes often undergo SCO²⁵. Since the divalent cobalt ion has smaller crystal field splitting than iron(II), the cobalt(II) complex of (32) was proposed as a potential SCO candidate (Figure 5.42);

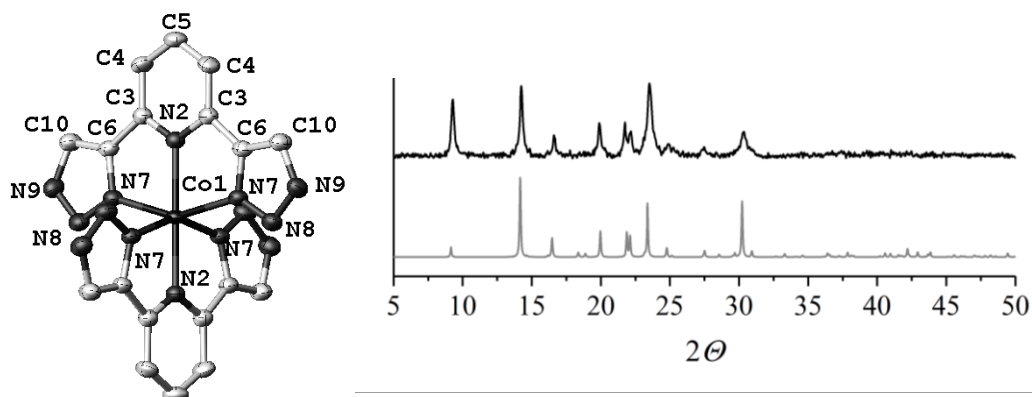


Figure 5.42: Crystal structure and powder diffraction pattern of [32]CoB. The colour assignment in the plot is black for the experimental and grey for the simulated XRD.

	[32]CoB
Fe–N[pyridinyl]	2.091(6)
Fe–N[triazolyl]	2.151(4)
V_{Oh}	12.13(2)
Σ	126.2(10)
Θ	413.4(16)
ϕ	180.0(0)
θ	90.000(8)

Table 5-15: Crystallographic parameters determined directly from the crystal structure by using Olex2¹⁶.

The spin state of cobalt(II) was ambiguous to assign from the crystallographic tables (Table 3-3). But the HS state was confirmed by SQUID (Figure 5.43).

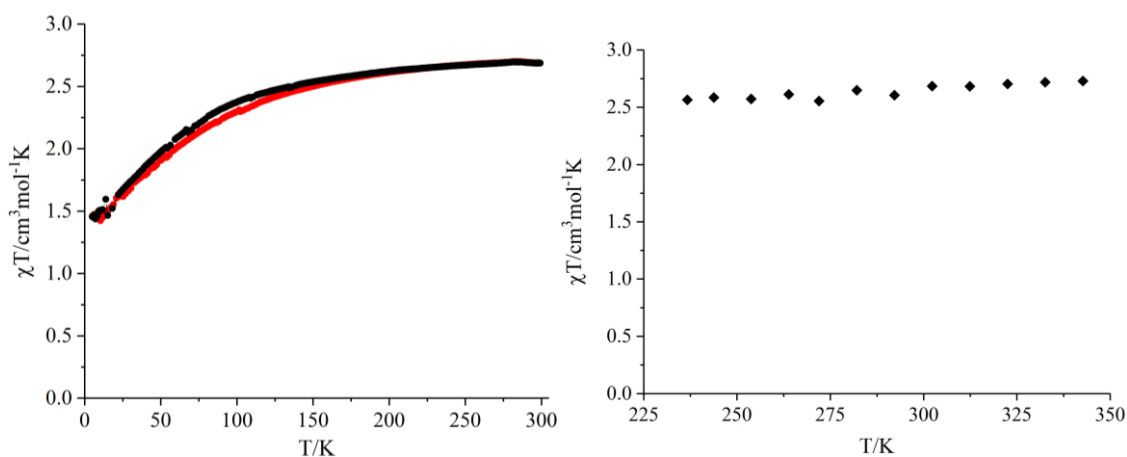


Figure 5.43: Magnetic susceptibility measurement in solid state by SQUID and in liquid solution of; [32]CoB black and [32]CoC red respectively.

In most 3d metal complexes the zero field splitting effect is only observed at low temperatures ($T < 50$ K). Large zero-field splitting values were observed (Figure 5.43). As expected for octahedral Co^{2+} complexes because the symmetry of the octahedral d^7 configuration allows efficient mixing of electronic states²⁶.

5.3 Conclusions

Modifications of bpp skeleton at 5-membered rings affected the magnetic properties of their iron(II) salts and also the coordination type of the ligand. Various transition metals were reacted with ligand (30) and all the structures observed present the M-N[3]triazolyl bond. DFT calculations were performed on several similar derived ligands. It has been found that orbitals corresponding to donor lone pair of N[3/14] are higher in energy than those for pyridyl and chelating nitrogens (N[6] and N[2/13] respectively). Also, ligand (30) presents greater natural and Mulliken charges for N[3/14] (linear) than for N[2/13] (chelating). The graphical representation of those charges revealed the parameter $\Delta N_{[\text{chelating}]} - N_{[\text{linear}]}$ which describes the coordination type of each ligand calculated. Some of the structures obtained from **M[30]** were not fully characterized but it is clear that 1-bTp ligand is a very interesting coordinating ligand which could promote new rare structures upon further investigation. Isomer (30) was fully characterized together with its iron(II) perchlorate complex, **[31]C** which was HS over the whole temperature range, whereas (33) was not isolated in a reproducible yield. When (33) reacted with the iron salt, no coloration of the solution was observed which could indicate a linear coordination.

Methylated derivatives of isomer (32) were coordinated to iron(II). The magnetic properties of all the compounds were measured by SQUID and Evans method. In the solid state, complexes **[34]** are LS up to 300 K, while complexes of **[35]** are HS with an exception of the solvatomorph **[35]γC** which undergoes an incomplete hysteretic (6 K) transition associated to a break in symmetry from $Z'=1$ to $Z'=3$. A terpyridine embrace was observed in the crystal packing of this structure. Cobalt(II) complexes from ligand (32) are HS. In solution the results are a bit different; **[34]** undergoes SCO above room temperature while **[31]**, **[35]**, and **[32]Co** remain HS.

5.4 Bibliography

1. Halcrow, M. A., Recent advances in the synthesis and applications of 2,6-dipyrazolylpyridine derivatives and their complexes. *New Journal of Chemistry* **2014**, 38 (5), 1868-1882.

Chapter 5

2. F. Carina, R.; Verzeqnessi, L.; F. Williams, A.; Bernardinelli, G., Modulation of iron reduction potential by deprotonation at a remote site. *Chemical Communications* **1998**, (24), 2681-2682.
3. Savchuk, M. O.; Litsis, O. O.; Znovjyak, K. O.; Sliva, T. Y.; Kobylinskaya, N. G.; Shishkina, S. V.; Dyakonenko, V. V.; Amirkhanov, V. M., Transition metal complexes of 2,6-bis(imidazol-2-yl)pyridine and its aliphatic derivative. *Polyhedron* **2017**, *133*, 162-168.
4. Sugiyarto, K.; Craig, D.; Rae, A.; Goodwin, H., Structural and Electronic Properties of Iron(II) and Nickel(II) Complexes of 2,6-Bis(triazol-3-yl)pyridines. *Australian Journal of Chemistry* **1993**, *46* (8), 1269-1290.
5. Glynn, C. W.; Turnbull, M. M., Synthesis and metal complexes of 2,6-bis(1-triazolo)pyridine: X-ray structure of 2,6-bis(1-triazolo)pyridine dihydrochloride. *Inorganica Chimica Acta* **2002**, *332* (1), 92-100.
6. Ryu, J. Y.; Han, J. H.; Lee, J. Y.; Hong, S. J.; Choi, S. H.; Kim, C.; Kim, S.-J.; Kim, Y., Crystal structures and catalytic activities of Zn(II) compounds containing btp ligands. *Inorganica Chimica Acta* **2005**, *358* (13), 3659-3670.
7. Youm, K.-T.; Kang, H. C.; Lee, G.-b.; Woo, H. K.; Park, Y. J.; Lee, N.-k.; Ko, J.; Jun, M.-J., Anion-templating self-assembly of [Cu₂(OMe)₂]²⁺ SBUs depending on the size of the anion in the solid state. *Polyhedron* **2006**, *25* (11), 2318-2324.
8. Youm, K.-T.; Ko, J.; Jun, M.-J., Non-classical hydrogen bonds (C–H···X, X=Cl and N) induced 3D architecture: Trigonal bipyramidal ferric complex, [Fe(btp)Cl₃]_n (btp=2,6-bis(N1-1,2,4-triazolyl)pyridine). *Polyhedron* **2006**, *25* (14), 2717-2720.
9. Zhu, Y.-Y.; Li, H.-Q.; Ding, Z.-Y.; Lu, X.-J.; Zhao, L.; Meng, Y.-S.; Liu, T.; Gao, S., Spin transitions in a series of [Fe(pybox)₂]²⁺ complexes modulated by ligand structures, counter anions, and solvents. *Inorganic Chemistry Frontiers* **2016**, *3* (12), 1624-1636.
10. Burrows, K. E.; McGrath, S. E.; Kulmaczewski, R.; Cespedes, O.; Barrett, S. A.; Halcrow, M. A., Spin States of Homochiral and Heterochiral Isomers of [Fe(PyBox)₂]²⁺ Derivatives. *Chemistry – A European Journal* **2017**, *23* (38), 9067-9075.
11. Byrne, J. P.; Kitchen, J. A.; Gunnlauqsson, T., The btp [2,6-bis(1,2,3-triazol-4-yl)pyridine] binding motif: a new versatile terdentate ligand for supramolecular and coordination chemistry. *Chemical Society Reviews* **2014**, *43* (15), 5302-5325.
12. Li, Y.; Huffman, J. C.; Flood, A. H., Can terdentate 2,6-bis(1,2,3-triazol-4-yl)pyridines form stable coordination compounds? *Chemical Communications* **2007**, (26), 2692-2694.
13. Kiskin, M. A.; Fomina, I. G.; Sidorov, A. A.; Aleksandrov, G. G.; Proshenkina, O. Y.; Dobrokhotova, Z. V.; Ikorskii, V. N.; Shvedenkov, Y. G.; Novotortsev, V. M.; Eremenko, I. L.; Moiseev, I. I., Polynuclear iron(III) pivalates. *Russian Chemical Bulletin* **2004**, *53* (11), 2508-2518.
14. Herold, S.; Lippard, S. J., Synthesis, Characterization, and Magnetic Studies of Two Novel Isostructural Pentanuclear Iron(II) Complexes. *Inorganic Chemistry* **1997**, *36* (1), 50-58.

Chapter 5

15. Boillot, M. L.; Sour, A.; Delhaès, P.; Mingotaud, C.; Soyer, H., A photomagnetic effect for controlling spin states of Iron(II) complexes in molecular materials. *Coordination Chemistry Reviews* **1999**, *190-192*, 47-59.
16. Dolomanov, O. V.; Bourhis, L. J.; Gildea, R. J.; Howard, J. A. K.; Puschmann, H., OLEX2: a complete structure solution, refinement and analysis program. *Journal of Applied Crystallography* **2009**, *42* (2), 339-341.
17. Kimura, A.; Ishida, T., Spin-Crossover Temperature Predictable from DFT Calculation for Iron(II) Complexes with 4-Substituted Pybox and Related Heteroaromatic Ligands. *ACS Omega* **2018**, *3* (6), 6737-6747.
18. Sugiyarto, K. H.; Scudder, M. L.; Craig, D. C.; Goodwin, H. A., Electronic and Structural Properties of the Spin Crossover Systems Bis(2,6-bis(pyrazol-3-yl)pyridine)iron(II) Thiocyanate and Selenocyanate. *Australian Journal of Chemistry* **2000**, *53* (9), 755-765.
19. Röhrig, U. F.; Majjigapu, S. R.; Grosdidier, A.; Bron, S.; Stroobant, V.; Pilotte, L.; Colau, D.; Vogel, P.; Van den Eynde, B. J.; Zoete, V.; Michielin, O., Rational Design of 4-Aryl-1,2,3-Triazoles for Indoleamine 2,3-Dioxygenase 1 Inhibition. *Journal of Medicinal Chemistry* **2012**, *55* (11), 5270-5290.
20. L. Scudder, M.; A. Goodwin, H.; G. Dance, I., Crystal supramolecular motifs: two-dimensional grids of terpy embraces in [ML₂] complexes (L=terpy or aromatic N₃-tridentate ligand). *New Journal of Chemistry* **1999**, *23* (7), 695-705.
21. Dance, I., Inorganic intermolecular motifs, and their energies. *CrystEngComm* **2003**, *5* (37), 208-221.
22. Pritchard, R.; Kilner, C. A.; Halcrow, M. A., Iron(ii) complexes with a terpyridine embrace packing motif show remarkably consistent cooperative spin-transitions. *Chemical Communications* **2007**, (6), 577-579.
23. (a) Holland, J. M.; McAllister, J. A.; Lu, Z.; Kilner, C. A.; Thornton-Pett, M.; Halcrow, M. A., An unusual abrupt thermal spin-state transition in [FeL][BF₄] [L = 2,6-di(pyrazol-1-yl)pyridine]. *Chemical Communications* **2001**, (6), 577-578; (b) Elhaïk, J.; Kilner, C. A.; Halcrow, M. A., Insight into Structure: Function Relationships in a Molecular Spin-Crossover Crystal, from a Related Weakly Cooperative Compound. *European Journal of Inorganic Chemistry* **2014**, *2014* (26), 4250-4253.
24. Elhaïk, J.; Money, V. A.; Barrett, S. A.; Kilner, C. A.; Evans, I. R.; Halcrow, M. A., The spin-states and spin-crossover behaviour of iron(ii) complexes of 2,6-dipyrazol-1-ylpyridazine derivatives. *Dalton Transactions* **2003**, (10), 2053-2060.
25. Hayami, S.; Komatsu, Y.; Shimizu, T.; Kamihata, H.; Lee, Y. H., Spin-crossover in cobalt(II) compounds containing terpyridine and its derivatives. *Coordination Chemistry Reviews* **2011**, *255* (17), 1981-1990.
26. Boča, R., Zero-field splitting in metal complexes. *Coordination Chemistry Reviews* **2004**, *248* (9), 757-815.

Chapter 6 – Pursuit of Bpp Derivatives Containing Tether Group for Covering Surfaces and Nanoparticles

6.1 Introduction

Applying spin-crossover in an information processing device is an important goal within the community. To achieve that, SCO materials have to be attached to substrates such as surfaces or nanoparticles¹. The growth of stable, homogeneous and reproducible thin films is an essential step towards application of functional materials. Thin films of switching materials have been manufactured by several techniques including Langmuir-Blodgett deposition², sublimation deposition³, surface-assisted molecular self-assembly⁴ or dip coating/drop casting⁵.

Our approach towards that aim was to add tether groups to SCO active molecules. In view of the results in chapter 2 and chapter 5, where modifications of 1-bpp scaffold (Figure 6.1) barely afforded SCO active iron(II) complexes⁶, in this work we focused on 1-bpp based compounds.

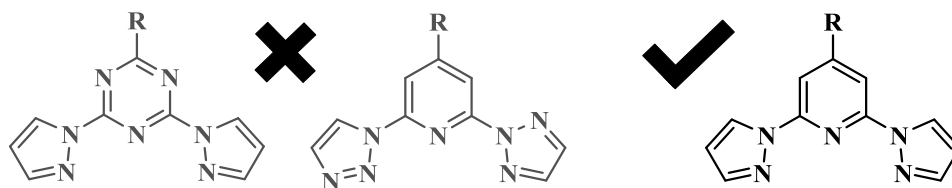


Figure 6.1: Modifications on the bpp scaffolds studied in previous chapters.

The affinity of sulphur compounds for gold is well known⁷. Several types of tether groups based on sulphur-containing substituents have been reported in the literature (Figure 6.2)⁸.

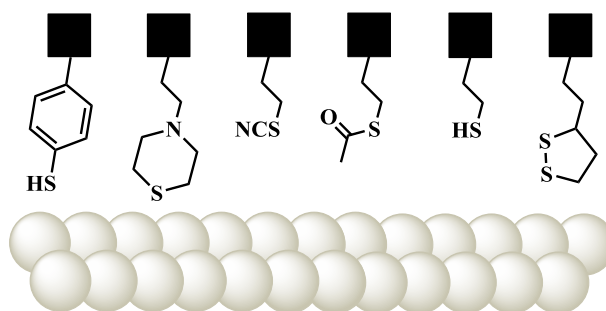


Figure 6.2: Examples of thiol-derived tether groups⁹.

Considering that (R)-lipoic acid is a commercially available compound (Figure 6.3), and several studies have been reported covering gold surfaces¹⁰, gold nanoparticles¹¹ or even quantum dots with functional materials containing 1,2-dithiolan as anchoring group¹². We investigate new potential linker groups that could be used between lipoate and the bpp scaffold.

In this chapter three target molecules containing lipoate bound to bpp through different linkers are discussed to see how accessible their synthesis is, and to investigate how each linker affects $T_{1/2}$ of their iron(II) complexes. Although none of the syntheses of the three target molecules (36), (41) and (43) was successfully achieved for several reasons detailed below, a series of interesting compounds derived from them are described in detail and fully characterized.

6.2 Result and discussion

6.2.1 Target molecule n.1; 2,6-di(pyrazol-1-yl)-4-(R)-thiolipoate-pyridine (36)

Iron(II) salts of bpp-SR derivatives have been previously prepared in the Halcrow group, and often undergo SCO¹³. Hence the first ligand proposed was (36).

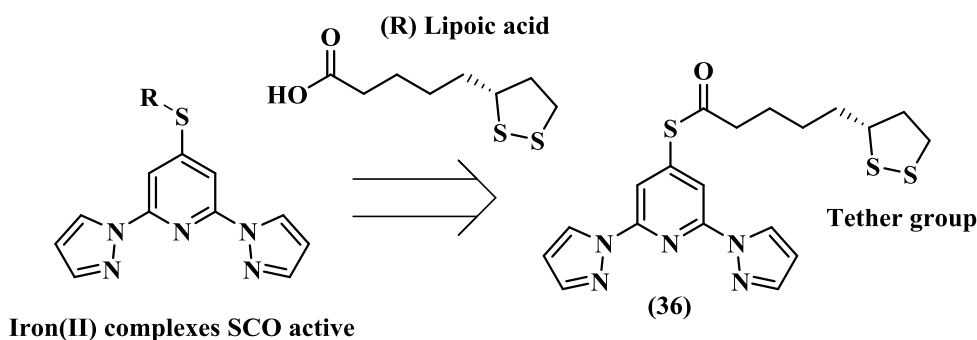


Figure 6.3: Designing target molecule 1, ligand (36).

The synthetic path for the precursor bpp-SH (38) was developed previously in the group by Dr Lawrence Kershaw Cook (Figure 6.4). However, only the first of these steps gave consistently high yields. Thus, obtaining good quantities of (38) to work with was challenging. Moreover, ligand (38) oxidizes to bpp-SS-bpp (39) very easily (Figure 6.5).

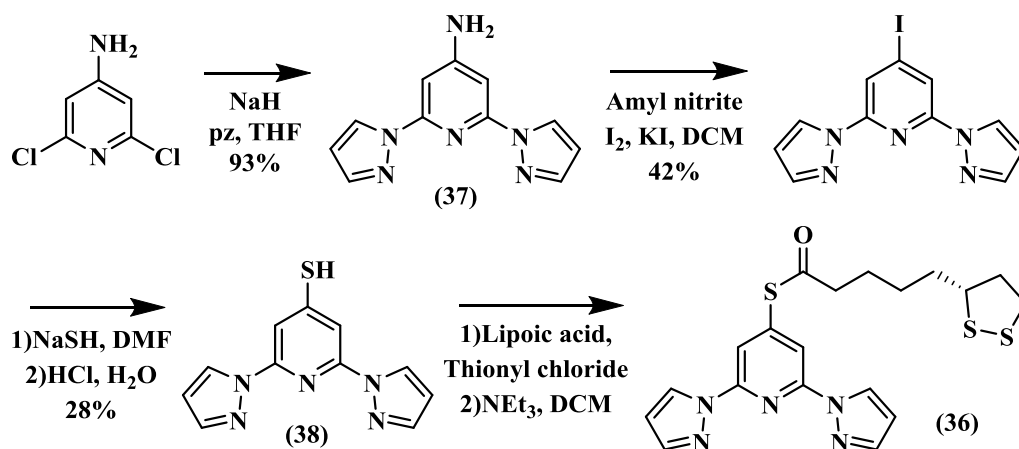


Figure 6.4: Multi-steps synthesis of ligand (36).

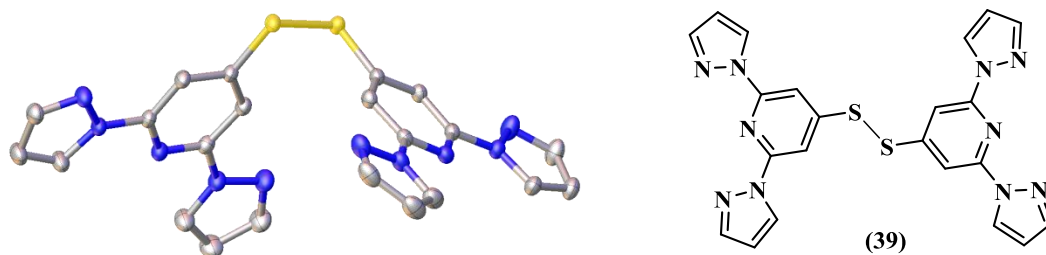


Figure 6.5: Crystal structure of ligand (39). Hydrogen atoms of the structure were removed for clarity. Crystals of (39) were repeatedly observed during (36) and (40) synthesis.

Several attempts to synthesise ligand (36) were without success, consistently giving an insoluble gum. Ligand (40) was therefore proposed as analogous to (36), with an easier synthesis owing to the availability of acetyl chloride (Figure 6.6).

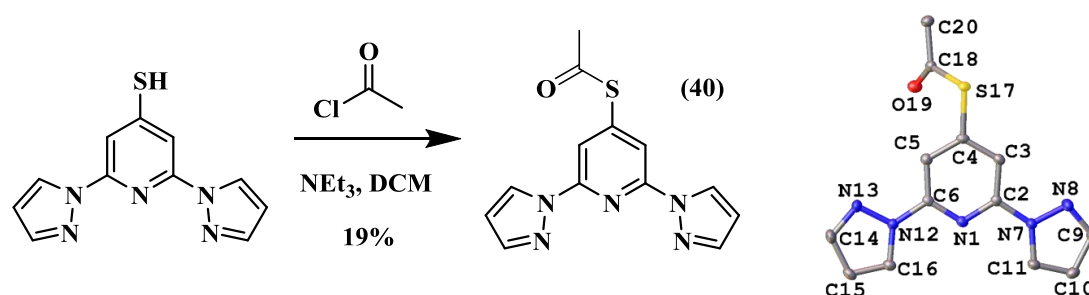


Figure 6.6: Scheme of synthesis and crystal structure of ligand (40). $P2_12_12_1$ space group, hydrogen atoms of the structure were removed for clarity.

Ligand (40) was synthesized in a very low yield, with bpp-S-S-bpp (39) instead being the major product. Hydrated iron(II) tetrafluoroborate and perchlorate salts of (40) were crystallized from nitromethane, yielding isostructural, but poor quality, single crystals (Figure 6.7).

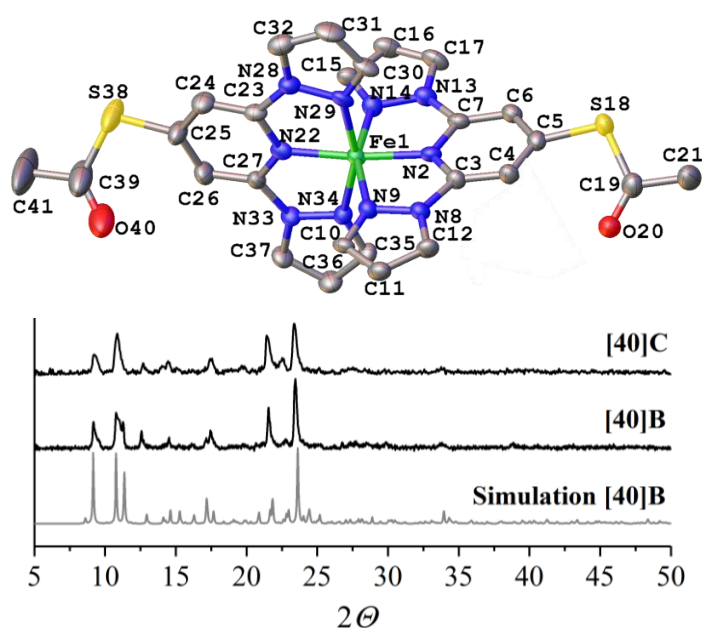


Figure 6.7: Crystal structure and powder pattern of [40]X from nitromethane. Solvent molecules, counter-anions and hydrogen atoms of the structure were removed for clarity. The colour assignment in the plot is black for the experimental and grey for the simulated XRD. $Pbca$ space group.

Chapter 6

VT experiments were collected showing a spin transition. The following table describes the geometric coordination parameters at different spin states (Table 6-1).

[40]B-MeNO ₂	120 K	270 K
Fe–N[pyridinyl]	1.894(6), 1.912(6)	2.110(6), 2.125(6)
Fe–N[pyrazolyl]	1.972(7) – 2.002(6)	2.161(7) – 2.185(7)
V _{Oh}	9.63(2)	12.06(3)
Σ	88.3(8)	152.7(9)
⊙	292(2)	506(3)
ϕ	173.2(3)	167.5(3)
θ	88.10 (7)	87.65(9)
[40]C-MeNO ₂	130 K	280 K
Fe–N[pyridinyl]	1.897(7), 1.923(7)	2.132(10), 2.152(9)
Fe–N[pyrazolyl]	1.973(7) – 1.990(7)	2.157(8) – 2.183(8)
V _{Oh}	9.62(2)	12.10(3)
Σ	90.2(8)	153.9(14)
⊙	298(2)	509(3)
ϕ	172.3(3)	167.0(3)
θ	88.46 (8)	87.84(9)

Table 6-1: Crystallographic parameters of [40]X-MeNO₂, LS vs HS state.

A gradual transition for these compounds in the solid state was confirmed by SQUID (Figure 6.8). A small step was observed for the perchlorate salt which is also observed in the VT cells.

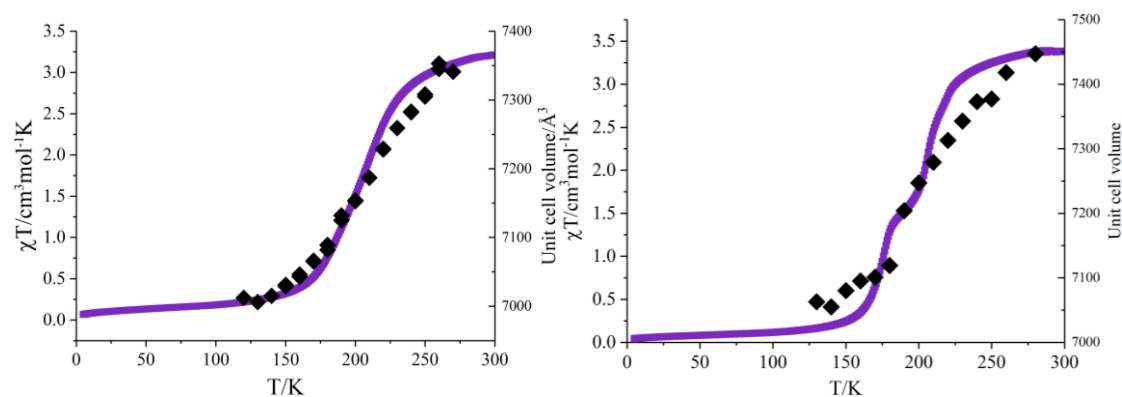


Figure 6.8: SQUID curve plotted with the VT unit cell volume parameters of both salts, [40]B-MeNO₂ (left) [40]C-MeNO₂ (right).

Chapter 6

This experiment showed a unit cell volume change (ΔV) of 4.84% and 5.4% for the tetrafluoroborate and the perchlorate salts respectively. These values are significant and a sign that the thermal contraction is accompanied by a gradual SCO on cooling. [40]C complex was also crystallized from acetone in the triclinic $P\bar{1}$ space group containing two unique molecules in the asymmetric unit cell (Figure 6.9).

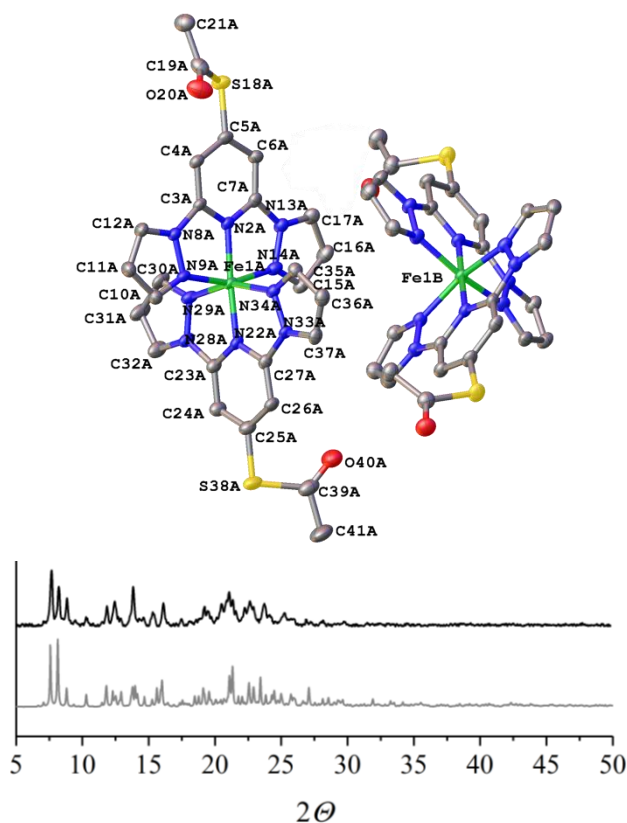


Figure 6.9: Crystal structure of [40]C-Me₂CO and powder diffraction pattern. Solvent molecules, counter-anions and hydrogen atoms of the structure were removed for clarity. The colour assignment in the plot is black for the experimental and grey for the simulated XRD.

In this case, [40]C-Me₂CO undergoes an abrupt SCO close to room temperature with a 5 K hysteretic loop, $T_{1/2\downarrow} = 270$ K, $T_{1/2\uparrow} = 275$ K (Figure 6.10).

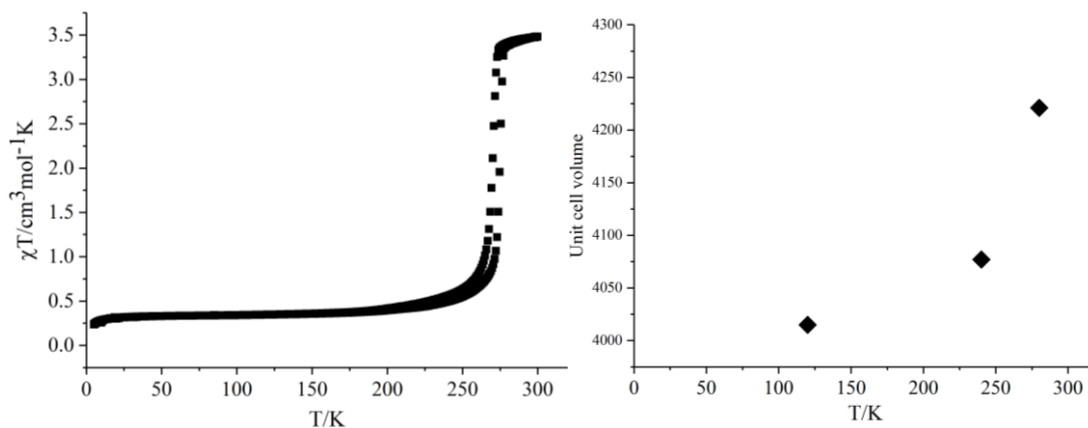


Figure 6.10: SQUID curve and unit cell volumes of [40]C-Me₂CO. Three crystallographic data points were taken at 120, 240 and 280 K which follow the trend described by SQUID.

Chapter 6

Complex **[40]C-Me₂CO** was LS at 120 K according to its crystallographic parameters (Table 6-2). Although no full data set was collected at high temperature, the variation of the cell volume data was in agreement with the SQUID curve. The variation of unit cell volume from 250 K to 280 K was 3.5 %, typical of SCO.

120 K	[40]C-Me₂CO Molecule A	Molecule B
Fe–N[pyridinyl]	1.905(3), 1.909(3)	1.898(3), 1.901(3)
Fe–N[pyrazolyl]	1.971(4) – 1.989(3)	1.968(3) – 1.987(4)
V_{Oh}	9.671(10)	9.611(10)
Σ	88.4(4)	89.0(5)
Θ	290.9(11)	287.3(11)
ϕ	176.80(14)	178.07(14)
θ	86.98 (4)	86.74 (3)

Table 6-2: Geometric parameters of [40]C-Me₂CO molecules A and B.

No more research on salts of complex **[40]** was performed despite their interesting magnetic properties, due to their genuinely poor quality single crystals together with the low yield for the synthesis of **(40)**. χT vs T was also determined in acetonitrile solution by paramagnetic NMR Evans Method. Data points were taken every 10 K from 340 K to 240 K (Figure 6.11).

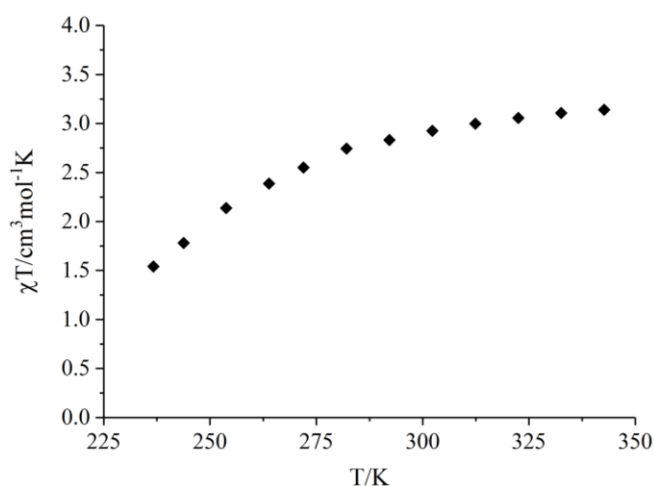


Figure 6.11: Magnetic susceptibility in solution of [40] in acetonitrile.

Complexes **[40]X** undergo SCO in solution ($T_{1/2} \approx 240$ K) and it was believed that complex **[36]** would behave similarly. Although “bpp-thioester” compounds are promising in terms of SCO activity, ligand **(36)** was discarded due to its low yields and the instability of this type of compounds towards pH variations¹⁴.

6.2.2 Target molecule n.2, (41); obtainment of 2,6-Di(pyrazol-1-yl)-4-(3,4-dimethoxythiophenol)-pyridine (42)

It is possible to obtain bpp-SR type of compounds avoiding the multi-steps synthesis mentioned before (Figure 6.4). This easier procedure only involves nucleophilic aromatic substitutions from the 2,4,6-trifluoropyridine with pyrazolate and thiolate derivative R-S⁻ (Figure 6.12).

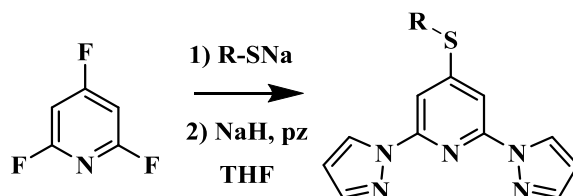


Figure 6.12: Synthetic procedure B of bpp-SR.

Although iron (II) complexes of bpp-SR ligands (R = hydrogen, methyl, isopropyl, tertbutyl and -SSR) have been recently examined as SCO active¹³, analogues with R = aromatic were unknown until now. With all that in mind, and due to the availability of different methoxy thiophenols (Figure 6.13), ligand (41) was proposed as an alternative to (36).

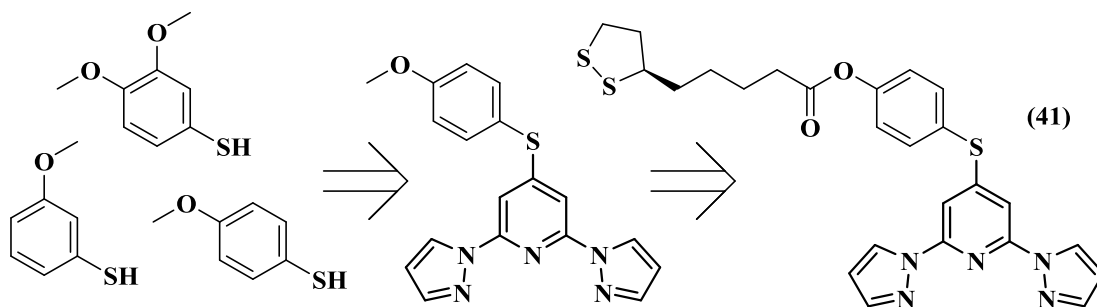


Figure 6.13: Scheme of the commercially available methoxy thiophenols and an example of the hypothetical tethered ligand (41).

(42) (Figure 6.14), was prepared from 3,4-dimethoxy-thiophenol, sodium hydride, pyrazole and trifluoropyridine (Figure 6.12).

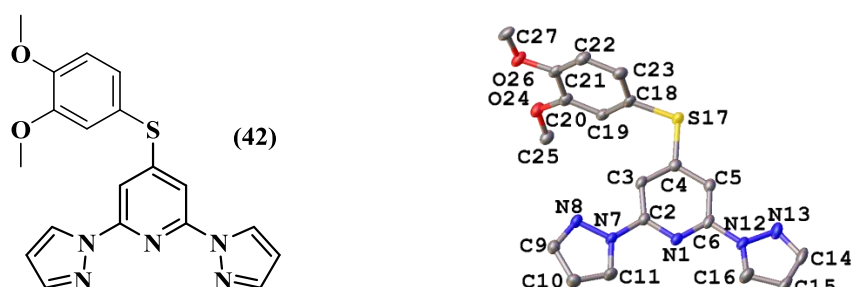


Figure 6.14: Scheme and crystal structure of ligand (42). *Cc* space group, hydrogen atoms of the structure were removed for clarity.

Ligand (42) was reacted with iron(II) tetrafluoroborate and perchlorate hydrate salts. Both complexes crystallized in the *C2/c* space group and were isostructural (Figure 6.15).

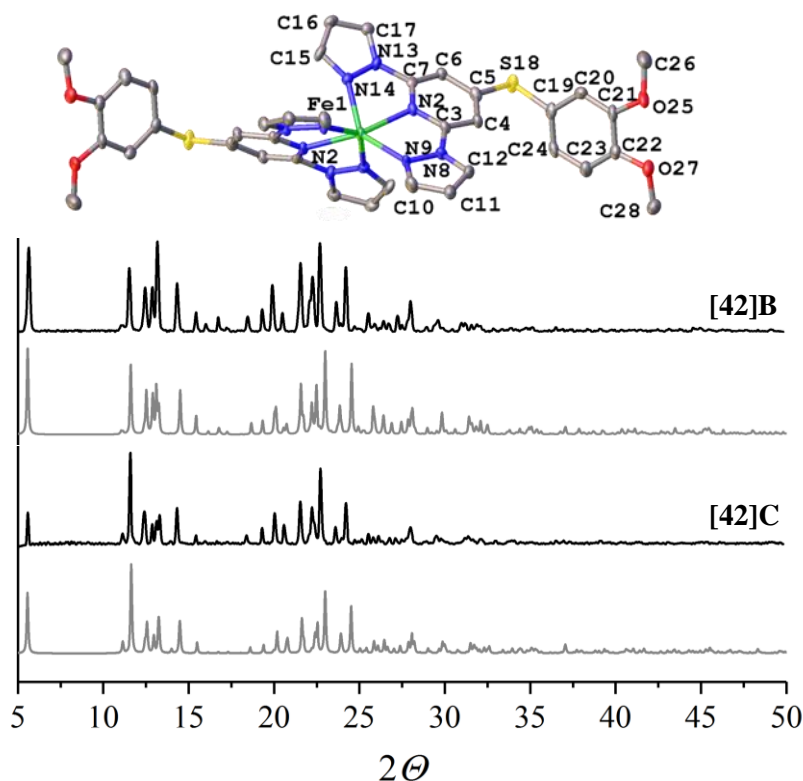


Figure 6.15: Crystal structure of [42]B and PDX spectra of both [42]B and [42]C. Counter-anions and hydrogen atoms of the structure were removed for clarity. The colour assignment in the plot is black for the experimental and grey for the simulated XRD.

120 K	[42]B	[42]C
Fe–N[pyridinyl]	2.163(5)	2.171(4)
Fe–N[pyrazolyl]	2.169(5), 2.218(6)	2.182(4), 2.218(4)
V_{Oh}	11.02(2)	11.021(17)
Σ	203.5(9)	208.4(7)
Θ	499.9(16)	505.2(13)
ϕ	143.6(3)	143.0(2)
θ	74.16(10)	73.37(7)

Table 6-3: Geometric parameters of [42]X molecules. Highlighted in bold the parameter (ideally $\phi = 180^\circ$) heavily distorted.

Not only were these unexpectedly high spin, they also showed the highest distortion parameter ϕ ever observed for the $[\text{Fe}(\text{bppR})_2]^{2+}$ type of complexes¹⁵ (Table 6-3). This could be attributed to the packing of the thiophenol rings in the lattice (Figure 6.16).

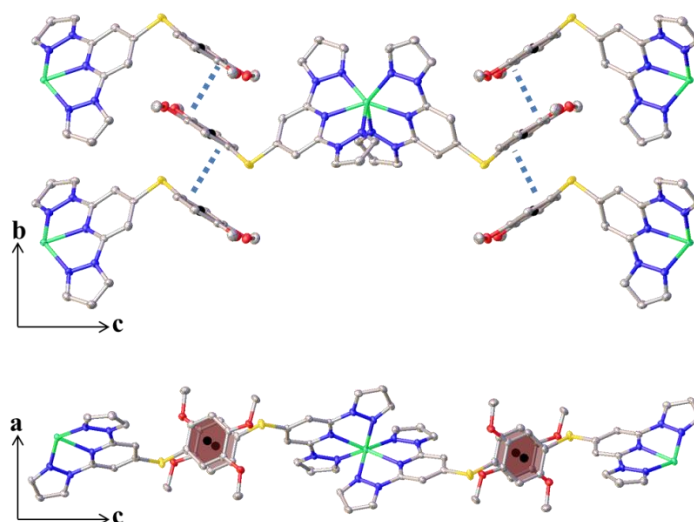


Figure 6.16: Views of π - π interactions between the thiophenol rings along a and b crystallographic axes respectively for the [42]C.

Two unique crystallographic parallel-displaced π - π stacking interactions were observed, with centroid-centroid distance 3.801(4) and 4.239(4) Å; plane-centroid distance 3.456(5) and 3.295(7) Å; and plane-plane angle, 0.0(8) and 0.0(6) $^\circ$, respectively.

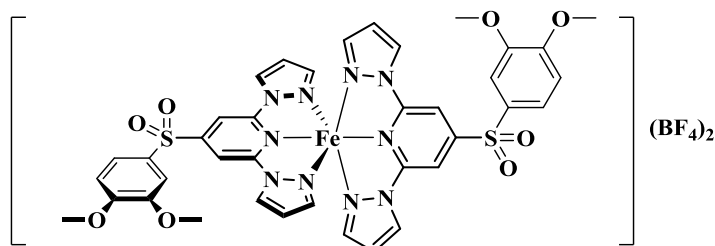


Figure 6.17: Scheme of the iron complex of the oxidized ligand (42).

Interestingly, complex [42]C was isolated in analytical purity, while precipitated powder samples of [42]B gave consistently low C,H,N values. The results fitted better with the sulphonate analogue of (42), (Figure 6.17). Oxidation of thioether groups in similar compounds was observed before^{13b}. Apparently, only tetrafluoroborate counter-anions catalyzed the oxidation.

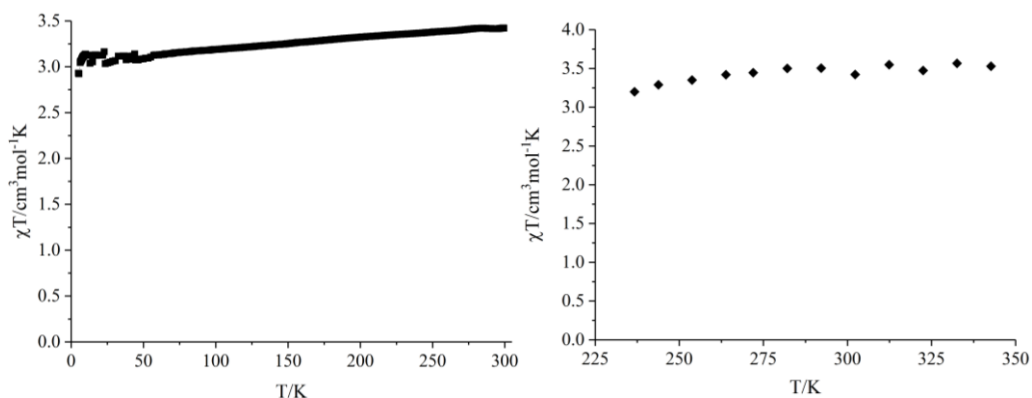


Figure 6.18: Magnetic susceptibility vs T of [42]C in the solid state and in solution in acetonitrile.

The fact that the complex [42]C also remains HS upon cooling in solution, could be a sign of the strong electron donating capacity of the two methoxy groups in the aromatic ring, then, decreasing the crystal ligand field. As a result of the magnetic properties of [42] complexes, ligand (41) and its derivatives were immediately discarded. A similar reaction will be described in Chapter 7 for the tethered ligand (66), which was fully characterized.

6.2.3 Target molecule n.3; 2,6-Di(pyrazol-1-yl)-4-(R)-(5-(1,2-dithiolan-3-yl)pentanecarbonyl)-pyridine (43) and 2,6-di(pyrazol-1-yl)-4-acetamide-pyridine (44)

Although iron(II) complexes from bpp ligands containing nitrogen donor in the 4-position of bpp scaffold were reported to be HS¹⁶, the less electron-donating N-amide group remained unexplored. Since the synthesis of bpp-NH₂ (37) is straightforward (Figure 6.4), ligand (43) was proposed as a potential solution to the previous problems.

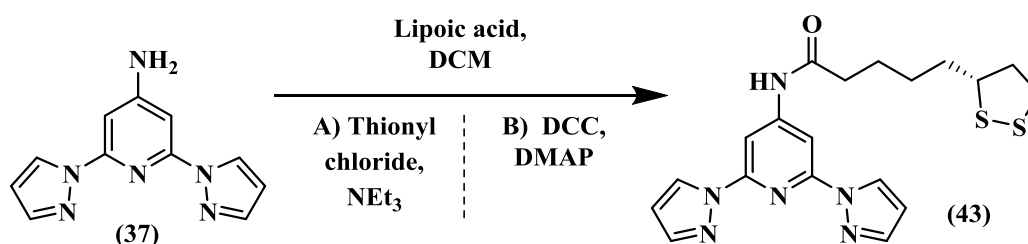


Figure 6.19: Scheme of synthesis of ligand (43).

Similar insoluble gum to the synthesis of (36) was observed here. It was believed that thionyl chloride could react with the lipoic acid polymerizing it into the sticky gum. Alternatively DCC coupling was approached (Figure 6.19). Unfortunately ligand (43) was obtained in a very low yield and its solubility prevented purification. The low reactivity could reflect the de-activated nature of (pyrid-4-yl)amino group¹⁷.

2,6-Di(pyrazol-1-yl)-4-(*N*-acetamido)-pyridine (44) (Figure 6.20) was synthesized from (37) with an excess of acetyl chloride in 67% yield. Ligand (44) was fully characterized and crystallized in *C2/c* space group, with two unique molecules and a water molecule sharing hydrogen bonds with the amide proton in the asymmetric unit cell.

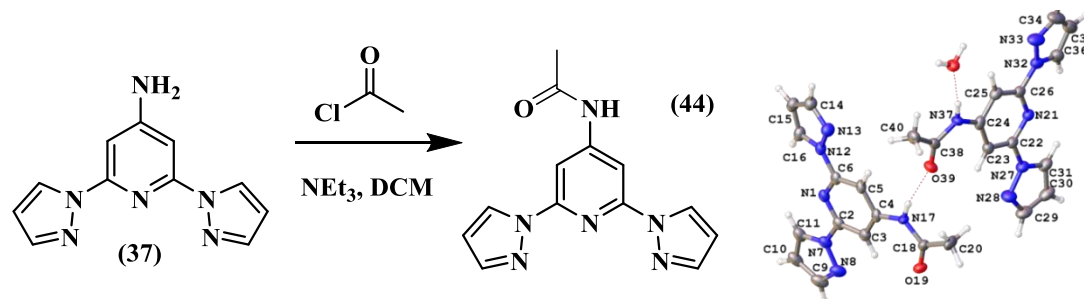


Figure 6.20: Scheme of synthesis and crystal structure of ligand (44). *C2/c* space group.

Chapter 6

Iron(II) tetrafluoroborate and perchlorate salts of ligand (**44**) (**[44]B** and **[44]C**) were crystallized from several solvents. The structures were all solvated lattices, and showed different magnetic properties (Table 6-8).

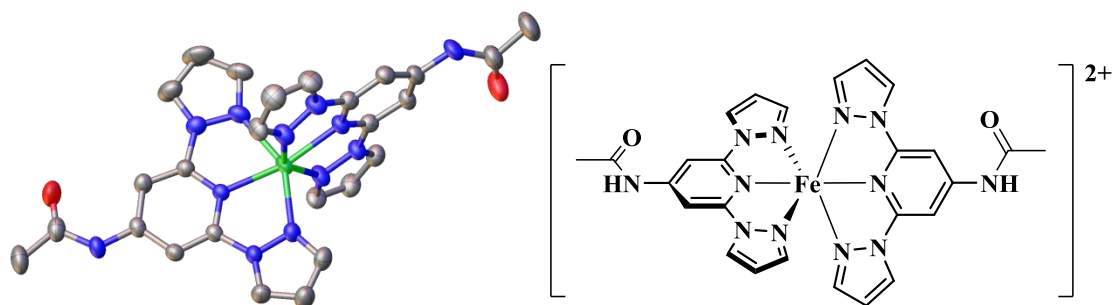


Figure 6.21: Crystal structure of **[44]B-EtCN** and schematic of the complex. Solvent molecules, counter-anions and hydrogen atoms of the structure were removed for clarity.

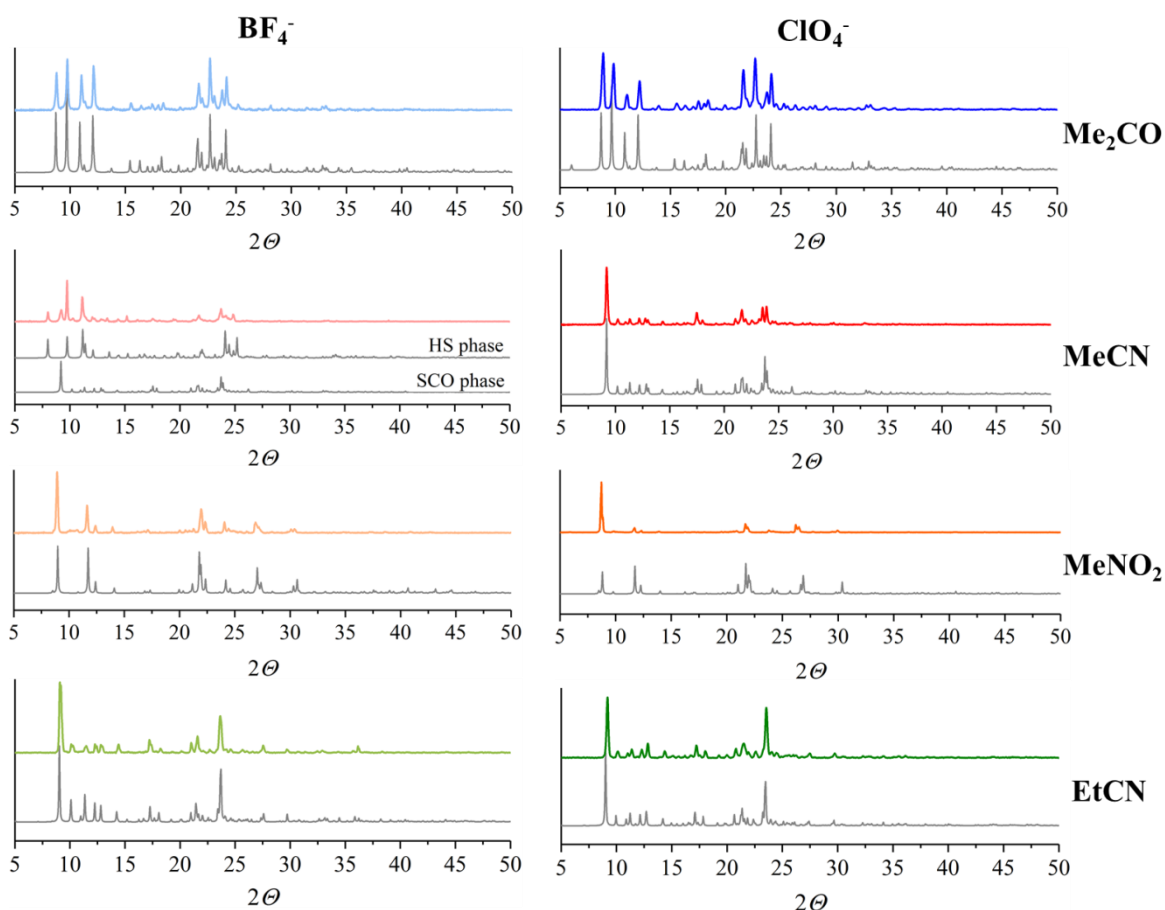


Figure 6.22: Powder XRD of the pairs of solvatomorphs **[44]X-Y**. The colour assignment in the plot is grey for the simulated XRD and each colour corresponds to an experimental spectrum; pale blue **[44]B-Me₂CO**, blue **[44]C-Me₂CO**, pale red **[44]B-MeCN**, red **[44]C-MeCN**, pale orange **[44]B-MeNO₂**, orange **[44]C-MeNO₂**, pale green **[44]B-EtCN** and green **[44]C-EtCN**.

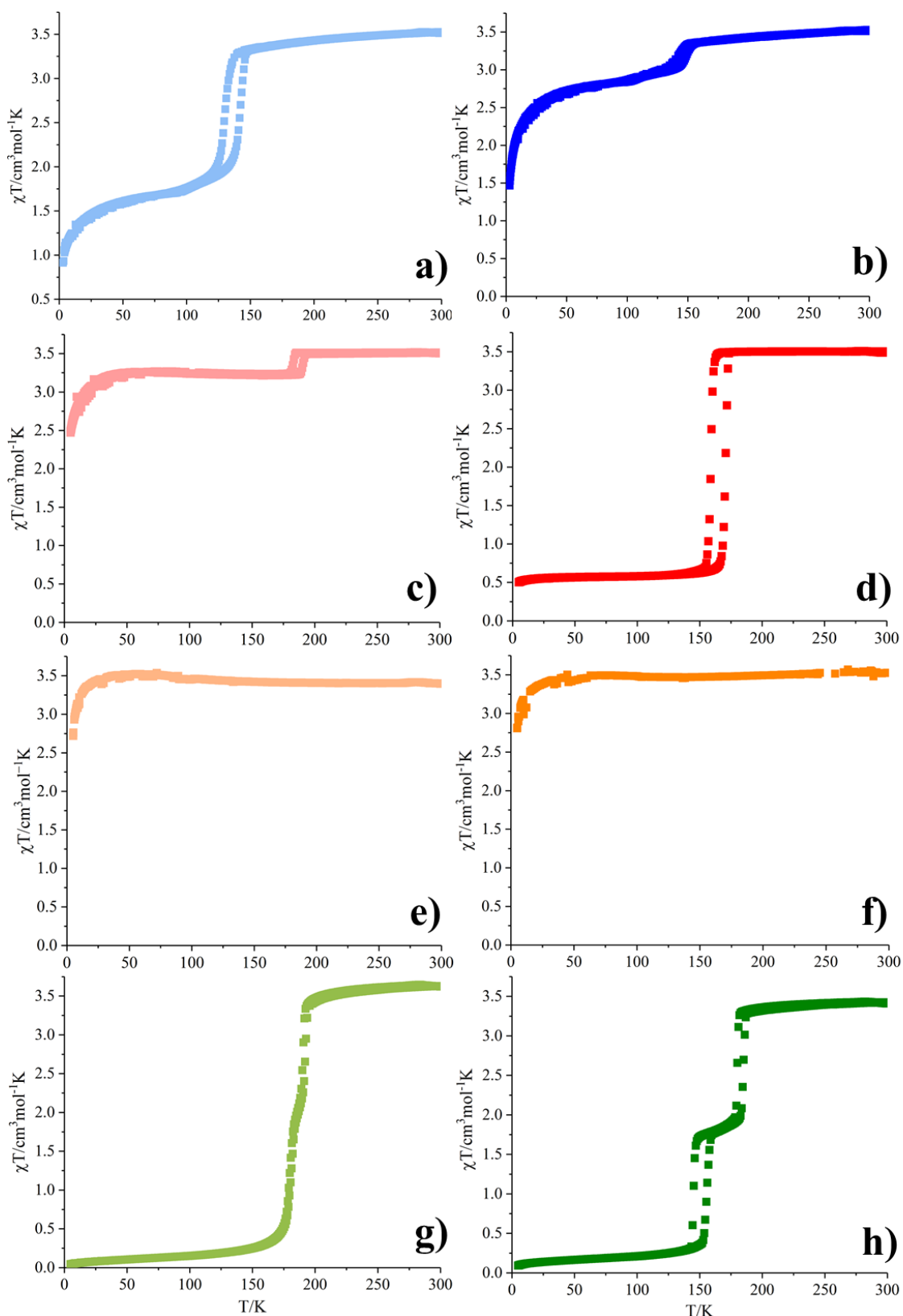


Figure 6.23: SQUID curves of [44]X-Y. The assignment is as follow; a) [44]B-Me₂CO, b) [44]C-Me₂CO, c) [44]B-MeCN, d) [44]C-MeCN, e) [44]B-MeNO₂, f) [44]C-MeNO₂, g) [44]B-EtCN, h) [44]C-EtCN.

The perchlorate and tetrafluoroborate salts from each solvate were isostructural, and show similar magnetic properties. Three solvates were crystallized from acetone (Me₂CO). [44]C-Me₂CO,

Chapter 6

[44]B-Me₂CO α and **[44]B-Me₂CO β** . The perchlorate salt contains one acetone molecule with one HS iron(II) complex in the asymmetric unit cell at room temperature. **[44]C-Me₂CO** undergoes a symmetry breaking at 135 ± 5 K from ($P2_1/c$, $Z = 4$) to ($P2_1/c$, $Z = 8$) without a change on its spin state (Table 6-4 and Figure 6.23, b)), where two HS complexes are found in the asymmetric unit¹⁷.

[44]C-Me₂CO	(170 K)	Molecule A (120 K)	Molecule B (120 K)
Fe-N[pyridinyl]	2.115(3), 2.125(3)	2.114(3), 2.120(3)	2.121(3), 2.128(3)
Fe-N[pyrazolyl]	2.177(4) – 2.193(3)	2.174(4) – 2.199(3)	2.176(4) – 2.198(3)
V_{Oh}	12.200(13)	12.263(3)	12.148(3)
Σ	155.2(5)	153.5(4)	155.3(4)
Θ	513.4(11)	505.6(11)	515.6(11)
ϕ	168.48(12)	172.57(13)	165.45(12)
θ	87.94(4)	87.50(4)	82.85(4)
[44]B-Me₂CO α	(240 K)	Molecule A (130 K)	Molecule K (130 K)
Fe-N[pyridinyl]	2.117(3), 2.121(3)	2.144(6), 2.157(6)	2.056(7), 2.077(7)
Fe-N[pyrazolyl]	2.180(3) – 2.200(3)	2.176(6) – 2.208(7)	2.099(7) – 2.151(6)
V_{Oh}	12.268(12)	12.147(3)	11.443(3)
Σ	154.4(4)	163.9(7)	138(1)
Θ	510.1(11)	517(1)	452(2)
ϕ	169.65(12)	162.4(2)	170.4(3)
θ	87.84(9)	79.80(6)	87.64(6)
[44]B-Me₂CO α	Molecule O (130 K)	[44]B-Me₂CO β	(120 K)
Fe-N[pyridinyl]	1.935(6), 1.948(6)	Fe-N[pyridinyl]	2.121(3), 2.138(3)
Fe-N[pyrazolyl]	1.953(6) – 2.006(6)	Fe-N[pyrazolyl]	2.158(3) – 2.204(3)
V_{Oh}	9.833(1)	V_{Oh}	12.116 (11)
Σ	94.9(9)	Σ	163.0(5)
Θ	311(2)	Θ	519.0(10)
ϕ	176.3(2)	ϕ	166.26(12)
θ	87.15(6)	θ	81.52(4)

Table 6-4: Geometric parameters of [44]X-Me₂CO crystal structures at different temperatures. Only three representative examples for [44]B-Me₂CO α low temperature phase shown.

Chapter 6

The tetrafluoroborate iron salt crystallized as two different pseudopolymorphs. The minor crystalline phase **[44]B-Me₂CO β**, crystallized in $P2_1/n$ space group and was only observed once. The asymmetric unit cell contained two acetone molecules and did not undergo SCO or symmetry breaking.

In contrast, the main crystalline phase is **[44]B-Me₂CO α** which is isostructural with the perchlorate salt, also containing one acetone molecule. In this case the symmetry breaking is ($P2_1/c$, $Z = 4$) to ($P2_1$, $Z = 48$) which is the largest symmetry breaking ever reported associated with SCO¹⁷. The hysteretic, incomplete spin transition occurs at $T_{1/2\downarrow} = 130$ K, $T_{1/2\uparrow} = 142$ K (Figure 6.23, a)). The asymmetric unit cell of **[44]B-Me₂CO α** below 130 K contains 24 crystallographically unique iron(II) complexes, 10 of which retain their HS state, 10 others switch to LS and four lie in a mixed HS/LS population (Table 6-4 and Figure 6.24).

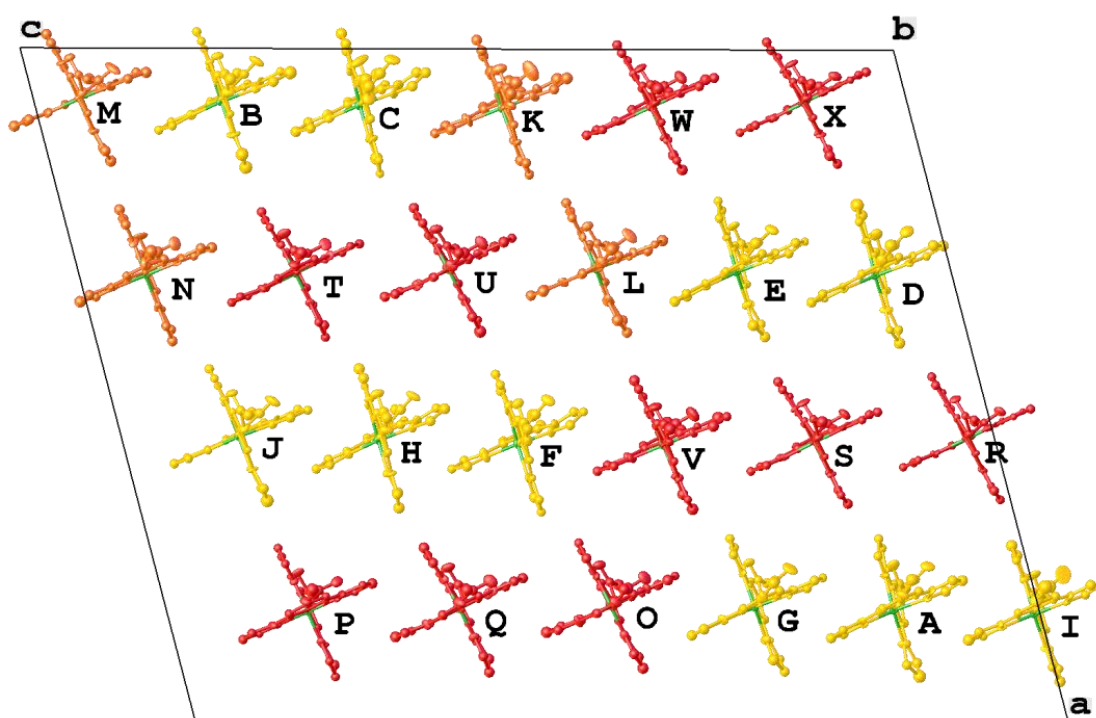


Figure 6.24: Asymmetric unit cell of **[44]B-Me₂CO α** at 120 K. Different spin states coloured as follow; HS (yellow), LS (red) and (orange) corresponds to intermediate states. Counter-anions and solvent are deleted for clarity. The letter labels for each unique molecule in the model are also shown.

The complexes are labelled alphabetically ordered according to their spin state, **A-J** are HS, **K-N** intermediate spin state and **O-X** low spin. The crystallographic parameters of one example of each subgroup are displayed in (Table 6-4). The Figure 6.25 displays a plot with the Jahn-Teller distortion parameters for the 24 unique complexes of **[44]B-Me₂CO α** at 130 K.

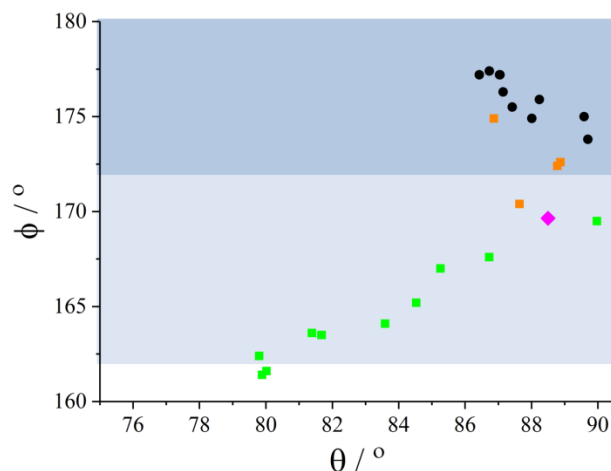


Figure 6.25: Molecular geometries of [44]B-Me₂CO α structure. The magenta diamond is the 240 K, while the 24 molecules of the 130 K structure are colour coded as; square green = HS, orange = intermediate state and circle black corresponds to LS complexes. High-spin [Fe(bpp)₂]²⁺ derivatives in the shaded parts of the graph commonly (dark blue) or rarely (pale blue) exhibit SCO on cooling. High-spin complexes in the unshaded part of the graph never exhibit SCO in the solid state.

Such symmetry breaking (unit cell volume of [44]B-Me₂CO α changes from 3688.95(14) to 42804(3) Å³) can be easily detected from the diffraction frames at different temperatures (Figure 6.26).

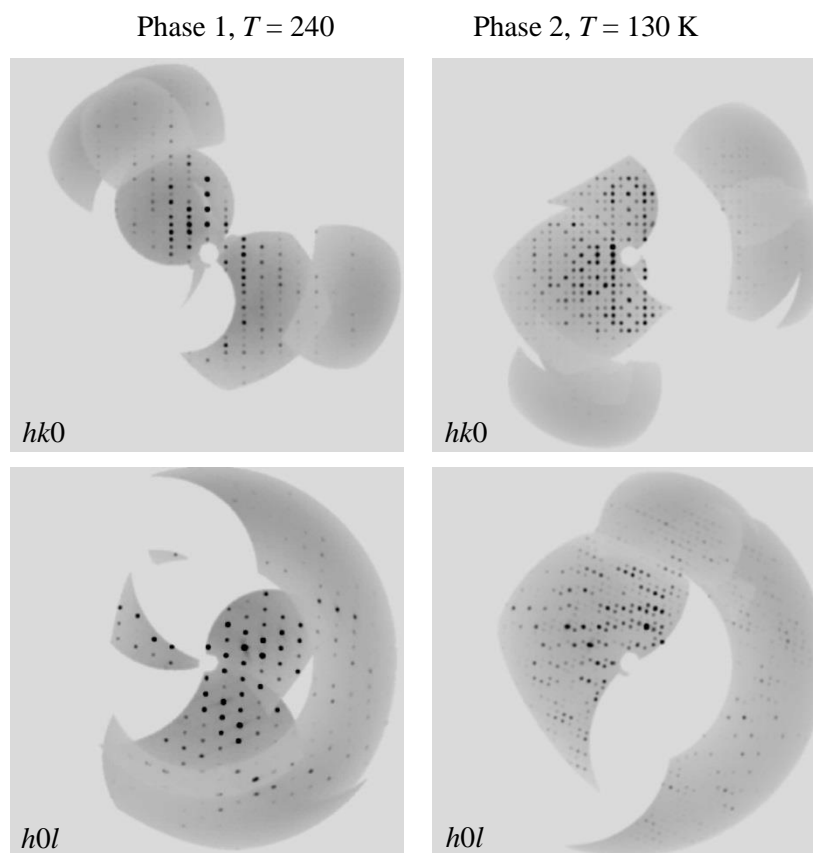


Figure 6.26 Diffraction images from [44]B-Me₂CO α in the $hk0$ (top) and $h0l$ (bottom) zones, showing the large number of additional diffraction spots afforded by the symmetry breaking.

Chapter 6

Single crystals of [44]C-Me₂CO and [44]B-Me₂CO α behaved like the bulk sample in agreement with the SQUID curves (Figure 6.27).

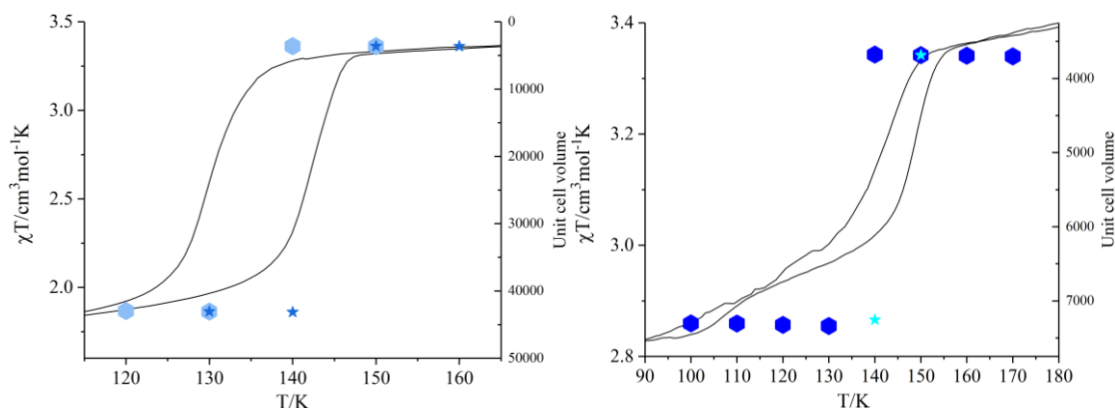


Figure 6.27: VT unit cell volumes of [44]B-Me₂CO α (left) and [44]C-Me₂CO (right) overlaying each SQUID curve (black line), large hexagons represent the cooling and stars warming data points.

[44]B-MeCN	α , 120 K	β , 125 K	β , 200 K
Fe-N[py]	2.1191(16), 2.1247(17)	1.893(8), 1.900(8)	2.110(5), 2.121(5)
Fe-N[pz]	2.1850(17) – 2.200(19)	1.960(8) – 1.988(9)	2.179(6) – 2.199(6)
V_{Oh}	12.414(7)	9.52 (3)	12.25(2)
Σ	155.7(2)	91.2(12)	156.3(8)
Θ	510.9(6)	292(3)	500(2)
ϕ	166.04(7)	174.5(4)	168.6(2)
θ	84.856(17)	86.87(8)	85.16(8)
[44]C-MeCN	160 K	180 K	
Fe-N[py]	1.921(5), 1.922(5)	2.116(4), 2.125(4)	
Fe-N[pz]	1.965(5) – 2.019(5)	2.170(5) – 2.199(4)	
V_{Oh}	9.803 (15)	12.236(16)	
Σ	94.6(7)	157.2(6)	
Θ	303.2(17)	502.7(14)	
ϕ	174.4(2)	167.91(16)	
θ	87.15(5)	84.69(5)	

Table 6-5: VT crystallographic parameters of [44]X-MeCN.

Chapter 6

Three solvates were also crystallized from acetonitrile (MeCN) which are $P\bar{1}$. [44]C-MeCN, containing one complex and one acetonitrile molecule in the asymmetric unit cell, exhibits an abrupt SCO with 12 K hysteretic loop, $T_{1/2\downarrow} = 159$ K, $T_{1/2\uparrow} = 171$ K (Figure 6.23, d)). In contrast, a mixture of two crystallographic phases are observed from crystallizations of [44]B-MeCN, α and β . The major pseudopolymorph α contained two molecules of MeCN in the asymmetric unit cell and it is HS at 120 K (Table 6-5). A small fraction of the material (β) is isostructural to [44]C-MeCN which only contains one MeCN molecule and also exhibits a hysteretic spin transition $T_{1/2\downarrow} = 182$ K, $T_{1/2\uparrow} = 190$ K (Figure 6.23, c)).

Single crystals of [44]C-MeCN and mixture of [44]B-MeCN α and β behaved like their bulk samples in agreement with the SQUID curves (Figure 6.28).

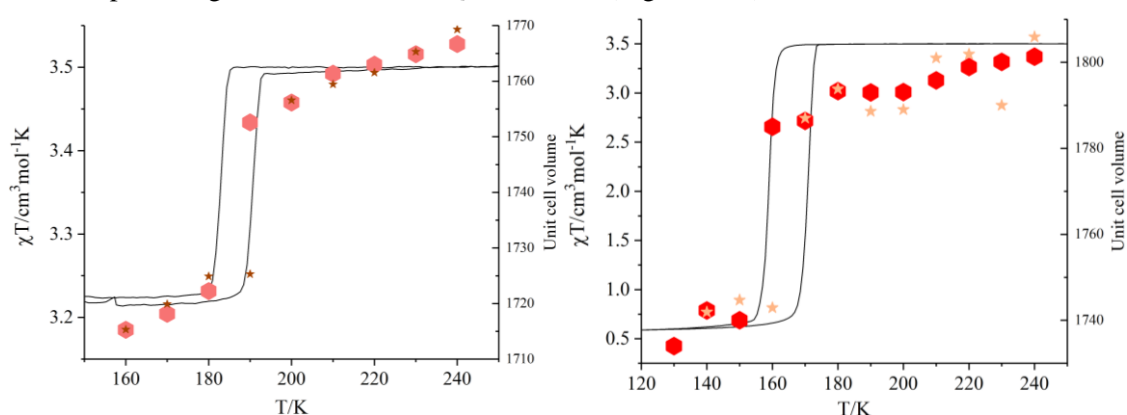


Figure 6.28: VT unit cell volumes of [44]B-MeCN β (left) and [44]C-MeCN (right) overlaying each SQUID curve (black line), large hexagons represent the cooling and stars warming data points.

The nitromethane solvates [44]X-MeNO₂ adopt the space group $Pbcn$. Both contain two molecules of MeNO₂ in the asymmetric unit and remain HS at all temperatures examined (Table 6-6).

120 K	[44]B-MeNO ₂	[44]C-MeNO ₂
Fe-N[pyridinyl]	2.1165(15)	2.1247(17)
Fe-N[pyrazolyl]	2.1771(16), 2.2056(16)	2.177(2), 2.206(2)
V_{Oh}	12.379(7)	12.412(9)
Σ	153.8(3)	153.9(4)
Θ	495.3(6)	499.2(7)
ϕ	176.47(9)	175.29(11)
θ	79.88(2)	79.49(3)

Table 6-6: Geometric parameters of [44]B-MeNO₂ molecules.

Chapter 6

Finally, the propionitrile (EtCN) complexes crystallized in the $P\bar{1}$ space group and are isostructural with [44]X-MeCN, but their SCO occurs in an abrupt two-step transition (Table 6-7).

[44]B-EtCN	160 K	187 K	200 K
Fe-N[py]	1.909(3), 1.910(4)	2.038(3), 2.056(3)	2.109(2), 2.121(3)
Fe-N[pz]	1.957(4) – 1.997(4)	2.081(3) – 2.113(3)	2.159(3) – 2.198(3)
V_{Oh}	9.608(12)	11.177(12)	12.055(11)
Σ	92.2(5)	134.8(5)	156.0(4)
Θ	299.9(14)	431.6(12)	499.3(9)
ϕ	173.79(18)	168.26(14)	165.78(11)
θ	87.55(4)	85.53(4)	84.57(3)
[44]C-EtCN	120 K		170 K, Molecule A
Fe-N[py]	1.905(5), 1.908(5)		1.896(5), 1.907(5)
Fe-N[pz]	1.969(5) – 1.994(5)		1.962(5) – 2.000(5)
V_{Oh}	9.655(15)		9.600(15)
Σ	89.6(8)		90.7(7)
Θ	292.4(17)		296.2(17)
ϕ	174.4(2)		173.4(2)
θ	88.12(5)		88.86(5)
[44]C-EtCN	170 K, Molecule A		240 K
Fe-N[py]	2.106(5), 2.121(5)		2.117(4), 2.131(4)
Fe-N[pz]	2.143(5) – 2.183(5)		2.178(4) – 2.206(5)
V_{Oh}	11.910(18)		12.140(15)
Σ	155.0(7)		158.7(6)
Θ	499.0(16)		510.6(13)
ϕ	165.19(19)		165.14(15)
θ	85.77(5)		84.48(5)

Table 6-7: VT crystallographic parameters of EtCN[44]C.

The asymmetric unit cell of [44]B-EtCN contains one propionitrile molecule and one HS iron(II) complex at room temperature. Between 192-180 K the complex is in an intermediate

spin state, below 180 K the complex is fully low spin. A narrow hysteresis loop of 2 K approximately is observed.

In contrast, [44]C-EtCN presents a better defined two-step transition with two wider hysteresis loops. The first hysteretic loop $T_{1/2\downarrow} = 180$ K, $T_{1/2\uparrow} = 185$ K spans 5 K and the second $T_{1/2\downarrow} = 145$ K, $T_{1/2\uparrow} = 156$ K spans 11 K. The asymmetric unit cell of [44]C-EtCN complex contains one propionitrile molecule and one HS iron(II) complex at room temperature. The intermediate step is prolonged between approximately 180-150 K, because a symmetry breaking is associated with the 50% SCO stage. Two crystallographically unique complex molecules are found in the intermediate phase, one being fully HS and the other fully LS (Table 6-7). Below 150 K the complex recovers its initial crystallographic symmetry, but is fully low spin.

Single crystals of [44]C-EtCN and mixture of [44]B-EtCN behave like their bulk samples, in agreement with the SQUID curves (Figure 6.29).

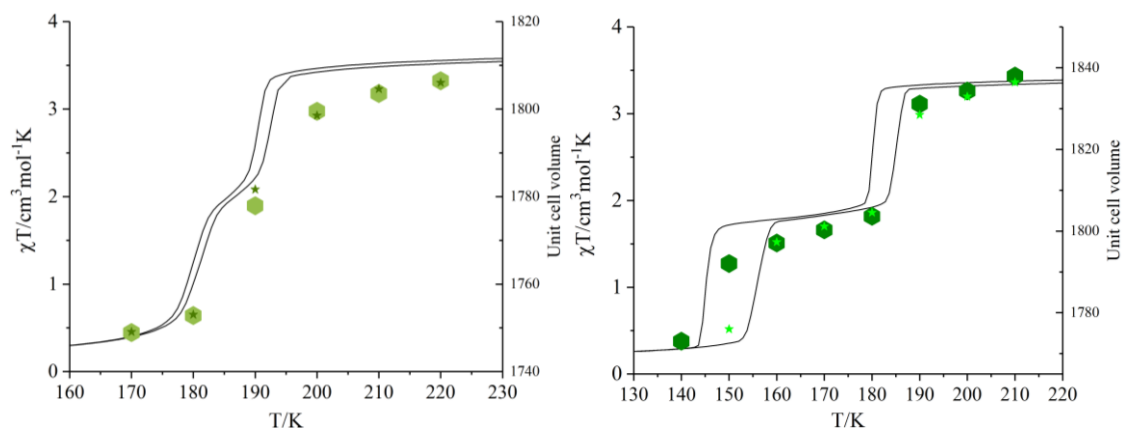


Figure 6.29: VT unit cell volumes of [44]B-EtCN (left) and [44]C-EtCN (right) overlaying each SQUID curve (black line), large hexagons represent the cooling and stars warming data points. In the right plot volume was normalized by dividing the expanded intermediate phase by two.

A 1:1 mixture of iron(II) perchlorate and tetrafluoroborate hydrates was reacted with (44) in propionitrile. [44]C+B-EtCN presents magnetic behaviour that is intermediate between [44]B-EtCN and [44]C-EtCN. A complex of (44) with iron(II) triflate was also crystallized from propionitrile, but in this case the compound remained HS upon cooling (Figure 6.30).

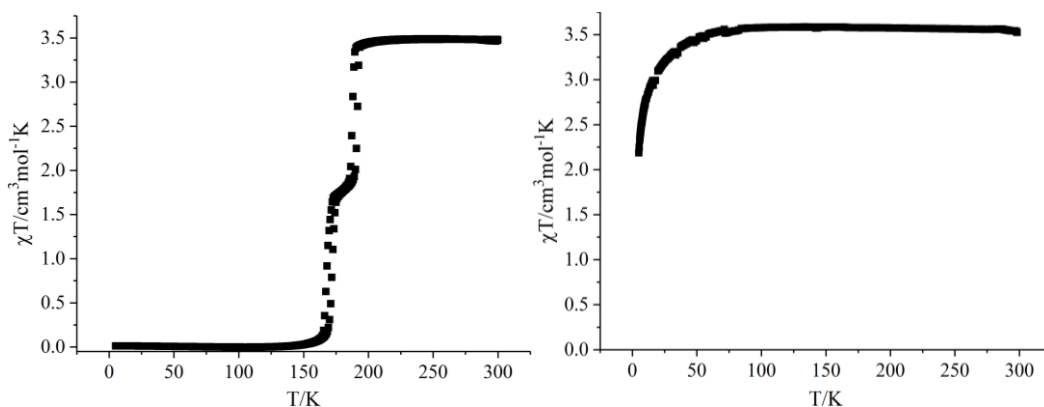


Figure 6.30: SQUID curves of [44]C+B-EtCN (left) and [44]triflate-EtCN (right).

Chapter 6

In attempts to obtain a solvent free material, other solvates were crystallized from dichloroethane, methanol or ethanol. These proved to be HS and uninteresting, and so were not fully characterized. All [44]X complexes in this work are plotted according to their Jahn-Teller distortion parameters (Figure 6.31).

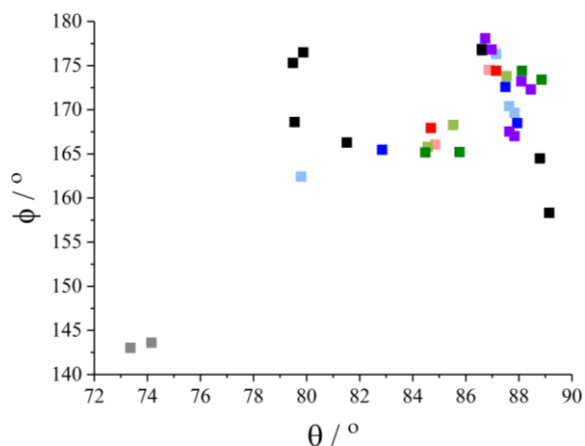


Figure 6.31: Jahn-Teller distortion parameters for all the crystal structures collected at different temperatures along the chapter, colour coded; red and pale red are [44]C and B-MeCN, green and pale green are [44]C and B-EtCN, blue and pale blue are [44]C and B-Me₂CO, black are all [44]X HS complexes, [40]X are violet and [42]X complexes the grey squares.

Magnetic susceptibility data from [44]B was also measured in solution by Evans Method (Figure 6.32). The lowest temperature data points could be considered to indicate the beginning of a spin transition.

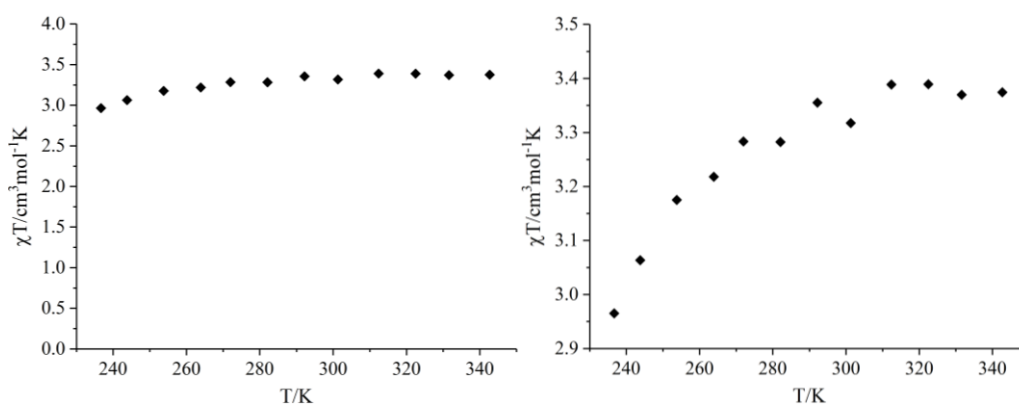


Figure 6.32: Magnetic susceptibility in solution of [44]B in acetonitrile. Expansion of the y axis of the same experiment is presented (right) for clarity.

Counter-anion	BF ₄ ⁻ , [44]B		ClO ₄ ⁻ , [44]C	
Acetone, Me ₂ CO	<i>P2₁/c</i>	Symmetry breaking SCO	<i>P2₁/c</i>	Symmetry breaking
Acetonitrile, MeCN	<i>P1̄ / P1̄</i>	High spin / SCO	<i>P1̄</i>	SCO
Nitromethane, MeNO ₂	<i>Pbcn</i>	High spin	<i>Pbcn</i>	High spin
Propionitrile, EtCN	<i>P1̄</i>	Two-step SCO	<i>P1̄</i>	Two-step SCO

Table 6-8: Summary of the solvate/counter-anions combinations crystallized of [44] during this work.

In summary, several combinations of iron(II) salts were crystallized from ligand (44) and some of them respond to a thermal stimulus. Even though the $T_{1/2}$ values of SCO-active [44] complexes were low, and they did not switch their spin state in solution, it was demonstrated that [43] complexes could potentially show interesting properties. Unfortunately, ligand (43) was synthesized in a low yield, and was not isolated in pure form due to solubility problems.

6.3 Conclusions

The target molecules; (36), (41) and (43) were not isolated in pure form, however their simplified analogue ligands (40), (42) and (44) were synthesized and fully characterized. The iron(II) complexes [40]X, [42]X and [44]X presented interesting magnetic properties which were measured by SQUID, Evans method and single crystal XRD.

The iron(II) complexes [40]X presented spin-crossover both in solid state and in fluid solution, as expected from other bpp-SR based iron(II) complexes. In contrast, [42]X were HS both in the liquid and the solid state. These complexes present a very low ϕ distortion parameter (ca 143 °), which has not been observed before for the bpp family of compounds.

Finally, several solvates were crystallized of the tetrafluoroborate and perchlorate salts of [44]. Different solvates behave differently and crystallized in different space groups, while both salts of the same solvate are isostructural and behave similarly. The size of the counter-anion together with the electronic effects of their interaction with the hydrogen of the amide in the 4-position of the pyridine define $T_{1/2}$ when SCO behavior is observed. The results however suggest that the size of the solvent molecule is more important in terms of the shape of the SCO curve. The changes in the crystal packing due to the addition of a solvent molecule of the complexes [44]X studied in this work stop the SCO activity. [44]X was HS in solution above the melting point of acetonitrile, however the beginning of transition could be recognized at low temperatures.

6.4 Bibliography

1. Rotaru, A.; Dugay, J.; Tan, R. P.; Gural'skiy, I. A.; Salmon, L.; Demont, P.; Carrey, J.; Molnár, G.; Respaud, M.; Bousseksou, A., Nano-electromanipulation of spin crossover nanorods: towards switchable nanoelectronic devices. *Adv Mater* **2013**, 25.
2. (a) White, N. G.; Feltham, H. L. C.; Gandolfi, C.; Albrecht, M.; Brooker, S., Towards Langmuir–Blodgett films of magnetically interesting materials: solution equilibria in amphiphilic iron(ii) complexes of a triazole-containing ligand. *Dalton Transactions* **2010**, 39 (15), 3751-3758; (b) Kitchen, J. A.; White, N. G.; Gandolfi, C.; Albrecht, M.; Jameson, G. N.

Chapter 6

L.; Tallon, J. L.; Brooker, S., Room-temperature spin crossover and Langmuir–Blodgett film formation of an iron(ii) triazole complex featuring a long alkyl chain substituent: the tail that wags the dog. *Chemical Communications* **2010**, 46 (35), 6464–6466.

3. Shalabaeva, V.; Rat, S.; Manrique-Juarez, M. D.; Bas, A.-C.; Vendier, L.; Salmon, L.; Molnár, G.; Bousseksou, A., Vacuum deposition of high-quality thin films displaying spin transition near room temperature. *Journal of Materials Chemistry C* **2017**, 5 (18), 4419–4425.

4. Poneti, G.; Poggini, L.; Mannini, M.; Cortigiani, B.; Sorace, L.; Otero, E.; Sainctavit, P.; Magnani, A.; Sessoli, R.; Dei, A., Thermal and optical control of electronic states in a single layer of switchable paramagnetic molecules. *Chemical Science* **2015**, 6 (4), 2268–2274.

5. Quintero, C. M.; Gural'skiy, I. y. A.; Salmon, L.; Molnár, G.; Bergaud, C.; Bousseksou, A., Soft lithographic patterning of spin crossover complexes. Part 1: fluorescent detection of the spin transition in single nano-objects. *Journal of Materials Chemistry* **2012**, 22 (9), 3745–3751.

6. Capel Berdiell, I.; Kulmaczewski, R.; Halcrow, M. A., Iron(II) Complexes of 2,4-Dipyrazolyl-1,3,5-triazine Derivatives—The Influence of Ligand Geometry on Metal Ion Spin State. *Inorganic Chemistry* **2017**, 56 (15), 8817–8828.

7. Love, J. C.; Estroff, L. A.; Kriebel, J. K.; Nuzzo, R. G.; Whitesides, G. M., Self-Assembled Monolayers of Thiolates on Metals as a Form of Nanotechnology. *Chemical Reviews* **2005**, 105 (4), 1103–1170.

8. (a) Stock, P.; Erbe, A.; Buck, M.; Wiedemann, D.; Ménard, H.; Hörner, G.; Grohmann, A., Thiocyanate Anchors for Salt-like Iron(II) Complexes on Au(111): Promises and Caveats. In *Zeitschrift für Naturforschung B*, 2014; Vol. 69, p 1164; (b) Devid, E. J.; Martinho, P. N.; Kamalakar, M. V.; Prendergast, Ú.; Kübel, C.; Lemma, T.; Dayen, J.-F.; Keyes, T. E.; Doudin, B.; Ruben, M.; van der Molen, S. J., The influence of molecular mobility on the properties of networks of gold nanoparticles and organic ligands. *Beilstein J Nanotechnol* **2014**, 5, 1664–1674; (c) Liu, K.; Li, G.; Wang, X.; Wang, F., Length Dependence of Electron Conduction for Oligo(1,4-phenylene ethynylene)s: A Conductive Probe-Atomic Force Microscopy Investigation. *The Journal of Physical Chemistry C* **2008**, 112 (11), 4342–4349.

9. (a) Pukenas, L.; Benn, F.; Lovell, E.; Santoro, A.; Kershaw Cook, L. J.; Halcrow, M. A.; Evans, S. D., Bead-like structures and self-assembled monolayers from 2,6-dipyrazolylpyridines and their iron(ii) complexes. *Journal of Materials Chemistry C* **2015**, 3 (30), 7890–7896; (b) Devid, E. J.; Martinho, P. N.; Kamalakar, M. V.; Šalitroš, I.; Prendergast, Ú.; Dayen, J.-F.; Meded, V.; Lemma, T.; González-Prieto, R.; Evers, F.; Keyes, T. E.; Ruben, M.; Doudin, B.; van der Molen, S. J., Spin transition in arrays of gold nanoparticles and spin crossover molecules. *ACS Nano* **2015**, 9 (4), 4496–4507; (c) Shen, C.; Haryono, M.; Grohmann, A.; Buck, M.; Weidner, T.; Ballav, N.; Zharnikov, M., Self-Assembled Monolayers of a Bis(pyrazol-1-yl)pyridine-Substituted Thiol on Au(111). *Langmuir* **2008**, 24 (22), 12883–12891.

Chapter 6

10. (a) Sakaguchi, I.; Fukasawa, T.; Fujimoto, K.; Inouye, M., Immobilization of Crosslinked Peptides that Possess High Helical Contents and Their Binding to Target DNAs on Au Surfaces. *Chemistry Letters* **2018**, *47* (3), 365-368; (b) Pukenas, L.; Prompinit, P.; Nishitha, B.; Tate, D. J.; Singh, N. D. P.; Wälti, C.; Evans, S. D.; Bushby, R. J., Soft Ultraviolet (UV) Photopatterning and Metallization of Self-Assembled Monolayers (SAMs) Formed from the Lipoic Acid Ester of α -Hydroxy-1-acetylpyrene: The Generality of Acid-Catalyzed Removal of Thiol-on-Gold SAMs using Soft UV Light. *ACS Applied Materials & Interfaces* **2017**, *9* (21), 18388-18397; (c) Kyllönen, L. E. P.; Chinuswamy, V.; Maffeo, D.; Kefalas, E. T.; Haider, J. M.; Pikramenou, Z.; Mavridis, I. M.; Yannakopoulou, K.; Glezos, N., Electronic transport between Au surface and scanning tunnelling microscope tip via a multipodal cyclodextrin host–metal–guest supramolecular system. *Journal of Physical Organic Chemistry* **2012**, *25* (3), 198-206.
11. (a) Feltham, H. L. C.; Dumas, C.; Mannini, M.; Otero, E.; Sainctavit, P.; Sessoli, R.; Meledandri, C. J.; Brooker, S., Proof of Principle: Immobilisation of Robust Cu^{II}3Tb^{III}-Macrocycles on Small, Suitably Pre-functionalised Gold Nanoparticles. *Chemistry – A European Journal* **2017**, *23* (11), 2517-2521; (b) Nag, R.; Kandi, R.; Rao, C. P., Host–Guest Complexation of a Lipoic Acid Conjugate of Calix[4]arene with Pyridinium Moiety on Gold Nanorods for Mitochondrial Tracking Followed by Cytotoxicity in HeLa Cells under 633 nm Laser Light. *ACS Sustainable Chemistry & Engineering* **2018**, *6* (7), 8882-8890.
12. Zhang, C.; Palui, G.; Zeng, B.; Zhan, N.; Chen, B.; Mattoussi, H., Non-Invasive Characterization of the Organic Coating of Biocompatible Quantum Dots Using Nuclear Magnetic Resonance Spectroscopy. *Chemistry of Materials* **2018**, *30* (10), 3454-3466.
13. (a) Kershaw Cook, L. J.; Shepherd, H. J.; Comyn, T. P.; Baldé, C.; Cespedes, O.; Chastanet, G.; Halcrow, M. A., Decoupled spin crossover and structural phase transition in a molecular iron(II) complex. *Chemistry – A European Journal* **2015**, *21* (12), 4805-4816; (b) Kershaw Cook, L. J.; Kulmaczewski, R.; Barrett, S. A.; Halcrow, M. A., Iron(II) complexes of 4-sulfanyl-, 4-sulfinyl- and 4-sulfonyl-2,6-dipyrazolylpyridine ligands. A subtle interplay between spin-crossover and crystallographic phase changes. *Inorganic Chemistry Frontiers* **2015**, *2* (7), 662-670; (c) Kershaw Cook, L. J.; Fisher, J.; Harding, L. P.; Halcrow, M. A., An iron(ii) spin-crossover metallacycle from a back-to-back bis-[dipyrazolylpyridine]. *Dalton Transactions* **2015**, *44* (20), 9417-9425; (d) Cook, L. J. K.; Kulmaczewski, R.; Cespedes, O.; Halcrow, M. A., Different spin-state behaviors in isostructural solvates of a molecular iron(II) complex. *Chemistry – A European Journal* **2016**, *22* (5), 1789-1799.
14. Jordan, F.; Kudzin, Z.; Witczak, Z.; Hoops, P., Nuclear magnetic resonance determination of the site of acylation of the tautomeric nucleophile 4(1H)-pyridinethione. *The Journal of Organic Chemistry* **1986**, *51* (4), 571-573.
15. Halcrow, M. A., Structure: function relationships in molecular spin-crossover complexes. *Chemical Society Reviews* **2011**, *40* (7), 4119-4142.

Chapter 6

16. Kershaw Cook, L. J.; Kulmaczewski, R.; Mohammed, R.; Dudley, S.; Barrett, S. A.; Little, M. A.; Deeth, R. J.; Halcrow, M. A., A Unified Treatment of the Relationship Between Ligand Substituents and Spin State in a Family of Iron(II) Complexes. *Angewandte Chemie International Edition* **2016**, *55* (13), 4327-4331.
17. Capel Berdiell, I.; Kulmaczewski, R.; Cespedes, O.; Halcrow, M. A., An Incomplete Spin Transition Associated with a $Z'=1 \rightarrow Z'=24$ Crystallographic Symmetry Breaking. *Chemistry – A European Journal* **2018**, *24* (20), 5055-5059.

Chapter 7 – Coating Surfaces with SAMs of Spin-Crossover Materials.

7.1 Introduction

Interest in the charge transport properties of SCO compounds has increased in the last few years for the integration of those compounds into devices as thin films¹, nanoparticles² or single molecules³. In this context, the deposition of SCO molecules onto surfaces has stimulated a lot of research in recent years⁴. Most of these have focused on ultrahigh vacuum deposition (UHV) of neutral, thermally evaporable SCO complexes⁵ (Figure 7.1). Submonolayers of a positively charged Fe(III) SCO complex obtained by sublimation have only been reported very recently⁶.

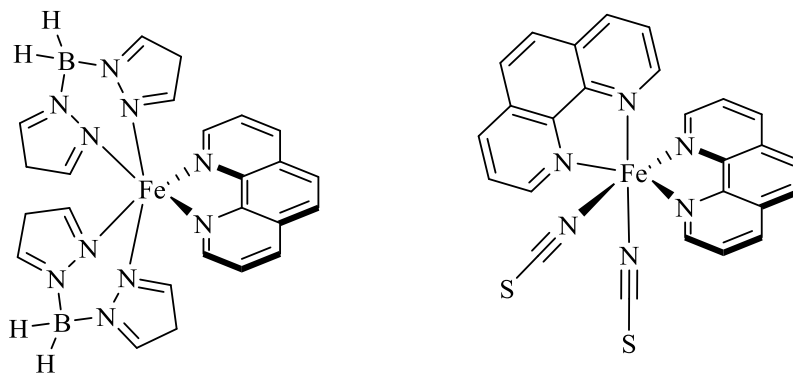


Figure 7.1: Examples of neutral SCO iron(II) complexes deposited in surfaces described in the literature⁷.

X-ray absorption (XAS), Scanning Tunneling Microscopy, and other techniques have shown that interactions between the surface and those evaporated molecules can decompose the complexes or change their SCO transition considerably with respect to that of the bulk⁸. For example, while the spin state of [Fe(bpz)₂phen] molecules in contact with a gold surface remain blocked, a second molecular layer deposited on top of the first one could be reversibly switched with an electric field⁹. Molecules of [Fe(phen)₂(NCS)₂] can only be individually switched between the HS and LS states using electric fields, when the molecules are not directly connected to a copper surface, but interact through an insulating thin layer^{3a}. The decomposition of [Fe(bpz)₂L] complexes was suppressed by deposition on bismuth, which has much lower conductivity¹⁰. In an analogous way, the replacement of the gold substrate by highly oriented pyrolytic graphite (HOPG) enabled thermal-induced and light-induced SCO of a submonolayer of [Fe(bpz)₂phen], even for molecules in direct contact with the solid surface¹¹.

Chapter 7

In contrast to UHV deposition, solution-based methods towards SCO thin films remain almost unexplored. The main advantage of this method is the simplicity. The monolayer is formed by immersion of the substrate into the complex solution, which also gives the option to use charged complexes like $[\text{Fe}(\text{bpp})_2]^{2+}$. However the method usually requires chemical functionalization of the SCO complexes with suitable anchoring groups capable of specifically interacting with the surface¹². (Figure 7.2). This method is also not so clean as sublimation, because of the involvement of solvent which must be removed from the thin film after its formation.

Previous results with the $[\text{Fe}(\text{bpp-R})_2]^{2+}$ family of complexes have afforded “chains-of-beads” self-assemblies by drop-casting solutions of the complex on HOPG and gold, giving rise to a spin-state interconversion detected by current-imaging tunneling spectroscopy (CITS)¹³.

The grafting of molecules functionalized with carboxylic acid groups onto metal-oxide surfaces is a well-known process¹⁴. Prior to my mobility visit to ICMol in Valencia, with Dr Miguel Clemente, a similar investigation was carried out by them, where cobalt(II) and iron(II) complexes containing the bppCOOH ligand¹⁵ were deposited onto metal-oxide surfaces by dipping the substrates into $[\text{Fe}(\text{bppCOOH})_2]^{2+}$ solution. Their results suggested that a SAM of the complex was formed, but no evidence of SCO was found (this study has not yet been published).

Based on these ideas, and after the unsuccessful attempts discussed in chapter 6, we developed new ligands containing a longer spacer between the anchor group and the bpp heterocyclic core. Deposition of new iron(II) complexes solutions onto gold and metal-oxide surfaces to give self-assembled monolayers (SAMs) of the positively charged dithiolane-functionalized and carboxyl-functionalized $[\text{Fe}(\text{bpp-R})_2]^{2+}$ SCO complexes, was investigated at ICMol in Valencia (Spain) funded by a RSC Researcher Mobility Grant.

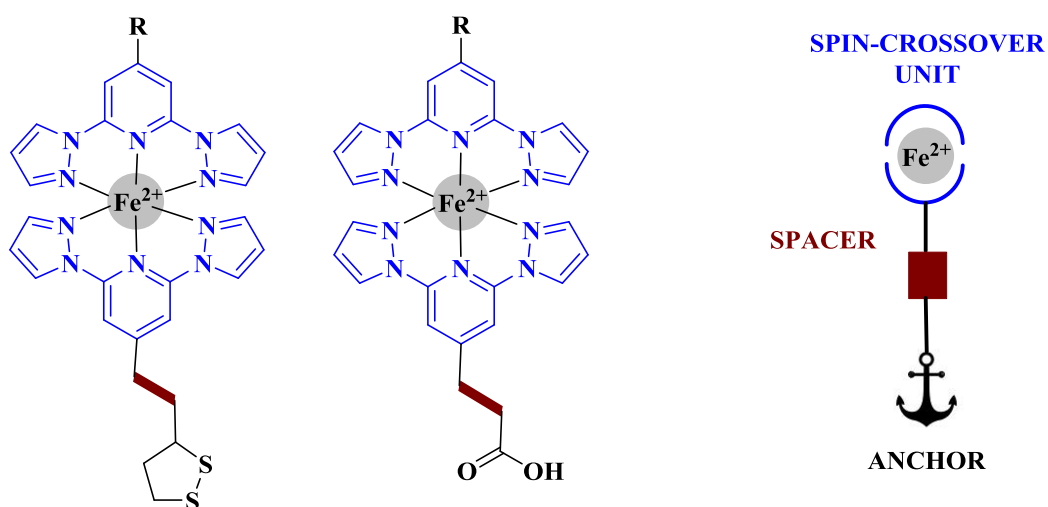


Figure 7.2: $[\text{Fe}(\text{bpp-R})_2]^{2+}$ complexes with the anchor types studied here.

7.2 Results and discussion

7.2.1 Synthesis and characterization of the 1,2-dithiolane tethered ligands and their iron(II) complexes

The first tethered ligand was synthesized from the aminomethyl-bpp precursor (**45**), which was first obtained by Ahmed Ahmed during his Masters by Research degree (Figure 7.3).

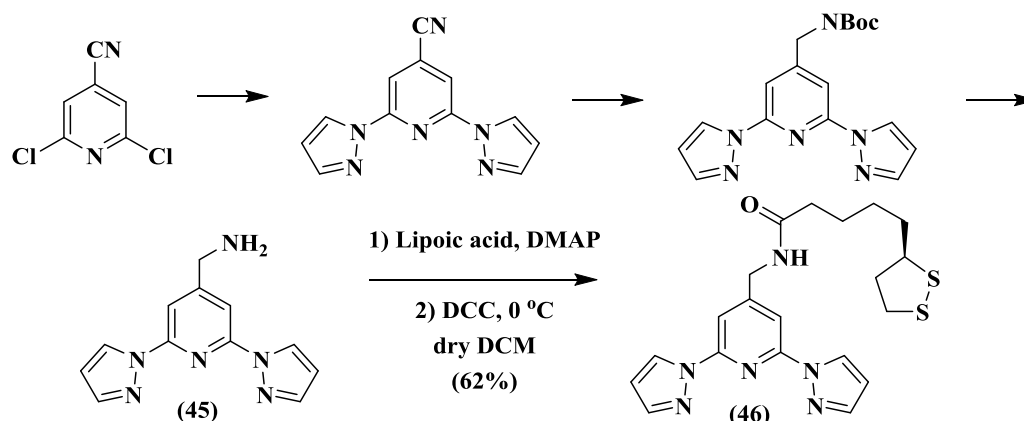


Figure 7.3: Synthetic scheme of ligand (**46**), $\text{bppCH}_2\text{NH}_2$ (**45**) was synthesized by Ahmed.

Unfortunately the synthesis of (**45**) was tedious and low yielding. Moreover, (**45**) easily oxidizes to the amide (**47**) under non-dry conditions (Figure 7.4).

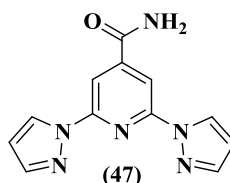


Figure 7.4: The major product obtained during the synthesis of (**45**).

Although (**46**) was fully characterized, it was discarded for the reasons stated above which limited the scale-up of its synthesis. It was also considered not worth pursuing because $[\text{46}]\text{C}$ did not present $T_{1/2}$ close to room temperature (Figure 7.7).

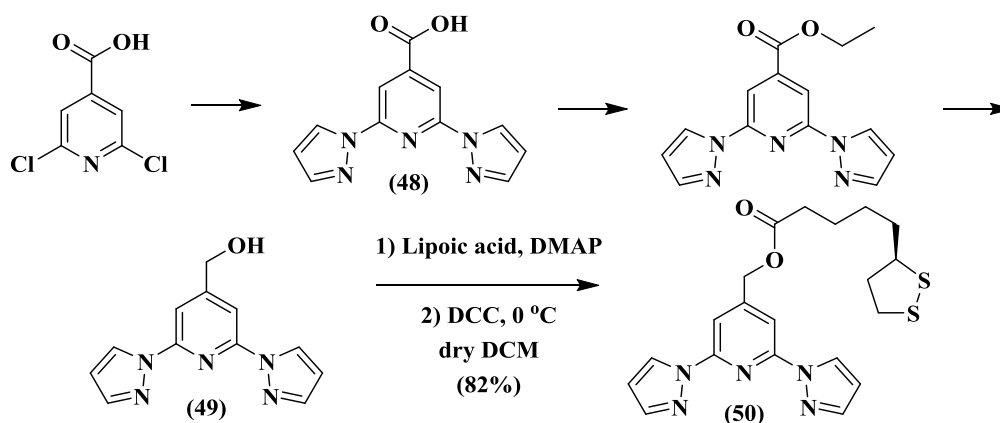


Figure 7.5: Synthetic scheme of ligand (**50**), bppCH_2OH (**49**) was synthesized following the reported procedure¹⁶.

The analogous reduction of bppCOOH (**48**), which was reported before,¹⁶ entails straightforward steps with high yields (Figure 7.5). Hence, (**50**) was the first tethered ligand whose iron(II) complex was fully characterized. The DCC coupling method is widely-known for activating carboxylic acids in the synthesis of amides¹⁷ or esters¹⁸. It worked well in presence of DMAP as base for both reactions in Figure 7.3 and Figure 7.5. (**50**) crystallized in the monoclinic space group C_2 (Figure 7.6).

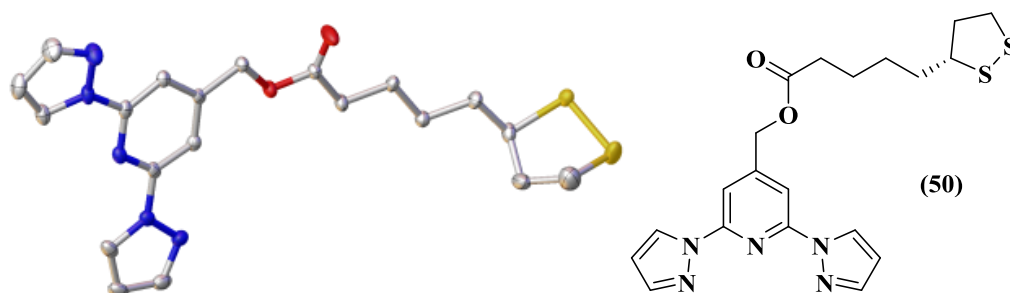


Figure 7.6: Crystal structure of (**50**). Hydrogen atoms were omitted for clarity.

In principle, once complexes are deposited on the surfaces they will not be influenced by any lattice effects. Hence, their spin state behaviour should be more similar to their solution properties than in the solid state. Magnetic susceptibility of the complexes [**46**]C and [**50**]C was calculated by EVANS method, from data points taken in 10 K increments from acetonitrile solutions (Figure 7.7).

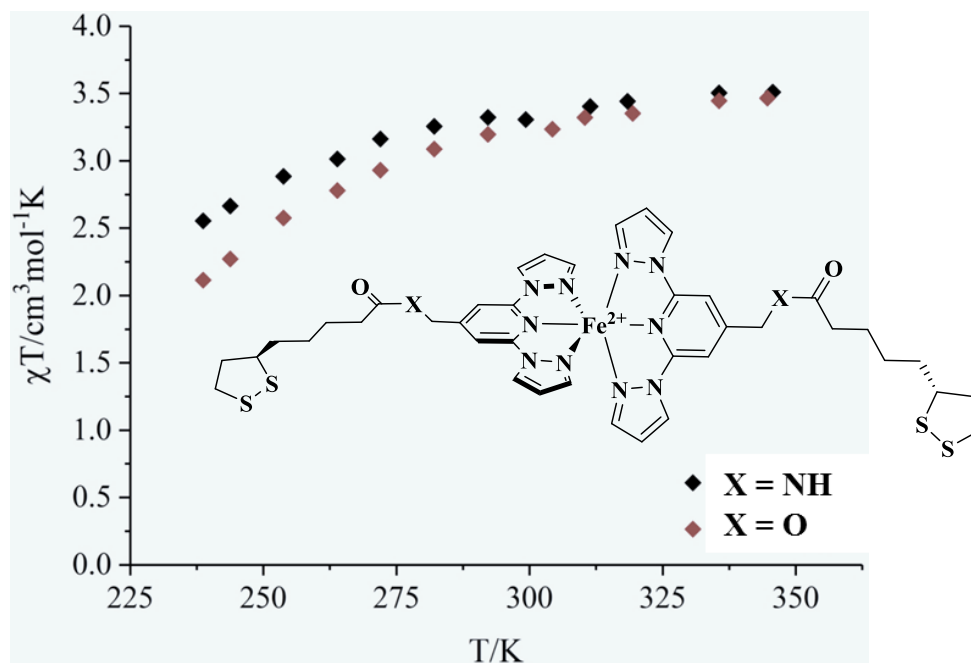


Figure 7.7: Evans method of [**46**] and [**50**].

The beginning of a spin transition was observed close to melting point of acetonitrile. The $T_{1/2}$ values of these transitions were too low for our purposes. Hence, more electron-withdrawing substituents at the 4-position of the pyridyl ring were needed, to raise $T_{1/2}$.¹⁹ The following ligands, derived directly from bppCOOH (**48**),²⁰ were proposed (Figure 7.8).

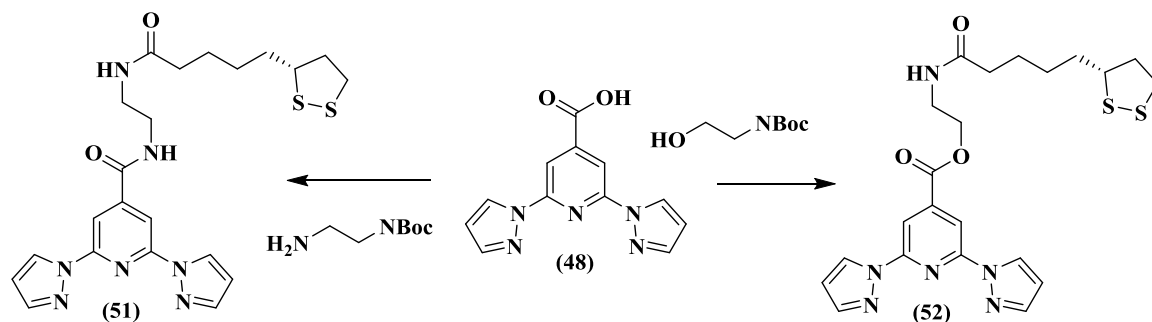


Figure 7.8: Designing accessible ligands (51) and (52) with EWG in the 4-position of the pyridyl ring.

Since the DCC coupling worked very well, a new family of ligands based on that chemistry was pursued, with ester or amide links between the tether group and the bpp backbone. The synthetic steps for (51) are presented in (Figure 7.9).

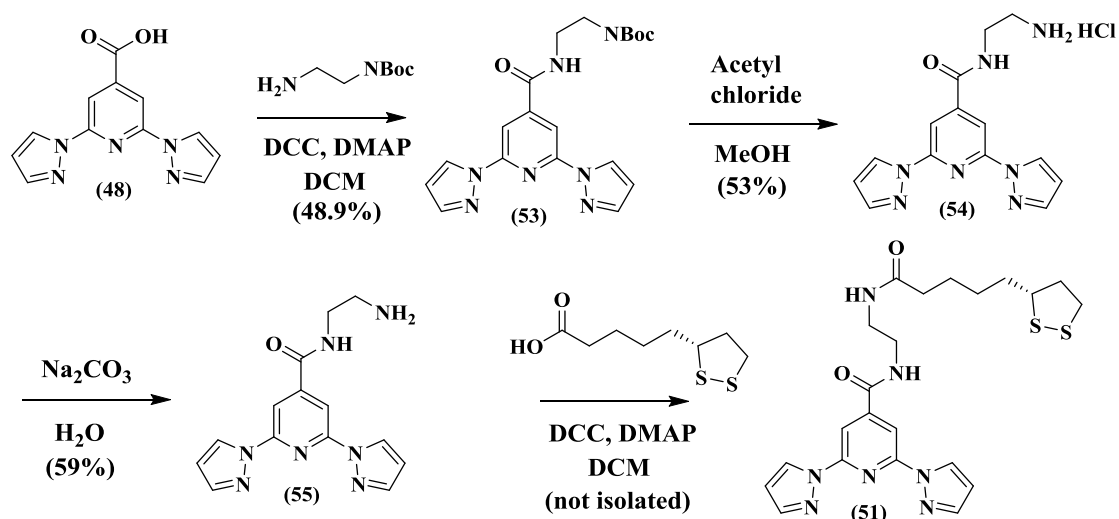


Figure 7.9: Synthetic scheme of ligand (51).

All steps were performed in moderate yields. The final ligand (51), containing two amide groups was extremely insoluble, and was not isolated in pure form by NMR or ESMS.

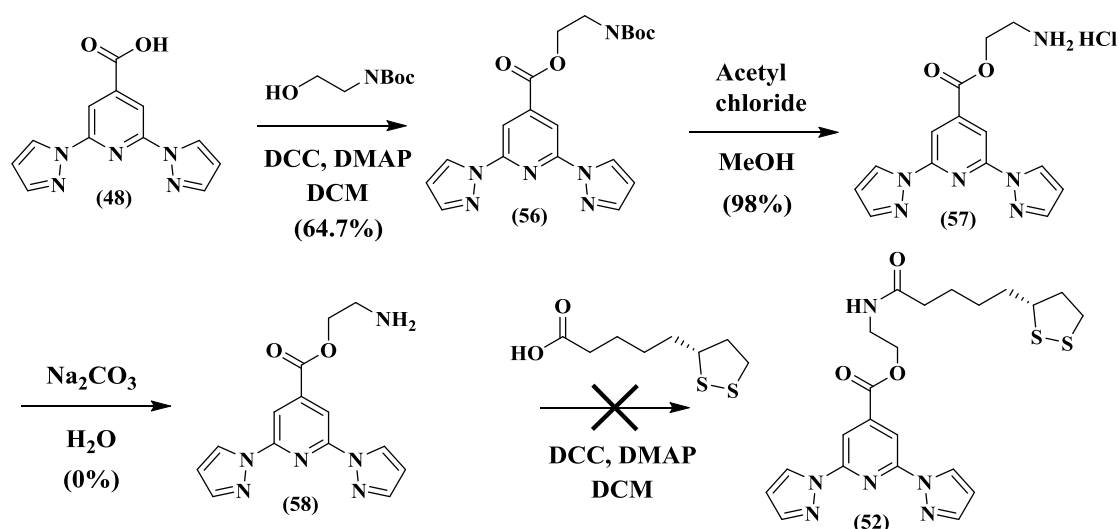


Figure 7.10: Synthetic scheme of ligand (52).

Chapter 7

During the synthesis of the second ligand (**52**), intermediate (**57**) was not soluble in water at room temperature, so DMSO was added and the mixture was heated to 100 °C, where the salt finally dissolved completely. However, after neutralization, ^1H NMR of (**58**) indicated that an isomerization had occurred (Figure 7.11). This was later confirmed by the crystal structure of (**60**) (Figure 7.12).

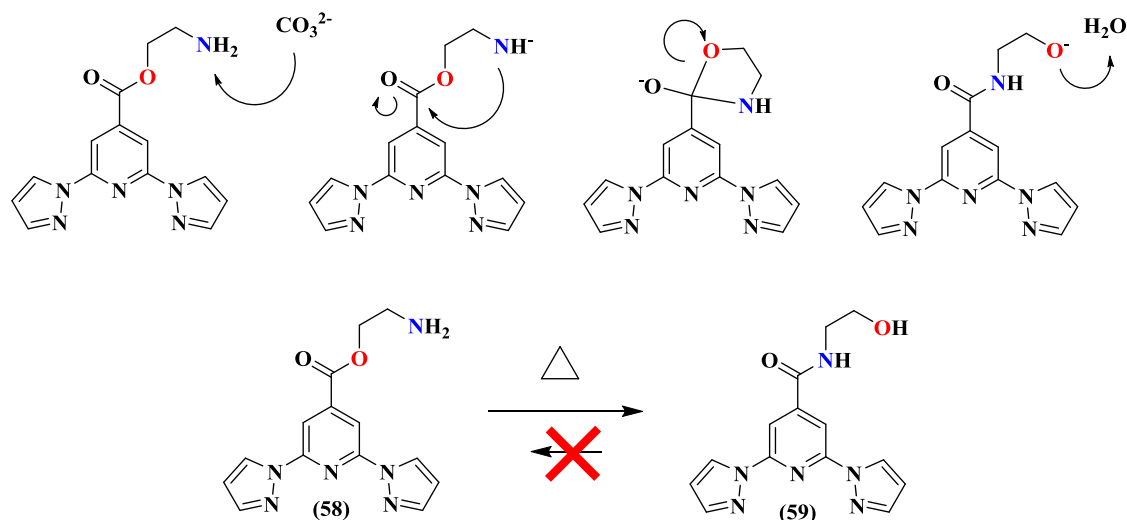


Figure 7.11: Mechanism of the irreversible isomerization from (**58**) to (**59**).

The equilibrium was shifted to the right because amides are thermodynamically more stable than esters and thus less reactive. Ligand (**60**), a regioisomer of (**52**), was successfully obtained upon DCC coupling again of (R)-lipoic acid to (**59**), and it crystallized in the orthorhombic $P2_12_12_1$ space group (Figure 7.12).

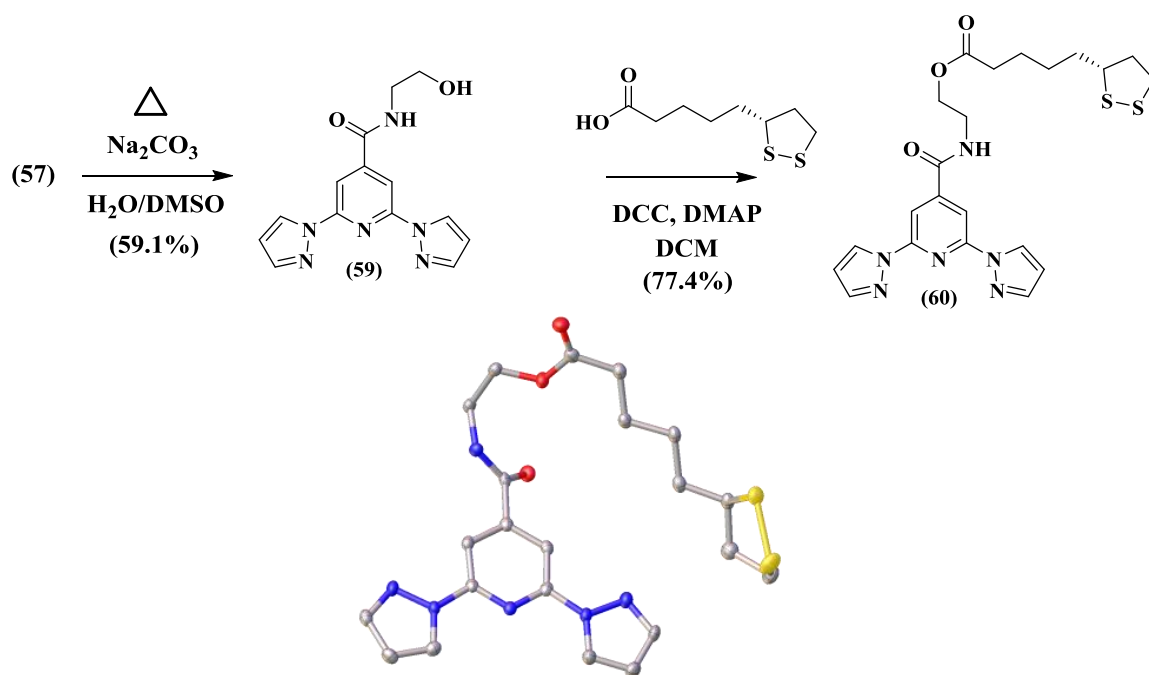


Figure 7.12: Synthetic scheme and crystal structure of (**60**). Hydrogen atoms were omitted for clarity.

Chapter 7

(61) was synthesized from (48) by an esterification using ethylene glycol as solvent (Figure 7.5)¹⁶. The resultant dithiolane derivative (62) crystallized in the monoclinic $P2_1$ space group (Figure 7.13).

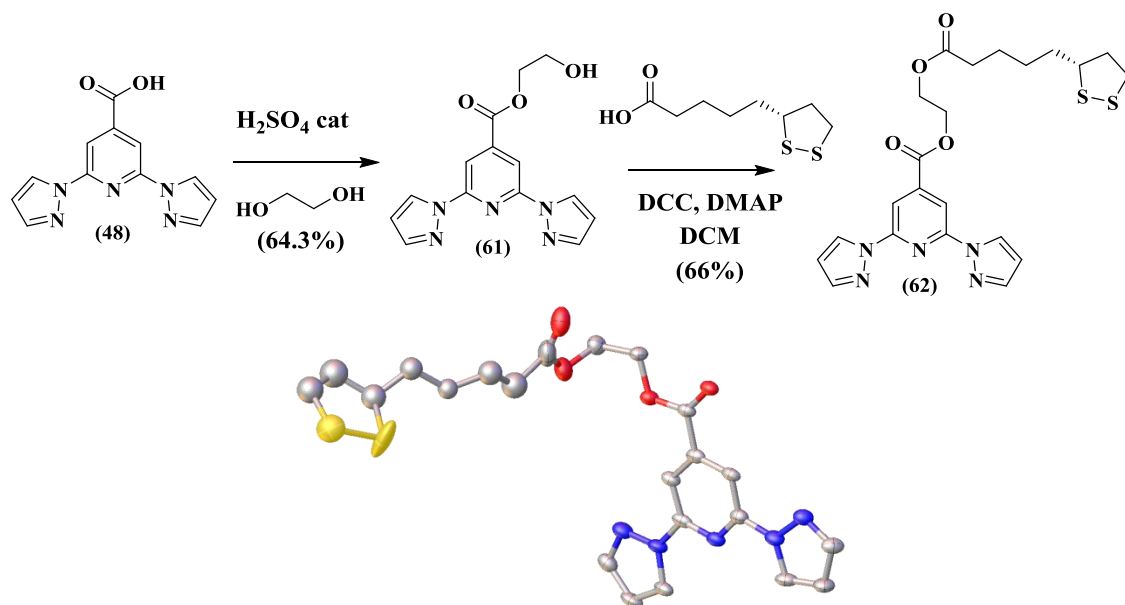


Figure 7.13: Synthetic scheme and crystal structure of (62). Hydrogen atoms were omitted and only one occupancy of the disordered alkyl chain shown for clarity.

A different approach, similar to ligand (42) (Chapter 6), was adopted for (66). Aromatic nucleophilic substitution reactions on trifluoropyridine yielded precursor (65) containing sulphur in the 4-position of the pyridyl ring and a primary amine available for attaching lipoic acid. (Figure 7.14).

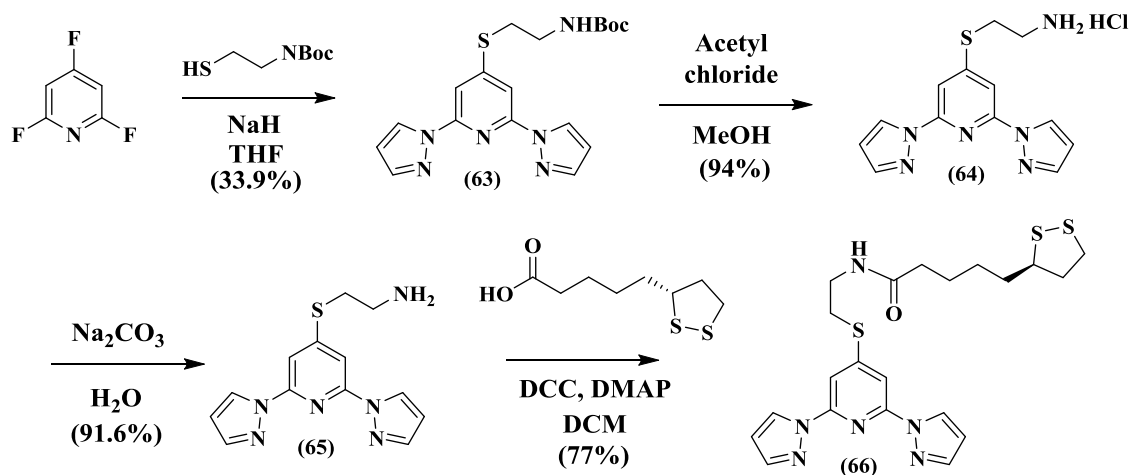


Figure 7.14: Synthetic scheme and crystal structure of (66).

In summary, (50), (60), (62), and (66) containing 1,2-dithiolane anchor groups were synthesized and fully characterized. Each ligand has a different linker at the 4-position of the pyridyl ring (-CH₂OR, -COOR, -CONR and -SR respectively). Thus, different SCO behaviour is expected for [50]C, [60]C, [62]C and [66]C (Figure 7.15).

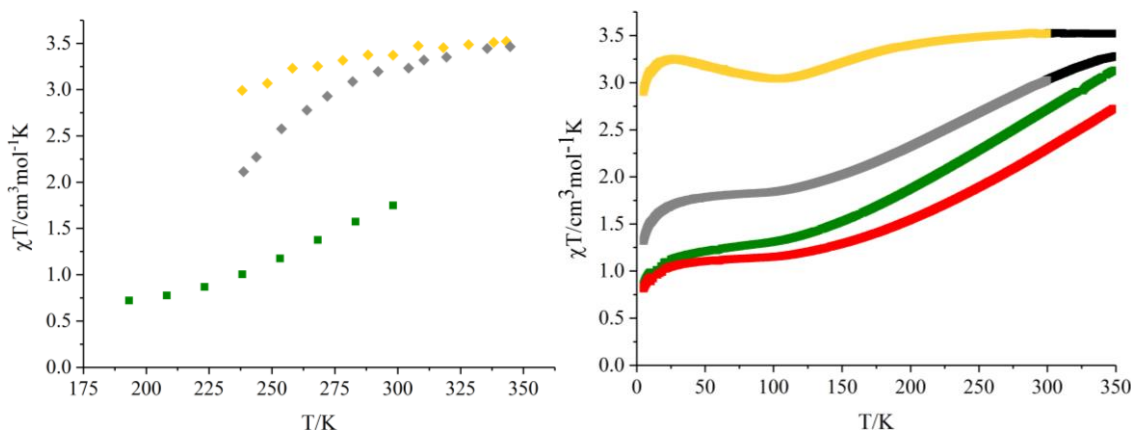


Figure 7.15: Evans method and SQUID data of [50]C (grey, MeCN), [60]C (green, acetone), [62]C (red) and [66]C (yellow, MeCN). SQUID curves of [50] and [66] were collected 300-5 K hence a simulation for the 350-300 K region is represented in black.

Complexes [60] and [62] stabilized the LS state compared to [50] as expected¹⁹. However the HS nature of [66] was unexpected.

7.2.2 Synthesis and characterization of carboxylic acid tethered ligands and their iron(II) complexes

The following ligands containing carboxylic acid tether groups were obtained (

Figure 7.16).

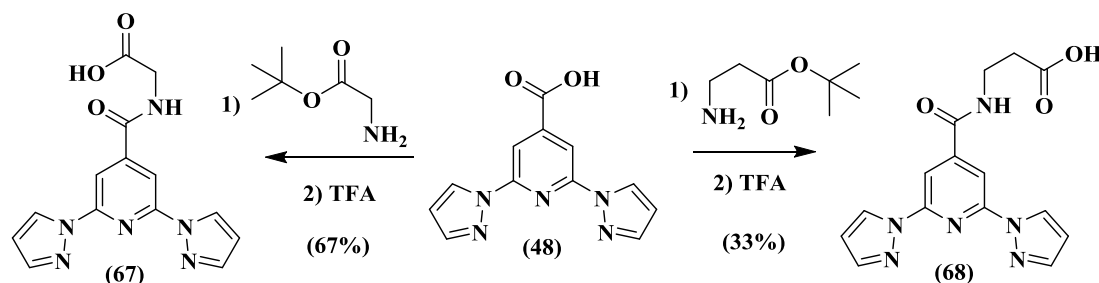


Figure 7.16: Designing accessible ligands (67) and (68) with EWG in the 4-position of the pyridyl ring.

In this case both ligands contain amide linkers between the bpp framework and the tether group. Therefore, similar SCO properties were expected for their iron(II) complexes. DCC coupling of bppCOOH was again used with amino-acids protected with *t*-butyl ester groups which can be easily removed with a trifluoroacetic acid treatment²¹.

Both iron(II) complexes crystallized from acetonitrile solutions by ether diffusion. Two polymorphs were observed of [67]C which crystallized in the monoclinic $P2_1/n$ space group as large red plates (α) and in the triclinic $P\bar{1}$ space group as thin red needles (β) (Figure 7.17). Both polymorphs contain one molecule of MeCN in the lattice, the main difference between them being that the [67] β C structure is heavily disordered. Crystals of [67] β C were

Chapter 7

considerably smaller than polymorph α , hence a VT study was only performed on $[67]\alpha\text{C}$ (Figure 7.18).

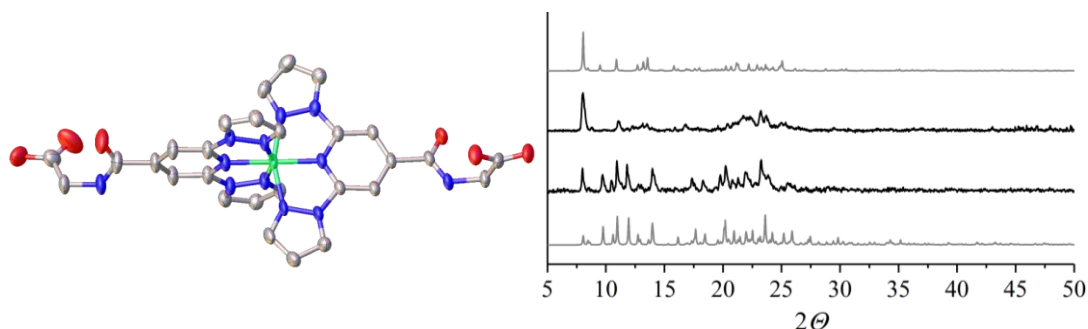


Figure 7.17: Crystal structure of $[67]\alpha\text{C}$ and powder patterns of both polymorphs (bottom α and top β). Hydrogen atoms and counter-anions were omitted for clarity. The colour assignment in the plot is black for the experimental and grey for the simulated XRD.

VT unit cells every 20 K (Figure 7.18), and full data sets at 125, 280 and 340 K, were collected for $[67]\alpha\text{C}$ (Table 7-1).

	$[67]\alpha\text{C}$ (125 K)	$[67]\alpha\text{C}$ (280 K)	$[67]\alpha\text{C}$ (340 K)	$[67]\beta\text{C}$ (120 K)
Fe–N _[py]	1.9008(14), 1.9034(15)	1.934(3), 1.946(3)	2.063(4), 2.076(3)	1.886(7), 1.892(6)
Fe–N _[pz]	1.9747(15)- 1.9847(15)	1.999(4) - 2.009(4)	2.111(4), 2.131(4)	1.961(6), 1.972(7)
V _{Oh}	9.636(5)	10.001(12)	11.565(14)	9.444(19)
Σ	88.06(19)	99.0(5)	135.7(5)	89.2(10)
Θ	289.5(4)	325.0(13)	444.8(13)	293(2)
ϕ	179.02(6)	178.93(14)	176.79(14)	179.4(3)
θ	89.402(14)	88.82(5)	89.06(5)	87.22(8)

Table 7-1: Crystallographic parameters determined directly from the crystal structure using Olex2²².

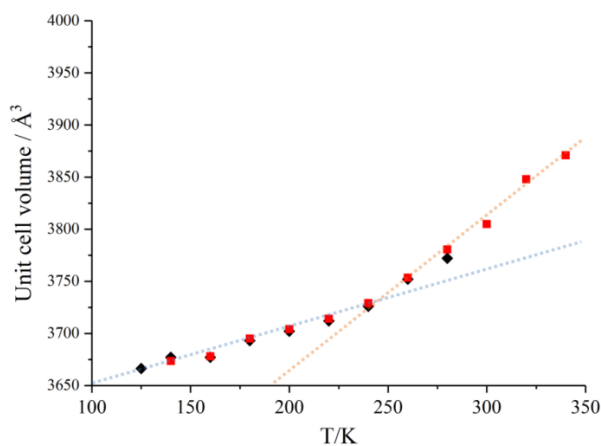


Figure 7.18: VT experiment every 20 K increments. Blue dashed line represents the constant thermal contraction of the unit cell volume. Orange dashed line represent the increment of the volume due to gradual SCO.

Chapter 7

[68]C crystallizes in the triclinic $P\bar{1}$ space group. Three unique complexes sharing hydrogen bonds between their terminal $-\text{COOH}$ groups forming a supramolecular trimer, are found in the asymmetric unit (Figure 7.19).

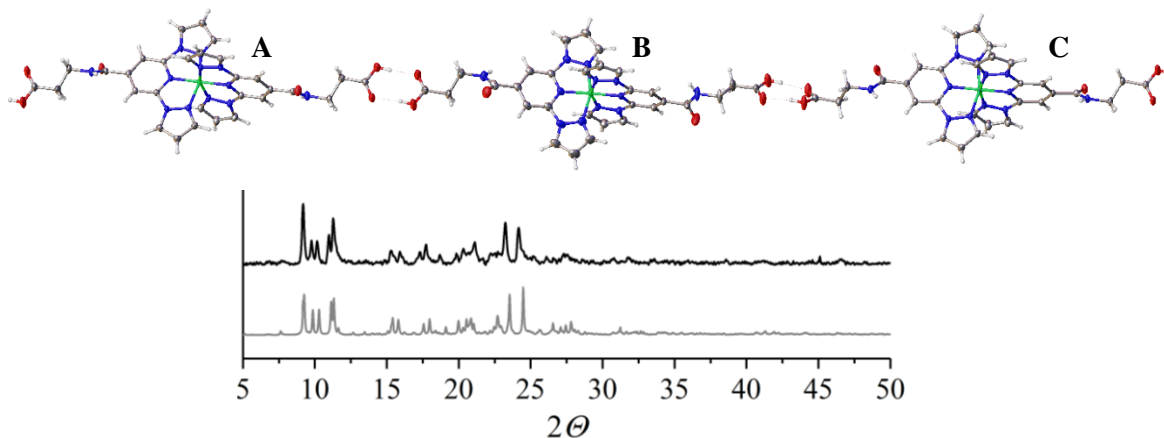


Figure 7.19: Crystal structure and powder patterns of [68]C. Counter-anions and solvent molecules were omitted for clarity. The colour assignment in the plot is black for the experimental and grey for the simulated XRD.

[68]C	Molecule A (120 K)	Molecule B (120 K)	Molecule C (120 K)
Fe–N _[py]	1.9021(4), 1.906(4)	1.90250(4), 1.92715(4)	1.88294(4), 1.88740(4)
Fe–N _[pz]	1.9698(5) - 1.9874(5)	1.98969(4) - 2.00512(3)	1.96508(3) - 1.97809(4)
V _{Oh}	9.6259(15)	9.89576(11)	9.50341(11)
Σ	88.20(4)	93.567(2)	83.173(2)
ϑ	289.748(4)	307.396(4)	273.711(3)
ϕ	177.28(3)	178.46668(5)	178.98060(3)
θ	85.2656(16)	89.2660(16)	88.9107(16)
[68]C	Molecule A (290 K)	Molecule B (290 K)	Molecule C (290 K)
Fe–N _[py]	1.9719(6), 1.9723(6)	2.01517(5), 2.04559(5)	1.89118(5), 1.90752(5)
Fe–N _[pz]	2.0299(7)- 2.0429(8)	1.98237(7) - 2.30155(7)	1.96709(6), 1.99201(7)
V _{Oh}	10.400(2)	11.4771(2)	9.60053(17)
Σ	109.364(4)	125.186(4)	86.396(6)
ϑ	358.817(6)	398.223(7)	283.800(5)
ϕ	176.01(5)	174.8560(2)	179.2830(3)
θ	84.413(3)	89.503(3)	87.599(3)

Table 7-2: Crystallographic parameters determined directly from the crystal structure using Olex2²².

Chapter 7

The magnetic behaviour of [67]C and [68]C was expected to be similar but, in contrast to [60]C which was an amorphous solid and presented gradual SCO (Figure 7.15), better defined transitions were observed by SQUID (Figure 7.20).

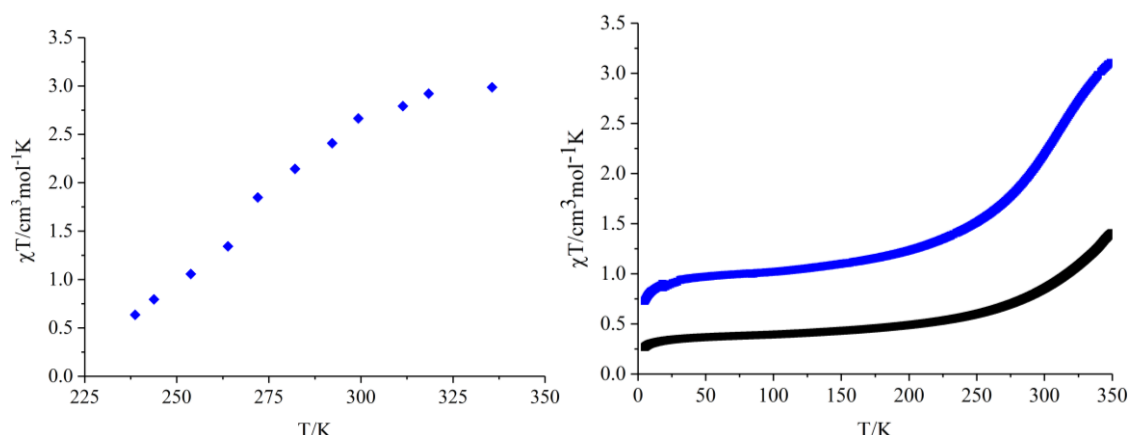


Figure 7.20: Evans method of [67] and SQUID of [67]C (blue) and [68]C (black).

In view of the results (Figure 7.20), the following modification of these ligands was proposed in order to favour the HS form of the complexes (Figure 7.21).

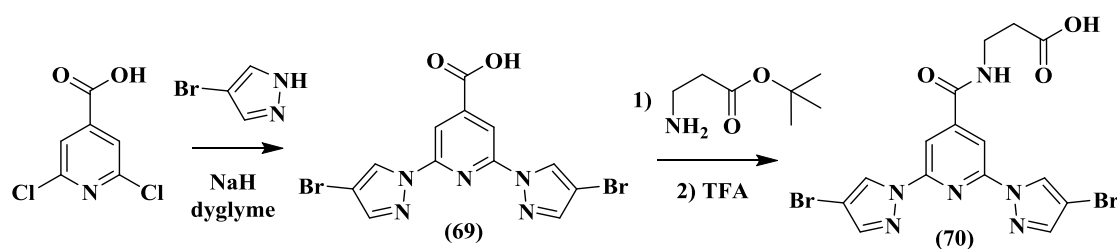


Figure 7.21: Designing (70) with weak EDG in the 4-position of the pyrazole which could lower $T_{1/2}$.

Ligand (69) was synthesized and fully characterized, but due to lack of time before going to Valencia, ligand (70) was discarded. (69) crystallized in the $P2_1/c$ space group (Figure 7.22).

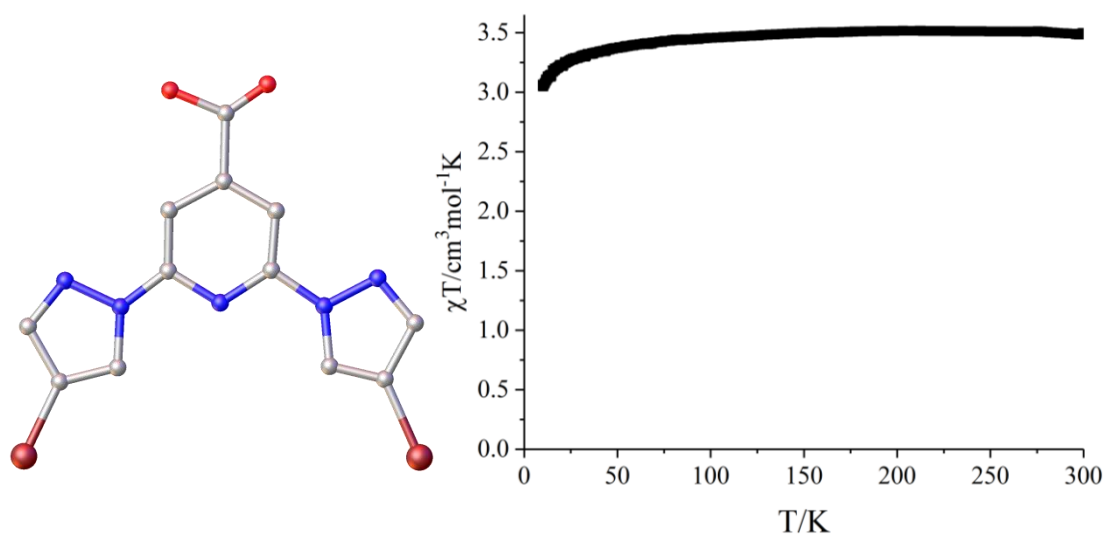


Figure 7.22: Crystal structure of (69). Hydrogen atoms were omitted for clarity. SQUID of [69]B.

7.2.3 Coating surfaces with the complexes

The general procedure for the complex deposition was dipping the substrates into $[\text{Fe}(\text{L})_2](\text{ClO}_4)_2$ solutions (direct deposition). The grafting was achieved by immersion of the substrates in 1mM solutions of the complexes for 16 h. Then, they were thoroughly rinsed with the same solvent to remove any physisorbed material not chemically bonded to the substrate, then dried under a N_2 stream. Sequential deposition²³ was also attempted where the substrates were first immersed into ligand solution, followed by a second dip step into iron(II) salt solution, and finally by repeating the first step the complete complex was prepared.

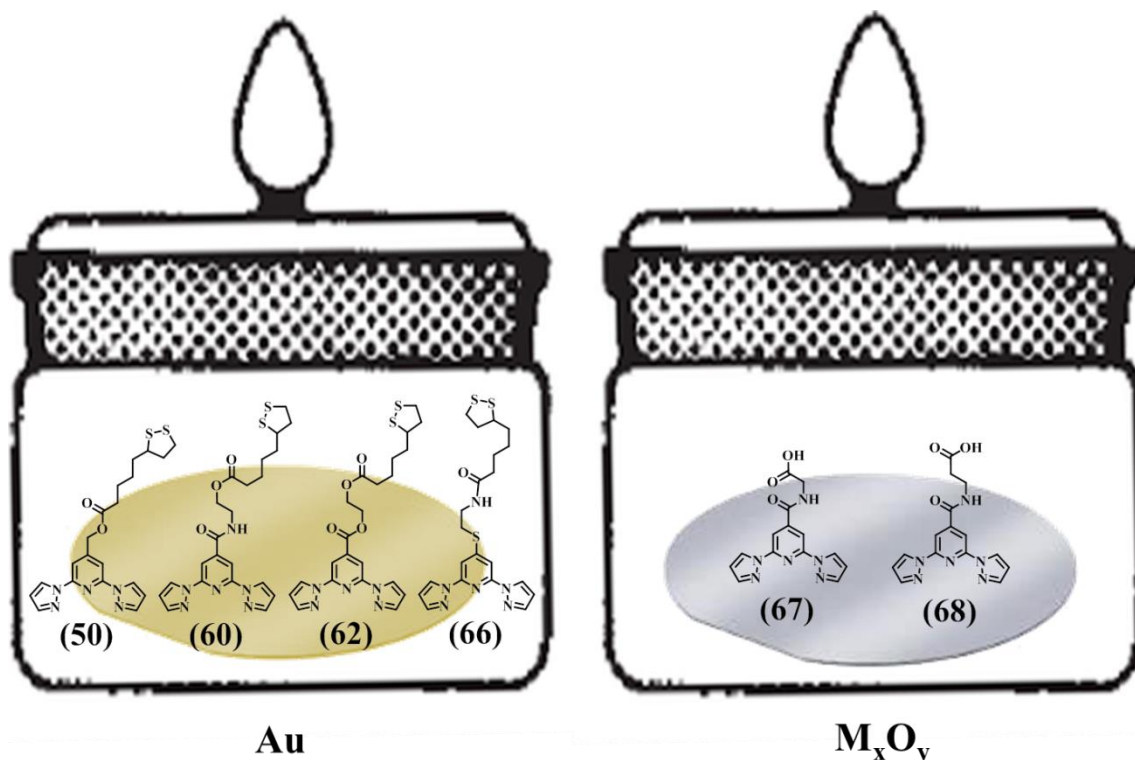


Figure 7.23: Scheme of ligands deposited onto gold and metal-oxide substrates.

The dithiolane ligands ((50), (60), (62) and (66)) were deposited on gold surfaces which were prepared by vacuum vapour deposition of Au onto Si/SiO₂ (native). The carboxylic acid ligands ((67) and (68)) were deposited onto four different metal-oxide surfaces: Si/SiO₂ (native) which is a Si substrate with a layer of SiO₂ on the surface due to oxidation with air; indium tin oxide (ITO) coated glass; zinc oxide (ZnO); and Al₂O₃-coated glass. The first three substrates were obtained from commercial sources (NOVA electronic materials), while Al₂O₃-coated glass was prepared by evaporation of Al onto glass.

Iron(II) complexes of bpp derived compounds are usually stable towards oxidation in solution. The stability of [60], [62], [66] and [68] solutions in different solvents was monitored by UV-vis. Spectra were collected at different concentrations from freshly prepared solutions, and after 24 h in the glovebox (Figure 7.24). The spectra are overlaid showing the stability of each complex in solution after 24 hours.

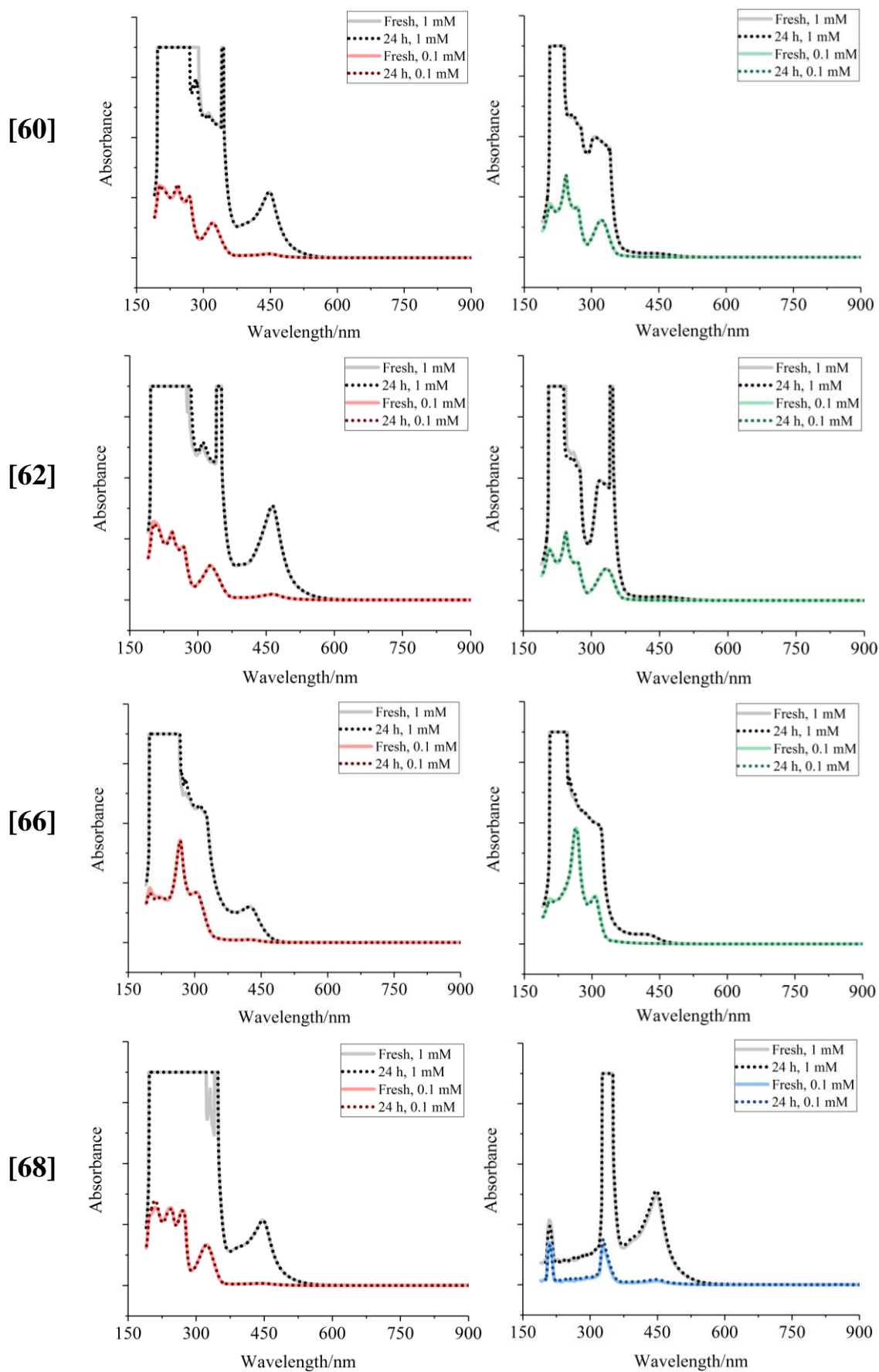


Figure 7.24: UV-vis spectra of [60], [62], [66] and [68] respectively. Colour code is MeCN (red), EtOH (green) and acetone (blue). The absorbance data are not normalised for concentration.

Chapter 7

Different grafting conditions were assessed with the aim of optimizing the process for synchrotron analysis. The gold substrates were activated by immersion in a solution of H₂O₂ and H₂SO₄ (1:1) for 40 seconds. All the experiments performed during the stay at ICMol are detailed bellow (Table 7-3).

Ligand	Substrate	Deposition	Solvent	Concentration
(50)	Au	Direct	EtOH	1 mM
(50)	Au	Sequential	EtOH	1 mM
(50)	Au	Sequential	EtOH/MeCN	1 mM
(50)	Au	Direct	MeCN	1 mM
(50)	Au	Direct	MeOH	1 mM
(60)	Au	Direct	EtOH	1 mM
(60)	Au	Direct	MeCN	1 mM
(60)	Au	Sequential	EtOH/MeCN	1 mM
(62)	Au	Direct	EtOH	1 mM
(62)	Au	Direct	MeCN	1 mM
(62)	Au	Sequential	EtOH/MeCN	1 mM
(66)	Au	Direct	EtOH	1 mM
(66)	Au	Direct	MeCN	1 mM
(66)	Au	Sequential	EtOH/MeCN	1 mM
(67)	Si/SiO ₂	Direct	Acetone	0.5 mM
(67)	Si/SiO ₂	Direct	MeCN	0.1 mM
(67)	Si/SiO ₂	Direct	MeCN	1 mM
(68)	Si/SiO ₂	Direct	MeCN	1 mM
(68)	Si/SiO ₂	Sequential	Acetone	1 mM
(68)	Si/SiO ₂	Sequential	Acetone/MeCN	1 mM
(68)	Si/SiO ₂	Direct	MeCN	0.1 mM
(68)	Si/SiO ₂	Direct	Acetone	1 mM
(68)	Si/SiO ₂ (activated)	Direct	Acetone	1 mM
(68)	ITO	Direct	Acetone	1 mM
(68)	Glass/Al ₂ O ₃	Direct	Acetone	1 mM
(68)	ZnO	Direct	Acetone	1 mM

Table 7-3: List of the different deposition conditions examined during this study.

7.2.4 Characterization of the coated surfaces

7.2.4.1 Atomic Force microscopy (AFM)

AFM was used to determine the surface morphology and to verify the occurrence of deposition without the presence of complex aggregates on the surface. The length of the molecules can be calculated from the single crystal X-ray diffraction structures. Complexes [67] and [68] present sizes close to 1.9 and 2.2 nm respectively (the distance between their two carboxylic acid end groups). However in the case of the thiolated ligands, only some ligands were crystallized, which contain long aliphatic chains as link between the bpp unit and the tether group. The spacer brings flexibility which makes difficult to predict the size of a monolayer. The morphology of naked substrates was determined as reference (Figure 7.25).

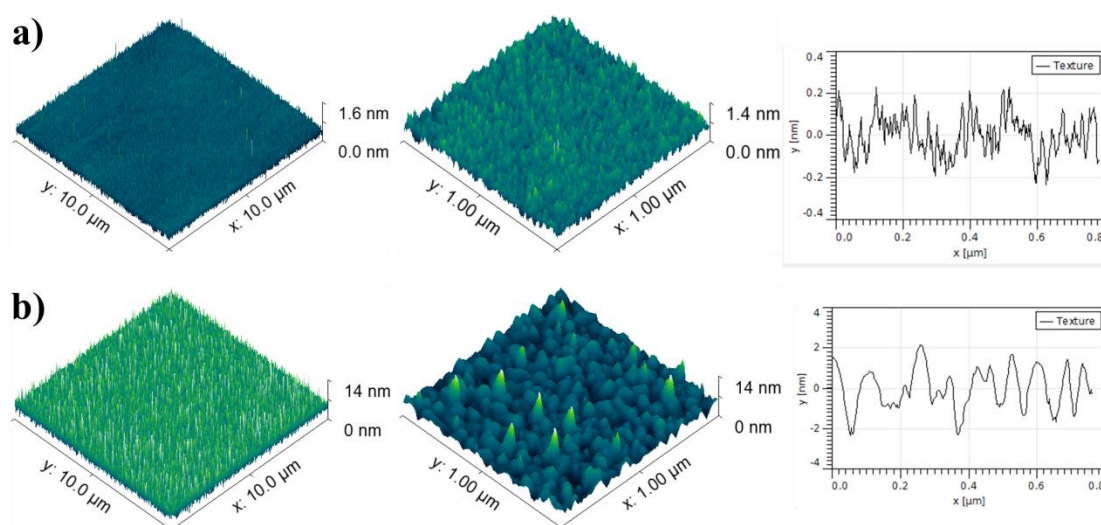


Figure 7.25: Reference AFM images and their profiles. Silicon oxide a) present root mean square roughness (RMS) of 0.07 nm while gold surface b) is more rugged, RMS = 0.5 nm.

On one hand, large aggregates were commonly observed for direct deposition of thiolated complexes on gold (Figure 7.26).

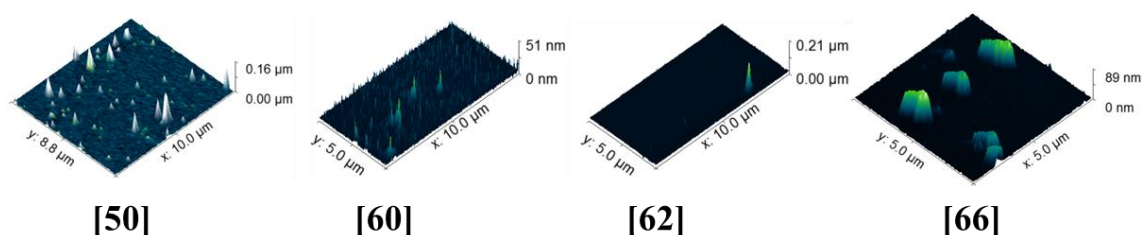


Figure 7.26: AFM examples of thiolated complexes deposited on gold where large aggregates are shown.

The sequential experiment of [50] presented cleaner AFM images (Figure 7.27). The same procedure afforded a monolayer of ligands (62) and (66) by XPS, but iron(II) did not coordinated the ligands (Table 7-4).

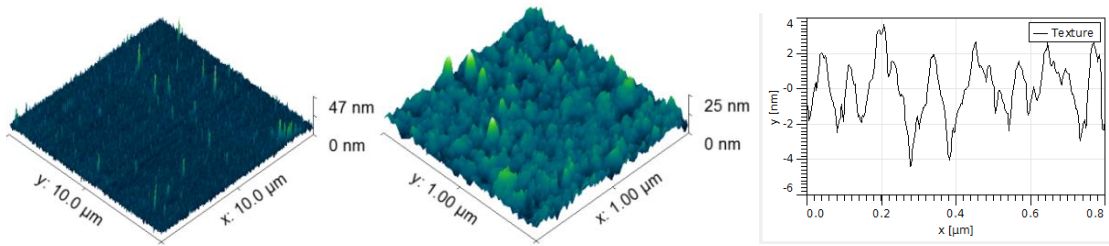


Figure 7.27: AFM of the sequential [50] experiment and the profile showing RMS of 0.8 nm.

In contrast, complexes with carboxylic acid tether groups presented notably better results on metal-oxide surfaces for the direct deposition method. The improvement was in the homogeneity of the sample, and in the observation of fewer and smaller aggregates (Figure 7.28).

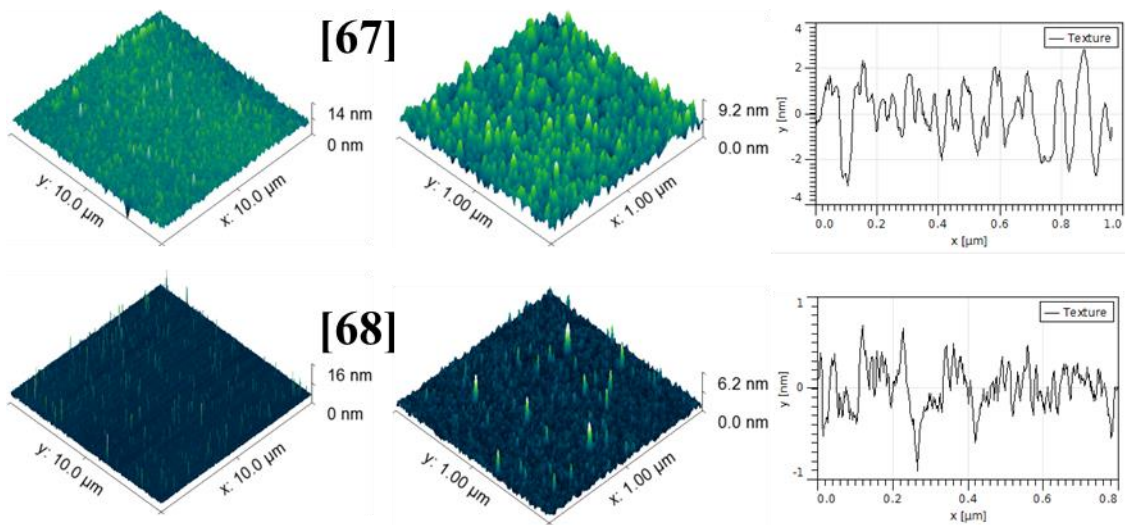


Figure 7.28: AFM of [67] RMS of 0.7 nm and [68] RMS of 0.2 nm over Si/SiO₂ substrates.

Root mean square roughness (RMS) measures how different the surface is from a mean plane. The RMS of Si/SiO₂ increased in both experiments compared to the naked substrate (Figure 7.25, a). However it is clear that deposition of [67] showed a more homogenous profile. Similar results of a grafting in solution were reported before on iron oxide (Fe₃O₄)¹². Deposition of [68] was also performed on different substrates (Figure 7.29).

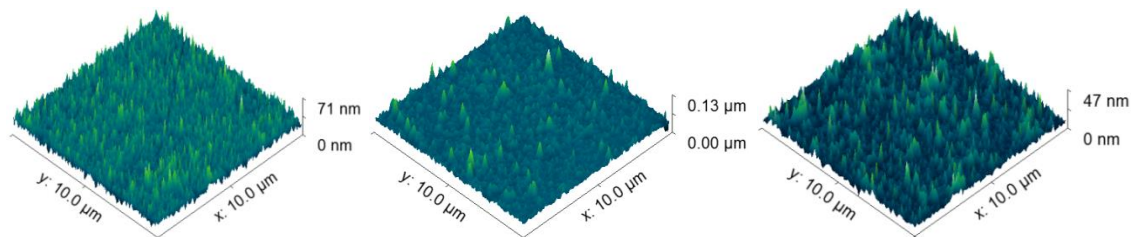


Figure 7.29: AFM of [68] deposition in ITO (left), Glass/Al₂O₃ (middle) and ZnO (right), RMS calculated; 2.4, 1.2 and 1.7 nm respectively.

No reference AFM pictures of the naked substrates were collected for the new metal-oxides, hence no comparison could be performed. In summary, all of our samples analysed by

Chapter 7

AFM present consistent maximum height differences compared to the naked substrates confirming the deposition of the SCO materials on Au or Si/SiO₂.

7.2.4.2 X-ray photoelectron spectroscopy (XPS)

Survey spectra at room temperature of [50], [60], [62], [66], [67] and [68] deposited onto Au or metal-oxides (Figure 7.23), clearly show the presence of the expected elements (N, S, Fe), except for Cl confirming the absence of ClO₄⁻ counter-anions (Table 7-4).

Ligand	Fe (cps)	(obs.) N (calc.)	(obs.) S (calc.)	Cl		
(50)	2500	10.34	10	5.3	4	0
(50)	5500	3.3	10	0.7	4	0
(60)	1500	12.1	10	7	4	0
(60)	0	20	10	4	4	0
(62)	1500	20.7	12	5	4	0
(62)	0	11.55	12	3	4	0
(66)	1200	19.9	12	9.8	6	0
(66)	0	13.25	12	5	6	0
(67)	5000	3.5	12	-	-	0.15
(67)	2500	6.05	12	-	-	0.3
(67)	400	9.8	12	-	-	2.2
(68)	300	10.1	12	-	-	0
(68)	700	9.5	12	-	-	0
(68)	Signal overlaid	10.3	12	-	-	0.43
(68)	4000	3.23	12	-	-	0
(68)	9000	4.5	12	-	-	0.32

Table 7-4: Representative results of survey XPS. The amounts of key elements are quoted relative to iron. Coloured in red two of the best results which are discussed below.

Three parameters are assessed in the above table: the intensity of iron signal; the relative intensities of representative elements of the ligands; and the absence of chlorine from the counter-anions. The earlier study of [Fe(bppCOOH)₂]²⁺ deposition performed by Miguel Clemente was also in agreement with the absence of counter-anions in the SAMs.

High-resolution XPS spectra at the Fe 2p edge exhibit broad Fe 2p_{1/2} and 2p_{3/2} peaks with high-energy satellite peaks (Figure 7.30). This could indicate the presence of complexes in the HS state^{13a} but it could also be due to partial oxidation of Fe(II) to Fe(III). In fact, XPS spectra of [Fe(bppCOOH)₂]²⁺ samples on Si/SiO₂ (300 nm), exposed to air for several days, display more intense satellite contributions when compared to samples prepared and measured

under N₂ (Figure 7.31). These experiments of [Fe(bppCOOH)₂]²⁺ deposition were performed by Dr Miguel Clemente before my stay at ICMol.

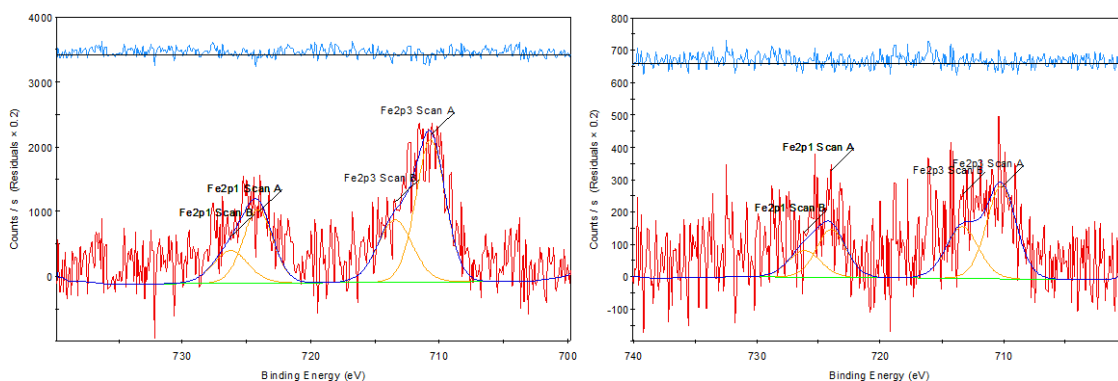


Figure 7.30: High-resolution XPS spectra at the Fe 2p edge of [50] (left) and [68] (right) deposited on Au and Si/SiO₂ respectively.

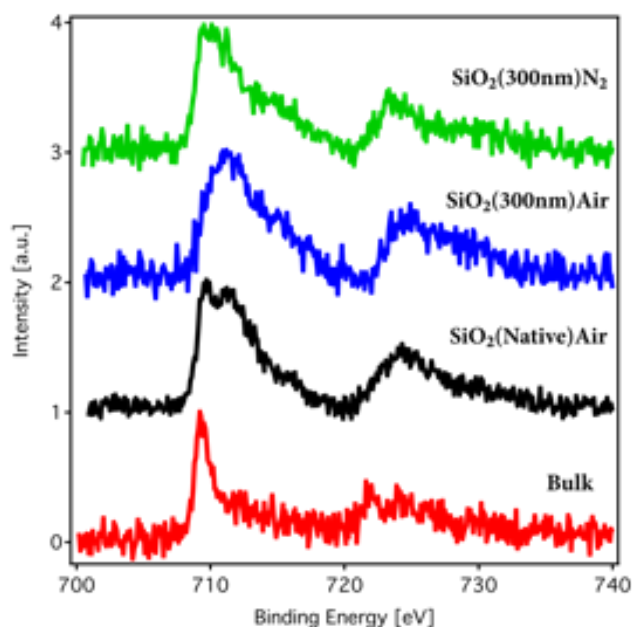


Figure 7.31: Normalized high-resolution XPS spectra at the Fe 2p edge of [Fe(bppCOOH)₂]²⁺ samples. A bulk reference spectrum (red) has been included for comparison. SiO₂(300nm) substrates present a thermal treatment, which affords a 300 nm layer of SiO₂ on Si.

7.2.4.3 X-ray absorption spectroscopy (XAS)

XAS was chosen to confirm the deposition of [Fe(L)₂]²⁺ on the substrates and to determine the spin state of Fe(II) at different temperatures. This technique has already been used to characterize the spin state of sub- and monolayers of SCO complexes evaporated on different surfaces²⁴. XAS spectrum of HS iron(II), LS iron(II) and HS iron(III) reference compounds were reported previously (Figure 7.32). The measurements were performed at the ALBA synchrotron (beamline BOREAS, Barcelona, Spain). XPS pointed to partial oxidation of iron by O₂, when the samples measured were stored under ambient atmosphere. To avoid these effects, XAS samples were prepared in a glovebox and directly transferred to the analysis chambers without breaking the inert atmosphere.

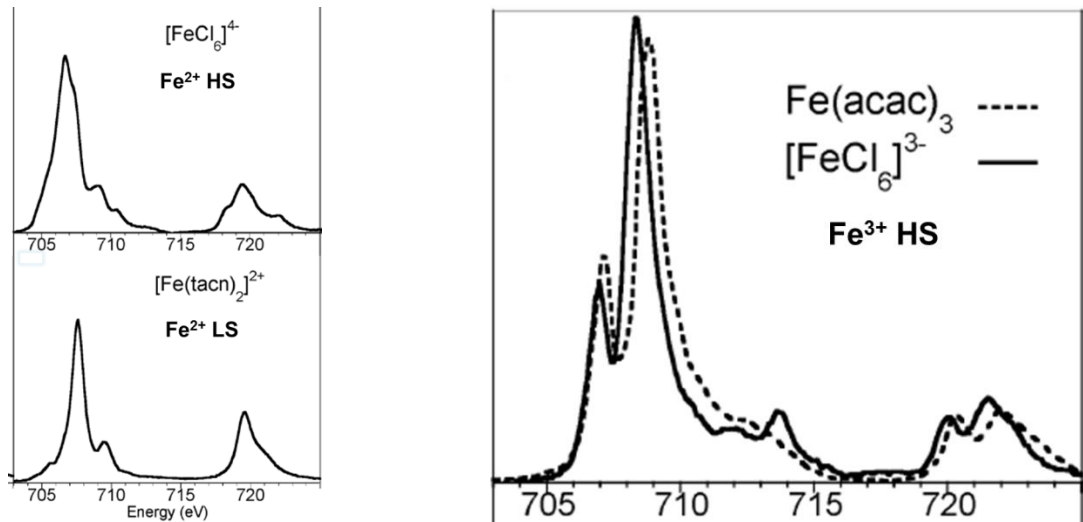


Figure 7.32: L-edge multiplets and integrated intensities for selected octahedral complexes reported by Wasinger *et. al.*²⁵.

The Fe L₃-edge of a typical octahedral iron(II) HS complex is composed by a peak at 708 eV with a shoulder at 709 eV. In contrast a LS complex presents the L₃ maximum shifted to higher energies (710 eV), with a less structured and more intense L₂-edge which is also shifted to higher energies (Figure 7.32). The spectrum of a HS iron(III) complex is characterized by two strong features in the L₃-edge at 707 and 709 eV, followed by small multiplet and satellite features (710-715 eV) and two relatively weak features in the L₂-edge (719-725 eV).

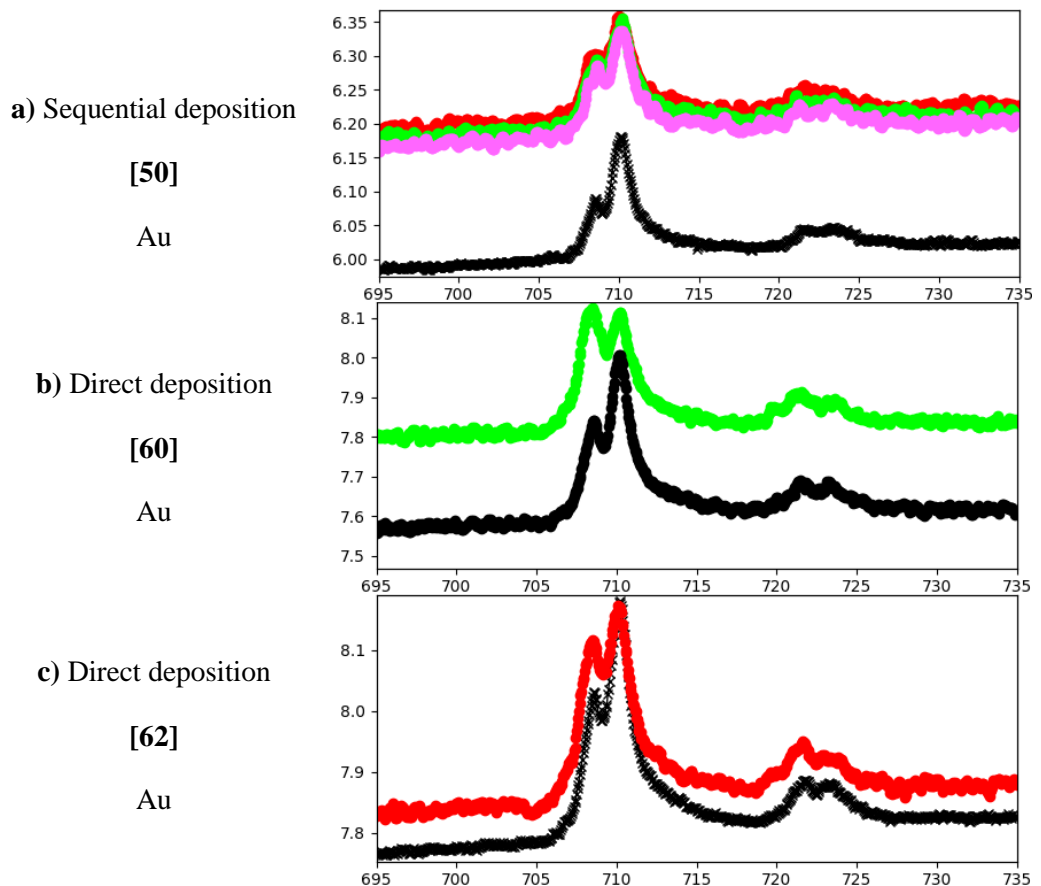


Figure 7.33: XAS spectra of [50], [60] and [62] complexes deposited on gold surfaces at 300 K.

Chapter 7

XAS is a global surface technique with high sensitivity able to detect spin state of a submonolayer. Per contra, the x-ray beam can destroy the complex, alter oxidation state²⁶ or spin state²⁷. Indeed the spectra collected in this study were evolving with time. The first spectrum (black line, Figure 7.33) of the three samples were typical of HS Fe(III) (Figure 7.32), small increase of HS Fe(II) was observed after successive spectra were collected on the same spot, implying possible photoreduction induced by soft X-rays. This effect could be reduced by decreasing the photon flux to less than 5% of its initial intensity, and by lowering the temperature. It may be related to chemical changes or degradation undergone by the compound, as the effect is irreversible even at low temperatures. Thus it is not due to soft x-ray induced excited spin state trapping (SOXIESST). This has been observed on other samples. For instance, bulk samples of $[\text{Fe}(\text{phen})_2(\text{NCS})_2]$ also showed a degradation over time in the same experiment, which is manifested by the freezing in of a LS state, probably through the removal of a ligand group²⁸.

The spectra of the SAMs deposited on Si/SiO₂ show a noisier and significantly weaker signal than those deposited on Au. This makes it very complicated to estimate the HS/LS fraction or the oxidation state (Figure 7.34).

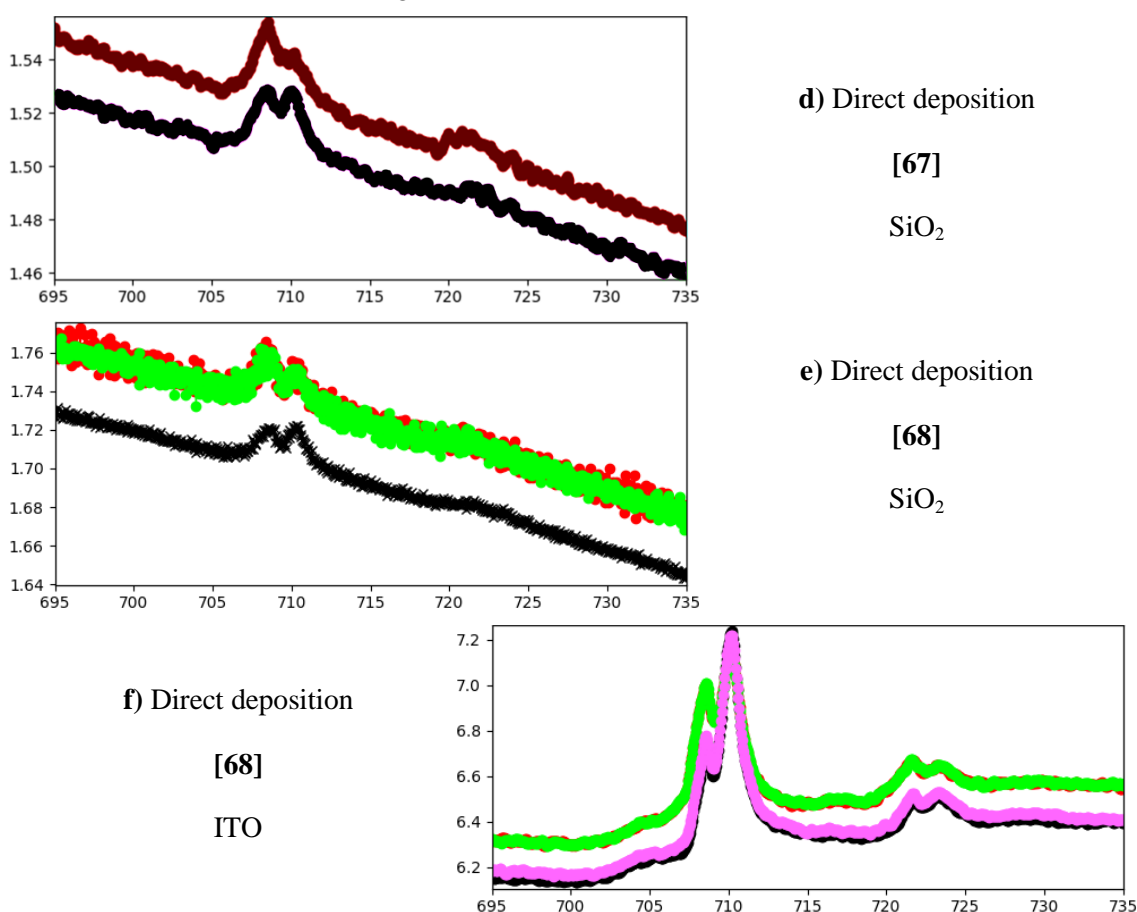


Figure 7.34: XAS spectra of [67] and [68] complexes deposited on metal-oxides substrates at 300 K.

However XAS spectra of the complexes deposited on ITO, which is a more conducting substrate, look very similar to the gold deposited samples. Again the spectrum (Figure 7.34, f)) corresponds to pure HS iron(III) (black and pink lines are the first spectra) and after irradiation

with the X-ray beam the relative intensity of 708 peak increases. Two peaks at 710 and 708 eV are always observed, their relative intensity varying during the measurement but not with temperature or light irradiation. Depending on the measurement conditions we have a variable amount of HS iron(II) (peak at 708 eV) which always increases in successive scans in an irreversible way. Hence this could be photoreduction of iron(III). In the most conducting substrates Au and ITO, the spectra are more consistent with HS iron(III). It seems that the less conducting Si/SiO₂ substrates favour photoreduction as they are charged by the soft X-ray used in the measurements. Oxidation to Fe(III) could take place after transferring the substrates from the solution into the measurement chamber or it could be intrinsic to the nature of those compounds deposited on surfaces where one bpp ligand is replaced by three water molecules for example.

Further research could be performed in two directions; either using analogous ligands based on the terpyridine scaffold²⁹ with cobalt (II), because the previous study at ICMol with [Co/Fe(bppCOOH)₂]²⁺ showed Co(II) complexes to be less sensitive towards oxidation deposited and they can also undergo SCO. Or the use of five³⁰ or six N-donor ligands which could potentially stabilize the coordination sphere of the iron(II) compared to bpp and hopefully maintain their SCO activity on the surfaces³¹. An interesting experiment for the carboxylated compounds deposited on metal-oxide surfaces could be to immerse the functionalized substrates in basic or acidic solutions to observe if the chemically induced deprotonation/protonation of the carboxylic acid has any influence in the spin or oxidation state of the monolayer.

7.2.5 Coating gold nanoparticles

A classical synthetic method of gold nanoparticles (AuNPs) where the solvent used is water and the particles are stabilized by citrate is known as the Turkevich method³². However the method described by Osterloh *et al.* has been proved to be a more practical method where easily size-tunable monodispersed spherical AuNPs are obtained by varying the concentration of the reagents³³. AuNPs of approximately 15 nm size were synthesised and characterized by TEM (Figure 7.35).

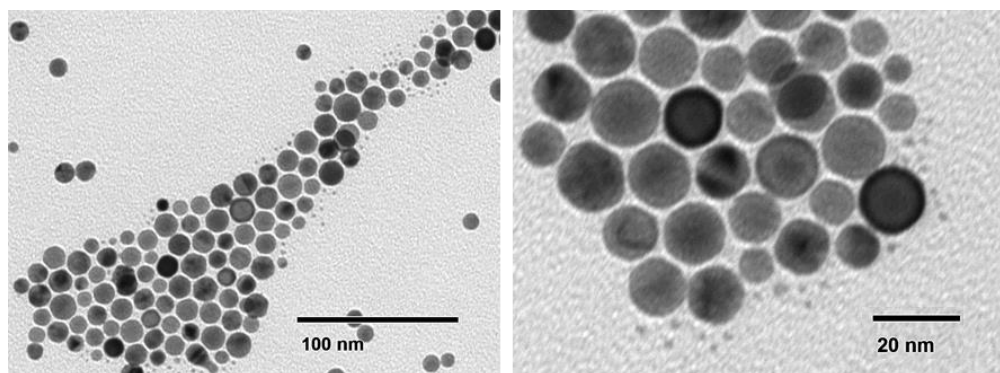


Figure 7.35: TEM image of AuNPs synthesized sizes vary from 8 to 15 nm.

Chapter 7

The size of the particles was also examined by DLS (Figure 7.36), which was in agreement with the result of the converted diameter calculated based on number (D)).

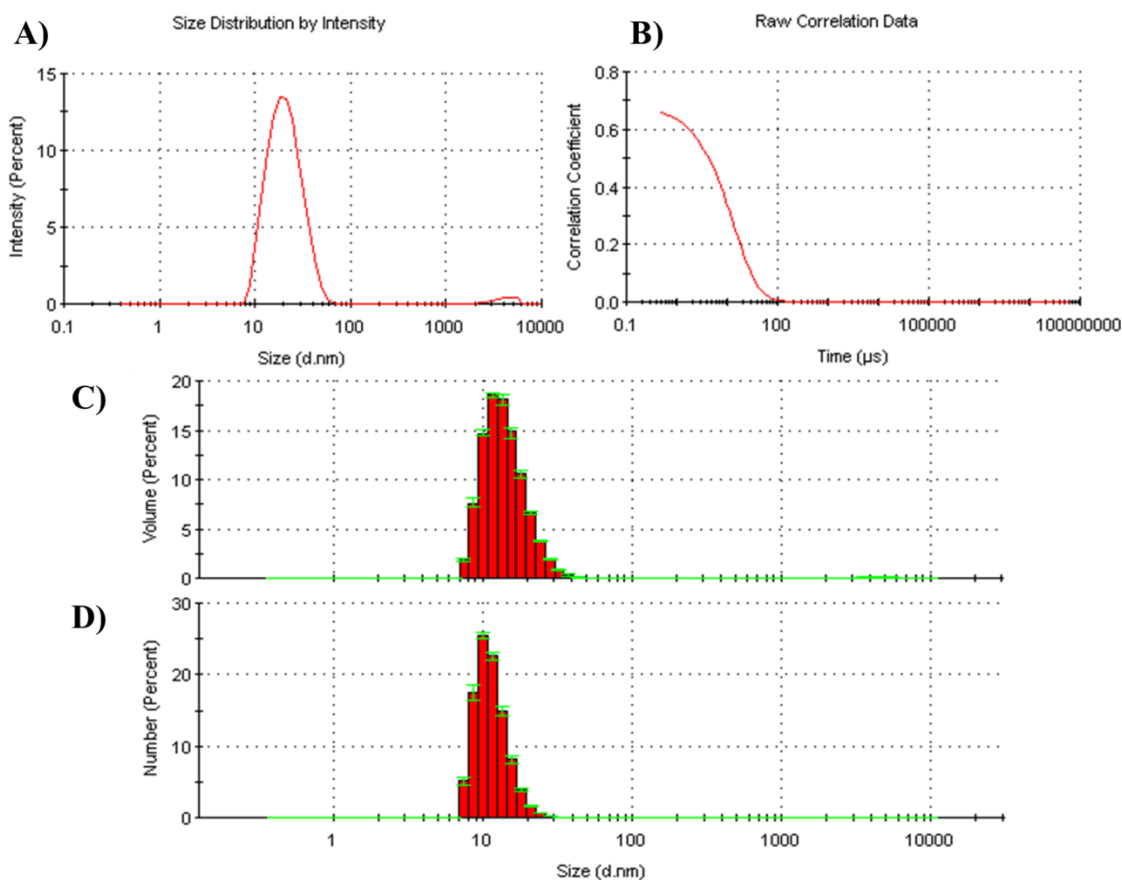


Figure 7.36: DLS analysis, mean diameter = 19.25 nm. A) Fundamental diameter measured by intensity. B) Correlation data showing the quality of the data. C) Mean diameter calculated based on volume, 14.48 nm. D) Mean diameter calculated based on number, 11.55 nm.

The concentration of the gold nanoparticles was calculated based on the Beer Lambert law with the absorption value at 400 nm ($A = 1.2$ equals 5×10^{-4} M). Expert advice at ICMol said that the optimum concentration for ligand exchange reactions was 1.67×10^{-4} mol Au/ mL. Hence, a grafting of 4 mL of AuNPs at that concentration was attempted where methanolic solutions of $[\text{Fe}(\mathbf{50})](\text{ClO}_4)_2$ (4 mL of 0.25 and 0.125 mM) were added dropwise with a perfuser stringe pump during 15 min. The characteristic plasmon vanished after few minutes as the nanoparticles precipitated. The precipitate was collected by centrifugation and was analysed by XPS (Table 7-5).

$[\text{Fe}(\mathbf{50})](\text{ClO}_4)_2$	Fe (cps)	N (relative)	S (relative)	Cl (relative)
expected	-	10	4	0
(0.25 mM)	0	1	3.6	1.9
(0.125 mM)	0	1.34	1	1.11

Table 7-5: XPS results of the AuNPs precipitated from toluene solution. Amounts of key elements relative to the minor element found.

Chapter 7

Poor results were obtained since the ratio N/S did not correspond to ligand (**50**), chlorine was present and no iron was observed in the particles.

In view of these results, a sequential approach was attempted. Interestingly, when a toluene solution (4 mL, 0.125 mM) of ligand (**50**) was added to 4 mL of AuNPs the plasmon was maintained for hours which could imply a successful partial ligand exchange. However this was not proved because once the methanolic solution of iron(II) salt was added the plasmon was repeatedly lost. An experiment where the same concentration of oleylamine-stabilized AuNPs in toluene was subjected to pure methanol addition, confirmed that the AuNPs are sensitive to small volumes of methanol, which causes aggregation. In order to solve the problem, two alternatives were proposed. First was to stabilize the AuNPs in a polar solvent in which the thiolated complexes are soluble (Figure 7.37).

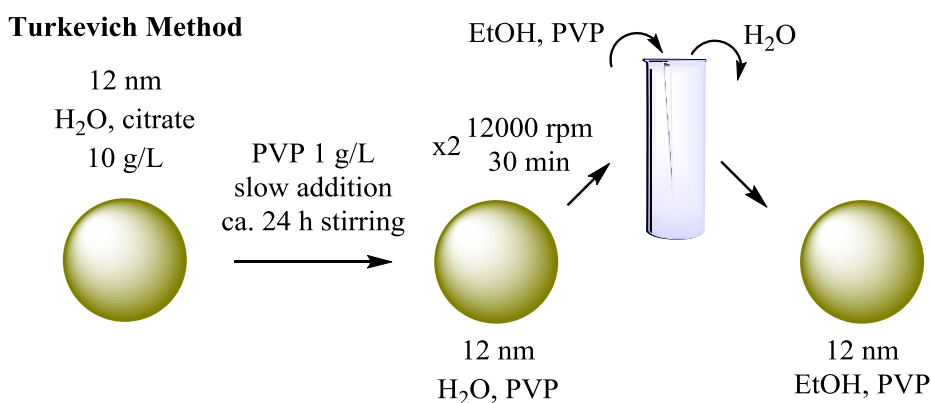


Figure 7.37: Preparation methodology proposed of AuNPs stabilized in EtOH.

However this was not successfully carried out due to the complexity of the process combined with lack of time at ICMol. The second approach was to deposit the AuNPs on a Si/SiO₂ substrate, then performing the grafting analogously to the work described above. The main advantage of this approach for AuNPs over the monolayers of the complexes directly on Au substrates, is that grafting onto deposited AuNPs could increase their sensitivity for Raman spectroscopy, enabling extra characterization of the deposited complexes. In order to do that, the Si/SiO₂ substrate needs to be functionalised first (Figure 7.38).

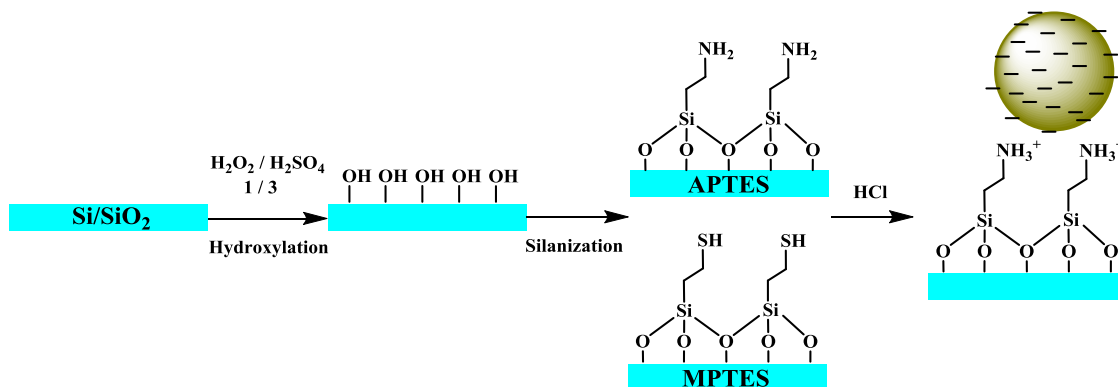


Figure 7.38: Scheme of functionalization of Si/SiO₂ with APTES and MPTES.

Chapter 7

Once the silicon oxide surfaces were silanized, AuNPs were deposited in both (3-aminopropyl)triethoxysilane (APTES) and (3-mercaptopropyl)trimethoxysilane (MPTES) by drop-casting of toluene solution (Figure 7.39).

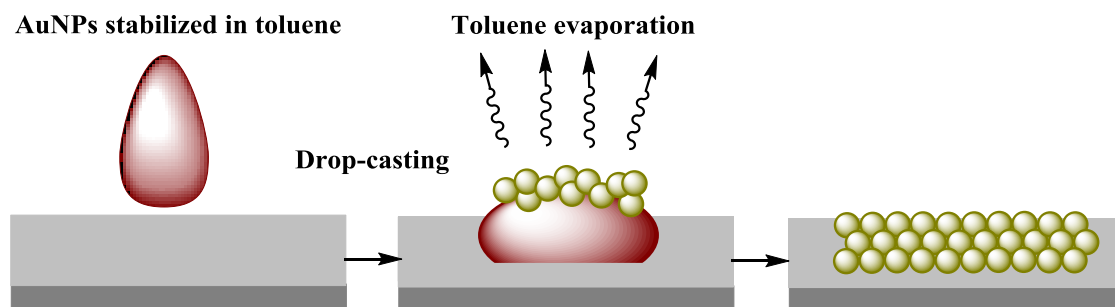


Figure 7.39: Scheme of the drop-casting of AuNPs.

The quality of the self-assembled monolayer of AuNPs was examined by AFM (Figure 7.40). On the one hand, the MPTES coverage was poor with few-separated AuNPs on the surface. Hence, this coating was discarded. In contrast, when APTES was used a rich populated AuNP SAM was obtained.

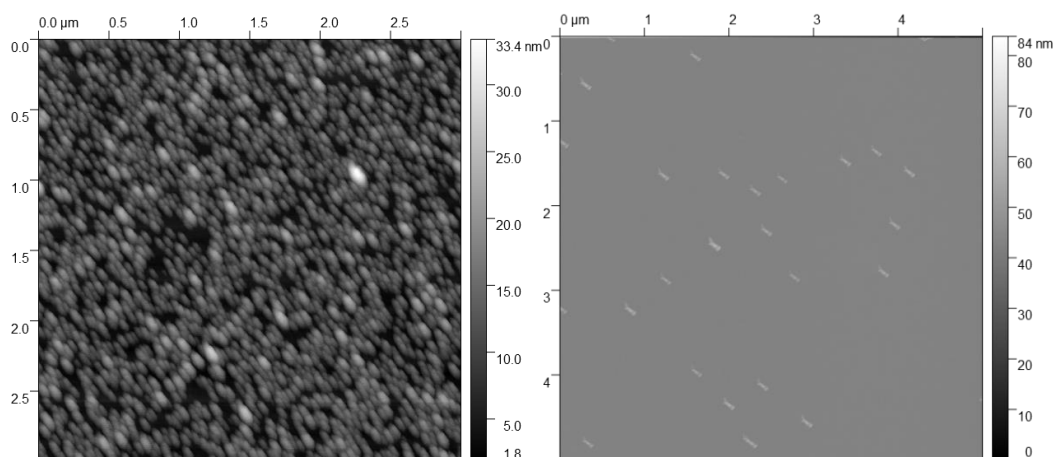


Figure 7.40: AFM images of the AuNPs deposited on Si/SiO₂; with APTES (left) and MPTES (right).

Sequential grafting of [Fe(50)](ClO₄)₂ was performed onto Si/SiO₂ substrate functionalised with APTES and AuNPs. Deposition of [50] was analysed by XPS (Table 7-6).

[Fe(50)](ClO ₄) ₂	Fe (cps)	N (relative)	S (relative)	Cl (relative)
expected	-	10	4	0
MeCN	1300	2.5	0	0
EtOH	110	3.06	0	0

Table 7-6: XPS results of the AuNPs deposited on Si/SiO₂ substrate. Amounts of key elements relative to iron.

Iron was found in the XPS analysis however the nitrogen content was rather low and no sulphur was observed. Hence, the coating of AuNPs with these SCO complexes was discontinued.

7.3 Conclusions

A number of novel 2,6-di(pyrazol-yl)pyridine-based ligands containing dithiolane [(50), (60), (62) and (66)] and carboxylic acid [(67) and (68)] tether groups were designed, synthesized and fully characterized. Iron(II) complexes of those ligands were prepared and most of them undergo SCO in solution or in solid state. Iron(II) complexes with dithiolane tethers are amorphous and show typical gradual SCO, while the carboxylic acid tethered complexes crystallized better because their spacers were shorter. The complexes were characterized by ^1H NMR, ESMS, SQUID, single crystal and powder XRD, Evans method and microanalysis. Large single crystals of [62]C were grown from acetonitrile solution upon atmospheric diffusion of diethyl ether, however the disorder of the aliphatic chain decreased the diffraction limit down to 1.5 Å ca. The refinement of that structure was incomplete where only $[\text{Fe}(\text{bppCOO-})_2](\text{ClO}_4)_2$ was modelled.

In this work, we have demonstrated the successful formation of SAMs by AFM and XPS. Complexes were deposited by immersion of solid substrates in their solution. [(50), (60), (62) and (66)] with dithiolane substituents formed SAMs on gold surface whereas the carboxylic acids (67) and (68) were deposited onto several metal-oxide substrates such as ITO, Al_2O_3 , ZnO and Si/SiO₂. However, the integrity of the SCO molecule was not proved by the techniques used to analyse them on the surface. The final conclusion is that iron(II) bpp complexes decompose or oxidize after deposition. Gold nanoparticles were easily synthesized by reported procedures, however any attempts of coat them with [50]C complex were unsuccessful in the time available.

With a view to publication, characterization of the SAMs could be completed with different techniques; electrochemistry. Matrix-Assisted Laser Desorption/Ionization Time-Of-Flight (MALDI- TOF), cyclic voltammetry, Infrared Reflection Absorption Spectroscopy (IRRAS), contact angle measurements and Raman spectroscopy at ICMol.

7.4 Bibliography

1. Lefter, C.; Rat, S.; Costa, J. S.; Manrique-Juárez, M. D.; Quintero, C. M.; Salmon, L.; Séguy, I.; Leichle, T.; Nicu, L.; Demont, P.; Rotaru, A.; Molnár, G.; Bousseksou, A., Current Switching Coupled to Molecular Spin-States in Large-Area Junctions. *Advanced Materials* **2016**, 28 (34), 7508-7514.
2. (a) Dugay, J.; Giménez-Marqués, M.; Kozlova, T.; Zandbergen, H. W.; Coronado, E.; van der Zant, H. S. J., Spin Switching in Electronic Devices Based on 2D Assemblies of Spin-Crossover Nanoparticles. *Advanced Materials* **2015**, 27 (7), 1288-1293; (b) Holovchenko, A.; Dugay, J.; Giménez-Marqués, M.; Torres-Cavanillas, R.; Coronado, E.; van der Zant, H. S. J.,

Chapter 7

Near Room-Temperature Memory Devices Based on Hybrid Spin-Crossover@SiO₂ Nanoparticles Coupled to Single-Layer Graphene Nanoelectrodes. *Advanced Materials* **2016**, 28 (33), 7228-7233; (c) Dugay, J.; Aarts, M.; Giménez-Marqués, M.; Kozlova, T.; Zandbergen, H. W.; Coronado, E.; van der Zant, H. S. J., Phase Transitions in Spin-Crossover Thin Films Probed by Graphene Transport Measurements. *Nano Letters* **2017**, 17 (1), 186-193.

3. (a) Miyamachi, T.; Gruber, M.; Davesne, V.; Bowen, M.; Boukari, S.; Joly, L.; Scheurer, F.; Rogez, G.; Yamada, T. K.; Ohresser, P.; Beaurepaire, E.; Wulfhekel, W., Robust spin crossover and memristance across a single molecule. *Nature Communications* **2012**, 3, 938; (b) Gopakumar, T. G.; Matino, F.; Naggert, H.; Bannwarth, A.; Tuczek, F.; Berndt, R., Electron-Induced Spin Crossover of Single Molecules in a Bilayer on Gold. *Angewandte Chemie International Edition* **2012**, 51 (25), 6262-6266; (c) Palamarciuc, T.; Oberg, J. C.; El Hallak, F.; Hirjibehedin, C. F.; Serri, M.; Heutz, S.; Létard, J.-F.; Rosa, P., Spin crossover materials evaporated under clean high vacuum and ultra-high vacuum conditions: from thin films to single molecules. *Journal of Materials Chemistry* **2012**, 22 (19), 9690-9695.

4. (a) Zhang, X.; N'Diaye, A. T.; Jiang, X.; Zhang, X.; Yin, Y.; Chen, X.; Hong, X.; Xu, X.; Dowben, P. A., Indications of magnetic coupling effects in spin cross-over molecular thin films. *Chemical Communications* **2018**, 54 (8), 944-947; (b) Rohlf, S.; Gruber, M.; Flöser, B. M.; Grunwald, J.; Jarausch, S.; Diekmann, F.; Kalläne, M.; Jasper-Toennies, T.; Buchholz, A.; Plass, W.; Berndt, R.; Tuczek, F.; Rosnagel, K., Light-Induced Spin Crossover in an Fe(II) Low-Spin Complex Enabled by Surface Adsorption. *The Journal of Physical Chemistry Letters* **2018**, 9 (7), 1491-1496; (c) Shalabaeva, V.; Rat, S.; Manrique-Juarez, M. D.; Bas, A.-C.; Vendier, L.; Salmon, L.; Molnár, G.; Bousseksou, A., Vacuum deposition of high-quality thin films displaying spin transition near room temperature. *Journal of Materials Chemistry C* **2017**, 5 (18), 4419-4425.

5. Bairagi, K.; Bellec, A.; Fourmental, C.; Iasco, O.; Lagoute, J.; Chacon, C.; Girard, Y.; Rousset, S.; Choueikani, F.; Otero, E.; Ohresser, P.; Saintavit, P.; Boillot, M.-L.; Mallah, T.; Repain, V., Temperature-, Light-, and Soft X-ray-Induced Spin Crossover in a Single Layer of FeII-Pyrazolylborate Molecules in Direct Contact with Gold. *The Journal of Physical Chemistry C* **2018**, 122 (1), 727-731.

6. (a) Jasper-Tönnies, T.; Gruber, M.; Karan, S.; Jacob, H.; Tuczek, F.; Berndt, R., Deposition of a Cationic FeIII Spin-Crossover Complex on Au(111): Impact of the Counter Ion. *The Journal of Physical Chemistry Letters* **2017**, 8 (7), 1569-1573; (b) Jasper-Toennies, T.; Gruber, M.; Karan, S.; Jacob, H.; Tuczek, F.; Berndt, R., Robust and Selective Switching of an FeIII Spin-Crossover Compound on Cu₂N/Cu(100) with Memristance Behavior. *Nano Letters* **2017**, 17 (11), 6613-6619.

7. (a) Kumar, K. S.; Studniarek, M.; Heinrich, B.; Arabski, J.; Schmerber, G.; Bowen, M.; Boukari, S.; Beaurepaire, E.; Dreiser, J.; Ruben, M., Engineering On-Surface Spin Crossover: Spin-State Switching in a Self-Assembled Film of Vacuum-Sublimable Functional Molecule. *Advanced Materials* **2018**, *30* (11), 1705416; (b) Gruber, M.; Miyamachi, T.; Davesne, V.; Bowen, M.; Boukari, S.; Wulfhekel, W.; Alouani, M.; Beaurepaire, E., Spin crossover in Fe(phen)₂(NCS)₂ complexes on metallic surfaces. *The Journal of Chemical Physics* **2017**, *146* (9), 092312.
8. (a) Naggert, H.; Rudnik, J.; Kipgen, L.; Bernien, M.; Nickel, F.; Arruda, L. M.; Kuch, W.; Näther, C.; Tuczek, F., Vacuum-evaporable spin-crossover complexes: physicochemical properties in the crystalline bulk and in thin films deposited from the gas phase. *Journal of Materials Chemistry C* **2015**, *3* (30), 7870-7877; (b) Beniwal, S.; Zhang, X.; Mu, S.; Naim, A.; Rosa, P.; Chastanet, G.; Létard, J. F.; Liu, J.; Sterbinsky, G. E.; Arena, D. A.; Dowben, P. A.; Enders, A., Surface-induced spin state locking of the [Fe(H₂B(pz)₂)₂(bipy)] spin crossover complex. *Journal of Physics: Condensed Matter* **2016**, *28* (20), 206002.
9. Gopakumar, T. G.; Bernien, M.; Naggert, H.; Matino, F.; Hermanns, C. F.; Bannwarth, A.; Mühlenberend, S.; Krüger, A.; Krüger, D.; Nickel, F.; Walter, W.; Berndt, R.; Kuch, W.; Tuczek, F., Spin-Crossover Complex on Au(111): Structural and Electronic Differences Between Mono- and Multilayers. *Chemistry – A European Journal* **2013**, *19* (46), 15702-15709.
10. Ossinger, S.; Naggert, H.; Kipgen, L.; Jasper-Toennies, T.; Rai, A.; Rudnik, J.; Nickel, F.; Arruda, L. M.; Bernien, M.; Kuch, W.; Berndt, R.; Tuczek, F., Vacuum-Evaporable Spin-Crossover Complexes in Direct Contact with a Solid Surface: Bismuth versus Gold. *The Journal of Physical Chemistry C* **2017**, *121* (2), 1210-1219.
11. Bernien, M.; Naggert, H.; Arruda, L. M.; Kipgen, L.; Nickel, F.; Miguel, J.; Hermanns, C. F.; Krüger, A.; Krüger, D.; Schierle, E.; Weschke, E.; Tuczek, F.; Kuch, W., Highly Efficient Thermal and Light-Induced Spin-State Switching of an Fe(II) Complex in Direct Contact with a Solid Surface. *ACS Nano* **2015**, *9* (9), 8960-8966.
12. Campbell, V. E.; Tonelli, M.; Cimatti, I.; Moussy, J.-B.; Tortech, L.; Dappe, Y. J.; Rivière, E.; Guillot, R.; Delprat, S.; Mattana, R.; Seneor, P.; Ohresser, P.; Choueikani, F.; Otero, E.; Koprowiak, F.; Chilkuri, V. G.; Suaud, N.; Guihéry, N.; Galtayries, A.; Miserque, F.; Arrio, M.-A.; Saintavit, P.; Mallah, T., Engineering the magnetic coupling and anisotropy at the molecule–magnetic surface interface in molecular spintronic devices. *Nature Communications* **2016**, *7*, 13646.
13. (a) Alam, M. S.; Stocker, M.; Gieb, K.; Müller, P.; Haryono, M.; Student, K.; Grohmann, A., Spin-State Patterns in Surface-Grafted Beads of Iron(II) Complexes.

Chapter 7

Angewandte Chemie International Edition **2010**, *49* (6), 1159-1163; (b) Pukenas, L.; Benn, F.; Lovell, E.; Santoro, A.; Kershaw Cook, L. J.; Halcrow, M. A.; Evans, S. D., Bead-like structures and self-assembled monolayers from 2,6-dipyrazolylpyridines and their iron(II) complexes. *Journal of Materials Chemistry C* **2015**, *3* (30), 7890-7896.

14. (a) Wei, T.-X.; Shi, Y.-R.; Zhai, J.; Gan, L.-B.; Huang, C.-H.; Liu, T.-T.; Ying, L.-M.; Luo, G.-B.; Zhao, X.-S., Synthesis, monolayer fabrication and photoelectric conversion property of two pyrrolidinofullerene carboxylic acid derivatives!The work was mainly done in State Key Laboratory of Rare Earth Materials Chemistry and Applications, Peking University, Beijing 100871, P.R. China.1. *Chemical Physics Letters* **2000**, *319* (1), 7-12; (b) Mottaghi, M.; Lang, P.; Rodriguez, F.; Rumyantseva, A.; Yassar, A.; Horowitz, G.; Lenfant, S.; Tondelier, D.; Vuillaume, D., Low-Operating-Voltage Organic Transistors Made of Bifunctional Self-Assembled Monolayers. *Advanced Functional Materials* **2007**, *17* (4), 597-604; (c) Bertazzo, S.; Rezwan, K., Control of α -Alumina Surface Charge with Carboxylic Acids. *Langmuir* **2010**, *26* (5), 3364-3371; (d) Choi, J.-H.; Kim, S.-O.; Linardy, E.; Dreaden, E. C.; Zhdanov, V. P.; Hammond, P. T.; Cho, N.-J., Adsorption of hyaluronic acid on solid supports: Role of pH and surface chemistry in thin film self-assembly. *Journal of Colloid and Interface Science* **2015**, *448*, 197-207.

15. (a) Abhervé, A.; Clemente-León, M.; Coronado, E.; Gómez-García, C. J.; López-Jordà, M., A spin-crossover complex based on a 2,6-bis(pyrazol-1-yl)pyridine (1-bpp) ligand functionalized with a carboxylate group. *Dalton Transactions* **2014**, *43* (25), 9406-9409; (b) García-López, V.; Palacios-Corella, M.; Abhervé, A.; Pellicer-Carreño, I.; Desplanches, C.; Clemente-León, M.; Coronado, E., Spin-crossover compounds based on iron(ii) complexes of 2,6-bis(pyrazol-1-yl)pyridine (bpp) functionalized with carboxylic acid and ethyl carboxylic acid. *Dalton Transactions* **2018**, *47* (47), 16958-16968.

16. Elhaïk, J.; Pask, C. M.; Kilner, C. A.; Halcrow, M. A., Synthesis of 2,6-di(pyrazol-1-yl)-4-bromomethylpyridine, and its conversion to other 2,6-di(pyrazol-1-yl)pyridines substituted at the pyridine ring. *Tetrahedron* **2007**, *63* (2), 291-298.

17. Biswas, N. N.; Yu, T. T.; Kimyon, Ö.; Nizalapur, S.; Gardner, C. R.; Manefield, M.; Griffith, R.; Black, D. S.; Kumar, N., Synthesis of antimicrobial glucosamides as bacterial quorum sensing mechanism inhibitors. *Bioorganic & Medicinal Chemistry* **2017**, *25* (3), 1183-1194.

18. Kocsis, L. S.; Brummond, K. M., Intramolecular Dehydro-Diels–Alder Reaction Affords Selective Entry to Arylnaphthalene or Aryldihydronaphthalene Lignans. *Organic Letters* **2014**, *16* (16), 4158-4161.

Chapter 7

19. Kershaw Cook, L. J.; Kulmaczewski, R.; Mohammed, R.; Dudley, S.; Barrett, S. A.; Little, M. A.; Deeth, R. J.; Halcrow, M. A., A unified treatment of the relationship between ligand substituents and spin state in a family of iron(II) complexes. *Angewandte Chemie* **2016**, *128* (13), 4399-4403.
20. Vermonden, T.; Branowska, D.; Marcelis, A. T. M.; Sudhölter, E. J. R., Synthesis of 4-functionalized terdentate pyridine-based ligands. *Tetrahedron* **2003**, *59* (27), 5039-5045.
21. (a) Ferreira, R. S.; Simeonov, A.; Jadhav, A.; Eidam, O.; Mott, B. T.; Keiser, M. J.; McKerrow, J. H.; Maloney, D. J.; Irwin, J. J.; Shoichet, B. K., Complementarity Between a Docking and a High-Throughput Screen in Discovering New Cruzain Inhibitors. *Journal of Medicinal Chemistry* **2010**, *53* (13), 4891-4905; (b) Dutta, R.; Scott, M. D.; Haldar, M. K.; Ganguly, B.; Srivastava, D. K.; Friesner, D. L.; Mallik, S., Fluorescent water soluble polymers for isozyme-selective interactions with matrix metalloproteinase-9. *Bioorg Med Chem Lett* **2011**, *21* (7), 2007-2010.
22. Dolomanov, O. V.; Bourhis, L. J.; Gildea, R. J.; Howard, J. A. K.; Puschmann, H., OLEX2: a complete structure solution, refinement and analysis program. *Journal of Applied Crystallography* **2009**, *42* (2), 339-341.
23. (a) Tricard, S.; Fleury, B.; Volatron, F.; Costa-Coquelard, C.; Mazerat, S.; Huc, V.; David, C.; Brisset, F.; Miserque, F.; Jegou, P.; Palacin, S.; Mallah, T., Growth and density control of nanometric nickel–iron cyanide-bridged objects on functionalized Si(100) surface. *Chemical Communications* **2010**, *46* (24), 4327-4329; (b) Tricard, S.; Raza, Y.; Mazerat, S.; Aissou, K.; Baron, T.; Mallah, T., Sequential growth of bistable copper–molybdenum coordination nanolayers on inorganic surfaces. *Dalton Transactions* **2013**, *42* (22), 8034-8040.
24. Davesne, V.; Gruber, M.; Studniarek, M.; Doh, W. H.; Zafeiratos, S.; Joly, L.; Sirotti, F.; Silly, M. G.; Gaspar, A. B.; Real, J. A.; Schmerber, G.; Bowen, M.; Weber, W.; Boukari, S.; Costa, V. D.; Arabski, J.; Wulfhekel, W.; Beaupaire, E., Hysteresis and change of transition temperature in thin films of Fe([Me₂Pyrz]₃BH)₂, a new sublimable spin-crossover molecule. *The Journal of Chemical Physics* **2015**, *142* (19), 194702.
25. Wasinger, E. C.; de Groot, F. M. F.; Hedman, B.; Hodgson, K. O.; Solomon, E. I., L-edge X-ray Absorption Spectroscopy of Non-Heme Iron Sites: Experimental Determination of Differential Orbital Covalency. *Journal of the American Chemical Society* **2003**, *125* (42), 12894-12906.
26. Zhang, X.; Costa, P. S.; Hooper, J.; Miller, D. P.; N'Diaye, A. T.; Beniwal, S.; Jiang, X.; Yin, Y.; Rosa, P.; Routaboul, L.; Gonidec, M.; Poggini, L.; Braunstein, P.; Doudin, B.; Xu,

Chapter 7

X.; Enders, A.; Zurek, E.; Dowben, P. A., Locking and Unlocking the Molecular Spin Crossover Transition. *Advanced Materials* **2017**, *29* (39), 1702257.

27. Kipgen, L.; Bernien, M.; Nickel, F.; Naggert, H.; Britton, A. J.; Arruda, L. M.; Schierle, E.; Weschke, E.; Tuczek, F.; Kuch, W., Soft-x-ray-induced spin-state switching of an adsorbed Fe(II) spin-crossover complex. *Journal of Physics: Condensed Matter* **2017**, *29* (39), 394003.

28. Davesne, V.; Gruber, M.; Miyamachi, T.; Costa, V. D.; Boukari, S.; Scheurer, F.; Joly, L.; Ohresser, P.; Otero, E.; Choueikani, F.; Gaspar, A. B.; Real, J. A.; Wulfhekel, W.; Bowen, M.; Beaupaire, E., First glimpse of the soft x-ray induced excited spin-state trapping effect dynamics on spin cross-over molecules. *The Journal of Chemical Physics* **2013**, *139* (7), 074708.

29. Salvatore, P.; Glargaard Hansen, A.; Moth-Poulsen, K.; Bjørnholm, T.; John Nichols, R.; Ulstrup, J., Voltammetry and in situscanning tunnelling spectroscopy of osmium, iron, and ruthenium complexes of 2,2':6',2''-terpyridine covalently linked to Au(111)-electrodes. *Physical Chemistry Chemical Physics* **2011**, *13* (32), 14394-14403.

30. Buron, C.; Groni, S.; Ségaud, N.; Mazerat, S.; Dragoë, D.; Fave, C.; Sénéchal-David, K.; Schöllhorn, B.; Banse, F., Self-assembled monolayer formation of a (N5)Fe(ii) complex on gold electrodes: electrochemical properties and coordination chemistry on a surface. *Dalton Transactions* **2016**, *45* (47), 19053-19061.

31. Kulmaczewski, R.; Cespedes, O.; Halcrow, M. A., Gradual Thermal Spin-Crossover Mediated by a Reentrant $Z' = 1 \rightarrow Z' = 6 \rightarrow Z' = 1$ Phase Transition. *Inorganic Chemistry* **2017**, *56* (6), 3144-3148.

32. (a) Turkevich, J.; Stevenson, P. C.; Hillier, J., A study of the nucleation and growth processes in the synthesis of colloidal gold. *Discussions of the Faraday Society* **1951**, *11* (0), 55-75; (b) Kimling, J.; Maier, M.; Okenve, B.; Kotaidis, V.; Ballot, H.; Plech, A., Turkevich Method for Gold Nanoparticle Synthesis Revisited. *The Journal of Physical Chemistry B* **2006**, *110* (32), 15700-15707.

33. Hiramatsu, H.; Osterloh, F. E., A Simple Large-Scale Synthesis of Nearly Monodisperse Gold and Silver Nanoparticles with Adjustable Sizes and with Exchangeable Surfactants. *Chemistry of Materials* **2004**, *16* (13), 2509-2511.

Chapter 8 – Experimental

8.1 Methods and instrumentation

8.1.1 NMR Spectroscopy

NMR spectra were recorded on a ULTRASHIELD Advance III 300 MHz, Ascend Advance III 400 MHz, Advance 500 MHz (Bruker Corp.) spectrometers using automated procedures, or by the Jeol ECA600 series II 600MHz NMR service. All deuterated solvents were purchased from Sigma Aldrich, Fluorochem or Fisher and used as received.

8.1.2 Mass Spectrometry

High resolution electrospray (ES) mass spectra were recorded on an open access MicroTOF mass spectrometer (Bruker Corp.) in either positive or negative ion mode. Samples were injected directly from feed solutions diluted to 10 $\mu\text{g} / \text{mL}$ and acquired over the m/z range 50 – 4000. Direct injection mass spectrometry data were collected by Dr Stuart Warriner. Low resolution electrospray mass spectra were recorded on an open access Micromass LCT (Bruker Corp.) after passing through a short HPLC column. All spectra were recorded using acetonitrile/water mix as an eluent and sodium formate calibrant.

8.1.3 X-ray Crystallography

Single crystal X-ray data were collected by the author. Crystals were mounted under Fomblin onto a nylon loop. Diffraction data were collected using an Agilent SuperNova diffractometer with an Atlas CCD detector using mirror monochromated Mo- K_{α} ($\lambda = 0.71073 \text{ \AA}$) or Cu- K_{α} ($\lambda = 1.54184 \text{ \AA}$) radiation. Data collected using synchrotron radiation were acquired at Diamond Light Source ($\lambda = 0.6889 \text{ \AA}$) using a Pilatus 2M detector by Dr Chris Pask, Dr Rafal Kulmaczewski, Kay Burrows or the author. The structures were solved using SHELXS direct methods, and the structural model refined by full matrix least squares using SHELXL. Molecular graphics and tables of bond lengths were carried out using Olex2.

Powder diffraction patterns were collected by the author on Bruker D2 Phaser equipped with a LynxEye detector using Long Fine Focused Cu radiation ($\lambda^{\circ} = 1.54060 \text{ \AA}$) and the data were processed by DIFFRAC. Measurement software.

8.1.4 Magnetic susceptibility

Magnetic measurements were performed by Dr Rafal Kulmaczewski on a Quantum Design SQUID magnetometer, in a applied field of 5000 Oe. A diamagnetic correction for the sample was estimated by using Pascal's constants¹; a diamagnetic correction for the sample holder was also applied to the data.

8.1.5 Elemental Analysis

Elemental composition of samples was determined by Tanya Marinko-Covell of the University of Leeds Microanalytical Service using a Carlo Erba 1108 Elemental Analyzer, or by Stephen Boyer of the School of Human Science at London Metropolitan University.

8.1.6 Scanning Electron Microscopy (SEM)

Scanning electron microscopy images of gel samples supported on a silicon wafer were mounted by Dr Alexander Kulak on an SEM stub using an adhesive copper film. Samples were coated with iridium (2 nm), prior to viewing with a FEI Nova NanoSEM 450 operating at 3 kV.

8.1.7 UV-vis/NIR

Absorption spectra were recorded by the author on a Perkin Elmer Lambda 900 spectrophotometer using tungsten-halogen lamps and R6872 photomultiplier/detector, at University of Leeds. At the ICMol (Valencia), UV-vis absorption spectra were recorded on an Jasco V-670 spectrophotometer, using quartz SUPRASIL® 1 cm path length cuvettes. The spectra were processed using Spectra Manager Software.

8.1.8 Evans Method

Variable temperature magnetic susceptibilities in solution were performed by Simon Barrett or Mark Howard on a Bruker DRX 500 spectrometer at a frequency of 500.57MHz. A diamagnetic correction for the solvent, and correction for the change in density of the solvent with temperature², were applied to these data.

8.1.9 Melting point

Melting points were determined by the author on a Stuart Scientific BIRBY SMP3 melting point apparatus.

8.1.10 Dynamic light scattering (DLS)

DLS measurements were collected on a Zetasizer Nano-S (Malvern Instrument, UK) at ICMol (Valencia). A He-Ne laser at $\lambda = 632$ nm was used as light source and the scattering was 173° . The results were analyzed via a non-negative least square algorithm (GP) as implemented in the Zetasizer Nano software.

8.1.11 Transmission electron microscopy (TEM)

TEM images were taken in a Jeol JEM-1010, electron microscope of transmission of 100KV with a ATM RX80 (8Mpx) digital camera, at the ICMol (Valencia). The TEM grid was prepared immediately after stopping the reaction. 10 μ L of the solution was dropped into the grid which was then dried under vacuum carefully for 10 minutes.

8.1.12 X-ray photoelectron spectroscopy (XPS)

X-ray photoelectron spectroscopy (K-ALPHA, Thermo Scientific) was used to analyse the surfaces of the samples. Samples were analysed ex-situ at the X-ray spectroscopy service at the Universidad de Alicante. All spectra were collected using Al K_α radiation (1486.6 eV), monochromatized by a twin crystal monochromator, yielding a focused X-ray spot (elliptical in shape with a major axis length of 400 μ m) at 3 mA \cdot C and 12 kV. The alpha hemispherical analyser was operated in constant energy mode with survey scan pass energies of 200 eV to measure the whole energy band, and at 50 eV in a narrow scan to selectively measure particular elements. XPS data were analysed with Advantage software. A smart background function was used to approximate the experimental backgrounds. Charge compensation was achieved with a system flood gun that provides low energy electrons and low energy argon ions from a single source. Spectra are referenced using the C 1s main peak (284.8 eV).

8.1.13 Atomic force microscopy (AFM)

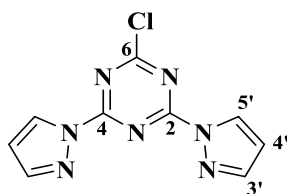
The substrates were imaged at ICMol (Valencia) with a Digital Instruments Veeco Nanoscope IVa AFM microscope, in tapping mode, using silicon tips with natural resonance frequency of 300 kHz and with an equivalent constant force of 40 N/m.

8.1.14 X-ray absorption spectroscopy (XAS)

Experiments were performed on synchrotron light at ALBA synchrotron (Barcelona, Spain), in the BOREAS Line.

8.2 Experimental details of ligands and metal complexes related to Chapter 2

8.2.1 2,4-Di(pyrazol-1-yl)-6-chloro-1,3,5-triazine (1)



To a stirred solution of pyrazole (1.0 g, 14.7 mmol) in THF (125 mL) cyanuric chloride (1.35 g, 7.3 mmol) was added carefully. The pale yellow suspension was stirred for 6 hr. Solvent was removed *in vacuo* and to give a white/blue solid. The compound was isolated by elution over silica gel (eluent: EtOAc, Rf: 0.58) to give a white solid, 0.61 g,

34% yield.

$^1\text{H NMR}$ ((400MHz, CDCl_3), 298 K, ppm) δ : 6.61 (dd, $J = 2.9, 1.5$ Hz, 2H, 4'), 7.96 (d, $J = 0.7$ Hz, 2H, 3'), 8.68 (d, $J = 2.8$ Hz, 2H, 5');

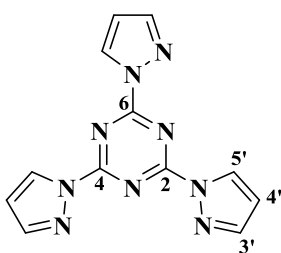
$^{13}\text{C NMR}$ ((100MHz, CDCl_3), 298 K, ppm) δ : 110.9 (4'), 130.7 (5'), 146.6 (3'), 162.9 (2 + 4), 173.6 (6);

$\text{ES}^+\text{-MS } m/z$ 248.0 [(M + H)]⁺, 270.0 [(M + Na)]⁺, 517.1 [(2M + Na)]⁺.

Mp: 170.2 °C.

Anal. Calcd for $\text{C}_9\text{H}_6\text{ClN}_7$: C, 43.65; H, 2.44; N, 39.59. **Found:** C, 43.4; H, 2.8; N, 39.2.

8.2.2 2,4,6-Tri(pyrazol-1-yl)-1,3,5-triazine (2)



To a stirred suspension of NaH 60% dispersion (1.3 g, 32.5 mmol) in THF (125 mL), pyrazole was added carefully (2.21 g, 32.5 mmol). After 5 minutes cyanuric chloride (2.0 g, 10.8 mmol) dissolved in THF was added. The solution was stirred for 8 hr at room temperature. Solvent was removed *in vacuo*, water was added and the crude was extracted with DCM. The compound was isolated by

eluting through silica gel (eluent gradient: EtOAc to acetone, Rf: 0.08 to 0.54 respectively) as a white powder. 2.58 g, 85.5% yield.

$^1\text{H NMR}$ ((400MHz, CDCl_3), 298 K, ppm) δ : 6.59 (dd, $J = 2.8, 1.5$ Hz, 3H, 4'), 7.95 (d, $J = 0.6$ Hz, 3H, 3'), 8.79 (d, $J = 2.8$ Hz, 3H, 5');

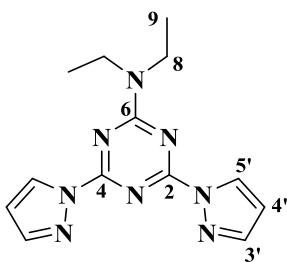
$^{13}\text{C NMR}$ ((100MHz, CDCl_3), 298 K, ppm) δ : 110.4 (4'), 130.7 (5'), 146.0 (3'), 163.7 (2 + 4 + 6);

$\text{ES}^+\text{-MS } m/z$ 280.1 [(M + H)]⁺, 302.1 [(M + Na)]⁺, 581.2 [(2M + Na)]⁺.

Mp: 240.8 °C.

Anal. Calcd for $\text{C}_{12}\text{H}_9\text{N}_9 \cdot 1/4\text{H}_2\text{O}$: C, 50.80; H, 3.37; N, 44.42. **Found:** C, 50.6; H, 3.1; N, 44.9.

8.2.3 2,4-Di(pyrazol-1-yl)-6-(diethylamino)-1,3,5-triazine (3)



Triethylamine (4.9 mL, 35.2 mmol) was stirring in THF when pyrazole (1.2 g, 17.6 mmol) was added. After 5 min of stirring cyanuric chloride (1.5 g, 8.1 mmol) was added and the solution was stirred overnight at room temperature. The compound was isolated by column flash chromatography (gradient eluent: from EtOAc to acetone, Rf: 0.36 to Rf: 0.83-0.26 respectively) as a colourless crystalline solid. 1.37 g, 59.2% yield.

$^1\text{H NMR}$ ((400MHz, CDCl_3), 298 K, ppm) δ : 3.81 (q, $J = 7$ Hz, 4H, 8), (1.3 (t, $J = 7.2$ Hz, 6H, 9), 6.49 (dd, $J = 2.6, 1.5$ Hz, 2H, 4'), 7.87 (s, 2H, 3'), 8.66 (d, $J = 2.6$ Hz, 2H, 5');

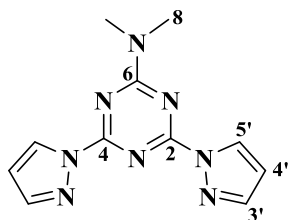
$^{13}\text{C NMR}$ ((100MHz, CDCl_3), 298 K, ppm) δ : 12.9 (9) 42.0 (8) 108.7 (4'), 129.9 (5'), 144.4 (3'), 162.4 (2 + 4), 165.2 (6);

$\text{ES}^+\text{-MS } m/z$ 285.2 [(M + H)]⁺, 307.1 [(M + Na)]⁺, 591.3 [(2M + Na)]⁺.

Mp: 104.3 °C.

Anal. Calcd for $\text{C}_{13}\text{H}_{16}\text{N}_8$: C, 54.92; H, 5.67; N, 39.41. Found: C, 54.4; H, 5.7; N, 40.2

8.2.4 2,4-Di(pyrazol-1-yl)-6-(dimethylamino)-1,3,5-triazine (4)



2,4,6-Tri(pyrazol-1'-yl)-1,3,5-triazine (2), (1.5 g, 5.3 mmol) was stirred in CHCl_3 solution (15 mL) when 40% aqueous dimethylamine (1.07 cm³, 8.4 mmol) was added. After stirring for 1.5 h, water was added and the two phases were stirred for 10 min. The organic phase was concentrated *in vacuo* and the crude was purified by silica gel chromatography (eluent: EtOAc, Rf: 0.23) as a white solid (884 mg, 3.4 mmol) 65.2% yield.

$^1\text{H NMR}$ ((400MHz, CDCl_3), 298 K, ppm) δ : 3.30 (s, 6H, 8), 6.42 (dd, $J = 2.5, 1.6$ Hz, 2H, 4'), 7.80 (s, 2H, 3'), 8.60 (d, $J = 2$ Hz, 2H, 5');

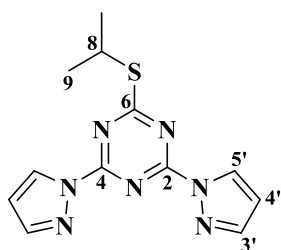
$^{13}\text{C NMR}$ ((100MHz, CDCl_3), 298 K, ppm) δ : 36.8 (8), 108.6 (4'), 129.8 (5'), 144.3 (3'), 162.0 (2 + 4), 166.0 (6);

$\text{ES}^+\text{-MS } m/z$ 257.1 [(M + H)]⁺, 279.1 [(M + Na)]⁺, 535.2 [(2M + Na)]⁺.

Mp: 210.6 °C.

Anal. Calcd for $\text{C}_{11}\text{H}_{12}\text{N}_8$: C, 51.55; H, 4.72; N, 43.73. Found: C, 51.6; H, 4.8; N, 43.9

8.2.5 2,4-Di(pyrazol-1-yl)-6-(isopropylsulfanyl)-1,3,5-triazine (5)



2,4,6-Tri(pyrazol-1'-yl)-1,3,5-triazine (**2**), (800 mg, 2.85 mmol) was stirred in DCM (10 mL) when sodium 2-propanethiolate (280 mg, 2.85 mmol) was added. After stirring for 3 h water was added to stop the reaction. The organic phase was concentrated *in vacuo* and the crude was purified by silica gel chromatography (eluent: EtOAc, Rf: 0.65) as a colourless solid (230 mg, 0.8 mmol) 28% yield.

$^1\text{H NMR}$ ((500MHz, CDCl_3), 298 K, ppm) δ : 1.51 (d, $J = 6.8$ Hz, 6H, 9), 4.15 (m, 1H, 8), 6.54 (dd, $J = 2.7, 1.5$ Hz, 2H, 4'), 7.90 (s, 2H, 3'), 8.66 (d, $J = 2.7$ Hz, 2H, 5');

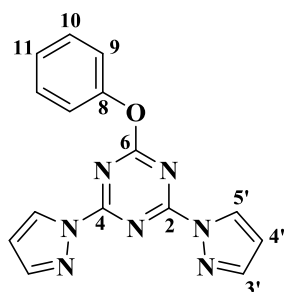
$^{13}\text{C NMR}$ ((100MHz, CDCl_3), 298 K, ppm) δ : 22.6 (9), 36.5 (8), 109.9 (4'), 130.2 (5'), 145.5 (3'), 161.1 (2 + 4), 186.2 (6);

$\text{ES}^+\text{-MS } m/z$ 288.1 [(M + H)]⁺, 305.1 [(M + NH_4)]⁺, 310.1 [(M + Na)]⁺, 597.2 [(2M + Na)]⁺.

Mp: 147.3 °C.

Anal. Calcd for $\text{C}_{12}\text{H}_{13}\text{N}_7\text{S}$: C, 50.16; H, 4.56; N, 34.12. Found: C, 50.1; H, 4.6; N, 33.9

8.2.6 2,4-Di(pyrazol-1-yl)-6-phenoxy-1,3,5-triazine (6)



Sodium hydroxide (440 mg, 10.8 mmol) was added to a phenol solution in acetone (1.02 g, 10.8 mmol). Cyanuric chloride (2 g, 10.8 mmol) was added after 5 min. The mixture was stirred for 15 minutes and pyrazole was added (1.47 g, 21.7 mmol). Finally, NaH 60% (0.83 g, 20 mmol) was added carefully over 3 min and the mixture was stirred for 2 h. This compound was purified by column flash chromatography (EtOAc, Rf 0.62) as a white solid (712mg, 2.33 mmol) 21.6% yield.

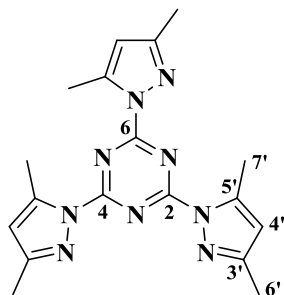
$^1\text{H NMR}$ ((400MHz, CDCl_3), 298 K, ppm) δ : 6.51 (d, $J = 0.7$ Hz, 2H, 4'), 7.28 (d, $J = 7.8$ Hz, 2H, 9), 7.34 (m, 1H, 11), 7.48 (m, 2H, 10), 7.90 (s, 2H, 3'), 8.51 (d, $J = 2.4$ Hz, 2H, 5');

$^{13}\text{C NMR}$ ((100MHz, CDCl_3), 298 K, ppm) δ : 110.2 (4'), 121.4 (9), 126.4 (11), 129.7 (10), 130.5 (5'), 145.8 (3'), 151.6 (8), 164.3 (2 + 4), 172.5 (6);

$\text{ES}^+\text{-MS } m/z$ 306.1 [(M + H)]⁺, 328.2 [(M + Na)]⁺, 633.2 [(2M + Na)]⁺.

Mp: 172.4 °C.

8.2.7 2,4,6-Tri(3,5-dimethylpyrazol-1-yl)-1,3,5-triazine (8)



This compound was obtained following an analogous synthesis for (2) by using 3,5-dimethyl pyrazole instead of pyrazole. The compound was purified by column flash chromatography (eluent: EtOAc, Rf: 0.15) as a white powder. 78% yield.

$^1\text{H NMR}$ ((400MHz, CDCl_3), 298 K, ppm) δ : 2.33 (s, 9H, 6'), 2.80 (s, 9H, 7') 6.09 (s, 3H, 4');

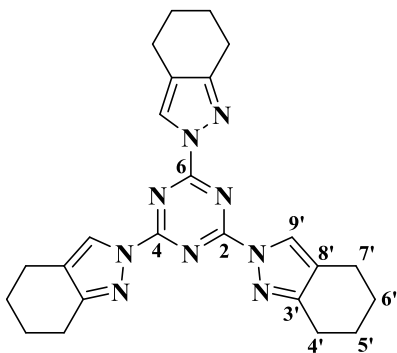
$^{13}\text{C NMR}$ ((100MHz, CDCl_3), 298 K, ppm) δ : 14.0 (7'), 15.6 (6'), 111.9 (4'), 144.4 (3'), 153.4 (5'), 164.4 (4 + 6 + 2);

ES^+ -MS m/z 364.2 [(M + H) $^+$], 386.2 [(M + Na) $^+$], 485.3 [(M + NC-dmpz + H) $^+$].

Mp: 246.1 °C.

Anal. Calcd for $\text{C}_{18}\text{H}_{21}\text{N}_9$: C, 59.49; H, 5.82; N, 34.69. Found: C, 57.2; H, 5.9; N, 34.1

8.2.8 2,4,6-Tri(4,5,6,7-tetrahydroindazol-2-yl)-1,3,5-triazine (9)



This compound was obtained following an analogous synthesis for (2) by using 4,5,6,7 tetrahydroindazole instead of pyrazole. The compound was isolated by eluting through silica gel (eluent gradient: EtOAc to acetone, Rf: 0.08 to 0.34 respectively) as a white powder. 23% yield.

$^1\text{H NMR}$ ((400MHz, CDCl_3), 298 K, ppm) δ : 1.79 (m, 6H, 5'), 1.86 (m, 6H, 6'), 2.64 (t, J = 6 Hz, 6H, 4'), 2.84 (t, J = 6.3 Hz, 6H, 7'), 8.45 (s, 3H, 9');

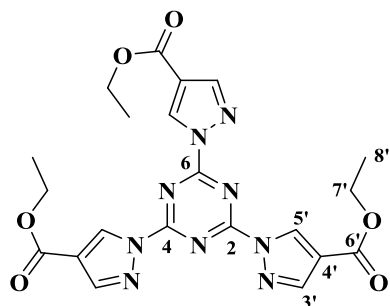
$^{13}\text{C NMR}$ ((100MHz, CDCl_3), 298 K, ppm) δ : 20.6 (7'), 23.0 (6' + 5'), 24.0 (4'), 121.1 (8'), 127.0 (9'), 157.0 (3'), 163.0 (2 + 4 + 6);

ES^+ -MS m/z 442.3 [(M + H) $^+$].

Mp: 344.9 °C.

Anal. Calcd for $\text{C}_{24}\text{H}_{27}\text{N}_9$ (1/11 $\cdot\text{CH}_2\text{Cl}_2$) : C, 64.41; H, 6.10; N, 28.06. Found: C, 64.7; H, 6.3; N, 28.1

8.2.9 Triethyl 1,1',1''-(2,4,6-tri(4-carboxylate-pyrazol-1-yl)-1,3,5-triazine) (10)



This compound was obtained following an analogous synthesis for (2) by using Ethyl 4-pyrazolecarboxylate instead of pyrazole. The compound was purified by column flash chromatography (eluent: EtOAc, Rf: 0.8) as a white powder. 24% yield.

$^1\text{H NMR}$ ((400MHz, CDCl_3), 298 K, ppm) δ : 1.43 (t, $J = 7.1$ Hz, 9H, 8'), 4.41 (q, $J = 7.1$ Hz, 6H, 7'), 8.33 (s, 3H, 3'),

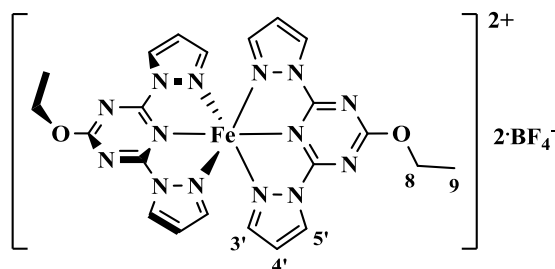
9.27 (s, 3H, 5');

$^{13}\text{C NMR}$ ((100MHz, CDCl_3), 298 K, ppm) δ : 14.3 (8'), 61.2 (7'), 119.8 (4'), 133.9 (5'), 146.3 (3'), 161.6 (6'), 163.8 (2 + 4 + 6);

$\text{ES}^+\text{-MS } m/z$ 496.2 [(M + H) $^+$], 513.2 [(M + NH_4) $^+$], 518.2 [(M + Na) $^+$], 1008.4 [(2M + NH_4) $^+$].

Mp: 216.2 °C.

8.2.10 Bis(2,4-di(pyrazol-1-yl)-6-ethoxy-1,3,5-triazine)iron(II) ditetrafluoroborate [12]B



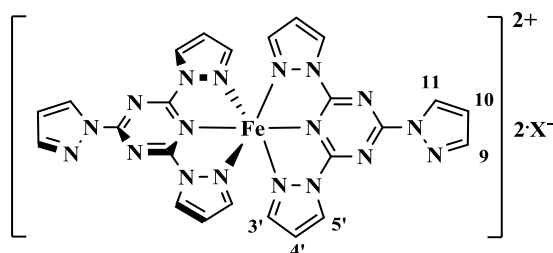
Iron(II) tetrafluoroborate hydrate (58 mg, 0.17 mmol) was dissolved in hot EtOH (60°) (30 mL), and mixed with a hot solution of 2,4-di(pyrazol-1-yl)-6-chloro-1,3,5-triazine (1), (100 mg, 0.4 mmol) in EtOH (20 mL). The solution turned yellow immediately, it was slowly cooled to room temperature then put into the freezer. Yellow crystals during a period of hours, and were isolated by decantation. (87 mg, 69% yield).

$^1\text{H NMR}$ ((300MHz, CD_3CN), 298 K, ppm) δ : -1.76 (s, 6H, 9) 4.07 (s, 4H, 8), 42.32 (s, 4H, 5'), 43.80 (s, 4H, 4'), 72.20 (s, 4H, 3');

$\text{ES}^+\text{-MS } m/z$ 195.5 [$\text{Na}_2\text{H}(\text{L})(\text{BF}_4)$] $^{2+}$, 258.1 [$\text{H}(\text{L})$] $^+$, 280.1 [$\text{Na}(\text{L})$] $^+$, 285.1 [$\text{Fe}(\text{L})_2$] $^{2+}$, 332.0 [$\text{Fe}(\text{L})\text{F}$] $^+$, 405.6 [$\text{K}(\text{L})_3\text{H}$] $^{2+}$, 537.2 [$\text{Na}(\text{L})_2$] $^+$, 589.1 [$\text{Fe}(\text{L})_2\text{F}$] $^+$.

Anal. Calcd for $\text{C}_{22}\text{H}_{22}\text{N}_{14}\text{O}_2\text{FeB}_2\text{F}_8$: C, 35.5; H, 2.98; N, 26.34. Found: C, 35.6; H, 3.0; N, 26.4

8.2.11 Bis(2,4,6-tri(pyrazol-1-yl)-1,3,5-triazine)iron(II) [2]X (X = BF₄⁻ and ClO₄⁻)



A solution of 2,4,6-tri(pyrazol-1'-yl)-1,3,5-triazine (**2**), (100 mg, 0.35 mmol) in hot nitromethane (15 mL) was added to a hot solution of iron(II) tetrafluoroborate hexahydrate (60 mg, 0.17 mmol) in nitromethane (30 mL) when it became intense yellow. The volume of NM was reduced *in vacuo* to 50%. Diethyl ether was added and yellow powder precipitated immediately (117 mg, 84.8% yield). Single crystals were obtained by diffusing diethyl ether onto NM solution of the complex. The same procedure using iron(II) perchlorate hydrate instead, produced 71% yield of [2]C.

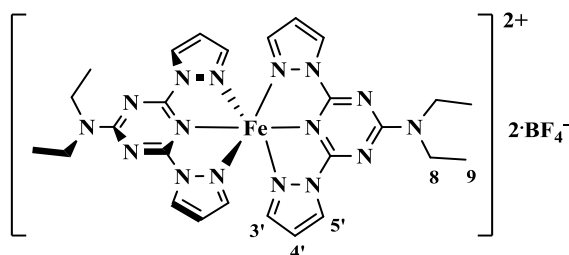
¹H NMR ((300MHz, CD₃NO₂), 298 K, ppm) δ: 5.25 (s, 2H, 10) 6.07 (s, 2H, 9), 8.35 (s, 2H, 11), 43.80 (s, 8H, 5' + 4'), 72.03 (s, 4H, 3');

ES⁺-MS *m/z* 280.1 [H(L)]⁺, 302.1 [Na(L)]⁺, 307.1 [Fe(L)₂]²⁺, 329.5 [Fe(L)₂(O₂CH)]²⁺, 338.5 [Fe(L)₂(O₂CH)(OH₂)]²⁺, 438.6 [K(L)₃H]²⁺, 513.1 [FeH(2,4-di[pyrazolyl]-6-oxo-1,3,5-triazinate)₂]⁺, 563.1 [Fe(L)(2,4-di[pyrazolyl]-6-oxo-1,3,5-triazinate)]⁺, 581.2 [Na(L)₂]⁺, 633.1 [Fe(L)₂F]⁺.

- [2]B, Anal. Calcd for C₂₄H₁₈B₂F₈FeN₁₈: C, 36.57; H, 2.30; N, 31.97. Found: C, 36.6; H, 2.3; N, 31.8

- [2]C, Anal. Calcd for C₂₄H₁₈N₁₈FeCl₂O₈: C, 35.45; H, 2.23; N, 31.00. Found: C, 35.3; H, 2.2; N, 30.9

8.2.12 Bis(2,4-di(pyrazol-1-yl)-6-(diethylamino)-1,3,5-triazine)iron(II) ditetrafluoroborate [3]B



A solution of 2,4-di(pyrazol-1-yl)-6-(diethylamino)-1,3,5-triazine (**3**), (25 mg, 0.09 mmol) in hot nitromethane (7 mL) was added to a hot solution of iron(II) tetrafluoroborate hexahydrate

Chapter 8

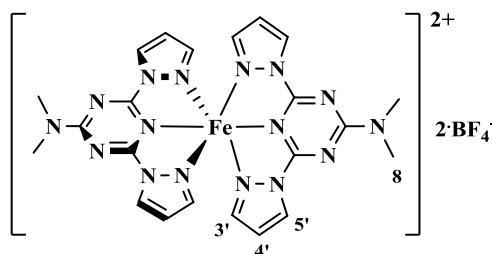
(15 mg, 0.04 mmol) in hot nitromethane (20 mL). The solution turned yellow. The solvent was reduced under vacuum and diisopropyl ether was diffused to yield large crystals. (20.1 mg, 63% yield).

$^1\text{H NMR}$ ((300MHz, CD_3CN), 298 K, ppm) δ : 0.17 (s, 12H, 9), 10.57 (s, 8H, 8), 49.14 (s, 8H, 4' + 5') 72.02 (s, 4H, 3');

$\text{ES}^+\text{-MS } m/z$ 285.2 $[\text{H}(\text{L})]^+$, 304.2 $[\text{K}(\text{L})_2\text{H}]^{2+}$, 307.1 $[\text{Na}(\text{L})]^+$, 312.1 $[\text{Fe}(\text{L})_2]^{2+}$, 446.2 $[\text{K}(\text{L})_3\text{H}]^{2+}$, 591.3 $[\text{Na}(\text{L})_2]^+$.

Anal. Calcd for $\text{C}_{26}\text{H}_{32}\text{N}_{16}\text{FeF}_2\text{B}_8$: C, 39.11 H, 4.04; N, 28.06. Found: C, 38.9; H, 3.9; N, 27.9

8.2.13 Bis(2,4-di(pyrazol-1-yl)-6-(dimethylamino)-1,3,5-triazine)iron(II) ditetrafluoroborate [4]B



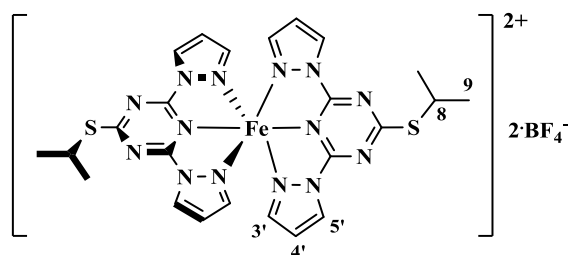
Iron(II) tetrafluoroborate hydrate (66 mg, 0.19 mmol) dissolved in MeCN was added to a stirred solution of 2,4-di(pyrazol-1-yl)-6-(dimethylamino)-1,3,5-triazine (**4**), (100 mg, 0.39 mmol) in DCM (10 mL). The solution turned yellow immediately. After 20 min stirring at room temperature yellow suspension was produced. The solvent was removed carefully by decantation to isolate a yellow powder (130 mg, 92% yield). Single crystals were obtained by diffusing ether onto MeCN solution of the complex.

$^1\text{H NMR}$ ((300MHz, CD_3CN), 298 K, ppm) δ : 16.00 (s, 12H, 8), 49.44 (s, 8H, 4' + 5'), 72.59 (s, 4H, 3');

$\text{ES}^+\text{-MS } m/z$ 257.1 $[\text{H}(\text{L})]^+$, 279.1 $[\text{Na}(\text{L})]^+$, 284.1 $[\text{Fe}(\text{L})_2]^{2+}$, 404.2 $[\text{K}(\text{L})_3\text{H}]^{2+}$, 535.2 $[\text{Na}(\text{L})_2]^+$, 587.2 $[\text{Fe}(\text{L})_2\text{F}]^+$.

Anal. Calcd for $\text{C}_{22}\text{H}_{24}\text{B}_2\text{F}_8\text{FeN}_{16}$: C, 35.61; H, 3.26; N, 30.20. Found: C, 35.7; H, 3.2; N, 30.1

8.2.14 Bis(2,4-di(pyrazol-1-yl)-6-(isopropylsulfanyl)-1,3,5-triazine)iron(II) ditetrafluoroborate [5]B



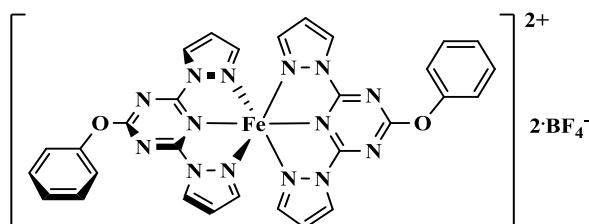
A solution of 2,4-di(pyrazol-1-yl)-6-(isopropylsulfanyl)-1,3,5-triazine (**5**), (20 mg, 0.07 mmol) in hot nitromethane (7 mL) was added to a hot solution of iron(II) tetrafluoroborate hexahydrate (9 mg, 0.03 mmol) in hot nitromethane (3 mL). The volume of NM was reduced *in vacuo* to 50%. Diisopropyl ether (15 mL) was added and yellow powder precipitated (20 mg, 83% yield). Single crystals were obtained by ether diffusion onto MeCN solution of [5]B.

$^1\text{H NMR}$ ((300MHz, CD_3NO_2), 298 K, ppm) δ : 0.99 (s, 12H, 9), 5.54 (s, 2H, 7), 44.2 (s, 8H, 4' + 5') 71.83 (s, 4H, 3');

$\text{ES}^+\text{-MS } m/z$ 273.0 $[\text{Fe}(\text{bppSH})_2]^{2+}$, 294.0 $[\text{Fe}(\text{bppSH})_2 + \text{Na} + \text{OH}]^{2+}$, 310.1 $[\text{Na}(\text{L})]^+$, 315.1 $[\text{Fe}(\text{L})_2]^{2+}$, 450.6 $[\text{K}(\text{L})_3\text{H}]^{2+}$, 597.2 $[\text{Na}(\text{L})_2]^+$, 649.1 $[\text{Fe}(\text{L})_2\text{F}]^+$.

Anal. Calcd for $\text{C}_{24}\text{H}_{26}\text{B}_2\text{F}_8\text{FeN}_{14}\text{S}_2$: C, 35.85; H, 3.26; N, 24.39. Found: C, 35.9; H, 3.4; N, 24.2

8.2.15 Bis(2,4-di(pyrazol-1-yl)-6-phenoxy-1,3,5-triazine)iron(II) ditetrafluoroborate [6]B

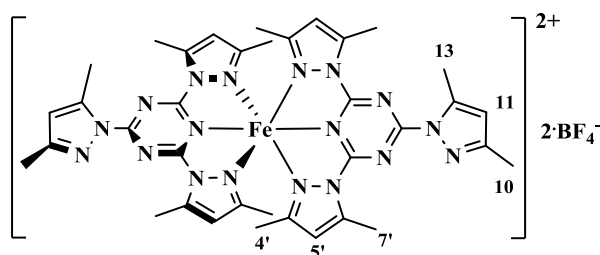


A solution of 2,4-di(pyrazol-1-yl)-6-phenoxy-1,3,5-triazine (**6**), (15 mg, 0.05 mmol) in hot nitromethane (6 mL) was added to a hot solution of iron(II) tetrafluoroborate hexahydrate (8.3 mg, 0.025 mmol) in hot nitromethane (7 mL). Then 10 mL of diethyl ether were added and yellow powder precipitated (12 mg, 56%). Poor and small single crystals were obtained by diffusion of ether onto MeCN solution of the complex.

$\text{ES}^+\text{-MS } m/z$ 306.1 $[\text{H}(\text{L})]^+$, 333.1 $[\text{Fe}(\text{L})_2]^{2+}$, 485.6 $[\text{Fe}(\text{L})_3]^{2+}$, 633.2 $[\text{Na}(\text{L})_2]^+$, 685.1 $[\text{Fe}(\text{L})_2\text{F}]^+$.

Anal. Calcd for $\text{C}_{30}\text{H}_{22}\text{N}_{14}\text{O}_2\text{FeB}_2\text{F}_8$: C, 42.89; H, 2.64; N, 23.34. Found: C, 42.1; H, 3.5; N, 20.6

8.2.16 Bis(2,4,6-tri(3,5-dimethylpyrazol-1-yl)-1,3,5-triazine)iron(II) ditetrafluoroborate [8]B



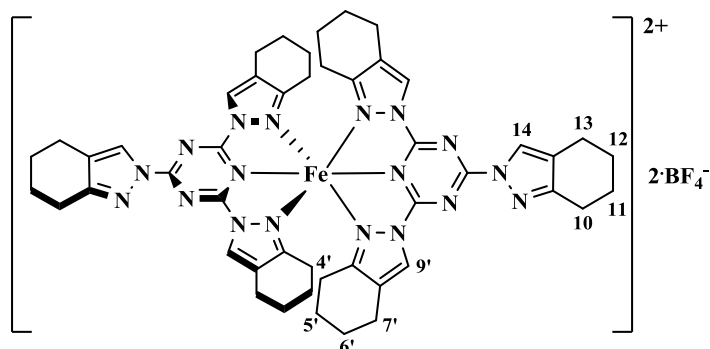
Iron(II) tetrafluoroborate hydrate (17 mg, 0.05 mmol) dissolved in MeCN was added to a stirred solution of 2,4,6-tri(3,5-dimethylpyrazol-1-yl)-1,3,5-triazine (**8**), (30 mg, 0.1 mmol) in DCM (8 mL). The solution turned orange. After 20 min stirring diethyl ether was diffused yielding nice orange crystals. Yield from 82%.

$^1\text{H NMR}$ ((300MHz, CD_3NO_2), 298 K, ppm) δ : 3.02 (s, 6H, 10), 3.66 (s, 6H, 13), 4.71 (s, 2H, 11), 7.40 (s, 12H, 7'), 18.32 (s, 12H, 4'), 76.67 (s, 4H, 5');

$\text{ES}^+\text{-MS}$ m/z 391.2 $[\text{Fe}(\text{L})_2]^{2+}$, 703.3 $[\text{Fe}(\text{L})(2,4\text{-di}(3,5\text{-dimethylpyrazolyl})\text{-6-oxo-1,3,5-triazinate})]^+$.

Anal. Calcd for $\text{C}_{36}\text{H}_{42}\text{N}_{18}\text{FeB}_2\text{F}_8$: C, 45.20; H, 4.42; N, 26.35. Found: C, 45.1; H, 4.3; N, 26.2

8.2.17 Bis(2,4,6-tri(4,5,6,7-tetrahydroindazol-2-yl)-1,3,5-triazine)iron(II) ditetrafluoroborate [9]B



Iron(II) tetrafluoroborate hydrate (30 mg, 0.08 mmol) dissolved in MeCN was added to a stirred solution of 2,4,6-tri(4,5,6,7-tetrahydroindazol-2-yl)-1,3,5-triazine (**9**), (80 mg, 0.17 mmol) in DCM (10 mL). The solution gradually turned yellow and after 40 min stirring at room temperature hexane was added to precipitate yellow powder (75 mg, 82%).

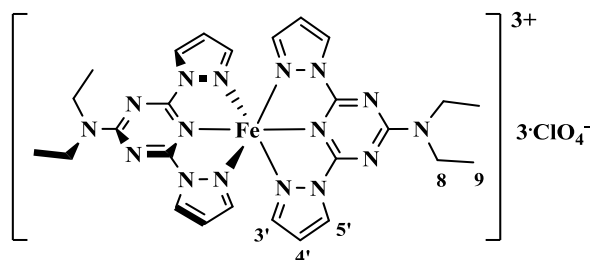
$^1\text{H NMR}$ ((300MHz, CD_3CN), 298 K, ppm) δ : 1.43 (s, 8H, 11 + 12), 2.97 (s, 8H, 6'), 4.03 (s, 8H, 7'), 4.95 (s, 4H, 10), 5.77 (s, 8H, 13), 7.97 (s, 2H, 14), 10.26 (s, 8H, 5'), 12.80 (s, 8H, 4'), 37.32 (s, 4H, 9');

Chapter 8

ES⁺-MS *m/z* 442.3 [L + H]⁺, 469.2 [Fe(L)₂]²⁺, 905.5 [Na(L)₂]⁺.

Anal. Calcd for C₄₈H₅₄N₁₈FeB₂F₈(CH₂Cl₂): C, 49.14; H, 4.71; N, 21.04. Found: C, 49.3; H, 4.5; N, 21.0

8.2.18 Bis(2,4-di(pyrazol-1-yl)-6-(diethylamino)-1,3,5-triazine)iron(III) triperchlorate Fe^{III}[3]C



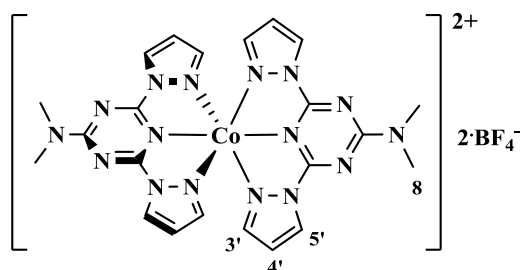
Iron(III) tetrafluoroborate hexahydrate (46 mg, 0.13 mmol) solution in MeCN was added to a solution of 2,4-di(pyrazol-1-yl)-6-(diethylamino)-1,3,5-triazine (**3**), (75 mg, 0.26 mmol) in DCM (8 mL). The solution turned black immediately. Diethyl ether was diffused through air and black needle shaped single crystals were obtained (64 mg, 61% yield).

¹H NMR ((300MHz, CD₃CN), 298 K, ppm) δ: 0.13 (s, 12H, 7), 10.71 (s, 8H, 6), 49.78 (s, 8H, 4' + 5') 72.95 (s, 4H, 3');

ES⁺-MS *m/z* 312.1 [Fe(L)₂]²⁺ (reduction), 446.2 [K(L)₃H]²⁺, 591.3 [Na(L)₂]⁺, 723.2 [Fe(L)₂(ClO₄)]⁺.

Anal. Calcd for C₂₆H₃₂N₁₆FeCl₃O₁₂: C, 33.84; H, 3.50; N, 24.29. Found: C, 33.9; H, 3.5; N, 24.1

8.2.19 Bis(2,4-di(pyrazol-1-yl)-6-(dimethylamino)-1,3,5-triazine)cobalt(II) ditetrafluoroborate Co[4]B



Cobalt (II) tetrafluoroborate hydrate (10 mg, 0.029 mmol) was added to a stirred solution of 2,4-di(pyrazol-1-yl)-6-(dimethylamino)-1,3,5-triazine (**4**), (15 mg, 0.059 mmol) in MeCN (10 mL). Dark blue/green solution was vigorously stirred and diethyl ether was diffused to yield single crystals. 89% yield.

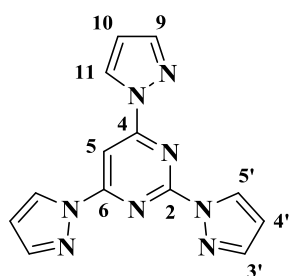
^1H NMR ((300MHz, CD_3CN), 298 K, ppm) δ : 13.41 (s, 4H, 5'), 24.13 (s, 12H, 6), 55.84 (s, 4H, 4'), 61.39 (s, 4H, 3');

ES⁺-MS m/z 257.1 $[\text{H(L)}]^+$, 276.1 $[\text{CoNa(L - CH}_2\text{)(L - (CH}_2\text{)}_2\text{)}]^{2+}$, 279.1 $[\text{Na(L)}]^+$, 404.1 $[\text{CoNa(L - CH}_2\text{)}_3]^{2+}$, 535.2 $[\text{Na(L)}_2]^+$.

Anal. Calcd for $\text{C}_{22}\text{H}_{24}\text{N}_{16}\text{CoF}_2\text{B}_8$: C, 35.46 H, 3.25; N, 30.08. Found: C, 34.7; H, 3.7; N, 29.3

8.3 Experimental details of ligands and metal complexes related to Chapter 3

8.3.1 2,4,6-Tri(pyrazol-1-yl)-1,3-pyrimidine (14)



To a NaH 60% mineral oil suspension in 30 mL of THF (1.28 g, 32.1 mmol), pyrazole (2.73 g, 40 mmol) dissolved in 25 ml of THF was added dropwise. The resulting solution was stirred at room temperature for 5 minutes. Trichloropyrimidine (1.5 g, 8.2 mmol) dissolved in THF was added carefully and the resulting solution was left overnight stirring at room temperature. The pale yellow precipitate obtained was cleaned with water and extracted with

chloroform. Yield: 81%.

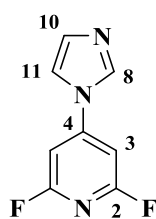
^1H NMR ((500MHz, CDCl_3), 298 K, ppm) δ : 6.56 (dd, $J = 2.7, 1.6$ Hz, 2H, 10), 6.57 (dd, $J = 2.7, 1.6$ Hz, 1H, 4'), 7.86 (d, $J = 0.9$ Hz, 2H, 9), 7.92 (d, $J = 0.9$ Hz, 1H, 3'), 8.41 (s, 1H, 5), 8.67 (d, $J = 2.7$ Hz, 1H, 5'), 8.73 (d, 2.5 Hz, 2H, 11);

^{13}C NMR ((75MHz, $\text{d}^6\text{-DMSO}$), 298 K, ppm) δ : 91.5 (5), 109.2 (4'), 109.8 (10), 128.8 (11), 130.8 (5'), 143.9 (3'), 144.8 (9), 154.8 (2), 159.4 (4 + 6);

ES⁺-MS m/z 279.1 $[(\text{M} + \text{H})]^+$, 301.1 $[(\text{M} + \text{Na})]^+$, 579.2 $[(2\text{M} + \text{Na})]^+$.

Mp: 257 °C.

8.3.2 2,6-Di(fluoro)-4-(imidazol-1-yl)-pyridine (15)



Imidazole (1 g, 14.7 mmol) was carefully added to a sodium hydride 60% (700 mg, 17 mmol) suspension in THF (35 mL). Then, 2,4,6-trifluoropyridine (5 g, 38 mmol) was added and the mixture was stirred at room temperature for 5 h. The compound was isolated as transparent crystalline needles through column flash chromatography (R_f 0.52, EtOAc), 1.29 g, 48.4 % yield.

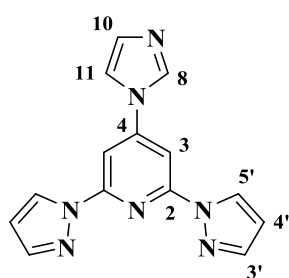
^1H NMR ((400MHz, $\text{d}^6\text{-DMSO}$), 298 K, ppm) δ : 7.19 (d, $J = 0.7$ Hz, 1H, 8), 7.71 (m, 2H, 3), 8.05 (m, 1H, 10), 8.63 (s, 1H, 11);

^{13}C NMR ((100MHz, $\text{d}^6\text{-DMSO}$), 298 K, ppm) δ : 96.6-97.0 (d, 3), 117.6 (11), 131.0 (10), 136.3 (8), 150.9 (t, 4), 160.7-163.3 (dd, 2),

ES⁺-MS m/z 182.1 [(M + H)⁺].

Mp: 164.6 °C.

8.3.3 2,6-Di(pyrazol-1-yl)-4-(imidazol-1-yl)-pyridine (16)



To a suspension of sodium hydride 60% (175 mg, 4.4 mmol) in THF (15 mL), pyrazole (300 mg, 4.4 mmol) was added carefully. 2,6-di(fluoro)-4-(imidazol-1-yl)-pyridine (760 mg, 4.2 mmol) was then added. After 24 h stirring at room temperature, column flash chromatography (R_f 0.33, EtOAc) yielded 980 mg of white solid 84% yield.

^1H NMR ((400MHz, CDCl_3), 298 K, ppm) δ : 6.55 (d, $J = 1.5$ Hz, 2H, 4'), 7.29 (s, 1H, 8), 7.58 (s, 1H, 10), 7.81 (s, 2H, 3'), 7.93 (s, 2H, 3), 8.22 (s, 1H, 11), 8.6 (d, $J = 2.7$ Hz, 2H, 5');

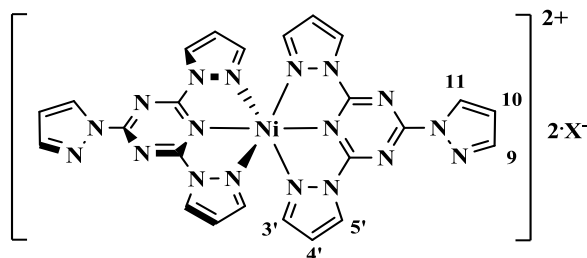
^{13}C NMR ((100MHz, CDCl_3), 298 K, ppm) δ : 99.7 (3), 108.6 (4'), 117.0 (11), 127.4 (5'), 131.7 (10), 135.2 (8), 143.0 (3'), 148.0 (4), 151.8 (2),

ES⁺-MS m/z 278.1 [(M + H)⁺], 300.1 [(M + Na)⁺], 577.2 [(2M + Na)⁺].

Mp: 196.8 °C.

Anal. Calcd for $\text{C}_{14}\text{H}_{11}\text{N}_7$: C, 60.65; H, 4.00; N, 35.35. Found: C, 60.2; H, 4.0; N, 35.6

8.3.4 Bis(2,4,6-tri(pyrazol-1-yl)-1,3,5-triazine)nickel(II) Ni[2]X (X = BF_4^- and ClO_4^-)



Two suspensions of 2,4,6-tri(pyrazol-1-yl)-1,3,5-triazine (**2**), (20 mg, 0.07mmol) and $\text{Ni}(\text{BF}_4)_2 \cdot 6\text{H}_2\text{O}$ (12 mg, 0.035 mmol) in 20 mL of NM were mixed, heated and sonicated together over 15 minutes. Diethyl ether was added to the pale blue solution and white

suspension appeared immediately. After stirring, pale blue powder precipitated (19 mg, 68% yield). The same procedure using nickel(II) perchlorate hydrate instead, 87% yield.

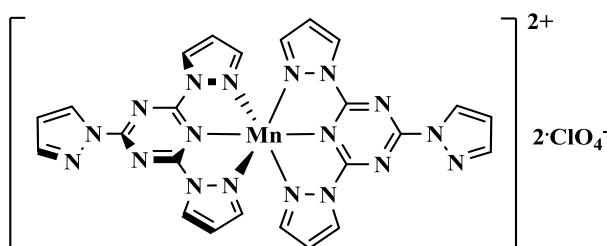
$^1\text{H NMR}$ ((300MHz, CD_3NO_2), 298 K, ppm) δ : 8.61 (s, 2H, 10), 10.57 (s, 2H, 9), 11.29 (s, 2H, 11), 46.93 (s, 4H, 5'), 55.45 (s, 4H, 4'), 61.54 (s, 4H, 3');

ES⁺-MS *m/z* 280.1 [H(L)]⁺, 302.1 [Na(L)]⁺, 308.1 [Ni(L)₂]²⁺, 513.1 [NiH(2,4-di(pyrazolyl)-6-oxo-1,3,5-triazinate)₂]⁺, 565.1 [Ni(L)(2,4-di(pyrazolyl)-6-oxo-1,3,5-triazinate)]⁺, 715.2 [Ni(L)₂(ClO₄)]⁺.

- Ni[2]B, Anal. Calcd for C₂₄H₁₈N₁₈NiB₂F₈: C, 36.45; H, 2.29; N, 31.88. Found: C, 36.3; H, 2.2; N, 31.7

- Ni[2]C, Anal. Calcd for C₂₄H₁₈N₁₈NiCl₂O₈: C, 35.32; H, 2.22; N, 30.89. Found: C, 35.2; H, 2.1; N, 30.8

8.3.5 Bis(2,4,6-tri(pyrazol-1-yl)-1,3,5-triazine)manganese(II) diperchlorate Mn[2]C



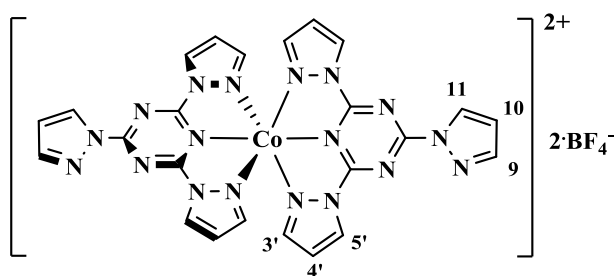
A solution of 2,4,6-tri(pyrazol-1-yl)-1,3,5-triazine (**2**), (40 mg, 0.14 mmol) in nitromethane (7 mL) was added to a suspension of manganese(II) perchlorate hexahydrate (26 mg, 0.07 mmol) in nitromethane (12 mL). The transparent mixture was sonicated over 10 min and diethyl ether was added to precipitate the compound as a white crystalline solid (37 mg, 59% yield).

$^1\text{H NMR}$ ((300MHz, CD_3NO_2), 298 K, ppm) δ : 6.52 (broad peak, s, 2H), 9.4 (broad peak, s, 1H), 18-26 (broad peak);

ES⁺-MS *m/z* 306.6 [Mn(L)₂]²⁺, 433.1 [Mn(L)(ClO₄)]⁺, 712.2 [Mn(L)₂(ClO₄)]⁺.

Anal. Calcd for C₂₄H₁₈N₁₈MnCl₂O₈: C, 35.50; H, 2.20; N, 31.00. Found: C, 35.2; H, 2.3; N, 31.0

8.3.6 Bis(2,4,6-tri(pyrazol-1-yl)-1,3,5-triazine)cobalt(II) ditetrafluoroborate Co[2]B



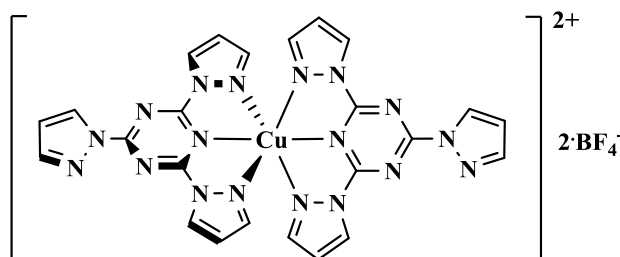
A solution of 2,4,6-tri(pyrazol-1-yl)-1,3,5-triazine (**2**), (40 mg, 0.14 mmol) in hot nitromethane (15 mL) was added to a hot solution of cobalt(II) tetrafluoroborate hexahydrate (24 mg, 0.07 mmol) in hot nitromethane (10 mL). The solution at this stage was pale violet. Diethyl ether was added and white/violet powder precipitated (41 mg, 74% yield).

$^1\text{H NMR}$ ((300MHz, CD_3NO_2), 298 K, ppm) δ : 11.77 (s, 2H, 10) 13.40 (s, 2H, 9), 20.37 (s, 2H, 11), 32.14 (s, 4H, 5'), 56.51 (s, 4H, 4'), 62.35 (s, 4H, 3');

$\text{ES}^+\text{-MS } m/z$ 308.6 $[\text{Co}(\text{L})_2]^{2+}$.

Anal. Calcd for $\text{C}_{24}\text{H}_{18}\text{N}_{18}\text{CoB}_2\text{F}_8$: C, 36.44; H, 2.29; N, 31.87. Found: C, 36.6; H, 2.4; N, 31.7

8.3.7 bis(2,4,6-tri(Pyrazol-1-yl)-1,3,5-triazine)copper(II) ditetrafluoroborate Cu[2]B



A solution of 2,4,6-tri(pyrazol-1-yl)-1,3,5-triazine (**2**), (25 mg, 0.09 mmol) in hot nitromethane (10 mL) was added to a hot solution of copper(II) tetrafluoroborate hexahydrate (15 mg, 0.05 mmol) in nitromethane (30 mL). The hot mixture was vigorously stirred. Mixtures of pale blue/grey small and big blue (hydrolysed species, containing (bptO)) single crystals were obtained by atmospheric diffusion of diethyl ether.

$\text{ES}^+\text{-MS } m/z$ 280.1 $[\text{H}(\text{L})]^+$, 310.6 $[\text{Cu}(\text{L})_2]^{2+}$, 361.0 $[\text{Cu}(\text{L})\text{F}]^+$, 570.1 $[\text{Cu}(\text{L})(\text{bptO})]^+$, 708.1 $[\text{Cu}(\text{L})_2(\text{BF}_4)]^+$, 950.1 $[\text{Cu}_2(\text{L})_2(\text{bptO})\text{F}_2]^+$.

Anal. Calcd for $\text{C}_{24}\text{H}_{18}\text{N}_{18}\text{CuB}_2\text{F}_8$: C, 36.23; H, 2.28; N, 31.69. Found: C, 37.5; H, 2.5; N, 30.5

8.3.8 [Bis(2,4,6-tri(pyrazol-1-yl)-1,3,5-triazine)iron(II) ditetrafluoroborate]-silver(I) tetrafluoroborate (Gel Fe-Ag-B)

Silver tetrafluoroborate (3.1 mg, 0.016 mmol) solution in nitromethane (0.25 mL) was added to a solution of [2]B in nitromethane (12.5 mg, 0.016 mmol) in 0.7 mL. After a briefly stir the coordination polymer gel was formed. All different CPG combinations were prepared analogously.

- **Gel Fe-Ag-B, ES⁺-MS *m/z*** 563.1 [Fe(L)(bptO)]⁺, 633.1 [Fe(L)₂F]⁺, 657.0 [Fe₂(L)(bptO)F₂]⁺, 665.1 [Ag(L)₂]⁺, 749.2 [Fe(L)₂F₃Na(H₂O)₃H]⁺, 849.0 [Fe₂(L)₂AgF₂(OH)₂]⁺, 936.1 [Fe₂(L)₂(bptO)F₂]⁺, 1062.0 [Fe₂(L)₂(bptO)AgF₃]⁺, 1152.0 [Fe₂(L)₃AgF₅H]⁺, 1278.0 [Fe₂(L)₃Ag₂F₆H]⁺, 1367.9 [Fe₃(L)₃Ag₂F₆(OH)(H₂O)]⁺ 1493.8 [Fe₃(L)₃Ag₃F₇(OH)(H₂O)]⁺.

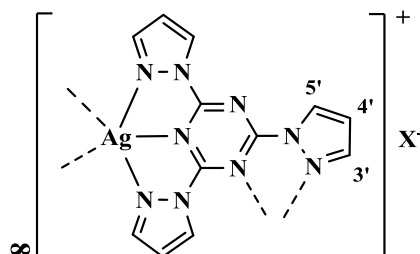
- **Gel Fe-Ag-C, ES⁺-MS *m/z*** 302.1 [Na(L)]⁺, 307.1 [Fe(L)₂]²⁺, 386.0 [Ag(L)]⁺, 665.1 [Ag(L)₂]⁺, 713.1 [Fe(L)₂(ClO₄)]⁺.

- **Gel Co-Ag-B, ES⁺-MS *m/z*** 566.1 [Co(L)(bptO)]⁺, 636.1 [Co(L)₂F]⁺, 665.1 [Ag(L)₂]⁺, 704.1 [Co(L)₂(BF₄)]⁺, 762.0 [Co(L)₂AgF₂]⁺, 942.1 [Co₂(L)₂(bptO)F₂]⁺, 1034.1 [Co₂(L-H)(L)₂F₃Na]⁺, 1080.2 [Co₂(L)₃F₂(BF₄)]⁺, 1148.2 [Co₂(L)₃F(BF₄)₂]⁺, 1206.1 [Co₂(L)₃AgF₃(BF₄)]⁺.

- **Gel Ni-Ag-B, ES⁺-MS *m/z*** 635.1 [Ni(L)₂F]⁺, 665.1 [Ag(L)₂]⁺, 703.1 [Ni(L)₂(BF₄)]⁺, 763.2 [Ni(L)₂AgF₂]⁺, 904.2 [Ni(L)₂(bptO)FNa(H₂O)]⁺, 940.3 [Ni₂(L)₂(bptO)F₂]⁺, 1008.2 [Ni₂(L)₃F₂(OH)]⁺, 1022.0 [Ni₂(L)(bptO)₂AgF(O₂CH)]⁺, 1066.0 [Ni₂(L)₂(bptO)AgF₃]⁺, 1146.2 [Ni₂(L)₃F(BF₄)₂]⁺.

- **Gel Ni-Ag-C, ES⁺-MS *m/z*** 665.2 [Ag(L)₂]⁺, 715.1 [Ni(L)₂(ClO₄)]⁺, 798.0 [Ag₂(L)₂(CN)]⁺, 822.1 [Ni(L-H)(L)Ag(ClO₄)]⁺, 872.0 [Ni₂(L-H)(L)(ClO₄)₂]⁺, 899.0 [Ni(L)₂Ag₂(OH)₃(H₂O)]⁺, 920.9 [Ni(L)₂Ag(ClO₄)₂]⁺, 1000.1 [Ni(L-H)₂(L)Ag]⁺, 1056.0 [Ni₂(L-H)₃Ag-H]⁺, 1074.0 [Ni₂(L-H)₃Ag(OH)]⁺, 1100.2 [Ni(L-H)(L)₂Ag(ClO₄)]⁺, 1158.0 [Ni₂(L-H)₃Ag(ClO₄)]⁺, 1206.0 [Ni(L-H)₂(L)Ag₂(ClO₄)]⁺, 1305.9 [Ni(L-H)₂(L)Ag₂(ClO₄)₂]⁺.

8.3.9 Catena-[2,4,6-tri(pyrazol-1-yl)-1,3,5-triazine]silver(I) Ag[2]X (X = BF₄⁻ and ClO₄⁻)



A solution of 2,4,6-tri(pyrazol-1-yl)-1,3,5-triazine (**2**), (20 mg, 0.07 mmol) in nitromethane (2.5 mL) was added to a hot solution of silver(I) tetrafluoroborate (14 mg, 0.07 mmol) in nitromethane (8 mL). Diethyl ether was added to a transparent solution and white powder

Chapter 8

precipitated immediately (33 mg, 98% yield). Second pseudopolymorph was crystallized from acetone. Silver perchlorate produced similar material, 68% yield.

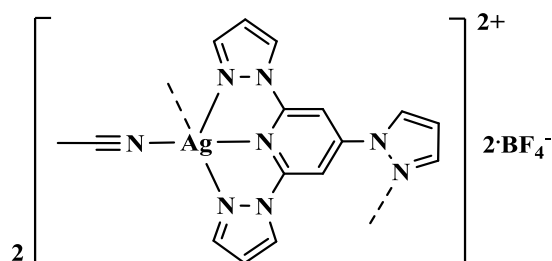
$^1\text{H NMR}$ ((300MHz, CD_3CN), 298 K, ppm) δ : 6.77 (br. s, 3H, 4'), 7.96 (br. s, 3H, 5'), 8.99 (d, $J = 2.7$ Hz, 3H, 3');

ES⁺-MS m/z 280.1 $[\text{H}(\text{L})]^+$, 302.1 $[\text{Na}(\text{L})]^+$, 386.0 $[\text{Ag}(\text{L})]^+$, 665.1 $[\text{Ag}(\text{L})_2]^+$, 581.2 $[\text{Na}(\text{L})_2]^+$, 733.0 $[\text{Ag}_2(\text{L})_2]^+$, 793.0 $[\text{Ag}_2(\text{L})_2\text{F}]^+$, 861.0 $[\text{Ag}_2(\text{L})_2(\text{BF}_4)]^+$, 966.9 $[\text{Ag}_3(\text{L})_2(\text{BF}_4)(-\text{H})]^+$, 971.0 $[\text{Ag}_2(\text{L})_2(\text{BF}_4)_2\text{Na}]^+$, 986.9 $[\text{Ag}_3(\text{L})_2(\text{BF}_4)\text{F}]^+$, 1054.9 $[\text{Ag}_3(\text{L})_2(\text{BF}_4)_2]^+$, 1140.1 $[\text{Ag}_2(\text{L})_3\text{BF}_4]^+$, 1335.0 $[\text{Ag}_3(\text{L})_3(\text{BF}_4)_2]^+$, 1444.0 $[\text{Ag}_3(\text{L})_3(\text{BF}_4)_3\text{Na}]^+$, 1529.9 $[\text{Ag}_4(\text{L})_3(\text{BF}_4)_3]^+$, 1809.0 $[\text{Ag}_4(\text{L})_4(\text{BF}_4)_3]^+$, 2088.1 $[\text{Ag}_4(\text{L})_5(\text{BF}_4)_3]^+$, 2282.0 $[\text{Ag}_5(\text{L})_5(\text{BF}_4)_4]^+$, 2562.1 $[\text{Ag}_5(\text{L})_6(\text{BF}_4)_4]^+$, 2758 $[\text{Ag}_6(\text{L})_6(\text{BF}_4)_5]^+$.

- **Ag[2]B**, Anal. Calcd for $\text{C}_{12}\text{H}_9\text{N}_9\text{AgBF}_4$: C, 30.41; H, 1.91; N, 26.60. Found: C, 30.6; H, 2.1; N, 26.7

- **Ag[2]C**, Anal. Calcd for $\text{C}_{12}\text{H}_9\text{N}_9\text{AgClO}_4$: C, 29.62; H, 1.86; N, 25.91. Found: C, 29.8; H, 1.8; N, 25.9

8.3.10 Bis[2,4,6-tri(pyrazol-1-yl)-pyridine]bis(acetonitrile)disilver(I) ditetrafluoroborate Ag[13]B-MeCN

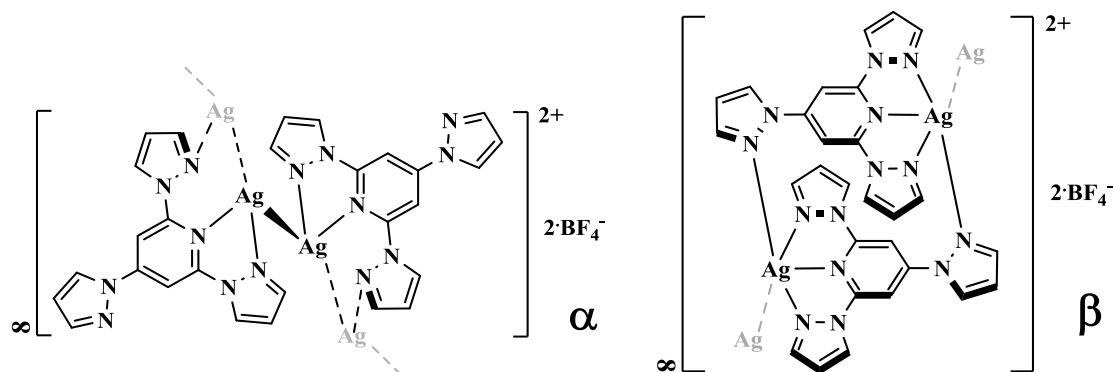


A solution of 2,4,6-tri(pyrazol-1-yl)-pyridine (**13**), (15 mg, 0.054 mmol) in acetonitrile (3 mL) was added to a solution of silver(I) tetrafluoroborate (11 mg, 0.056 mmol) in MeCN (4 mL). Diethyl ether was diffused into a transparent solution and thick needle shaped transparent crystals were obtained, 18 mg, 62% yield.

ES⁺-MS m/z 384.1 $[\text{Ag}(\text{L})]^+$;

Anal. Calcd for $\text{C}_{16}\text{H}_{11}\text{N}_8\text{AgBF}_4$: C, 37.46; H, 2.75; N, 21.84. Found: C, 37.5; H, 2.8; N, 21.7

8.3.11 Catena-Bis[2,4,6-tri(pyrazol-1-yl)-pyridine]disilver(I) ditetrafluoroborate Ag[13]B α and β

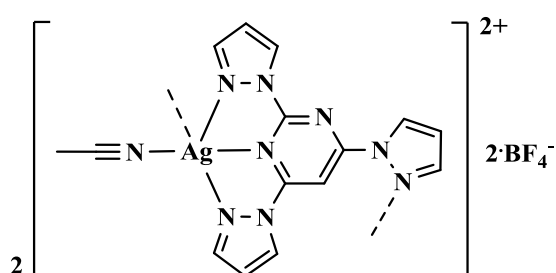


A solution of 2,4,6-tri(pyrazol-1-yl)-pyridine (**13**), (17 mg, 0.061 mmol) in nitromethane (2.5 mL) was added to a solution of silver(I) tetrafluoroborate (11.9 mg, 0.061 mmol) in nitromethane (8 mL). Diethyl ether was diffused into a transparent solution and white/transparent long and thick needle-shaped crystals were obtained (α). The solvent was decanted and before drying once the diethyl ether escaped, the crystals dissolved and recrystallized into small cubic blocks upon drying (β). 23 mg, 83% yield.

ES⁺-MS m/z 384.0 [Ag(L)]⁺, 661.1 [Ag(L)₂]⁺, 857.0 [Ag₂(L)₂(BF₄)₂]⁺;

Anal. Calcd for C₂₉H₂₅N₁₅Ag₂B₂F₈O₂: C, 34.63; H, 2.51; N, 20.90. Found: C, 34.5; H, 2.4; N, 20.7

8.3.12 Bis[2,4,6-tri(pyrazolyl-1-yl)pyrimidine]bis(acetonitrile)disilver(I) ditetrafluoroborate Ag[14]B-MeCN

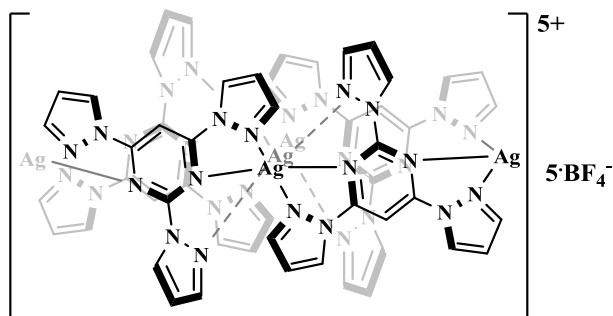


A solution of 2,4,6-tri(pyrazol-1-yl)-1,3-pyrimidine (**14**), (21 mg, 0.075 mmol) in acetonitrile (2.5 mL) was added to a solution of silver(I) tetrafluoroborate (14.6 mg, 0.075 mmol) in MeCN (8 mL). Diethyl ether diffusion produced transparent crystals (Yield 87%)

ES⁺-MS m/z 385.1 [Ag(L)]⁺, 663.2 [Ag(L)₂]⁺;

Anal. Calcd for C₁₅H₁₃N₉AgBF₄: C, 35.05; H, 2.55; N, 24.53. Found: C, 34.7; H, 2.3; N, 24.0

8.3.13 Tetrakis(2,4,6-tri(pyrazol-1-yl)-1,3,-pyrimidine)-pentasilver(I) penta-tetrafluoroborate Ag[14]B

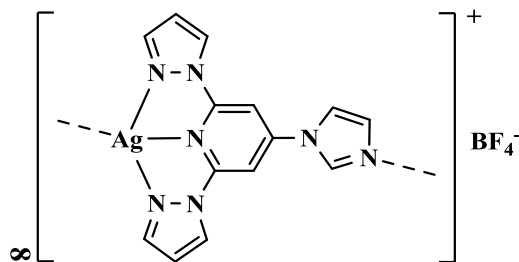


A solution of 2,4,6-tri(pyrazol-1-yl)-1,3-pyrimidine (**14**), (26 mg, 0.09 mmol) in nitromethane (4 mL) was added to a hot solution of silver(I) tetrafluoroborate (23 mg, 0.12 mmol) in nitromethane (6 mL). Diethyl ether was added to a transparent solution and white powder precipitated immediately (34 mg, 71% yield).

ES⁺-MS *m/z* 663.1 [Ag(L)₂]⁺, 772.0 [Ag₂(L)₂(-H)]⁺, 791.0 [Ag₂(L)₂F]⁺, 859.0 [Ag₂(L)₂(BF₄)]⁺, 984.9 [Ag₃(L)₂(BF₄)F]⁺, 1526.9[Ag₄(L)₃(BF₄)₃]⁺;

Anal. Calcd for C₅₂H₄₀N₃₂Ag₅B₅F₂₀: C, 29.93; H, 1.93; N, 21.48. Found: C, 29.8; H, 2.0; N, 21.3

8.3.14 Catena-[2,6-di(pyrazol-1-yl)-4-(imidazol-1-yl)-pyridine]silver(I) tetrafluoroborate Ag[16]B

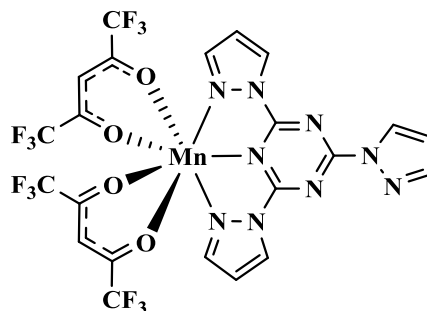


A solution of 2,6-di(pyrazol-1-yl)-4-(imidazol-1-yl)-pyridine (**16**), (19 mg, 0.068 mmol) in acetonitrile (2.5 mL) was added to a solution of silver(I) tetrafluoroborate (13.2 mg, 0.068 mmol) in MeCN (8 mL). Transparent single crystals were obtained after 3 months in a closed vial upon very slow evaporation of the solvent, 15 mg, 47%.

ES⁺-MS *m/z* 278.2 [H(L)]⁺, 386.1 [Ag(L)]⁺, 512.0 [Ag₂(L)F]⁺, 769.2 [Ag₂(L)₂(-H)]⁺, 789.2 [Ag₂(L)₂F]⁺;

Anal. Calcd for C₁₄H₁₁N₇AgBF₄ + (H₂O)_{0.625}: C, 34.80; H, 2.56; N, 20.29. Found: C, 34.5; H, 2.4; N, 20.3

8.3.15 2,4,6-Tri(pyrazol-1-yl)-1,3,5-triazine-bis(1,1,1,5,5,5-hexafluoro-2,4-pentanedionato)manganese(II)

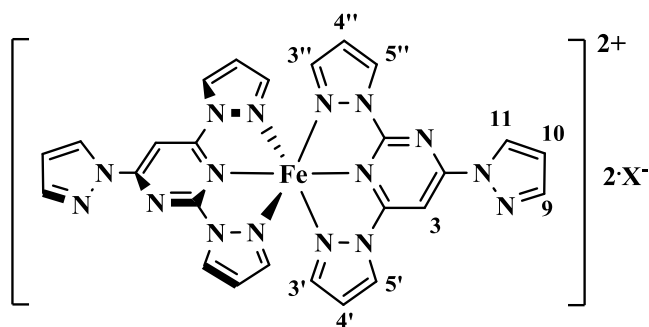


2,4,6-Tri(pyrazol-1-yl)-1,3,5-triazine (**2**), (30 mg, 0.107 mmol) was dissolved in MeCN and 50 mg of $\text{Mn}(\text{tFacac})_2$ (0.107 mmol) dissolved in MeCN were added. The yellow mixture was strongly stirred for two hours. The solution was left resting open air few days and large yellow crystals were obtained. (60 mg, 78% yield).

$^1\text{H NMR}$ (300MHz, CH_3CN) δ : 3.89 (s, 1H), 7.6-9.6 (broad peak), 10-12 (broad peak);

Anal. Calcd for $\text{C}_{22}\text{H}_{11}\text{N}_9\text{MnF}_{12}\text{O}_4$: C, 35.31; H, 1.48; N, 16.85. Found: C, 35.3; H, 1.4; N, 16.9

8.3.16 Bis(2,4,6-tri(pyrazol-1-yl)-1,3-pyrimidine)iron(II) [**14**] X ($\text{X} = \text{BF}_4^-$ and ClO_4^-)



A solution of 2,4,6-tri(pyrazol-1-yl)-1,3-pyrimidine (**14**), (21 mg, 0.076 mmol) in acetonitrile (8 mL) was added to a solution of iron(II) tetrafluoroborate hexahydrate (13 mg, 0.038 mmol) in MeCN (1 mL). Diethyl ether was added and yellow powder precipitated immediately (29 mg, 76% yield). Single crystals were obtained by diffusing diethyl ether onto MeCN solution of the complex. The same procedure using nitromethane and iron(II) perchlorate hydrate instead. 81% yield.

$^1\text{H NMR}$ ((300MHz, CD_3NO_2), 298 K, ppm) δ : 5.16 (s, 2H, 8), 6.41 (s, 2H, 7), 8.34 (s, 2H, 9), 42.20 (s, 2H, 5') 43.75 (s, 2H, 4'), 44.36 (s, 2H, 4''), 47.51 (s, 2H, 5''), 60.80 (s, 2H, 3) 73.73 (s, 2H, 3'), 75.01 (s, 2H, 3'');

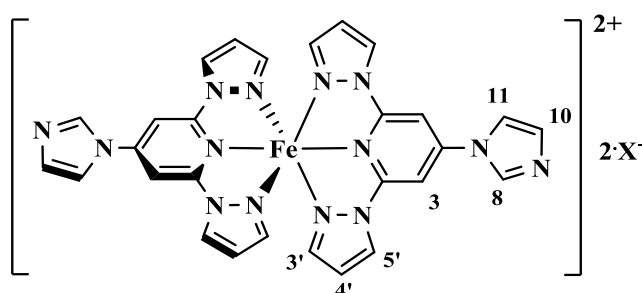
Chapter 8

ES⁺-MS *m/z* 306.1 [Fe(L)₂]²⁺, 369.1 [Fe(L)(H₂O)(OH)]⁺, 579.3 [Na(L)₂]⁺, 631.3 [Fe(L)₂F]⁺, 699.1 [Fe(L)₂(BF₄)]⁺.

- [14]B, Anal. Calcd for C₂₆H₂₀N₁₆FeB₂F₈: C, 39.73; H, 2.56; N, 28.51. Found: C, 39.5; H, 2.6; N, 28.3

- [50]C, Anal. Calcd for C₂₆H₂₀N₁₆FeCl₂O₈ (CH₃NO₂): C, 37.17; H, 2.66; N, 27.30. Found: C, 37.3; H, 2.5; N, 27.2

8.3.17 Bis(2,6-di(pyrazol-1-yl)-4-(imidazol-1-yl)-pyridine)iron(II) [16]X (X = BF₄⁻ and ClO₄⁻)



A solution of 2,6-di(pyrazol-1-yl)-4-(imidazol-1-yl)-pyridine (**16**), (10 mg, 0.036 mmol) either in acetonitrile or nitromethane (3 mL) was added to a solution of iron(II) tetrafluoroborate hexahydrate (6 mg, 0.018 mmol) in MeCN (1 mL). Diethyl ether was added and yellow powder precipitated immediately (11 mg, 82.4% yield). Single crystals were obtained by diffusing diethyl ether onto MeCN solution of the complex. The same procedure using iron(II) perchlorate hydrate instead, 71% yield.

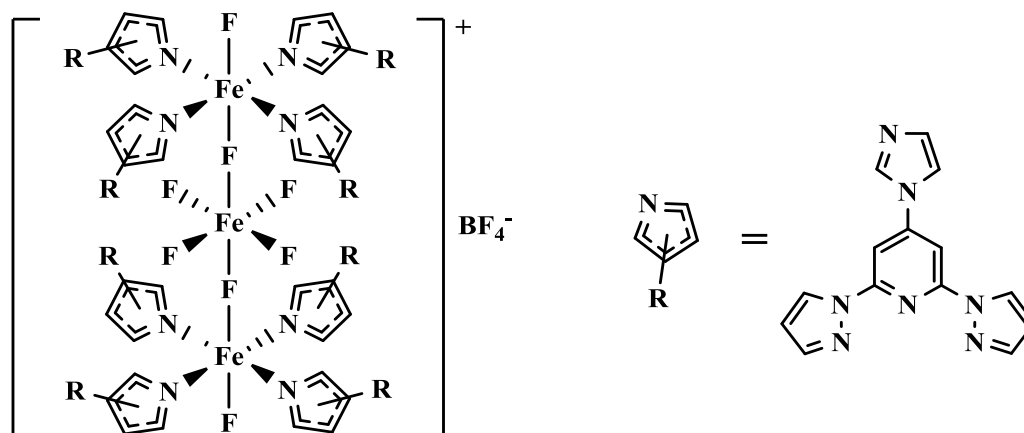
¹H NMR ((300MHz, CD₃CN), 298 K, ppm) δ: 5-10 (m, 6H, 8 + 10 + 11), 42.13 (s, 8H, 4' + 5'), 60.66 (s, 4H, 3), 71.71 (s, 4H, 3');

ES⁺-MS *m/z* 306.1 [Fe(L)₂]²⁺,

- [16]B, Anal. Calcd for C₂₈H₂₂N₁₄FeB₂F₈: C, 42.89; H, 2.83; N, 25.01. Found: C, 43.0; H, 3.0; N, 24.9

- [16]C, Anal. Calcd for C₂₈H₂₂N₁₄FeCl₂O₈: C, 41.55; H, 2.74; N, 24.23. Found: C, 41.7; H, 2.6; N, 24.1

8.3.18 Octakis-[2,6-di(pyrazol-1-yl)-4-(imidazol-1-yl)pyridine]octafluoro-tris-iron(III) tetrafluoroborate. $\text{Fe}^{\text{III}}_3[\text{16}]_8\text{F}_8$



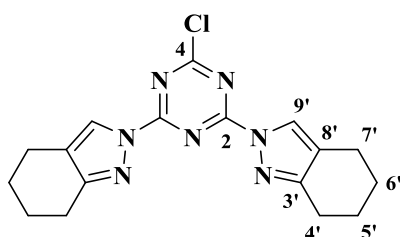
A solution of 2,6-di(pyrazol-1-yl)-4-(imidazol-1-yl)-pyridine (**16**), (35 mg, 0.126 mmol) in methanol (4 mL) was mixed with a suspension of sodium hexafluoroferrate in the same solvent (3.8 mg, 0.016 mmol in 2 mL), when a solution of iron(II) tetrafluoroborate hydrate (10.7 mg, 0.032 mmol) in 3 mL of methanol was added to the mixture a pale green/yellow color appeared. Slow evaporation of the solvent yielded big cubic shaped crystalline phase 18 mg, 0.007 mmol, 44 % yield. In contrast, diffusion of diethyl ether into the same solution produced needles which were suitable for single crystal X-ray diffraction.

ES⁺-MS m/z 1259.3 [$\text{Fe}_3(\text{L})_8\text{F}_7$]²⁺, 2537.7 [$\text{Fe}_3(\text{L})_8\text{F}_8$]⁺.

Anal. Calcd for $\text{C}_{112}\text{H}_{88}\text{N}_{56}\text{Fe}_3\text{BF}_{12}$: C, 51.3; H, 3.4; N, 29.9. Found: C, 46.8; H, 3.5; N, 27.2, alternatively, calcd for $\text{C}_{112}\text{H}_{88}\text{N}_{56}\text{Fe}_3\text{BF}_{12} + (\text{H}_2\text{O})_6 + ([\text{16}]\text{B})_2$: C, 46.92; H, 3.37; N, 27.36.

8.4 Experimental details of ligands and metal complexes related to Chapter 4

8.4.1 2,4-Di(4,5,6,7-tetrahydroindazol-2-yl)-6-chloro-1,3,5-triazine (**17**)



This compound was isolated from a column flash chromatography of reaction (**9**). The eluent applied was a gradient from EtOAc to acetone; R_f (0.5 to 0.65). 300 mg were isolated as a white powder, 15.6% yield. The compound was obtained with higher yield from the same procedure without sodium hydride.

¹H NMR ((400MHz, CDCl_3), 298 K, ppm) δ : 1.74 (m, 4H 7'), 1.82 (m, 4H, 8'), 2.6 (t, $J = 6.1$ Hz, 4H, 6'), 2.79 (t, $J = 6.3$ Hz, 4H, 9'), 8.27 (s, 2H, 5');

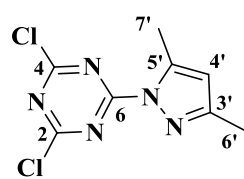
^{13}C NMR ((100MHz, CDCl_3), 298 K, ppm) δ : 20.6 (7'), 22.8 (6' + 5'), 24.0 (4'), 122.1 (8'), 126.8 (9'), 158.0 (3'), 162.2 (2 + 6), 173.1 (4);

ES⁺-MS m/z 356.1 [(M + H)⁺], 728.3 [(2M + NH_4)⁺].

Mp: 253.2 °C.

Anal. Calcd for $\text{C}_{17}\text{H}_{18}\text{ClN}_7 \cdot (3/10) \cdot \text{CHCl}_3$: C, 53.06; H, 4.71; N, 25.04. Found: 52.6; H, 4.7; N, 25.5

8.4.2 2,4-Di-chloro-6-(3,5-dimethylpyrazol-1-yl)-1,3,5-triazine (19)



This compound was isolated from a column flash chromatography of reaction (8). The eluent applied was a gradient from EtOAc; R_f (0.82) 45 mg were isolated as a white powder, 10 % yield.

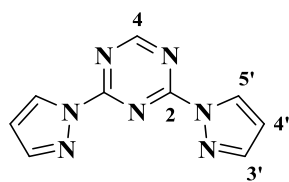
^1H NMR ((300MHz, CDCl_3), 298 K, ppm) δ : 2.36 (s, 3H 6'), 2.70 (s, 3H, 7'), 6.15 (s, 1H, 4');

^{13}C NMR ((75MHz, CDCl_3), 298 K, ppm) δ : 14.1 (7'), 16.0 (6'), 113.8 (4'), 145.6 (3'), 155.8 (5'), 163.1 (6), 172.3 (2 + 4);

ES⁺-MS m/z 244.0 [(M + H)⁺].

Mp: 228.8 °C.

8.4.3 2,6-Di(pyrazol-1-yl)-1,3,5-triazine (21)



Pyrazole (480 mg, 7 mmol) was added carefully to a NaH 60% dispersion (280 mg, 7 mmol) suspension in THF (30 mL). After 5 minutes stirring under nitrogen, the solution went transparent and 2,6-Dichloro-1,3,5-triazine (500 mg, 3.5 mmol) was added suspended in THF. The mixture was stirred for 12 hours at room temperature. The solvent was removed under vacuum, water was added (15 mL) and the compound was extracted with dichloromethane. After short column flash chromatography in EtOAc (R_f 0.22) pure compound was obtained as a white solid, 358mg, 1.68 mmol, 48.1% yield.

^1H NMR ((300MHz, CDCl_3), 298 K, ppm) δ : 6.59 (dd, J = 2.8, 1.5 Hz, 2H, 4'), 7.94 (d, J = 0.9 Hz, 2H, 3'), 8.72 (dd, J = 2.8, 0.5 Hz, 2H, 5'), 9.09 (s, 1H, 4);

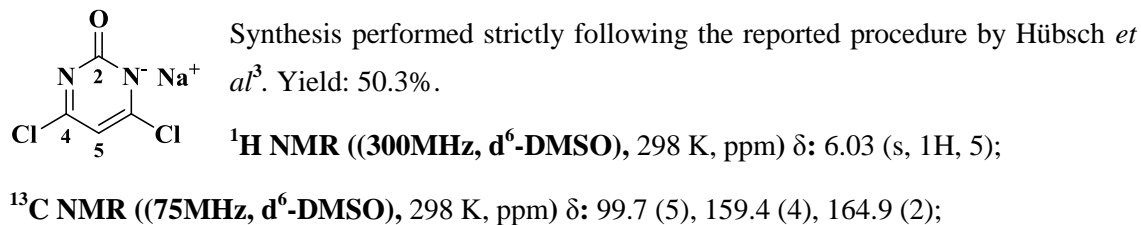
^{13}C NMR ((75MHz, CDCl_3), 298 K, ppm) δ : 109.8 (4'), 129.6 (5'), 145.2 (3'), 161.7 (2), 168.9 (4);

ES⁺-MS m/z 214.1 [(M + H)⁺], 236.1 [(M + Na)⁺], 449.1 [(2M + Na)⁺].

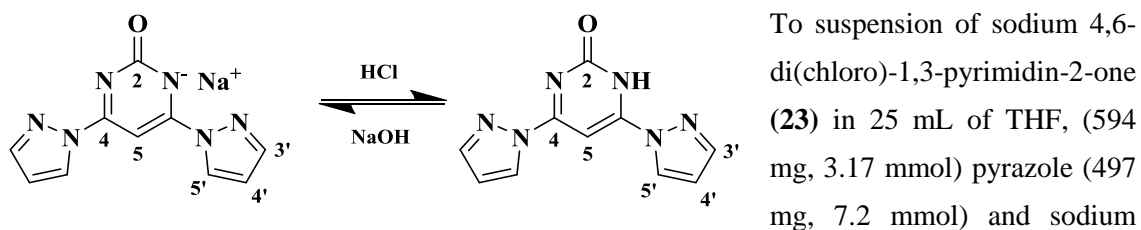
Mp: 101 °C.

Anal. Calcd for C₉H₇N₇: C, 50.70; H, 3.31; N, 45.99. Found: C, 50.7; H, 3.3; N, 45.9

8.4.4 Sodium 4,6-di(chloro)-1,3-pyrimidin-2-one (23)



8.4.5 Sodium 4,6-di(pyrazol-1-yl)-1,3-pyrimidin-2-one (22) and 2-hydroxy-4,6-bis(pyrazol-1-yl)-1,3-pyrimidine (24)



hydride (292 mg, 7.2 mmol) were added in 40 mL of THF. The mixture was stirred overnight at 65°C. The solvent was removed under vacuum and 35 mL of water were added. HCl was added from pH basic until pH = 5. The product (24) precipitated as a white solid which was filtered and dried under vacuum, 630 mg, 68.8% yield. Ligand (24) once purified can be converted back into (22) by NaOH addition in acetonitrile.

(22) ¹H NMR ((400MHz, d⁶-DMSO), 298 K, ppm) δ: 6.49 (dd, J = 2.5, 1.6, 2H, 8), 7.13 (s, 1H, 5), 7.75 (m, 2H, 7), 8.59 (d, J = 2.4 Hz, 2H, 9);

(22) ¹³C NMR ((100MHz, d⁶-DMSO), 298 K, ppm) δ: 78.2 (5), 107.2 (8), 127.0 (9), 141.8 (7), 159.7 (4 + 6), 167.2 (2);

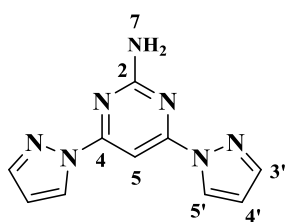
(24) ¹H NMR ((400MHz, d⁶-DMSO), 298 K, ppm) δ: 6.66 (dd, J = 2.6, 1.7, 2H, 4'), 7.82 (s, 1H, 5), 7.96 (d, J = 0.9 Hz, 2H, 3'), 8.59 (m, 2H, 5');

(24) ¹³C NMR ((100MHz, d⁶-DMSO), 298 K, ppm) δ: 87.1 (5), 109.4 (4'), 127.9 (5'), 144.1 (3'), 159.9 (4 + 6), 164.7 (2);

(24) ES⁺-MS *m/z* 229.1 [(M + H)]⁺, 251.1 [(M + Na)]⁺.

(24) Mp: 223.8°C.

8.4.6 2-Amino-4,6-bis(pyrazol-1-yl)-1,3-pyrimidine (26)



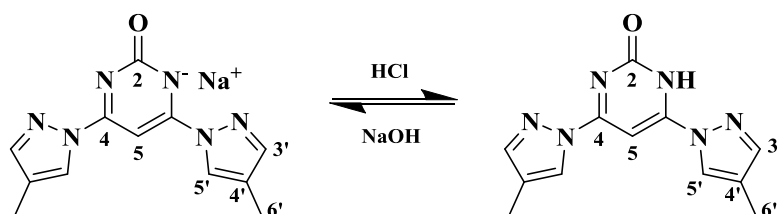
Synthesis performed strictly following the reported procedure by Ortiz *et al.*⁴. Yield: 56.3%. Different NMR shifts from the ones reported were observed.

¹H NMR ((300MHz, CDCl₃), 298 K, ppm) δ: 5.13 (s, 2H, 7), 6.47 (dd, 2.6, 1.7 Hz, 2H, 4'), 7.78 (d, 1.3 Hz, 2H, 3'), 7.87 (s, 1H, 5),

8.49 (d, J = 2.8 Hz, 2H, 5');

¹³C NMR ((75MHz, CDCl₃), 298 K, ppm) δ: 86.7 (5), 108.4 (4'), 127.5 (5'), 143.3 (3'), 159.9 (4), 162.2 (2);

8.4.7 2-Hydroxy-4,6-bis(4-methylpyrazol-1-yl)-1,3-pyrimidine (28)



To suspension of sodium 4,6-di(chloro)-1,3-pyrimidin-2-one (23) in 40 mL of THF, (820 mg, 4.4 mmol) 4-methylpyrazole (900 mg, 10.9 mmol) and

sodium hydride (0.5 g, 12.5 mmol) were added in 60 mL of THF. The mixture was stirred overnight at 65°C. The solvent was removed under vacuum and 65 mL of water were added. HCl was added from pH basic until pH = 4 when the product precipitated as white solid which was then filtered and washed thoroughly with water. Yield 68.8%, 775 mg.

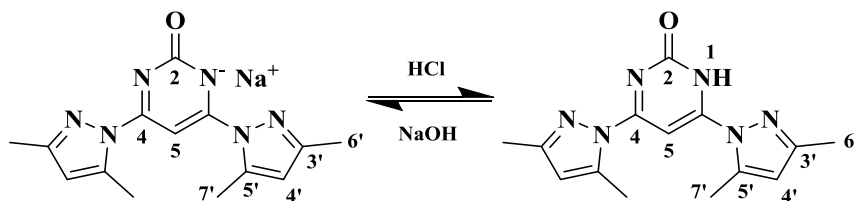
¹H NMR ((400MHz, d⁶-DMSO), 298 K, ppm) δ: 2.12 (s, 6H, 6'), 7.68 (s, 1H, 5), 7.78 (s, 2H, 5'), 8.33 (s, 2H, 3') 12.53 (br. s, 1H 1);

¹³C NMR ((100MHz, d⁶-DMSO), 298 K, ppm) δ: 8.7(6'), 86.1 (5), 119.4 (4'), 125.9 (3'), 145.1 (5'), 159.7 (4), 164.6(2);

ES⁺-MS *m/z* 257.1 [(M + H)]⁺, 279.1 [(M + Na)]⁺, 295.1 [(M + K)]⁺, 301.1 [(M + 2Na - H)]⁺, 535.2 [(2M + Na)]⁺.

Mp: 228.4°C.

8.4.8 2-Hydroxy-4,6-bis(3,5-dimethylpyrazol-1-yl)-1,3-pyrimidine (29)



To suspension of sodium 4,6-bis(3,5-dimethylpyrazol-1-yl)-1,3-pyrimidin-2-olate (29) in 50 mL of THF,

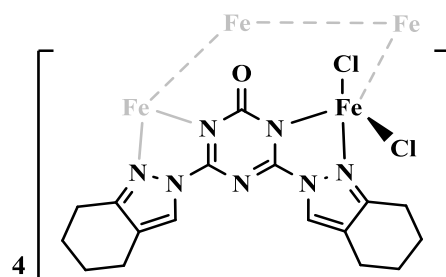
(1.3 g, 6.95 mmol) 3,5-dimethylpyrazole (1.54 g, 15.6 mmol) and sodium hydride (0.8 g, 20 mmol) were added in 80 mL of THF. The mixture was stirred overnight at 65°C. The solvent was removed under vacuum and 80 mL of water were added. HCl was added from pH basic until pH = 4 when the product precipitated as white solid which was then filtered and washed thoroughly with water. Yield 70.9%, 1.4 g.

$^1\text{H NMR}$ ((400MHz, $\text{d}^6\text{-DMSO}$), 298 K, ppm) δ : 2.22 (s, 6H, 6'), 2.66 (s, 6H, 7'), 6.18 (s, 2H, 4'), 7.73 (s, 1H, 5), 12.03 (s, 1H, 1);

$^{13}\text{C NMR}$ ((100MHz, $\text{d}^6\text{-DMSO}$), 298 K, ppm) δ : 13.4(6'), 15.2(7'), 90.6 (5), 110.7 (4'), 142.5 (3'), 150.9 (5'), 161.7 (4), 163.7(2);

$\text{ES}^+\text{-MS } m/z$ 285.1 [(M + H)]⁺, 307.1 [(M + Na)]⁺, 329.1 [(M + 2Na - H)]⁺, 591.3 [(2M + Na)]⁺.

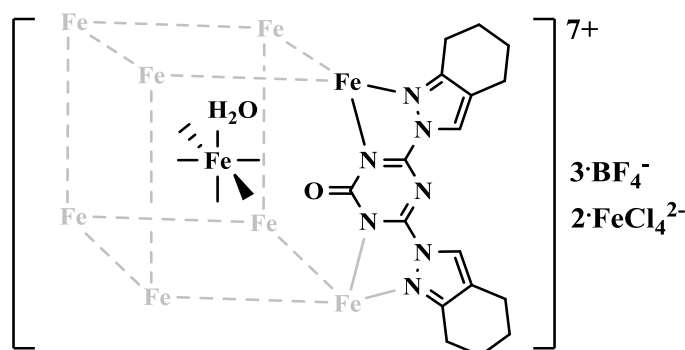
Mp: 180.1°C.

8.4.9 Tetra-[2,4-di(4,5,6,7-tetrahydro-2-indazol-2-yl)-1,3,5-triazin-4-one]octachloro-tetra-iron(III) [18] α 

Ligand (17) (13 mg, 0.037 mmol) was dissolved in acetone and mixed with iron(II) tetrafluoroborate hexahydrate (9.5 mg, 0.028 mmol) in the same solvent, orange solution. After a few weeks in a closed vial, orange/red needle shaped crystal appeared upon slow evaporation, (2 mg, 15.2% yield).

Anal. Calcd for $\text{C}_{68}\text{H}_{72}\text{N}_{28}\text{Fe}_4\text{O}_4\text{Cl}_8$: C, 44.09; H, 3.92; N, 21.17. Not enough sample.

8.4.10 Dodecakis-[2,4-di(4,5,6,7-tetrahydro-2-indazol-2-yl)-1,3,5-triazin-4-one]octa-iron(II) hexa-aqua-iron(III) tri-tetrafluoroborate-di(iron(II)-tetrachloride)[18]β

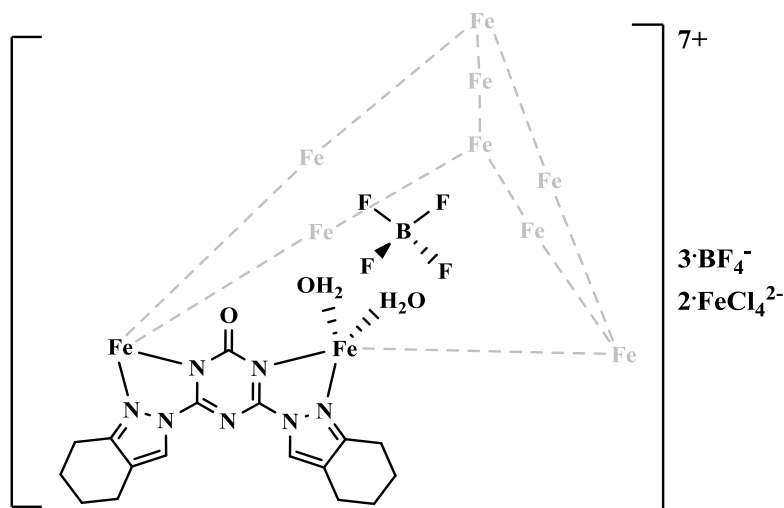


Ligand (**17**) (25 mg, 0.07 mmol) was dissolved in acetonitrile and mixed with iron(II) tetrafluoroborate hexahydrate (14 mg, 0.041 mmol) in the same solvent, yellow solution. Diethyl ether was diffused and long yellow/orange plate-shaped crystals appeared in 2-3 days, (14 mg, 35.6% yield).

ES⁺-MS *m/z* 663.9 [[Fe(H₂O)₆⊂Fe₈(L)₁₂]]⁷⁺, 774.4 [[Fe(H₂O)₆⊂Fe₈(L)₁₂](-H)]⁶⁺, 789.1 [[Fe(H₂O)₆⊂Fe₈(L)₁₂](BF₄)⁶⁺, 807.4 [[Fe(H₂O)₆⊂Fe₈(L)₁₂](FeCl₄)⁶⁺, 946.7 [[Fe(H₂O)₆⊂Fe₈(L)₁₂](BF₄)(-H)]⁵⁺, 964.1 [[Fe(H₂O)₆⊂Fe₈(L)₁₂](BF₄)₂]⁵⁺, 986.3 [[Fe(H₂O)₆⊂Fe₈(L)₁₂](BF₄)(FeCl₄)]⁵⁺, 1008.4 [[Fe(H₂O)₆⊂Fe₈(L)₁₂](FeCl₄)₂]⁵⁺.

Anal. Calcd for C₂₀₄H₂₂₈N₈₄Fe₁₁O₁₈B₃F₁₂Cl₈: C, 46.21; H, 4.33; N, 22.19. Found: C, 41.9; H, 3.8; N, 19.3

8.4.11 Decakis-[2,4-di(4,5,6,7-tetrahydro-2-indazol-2-yl)-1,3,5-triazin-4-one]deca-iron(II) tetrafluoroborate dodeca-aqua tri-tetrafluoroborate-di(iron(II)-tetrachloride)[18]γ

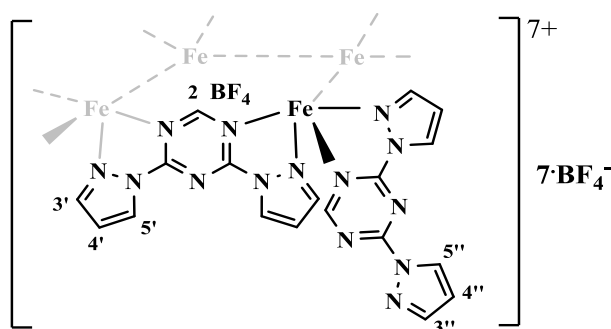


Large crystals of **[18]** γ were observed inside an aged and dried vial of the previous assembly, and could be a decomposition product.

ES⁺-MS *m/z* 781.86 $[\text{BF}_4\text{CFe}_9(\text{L})_{11}](\text{H}_2\text{O})_{11}(\text{FeCl}_4)(\text{H})]^{6+}$, 784.7 $[\text{BF}_4\text{CFe}_9(\text{L})_{11}](\text{H}_2\text{O})_{12}(\text{FeCl}_4)(\text{H})]^{6+}$.

Anal. Calcd for C₂₀₄H₂₄₀N₈₄Fe₁₂O₂₄B₄F₁₆: C, 44.12; H, 4.36; N, 21.19. Found: Not enough sample.

8.4.12 Octakis[2,4-di(pyrazol-1-yl)-1,3,5-triazine]-tetra-iron(II) octa-tetrafluoroborate, hemi[trifluoroboryl-pyrazole] **[21]B**



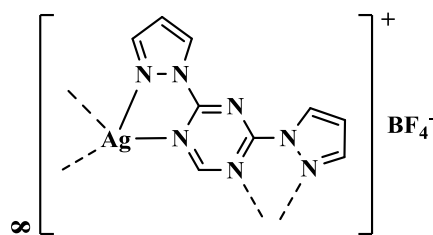
Ligand (**21**) (14 mg, 0.07 mmol) was dissolved in acetonitrile and mixed with iron(II) tetrafluoroborate hexahydrate (11 mg, 0.035 mmol) in the same solvent. Yellow powder was precipitated with diethyl ether addition. Once, the solution was kept in the NMR tube. After a few days yellow crystals appeared.

¹H NMR ((300MHz, CD₃NO₂), 298 K, ppm) δ : 1.12 (4''), 2.16 (3''), 3.43 (5''), 11.02 (s, 2H, 5'), 39.65 (s, 1H, 2), 42.15 (s, 2H, 4'), 70.65 (s, 2H, 3');

ES⁺-MS *m/z* 595.0 $[\text{Fe}_2(\text{L})_2\text{F}_3]^+$, 876.1 $[\text{Fe}_2(\text{L})_3(\text{BF}_4)\text{F}_2]^+$, 902.0 $[\text{Fe}_3(\text{L})_3\text{F}_5]^+$, 944.1 $[\text{Fe}_2(\text{L})_3(\text{BF}_4)_2\text{F}]^+$, 970.0 $[\text{Fe}_3(\text{L})_3(\text{BF}_4)\text{F}_4]^+$, 1038.0 $[\text{Fe}_3(\text{L})_3(\text{BF}_4)_2\text{F}_3]^+$, 1277.0 $[\text{Fe}_4(\text{L})_4(\text{BF}_4)\text{F}_6]^+$, 1345.0 $[\text{Fe}_4(\text{L})_4(\text{BF}_4)_2\text{F}_5]^+$, 1413.0 $[\text{Fe}_4(\text{L})_4(\text{BF}_4)_3\text{F}_4]^+$, 1694.1 $[\text{Fe}_4(\text{L})_5(\text{BF}_4)_4\text{F}_3]^+$.

Anal. Calcd for C₁₄₇H₁₁₆N₁₁₄Fe₈B₁₇F₆₇: C, 32.81; H, 2.15; N, 29.67. Found: C, 33.0; H, 2.3; N, 29.3.

8.4.13 Catena-[2,6-di(pyrazol-1-yl)-1,3,5-triazine]silver(I) tetrafluoroborate Ag[21]B

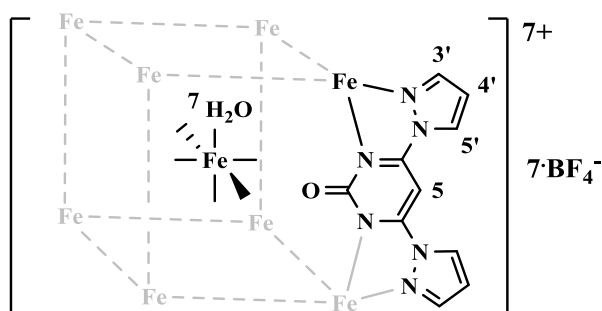


A solution of 2,6-di(pyrazol-1-yl)-1,3,5-triazine (**21**), (15 mg, 0.07 mmol) in nitromethane (3 mL) was added to a solution of silver(I) tetrafluoroborate (14 mg, 0.07 mmol) in the same solvent (6 mL). Diethyl ether was diffused into a transparent solution and white/transparent crystals were obtained, 16 mg, 57% yield.

ES⁺-MS *m/z* 236.1 [Na(L)]⁺, 320.0 [Ag(L)]⁺, 449.1 [Na(L)₂]⁺, 533.1 [Ag(L)₂]⁺;

Anal. Calcd for C₉H₇N₇AgBF₄: C, 26.50; H, 1.73; N, 24.04. Found: C, 26.43; H, 1.67; N, 23.94

8.4.14 Dodecakis-[4,6-di(pyrazol-1-yl)-2-hydroxypyrimidinate]octa-iron(II) hexa-aqua-iron(III) hepta-tetrafluoroborate [22]B



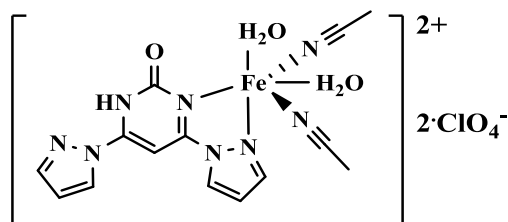
2-Hydroxy-4,6-bis(pyrazol-1-yl)-1,3-pyrimidine (200 mg, 0.88 mmol) in 85 mL of acetonitrile was mixed with iron tetrafluoroborate hydrate (179 mg, 0.53 mmol). An intense yellow/orange color appeared immediately. The mixture was vigorously stirred at room temperature for 2.5 h. The solution was filtered and red/orange single crystals were obtained by atmospheric diffusion of diethyl ether after 3-5 days. Yield 182 mg, 63%.

¹H NMR ((300MHz, CD₃NO₂), 298 K, ppm) δ: 2.53 (s, 12H, 7), 5.87 (s, 24H, 4'), 60.06 (s, 24H, 5'), 79.71 (s, 24H, 3'); 114.07 (s, 12H, 5).

ES⁺-MS *m/z* 570.7 [[Fe(H₂O)₆Fe₈(L)₁₂](BF₄)⁶⁺], 702.3 [[Fe(H₂O)₆Fe₈(L)₁₂](BF₄)₂]⁵⁺, 899.3 [[Fe(H₂O)₆Fe₈(L)₁₂](BF₄)₃]⁴⁺, 1228.1 [[Fe(H₂O)₆Fe₈(L)₁₂](BF₄)₄]³⁺, 1885.6 [[Fe(H₂O)₆Fe₈(L)₁₂](BF₄)₅]²⁺.

Anal. Calcd for C₁₂₀H₉₆N₇₂Fe₉O₁₈B₇F₂₈: C, 36.52; H, 2.45; N, 25.57. Found: C, 36.7; H, 2.2; N, 25.4

8.4.15 [2-oxo-4,6-(pyrazol-1-yl)-1,3-pyrimidine]-diaqua-diacetonitrile-iron(II) dip perchlorate [24]C

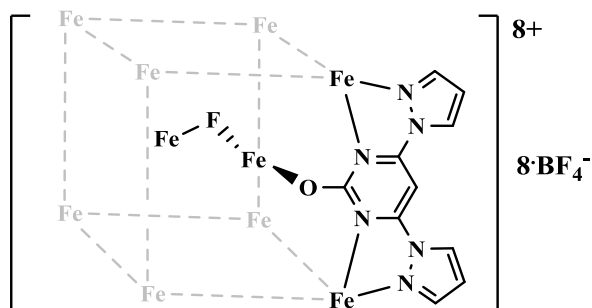


Ligand (**24**) (22 mg, 0.097 mmol) solution in 7 mL of acetone was mixed with iron(II) perchlorate hydrate (29 mg, 0.08 mmol) in 5 mL of acetone. The intense yellow solution was filtered. Yellow crystals were obtained by atmospheric diffusion of diisopropyl ether. 7 mg, 14% yield.

ES⁺-MS *m/z* 316.0 [Fe(L)(O₂)]⁺, 401.0 [Fe(L)(H₂O)(ClO₄)]⁺, 611.0 [Fe(L)₂(ClO₄)]⁺, 793.1 [Fe₂(L)₃(-H)₃]⁺, 1108.1 [Fe₃(L)₄(-H)₄(O₂)]⁺.

Anal. Calcd for C₁₄H₁₈N₈FeO₁₁Cl₂: C, 27.97; H, 3.02; N, 18.64. **Found:** C, 27.84; H, 2.78; N, 18.49

8.4.16 Decakis-[4,6-di(pyrazol-1-yl)-2-hydroxypyrimidinate]octa-iron(II) trifluorine-di-iron(III) octa-tetrafluoroborate [22]βB

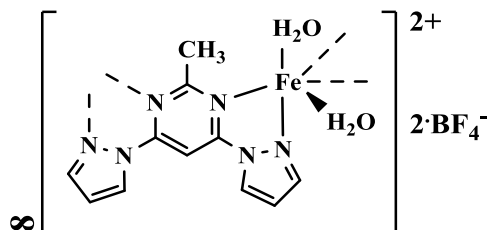


2-Hydroxy-4,6-bis(pyrazol-1-yl)-1,3-pyrimidine (50 mg, 0.22 mmol) in 85 mL of acetonitrile was mixed with sodium hydroxide (9 mg, 0.22 mmol) and the mixture was stirred for 1 h. The solvent was removed under vacuum and iron tetrafluoroborate hydrate (74 mg, 0.22 mmol) dissolved in acetonitrile was added. The mixture was stirred at 65 °C for 24 h and the solution turned red. Single crystals were obtained by atmospheric diffusion of diisopropyl ether after 2 days.

ES⁺-MS *m/z* 734.8 [Fe^{III}F-Fe^{III}⊂Fe^{II}₈(**22**)₁₀O₂F₃]⁴⁺.

Anal. Calcd for C₁₀₄H₈₀N₆₂B₉F₃₉Fe₁₀O₁₂: C 32.99; H, 2.13; N, 22.93. **Found:** C, 29.5; H, 2.1; N, 20.0

8.4.17 Catena-[2-methyl-4,6-(pyrazol-1-yl)pyrimidine]-diaqua-iron(II) [25]B

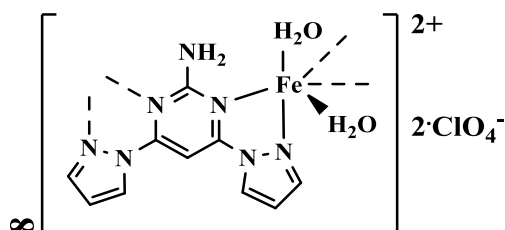


Ligand (**25**) (22 mg, 0.097 mmol) solution in 7 mL of acetone was mixed with iron(II) tetrafluoroborate hydrate (30 mg, 0.089 mmol) in 5 mL of acetone. The intense yellow solution was filtered. Yellow crystals were obtained by atmospheric diffusion of diethyl ether. The crystals once formed are not soluble into acetone, 21 mg, 42.9% yield.

ES⁺-MS *m/z* 367.1 [Fe₂(L)₂(BF₄)₂]²⁺, 527.1 [Fe(L)₂F]⁺.

Anal. Calcd for C₁₁H₁₄N₆FeO₂B₂F₈: C, 26.87; H, 2.87; N, 17.09. Found: C, 26.72; H, 2.78; N, 16.98

8.4.18 Catena-[2-amino-4,6-(pyrazol-1-yl)pyrimidine]-diaqua-iron(II) [26]X

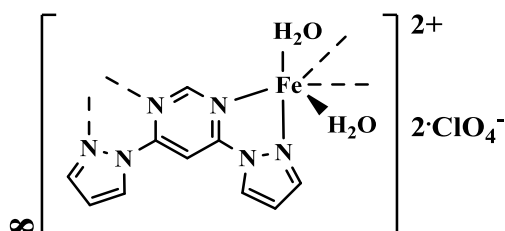


Ligand (**18**) (30 mg, 0.132 mmol) solution in 7 mL of acetonitrile was mixed with iron(II) perchlorate hydrate (44.6 mg, 0.132 mmol) in 5 mL of acetonitrile. The intense yellow solution was filtered. Yellow crystals were obtained by atmospheric diffusion of 1:1 diethyl and diisopropyl ether. 18 mg, 42.9% yield.

ES⁺-MS *m/z* 529.2 [Fe(L)₂F]⁺, 850.3 [Fe₂(L)₃F₃]⁺.

Anal. Calcd for C₂₂H₂₇N₁₅Fe₂O₁₉Cl₄: C, 24.95; H, 2.57; N, 19.84. Found: C, 24.9; H, 2.5; N, 19.7

8.4.19 Catena-[4,6-(pyrazol-1-yl)pyrimidine]-diaqua-iron(II) diperchlorate [27]X



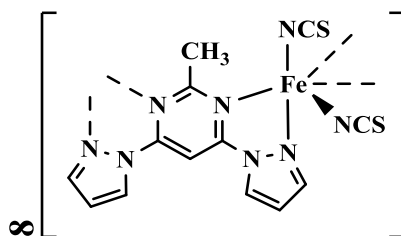
Chapter 8

Ligand (**27**) (30 mg, 0.141 mmol) solution in 7 mL of nitromethane was mixed with iron(II) perchlorate hydrate (51 mg, 0.141 mmol) in 4 mL of nitromethane. The intense orange solution was filtered. The cap of the vial was pierced with a needle and yellow crystals were obtained through slow evaporation of the solvent, 67 mg, 94% yield.

ES⁺-MS *m/z* 499.1 [Fe(L)₂F]⁺, 593.0 [Fe₂(L)₂F₃]⁺, 641.0 [Fe₂(L)₂F(BF₄)(-H)]⁺, 805.1 [Fe₂(L)₃F₃]⁺, 873.1 [Fe₂(L)₃F₂(BF₄)]⁺, 941.1 [Fe₂(L)₃F(BF₄)₂]⁺, 1153.2 [Fe₂(L)₄F(BF₄)₂]⁺.

Anal. Calcd for C₁₀H₁₂N₆FeO₁₀Cl₂: C, 23.88; H, 2.40; N, 16.71. Found: C, 23.6; H, 2.4; N, 16.6

8.4.20 Catena-[2-methyl-4,6-(pyrazol-1-yl)pyrimidine]-di-isothiocyanate iron(II) [25]NCS

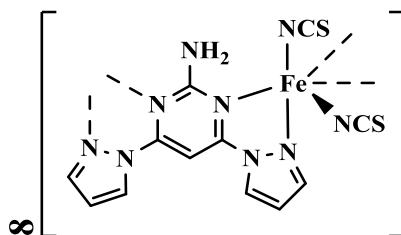


Iron(II) perchlorate hydrate dissolved in methanol (9 mg, 0.025 mmol) was mixed with potassium thiocyanate (5 mg, 0.051 mmol) in the same solvent. After stirring for 5 min, the solution was centrifuged and ligand (**25**) dissolved in methanol (6 mg, mmol) was added. After a few days in a crystallization dish, dark red/purple single crystals appeared on the walls, 2 mg, 21% yield.

ES⁺-MS *m/z* 566.1 [Fe(L)₂(NCS)]⁺ 738.0 [Fe₂(L)₂(NCS)₃]⁺.

Anal. Calcd for C₁₃H₁₀N₈FeS₂: C, 39.21; H, 2.53; N, 28.14. Found: C, 39.30; H, 2.62; N, 28.21

8.4.21 Catena-[2-amino-4,6-(pyrazol-1-yl)pyrimidine]-di-isothiocyanate iron(II) [26]NCS



Iron(II) perchlorate hydrate dissolved in methanol (15 mg, 0.041 mmol) was mixed with potassium thiocyanate (8 mg, 0.082 mmol) in the same solvent. After stirring for 5 min, the

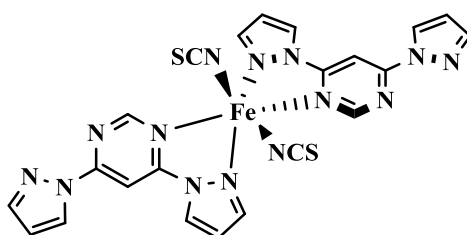
Chapter 8

solution was centrifuged and ligand (**26**) dissolved in methanol (10 mg, 0.041 mmol) was added. The cap of the vial was pierced few times with a needle and red single crystals appeared on the walls after 2 days. 12 mg, 78% yield.

ES⁺-MS *m/z* 568.1 [Fe(L)₂(NCS)]⁺ 740.0 [Fe₂(L)₂(NCS)₃]⁺.

Anal. Calcd for C₁₂H₉N₉FeS₂: C, 36.10; H, 2.27; N, 31.58 Found: C, 36.18; H, 2.21; N, 31.49

8.4.22 Bis-[4,6-(pyrazol-1-yl)pyrimidine]-di-isothiocyanate iron(II) [27]NCS

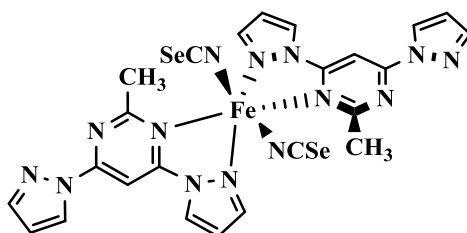


Iron(II) perchlorate hydrate dissolved in methanol (20 mg, 0.094 mmol) was mixed with potassium thiocyanate (18 mg, 0.189 mmol) in the same solvent. After stirring for 5 min, the solution was centrifuged and ligand (**27**) dissolved in methanol (20 mg, 0.094 mmol) was added. The cap of the vial was pierced few times with a needle and red single crystals appeared on the walls after 4 days. 48 mg, 85% yield.

ES⁺-MS *m/z* 240.1 [Fe(L)₂]²⁺, 346.1 [Fe(L)₃]²⁺, 538.1 [Fe(L)₂(NCS)]⁺ 710.0 [Fe₂(L)₂(NCS)₃]⁺.

Anal. Calcd for C₂₂H₁₆N₁₄FeS₂: C, 44.30; H, 2.70; N, 32.88. Found: C, 44.17; H, 2.75; N, 32.66

8.4.23 Bis-[2-methyl-4,6-(pyrazol-1-yl)pyrimidine]-di-isoselenocyanate iron(II) [25]NCSe

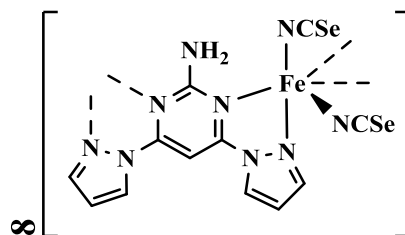


Iron(II) perchlorate hydrate dissolved in methanol (15 mg, 0.066 mmol) was mixed with potassium selenocyanate (19 mg, 0.133 mmol) in the same solvent. The suspension was centrifuged and ligand (**25**) dissolved in methanol (30 mg, 0.133 mmol) was added. The cap of the vial was pierced with a needle and yellow crystals were obtained through slow evaporation of the solvent after 3 or 4 days. 13 mg, 27% yield.

ES⁺-MS *m/z* 614.0 [2L + Fe + NCSe]⁺ 879.8 [2L + 2Fe + 3NCSe]⁺.

Anal. Calcd for C₂₄H₂₀N₁₄FeSe₂: C, 40.13; H, 2.81; N, 27.30. Found: C, 40.0; H, 2.9; N, 27.1

8.4.24 Catena-[2-amino-4,6-(pyrazol-1-yl)pyrimidine]-di-isoselenocyanato iron(II) [26]NCSe

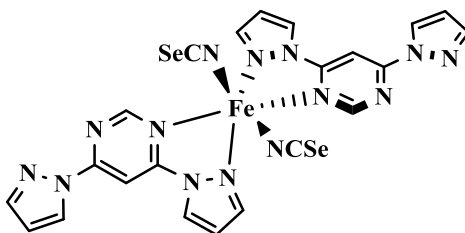


Iron(II) perchlorate hydrate dissolved in methanol (15 mg, 0.041 mmol) was mixed with potassium selenocyanate (12 mg, 0.082 mmol) in the same solvent. After stirring for 5 min, the solution was centrifuged and ligand (**26**) dissolved in methanol (10 mg, 0.041 mmol) was added. The cap of the vial was removed and orange single crystals appeared on the walls after 1-2 days. 13 mg, 64% yield.

ES⁺-MS *m/z* 616.0 [2L + Fe + NCSe]⁺ 881.8 [2L + 2Fe + 3NCSe]⁺.

Anal. Calcd for C₁₂H₉N₉FeSe₂: C, 29.23; H, 1.84; N, 25.57 Found: C, 29.3; H, 1.8; N, 25.4

8.4.25 Bis-[4,6-(pyrazol-1-yl)pyrimidine]-di-isoselenocyanato iron(II) [27]NCSe

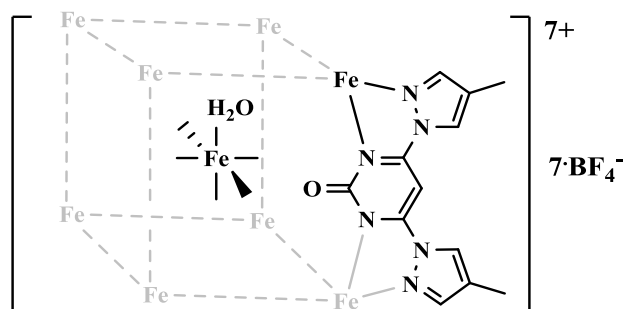


Iron(II) perchlorate hydrate dissolved in methanol (45 mg, 0.124 mmol) was mixed with potassium selenocyanate (36 mg, 0.248 mmol) in the same solvent. The suspension was centrifuged and ligand (**27**) dissolved in methanol (20 mg, 0.094 mmol) was added. The cap of the vial was pierced few times with a needle and red single crystals appeared on the walls after 4 days. 32 mg, 37% yield. The same procedure using ethanol or acetone yielded the isostructural solvates of [27]NCSe.

ES⁺-MS *m/z* 240.1 [Fe(L)₂]²⁺, 346.1 [Fe(L)₃]²⁺, 373.9 [Fe(L)(NCSe)]⁺, 391.9 [Fe(L)(NCSe)(H₂O)]⁺, 518.9 [Fe(L)(NCS)₂(H₃O)HF]⁺, 586.0 [Fe(L)₂(NCS)]⁺ 851.8 [Fe₂(L)₂(NCS)₃]⁺.

Anal. Calcd for C₂₂H₁₆N₁₄FeSe₂: C, 38.28; H, 2.34; N, 28.41. Found: C, 38.4; H, 2.5; N, 28.3

8.4.26 Dodecakis-[4,6-di(4-methylpyrazol-1-yl)-2-hydroxypyrimidinate]octa-iron(II) hexa-aqua-iron(III) hepta-tetrafluoroborate [28]B



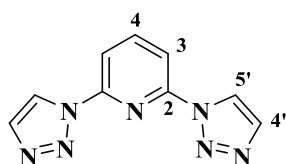
2-Hydroxy-4,6-bis(4-methylpyrazol-1-yl)-1,3-pyrimidine (100 mg, 0.39 mmol) was mixed with iron tetrafluoroborate hydrate (66 mg, 0.19 mmol) in 65 mL of acetonitrile and an intense orange colour appeared immediately. The mixture was vigorously stirred at room temperature for 2 h. The solution was filtered and red single crystals were obtained by atmospheric diffusion of mixture of diethyl ether and diisopropyl ether after 3-5 days. Yield 71 mg, 79%.

ES⁺-MS *m/z* 1340.2 [[Fe(H₂O)₆⊂Fe₈(L)₁₂](BF₄)₄]³⁺, 2053.8 [[Fe(H₂O)₆⊂Fe₈(L)₁₂](BF₄)₅]²⁺.

Anal. Calcd for C₁₄₄H₁₄₄N₇₂Fe₉O₁₈B₇F₂₈: C, 40.40; H, 3.39; N, 23.56. Found: C, 40.5; H, 3.5; N, 23.3

8.5 Experimental details of ligands and metal complexes related to Chapter 5

8.5.1 2,6-Di(1,2,3-triazol-1-yl)pyridine (30)



1,2,3-Triazole (930 mg, 13.4 mmol) was added to a stirred suspension of NaH 60% dispersion (540 mg, 13.4 mmol) in DMF (40 mL). When H₂ was no longer being expelled, 2,6-difluoropyridine (1 g, 6.4 mmol) in 25 mL of DMF was added and the reaction was stirred for 3 days at 70°C. Water (100 mL) was added to the beige suspension which turned white, and was filtered. The compound was isolated following 3 recrystallizations (hexane : chloroform, 1:1) as a white solid. 345 mg, 3.6 mmol 57% yield.

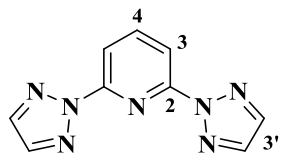
¹H NMR (300 MHz, CDCl₃), 298 K, ppm δ: 7.91 (d, J = 1.2 Hz, 1H, 5'), 8.20 (dd, J = 7.3, 1.3 Hz, 1H, 4), 8.30 (m, 2H, 3), 8.58 (d, J = 1.2 Hz, 2H, 4');

¹³C NMR (126 MHz, CDCl₃), 298 K, ppm δ: 113.4 (3), 121.0 (4'), 134.5 (5'), 142.6 (4), 148.0 (2);

ES⁺-MS *m/z* 214.1 [(M + H)]⁺, 236.1 [(M + Na)]⁺, 449.1 [(2M + Na)]⁺.

Mp: 194.8 °C.

8.5.2 2,6-Di(1,2,3-triazol-2-yl)pyridine (31)



Isomer (**31**) was isolated from the same crude for 2,6-di(1,2,3-triazol-1-yl)-pyridine (**30**), by eluting through silica gel (eluent, EtOAc : hexane (7:3), Rf: 0.3) as a white powder, 142 mg, 10% yield). The compound in the crude was present in approximately 40% however the yield upon purification was very low because (**33**) has a similar Rf value to (**31**).

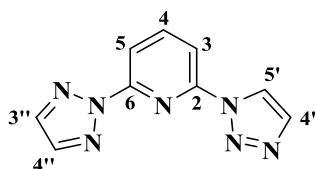
$^1\text{H NMR}$ (400MHz, CDCl_3), 298 K, ppm) δ : 7.93 (s, 4H, 3'), 8.09 (s, 3H, 3 + 4);

$^{13}\text{C NMR}$ (100MHz, CDCl_3), 298 K, ppm) δ : 112.6 (3), 137.0 (3' + 4'), 141.6 (4), 149.9 (2);

$\text{ES}^+\text{-MS } m/z$ 214.1 [(M + H)]⁺, 236.1 [(M + Na)]⁺, 449.1 [(2M + Na)]⁺.

Mp: 207.6 °C.

8.5.3 2-(1,2,3-Triazol-1-yl)-6-(1,2,3-triazol-2-yl)pyridine (33)



Isomer (**33**) was isolated from the same crude for 2,6-di(1,2,3-triazol-1-yl)-pyridine (**30**), by eluting through silica gel (eluent, EtOAc : hexane (7:3), Rf: 0.5) as a white powder. The compound in the crude was present in approximately 25% however the yield was negligible upon purification because (**33**) has the same Rf value as part of (**31**).

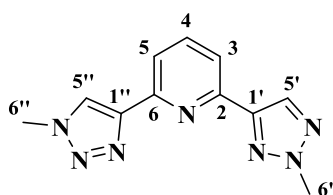
$^1\text{H NMR}$ (400MHz, CDCl_3), 298 K, ppm) δ : 7.88 (d, J = 1.1 Hz, 1H, 4'), 7.97 (s, 2H, 3'' + 4''), 8.15 (m, 2H, 3 + 5), 8.27 (m, 1H, 4), 8.77 (d, J = 1.1 Hz, 1H, 5');

$^{13}\text{C NMR}$ (100MHz, CDCl_3), 298 K, ppm) δ : 112.8 (5), 113.4 (3), 121.7 (5'), 134.3 (4'), 137.2 (3'' + 4''), 142.0 (4), 148.3 (2), 149.7 (6);

$\text{ES}^+\text{-MS } m/z$ 214.1 [(M + H)]⁺, 236.1 [(M + Na)]⁺, 449.1 [(2M + Na)]⁺.

Mp: 159.1 °C.

8.5.4 2-(2-Methyl-1,2,3-triazol-4-yl)-6-(1-methyl-1,2,3-triazol-4-yl)pyridine (34)



To a stirred solution of 2,6-di(1,2,3-triazol-4-yl)pyridine (**32**) (0.3 g, 1.41 mmol) in DMF (40 mL) potassium carbonate was added (0.136 g, 0.987 mmol). After 5 minutes, methyl iodide (0.76 g, 5.4 mmol) was added to the mixture and refluxed at 145 °C for 5 hr. Solvent was removed *in vacuo* and H_2O was added (35 mL) and extracted two times with DCM (100 mL). The compound was isolated by eluting through silica gel (eluent gradient: EtOAc : hexane (1:1) to EtOAc, Rf: 0.27 to 0.56 respectively) as a white powder. (91 mg, 0.38 mmol, 27% yield).

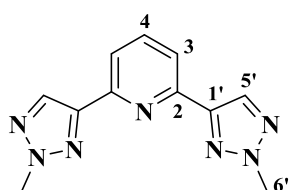
$^1\text{H NMR}$ ((300MHz, CDCl_3), 298 K, ppm) δ : 4.19 (s, 3H, 6''), 4.28 (s, 3H, 6'), 7.83-7.85 (m, 2H, 3 and 5), 8.13 (m, 1H, 4), 8.16 (s, 1H, 5''), 8.23 (s, 1H, 5')

$^{13}\text{C NMR}$ ((75MHz, CDCl_3), 298 K, ppm) δ : 36.8 (6''), 41.9(6'), 119.4(5), 119.5(3), 123.3(5''), 132.9(5'), 137.7(4), 148.1(2), 148.6(6), 149.5(1'), 150.2(1'')

$\text{ES}^+\text{-MS } m/z$ 242.1 [(M + H) $^+$], 264.1 [(M + Na) $^+$].

Mp: 136.3 $^\circ\text{C}$.

8.5.5 2,6-Di(2-methyl-1,2,3-triazol-4-yl)pyridine (35)



The compound was isolated from the same crude for 2-(3-Methyl(1,2,3-triazol-4-yl)-6-(4-methyl(1,2,3-triazol-4-yl)-pyridine (34), by eluting through silica gel (eluent gradient: EtOAc : hexane (1:1) to EtOAc, Rf: 0.58 to 0.84 respectively) as a white powder (114 mg, 0.47 mmol, 33% yield).

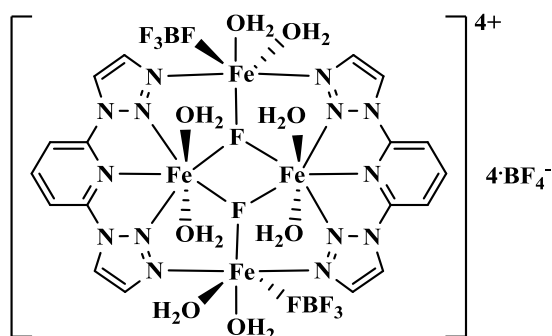
$^1\text{H NMR}$ ((300MHz, CDCl_3), 298 K, ppm) δ : 4.28 (s, 6H, 6'), 7.82-7.88 (m, 3H, 3 and 4), 8.23 (s, 2H, 5')

$^{13}\text{C NMR}$ ((75MHz, CDCl_3), 298 K, ppm) δ : 41.9(6'), 119.6(3), 133.1(5'), 137.6(4), 148.0(2), 149.7(1')

$\text{ES}^+\text{-MS } m/z$ 242.1 [(M + H) $^+$], 264.1 [(M + Na) $^+$], 505.2 [(2M + Na) $^+$].

Mp: 189.4 $^\circ\text{C}$.

8.5.6 Bis[μ_2 -2,6-di(1,2,3-triazol-1-yl)pyridine]di(μ_3 -fluoro)octaaqua-tetrakis-iron(II) hexatetrafluoroborate[30]B

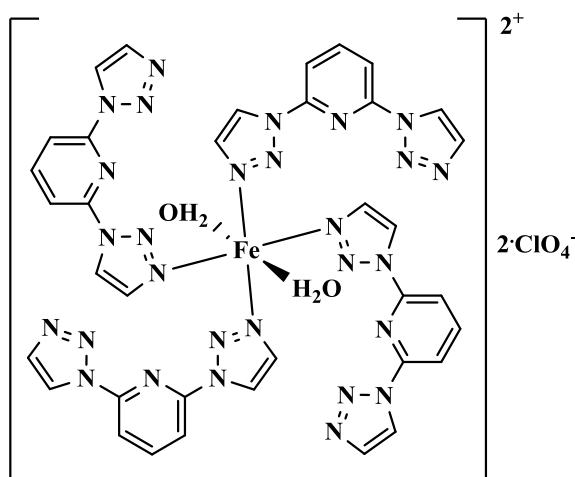


Iron(II) tetrafluoroborate hydrate (7.1 mg, 0.02 mmol) was mixed with 2,6-di(1,2,3-triazol-1-yl)pyridine (30), (9 mg, 0.04 mmol) in hot solution of nitromethane (1 mL). The solution turned red/orange immediately and was kept in a closed NMR tube. After 2 h the solution

turned into a pale yellow suspension which contained yellow single crystals. With time, the compound converts into a pale yellow insoluble powder.

Anal. Calcd for $C_{18}H_{32}N_{14}O_9Fe_4B_6F_{26}$: C, 15.77; H, 2.35; N, 14.31. Found: C, 35.0; H, 3.3; N, 29.8

8.5.7 Tetrakis-[2,6-di(1,2,3-triazol-1-yl)pyridine]diaqua-iron(II) diperchlorate [30]C

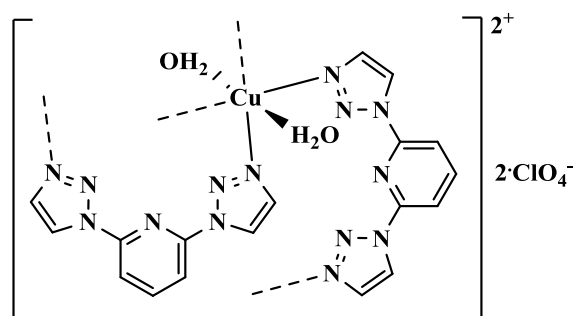


Iron(II) perchlorate hydrate (5.1 mg, 0.02 mmol) was mixed with 2,6-di(1,2,3-triazol-1-yl)pyridine (**30**), (12 mg, 0.06 mmol) in 6 mL of acetonitrile and the solution was almost transparent. Atmospheric diffusion of diethyl ether yielded transparent single crystals, 11 mg, 69% yield.

ES⁺-MS m/z 301.0 $[Fe(L)(O_2)]^+$, 368.0 $[Fe(L)(ClO_4)]^+$, 386.0 $[Fe_2(L)(ClO_4)(H_2O)]^+$, 581.0 $[Fe(L)_2(ClO_4)]^+$, 834.9 $[Fe_2(L)_2(ClO_4)_3]^+$, 1303.8 $[Fe_3(L)_3(ClO_4)_5]^+$.

Anal. Calcd for $C_{36}H_{32}N_{28}FeCl_2O_{10}$: C, 37.81; H, 2.82; N, 34.30. Found: C, 37.9; H, 2.7; N, 34.2

8.5.8 Catena-bis-[2,6-di(1,2,3-triazol-1-yl)pyridine]diaquacopper(II) ditetrafluoroborate Cu[30]B



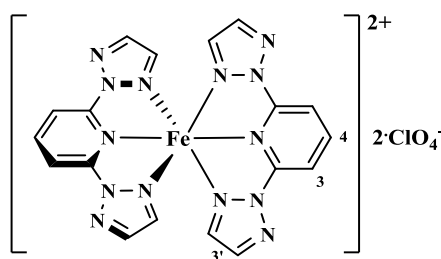
Chapter 8

Copper(II) tetrafluoroborate hydrate (12 mg, 0.04 mmol) was mixed with 2,6-di(1,2,3-triazol-1-yl)pyridine (**30**), (15 mg, 0.07 mmol) in 8 mL of acetonitrile producing a blue suspension which completely dissolved upon heating. Crystals were obtained by slowly cooling the solution. 12 mg, 48% yield.

ES⁺-MS *m/z* 295.0 [Cu(L)F]⁺, 508.1 [Cu(L)₂F]⁺, 576.1 [Cu(L)₂(BF₄)]⁺.

Anal. Calcd for C₁₈H₁₈B₂CuF₈N₁₄O₂: C, 30.9; H, 2.59; N, 28.03. **Found:** C, 30.8; H, 2.5; N, 27.9

8.5.9 Bis(2,6-di(1,2,3-triazol-2-yl)pyridine) iron(II) diperchlorate [31]C



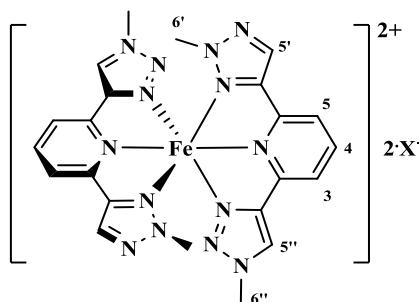
Iron(II) perchlorate hydrate (19 mg, 0.05 mmol) was mixed with 2,6-di(1,2,3-triazol-2-yl)pyridine (**13**), (22 mg, 0.10 mmol) in 9 mL of nitromethane. The solution turned yellow immediately and yellow single crystals were obtained by atmospheric diffusion of diethyl ether, 35 mg, 74% yield.

¹H NMR ((300MHz, CD₃NO₂), 298 K, ppm) δ: -13.66 (s, 2H, 4), 57.21 (d, 8H, 3'), 69.69 (s, 4H, 3)

ES⁺-MS *m/z* 236.1 [Na(L)]⁺, 301.0 [Fe(L)(O₂)]⁺, 368.0 [Fe(L)(ClO₄)]⁺, 581.0 [Fe(L)₂(ClO₄)]⁺.

Anal. Calcd for C₁₈H₁₄N₁₄FeCl₂O₈ + 3(H₂O): C, 29.41; H, 2.74; N, 26.67. **Found:** C, 29.3; H, 2.7; N, 26.5

8.5.10 Bis(2-(2-methyl-1,2,3-triazol-4-yl)-6-(1-methyl-1,2,3-triazol-4-yl)pyridine) iron(II) [34]X (X = BF₄⁻ and ClO₄⁻)



Chapter 8

Iron(II) tetrafluoroborate hydrate (12.6 mg, 0.04 mmol) was mixed with 2-methyl-1,2,3-triazol-4-yl)-6-(1-methyl-1,2,3-triazol-4-yl)pyridine (**34**), (18 mg, 0.08 mmol) in acetonitrile (1 mL). The solution turned red/orange immediately and red single crystals were obtained by atmospheric diffusion of diethyl ether, 20.5 mg, 77% yield. The same procedure using iron(II) perchlorate hydrate instead, produced 71% yield of [**34**]C.

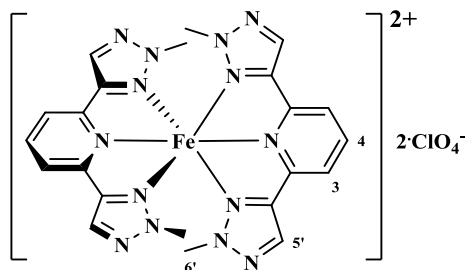
$^1\text{H NMR}$ ((300MHz, CD_3CN), 298 K, ppm) δ : 3.24 (s, 3H, 6'), 6.32 (s, 3H, 6''), 7.16 (s, 1H, 5'), 10.69 (s, 1H, 5''), 13.60 (s, 1H, 4), 16.52 (s, 2H, 3)

$\text{ES}^+\text{-MS } m/z$ 316.0 [$\text{Fe}(\text{L})\text{F}$] $^+$, 557.1 [$\text{Fe}(\text{L})_2\text{F}$] $^+$.

- [**34**]C, Anal. Calcd for $\text{C}_{22}\text{H}_{22}\text{N}_{14}\text{FeCl}_2\text{O}_8$: C, 35.84; H, 3.01; N, 26.60. Found: C, 35.7; H, 2.9; N, 26.4

- [**34**]B, Anal. Calcd for $\text{C}_{22}\text{H}_{22}\text{N}_{14}\text{FeB}_2\text{F}_8$: C, 37.11; H, 3.11; N, 27.54. Found: C, 37.3; H, 3.0; N, 27.4

8.5.11 Bis(2,6-di(2-methyl-1,2,3-triazol-4-yl)pyridine) iron(II) diperchlorate [**35**]C

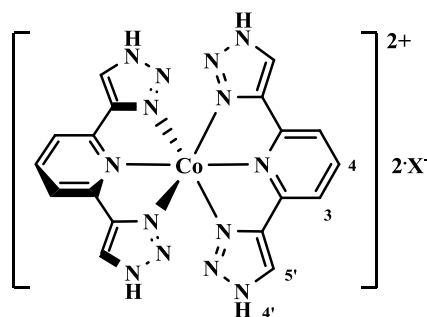


Iron(II) perchlorate hydrate (11.3 mg, 0.03 mmol) was mixed with 2,6-di(2-methyl-1,2,3-triazol-4-yl)pyridine (**35**), (15 mg, 0.6 mmol) in 7 mL of nitromethane. The solution turned yellow immediately, few drops of triethyl orthoformate were added and yellow single crystals were obtained by atmospheric diffusion of diethyl ether, 15 mg, 66% yield.

$^1\text{H NMR}$ ((300MHz, CD_3NO_2), 298 K, ppm) δ : -3.32 (s, 6H, 6'), 8.17 (d, 1H, 4), 25.15 (s, 2H, 3), 57.07 (s, 2H, 5')

$\text{ES}^+\text{-MS } m/z$ 242.1 [(L)H] $^+$, 264.1 [Na(L)] $^+$, 316.0 [Fe(L)F] $^+$, 342.0 [Fe(L)(O₂CH)] $^+$.

Anal. Calcd for $\text{C}_{22}\text{H}_{22}\text{N}_{14}\text{FeCl}_2\text{O}_8$: C, 35.84; H, 3.01; N, 26.60. Found: C, 35.9; H, 3.0; N, 26.5

8.5.12 Bis(2,6-di(1,2,3-triazol-4-yl)pyridine) cobalt(II) [32]X (X = BF₄⁻ and ClO₄⁻)

Cobalt(II) tetrafluoroborate hydrate (9.6 mg, 0.03 mmol) was mixed with 2,6-di(1,2,3-triazol-4-yl)pyridine (**32**), (12 mg, 0.06 mmol) acetone (10 mL). The solution was flesh coloured and transparent single crystals were obtained upon slow evaporation of the solvent. 9.8 mg, 53% yield. By using cobalt(II) perchlorate, 42%.

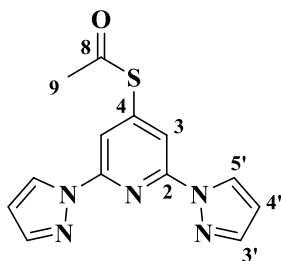
¹H NMR ((300MHz, CD₃CN), 298 K, ppm) δ: 17.93 (s, 2H, 4), 33.21 (d, 4H, 3), 68.53 (s, 4H, 5'), 93.50 (s, 4H, 4')

ES⁺-MS *m/z* 484.1 [Co(L)₂ - H]⁺.

- Co[32]C, Anal. Calcd for C₁₈H₁₄N₁₄FeCl₂O₈: C, 31.60; H, 2.06; N, 28.66. Found: C, 31.4; H, 2.1; N, 28.5

- Co[32]B, Anal. Calcd for C₁₈H₁₄N₁₄FeB₂F₈: C, 32.81; H, 2.14; N, 29.76. Found: C, 32.9; H, 2.3; N, 29.6

8.6 Experimental details of ligands and metal complexes related to Chapter 6

8.6.1 2,6-Di(pyrazol-1-yl)pyrid-4-yl thioacetate (**40**)

Triethylamine (300 mg, 3 mmol) in 5 mL of DCM were mixed with a white suspension of 2,6-di(pyrazol-1-yl)pyrid-4-yl thiol (350 mg, 1.44 mmol) in 12 mL of DCM. The mixture was stirred at 50°C when acetyl chloride (340 mg, 4.32 mmol) dissolved in 3 mL of DCM was added. The solution turned from yellowish to pale white immediately. After 2 minutes, 200 mg of triethylamine were added and the solution turned orange. 3 mL of water were added and the organic phase was dried with magnesium sulphate anhydrous. The solvent was removed under vacuum and the white product was purified through column flash chromatography (eluent: 15 : 1, hexane : EtOAc, R_f 0.68). Yielding crystalline transparent solid, 80 mg, 19% yield.

¹H NMR ((400MHz, CDCl₃), 298 K, ppm) δ: 2.51 (s, 3H, 9), 6.51 (m, 2H, 4'), 7.77 (s, 2H, 3'), 7.96 (s, 2H, 3), 8.56 (d, J = 2.7 Hz, 2H, 5');

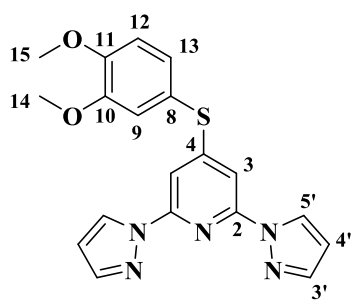
¹³C NMR ((100MHz, CDCl₃), 298 K, ppm) δ: 30.8 (9) 108.3 (4'), 113.3 (3), 127.2 (5'), 142.7 (3'), 144.2 (4), 150.2 (2), 190.5 (8)

ES⁺-MS *m/z* 244.1 [(bppSH + H)]⁺, 266.0 [(bppSH + Na)]⁺, 286.1 [(M + H)]⁺, 308.1 [(M + Na)]⁺, 340.0 [bppsSAC + Na]⁺, 507.1 [(bppsSbpp + Na)]⁺, 593.1 [(2M + Na)]⁺.

Mp: 162.1 °C.

Anal. Calcd for C₁₃H₁₁N₅OS: C, 54.72; H, 3.89; N, 24.55. **Found:** C, 54.6; H, 3.8; N, 24.3

8.6.2 2,6-Di(pyrazol-1-yl)-4-(3,4-dimethoxyphenylsulfanyl)pyridine (42)



Sodium hydride 60% (48 mg, 1.2 mmol) was suspended in THF (20 mL) and 3,4-dimethoxythiophenol (200 mg, 1.17 mmol) was added. After 2 minutes 2,4,6-trifluoropyridine (155 mg, 1.17 mmol) was added. After 3 hours, pyrazole (170 mg, 2.5 mmol) were added with NaH 60% (100 mg, 2.5 mmol). After 2 h stirring at room temperature the evolution of the reaction stopped. The crude was purified by column flash

chromatography (eluent: 4 : 1, hexane : EtOAc, R_f 0.37) yielding a beige solid 134 mg, 30.2% yield.

¹H NMR ((400MHz, CDCl₃), 298 K, ppm) δ: 3.9 (s, 3H, 15), 3.97 (s, 3H, 14), 6.46 (dd, J = 2.6, 1.7 Hz, 2H, 4'), 6.98 (d, J = 8.4 Hz, 1H, 12), 7.11 (d, J = 2 Hz, 1H, 9), 7.24 (dd, J = 8.3, 2.1 Hz, 1H, 13), 7.54 (s, 2H, 3) 7.7 (m, 2H, 3'), 8.51 (m, 2H, 5');

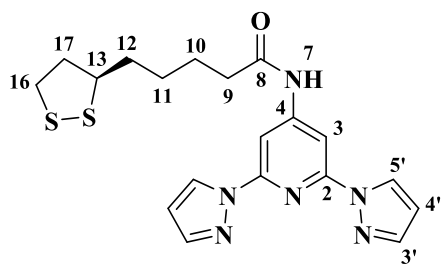
¹³C NMR ((100MHz, CDCl₃), 298 K, ppm) δ: 56.0 (14), 56.1 (15), 105.6 (3), 107.9 (4'), 112.1 (12), 117.9 (9), 119.1 (13), 127.2 (5'), 129.0 (8), 142.3 (3'), 149.8 (4), 150.0 (2), 150.8 (10), 157.4 (11);

ES⁺-MS *m/z* 380.1 [(M + H)]⁺, 402.1 [(M + Na)]⁺, 781.2 [(2M + Na)]⁺.

Mp: 97.2°C.

Anal. Calcd for C₁₉H₁₇N₅O₂S: C, 60.14; H, 4.52; N, 18.46. **Found:** C, 60.0; H, 4.4; N, 18.3

8.6.3 (R)-Lipoamide N-[2,6-di(pyrazol-1-yl)pyrid-4-yl] (43)



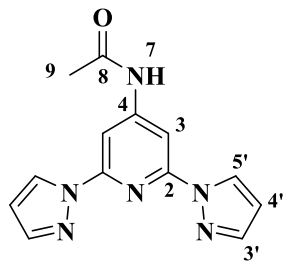
Thionyl chloride (2 mL, 27 mmol) was added to (R)-S-(dithiolan-3-yl)pentanoic acid (844 mg, 4 mmol) under nitrogen atmosphere. The orange mixture was stirred for half hour at 0 °C before the excess of thionyl chloride was removed under vacuum and 8 mL of DCM were added. In a separated flask, 0.4 mL of triethylamine were added to a suspension of 2,6-di(pyrazol-1-yl)-4-amino-pyridine (310 mg, 1.4 mmol) in 30 mL of DCM. The solutions were mixed and stirred 2h at room temperature. The solvent was removed under vacuum yielding a brown sticky solid which did not dissolved completely again.

¹H NMR ((400MHz, d⁶-DMSO), 298 K, ppm) δ: 1.4-1.9 (m, 6H, 10, 11, 12), 2.2 (t, J = 7.2 Hz, 2H, 9), 2.42 (m, 2H, 17), 3.10 (m, 2H, 16), 3.62 (m, 1H, 13), 6.60 (d, J = 1.7 Hz, 2H, 4'), 7.83 (s, 2H, 3'), 8.13 (s, 2H, 3), 8.88 (d, J = 2.6 Hz, 2H, 5'), 10.71 (s, 1H, 7);

¹³C NMR ((100MHz, d⁶-DMSO), 298 K, ppm) δ: 24.3, 28.2, 33.5, 34.1, 38.1, 40 (overlapped), 56.1, 98.0 (3), 108.2 (4'), 127.9 (5'), 142.4 (3'), 150.4 (4), 150.6 (2), 172.6 (8)

ES⁺-MS *m/z* 478.2 [(M + H₂ + Na + K)]⁺.

8.6.4 N-[2,6-Di(pyrazol-1-yl)pyrid-4-yl]acetamide (44)



Triethylamine (0.3 mL 2.19 mmol) was added to a suspension of 200 mg, 0.89 mmol of 2,6-di(pyrazol-1-yl)-4-amino-pyridine in 35 mL of DCM. Acetyl chloride diluted in DCM (210 mg, 2.66 mmol in 5 mL) was added at once. The mixture was stirred for 1 hour at room temperature when 0.5 mL of triethylamine were added and the solution turned red/orange while vapour was vigorously released. The solvent was removed under vacuum and water was added (25 mL) precipitating a pale brown solid. The compound was extracted with chloroform and dried with anhydrous MgSO₄. The crude was purified by column flash chromatography (eluent: 1:1, hexane : EtOAc, R_f 0.31) yielding white solid 159 mg, 67.1% yield.

¹H NMR ((300MHz, CDCl₃), 298 K, ppm) δ: 2.25 (s, 3H, 9), 6.48 (s, 2H, 4'), 7.74 (s, 2H, 3'), 7.98 (s, 1H, 7) 8.04 (s, 2H, 3), 8.53 (d, J = 2.3 Hz, 2H, 5');

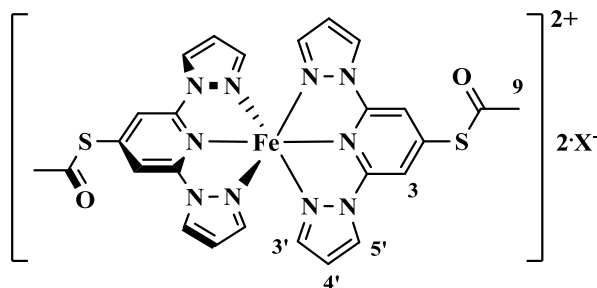
¹³C NMR ((75MHz, CDCl₃), 298 K, ppm) δ: 24.8 (9) 99.1 (3), 107.9 (4'), 127.2 (5'), 142.3 (3'), 149.4 (4), 151.1 (2), 168.8 (8)

ES⁺-MS *m/z* 269.1 [(M + H)]⁺, 291.1 [(M + Na)]⁺, 288.1 [(2M + K + H)]²⁺, 559.2 [(2M + Na)]⁺.

Mp: 211.4 °C.

Anal. Calcd for $C_{13}H_{12}N_6O$: C, 58.20; H, 4.51; N, 31.33. Found: C, 58.1; H, 4.7; N, 30.9

8.6.5 Bis(2,6-di(pyrazol-1-yl)pyrid-4-yl thioacetate)iron(II) [40]X



Iron(II) tetrafluoroborate hydrate (6 mg, 0.02 mmol) was mixed with 2,6-di(pyrazol-1-yl)pyrid-4-yl thioacetate (**19**), (10 mg, 0.04 mmol) in nitromethane (4 mL). The solution turned yellow immediately and yellow single crystals were obtained by atmospheric diffusion of diethyl ether, 6.5 mg, 46% yield. The same procedure using iron(II) perchlorate hydrate and acetone as solvent, produced red crystals, 67% yield of **[40]C**.

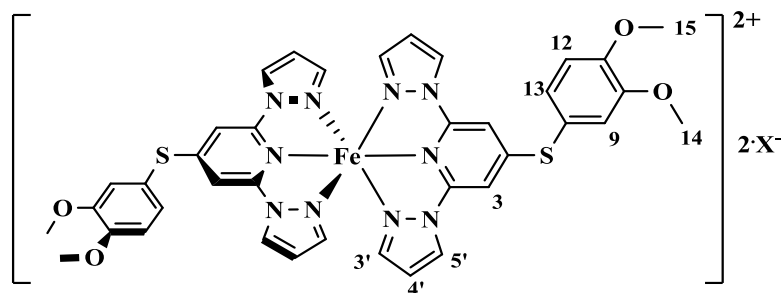
$^1\text{H NMR}$ (300MHz, CD_3NO_2) δ = 2.51 (s, 6H, 9), 34.07 (s, 2H, 5') 36.44 (s, 2H, 4'), 55.52 (s, 2H, 3), 61.33 (s, 2H, 3');

$\text{ES}^+\text{-MS } m/z$ 292.0 $[\text{Fe}(\text{L})(\text{bppSH})]^{2+}$, 313.1 $[\text{Fe}(\text{L})_2]^{2+}$, 360.0 $[\text{Fe}(\text{L})\text{F}]^+$, 386.0 $[\text{Fe}(\text{L})(\text{CO}_2\text{H})]^+$, 412.6 $[\text{Fe}(\text{L})(\text{bppSSbpp})]^{2+}$, 645.1 $[\text{Fe}(\text{L})_2\text{F}]^+$, 713.1 $[\text{Fe}(\text{L})_2(\text{BF}_4)]^+$.

- **[40]B**, Anal. Calcd for $C_{26}H_{22}N_{10}FeB_2F_8O_2S_2$: C, 39.03; H, 2.77; N, 17.51. Found: C, 39.1; H, 2.9; N, 17.6

- **[40]C**, Anal. Calcd for $C_{26}H_{22}N_{10}FeCl_2O_{10}S_2$: C, 37.84; H, 2.69; N, 16.97. Found: C, 37.7; H, 2.6; N, 16.9

8.6.6 Bis(2,6-di(pyrazol-1-yl)-4-(3,4-dimethoxyphenylsulfanyl)pyridine)iron(II) [42]X



Iron(II) perchlorate hydrate (10 mg, 0.027 mmol) was mixed with 2,6-di(pyrazol-1-yl)pyrid-4-yl thioacetate (**42**), (20 mg, 0.053 mmol) in acetonitrile (6 mL). The solution turned yellow immediately and yellow single crystals were obtained by atmospheric diffusion of diethyl

ether, 19 mg, 69% yield. The same procedure using iron(II) tetrafluoroborate hydrate, 77% yield of [40]B.

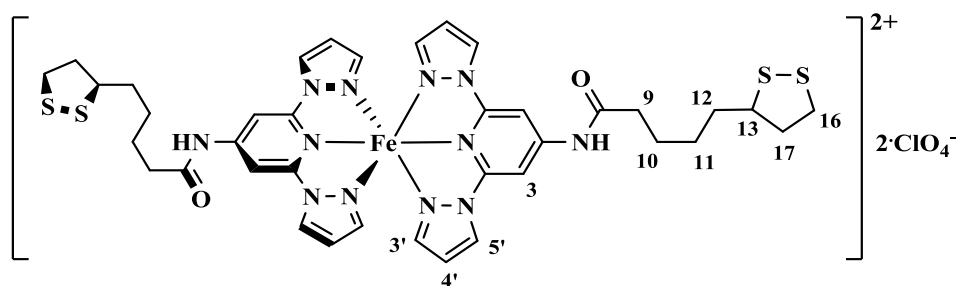
¹H NMR (300MHz, CD₃NO₂) δ = 3.65 (s, 3H, 14), 3.92 (s, 3H 15), 6.50 (s, 2H, 9 and 12), 7.05 (s, 1H, 13), 41.59 (s, 4H, 4' and 5'), 60.13 (s, 2H, 3), 71.11 (s, 2H, 3');

ES⁺-MS *m/z* 407.1 [Fe(L)₂]²⁺, 454.0 [Fe(L)F]⁺, 833.1 [Fe(L)₂F]⁺, 901.2 [Fe(L)₂(BF₄)]⁺.

- [21]B, Anal. Calcd for C₃₈H₃₄N₁₀FeB₂F₈O₄S₂: C, 43.37; H, 3.26; N, 13.31. Found: C, 42.9; H, 2.9; N, 12.8

- [21]C, Anal. Calcd for C₃₈H₃₄N₁₀FeCl₂O₁₂S₂: C, 45.03; H, 3.38; N, 13.82. Found: C, 44.87; H, 3.19; N, 13.62

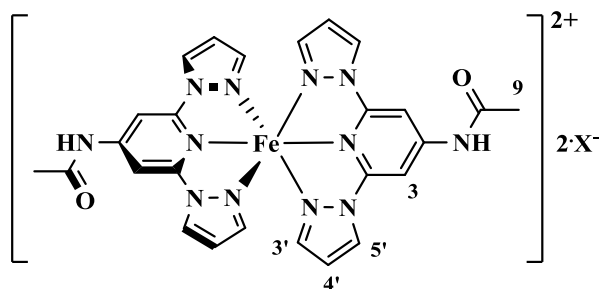
8.6.7 Bis((R)-lipoamide N-[2,6-di(pyrazol-1-yl)pyrid-4-yl])iron(II) [43]C



Ligand (43) (5 mg, 0.012 mmol) was suspended in a mixture of MeCN, MeOH, DCM, heated and sonicated for 30 minutes. A solution of iron(II) perchlorate hydrate (2 mg, 0.006 mmol) in the MeOH (1 mL) was added to the previous suspension. The liquid turned yellow and the reaction was filtered. The filtrate was analysed by ESMS but no product precipitated upon ether addition.

ES⁺-MS *m/z* 442.1 [Fe(L)₂]²⁺, 477.1 [NaK(L)(-H)]⁺, 569.0 [Fe(L)(ClO₄)]⁺, 983.1 [Fe(L)₂(ClO₄)]⁺.

8.6.8 Bis(N-[2,6-di(pyrazol-1-yl)pyrid-4-yl]acetamide)iron(II) [44]X (Y)



A solution of (44) (25 mg, 0.093 mmol) in several solvents (Y) (6 mL) was added to a solution of iron(II) tetrafluoroborate hexahydrate (16 mg, 0.047 mmol) in the same solvent (1-3 mL).

Chapter 8

Diethyl ether was diffused yielding single crystals of the complex. Yields were between 70-90%.

$^1\text{H NMR}$ (300MHz, $(\text{CD}_3)_2\text{CO}$) δ = 1.18 (s, 6H, 9), 44.96 (s, 2H, 5'), 46.44 (s, 2H, 4'), 64.27 (s, 2H, 3), 74.77 (s, 2H, 3');

ES^+ -MS m/z 296.1 $[\text{Fe}(\text{L})_2]^{2+}$, 691.1 $[[\text{Fe}(\text{L})_2(\text{ClO}_4)]^+$.

- [44]C (acetone), Anal. Calcd for $\text{C}_{26}\text{H}_{24}\text{N}_{12}\text{FeCl}_2\text{O}_{10}$ ($\text{C}_3\text{H}_6\text{O}$): C, 41.01; H, 3.56; N, 19.79. Found: C, 40.9; H, 3.4; N, 19.9

- [44]C (solvent free), Anal. Calcd for $\text{C}_{26}\text{H}_{24}\text{N}_{12}\text{FeCl}_2\text{O}_{10}$: C, 39.47; H, 3.06; N, 21.24. Found: C, 39.6; H, 3.2; N, 21.1

- [44]C (acetonitrile), Anal. Calcd for $\text{C}_{26}\text{H}_{24}\text{N}_{12}\text{FeCl}_2\text{O}_{10}$ ($\text{C}_2\text{H}_3\text{N}$): C, 40.40; H, 3.37; N, 21.88. Found: C, 40.3; H, 2.9; N, 21.4

- [44]C (propionitrile), Anal. Calcd for $\text{C}_{26}\text{H}_{24}\text{N}_{12}\text{FeCl}_2\text{O}_{10}$ ($\text{C}_3\text{H}_5\text{N}$): C, 41.15; H, 3.45; N, 21.51. Found: C, 41.4; H, 3.3; N, 21.7

- [44]C (nitromethane), Anal. Calcd for $\text{C}_{26}\text{H}_{24}\text{N}_{12}\text{FeCl}_2\text{O}_{10}$ (CH_3NO_2): C, 38.05; H, 3.19; N, 21.36. Found: C, 37.8; H, 3.2; N, 21.3

- [44]C+B, Anal. Calcd for $\text{C}_{26}\text{H}_{24}\text{N}_{12}\text{FeBF}_4\text{ClO}_6$: C, 40.11; H, 3.11; N, 21.59. Found: C, 40.1; H, 3.3; N, 21.7

- [44]TF, Anal. Calcd for $\text{C}_{28}\text{H}_{24}\text{N}_{12}\text{FeF}_6\text{O}_8\text{S}_2$: C, 37.76; H, 2.72; N, 18.87. Found: C, 37.6; H, 2.7; N, 1.7

- [44]B (acetone), Anal. Calcd for $\text{C}_{26}\text{H}_{24}\text{N}_{12}\text{FeB}_2\text{F}_8\text{O}_2$ ($\text{C}_3\text{H}_6\text{O}$): C, 42.27; H, 3.67; N, 20.40. Found: C, 42.2; H, 3.5; N, 20.3

- [44]B (solvent free), Anal. Calcd for $\text{C}_{26}\text{H}_{24}\text{N}_{12}\text{FeB}_2\text{F}_8\text{O}_2$: C, 40.77; H, 3.16; N, 21.94. Found: C, 40.6; H, 3.2; N, 21.8

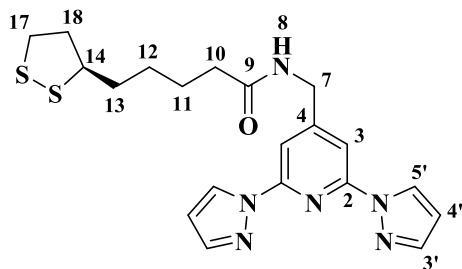
- [44]B (acetonitrile), Anal. Calcd for $\text{C}_{26}\text{H}_{24}\text{N}_{12}\text{FeB}_2\text{F}_8\text{O}_2$ ($\text{C}_2\text{H}_3\text{N}$): C, 41.67; H, 3.37; N, 22.56. Found: C, 41.7; H, 3.4; N, 22.7

- [44]B (propionitrile), Anal. Calcd for $\text{C}_{26}\text{H}_{24}\text{N}_{12}\text{FeB}_2\text{F}_8\text{O}_2$ ($\text{C}_3\text{H}_5\text{N}$): C, 42.42; H, 3.56; N, 22.18. Found: C, 42.3; H, 3.4; N, 22.1

- [44]B (nitromethane), Anal. Calcd for $\text{C}_{26}\text{H}_{24}\text{N}_{12}\text{FeB}_2\text{F}_8\text{O}_2$ (CH_3NO_2)₂: C, 37.87; H, 3.41; N, 22.08. Found: C, 37.5; H, 3.6; N, 22.1

8.7 Experimental details of ligands and metal complexes related to Chapter 7

8.7.1 (R)-Lipoamide N-[2,6-di(pyrazol-1-yl)pyrid-4-yl]methyl (46)



2,6-Di(pyrazol-1-yl)-4-methylamine-pyridine (**45**), (400 mg, 1.67 mmol), lipoic acid (344 mg, 1.67 mmol) and DMAP (71 mg, 0.47 mmol) were mixed in previously dried over anhydrous magnesium sulphate dichloromethane (50 mL) at 0°C. DCC (516 mg, 2.5 mmol) in dried dichloromethane (26 mL) was added drop by drop to the cooled suspension over half hour. After half hour stirring, the ice bath was removed and the mixture was left stirring overnight at room temperature. The suspension was filtered and the liquid phase was concentrated under vacuum yielding a pale yellow solid. The compound was isolated by eluting through silica gel in ethyl acetate, Rf: 0.73 as a pale yellow powder (443 mg, 1.04 mmol, 62% yield).

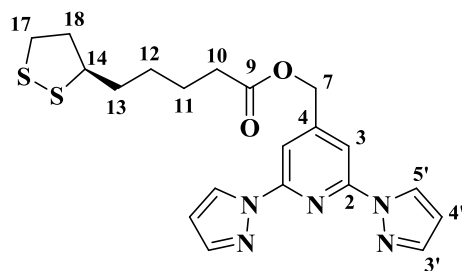
$^1\text{H NMR}$ ((400MHz, CDCl_3), 298 K, ppm) δ : 1.52 (m, 2H, 12), 1.74 (m, 4H, 11 and 13), 1.91 (dq $J = 13.2, 6.8$ Hz, 1H, 18A), 2.33 (td, $J = 7.4, 1.8$ Hz, 2H, 10), 2.45 (dq, $J = 12.6, 6.2$ Hz, 1H, 18B), 3.13 (m, 2H, 17), 3.59 (quin, $J = 6.8$ Hz, 1H, 14), 4.60 (d, $J = 5.9$ Hz, 2H, 7), 6.04 (d, $J = 5.6$ Hz, 1H, 8), 6.5 (m, 2H, 4'), 7.75 (s, 4H, 3' and 3), 8.54 (d, $J = 2.4$ Hz, 2H, 5').

$^{13}\text{C NMR}$ ((100MHz, CDCl_3), 298 K, ppm) δ : 25.3(11), 28.9(12), 34.6(13), 36.3(10), 38.4(17), 40.2(18), 42.6(7), 56.3(14), 107.6(3), 108.1(4'), 127.2(5'), 142.4(3'), 150.4(2), 153.9(4), 172.9(9).

$\text{ES}^+\text{-MS } m/z$ 225.2 [$\text{DCU} + \text{H}$] $^+$, 429.1 [($\text{M} + \text{H}$) $^+$], 449.4 [($\text{M} + \text{Na}$) $^+$].

Mp: 128.2 °C.

8.7.2 (R)-Lipoate [2,6-di(pyrazol-1-yl)pyrid-4-yl]methyl (50)



2,6-Di(pyrazol-1-yl)-4-methanol-pyridine (**49**), (232 mg, 0.96 mmol), lipoic acid (297 mg, 1.44 mmol) and DMAP (44 mg, 0.28 mmol) were mixed in previously dried over anhydrous magnesium sulphate dichloromethane (70 mL) at 0°C. DCC (437 mg, 2.12 mmol) in dried dichloromethane (15 mL) was added drop by drop to the cooled suspension over half hour. After half hour stirring, the ice bath was removed and the mixture was left stirring overnight at room temperature. The suspension was filtered and the liquid phase was concentrated under

vacuum yielding a pale yellow solid. The compound was isolated by eluting through silica gel in 1:1, ethyl acetate:hexane, Rf: 0.68 as a pale yellow powder (338 mg, 0.79 mmol, 82% yield).

¹H NMR ((300MHz, CDCl₃), 298 K, ppm) δ: 1.51 (m, 2H, 12), 1.71 (m, 4H, 11 and 13), 1.89 (m, 1H, 18A), 2.45 (m, 3H, 10 and 18B), 3.13 (m, 2H, 17), 3.57 (m, 1H, 14), 5.23 (s, 2H, 7), 6.49 (dd, J = 2.5, 1.7 Hz, 2H, 4'), 7.76 (d, J = 0.9 Hz, 2H, 3'), 7.81 (s, 2H, 3), 8.55 (m, 2H, 5')

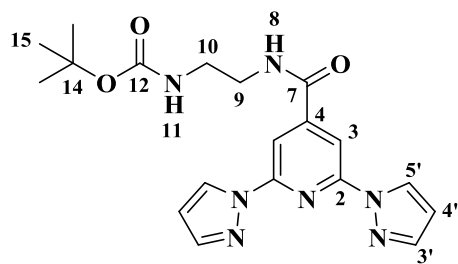
¹³C NMR ((75MHz, CDCl₃), 298 K, ppm) δ: 24.6(11), 28.7(12), 33.8(10), 34.5(13), 38.4(17), 40.1(18), 56.2(14), 64.1(7), 107.3(3), 108.1(4'), 127.1(5'), 142.4(3'), 150.3(2), 151.3(4), 172.8(9).

ES⁺-MS *m/z* 225.2 [DCU + H]⁺, 430.1 [(M + H)]⁺, 452.1 [(M + Na)]⁺, 881.2 [(2M + Na)]⁺.

Mp: 62.4 °C.

Anal. Calcd for C₂₀H₂₃N₅O₂S₂: C, 55.92; H, 5.40; N, 16.30. Found: C, 55.9; H, 5.6; N, 16.1

8.7.1 [(2,6-Di(pyrazol-1-yl)pyridine)-4-carbonylamino]-N-Boc-2-ethylamino (53)



DMAP (400 mg, 2.66 mmol), tert-butyl N-(2-aminoethyl)carbamate (2.43 g, 15 mmol) and 2,6-di(pyrazol-1-yl)pyridine-4-carboxylic acid (3 g, 11.8 mmol) were mixed in dry dichloromethane and the mixture was stirred for 5 minutes at 0 °C when DCC dissolved in DCM was added dropwise (3.85 g, 18.66

mmol). The final mixture was stirred at 0 °C for 30 minutes and then heated to room temperature and left overnight. The suspension was filtered and the filtrate was purified through silica column chromatography in (1:4, hexane:ethyl acetate to ethyl acetate, Rf 0.69-0.9). 2.3 g, 48.9% yield.

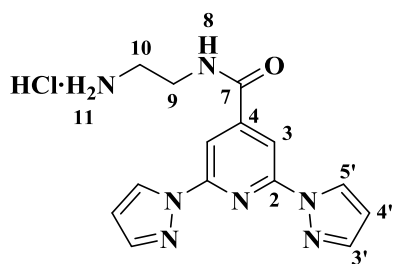
¹H NMR ((300MHz, CDCl₃), 298 K, ppm) δ: 1.43 (s, 9H, 15), 3.41 (m, 2H, 10), 3.61 (q, J = 5.2 Hz, 2H, 9), 5.39 (s, 1H, 11), 6.45 (s, 2H, 4'), 7.71 (s, 2H, 3'), 7.91 (s, 1H, 8), 8.12 (s, 2H, 3), 8.44 (s, 2H, 5');

¹³C NMR ((75MHz, d⁶-DMSO), 298 K, ppm) δ: 28.3 (15), 40.0 (10), 42.0 (9), 80.0 (14), 107.1 (3), 108.2 (4'), 127.0 (5'), 142.5 (3'), 147.4 (4), 150.5 (2), 157.4(12), 164.9 (7);

ES⁺-MS *m/z* 225.2 [DCU + H]⁺, 298.1 [(M - Boc)]⁺, 342.1 [(M - tert-butylate + H₂O)]⁺, 420.2 [M + Na]⁺, 817.4 [(2M + Na)]⁺.

Mp: 193.1 °C.

8.7.2 [(2,6-Di(pyrazol-1-yl)pyridine-4-carbonyl)amino]-2-(ethylammonium-chloride) (54)



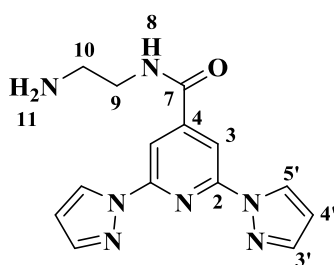
Acetyl chloride, 11 mL was added dropwise into a cooled methanol (120 mL, 0 °C) and the mixture was stirred for 50 min. The solution was added to [(2,6-di(pyrazol-1-yl)pyridine)-4-carbonyl)amino]-N-Boc-2-ethylamino (**53**), (1.3g, 3.3 mmol) and the mixture was stirred overnight at room temperature. A pure white precipitate was isolated by

filtration, 574 mg, 53% yield.

$^1\text{H NMR}$ ((400MHz, $\text{d}^6\text{-DMSO}$), 298 K, ppm) δ : 3.04 (m, 2H, 10), 3.5 (q, $J = 5.9$ Hz, 2H, 9), 6.67 (m, 2H, 4'), 7.92 (s, 2H, 3'), 8.18 (s, 3H, 11), 8.24 (s, 2H, 3), 8.99 (d, $J = 2.4$ Hz, 2H, 5'), 9.28 (t, $J = 5.3$ Hz, 1H, 8);

$^{13}\text{C NMR}$ ((100MHz, $\text{d}^6\text{-DMSO}$), 298 K, ppm) δ : 37.3 (10), 38.2 (9), 107.0 (3), 108.7 (4'), 128.4 (5'), 143.0 (3'), 147.6 (4), 150.1 (2), 164.1 (7);

8.7.3 [(2,6-Di(pyrazol-1-yl)pyridine-4-carbonyl)amino]-2-ethylamino (55)



(2,6-Di(pyrazol-1-yl)pyridine-4-carbonyl)amino]-2-(ethylammonium-chloride) (**54**), (468 mg, 1.4 mmol) was dissolved in 45 mL of water (acidic pH) and Na_2CO_3 was added until neutral pH (170 mg approx). The mixture was stirred overnight at room temperature. A white compound precipitated which was obtained pure by filtration. 246 mg, 59% yield.

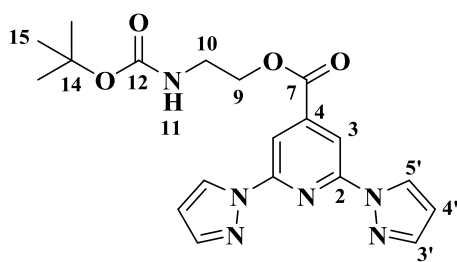
$^1\text{H NMR}$ ((300MHz, CDCl_3), 298 K, ppm) δ : 1.54 (s, 2H, 11), 2.98 (t, 5.6 Hz, 2H, 10), 3.54 (q, 5.6 Hz, 2H, 9), 6.50 (s, 2H, 4'), 7.22 (s, 1H, 8), 7.77 (s, 2H, 3'), 8.16 (s, 2H, 3), 8.53 (d, $J = 2.5$ Hz, 2H, 5');

$^{13}\text{C NMR}$ ((100MHz, CDCl_3), 298 K, ppm) δ : 41.0 (10), 42.6 (9), 107.2 (3), 108.3 (4'), 127.2 (5'), 142.7 (3'), 147.9 (4), 150.7 (2), 164.8 (7);

$\text{ES}^+\text{-MS } m/z$ 281.1 $[(\text{M} - \text{NH}_2)]^+$, 298.1 $[(\text{M} + \text{H})]^+$, 595.3 $[(2\text{M} + \text{H})]^+$.

Mp: 181.6 °C.

8.7.4 [(2,6-Di(pyrazol-1-yl)pyridine)-4-carbonyl]alkoxy]-N-Boc-2-ethylamino (56)



DMAP (270 mg, 1.78 mmol), N-Boc-ethanolamine (1.6 g, 10 mmol) and 2,6-di(pyrazol-1-yl)pyridine-4-carboxylic acid (2 g, 7.9 mmol) were mixed in dry dichloromethane and the mixture was stirred for 5 minutes at 0 °C when DCC dissolved in DCM was added dropwise (2.4 g, 11.6 mmol). The final mixture was stirred at 0 °C for 30 minutes and then heated to room temperature for 6 h, the mixture was refluxed at 50 °C for 3 h. The suspension was filtered and the filtrate was purified through silica column chromatography in 1:4 hexane/ethyl acetate, R_f 0.9. 2.04 g, 64.7% yield.

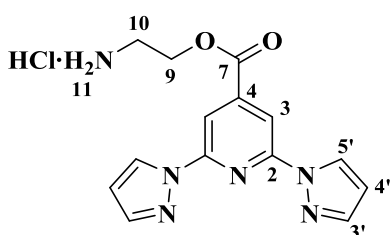
¹H NMR ((300MHz, CDCl₃), 298 K, ppm) δ: 1.45 (s, 9H, 15), 3.58 (q, J = 5.2 Hz, 2H, 10), 4.48 (q, J = 5.1 Hz, 2H, 9), 4.98 (s, 1H, 11), 6.54 (t, J = 1.9 Hz, 2H, 4'), 7.81 (s, 2H, 3'), 8.39 (s, 2H, 3), 8.58 (d, J = 2.6 Hz, 2H, 5');

¹³C NMR ((100MHz, CDCl₃), 298 K, ppm) δ: 28.4 (15), 39.6 (10), 65.6 (9), 79.8 (14), 108.5 (4'), 109.2 (3), 127.2 (5'), 142.9 (3'), 143.0 (4), 150.8 (2), 155.8 (12), 163.9 (7);

ES⁺-MS *m/z* 225.2 [DCU + H]⁺, 343.1 [(M – tert-butylate + H₂O)]⁺, 421.2 [(M + Na)]⁺, 819.3 [(2M + Na)]⁺.

Mp: 146.4 °C.

8.7.5 [(2,6-Di(pyrazol-1-yl)pyridine-4-carbonyl]alkoxy]-2-(ethylammonium-chloride) (57)



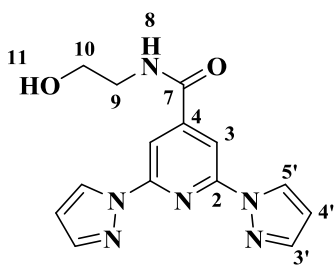
Acetyl chloride, 14 mL was added dropwise into a cooled methanol (140 mL, 0 °C) and the mixture was stirred for 50 min. The solution was added to [(2,6-di(pyrazol-1-yl)pyridine)-4-carbonyl] alkoxy]-N-Boc-2-ethylamino (56), (1.56g, 3.8 mmol) and the mixture was stirred overnight at room temperature. Pure white precipitate was isolated by filtration, 1.3 g, 98% yield.

¹H NMR ((400MHz, d⁶-DMSO), 298 K, ppm) δ: 3.29 (m, 2H, 10), 4.61 (m, 2H, 9), 5.55 (s, ,), 6.69 (dd, J = 2.6, 1.8 Hz, 2H, 4'), 7.94 (d, J = 1 Hz, 2H, 3'), 8.29 (s, 2H, 3), 8.40 (s, ,), 9.03 (d, J = 2.4 Hz, 2H, 5');

¹³C NMR ((100MHz, d⁶-DMSO), 298 K, ppm) δ: 37.7 (10), 62.7 (9), 108.3 (4'), 109.0 (3), 128.5 (5'), 142.9 (4), 143.3 (3'), 150.3 (2), 163.6 (7);

ES⁺-MS *m/z* 256.1 [(bppCOOH + H)]⁺, 299.1 [(M – Cl)]⁺

8.7.6 [(2,6-Di(pyrazol-1-yl)pyridine)-4-carbonyl]amino]-2-hydroxyethyl (59)



[(2,6-Di(pyrazol-1-yl)pyridine)-4-carbonyl]amino]-2-(ethylammonium-chloride) (57), (1.53 g, 4.5 mmol) was suspended in 100 mL of water (acidic pH) and 5 mL of DMSO, the mixture was refluxing at 110 °C until everything went into a yellowish solution (10-15 min) and then Na₂CO₃ was added until neutral pH (581 mg). The mixture was stirred for 1h at room temperature. A white compound precipitated which was obtained pure by filtration. 845 mg, 59.1% yield.

¹H NMR ((400MHz, CDCl₃), 298 K, ppm) δ: 3.69 (m, 2H, 9), 3.89 (t, J = 4.8 Hz, 2H, 10), 6.53 (s, 2H, 4'), 7.05 (s, 1H, 8), 7.79 (s, 2H, 3'), 8.19 (s, 2H, 3), 8.56 (d, J = 2.4 Hz, 2H, 5');

¹H NMR ((400MHz, d⁶-DMSO), 298 K, ppm) δ: 3.38 (q, J = 6 Hz, 2H, 9), 3.56 (q, J = 5.9 Hz, 2H, 10), 4.78 (t, J = 5.7 Hz, 1H, 11), 6.67 (dd, J = 2.6, 1.7 Hz, 2H, 4'), 7.91 (d, J = 1.1 Hz, 2H, 3'), 8.22 (s, 2H, 3), 8.99 (d, J = 2.6 Hz, 2H, 5'), 9.09 (t, J = 5.4 Hz, 1H, 8);

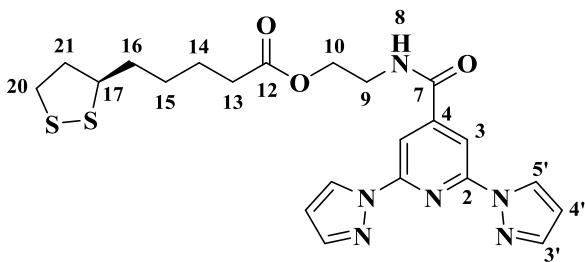
¹³C NMR ((100MHz, CDCl₃), 298 K, ppm) δ: 42.8 (9), 61.8 (10), 107.2 (3), 108.4 (4'), 127.3 (5'), 142.8 (3'), 147.5 (4), 150.8 (2), 165.3 (7);

¹³C NMR ((100MHz, d⁶-DMSO), 298 K, ppm) δ: 42.5 (9), 59.4 (10), 106.9 (3), 108.7 (4'), 128.3 (5'), 142.9 (3'), 147.9 (4), 150.1 (2), 163.5 (7);

ES⁺-MS *m/z* 299.1 [(M + H)]⁺, 321.1 [(M + Na)]⁺, 619.2 [(2M + Na)]⁺.

Mp: 196.3 °C.

8.7.7 (R)-Lipoate 2-[(2,6-di(pyrazol-1-yl)pyridine)-4-carbonyl]amino]ethyl (60)



[(2,6-Di(pyrazol-1-yl)pyridine)-4-carbonyl]amino]-2-hydroxyethyl (59), (664 mg, 2.23 mmol), lipoic acid (460 mg, 2.23 mmol) and DMAP (67 mg, 0.45 mmol) were mixed in dried over anhydrous magnesium sulphate dichloromethane (75 mL) at 0°C. DCC (529 mg, 2.56 mmol) in solution of

dried dichloromethane (22 mL) was added drop by drop to the cooled suspension over half hour. After half hour stirring, the ice bath was removed and the mixture was left stirring overnight at room temperature. The suspension was filtered and the liquid phase was concentrated under vacuum yielding a pale yellow solid. The compound was isolated by eluting through silica gel in 1:1, hexane/ethyl acetate, Rf: 0.45 as a pale beige powder (839 mg, 1.72 mmol, 77.4% yield).

$^1\text{H NMR}$ ((600MHz, CDCl_3), 298 K, ppm) δ : 1.46 (m, 2H, 15), 1.69 (m, 4H, 14 and 16), 1.86 (m, 1H, 21A), 2.40 (m, 3H, 13 and 21B), 3.07 (dt, $J = 11.0, 6.9$ Hz, 1H, 20B), 3.13 (ddd, $J = 11.3, 7.0, 5.4$ Hz, 1H, 20A), 3.53 (dq, $J = 8.5, 6.3$ Hz, 1H, 17), 3.77 (dd, $J = 10.7, 5.6$ Hz, 2H, 9), 4.32 (m, 2H, 10), 6.51 (dd, $J = 2.5, 1.7$ Hz, 2H, 4'), 6.94 (m, 1H, 8), 7.77 (d, $J = 1.2$ Hz, 2H, 3'), 8.12 (s, 2H, 3), 8.52 (d, $J = 2.4$ Hz, 2H, 5')

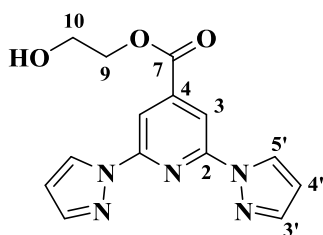
$^{13}\text{C NMR}$ ((150MHz, CDCl_3), 298 K, ppm) δ : 24.5(14), 28.7(15), 33.9(13), 34.5(16), 38.4(20), 39.7(9), 40.1(21), 56.2(17), 62.8(10), 107.0(3), 108.4(4'), 127.2(5'), 142.8(3'), 147.4(4), 150.7(2), 164.7(7), 173.6(12).

$\text{ES}^+\text{-MS } m/z$ 487.2 [(M + H)]⁺, 509.1 [(M + Na)]⁺, 973.3 [(2M + H)]⁺, 995.3 [(2M + Na)]⁺.

Mp: 125.1 °C.

Anal. Calcd for $\text{C}_{22}\text{H}_{26}\text{N}_6\text{O}_3\text{S}_2$: C, 54.30; H, 5.39; N, 17.27. **Found:** C, 54.5; H, 5.4; N, 17.3

8.7.8 [(2,6-Di(pyrazol-1-yl)pyridine)-4-carbonyl]alkoxy]-2-hydroxyethyl (61)



2,6-Di(pyrazol-1-yl)pyridine-4-carboxylic acid (1 g, 4 mmol) was dissolved in 150 mL of hot ethylene glycole (120 °C) and H_2SO_4 cat. (0.07 mL) was added. The mixture was stirred for 3 h. The mixture was cooled to room temperature when a white compound precipitated and was obtained pure by filtration. 769 mg, 64.3% yield.

$^1\text{H NMR}$ ((400MHz, CDCl_3), 298 K, ppm) δ : 4.03 (m, 2H, 10), 4.54 (m, 2H, 9), 6.53 (m, 2H, 4'), 7.81 (d, $J = 1.1$ Hz, 2H, 3'), 8.40 (s, 2H, 3), 8.56 (d, $J = 2.6$ Hz, 2H, 5');

$^1\text{H NMR}$ ((400MHz, $\text{d}^6\text{-DMSO}$), 298 K, ppm) δ : 3.76 (m, 2H, 10), 4.40 (m, 2H, 9), 6.67 (m, 2H, 4'), 7.91 (d, $J = 1.5$ Hz, 2H, 3'), 8.20 (s, 2H, 3), 8.99 (d, $J = 2.8$ Hz, 2H, 5');

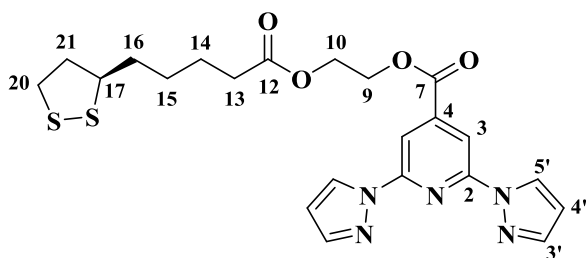
$^{13}\text{C NMR}$ ((100MHz, CDCl_3), 298 K, ppm) δ : 60.9 (10), 67.7 (9), 108.5 (4'), 109.2 (3), 127.3 (5'), 142.9 (3'), 143.0 (4), 150.8 (2), 164.2 (7);

$^{13}\text{C NMR}$ ((100MHz, $\text{d}^6\text{-DMSO}$), 298 K, ppm) δ : 58.9 (10), 67.9 (9), 108.0 (4'), 108.9 (3), 128.5 (5'), 143.2 (4), 143.3 (3'), 150.4 (2), 163.7 (7);

$\text{ES}^+\text{-MS } m/z$ 300.1 [(M + H)]⁺, 322.1 [(M + Na)]⁺.

Mp: 159.2 °C.

8.7.9 (R)-Lipoate 2-[(2,6-di(pyrazol-1-yl)pyridine)-4-carbonyl]alkoxy]ethyl (62)



[(2,6-Di(pyrazol-1-yl)pyridine)-4-carbonyl]alkoxy]-2-hydroxyethyl (61), (558 mg, 1.87 mmol), lipoic acid (385 mg, 1.87 mmol) and DMAP (56 mg, 0.37 mmol) were mixed in dried over anhydrous magnesium sulphate dichloromethane (50

mL) at 0°C. DCC (443 mg, 2.15 mmol) in solution of dried dichloromethane (26 mL) was added drop by drop to the cooled suspension over half hour. After half hour stirring, the ice bath was removed and the mixture was left stirring overnight at room temperature. The suspension was filtered and the liquid phase was concentrated under vacuum yielding a pale yellow solid. The compound was isolated by eluting through silica gel in 1:4, hexane/ethyl acetate, Rf: 0.88 as a pale yellow powder (558 mg, 1.25 mmol, 66% yield).

¹H NMR ((400MHz, CDCl₃), 298 K, ppm) δ: 1.47 (m, 2H, 15), 1.69 (m, 4H, 14 and 16), 1.87 (m, 1H, 21A), 2.41 (m, 3H, 13 and 21B), 3.12 (m, 2H, 20), 3.53 (m, 1H, 17), 4.46 (m, 2H, 9), 4.62 (m, 2H, 10), 6.54 (m, 2H, 4'), 7.82 (m, 2H, 3'), 8.40 (s, 2H, 5), 8.58 (m, 2H, 5')

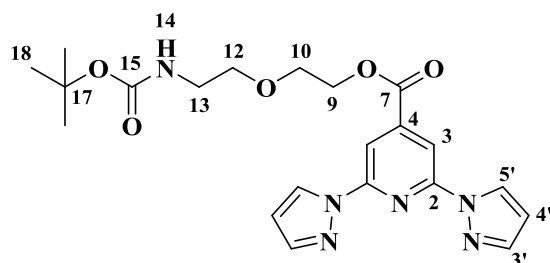
¹³C NMR ((100MHz, CDCl₃), 298 K, ppm) δ: 24.6(14), 28.7(15), 33.9(13), 34.5(16), 38.4(20), 40.2(21), 58.3(17), 61.8(10), 63.8(9), 108.5(4'), 109.2(3), 127.2(5'), 142.9(4 + 3'), 150.9(2), 163.8(7), 173.2(12).

ES⁺-MS *m/z* 448.1 [(M + H)]⁺, 510.1 [(M + Na)]⁺.

Mp: 104.8 °C.

Anal. Calcd for C₂₂H₂₅N₅O₄S₂: C, 54.19; H, 5.17; N, 14.36. Found: C, 54.3; H, 5.3; N, 14.2

8.7.10 [(2,6-Di(pyrazol-1-yl)pyridine)-4-carbonyl]alkoxy]-2-(hydroxyethoxy)-N-Boc-2-(ethylamine)



DMAP (238 mg, 1.6 mmol), N-Boc-2-(2-hydroxyethoxy)-ethylamine (1.85 g, 9 mmol) and 2,6-di(pyrazol-1-yl)pyridine-4-carboxylic acid (2 g, 7.84 mmol) were mixed in dry dichloromethane and the mixture was stirred for 5 minutes at 0 °C when DCC dissolved in

DCM was added dropwise (2.02 g, 9.8 mmol). The final mixture was stirred at 0 °C for 30 minutes and then heated to room temperature and left overnight. The suspension was filtered and the filtrate was purified through silica column chromatography in (1:1, hexane:ethyl acetate to ethyl acetate, Rf 0.77. 1.38 g, 39.8% yield.

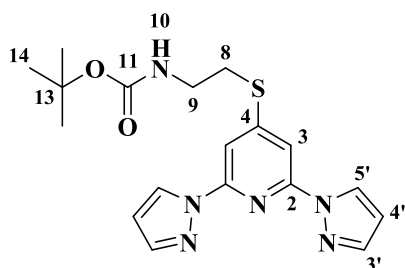
^1H NMR ((400MHz, CDCl_3), 298 K, ppm) δ : 1.41 (s, 9H, 18), 3.36 (m, 2H, 12), 3.61 (t, $J = 5.1$ Hz, 2H, 13), 3.83 (m, 2H, 10), 4.54 (m, 2H, 9), 4.99 (s, 1H, 14), 6.54 (m, 2H, 4'), 7.81 (d, $J = 1$ Hz, 2H, 3'), 8.41 (s, 2H, 3), 8.58 (d, $J = 2.4$ Hz, 2H, 5');

^{13}C NMR ((100MHz, CDCl_3), 298 K, ppm) δ : 28.4 (18), 40.4 (13), 65.0 (12), 68.6 (9), 70.4 (10), 79.3 (17), 108.4 (4'), 109.3 (3), 127.2 (5'), 142.9 (3'), 143.2 (4), 150.8 (2), 156.0 (15), 164.0 (7);

ES^+ -MS m/z 343.2 [(M - Boc)]⁺, 387.1 [(M - tBuO⁻)]⁺, 465.2 [M + Na]⁺, 907.4 [(2M + Na)]⁺.

Mp: 119.4 °C.

8.7.11 2,6-Di(pyrazol-1-yl)pyrid-4-yl-(N-Boc-2-ethylamino)sulphide (63)



Boc-cysteamine (2.2 g, 12.4 mmol) was added to a suspension on NaH 60% in THF (512 mg 11.3 mmol) and the mixture (50 mL) was stirred at room temperature for 10 min and trifluoropyridine was added (1.5 g, 11.3 mmol). The suspension turned thick when pyrazole (1.62 g, 23.7 mmol) and NaH 60% (930 mg, 23.3 mmol) were added and the mixture then became a clear solution which was stirred at

room temperature for 6 h, solvent was removed in vacuo and water was added (30 mL). The crude was extracted with chloroform and dried over MgSO_4 anhydrous. The compound was isolated through silica column chromatography in (4:1, hexane : ethyl acetate, Rf 0.25). 1.5 g, 33.9% yield.

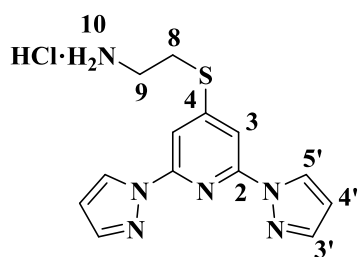
^1H NMR ((400MHz, CDCl_3), 298 K, ppm) δ : 1.43 (s, 9H, 14), 3.25 (t, $J = 6.2$ Hz, 2H, 9), 3.46 (q, $J = 5.6$ Hz, 2H, 8), 5.1 (s, 1H, 10), 6.45 (d, $J = 1.5$ Hz, 2H, 4'), 7.67 (s, 2H, 3), 7.72 (s, 2H, 3'), 8.49 (d, $J = 2.4$ Hz, 2H, 5');

^{13}C NMR ((100MHz, CDCl_3), 298 K, ppm) δ : 28.3 (14), 31.3 (8), 39.1 (9), 79.6 (13), 105.8 (3), 107.9 (4'), 127.2 (5'), 142.3 (3'), 149.8 (2), 154.2 (4), 155.6(11);

ES^+ -MS m/z 387.2 [(M + H)]⁺, 409.1 [M + Na]⁺, 795.3 [(2M + Na)]⁺.

Mp: 119.1 °C.

8.7.12 2,6-Di(pyrazol-1-yl)pyrid-4-yl-(2-ethylammonium-chloride)sulphide (64)



Acetyl chloride, 3.5 mL was added dropwise into a cooled methanol (40 mL, 0 °C) and the mixture was stirred for 30 min. The solution was added to 2,6-di(pyrazol-1-yl)pyrid-4-yl-(N-Boc-2-ethylamino)sulfide (**63**), (1.4g, 3.6 mmol) and the mixture was stirred overnight at room temperature. Pure white precipitate was isolated by filtration, 1.1 g, 94% yield.

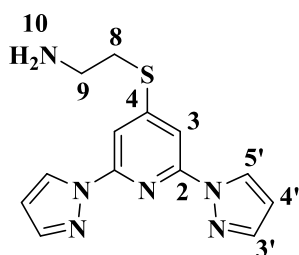
^1H NMR ((400MHz, $\text{d}^6\text{-DMSO}$), 298 K, ppm) δ : 3.13 (m, 2H, 10), 3.51 (t, $J = 7.2$ Hz, 2H, 9), 6.64 (dd, $J = 2.4, 1.8$ Hz, 2H, 4'), 7.67 (s, 2H, 3), 7.88 (d, $J = 0.9$ Hz, 3H, 3'), 8.35 (br. S, 3H, 10), 8.93 (d, $J = 2.4$ Hz, 2H, 5');

^{13}C NMR ((100MHz, $\text{d}^6\text{-DMSO}$), 298 K, ppm) δ : 27.5 (9), 37.6 (8), 105.2 (3), 108.7 (4'), 128.5 (5'), 143.0 (3'), 149.8 (2), 153.4 (4);

ES⁺-MS m/z 309.1 [M + Na]⁺.

Mp: 220.5 °C.

8.7.13 2,6-Di(pyrazol-1-yl)pyrid-4-yl-(2-ethylamino)sulphide (65)



2,6-Di(pyrazol-1-yl)pyrid-4-yl-(2-ethylammonium-chloride)sulfide (64), (1.2 g, 3.7 mmol) was dissolved in 65 mL of water (acidic pH) and Na_2CO_3 was added until neutral pH (200 mg approx). The mixture was stirred overnight at room temperature. A white compound was suspended in the aqueous solution which was extracted with 3 volumes of chloroform (x 100 mL) obtained pure.

970 mg, 91.6% yield.

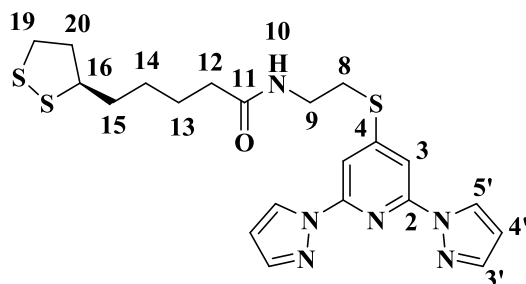
^1H NMR ((400MHz, CDCl_3), 298 K, ppm) δ : 1.48 (br. s, 2H, 10), 3.10 (m, 2H, 9), 3.24 (t, $J = 6.4$ Hz, 2H, 8), 6.49 (m, 2H, 4'), 7.74 (s, 2H, 3), 7.75 (d, $J = 1.5$ Hz, 2H, 3'), 8.54 (d, $J = 2.6$ Hz, 2H, 5');

^{13}C NMR ((100MHz, CDCl_3), 298 K, ppm) δ : 35.2 (8), 40.7 (9), 106.0 (3), 108.0 (4'), 127.2 (5'), 142.4 (3'), 149.9 (2), 154.9 (4);

ES⁺-MS m/z 270.1 [M - NH_2]⁺, 287.1 [(M + H)]⁺.

Mp: 85.1 °C.

8.7.14 (R)-Lipoamide N-([2,6-di(pyrazol-1-yl)pyrid-4-yl]-2-ethyl sulphide) (66)



2,6-Di(pyrazol-1-yl)pyrid-4-yl-(2-ethylamino)sulfide (65), (777 mg, 2.72 mmol), lipoic acid (616mg, 2.99 mmol) and DMAP (83 mg, 0.54 mmol) were mixed in dried over anhydrous magnesium sulphate dichloromethane (50 mL) at 0°C. DCC (673 mg, 3.25 mmol) in solution of dried dichloromethane (26 mL) was added

drop by drop to the cooled suspension over half hour. After half hour stirring, the ice bath was removed and the mixture was left stirring overnight at room temperature. The suspension was

filtered and the liquid phase was concentrated under vacuum yielding a pale yellow solid. The compound was isolated by eluting through silica gel in ethyl acetate, Rf: 0.51 as a pale yellow powder (994 mg, 2.09 mmol, 77% yield).

¹H NMR ((400MHz, CDCl₃), 298 K, ppm) δ: 1.46 (m, 2H, 14), 1.67 (m, 4H, 13 and 15), 1.9 (m, 1H, 20A), 2.2, (t, 7.5 Hz, 2H, 12), 2.45 (dq, J = 12.5, 6.3 Hz, 1H, 20B), 3.14 (m, 2H, 19), 3.32 (t, J = 6.4 Hz, 2H, 8), 3.55 (quin, J = 6.8 Hz, 1H, 16), 3.63 (q, J = 6.1 Hz, 2H, 9), 5.95 (br. s, 1H, 10), 6.5 (m, 2H, 4'), 7.73 (s, 2H, 3), 7.76 (s, 2H, 3'), 8.55 (d, J = 2.7 Hz, 2H, 5');

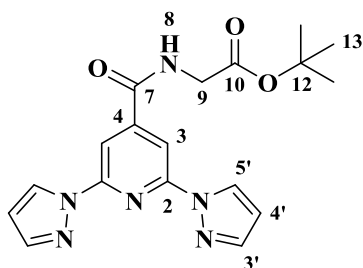
¹³C NMR ((100MHz, CDCl₃), 298 K, ppm) δ: 25.2 (13), 28.8 (14), 31.0 (8), 34.6 (15), 36.3(12), 38.0(9), 38.4(19), 40.2 (20), 56.3 (16), 105.9 (3), 108.1 (4'), 127.3 (5'), 142.5 (3'), 150.0 (2), 154.0 (4), 172.9 (11);

ES⁺-MS *m/z* 475.2 [(M + H)]⁺, 497.2 [M + Na]⁺, 971.3 [(2M + Na)]⁺.

Mp: 117.9. °C.

Anal. Calcd for C₂₁H₂₆N₆OS₃: C, 53.14; H, 5.52; N, 17.71. Found: C, 53.1; H, 5.6; N, 17.7

8.7.15 [(2,6-Di(pyrazol-1-yl)pyridine-4-carbonyl)amino]acetic acid tert-butyl ester (71)



DMAP (357 mg, 2.35 mmol), tert-butyl-2 aminoacetate (1.63 g, 12.4 mmol) and 2,6-di(pyrazol-1-yl)pyridine-4-carboxylic acid (3 g, 11.8 mmol) were mixed in dry dichloromethane and the mixture was stirred for 5 minutes at 0 °C when DCC dissolved in DCM was added dropwise (2.79 g, 13.5 mmol). The final mixture was stirred at 0 °C for 30 minutes and then heated to room temperature and left overnight. The

suspension was filtered and the filtrate was purified through silica column chromatography in (1:4, hexane:ethyl acetate to ethyl acetate, Rf 0.63-0.87. 3.47 g, 79.8% yield.

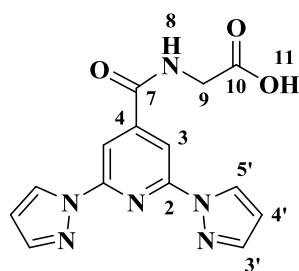
¹H NMR ((400MHz, CDCl₃), 298 K, ppm) δ: 1.52 (s, 9H, 13), 4.18 (d, J = 5 Hz, 2H, 9), 6.51 (m, 2H, 4'), 6.96 (br. s, 1H, 8), 7.78 (d, J = 0.9 Hz, 2H, 3'), 8.20 (s, 2H, 3), 8.55 (d, J = 2.4 Hz, 2H, 5');

¹³C NMR ((100MHz, CDCl₃), 298 K, ppm) δ: 28.1 (13), 42.6 (9), 82.8(12), 107.2 (4'), 108.4 (3), 127.2 (5'), 142.8 (3'), 147.0 (2), 150.8 (4), 164.4(7), 168.6(10);

ES⁺-MS *m/z* 313.1 [(M + H₂O - tBuO⁻)]⁺, 369.2 [(M + H)]⁺, 391.2 [(M + Na)]⁺, 759.3 [(2M + Na)]⁺.

Mp: 151.3 °C.

8.7.16 [(2,6-Di(pyrazol-1-yl)pyridine-4-carbonyl)amino]acetic acid (67)



[(2,6-Di(pyrazol-1-yl)pyridine-4-carbonyl)amino]acetic acid tert-butyl ester (**69**) (1 g, 0.027 mmol) was dissolved in 50 mL of DCM, then 10 mL of TFA were added carefully and the mixture was stirred at r.t. for 1 h. Solvent was removed *in vacuo*. Yielding a white solid (713 mg, 0.023 mmol, 84%).

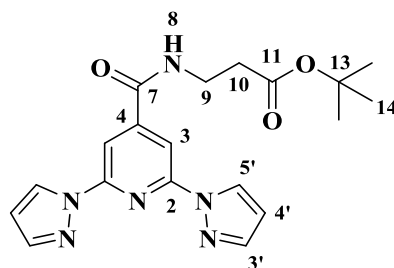
$^1\text{H NMR}$ ((400MHz, $\text{d}^6\text{-DMSO}$), 298 K, ppm) δ : 3.98 (m, 2H, 9), 6.67 (dd, $J = 2.6, 1.7$ Hz, 2H, 4'), 7.92 (d, $J = 1.1$ Hz, 2H, 3'), 8.23 (s, 2H, 3), 9.00 (d, $J = 2.6$ Hz, 2H, 5'), 9.51 (t, $J = 5.9$ Hz, 1H, 8);

$^{13}\text{C NMR}$ ((100MHz, $\text{d}^6\text{-DMSO}$), 298 K, ppm) δ : 41.3 (9), 106.8 (4'), 108.8 (3), 128.4 (5'), 143.0 (3'), 147.2 (2), 150.2 (4), 163.8(7), 170.8(10);

$\text{ES}^+\text{-MS } m/z$ 313.1 [(M + H) $^+$].

Mp: 272.6 °C.

8.7.17 [(2,6-Di(pyrazol-1-yl)pyridine-4-carbonyl)amino]propanoic acid tert-butyl ester (72)



DMAP (357 mg, 2.35 mmol), tert-butyl-2-aminopropanoate (**70**) (1.8 g, 12.4 mmol) and 2,6-di(pyrazol-1-yl)pyridine-4-carboxylic acid (3 g, 11.8 mmol) were mixed in dry dichloromethane and the mixture was stirred 5 minutes at 0 °C when DCC dissolved in DCM was added dropwise (2.79 g, 13.5 mmol). The final mixture was stirred at 0 °C for 30 minutes and then heated to room

temperature and left overnight. The suspension was filtered and the filtrate was purified through silica column chromatography in (1:4, hexane:ethyl acetate to ethyl acetate, R_f 0.69-0.9). 2.3 g, 43.6% yield.

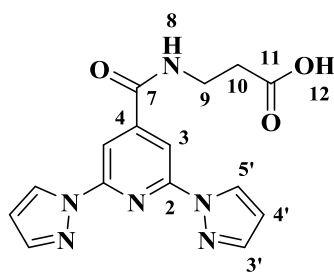
$^1\text{H NMR}$ ((400MHz, CDCl_3), 298 K, ppm) δ : 1.48 (s, 9H, 13), 2.6 (t, $J = 6.1$ Hz, 2H, 9), 3.73 (q, $J = 6$ Hz, 2H, 10), 6.52 (dd, $J = 2.4, 1.7$ Hz, 2H, 4'), 7.05 (br.s, 1H, 8), 7.78 (d, $J = 1$ Hz, 2H, 3'), 8.15 (s, 2H, 3), 8.55 (d, $J = 2.2$ Hz, 2H, 5');

$^{13}\text{C NMR}$ ((100MHz, CDCl_3), 298 K, ppm) δ : 28.1 (14), 34.9 (9), 35.8 (10), 81.5(13), 107.1 (3), 108.3 (4'), 127.2 (5'), 142.7 (3'), 147.8 (4), 150.8 (2), 164.5(7), 171.8(11);

$\text{ES}^+\text{-MS } m/z$ 327.1 [(M + $\text{H}_2\text{O} - \text{tBuO}^-)$] $^+$, 383.2 [(M + H) $^+$], 405.2 [(M + Na) $^+$], 787.3 [(2M + Na) $^+$].

Mp: 132.8 °C.

8.7.18 [(2,6-Di(pyrazol-1-yl)pyridine-4-carbonyl)amino]propanoic acid (68)



[(2,6-Di(pyrazol-1-yl)pyridine-4-carbonyl)amino]propanoic acid tert-butyl ester (**47**) (1 g, 0.026 mmol) was dissolved in 50 mL of DCM, then 10 mL of TFA were added carefully and the mixture was stirred at r.t. for 1 h. Solvent was removed *in vacuo* yielding a pale white solid (648 mg 0.02 mmol, 76%).

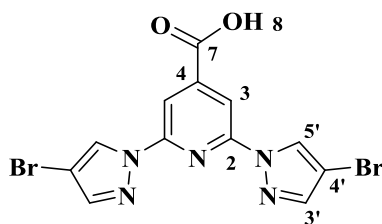
$^1\text{H NMR}$ ((400MHz, $\text{d}^6\text{-DMSO}$), 298 K, ppm) δ : 2.58 (t, $J = 7.1$ Hz, 2H, 9), 3.52 (m, 2H, 10), 6.52 (dd, $J = 2.6, 1.7$ Hz, 2H, 4'), 7.91 (d, $J = 0.9$ Hz, 2H, 3'), 8.20 (s, 2H, 3), 8.98 (m, 2H, 5') 9.19 (t, $J = 5.3$ Hz, 1H, 8);

$^{13}\text{C NMR}$ ((100MHz, $\text{d}^6\text{-DMSO}$), 298 K, ppm) δ : 33.3 (9), 35.8 (10), 106.8 (3), 108.7 (4'), 128.4 (5'), 142.9 (3'), 147.7 (4), 150.1 (2), 163.4(7), 172.7(11);

$\text{ES}^+\text{-MS } m/z$ 349.1 [(M + Na)]⁺.

Mp: 214.7 °C.

8.7.19 2,6-Di(4-bromo-pyrazol-1-yl)pyridine-4-carboxylic acid (69)



2,6-Di(chloro)pyridine-4-carboxylic acid (826 mg, 4.3 mmol) was added to suspension of 4-bromo-pyrazole (3 g, 20 mmol) and NaH 60% (1.3 g, 30 mmol) in 130 mL of diglyme. The mixture was refluxed at 140 °C for 8 days. The mixture was cooled to room temperature and water was added until brownish solution was observed with basic pH.

HCl (16%) was added carefully until the precipitated was observed (pH was still neutral). The mixture was filtered and the solid was washed thoroughly with water three times. The pale brown compound was dried under vacuum (Yield; 1.066 g 2.6 mmol, 60.5%).

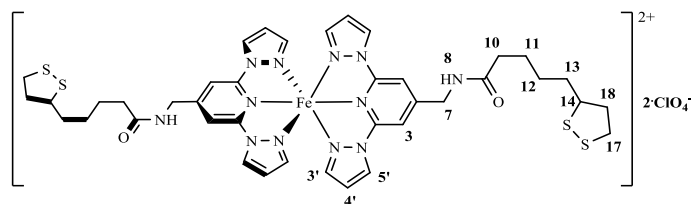
$^1\text{H NMR}$ ((400MHz, $\text{d}^6\text{-DMSO}$), 298 K, ppm) δ : 8.02 (s, 2H, 3'), 8.14 (s, 2H, 3), 9.37 (s, 2H, 5');

$^{13}\text{C NMR}$ ((100MHz, $\text{d}^6\text{-DMSO}$), 298 K, ppm) δ : 96.3 (3), 108.4 (4'), 128.8 (5'), 143.0 (3'), 149.2 (2), 165.0(4), 185.9(7);

$\text{ES}^+\text{-MS } m/z$ 413.9 [(M + H)]⁺, 435.9 [(M + Na)]⁺ (many unassigned strong peaks)

Mp: 247.7 °C (decomposition).

8.7.20 Bis-[(R)-lipoamide N-[2,6-Di(pyrazol-1-yl)pyrid-4-yl]methyl]iron(II) perchlorate [46]C



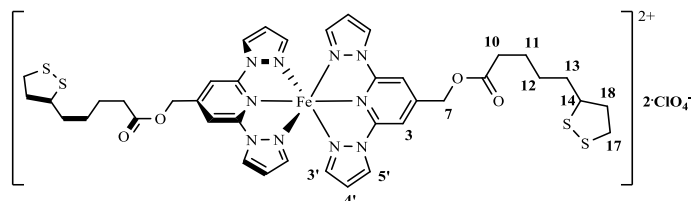
Solutions of iron(II) perchlorate hydrate and (R)-Lipoamide N-[2,6-Di(pyrazol-1-yl)pyrid-4-yl]methyl (**46**) in acetonitrile were mixed. The compound was precipitated as yellow powder upon diethyl ether addition.

$^1\text{H NMR}$ ((300MHz, CD_3CN), 298 K, ppm) δ : 1.27 (m, 2H, 12), 1.45 (m, 4H, 13), 1.58 (m, 2H, 11), 1.79 (m, 1H, 18A), 2.12 (m, 3H, 10 and 18B), 3.08 (m, 2H, 17), 3.47 (s, 1H, 14), 6.69 (s, 1H, 8) 9.16 (s, 2H, 7), 40.68 (s, 2H, 5'), 41.36 (s, 2H, 4'), 61.70 (s, 2H, 3), 70.13 (s, 2H, 3').

$\text{ES}^+\text{-MS } m/z$ 456.1 $[\text{Fe}(\text{L})_2]^{2+}$, 583.0 $[\text{Fe}(\text{L})(\text{ClO}_4)]^+$, 1011.2 $[\text{Fe}(\text{L})_2(\text{ClO}_4)]^+$.

Anal. Calcd for $\text{C}_{40}\text{H}_{48}\text{N}_{12}\text{FeCl}_2\text{O}_{10}\text{S}_4$: C, 43.20; H, 4.35; N, 15.12. Found: C, 43.3; H, 3.9; N, 13.4

8.7.21 Bis-[(R)-lipoate [2,6-Di(pyrazol-1-yl)pyrid-4-yl]methyl]iron(II) perchlorate [50]C



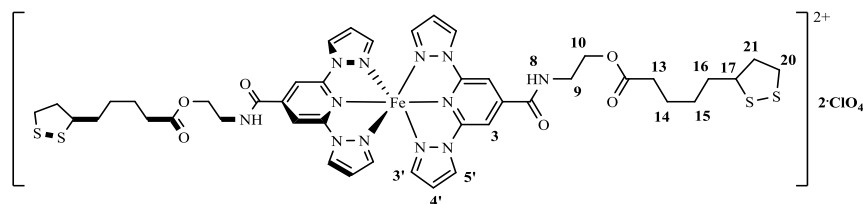
Solutions of iron(II) perchlorate hydrate and (R)-Lipoate N-[2,6-Di(pyrazol-1-yl)pyrid-4-yl]methyl (**50**) in acetonitrile were mixed. The compound was precipitated as a yellow powder upon diethyl ether addition.

$^1\text{H NMR}$ ((300MHz, CD_3CN), 298 K, ppm) δ : 1.36 (m, 2H, 12), 1.57 (m, 4H, 11 and 13), 1.83 (m, 1H, 18A), 2.41 (m, 3H, 10 and 18B), 3.07 (m, 2H, 17), 3.51 (m, 1H, 14), 8.81 (s, 2H, 7), 38.67 (s, 2H, 5'), 39.99 (s, 2H, 4'), 60.09 (s, 2H, 3), 67.57 (s, 2H, 3').

$\text{ES}^+\text{-MS } m/z$ 457.1 $[\text{Fe}(\text{L})_2]^{2+}$, 584.0 $[\text{Fe}(\text{L})(\text{ClO}_4)]^+$, 1013.1 $[\text{Fe}(\text{L})_2(\text{ClO}_4)]^+$.

Anal. Calcd for $\text{C}_{40}\text{H}_{46}\text{N}_{10}\text{FeCl}_2\text{O}_{12}\text{S}_4$: C, 43.13; H, 4.16; N, 12.58. Found: C, 43.0; H, 4.0; N, 12.5

8.7.22 Bis-[(R)-lipoate 2-[(2,6-di(pyrazol-1-yl)pyridine)-4-carbonyl] amino] ethyl]iron(II) perchlorate [60]C



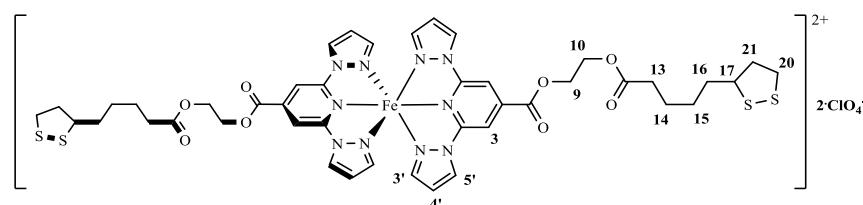
Solutions of iron(II) perchlorate hydrate and (R)-Lipoate 2-[(2,6-di(pyrazol-1-yl)pyridine)-4-carbonyl] amino] ethyl (**60**) in acetonitrile were mixed. The compound was precipitated as an orange powder upon diethyl ether addition.

$^1\text{H NMR}$ ((300MHz, CD_3CO), 298 K, ppm) δ : 1.45 (m, 2H, 15), 1.63 (m, 4H, 14 and 16), 1.84 (m, 1H, 21A), 2.38 (s, 3H, 13 and 21B), 3.06 (m, 2H, 20), 3.55 (s, 1H, 17), 3.80 (s, 2H, 9), 4.35 (s, 2H, 10), 8.48 (s, 1H, 8), 27.65 (s, 2H, 5'), 30.75 (s, 2H, 4'), 45.05 (s, 2H, 3), 48.32 (s, 2H, 3').

$\text{ES}^+\text{-MS } m/z$ 420.1 $[\text{Fe}(\text{L})(\text{L-LA})]^{2+}$, 487.2 $[\text{H}(\text{L})]^+$, 514.1 $[\text{Fe}(\text{L})_2]^{2+}$, 641.0 $[\text{Fe}(\text{L})_2(\text{ClO}_4)]^+$, 757.2 $[\text{Fe}(\text{L})_3]^{2+}$, 1000.3 $[\text{Fe}(\text{L})_4]^{2+}$, 1127.2 $[\text{Fe}(\text{L})_2(\text{ClO}_4)]^+$.

Anal. Calcd for $\text{C}_{44}\text{H}_{52}\text{N}_{12}\text{FeCl}_2\text{O}_{14}\text{S}_4$: C, 43.04; H, 4.27; N, 13.69. Found: C, 42.9; H, 4.2; N, 13.5

8.7.23 Bis-[(R)-lipoate 2-[(2,6-di(pyrazol-1-yl)pyridine)-4-carbonyl]alkoxy] ethyl]iron(II) perchlorate [62]C



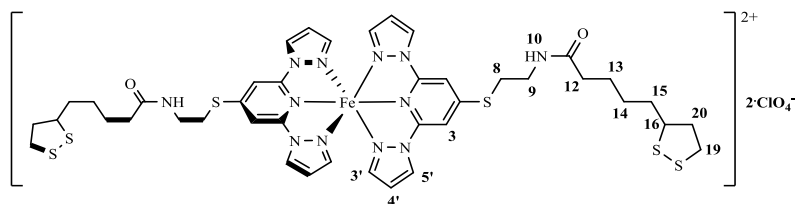
Solutions of iron(II) perchlorate hydrate and (R)-Lipoate 2-[(2,6-di(pyrazol-1-yl)pyridine)-4-carbonyl]alkoxy]ethyl (**62**) in acetonitrile were mixed. The compound was precipitated as a red powder upon diethyl ether addition. Slow diffusion of diethyl ether into the acetonitrile solution of [**62**]C yielded large red single crystals which were not suitable for XRD experiment.

$^1\text{H NMR}$ ((300MHz, CD_3CN), 298 K, ppm) δ : 1.44 (m, 2H, 15), 1.56 (m, 4H, 14 and 16), 1.78 (m, 1H, 21A), 3.03 (s, 3H, 13 and 21B), 3.50 (m, 2H, 20), 3.66 (s, 1H, 17), 4.65 (s, 2H, 9), 4.78 (s, 2H, 10), 22.92 (s, 2H, 5'), 26.38 (s, 2H, 4'), 39.1-41.6 (br. s, 4H, 3 and 3').

$\text{ES}^+\text{-MS } m/z$ 515.1 $[\text{Fe}(\text{L})_2]^{2+}$, 758.7 $[\text{Fe}(\text{L})_3]^{2+}$.

Anal. Calcd for $\text{C}_{44}\text{H}_{50}\text{N}_{10}\text{FeCl}_2\text{O}_{16}\text{S}_4$: C, 42.97; H, 4.10; N, 11.39. Found: C, 43.1; H, 3.9; N, 11.4

8.7.24 Bis-[(R)-lipoamide N-([2,6-di(pyrazol-1-yl)pyrid-4-yl]-2-ethyl sulfide)] iron(II) perchlorate [66]C



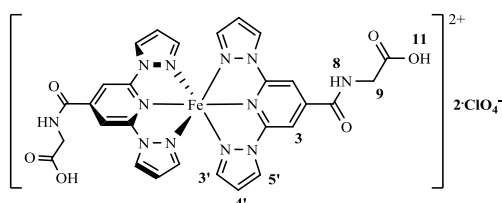
Solutions of iron(II) perchlorate hydrate and (R)-Lipoamide N-([2,6-di(pyrazol-1-yl)pyrid-4-yl]-2-ethyl sulfide)] ethyl (**66**) in acetonitrile were mixed. The compound was precipitated as a yellow powder upon diethyl ether addition.

$^1\text{H NMR}$ ((300MHz, $(\text{CD}_3)_2\text{CO}$), 298 K, ppm) δ : 1.29 (s, 2H, 14), 1.54 (s, 2H, 15), 1.80 (s, 4H, 13 and 20A), 2.29 (s, 1H, 12), 2.56 (m, 1H, 20B), 2.84 (s, 2H, 19), 3.24 (m, 2H, 8), 3.70 (s, 1, 16), 5.05 (s, 2H, 9) 7.84 (s, 1H, 10), 44.20 (s, 2H, 5'), 45.43 (s, 2H, 4'), 61.62 (s, 2H, 3), 73.44 (s, 2H, 3').

$\text{ES}^+\text{-MS } m/z$ 502.1 $[\text{Fe}(\text{L})_2]^{2+}$, 1103.1 $[\text{Fe}(\text{L})_2(\text{ClO}_4)]^+$.

Anal. Calcd for $\text{C}_{42}\text{H}_{52}\text{N}_{12}\text{FeCl}_2\text{O}_{10}\text{S}_6$: C, 41.90; H, 4.35; N, 13. 96. Found: C, 41.8; H, 4.2; N, 13.7

8.7.25 Bis-[[2,6-di(pyrazol-1-yl)pyridine-4-carbonyl]amino]acetic acid]iron(II) perchlorate [67]C



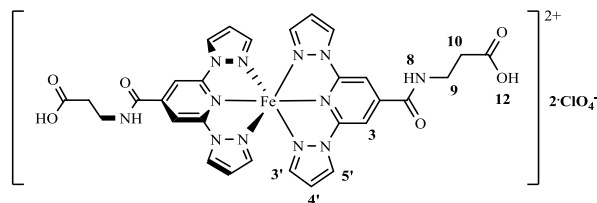
Solutions of iron(II) perchlorate hydrate and [(2,6-di(pyrazol-1-yl)pyridine-4-carbonyl)amino]acetic acid (**67**) in acetonitrile were mixed. The compound was precipitated as a red powder upon diethyl ether addition. Slow diffusion of diethyl ether into acetonitrile solution of [67]C yielded red single crystals, 78 % yield.

$^1\text{H NMR}$ ((300MHz, CD_3CN), 298 K, ppm) δ : 4.29 (s, 2H, 9), 8.06 (s, 1H, 8), 9.87 (br. s, 1H, 11) 27.22 (s, 2H, 5'), 30.90 (s, 2H, 4'), 46.16 (s, 2H, 3), 49.74 (s, 2H, 3').

$\text{ES}^+\text{-MS } m/z$ 313.1 $[\text{H}(\text{L})]^+$, 335.1 $[\text{Na}(\text{L})]^+$, 340.1 $[\text{Fe}(\text{L})_2]^{2+}$, 647.2 $[\text{Na}(\text{L})_2]^+$, 679.1 $[\text{Fe}(\text{L})_2\text{-H}]^+$, 779.1 $[\text{Fe}(\text{L})_2(\text{ClO}_4)]^+$, 991.2 $[\text{Fe}(\text{L})_3\text{-H}]^+$.

Anal. Calcd for $\text{C}_{28}\text{H}_{24}\text{N}_{12}\text{FeCl}_2\text{O}_{14}$: C, 38.25; H, 2.75; N, 19.12. Found: C, 38.0; H, 2.7; N, 19.1

8.7.26 Bis-[[2,6-Di(pyrazol-1-yl)pyridine-4-carbonyl]amino]propanoic acid]iron(II) perchlorate [68]C



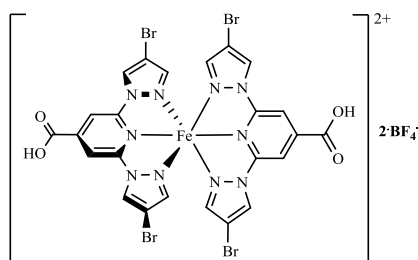
Solutions of iron(II) perchlorate hydrate and [(2,6-Di(pyrazol-1-yl)pyridine-4-carbonyl)amino]propanoic acid (**68**) in acetonitrile were mixed. The compound was precipitated as a red powder upon diethyl ether addition. Slow diffusion of diethyl ether into acetonitrile solution of [**68**]C yielded red single crystals, 53 % yield.

¹H NMR ((300MHz, CD₃CN), 298 K, ppm) δ: 2.75 (s, 2H, 10), 3.79 (s, 2H, 9), 7.72 (s, 1H, 8), 9.38 (br. s, 1H, 11) 29.08 (s, 2H, 5'), 32.36 (s, 2H, 4'), 48.55 (s, 2H, 3), 52.45 (s, 2H, 3').

ES⁺-MS *m/z* 327.1 [H(L)]⁺, 349.1 [Na(L)]⁺, 354.1 [Fe(L)₂]²⁺.

Anal. Calcd for C₃₀H₂₈N₁₂FeCl₂O₁₄: C, 39.71; H, 3.11; N, 18.52. Found: C, 39.6; H, 3.0; N, 18.3

8.7.27 Bis-[2,6-di(4-bromo-pyrazol-1-yl)pyridine-4-carboxylic acid]iron(II) tetrafluoroborate [71]B



Iron(II) tetrafluoroborate (10 mg, 0.03 mmol) was mixed with 2,6-di(4-bromo-pyrazol-1-yl)pyridine-4-carboxylic acid (**71**), (25 mg, 0.06 mmol) in nitromethane (5 mL). The suspension turned dark red upon sonication. The suspension was filtered and the complex was precipitated as red powder by addition of diethyl ether, 14 mg, 47% yield.

8.7.28 Deposition of complexes in surfaces

DIRECT. Under a dry atmosphere, the substrates having been activated when required, (the gold substrates were activated by immersion in a solution of H₂O₂ and H₂SO₄ (1:1) for 40

seconds) were placed in a weighing bottle containing a solution of the perchlorate salt $[\text{Fe}(\text{L})_2](\text{ClO}_4)_2$ (1 mM) which was previously filtered. After 24 h the substrates were vigorously washed with the same solvent and dried with a high pressure nitrogen flow.

SEQUENTIAL. Under dry atmosphere, the substrates (activated when required) were placed in a weighing bottle containing a solution (1 mM) of the tethered ligand L in varying solvents (EtOH or Acetone) which was previously filtered. After 24 h the substrates were vigorously washed with the same solvent and placed in a second weighing bottle containing a solution (1 mM) of $\text{Fe}(\text{ClO}_4)_2$ salt in acetonitrile which was previously filtered. After 24 h the substrates were vigorously washed with the same solvent and placed in a third weighing bottle containing a solution (1 mM) of the ligand L which was previously filtered. After 24 h the substrates were vigorously washed with the same solvent and dried with a high pressure nitrogen flow.

8.7.29 Preparation of gold nanoparticles

1.45 mL of oleylamine (80-90%) was added to a suspension of gold(III) chloride tri hydrate in 1 mL of toluene and the solution turned red. This mixture was quickly added into a refluxed mixture of 49 mL of toluene with 2.46 mL of oleylamine. After 2 h the reaction was stopped and 100 mL of methanol were added to precipitate the AuNPs. The particles were isolated by centrifugation, washed with methanol and redissolved in toluene.

8.8 Crystallographic tables

All Tables are appended on a supplementary annex, on a DVD-RW.

8.9 Bibliography

1. Bain, G. A.; Berry, J. F., Diamagnetic Corrections and Pascal's Constants. *Journal of Chemical Education* **2008**, 85 (4), 532.
2. NMR Manual for Evans Method. <http://imserc.facilities.northwestern.edu/nmr/nmr-manuals/>.
3. Hübsch, W.; Pflleiderer, W., Pteridines. Part XLI. Synthesis and properties of 6,7,8-trimethyl-4-thiolumazine. *Helvetica Chimica Acta* **1989**, 72 (4), 738-743.
4. Ortiz, M. I.; Soriano, M. L.; Carranza, M. P.; Jalón, F. A.; Steed, J. W.; Mereiter, K.; Rodríguez, A. M.; Quiñonero, D.; Deyà, P. M.; Manzano, B. R., New [2 × 2] Copper(I) Grids as Anion Receptors. Effect of Ligand Functionalization on the Ability to Host Counteranions by Hydrogen Bonds. *Inorganic Chemistry* **2010**, 49 (19), 8828-8847.